Beam Centrifuge Modelling of Caprock Integrity

By

Shenglong Jia

A thesis submitted in partial fulfillment of the requirements for the degree of

Doctor of Philosophy

in

Geotechnical Engineering

Department of Civil and Environmental Engineering
University of Alberta

Abstract

Although it has been widely used in geotechnical engineering to tackle complex geotechnical problems, geotechnical centrifuge modelling has not been used to solve geotechnical problems induced by SAGD process. This study, which adopts the physical modelling technique to investigate caprock deformation behaviour, intends to elucidate the impact of steam chamber expansion rate on caprock integrity.

To overcome the barrier of the shortage of the Clearwater shale samples, this study also develops a synthetic material to replicate the behaviour of Clearwater Formation shale for the physical modelling tests. Initial experimental results with consolidated Speswhite kaolin clay show that the material is too ductile to represent the Clearwater shales. Subsequently, a mixture of Speswhite kaolin clay, Sil325 (38-75µm), cement and water is assessed but again, unconfined compressive strength of the mixture material indicates that this mixture material is relatively soft when compared with the Clearwater shale. This leads to undertaking an extensive program to understand the components of synthetic Clearwater shale more efficiently, which involves collecting and analyzing previous studies pertaining to synthetic soils/rocks. An experimental program, which includes 160 separate formulations and considers the effect of water content, cement content, Atterberg limits and soil particle size distribution, is developed for the establishment of the database for the synthetic Clearwater shales. The results of this program provide the most suitable formulation (Speswhite kaolin clay: Sil325= 40:60, total soil-water content= 2.5 times the liquid limit, total soil-water to cement ratio= 3), which is used for the geotechnical centrifuge modelling tests. The mechanical properties of the synthetic Clearwater shale, including friction angle and cohesive strength, are quite close to those of the Clearwater shales.

Three centrifuge modelling tests are performed by using the synthetic Clearwater shales. An appropriate thickness of lead bars is used to simulate the overburden pressure applied to the prototype. A Mariotte bottle controls the water level in the plane strain box (PSB). The geomechanical caprock deflection mechanism, or GeoCDM, mimics the expansion of the steam chamber. A DIC camera records soil particle displacement at constant time intervals as the GeoCDM shears the sample. These images analyzed with GeoPIV_RG demonstrate the caprock failure evolution at different stages.

Experimental results of the geotechnical centrifuge modelling test reveal that vertical displacement of the soil particles decreases as the distance from the uplifting table increases. On any horizontal plane above the uplifting table, vertical displacement decreases as the horizontal distance between the soil particle and the centreline of the model increases. The model can be divided into four regions based on the horizontal displacement contours. Intuitively, the soil particles at the left side of the centreline of the model should move towards the –X direction, while those at the right side should move towards the +X direction. However, at the bottom of the model, soil particles at the left side of the centreline move towards the +X direction while those at the right side move towards the –X direction. The top surface of the model heaves as the uplifting table moves up. The geotechnical centrifuge modelling results not only show the surface heave but also the development of vertical fractures at the top surface of the model as the uplifting table moves up. Based on the analysis of the horizontal displacement contours, the vertical fractures at the top of the model are the combined result of uplift movement of the model and the low tensile strength of the model material. However, vertical fractures of the three tests only propagate towards the mid-height of the model for a few centimeters and then stops propagating as the uplifting table still moves up. Moreover, with the increase of model depth, the width of these vertical fractures decreases, indicating that high horizontal stress can effectively prohibit the development of vertical fractures.

A comparison is made between results from the geotechnical centrifuge modelling tests and those from the finite element model in "*Summary of investigations into the Joslyn May 18th 2006 Steam Release*". Both geotechnical centrifuge modelling test and numerical simulation test reveal that vertices of the pressurized zone are the highly strained area. The finite element model points out that the sheared zone has turned into wide fractures providing conduit for injected steam as the SAGD process continues. Similarly, geotechnical centrifuge modelling tests reveal that the inclined fractures originate from the vertices of the uplifting table and then propagate towards from the model surface.

This study uses the maximum total shear strains as the indication of the failure planes. The failure planes emerge from the uplifting table and propagate towards the model surface. This study finds that it is difficult to find the relationship between uplifting velocity and dip angles of these highly strain areas.

Preface

Caprock deformation behaviour is of major concern for thermal recovery projects. This thesis is based on the passion of the author for identifying caprock failure process using the world's mostly advanced technology, geotechnical centrifuge modelling, and the enthusiasm for developing synthetic soils to overcome the shortage of prototype samples for centrifuge modelling tests.

This thesis was completed by Shenglong Jia who was responsible for the work and results shown herein. Dr. Rick Chalaturnyk, Dr. Gonzalo Zambrano-Narvaez and Dr. Nathan Deisman have provided valuable guidance for the research. Gilbert Wong, Yazhao Wang, Keivan Khaleghi and Dmytro Pantov contributed extensive assistance in performing the laboratory tests.

One conference paper listed below has been published in GeoConvention 2016:

Jia, S., Chalaturnyk, R. J., & Zambrano-Narvaez, G. *Physical Modeling for SAGD Caprock Integrity with the Centrifuge Facility*

An additional conference paper is in preparation with Dr. Gonzalo Zambrano-Narvaez and Dr. Rick Chalaturnyk in 10th International Conference on Physical Modelling in Geotechnics.

Two journal papers based on the work in Chapter 4 is in preparation with Dr. Gonzalo Zambrano-Narvaez and Dr. Rick Chalaturnyk.

Acknowledgements

I would like to extend my sincere gratitude to my supervisor, Dr. Rick Chalaturnyk, for his guidance, encouragement and advice during my study. Without his persistent help and financial support, this dissertation would not have been possible.

I would like to thank Dr. Nathan Deisman for the technical discussions which helped me greatly to make the experimental plan, and for the guidance and the assistance with the laboratory tests and the numerical modelling. I would also like to thank Gilbert Wong, Keivan Khaleghi, Yujia Guo, Nathalia Ardila Angulo and Stephen Talman for all their assistance with the experimental work.

I am grateful for Dr. Zambrano Narvaez for the guidance in the geotechnical centrifuge modelling test. I would also like to thank Yazhao Wang, Jakob Brandl, Dmytro Pantov, Jingyu Wu and Anil Stephen for all their assistance with the geotechnical centrifuge modelling test.

I would like to thank Dr. Jun Xiong for his support and encouragement during the research and course work, and for his guidance on the numerical modelling and experimental design. I would also like to thank all my friends and colleagues at the Reservoir Geomechanics Research Group. In particular, I appreciate the help and encouragement from Lang Liu, Chuan Lu, Xiaoyan Teng, Bo Zhang, Boyang Du, Steve Zheng, Xinkui Wang, Juan Alejandro Arias Buitrago, Masoud Khademi and Susan Lizeth Sarmiento Navas. I would like to thank Hope Walls and Cecilia Guzman for the administrative support.

I would like to thank my family, my relatives and my friends for their patience, encouragement and support.

Table of Contents

Chapter 4 Development of an alternative material for Clearwater shale 137

List of Tables

List of Figures

Chapter 1 Introduction

1.1 Introduction

Oil sands, which have been found in many countries, consist of a mixture of sand, clay, crude bitumen and water. Over the past few decades, due to the increasing demand of energy and the rapid development of human society, significant investment in the development of unconventional oil sources has occurred. Unlike conventional oil, the crude bitumen contained in oil sands is slightly denser than water and very viscous such that it does not flow in its natural state. After being heated or diluted with lighter hydrocarbon, the crude bitumen becomes less viscous and can be extracted from the reservoir and then transported to oil refineries.

The oil sands deposits in Canada, most of which are in Alberta, are the third largest reserve in the world. Over the past few decades, the rapid development of the economy and the high oil price have made the recovery of Canada's oil sands commercially viable. However, only a small portion of the oil sands deposits in Alberta is shallow enough for surface mining, while the vast majority of these deposits lie sufficiently deep beneath the ground surface. Suitable in situ recovery methods are therefore required for efficient development. As such, numerous researchers have promoted the development of new recovery techniques, such as cyclic steam stimulation (CSS), steam flooding, steam assisted gravity drainage (SAGD), etc. (Butler, 1994, 1998, 2004). Some of these techniques, such as CSS and SAGD, are commercially used, while others are developed but not yet commercially adopted. Cyclic-steam stimulation (CSS) and steam-assisted gravity drainage (SAGD) are the two most predominant in-situ recovery methods in Alberta.

As shown in Figure 1-1(a), CSS involves three stages. The first stage is the injection phase during which the steam is injected into the oil sands reservoirs. The second stage is the soak phase during which the wells are shut-in at the surface to allow the steam in the reservoir to release the heat to the oil sand formations. In the third stage, the wells are put on production. The hot bitumen, condensed steam and water are pumped to the ground surface. If the bitumen-production rate is below a certain limit, the three stages are then repeated.

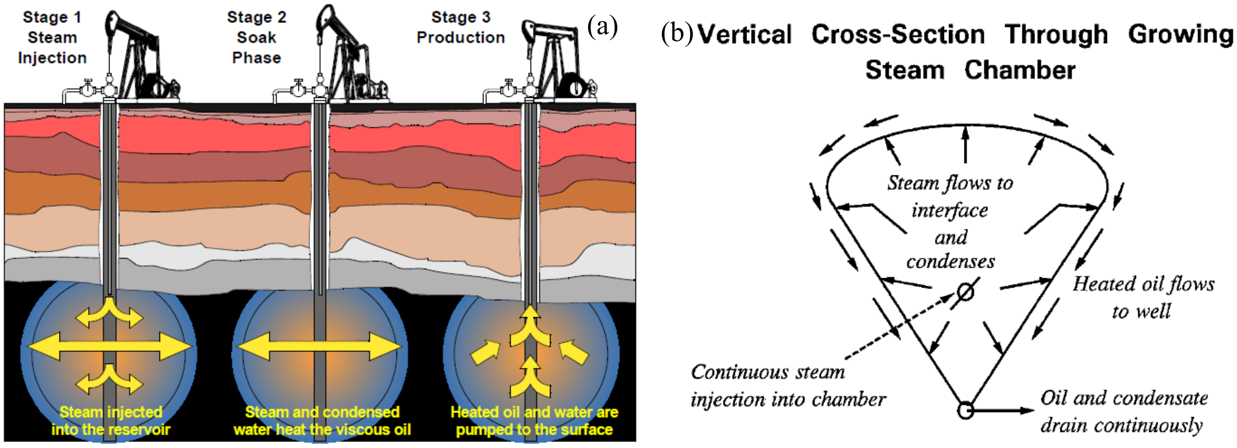

Figure 1-1 Schematic diagram of (a) Cyclic Steam Stimulation Process (G. R. Scott, 2002) and (b) SAGD configuration (Butler, 1998)

Figure 1-1(b) illustrates the basic procedure of the SAGD process. A pair of horizontal wells is drilled near the bottom of the oil sands pay zone. The upper well is referred to as the injector well, while the lower one is known as the producer well. The vertical distance between the two wells ranges from 4 to 6 m. In the initial stage or the steam circulation stage, high-pressure steam is circulated within these wells, resulting in the formation of heated annuli around each well. After the two annuli coalesce with each other, the next stage, or the SAGD stage, starts. High-pressure steam is continuously injected into the injector well while the producer well is used to collect the heated oil and condensed steam and pump the mixture to the ground surface.

Compared with CSS, the steam injection pressure required by SAGD is below the fracture pressure of the oil sands formation and does not create tensile fractures within the oil sands reservoirs (Collins et al., 2013; Yuan et al., 2013). Therefore, SAGD causes fewer disturbances on caprock integrity and is thought to be a gentler process on caprock. But, with the growth of the operational experience, many researchers point out that proactive precautions are needed to maintain caprock integrity (Yuan et al., 2013). On May 18, 2006, a catastrophic steam release known as the Joslyn Steam Release incident occurred near the heel of well pair 204 –P1I1, as shown in Figure 1-2. It caused a surface disturbance zone of approximately 125 m by 75 m. Dust and rock ejection accompanying the steam release was spread over a distance in excess of 300 meters, creating limited damage to nearby facilities. The incident, which significantly affects the approval process for future SAGD processes, once again indicates that caprock integrity is a major issue of the SAGD process.

Immediately after the incident, an investigation was conducted on possible root causes. Two reports were released by the Alberta government. One of them was "*Summary of investigations into the Joslyn May 18th 2006 Steam Release*," while the other was "*Total E&P Canada Ltd., Surface Steam Release of May 18, 2006 Joslyn Creek SAGD Thermal Operation ERCB Staff review and Analysis*." Both have presented extensive information about the steam release area and have greatly contributed to the performance of both the numerical simulation and the physical modelling tests. However, due to the complexities of the material properties, ground conditions and other unknown factors, there is no concise conclusion of the incident.

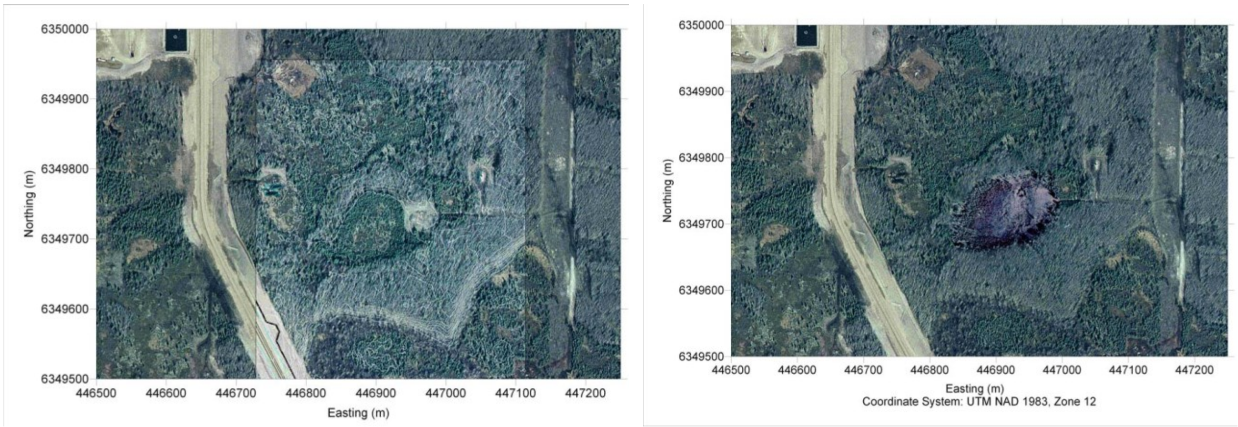

Figure 1-2 Aerial photography of the steam release area before and after the steam release (Total E&P Canada, 2007)

Caprock, which mainly comprises shales and mudstones, is made up of fine-grained sedimentary rocks with high clay content. It is of great importance for safely and efficiently recovering bitumen from oil sands reservoirs. During the geological history of the caprock, its low permeability has effectively trapped resources within reservoirs. However, human activities, such as the in-situ recovery process, may compromise the caprock hydraulic and mechanical integrity. The hydraulic integrity of the caprock prevents reservoir fluid from entering the shallow groundwater, while the mechanical integrity guarantees that the caprock deformation is within tolerable values and the stress state in the caprock is below the failure envelope (Yuan et al., 2013). The compromise of the caprock may induce many problems, such as personal injury, damage of facility at the ground surface, pollution of environment and local ecology.

In general, caprock integrity assessment is achieved through in-situ stress determination, caprock geological studies, constitutive property characterization and reservoir geomechanical simulations (Shafie Zadeh & Chalaturnyk, 2015). Numerous researchers have adopted analytical or numerical simulation methods to identify the reservoir pressure, temperature and other factors of caprock integrity (Bruno et al., 2000; Haekes et al., 2005; Dusseault et al., 2001; Vilarrasa et al., 2014). Recent efforts in surface-heave monitoring combined with pore pressure and temperature observations greatly contribute to the validity of these modelling efforts, but significant uncertainty still remains concerning the failure mechanisms within the caprock zones (Gu et al., 2011; P.M. Collins, 199; Dusseault, 2009). Under the lack of field monitoring data and validity of numerical simulation results, a physical modelling test becomes the most reliable way to recreate the failure process of caprock, to calibrate inputs of the numerical simulation test, to validate the numerical simulation test and to provide reliable calibration guidance for numerical models.

Scott (1987) suggested that three components of a failure needed to be understood before any subsequent steps could be taken – 1) mechanics involved in a failure, 2) properties of materials involved in the failure and 3) analysis incorporating mechanism and properties (R. F. Scott, 1987). If there is not enough information to elucidate the failure mechanism, then prototype or model tests are essential to provide guidance for design procedures. For the failure process of the Joslyn steam release incident, the most likely scenario involves the expansion of the steam chamber, the lateral extension of the pressurized area, the development of the shear failures on the edge of the pressurized area and the water/steam storage in the chamber as well as those fractures in the caprock. However, due to the shortage of field monitoring data, significant uncertainties remain.

While many studies use numerical simulation techniques to assess caprock failure mechanisms, this study adopts the geotechnical centrifuge or physical modelling as a tool to reveal caprock deformation mechanisms. The geotechnical centrifuge, which accelerates reduced scale models to a magnitude many times stronger than the Earth's gravity, reproduces the self-weight stresses and gravity-dependent processes. Test results are related to the prototype (i.e., field scale) through scaling laws. This technique has been recognized as a major tool in tackling complex geotechnical problems and provides reliable data for validation of numerical analysis as well as design procedures (Ng, 2014). Although caprock deformation, which involves the uplift behaviour of the shale barrier, has never been studied through geotechnical centrifuge modelling, similar studies pertaining to the uplift resistance of soils are extensive, such as horizontal plate anchor and "trap-door" tests.

One of the biggest challenges of geotechnical centrifuge modelling is the samples used in the tests. Because of the extremely friable nature of shale, the material is quite easy to disintegrate into slurry after being exposed to water, thus making it impossible to obtain samples using conventional methods. To overcome the shortage of Clearwater shale samples, this study attempts to develop synthetic Clearwater shale with physical and mechanical properties similar to the prototype material. Consolidated Speswhite kaolin clay was first used to replace the Clearwater shale for the physical modelling test, however, the experimental results showed that the material was too ductile to represent Clearwater shale. A modified formula based on an extensive literature review of reconstituted shales was then proposed. The unconfined compressive strength of this material was around 450 kPa, which was relatively low when compared with the Clearwater shale, thus motivating a more rigorous program to identify a suitable formulation for a synthetic material that more closely captured the constitutive behavior of Clearwater Formation clay shale.

Consequently, a larger experimental program was undertaken to develop a database of properties over a wide range of formulations to aid in identifying the most appropriate combination of materials for preparing a synthetic Clearwater shale. There were three essential parts in establishing the database: the first involved the physical and mechanical properties of the Clearwater shale, which were obtained from extensive experimental testing conducted within the Reservoir Geomechanics Research Group (RG^2); the second involved the components of the synthetic Clearwater shale; and the third involved a systematic experimental plan which should take into account the impact of the components of the synthetic Clearwater shale on the strength development of the synthetic Clearwater shale.

Several critical points, such as the development of the synthetic soil, the geological information of the Joslyn steam release area and the preparation of the geotechnical centrifuge models, are presented in this study. Meanwhile, the comparison between geotechnical centrifuge modelling and numerical simulation is performed to validate the numerical modelling results and to provide guidance for industrial production.

1.2 Problem statement

Only a small proportion of the Alberta oil sands deposits are shallow enough for surface mining, while the vast majority lies deep beneath the ground surface. Thermal oil recovery techniques, such as steam assisted gravity drainage (SAGD), are becoming more popular in Alberta. However, the incident regarding the Total E&P Canada Ltd. (Total) Joslyn Creek SAGD project that occurred on May 18, 2006, indicated that understanding the impact of SAGD on caprock integrity is essential for industrial production. Previous SAGD projects mainly relied on numerical simulation and field observations to enhance understanding and provide guidance for production. However, the steam release incident indicates that these approaches need to be complemented with a more sophisticated method such as geotechnical centrifuge modelling to verify numerical simulation results and to provide guidance for production.

The first challenge of this study is to find analogue material of the Clearwater shale for centrifuge modelling test. Clearwater shale, which is highly over-consolidated during geological history, is mainly composed of clay and silt. Compared with normally consolidated clay, Clearwater shale shows relatively high cohesive strength.

The second challenge of the study is the identification of caprock failure mechanisms through geotechnical centrifuge modelling test. Despite the wide usage of this technique in tackling complex geotechnical problems, it has never been used to identify caprock failure mechanisms. The overburden pressure applied to the caprock is simulated through weighting with lead bars while a Mariotte bottle is used to control the water level in the plane strain box (PSB). A custom-designed and built device called the Geomechanical Caprock Deflection Mechanism, or GeoCDM, is used to mimic the expansion of the steam chamber. The caprock failure process under different uplifting velocities is recorded with a camera to investigate the effect of expansion rate on caprock failure mechanism.

The third challenge of this study is to make a comparison between the experimental results of the geotechnical centrifuge modelling tests and those of the numerical modelling tests pertained to Joslyn steam release incident from the report "*Summary of investigations into the Joslyn May 18th 2006 Steam Release"*. Although this study mainly focuses on physical modelling tests, the comparison is still made to verify the numerical simulation tests.

1.3 Scientific hypothesis

The scientific hypothesis for this research is that physical model tests conducted in the centrifuge can successfully capture caprock failure mechanisms resulting for SAGD operations.

1.4 Research objectives

To explore the issues embodied in the research hypothesis, this research is divided into three main objectives: 1) develop a synthetic soil to represent Clearwater shale for the centrifuge modelling test; 2) recreate caprock failure process with geotechnical centrifuge facility; 3) analyze images captured during geotechnical centrifuge modelling test by using GeoPIV to detect caprock deformation behavior.

1.4.1 Short-term objectives

The main short-term objective of this research is the development of suitable synthetic Clearwater shales for geotechnical centrifuge testing. This will be pursued through the following steps:

1. Conducting an extensive literature review to determine the possible components of the synthetic soil and bonding agents for creating cementitious bonds between soil particles.
2. Establishing a testing matrix of unconfined compression tests to determine the most suitable "recipe" or formula for creating synthetic soil.
3. Performing tests to determine the constitutive properties of the selected synthetic soil; and
4. Comparing the mechanical properties of synthetic soil with those of Clearwater shale to defend its suitability for physical model tests.

1.4.2 Long-term objectives

The longer-term objectives of this research are design, assembly, and execution of the physical model tests. This will be pursued through the following steps:

1. Perform a centrifuge modelling test to get initialization and propagation of both tensile and shear fractures, to observe distribution of vertical displacement as well as horizontal displacement at different stages, and to identify caprock failure mechanism under different uplifting velocities.
2. Analyze images captured during geotechnical centrifuge modelling tests by using GeoPIV to detect caprock deformation behavior and make a comparison with the numerical simulation tests pertained to Joslyn steam release incident.

1.5 Research scope

The geotechnical centrifuge tests conducted in this research will utilize synthetic soil and will not attempt to use field block samples of caprock formation material. The use of field samples directly in centrifuge modelling is problematic and is generally not adopted in most centrifuge testing workflows. The use of a synthetic soil that captures the key features of the constitutive behaviour of caprock formations is deemed sufficient since this research is focusing on elucidating failure processes and not history matching a particular case study.

While it would be ideal to progress centrifuge testing to the stage where an inert gas could be injected into the physical models to better simulate the process of an expanding steam chamber, this study will continue to utilize the GeoCDM device, which imposes a displacement boundary condition at the base of the specimen, with the centrifuge. This device provides a significant advantage in being able to conduct both “slow” and “fast” loading tests to study how this affects failure mechanisms.

Geotechnical centrifuge modelling, which uses the abovementioned synthetic soil, intends to reproduce the failure process of caprock. It focuses on the initialization and propagation of fractures, the distribution of displacements in the sample and the evolution of the failure process.

Although this study mainly focuses on physical modelling test, the comparison between results of geotechnical centrifuge modelling tests and the numerical simulation tests from the report, *Summary of investigations into the Joslyn May 18th 2006 Steam Release*, is still made. To deepen the understanding of caprock deformation behaviour and help with the performance of geotechnical centrifuge modelling test. FLAC3D is used to model caprock deformation behaviour induced by uplifted forces, as shown in Appendix E.

1.6 Research methodology

The research methodology of this study includes three components: 1) perform geotechnical centrifuge modelling tests; 2) develop synthetic soil; 3) analyze results from geotechnical centrifuge modelling tests to detect caprock deformation behavior.

1.6.1 Development of synthetic Clearwater shale

The synthetic soil or analogue material must satisfy the following requirements:

1. From a practical point of view, the components of the synthetic soil should be easy access and low cost because large quantities of materials are needed.
2. Large blocks of synthetic soil should be isotropic and homogeneous as behaviour of different samples should be consistent.
3. Deformational/mechanical behaviour of the synthetic soil should be as close to the Clearwater shale as possible. Extensive literature adopting reconstituted soil with carefully controlled properties for experimental work is available (Stimpson, 1970). However, due to dissimilar engineering properties, these model materials are not qualified to be representative of Clearwater shale. Clearwater shale has quite strong cementitious bonds and shows quite high cohesive strength.

To find a suitable formula for the synthetic soil, a matrix of unconfined compression tests, including 320 samples, is performed to study the effect of water content, cement content, Atterberg limits and soil particle size distribution on the strength development of the synthetic soil. Principal components of the synthetic soil are Speswhite kaolin clay supplied by IMERYS Minerals Ltd. and Sil325 supplied by Sil Industrial Minerals. Ordinary Portland cement is used as the bonding agent to create cementitious bonds between soil particles.

For the unconfined compression tests, cylindrical molds 45 mm in diameter and 120 mm high are used to assure sufficient specimen height for unconfined compression tests. A thin layer of petroleum jelly is applied on the inner surface of the mold so that samples can be easily moved from the mold after the curing period. The total soil-water content of the soil-water-cement mixture for the entire testing program is adjusted to the range of liquid limit of 1.1, 1.5, 2.0 and 2.5, each of which is in combination with 3, 5, 7 and 8 total soil-water to cement ratio. In preparing the specimens, quantities of soil, distilled water and cement required for at least two specimens at a prescribed water content and the total soil-water to cement ratio are calculated and weighed.

The well-mixed slurry is then poured into the mold in three separate layers. After filling each layer, trapped air bubbles are removed by subjecting the mold to vibration until no air bubbles erupt from the sample. Immediately after completing the soil-filling process, the specimen along with the mold is sealed with plastic film to prevent moisture loss. After 24 hours, the cylindrical sample is dismantled, wrapped with plastic film and then carefully stored in a custom-built humidity container that would be stored in the laboratory at a constant temperature (20±2ºC).

Unconfined compression tests are carried out on specimens that have been cured for 28 days. All specimens are trimmed to 45 mm (diameter) by 90 mm (height) for unconfined compression tests. The rate of vertical displacement is chosen to produce an axial deformation rate of approximately 0.5% per minute. The axial strain measurements are made using a linear variable differential transformer (LVDT). The radial strain measurements are made using a radial chain. The formula, which shows a similar unconfined compressive strength as Clearwater shale, is screened out and then used to make the samples for triaxial tests.

For the triaxial tests, a cylindrical mold 63.5 mm in diameter and 127 mm high is used to assure sufficient specimen height. The procedure of making the soil slurry, transferring the slurry to the moulds and storing samples, is the same as that for the unconfined compression tests. Isotopically consolidated drained/undrained triaxial compression tests are run on samples after 28 days of curing. Tensile strength and permeability are also determined for the comparison with the Clearwater shale and for the inputs of the numerical simulation test.

1.6.2 Geotechnical centrifuge modelling test

A Broadbent G-Max GT50/1.7 geotechnical beam centrifuge is used in this study. GT50 indicates that the nominal capacity of the beam centrifuge is 50 g-tones. This means that a maximum payload of 500 kg can be spun at 100 g. The number 1.7 indicates that the nominal effective radius of the payload is 1.7 m although the radius of the swing platform is 2.0 m.

Quantities of soil, distilled water and cement are calculated and weighed based on the requirement that the final height of the centrifuge modelling samples after the curing/consolidation period should be 20 cm. The soil and water are then transferred to the mixing pot of the GS1500 vacuum mixer to mix for 120 minutes. Cement slurry, which is thoroughly mixed by hand, is then added to the mixing pot and mixed for another 30 minutes. The thoroughly mixed slurry is then transferred to the PSB in five separate layers. After filling each layer, trapped air bubbles are removed by tapping the PSB with a rubber hammer until no air bubbles erupt from the sample.

Immediately after completing the soil filling process, the sample is sealed with plastic film and cured for 28 days. After reaching the desired number of curing days, the front plate is replaced with the glass window, and an appropriate thickness of lead bars is placed on top of the sample to mimic the overburden pressure. A Mariotte bottle is used to control the water level in the PSB. The Parker Servo motor is used to control the uplifting velocity. The experimental package is then placed in the swing cradle for the centrifuge modelling test.

Table 1-1 Major components of the centrifuge modelling test

Components	Function
Plane Strain Box	Contains sample
Parker Servo motor	Supplies power and control velocity for GeoCDM
Mariotte bottle	Controls water level in the plane strain
GeoCDM	Mimics effect of the expanding steam chamber
Lead bars	Create overburden pressure
Kulite pore pressure transducer	Monitors pore water pressure
External pore pressure transducer	Monitors water level change
Perspex glass	Visualizes soil particle movements
Camera	Records soil particle movements
Light	Supplies suitable light for capturing images

Prior to motivating the GeoCDM, the sample is first consolidated in the centrifuge for 8 hours. After that, the shearing process starts, and photos are taken at constant time intervals. Those photos are used for the analysis to track the soil particles displacements and the caprock deformation behaviour. Table 1-1 illustrates the major components used for the geotechnical centrifuge modelling.

1.7 New contributions

It is expected that this research will provide the following academic and applied engineering contributions.

1.7.1 Academic contributions

1. The development of a synthetic soil that has similar physical and mechanical properties as Clearwater shale. This overcomes the shortage of the Clearwater shale samples.
2. The establishment of an experimental workflow for physical modelling studies of caprock uplift behaviour that includes depth of burial, shale thickness, strength and rate of loading.

3. The discovery of failure mechanisms in caprocks, including the initialization and propagation of both tensile cracks and shear cracks and the distribution of both vertical and horizontal displacement in the sample.

1.7.2 Applied contributions

1. The provision of guidance for the design of SAGD projects. The centrifuge modelling technique has been widely used in geotechnical engineering for the study of specific geotechnical problems. This study is the first to introduce centrifuge modelling technique for the study of caprock behaviour.
2. The provision of calibration of input parameters for numerical modelling. Due to the limitation of monitoring technology, few data can be obtained from the field. Moreover, these data may be very sensitive to the external environment such as vibration, temperature variation, etc. Centrifuge modelling can eliminate most of these external interferences and provide reliable calibration for numerical modelling.
3. Validate numerical simulation test from “*Summary of Investigations into the Joslyn May 18th 2006 Steam Release*”. Due to the simplifications and assumptions made by numerical modelling, test results from the approach should be complemented with the centrifuge modelling test.

1.8 Thesis outline

Chapter 1 provides a discussion on the motivation for this research, and background information, research objectives and methodology employed in the research.

Chapter 2 intends to be the theoretical background of this thesis. It presents the available literature that can promote the contribution of this study in industrial production and within the academic domain.

Chapter 3 summarizes geological information from the Joslyn Creek steam release area, possible reasons for the incident proposed by other researchers, advantages and disadvantages of geotechnical centrifuge modelling, the principles of this technique, inherent centrifuge modelling errors, the procedure of preparing the model for the physical modelling tests and the experimental results of the geotechnical centrifuge modelling test by using the consolidated Speswhite kaolin clay and the synthetic Clearwater shale-I.

Chapter 4 illustrates the procedure for the development of synthetic soil. It describes the methodology used for achieving this goal. The principal components of the model material as well as the bonding agent are determined through literature review. A matrix of unconfined compression tests considering the effect of the total soil-water content, the cement content and the soil particle size distribution is presented. Experimental results are then analyzed to study the impact of these factors on the after-curing properties of the synthetic soil. The relationship between the initial parameters and the after-curing properties such as the unconfined compressive strength, the after-curing void ratio, etc. is established, which is of great value for the establishment of the database.

The comparison between the Clearwater shale and the database is then made for the selection of the formula for the synthetic Clearwater shales. The mechanical properties of the synthetic Clearwater shale are then compared with the Clearwater shale to defend the suitability of the synthetic Clearwater shale for the physical modelling tests.

Chapter 5 presents experimental results of geotechnical centrifuge modelling tests. It includes the initiation and propagation of the fractures in the sample, the evolution of the vertical displacement, the horizontal displacement, the resultant displacement and the maximum total shear strains.

Chapter 6 presents the analysis of the experimental results shown in Chapter 5. It focuses on the analysis of the experimental results of the geotechnical centrifuge modelling tests. It intends to find the engine of the deformation, the most highly strained area from which the failure starts, and the type of forces resulting in these fractures.

Chapter 7 summarizes the major findings of this study and the contributions of these findings to the study of the caprock failure mechanism. Recommendations for further study are also presented in this chapter.

The appendix presents results of the geotechnical centrifuge modelling tests, code for the numerical simulation test using FLAC3D, results of the numerical simulation test as shown in Appendix E and images, captured as GeoCDM moves up, illustrating the failure process of caprock

.

Chapter 2 Literature review

2.1 Introduction

Caprock failure induced by the SAGD process is not common, but it has occurred. To design operational parameters that prevent caprock failure, SAGD projects mainly adopt numerical simulation studies combined with reservoir surveillance during operation. However, due to the complexity of the geologic media and the limitations of the research methodologies, assumptions, and simplifications must be made when using the numerical modelling approach. Meanwhile, due to the cost of extensive field monitoring, there is a paucity of data for the validation of the numerical modelling results. Therefore, numerous uncertainties pertaining to the caprock failure mechanism exist.

The Joslyn steam release incident (Total E&P Canada, 2007) has stimulated the interest of many researchers. Most of this literature about the failure mechanism of the Joslyn steam release incident adopts either numerical modelling approaches or analytical methods. This thesis, being part of the project focusing on the identification of the caprock failure mechanism, intends to investigate the caprock failure process through the geotechnical centrifuge modelling test.

This chapter, which provides the background of the research includes four sections:

The first section describes the basic information of the Joslyn Creek steam release incident, including geologic information, the possible shale barriers and the possible reasons resulting in the failure. Concurrently, the caprock failure mechanism proposed by other researchers is also presented.

The second section describes the research topics pertaining to soil deformation behaviour induced by the uplift force such as the horizontal plate anchor, trap-door tests, buried pipe, etc.

The third section intends to describe the research status of the caprock failure process.

The fourth section describes the methodologies and materials used by different researchers for preparation of synthetic soil/rock materials for physical experiments.

Overall, this literature review includes: 1) failure mode induced by uplift force; 2) caprock integrity assessment; 3) geotechnical centrifuge modelling test; 4) the development of synthetic soil.

2.2 Geology of steam release area

The Joslyn Creek Project, located approximately 60 km north of Fort McMurray, adopted steam-assisted gravity drainage (SAGD) process for the recovery of bitumen. Geological information of the Joslyn steam release area is obtained from "*Summary of investigations into the Joslyn May 18th 2006 Steam Release*" and "*Total E&P Canada Ltd., Surface Steam Release of May 18, 2006 Joslyn Creek SAGD Thermal Operation ERCB Staff review and Analysis.*"

As shown in Figure 2-1, oil sands reservoirs which are suitable for commercial exploitation are found to be with a buried depth ranging from 65 to 110 m and are primarily in the Middle McMurray Formation. A horizontal SAGD injector, which is about 28 m below the top of the Middle McMurray, is drilled at the base of the formation. A producer used to collect bitumen is drilled 5 m below the injector. Above the bitumen-bearing formation, there is a 25 m thick Middle / Upper McMurray and Wabiskaw interval. The top of the McMurray reservoir is less than 50 m from ground surface, which indicates that it is a shallow deposit.

The Waterways Formation, which is below the McMurray Formation, is an argillaceous limestone. From bottom to top, the McMurray formation has been divided into three informal members based on their depositional environments: Lower, Middle, and Upper McMurray. Overlying the McMurray Formation, the Wabiskaw Member of the Clearwater Formation is comprised of silts, fine grained sands and shales. It does not contribute to the in-situ bitumen recovery due to the low grades of bitumen. From bottom to top, it has been divided into three separate units: Kcw1, Kcw2 and Kcw3. Although the Kcw1 is depositionally continuous, Total E&P Canada Ltd. does not consider the unit as an efficient pressure seal, or a lateral pressure drain due to its thin thickness. The Kcw2 is considered to be an effective caprock for the commercial SAGD steam chamber for a long run due to its constant thickness of approximately 4.8 m. Kcw3, with a constant thickness of 2 m, is not considered to be an effective caprock for the steam chamber due to the pressure drain of low-to fair quality.

The overburden thickness of the Wabiskaw Member ranges from 40 to 60 m. The formation that directly overlies the Wabiskaw Member is the Clearwater Formation, which has a thickness ranging from 20 to 30 m. The material overlying the Clearwater formation mainly consists of the Pleistocene, low-quality sands and shales. The Clearwater formation mainly consists of marine clay which has very low permeability. Because of that, the formation is considered an effective caprock for the SAGD project.

Based on the two reports, the Clearwater formation is separated into 5 stratigraphic units: Kc1, Kc2, Kc3, Kc4, Kc5. Being the approved caprock for the Joslyn Creek SAGD project, the Clearwater Formation with a thickness of 20 to 30 m is found to be continuous in the scheme area. Meanwhile, no evidence shows that the overburden interval has pre-existing fractures.

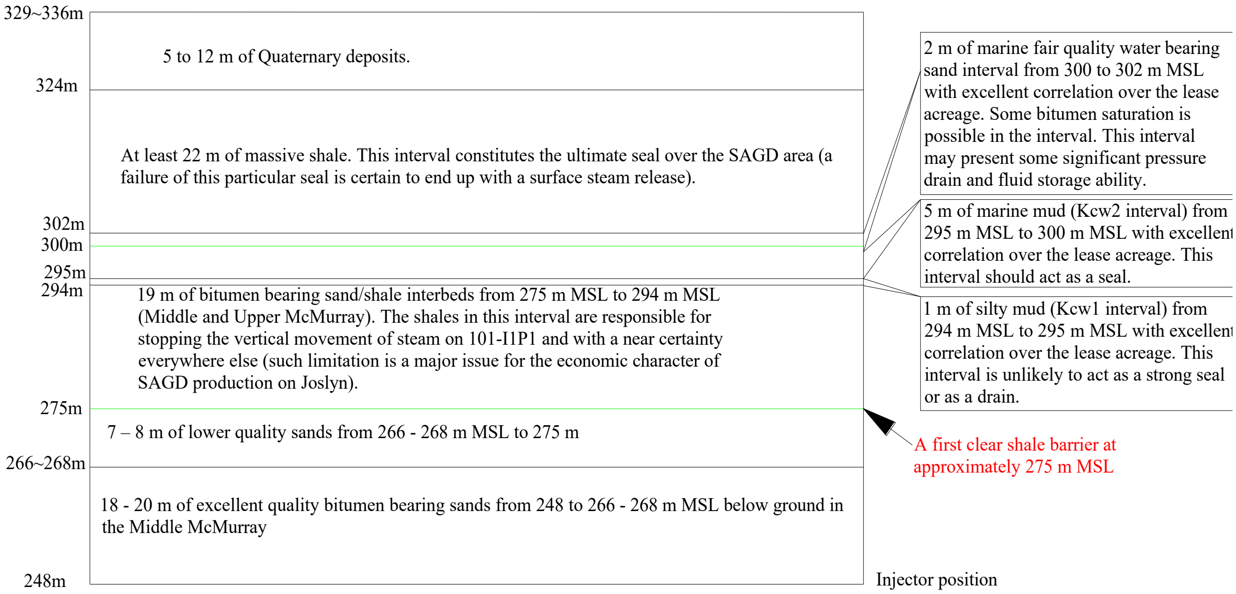

5 to 12 m of Quaternary deposits.

At least 22 m of massive shale. This interval constitutes the ultimate seal over the SAGD area (a failure of this particular seal is certain to end up with a surface steam release).

19 m of bitumen bearing sand/shale interbeds from 275 m MSL to 294 m MSL (Middle and Upper McMurray). The shales in this interval are responsible for stopping the vertical movement of steam on 101-I1P1 and with a near certainty everywhere else (such limitation is a major issue for the economic character of SAGD production on Joslyn).

7 – 8 m of lower quality sands from 266 - 268 m MSL to 275 m

18 - 20 m of excellent quality bitumen bearing sands from 248 to 266 - 268 m MSL below ground in the Middle McMurray

2 m of marine fair quality water bearing sand interval from 300 to 302 m MSL with excellent correlation over the lease acreage. Some bitumen saturation is possible in the interval. This interval may present some significant pressure drain and fluid storage ability.

5 m of marine mud (Kcw2 interval) from 295 m MSL to 300 m MSL with excellen correlation over the lease acreage. This interval should act as a seal.

1 m of silty mud (Kcw1 interval) from 294 m MSL to 295 m MSL with excellen correlation over the lease acreage. This interval is unlikely to act as a strong seal or as a drain.

A first clear shale barrier at approximately 275 m MSL

Figure 2-1 Stratigraphy of the Joslyn Creek SAGD project area (Total E&P Canada, 2007)

2.3 Failure mechanism

2.3.1 Failure mechanism proposed by Total E&P Canada

Total concluded from their investigations that the pre-existing fractures (within the caprock) and nearby observation wells were not the primary cause of the Joslyn steam release incident. The report demonstrated that one of the major reasons leading to the incident was the condensed steam accumulated under the Clearwater shale barrier. During the circulation and the semi-SAGD phase, the steam pressure disturbed the Wabiskaw Member and eventually lead to the formation of flow paths to the base of the Clearwater Formation. The condensed steam accumulates in the pores, fractures and other possible spaces in the Middle and Upper McMurray Formation. As the SAGD process continued, the volume of the pressurized zone expands, and eventually led to the steam release incident.

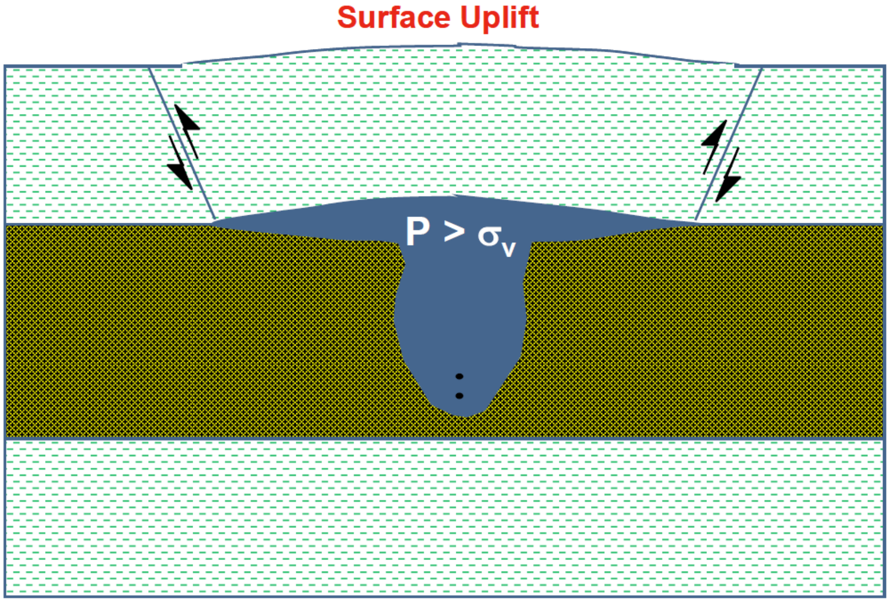

Figure 2-2 Failure mechanism proposed by Total E&P Canada (Total E&P Canada, 2007)

Based on analyses of in-situ stress tests and numerical modelling studies, the initiation and propagation of a tensile fracture induced by the steam pressure is designed to be prevented. The geomechanical modelling demonstrates that the caprock integrity can be significantly affected by the steam pressure and the surface area of the pressurized zone. By enlarging the radius of the pressurized area from 15 m by steps of 5 m, the result of the geomechanical modelling provided by Total E&P Canada shows that if the radius reaches 45 m, the plastic shear strain reaches the top surface of the overburden, indicating that the shear fault has already provided a flow path for the accumulated steam (Total E&P Canada, 2007). Figure 2-2 demonstrates the schematic diagram of the Joslyn caprock failure mechanism provided by Total E&P Canada. The accumulated steam under the shale barrier displaces the caprock, induces the surface heave and eventually results in the shear zones at the shoulder of the pressurized zone.

2.3.2 Failure mechanism proposed by Collins (2007)

The caprock integrity has to satisfy two requirements: the first is the hydraulic integrity or mechanical integrity, and the second is that the seal should have low vertical transmissibility and be laterally continuous over the region (Collins, 2007). Collins (2007) presented several critical factors affecting the caprock integrity:

1. Burial depth
2. Dimensions of the pressurized zone
3. Caprock thickness and strength
4. Pay zone thickness
5. Injection pressure of the steam
6. Stress changes induced by the thermal jacking

Figure 2-3 demonstrates the formation-steam chamber interaction during the SAGD process (Collins, 2007). This schematic diagram shows that dilation of the oil sands produces vertical displacements within the caprock and induces a redistribution of the original stress state. With the increase of steam injection pressure and the expansion of the steam chamber, the caprock integrity can be seriously compromised and may eventually reach a critical state at which failure could occur.

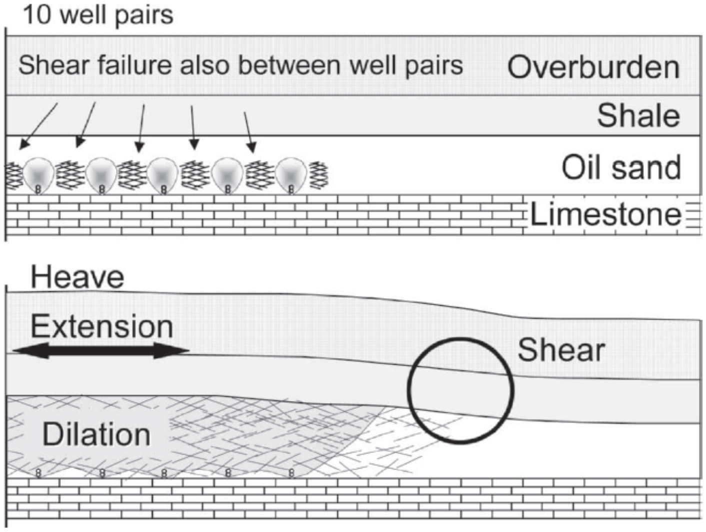

Figure 2-3 Schematic diagram of the effect of the SAGD process on caprock integrity (Collins, 2007)

2.3.3 Failure mechanism proposed by Khan

During the SAGD process, a few well-established factors can impact the reservoir and caprock, including the temperature, injection pressure, in-situ stress, mechanical properties of the reservoir and caprock (e.g., dilation angle, friction angle). Theoretically, tensile failure occurs when the injection pressure is higher than the fracture pressure, which can be deduced from a mini-fracturing test. However, keeping the injection pressure lower than the fracture pressure does not necessarily guarantee caprock integrity (Khan et al., 2010, 2011). Due to varying boundary conditions, the vertical stress changes slightly while the horizontal stress greatly increases and such a situation can lead to the formation of shear fractures in the oil sands reservoirs. If permeability increases due to shear deformations, this may be beneficial for the recovery process. However, the propagation of shear fractures can be a great challenge for caprock integrity if they extend out of the reservoir and into the caprock horizons. Additionally, the combined effects of dehydration (heat) and exposure to fresh water (condensed steam) can lead to a reduction of the mechanical properties of the shale barrier.

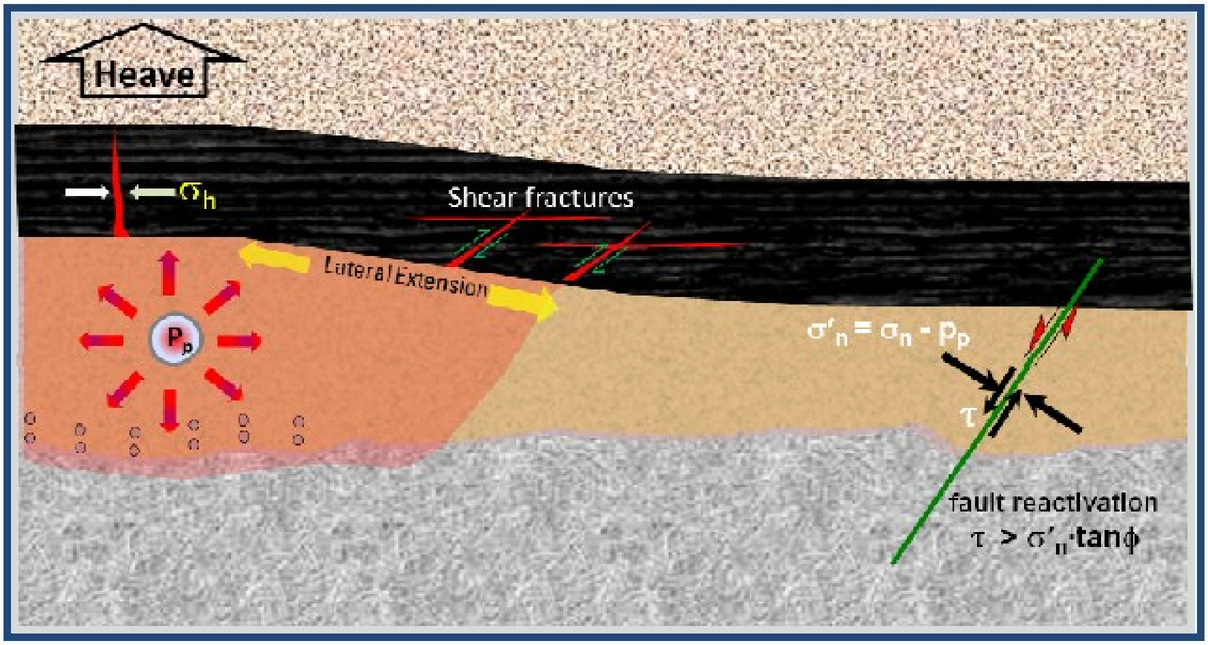

Figure 2-4 Schematic diagram of the caprock failure mechanism proposed by Khan et al. (Khan et al., 2010, 2011)

2.3.4 Other Proposed Failure Mechanisms

Rahmati, Nouri, and Fattahpour (2014) and Uwiera-Gartner, Carlson, Walters, and Palmgren (2011) have also qualitatively described the geomechanical mechanisms induced by the SAGD operation. From their perspective, during the SAGD process, the following phenomena happen in and around the oil sands reservoirs (as shown in Figure 2-5):

1. The pore pressure change induced by the injected steam redistributes the in-situ stress state of the oil sands reservoirs and the surrounding strata.
2. The injected steam leads the oil sands reservoirs to expand, which can eventually compress the caprock.
3. Geomechanical processes such as dilation, tensile fracturing and shearing can significantly affect the physical and mechanical properties of the reservoir, which can compromise caprock integrity.

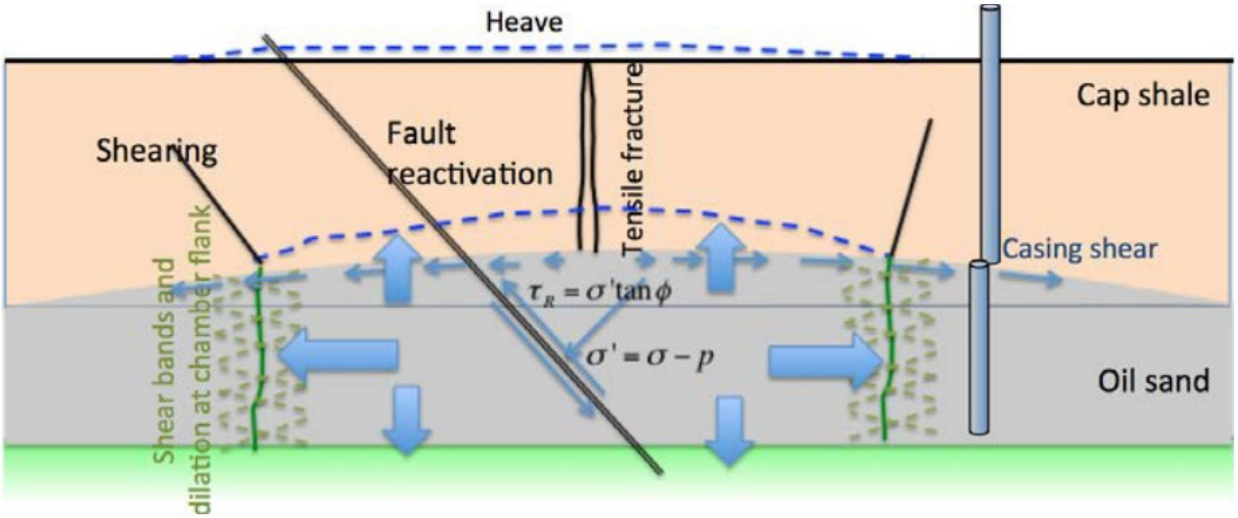

Figure 2-5 Geomechanical mechanisms induced by the SAGD process (Rahmati et al., 2014)

2.4 Soil deformation behaviour induced by uplift forces

The literature review of the failure mechanisms of the Joslyn steam release incident indicates that the uplift force resulting from either the accumulated water beneath the shale barrier or the thermal expansion of the oil sands reservoir is likely the main contributor to the caprock containment issues. Some researchers also propose similar reasons for the eruptions of volcanoes, concluding that the accumulation of magma leads to the eruption, and the "trapdoor" faulting forms arcuate intra-caldera ridge (Amelung et al., 2000). The occurrence of the abovementioned disasters involves the interaction between the underground processes, such as condensed steam/magma, and the surrounding soil/rock. Under this condition, collecting and analyzing literature related to the soil deformation behaviour induced by the uplift force may contribute to an understanding of the caprock deformation behaviour.

Numerous geotechnical problems such as uplift piles, horizontal plate anchors, and buried pipelines also involve the interaction between a subsurface structure or process and the surrounding soil mass. Moreover, ground heave induced by the uplift force is a commonly seen phenomenon in geotechnical engineering. Many factors can produce the uplift force, such as expansive soil, wind, hydraulic pressure beneath the dam, accumulated magma and so on. In the past few decades, researchers have adopted approaches such as physical modelling, field tests, numerical modelling, and theoretical analysis to investigate the failure mechanisms of these problems. The methodology of these research studies and the definition of the failure plane adopted by these researchers would provide guidance for the current research study.

2.4.1 Soil arching

In 1895, Janssen developed an approach known as Janssen's silo theory for the design of silos (Janssen, 1895). It was the first time that the arching effect was realized and studied by researchers. From the awareness of the soil arching effect, numerous studies have attempted to investigate the phenomenon using methods including experimental approaches, theoretical and analytical methods, numerical modelling, and empirical approaches. From 1906 to the 1940s, Spangler and Handy performed extensive experiments and theoretical analysis to investigate the pressure on the buried conduit and proposed the well-known Marston-Spangler theory, which is still widely used today (Spangler & Handy, 2007). In 1943, Terzaghi proposed the definition of the arching effect and presented a detailed derivation of the arching problem. It is worth noting that the trap door tests and the corresponding analysis performed by Terzaghi laid a foundation for the future study of the arching effect (Terzaghi, 1943). Moradi and Abbasnejad (2013) and Tien (1996) summarized the development of the soil arching theory and the experimental, theoretical and empirical approaches adopted by different researchers.

The arching, which includes active arching and passive arching, widely exists in geotechnical engineering and plays an important role in both the natural terrain and man-made structures. The shearing resistance to the relative motion between the yielding soil mass and the adjacent stationary soil mass is the principal reason for the soil arching. As external factors such as forces or high-pressure steam during the SAGD process uplift the yielding mass, the shearing resistance acts download, leading to a load increase over the base of the yielding mass and a load decrease over the adjacent stationary mass. If the yielding mass moves download, the shearing resistance acts upward, resulting in a load decrease over the base of the yielding mass and a load increase over the adjacent stationary mass.

From the perspective of the man-made structure, the principal reason for the relative motion can be attributed to the difference in the stiffness between the installed structure and the surrounding soils. The active arching occurs if the installed structure is less stiff than the surrounding soils, and the stress redistribution transfers load from the yielding areas of the installed structure to the less deformable soils, leading to the decrease in the load over the yielding areas of the installed object and the increase in load over the surrounding soils. The passive arching occurs if the surrounding soil is less stiff than the installed structure. The stress redistribution transfers load from the surrounding soils to the installed structure, leading to the load decrease over the adjoining soils and a load increase over the installed structure (Iglesia et al., 2013; Terzaghi, 1943).

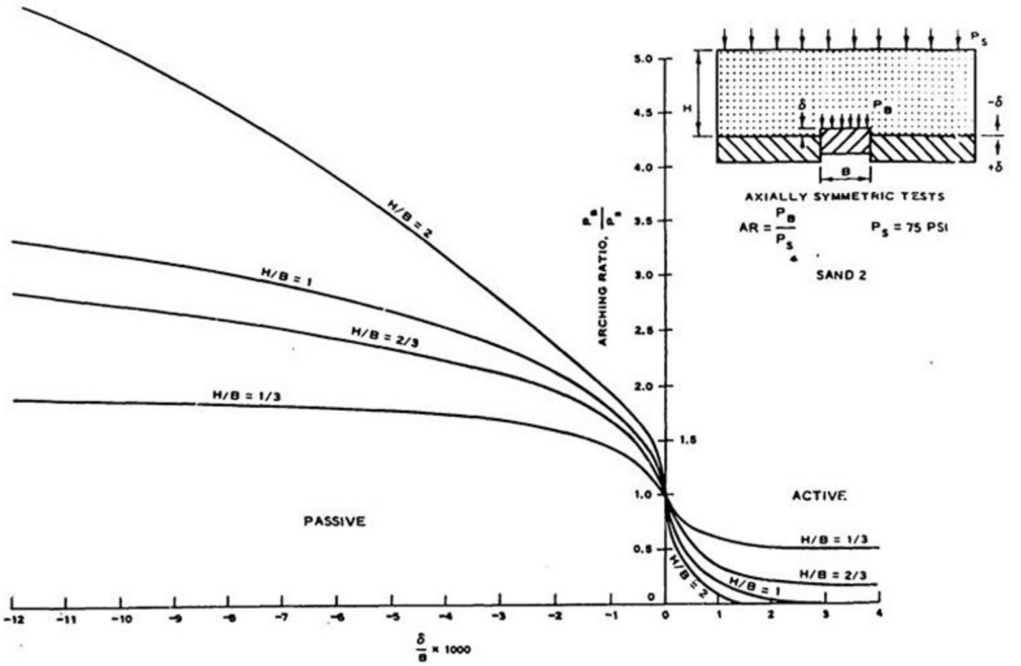

Figure 2-6 Arching curves induced by active and passive arching (Mcnulty, 1965)

Mcnulty (1965) performed a series of experiments to investigate the stress redistribution induced by the arching effect, as shown in Figure 2-6. The study adopted a parameter referred to as dimensionless deflection ($\frac{\delta}{B}$), which was defined as the ratio of the vertical displacement of the trapdoor to the width of the trapdoor, to quantitatively describe the effect of arching. As shown in Figure 2-6, when the dimensionless deflection is very small (-0.001 to 0.001), the stress change of passive arching is symmetrical about point (1.0, 0) with that of the active arching. However, beyond these bounds, for the active arching, the pressure on the trap door sharply drops to a small value; for the passive arching, the pressure on the trap door gradually reaches the ultimate state where the pressure changes slowly with the uplift deflection.

Tanaka and Sakai (1993) performed a series of trap-door tests to investigate the load-displacement relationship and the development of the shear band, as shown in Figure 2-7. The height of the sample is 20 cm, while the width of the trap door is 10 cm. The sample utilized in the study is made by pouring the air-dried Toyoura sand into the container with great care. To photographically track the development of the shear bands, the sample is marked by a few thin layers of red sand at intervals of about 1.5 cm adjacent to the glass wall of the container.

Similar to the results presented by Mcnulty (1965), the load on the trap door increases sharply at the initial stage of the passive arching. As the trap door continues moving up, the load gradually stabilizes and reaches the so-called ultimate state. As shown in Figure 2-7, the researchers define the shear band as the point at which the horizontal line deflects. At the initial stage, the shear band seems to be a linear line. As the trap door moves up, the shear band gradually increases to the ground surface and bends toward the horizontal line.

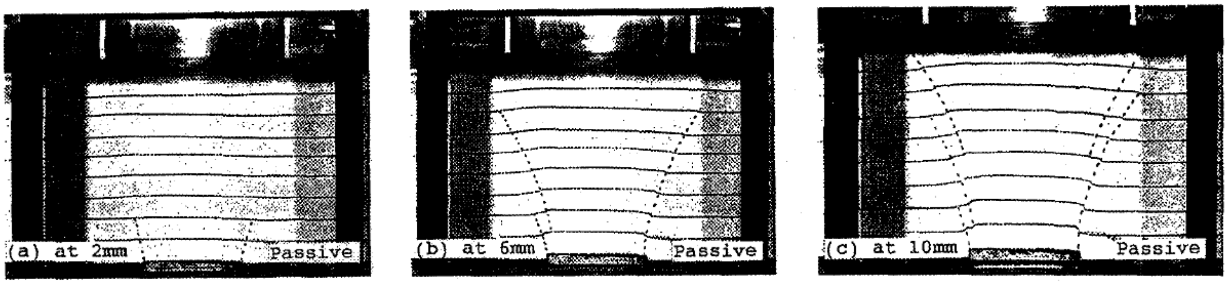

Figure 2-7 Propagation of shear bands in the sand mass (Tanaka & Sakai, 1993)

Vardoulakis, Graf, and Gudehus (1981) performed physical modelling tests to investigate the propagation of the shear bands and the factors controlling the inclination of the shear bands, as shown in Figure 2-8. The experimental results reveal that a small upward deflection of the trap door in the dense sand can clearly result in the occurrence of the shear bands extending from the edge of the trap door. After the shear band tip reaches a certain height in the sample, the rigid body motion of the wedge bounded by the shear bands dominates. As the deflection enlarges, the shear bands propagate into the soil body and eventually reach the free surface. If the trap door continues moving upward, a new set of shear bands with a steeper inclination angle extending from the edge of the trap door emerges. The researchers infer that the major reason resulting in the steeper shear bands is the sand dilation. The inclination angle of the shear bands depends on the porosity of the soil sample. For loose sand with a small embedment ratio, the shear bands are almost vertical. For loose sand with a large embedment ratio, the shear bands are not observed in the sample.

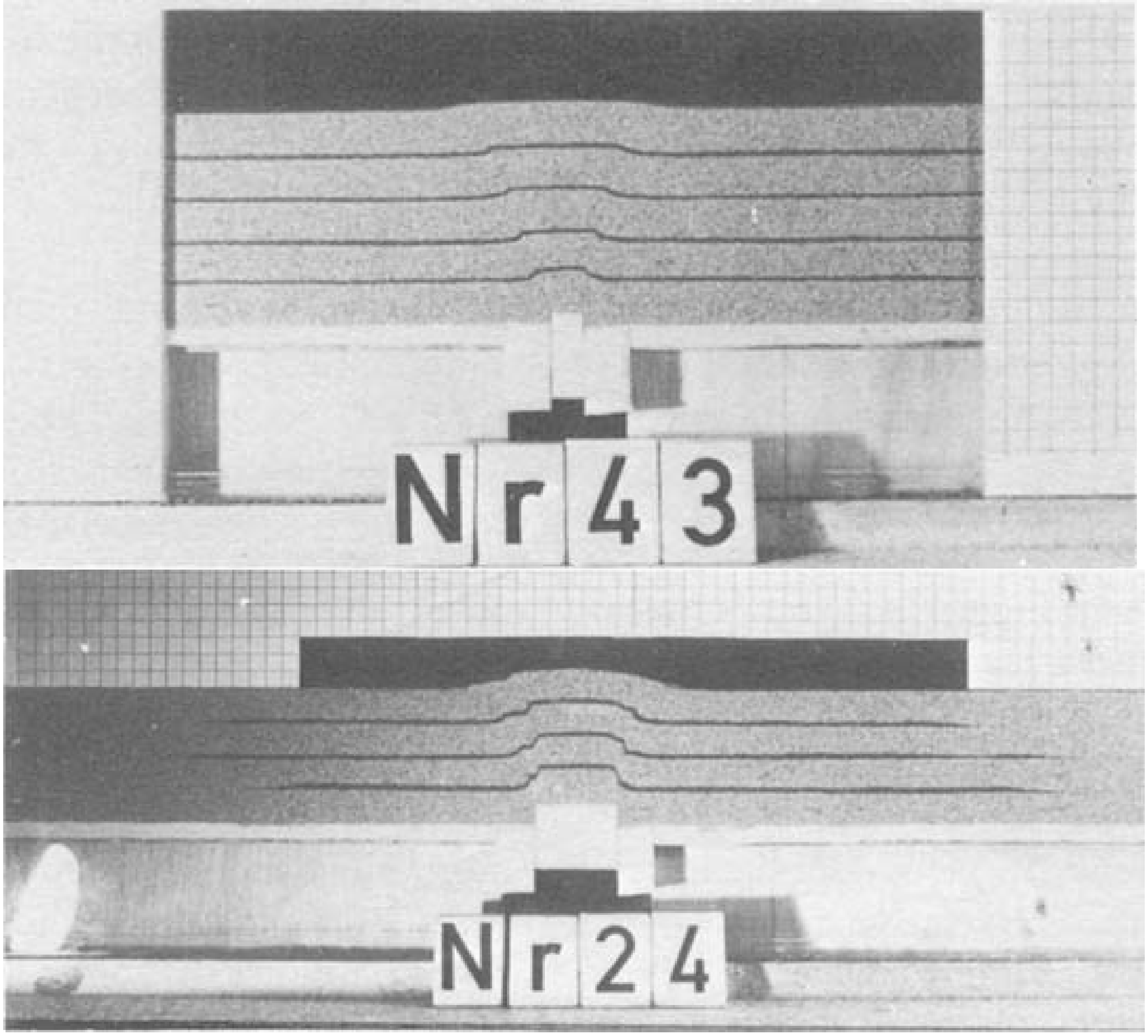

Figure 2-8 Passive arching after small trap-door displacement (Nr43) and large trap-door displacement (Nr24) (Vardoulakis et al., 1981)

The trap door is a classic experimental setup to study the arching effect and has been adopted by numerous researchers. In recent years, with the development of the advanced instruments, some researchers utilize the geotechnical centrifuge to investigate the arching effect. Meanwhile, the development of the Tactile Pressure Sensor (El Ganainy et al., 2013), load cell (Sadrekarimi &

Abbasnejad, 2010) and other instruments have made it possible to track pressure variation during the trap-door tests.

2.4.2 Horizontal plate anchor

Experimental investigations into the soil deformation behaviour induced by the plate anchor at the laboratory scale can be classified into two categories: the conventional method under “normal gravity” conditions and the geotechnical centrifuge modelling test.

The horizontal plate anchor is used to resist the uplift forces acting on structures such as transmission towers, foundations and so on. Anchor geometry, embedded depth, local soil conditions, etc. have been recognized as major factors affecting the behaviour of the soil around the anchor. Large-scale field tests (Sutherland, 1988), small-scale model tests (Ilamparuthi et al., 2002; Vesic, 1971), numerical methods (R. K. Rowe & Davis, 1982; Sakai & Tanaka, 2007) and analytical solutions (Baker & Konder, 1966; Meyerhof & Adams, 1968a; Murray & Asce, 1987) have been adopted by different researchers for the investigation of soil deformation behaviour under different conditions.

Despite the extensive research performed by many researchers, discrepancies between model prediction and the actual measurement still exist, indicating that a full understanding of the interaction between the plate anchor and the surrounding soils is necessary. The embedment ratio, which is defined as the embedment depth of the anchor to the width of the anchor, classifies the horizontal plate anchor into shallow anchor and deep anchor. If the embedment ratio is less than a certain value, the failure surface can extend to the ground surface. This situation is referred to as the shallow anchor condition. Beyond this certain value, the failure surface does not extend to the ground surface. Instead, a localized shear failure with a flow-around mechanism occurs. This situation is referred to as the deep anchor condition. The critical embedment ratio is a function of soil friction angle (Das & Shukla, 2013; Ilamparuthi & Muthukrishnaiah, 1999; Meyerhof & Adams, 1968a).

Failure surfaces presented by previous studies can be primarily classified into three failure modes: the first mode, which is proposed by Majer in 1955, considers the failure surface as a frictional cylinder; the second mode, which is proposed by Mors in 1959, considers the failure surface as a truncated cone extending from the anchor edge with an apex angle of $90°+\phi$, where ϕ is the soil friction angle; the third failure mode, which is proposed by Balla in 1961 and Baker and Kondner in 1966, considers the failure as it occurs along an arc of a circle. This theory considers that the failure surface extends from the anchor edge and intersects with the ground surface at an angle of approximately $45° - \phi/2$ (Das & Shukla, 2013).

For a shallow plate anchor, from the plate up to a certain height, the vertical displacement of soil particles is greater than that of the plate. Beyond this height, the vertical displacement of soil particles is less than that of the plate. For a deep plate, the vertical displacement of soil particles decreases rapidly with the increase of distance from the plate. The rupture surface of a deep anchor consists of two parts: the first part is a plane surface emerging from the top edge of the plate and extends to a certain depth within the sample; the second part emerges from the end of the plane surface, bulges radially and forms a "balloon" shaped cap, as shown in Figure 2-9 (Ilamparuthi et al., 2002).

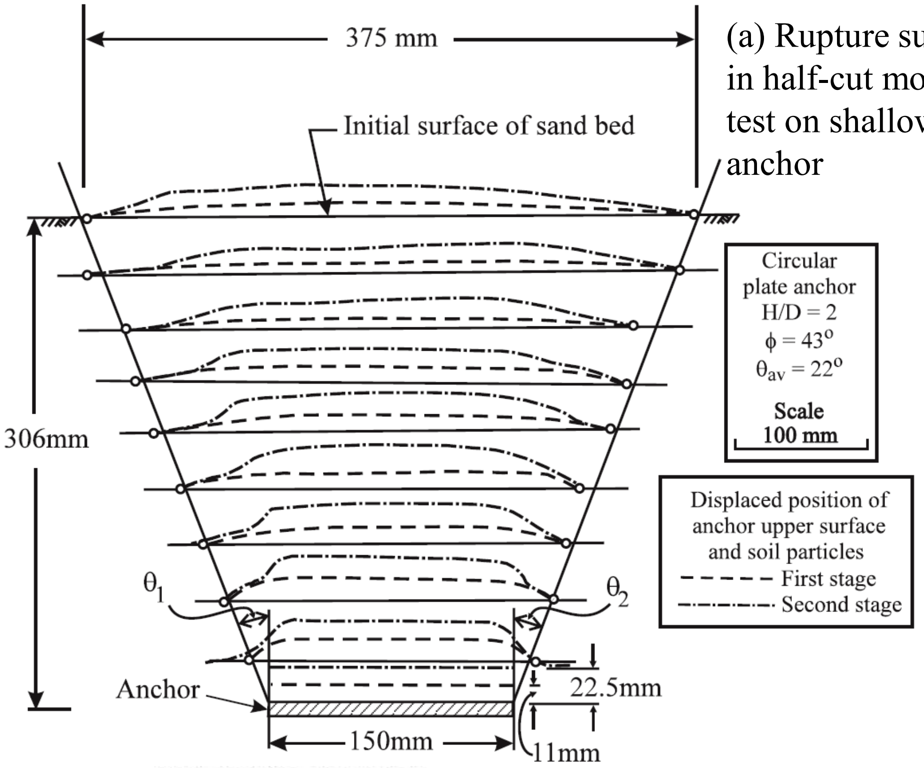

(a) Rupture surface in half-cut model test on shallow anchor

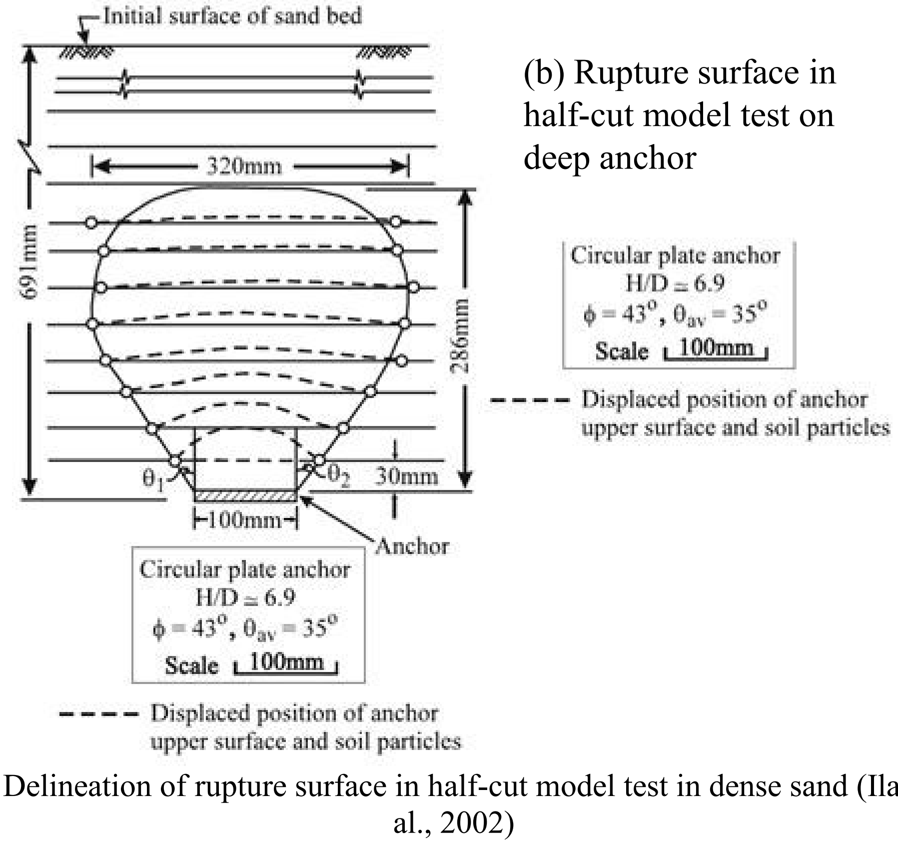

(b) Rupture surface in half-cut model test on deep anchor

Figure 2-9 Delineation of rupture surface in half-cut model test in dense sand (Ilamparuthi et al., 2002)

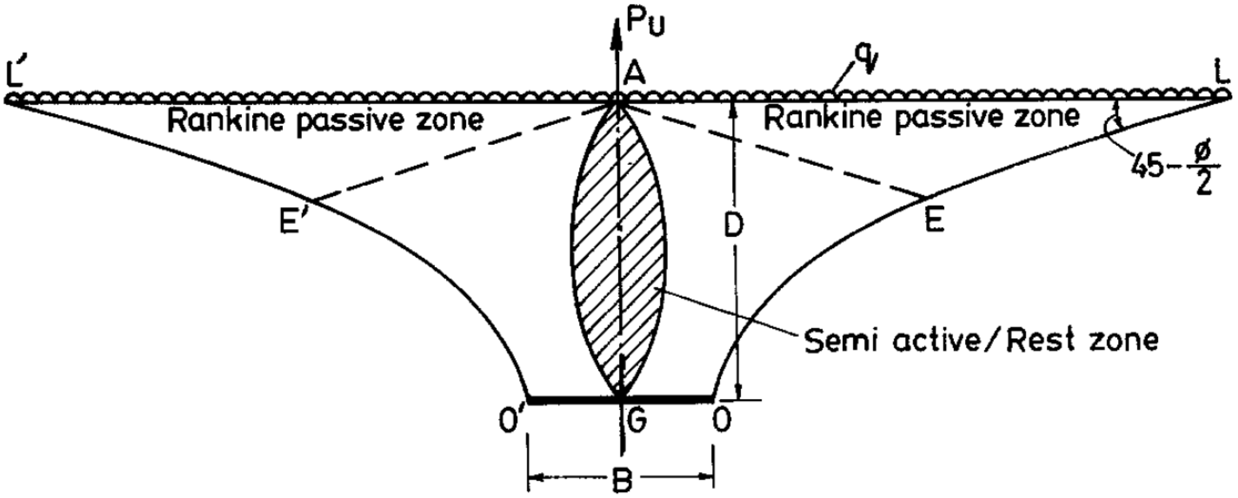

Figure 2-10 Failure mechanism induced by the uplift movement of horizontal plate anchor
(Rao & Kumar, 1994)

Uplift force changes in-situ stress distribution in various regions around the affected soil (Rahmati et al., 2014; Thorne et al., 2004). When the shear failure occurs, earth pressure in the vicinity of the footing slab could be at the semi-active condition while that near the ground surface could be Rankine passive earth pressure, as shown in Figure 2-10 (Matsuo, 1967; K. S. S. Rao & Kumar, 1994). As the uplift forces commence, a very small relative deflection can result in a significant change in the vertical pressure on the trap door (Mcnulty, 1965). Consequently, this uplift force can lead to surface heave, resulting in the decrease of horizontal stresses and eventually leading to the occurrence of tensile stresses or tensile failure (Thorne et al., 2004).

Although extensive research is available for the investigation of the soil uplifting behaviour under various conditions, most of these studies focus on the final shape of the failure planes. The lack of tracking the soil failure process can lead to discrepancies between the model prediction and the actual measurement.

Liu, Liu, and Zhu (2012) adopted DIC (digital image correlation) to track the soil deformation around an uplift plate anchor in sand. The researchers performed a series of model tests to study the influence of soil particle size, soil density, and anchor embedment depth on the soil deformation behaviour. The soil density can significantly affect the anchor displacement at the peak pullout resistance (δ_p), while the particle size has minimum influence on the value. The denser the sand is, the smaller the anchor displacement at the peak pullout resistance is. Moreover, the peak pullout resistance in dense sand is more than double that in loose sand. In loose sand, if the embedment ratio is 1, a cylindrical influence zone occurs. As the embedment depth increases, the deformation mainly occurs within a bulb-shaped zone extending from the anchor edge. In dense sand, the failure zone can be described as a truncated cone extending from the anchor edge to the ground surface. The experimental results reveal that the soil density rather than the soil particle size can significantly affect the soil deformation behaviour. By comparing experimental results with those from other studies, the researchers find that the results coincide well with other studies and conclude that the influence of the interface between the anchor and the Perspex glass window on the failure planes and the anchor displacement at the peak pullout resistance is negligible.

2.4.3 Buried pipe

Oil and gas from offshore production plants are usually transported to the mainland through buried pipelines. The high temperature-high pressure (HPHT) fluid inside the pipeline causes axial thermal expansion, resulting in the possibility of either vertical or lateral buckling. The widely seen problem is the upheaval buckling in the vertical direction as the high passive resistance in the horizontal direction can effectively resist the lateral buckling. Numerous researchers have performed model tests and analytical/numerical analysis to investigate the uplift capacity and the corresponding failure mechanism of the buried pipe (Berghe et al., 2005; Schupp et al., 2016; Trautmann et al., 1985; White et al., 2001).

Based on the experimental, analytical and numerical studies performed by different researchers, the failure mechanisms of the buried pipe can be primarily classified into three failure modes: the commonly used failure mode is the vertical slip failure mechanism; the second failure mechanism is based on the experimental observation, it considers that the failure surface of the medium to dense soils with shallow buried pipe can be approximately expressed by an inclined slip surface model (Thusyanthan et al., 2010), the failure mechanism of loose sand or initially dense sand with deep buried pipe is a localized shear with a flow around mechanism (Berghe et al., 2005; White et al., 2001). Many researchers point out that the inclination of the shear band is approximately equal to the dilation angle (Berghe et al., 2005; White et al., 2001).

By adopting GeoPIV which is a novel image-based deformation measurement technique, White, Cheuk, and Bolton (2008) performed a series of physical modelling tests to investigate the effect of the soil particle size and density on the uplift response of the buried pipe. This study reveals that soil density can significantly affect the inclination of the distributed shear zone. The inclination of the distributed shear zone to the vertical of the dense sand is obviously larger than that of the loose sand. The soil grain size can affect the infilling mechanism and the width of the shear zones, but the peak uplift resistance is independent of the soil grain size.

2.4.4 Uplifting velocity

The deformation behaviour of the soil surrounding the horizontal plate anchors embedded in clay is not only affected by the suction developed at the anchor/clay interface but also the uplifting velocity, which can significantly affect the drainage condition. With the increase of the uplifting velocity, the pore water may be drained, partially drained and fully undrained. Experimental results through the penetration resistance show that the mobilized drained soil strength is higher than that of the undrained soil strength in normally consolidated kaolin clay. A dimensionless velocity of the anchor plate, $V=\frac{vB}{c_v}$ is used, where v is anchor velocity, c_v is coefficient of consolidation, and B is width of plate anchor, as shown in Figure 2-11 (Han et al., 2016).

Time effect can also significantly affect soil uplift behaviour. Experimental results by Meyerhof and Adams in 1968 reveal that the uplift capacity under sustained load in clay is less than that under short-term conditions. In stiff clays, the long-term capacity is only a small fraction of the short-term capacity. However, in soft clay, the long-term capacity is a much higher fraction of the short-term capacity (Meyerhof & Adams, 1968b).

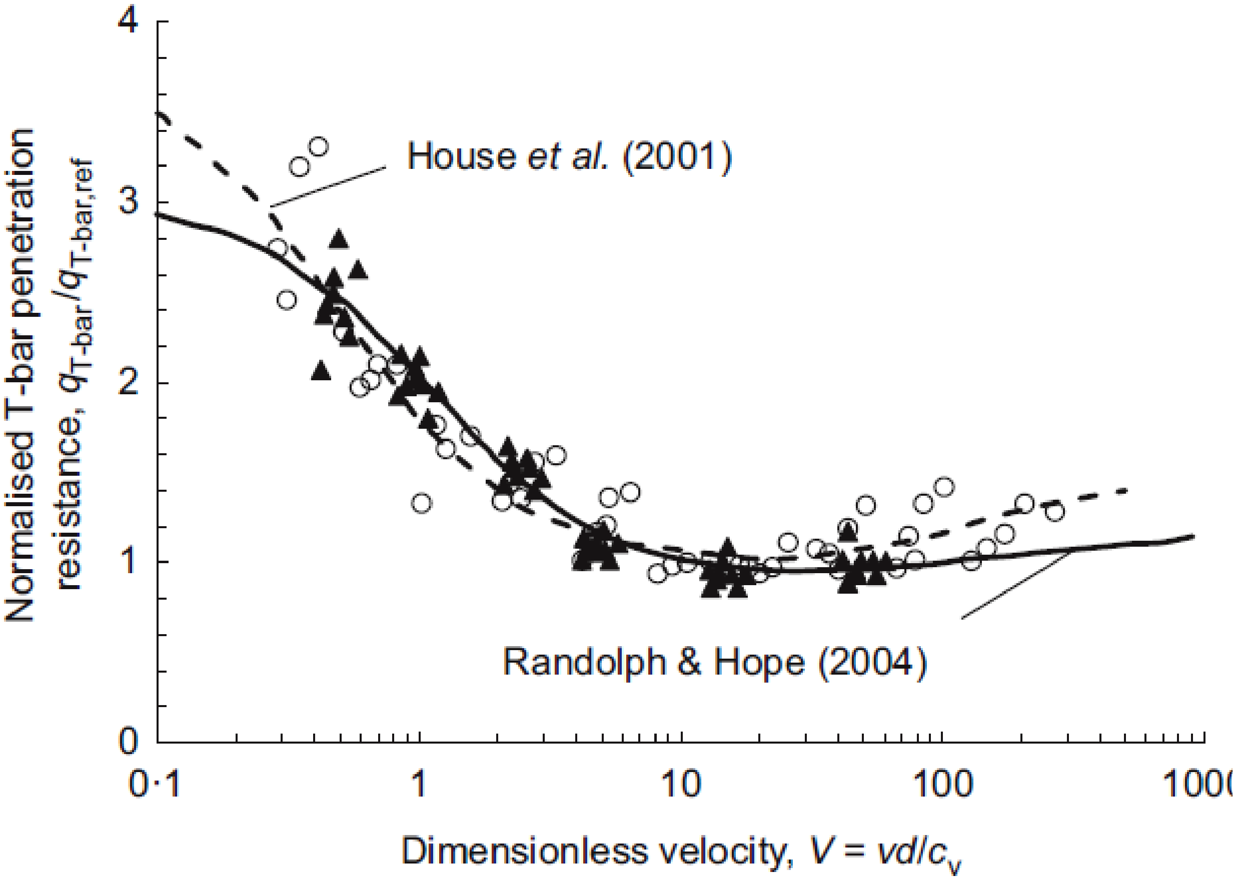

Figure 2-11 Normalized T-bar resistance variation with dimensionless velocity (Han et al., 2016)

2.5 Caprock integrity assessment

Assessing operating data in other mature analogue projects has been considered the most reliable way for assessing the effectiveness of a formation as a caprock (Collins et al., 2013). During the SAGD process, firstly the elevated pore pressure front followed by the high temperature front will reach the base of the caprock prior to arrival of the steam chamber itself. The pore pressure and temperature changes can alter the physical and mechanical properties of the shale barrier potentially resulting in the formation of the micro-fractures, an increase in permeability and compromised caprock hydraulic integrity. With the expansion of the steam chamber, the steam can eventually reach the shale barrier. The condensed water accumulates in these micro-fractures, softening the shale barrier and decreasing cohesion as well as internal friction angle (Collins, 2007; Khan et al., 2011; Rahmati, 2016).

In a SAGD operation, numerous processes such as thermal expansion, shearing and tensile fracturing, pore pressure change and dilation can occur (Uwiera-Gartner et al., 2011). These processes may change material properties and the initial stress state, and induce caprock deformation and surface heave (Azad & Chalaturnyk, 2011).

Assessment of caprock integrity is essentially composed of four parts: caprock geological studies, in-situ stress assessment, constitutive property characterization, and numerical simulation (Shafie Zadeh & Chalaturnyk, 2015). It is generally achieved through reservoir geomechanical simulations combined with results from in-situ test and laboratory-measured material properties (Azad & Chalaturnyk, 2011; Walters et al., 2012; Yuan et al., 2013). Recent efforts in surface heave monitoring combined with pore pressure and temperature observations greatly contribute to the validity of these modelling efforts, but significant uncertainty still remains concerning the failure mechanisms within the caprock zones (Collins, 1994; M. B. Dusseault, 2009; Gu et al., 2011).

The derivation of caprock deflection induced by the CO_2 injection considers the caprock as a thin plate sandwiched between the CO_2 storage region and the overburden region. Compared with the radius of the pressurized zone, the caprock thickness is a relatively small value and therefore can be simplified as a thin plate (C. Li et al., 2015; Selvadurai, 2009). Simplifying the geologic formation as thin plates not only provides convenience for theoretical analysis but also makes possible the experimental investigation. Papamichos, Vardoulakis, and Heil (2001) simplified the hydrocarbon reservoir as a thin plate for the investigation of the effect of the reservoir compaction on the stress redistribution in the reservoir and the overburden.

2.6 Geotechnical centrifuge modelling

Centrifuge modelling has been considered one of the most important developments in geotechnics (Ng, 2014). Over the past few decades, it has been successfully used in practice to tackle complex geotechnical problems (Nomoto et al., 1999; Feng and Yin, 2014; Ling et al., 2009). The numerous applications of the geotechnical centrifuge can be categorized into four types: investigation of new phenomena, modelling of prototypes, validation of numerical methods and parametric studies (Ko & Craig, 1988).

It is well-known that stress level and stress history are the two main factors affecting soil behaviour (Abdulhadi, 2009; Ti et al., 2009; Wood, 1991). The biggest advantage of the geotechnical centrifuge is its ability to replicate the self-weight stresses and the stress-dependent processes. A $1/N$ scaled sample would be placed in the swing cradle that is suspended from the ends of a pair of tubular arms. While the centrifuge is spinning, the swing cradle rotates from the vertical direction to the horizontal direction parallel to the tubular arms in a short time. The high centripetal acceleration provides the $1/N$ scaled sample with an acceleration field of magnitude n times stronger than Earth's gravity. Therefore, the vertical stress in the model at depth h_m, $\rho N g h_m$, where

ρ is the sample density, will be identical to that in the corresponding prototype at depth $h_p=Nh_m$. Scaling law, which is the connection between the geotechnical models under centrifugal acceleration and the prototype under Earth gravity, are used to maintain the similarity between the model and the prototype, and to extrapolate test results to practice design (Taylor, 2005).

The scale factor for time of consolidation/seepage is $1:N^2$, while that for the dynamic event is $1:N$. Some researchers ascribe the conflict of the scaling laws to the reduced model size, which shortens flow path of pore water, thus leading to the reduction of consolidation time (Taylor, 2005).

Experimental conditions such as the interface friction and adhesion between the soil sample and the container can also affect experimental results. It may induce pressure deficiency at the base of the container (Mitchell & Liang, 1986). Commonly adopted methods to reduce side friction effects are increasing the width-to-height ratio or lubricating the internal sidewall of the container with a lubricant such as high-viscosity silicon oil. Additionally, this side effect can be reduced in centrifuge tests due to the interaction between the curved vertical stress and the side friction effect (Moo-young et al., 2003; P. W. Rowe, 1971).

2.7 Development of synthetic soils

Reconstituted Speswhite kaolinite clay, which was used for initial caprock integrity centrifuge modelling tests, is far too weak to represent the behaviour of Clearwater shale (Wu, 2015). Therefore, it is essential to develop a suitable synthetic soil that can appropriately capture the behaviour of Clearwater shale for the physical modelling test.

A summary of previous studies provides valuable guidance for the development of model material (Stimpson, 1970). Johnston and Choi (1986) developed a synthetic soft rock to predict the behaviour of the Melbourne mudstone under external forces or displacement. The principal component of the synthetic soft rock is reconstituted mudstone, while ordinary Portland cement is chosen as the cementing agent. Tavenas, Roy, and Rochelle (1973) developed a synthetic material to model mechanical properties of the Champlain clay. This synthetic soil is a mixture of kaolinite, bentonite, Portland cement, and water. These studies not only contribute to the design of a test plan for making synthetic soil but also provide detailed information about the procedure of making the synthetic soil.

The concept of mixing cement with soft clay to improve soil strength has been widely recognized by researchers around the world (Cuccovillo & Coop, 1997; Haralambos, 2009; Horpibulsk et al., 2011; Horpibulsuk et al., 2003; Rotta et al., 2003). Some researchers point out that there exists an optimum clay water content at which the strength of the cement-treated soil reaches the highest value at a given cement content. Figure 2-12 and Figure 2-13 describe the relationship between the unconfined compressive strength and the normalized water content defined as the ratio of the total clay water content (w_c) to the liquid limit (LL). These figures point out that the optimum clay water content is between the liquid limit and 1.2 times the liquid limit irrespective of the cement content (Bergado & Lorenzo, 2005; Lorenzo, G. A. & Bergado, 2004).

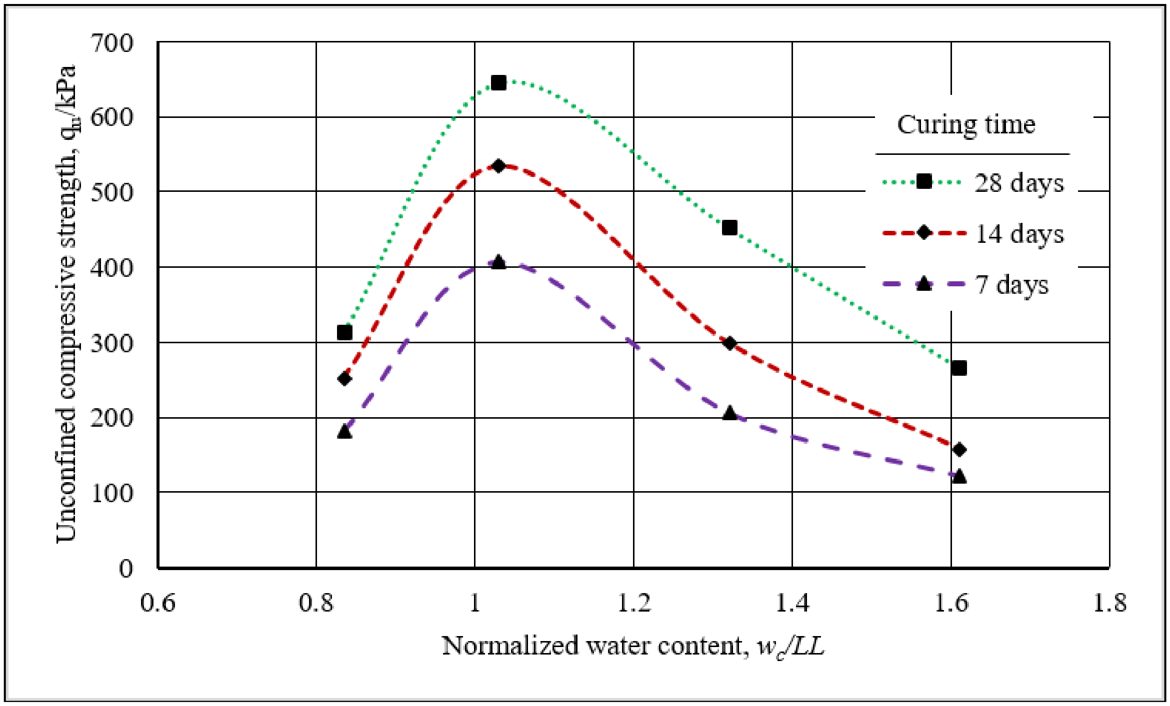

Figure 2-12 Effect of water content on the unconfined compressive strength (Lorenzo, G. A. & Bergado, 2004)

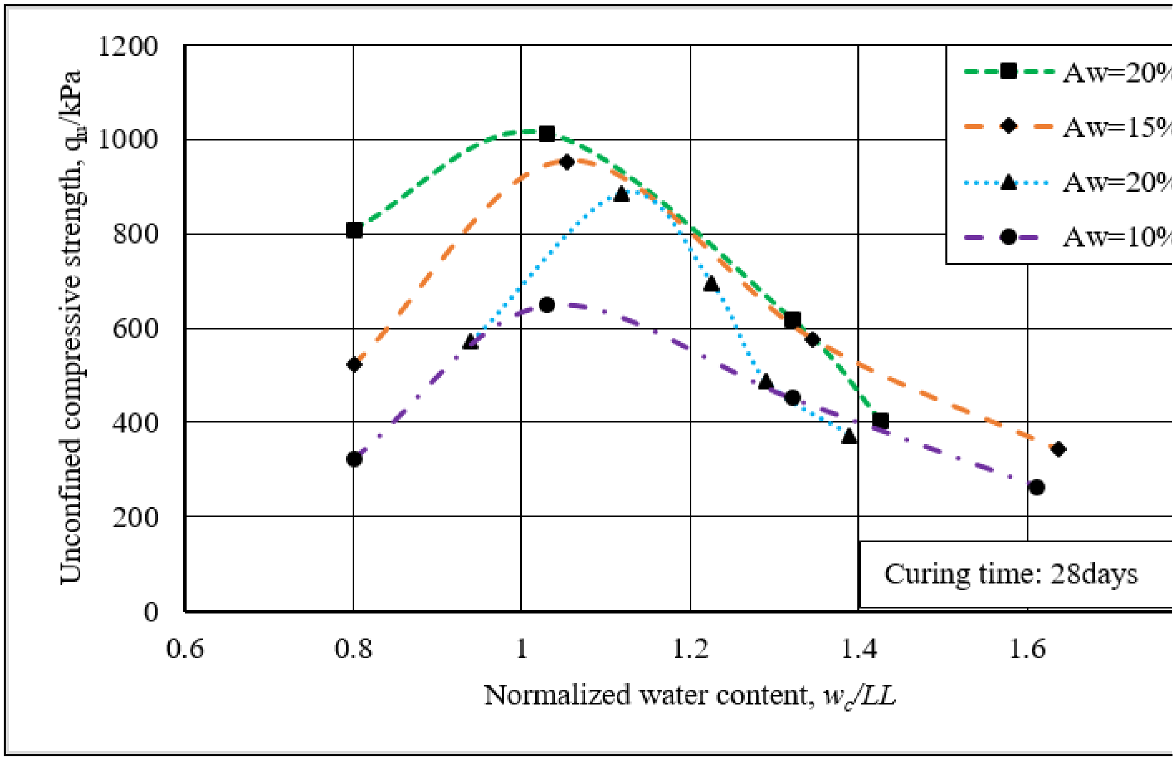

Figure 2-13 Effect of water content on the cement-treated soil strength. A_w is cement content defined as the percentage ratio of weight of cement powder to the weight of dry soil (Bergado & Lorenzo, 2005).

Miura N. et al. (2001) proposed a clay-water/cement ratio defined as the ratio of the total soil-water content to the cement content to reflect the effect of the water content and the cement content on cemented soil strength. The higher the clay-water/cement ratio is, the lower the soil strength is (Miura et al., 2001).

Terashi (1997) proposed that factors affecting strength development of cement-treated soil could be divided into four categories: I. Characteristics of binder, II. Characteristics and conditions of soil, III. Mixing condition, IV. Curing condition, as presented in Table 2-1 (Babasaki et al., 1997). Kitazume and Terashi give a comprehensive summary of studies that present factors affecting cement-treated soil strength. The book, *The Deep Mixing Method*, quantitatively demonstrates the relationship between those factors and the stabilized soil strength (Kitazume & Terashi, 2013).

Table 2-1 Factors affecting cement-treated soil strength (Babasaki et al., 1997)

I. Characteristics of binder	1. Type of binder 2. Quality 3. Mixing water and additives
II. Characteristics and conditions of soil (especially important for clays)	1. Physical, chemical and mineralogical properties of soil 2. Organic content 3. Potential Hydrogen (pH) of pore water 4.Water content
III. Mixing conditions	1. Degree of mixing 2. Timing of mixing/re-mixing 3. Quantity of binder
IV. Curing conditions	1. Temperature 2. Curing period 3. Humidity 4.Wetting and drying/freezing and thawing, *etc.* 5. Overburden pressure

2.8 Summary

Undoubtedly, geotechnical centrifuge modelling is a valuable tool in tackling complex geotechnical problems. However, this technique has never been adopted by researchers in identifying the caprock failure mechanism.

From the perspective of geotechnical engineering, the steam release incident of the Joslyn Creek SAGD project is mainly induced by the accumulated water beneath the Clearwater shale barrier. As the SAGD process goes on, the pressurized zone expands, uplifts the caprock, and eventually leads to the failure. The reports provided by Total E&P Canada also describes that the failure plane can eventually extend to the ground surface as the dimension of the pressurized zone enlarges. Burial depth, dimensions of pressurized zone, caprock thickness and strength, pay zone thickness, injection pressure of the steam and the stress changes induced by the thermal jacking are considered major factors controlling the caprock integrity.

In general, caprock integrity assessment is achieved through either the numerical simulation approaches, which is then verified through the field test or the operating data in other mature analogue projects. Although field data greatly contribute to the validation of the numerical modelling results, significant uncertainty concerning the caprock failure mechanism remains unknown. At the same time, simplifying the caprock as a thin plate has made the calculation easy and efficient.

Although literature related to the caprock deformation behaviour induced by the uplift force is rarely seen, there are numerous studies pertaining to the soil deformation behaviour induced by the uplift force in geotechnical engineering. To strengthen the understanding of the caprock failure mechanism, collecting and analyzing this literature becomes essential, such as has been done by the studies on horizontal plane anchor, trap door, buried pipe, etc. The factors affecting soil deformation behaviour and the definition of the failure planes greatly contribute to the study of caprock deformation behaviour.

One of the challenges of this study is to make synthetic Clearwater shale for the physical modelling test. The adoption of synthetic soil/rock for physical modelling tests is commonly seen in geotechnical engineering. However, the problem is in choosing suitable components for the synthetic Clearwater shale. Moreover, the Clearwater shale has relatively high cohesive strength, indicating that a bonding agent may be needed to create cementitious bonds between soil particles. The literature presented by other researchers provides valuable guidance for the preparation of synthetic Clearwater shale. Moreover, the wide application of cement has made the factors controlling the strength development of cement-treated soil clear.

Chapter 3 Background and Application of Centrifuge Modelling for Caprock Integrity

3.1 Introduction

Physical modelling tests can be troublesome because the model materials and setup must be prepared with great effort and are time-consuming when compared with conventional tests such as the triaxial test or the direct shear test. This may be one of the reasons that centrifuge modelling is not commonly considered in geotechnical practice. Therefore, it becomes essential to introduce the basic information of the technology prior to discussing the experimental results of the centrifuge modelling test.

In short, the objective of this chapter is to elucidate the technology and its primary application in the identification of the caprock failure process. This chapter includes three parts:

1. The first section briefly introduces the centrifuge facility, the major components of the experimental package, and the procedure of preparing the model and conducting the centrifuge test.
2. The second section presents the consolidation behaviour of the Speswhite kaolin clay; and
3. The third section presents the experimental results of the geotechnical centrifuge modelling test by using the consolidated Speswhite kaolin clay as the synthetic Clearwater shale. The analysis of the experimental results reveals that the consolidated Speswhite kaolin clay is too soft to represent the Clearwater shale.

3.2 Principle of geotechnical centrifuge modelling

Vertical stress is equal to the product of soil density, burial depth and Earth-gravity. Therefore, there are two ways to replicate the in-situ stress state in a small-scale sample. The first method is to increase the Earth's gravity while the other is to increase the soil density. Changing the soil density indicates that the material properties may be different from those of the prototype material, producing unreliable results. Under this circumstance, increasing the Earth's gravity is the best choice.

The original purpose of the geotechnical centrifuge was to recreate the self-weight body forces that exist in a prototype in a small-scale sample subjected to a high acceleration field. Two approaches can achieve this goal. The first method involves the acceleration motion along a straight line. The second method is the circular motion, which is the theoretical basis of geotechnical centrifuge modelling.

Soil samples placed in the swing cradle suspended from the ends of a pair of tubular arms will spin at high speed to increase the g-force so that the self-weight stress in the model is identical to that in the prototype. Compared with the in-situ test, the geotechnical centrifuge modelling test has the advantage of high efficiency and low cost. Meanwhile, the geotechnical centrifuge tests supply data for understanding deformational behaviour of complex geotechnical problems and are widely considered to be benchmarks useful for the verification of the numerical modelling results.

As shown in Figure 3-1, the model is being rotated around a fixed axis known as the rotation shaft, resulting in the centrifugal force perpendicular to the rotation shaft. To create a stable acceleration field, the rotation shaft should be parallel to the direction of the Earth's gravity. Otherwise, the acceleration and the velocity of the object changes with the object's position.

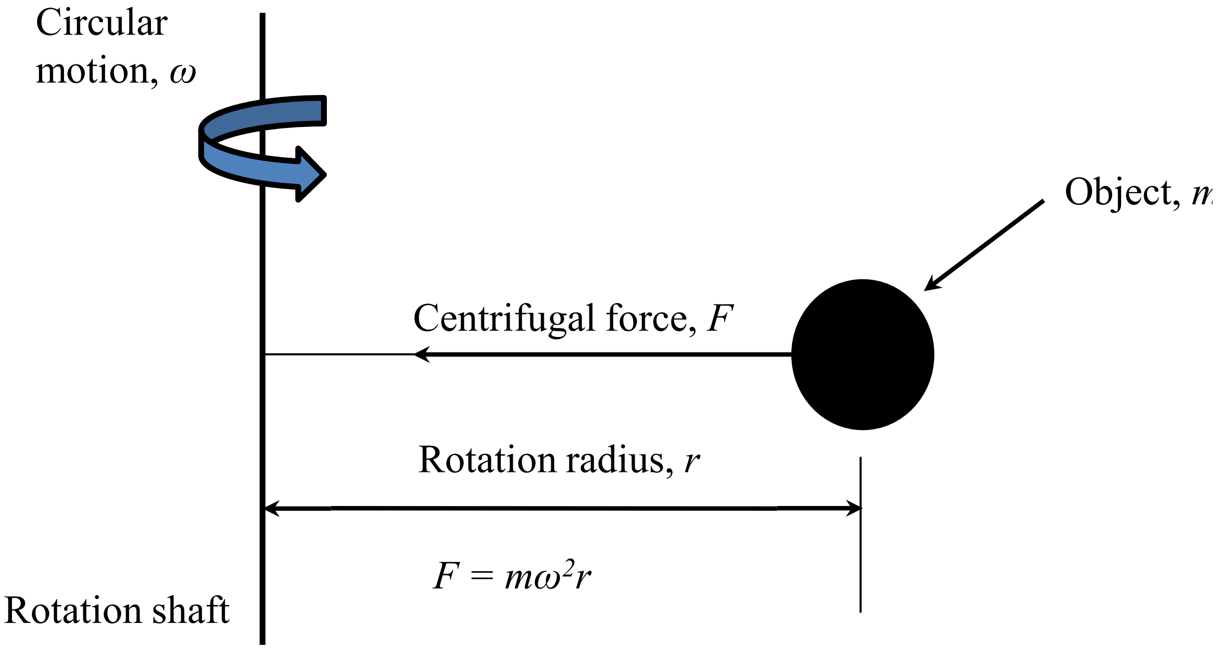

Figure 3-1 Schematic diagram of the uniform circular motion

According to Newton's second law: *In an inertial reference frame, the vector* sum *of the forces F on an object is equal to the mass m of that object multiplied by the acceleration aof the object: F = ma*, an external force commonly known as centrifugal force, which points to the rotational axis, is needed to maintain the motion.

$$F = ma = m\omega^2 r = m\frac{v^2}{r} \qquad \text{Equation (3-1)}$$

The centrifugal acceleration induced by the centrifugal force can be many times stronger than the Earth's gravity and is expressed as below:

$$a = \omega^2 r = \frac{v^2}{r} = Ng \qquad \text{Equation (3-2)}$$

where ω, v and r are angular velocity, tangential velocity and effective radius of the centrifuge facility arm, respectively.

As shown in Figure 3-2, the samples in the swing cradle are suffering an Ng gravitational field. At the top of the sample, vertical stress is zero if there is no overburden on the sample. At depth H_m, vertical stress is equal to ρNgh_m which corresponds to the vertical stress of the prototype at depth $H_p = NH_m$.

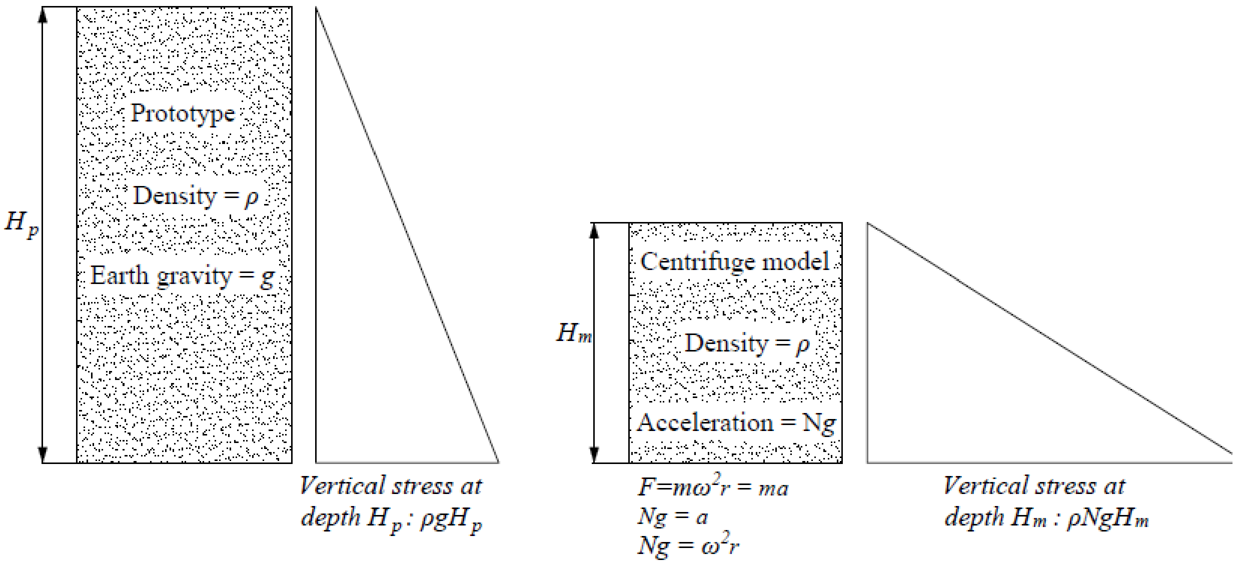

Figure 3-2 Principle of geotechnical centrifuge modelling

The principle of the geotechnical centrifuge modelling supports centrifuge facilities being a powerful tool for the study of these geotechnical problems highly dependent upon the Earth's gravity, such as the slope stability, self-weight consolidation, horizontal plate anchor, groundwater contaminant migration, etc. In practice, the soil/rock self-weight is the driving force of many geotechnical problems. As the engineering activities change the original topography, the in-situ stress state also changes and results in stress redistribution. During this process, the stress concentration at certain points may exceed the material yield criteria and eventually leads to failure.

3.3 Scaling laws

Experimental results of the geotechnical centrifuge modelling tests are extrapolated to the prototype situation through scaling laws, which describe the similarity between the prototype and the model. In 1951, Henry L. Langhaar proposed that three similarities—geometric similarity, kinematic similarity and dynamic similarity—should be fulfilled in order to achieve a strict similitude (Langhaar, 1951).

Geometric similarity requires that the ratio of the physical dimensions in the model to the corresponding dimensions in the prototype should be constant. For example,

$$\frac{L_m}{L_p} = \frac{R_m}{R_p} = \frac{\phi_m}{\phi_p} = \frac{1}{N} \qquad \text{Equation (3-3)}$$

$$\frac{A_m}{A_p} = \frac{1}{N^2} \qquad \text{Equation (3-4)}$$

$$\frac{V_m}{V_p} = \frac{1}{N^3} \qquad \text{Equation (3-5)}$$

where the subscript *m* and *p* represent the model and the prototype, respectively; *L*, *A* and *V* represent the length, area and volume of an objective, respectively; *N* represents the scale factor.

Kinematic similarity requires the similarity of motion between the model and the prototype. It means that the particle flow direction at a certain point in the model should be the same as that in the prototype. The ratio of the particle's velocity in the model to that in the prototype should be a constant for all the particles. At the same time, the ratio of the particle's acceleration to that in the prototype should also be a constant for all the particles.

$$\frac{v_m}{v_p} = v^* \qquad \text{Equation (3-6)}$$

$$\frac{a_m}{a_p} = a^* \qquad \text{Equation (3-7)}$$

where v and a represent the velocity and the acceleration, respectively; v^* and a^* represent the scale factor.

Table 3-1 Common scale factors for centrifuge tests

Parameter	Scale factor (model/prototype)
Length (linear dimension)	$1/N$
Area	$1/N^2$
Volume	$1/N^3$
Acceleration	N
Stress	1
Strain	1
Density	1
Unit weight	N
Force	$1/N^2$
Time (dynamic)	$1/N$
Time (consolidation/diffusion)	$1/N^2$
Time (creep)	1
Pore fluid velocity	N
Velocity (dynamic)	1

Dynamic similarity requires the similarity of forces between the model and the prototype. It means that not only the direction of the forces acting on the geotechnical model should be the same as that in the prototype but also the ratio of the forces acting on the geotechnical model to that on the corresponding point in the prototype should be a constant:

$$\frac{F_m}{F_p} = F^* \quad \text{Equation (3-8)}$$

where F represents forces acting on the model or prototype; F^* represents the scale factor.

These three similarities (geometric, kinematic and dynamic) form the foundation of the scaling laws. Before deducing the centrifuge scaling laws, it is worth noting that the objective of the geotechnical centrifuge is to create the stress state of the prototype in a small-scale sample, indicating that the stress scale factor defined as the ratio of the stress in the model to the stress in the prototype should be equal to 1. Table 3-1 lists the scale factors of the geotechnical centrifuge modelling. Obviously, the time scale factor for consolidation/diffusion is quite different from that for the dynamic condition. The major reason for the conflict can be attributed to the fact that the driving force of the consolidation/diffusion in the model is different from that in the prototype.

3.4 Conflict of scaling laws

Table 3-1 shows the classic scaling laws widely adopted by researchers for the geotechnical physical modelling test. Obviously, the scale factor of time for the dynamic events is quite different from that for the consolidation/diffusion events. Many researchers have attempted to determine the root cause of the conflict, but the controversy remains. By summing up the research pertaining to the scaling laws and the similitude questions, Garnier et al. (2007) published a paper that clearly demonstrated recent developments in scaling laws. Thusyanthan and Madabhushi (2003) explained the reason leading to the conflict of the scaling laws. The researchers found that the water pressure difference of the model was the same as that of the prototype, but the flow path of the model was *N* times shorter than that of the prototype. The derivation is described as below:

Based on Darcy's law, the total head difference is the driving force of the fluid motion in the porous media:

$$v = ki \qquad \text{Equation (3-9)}$$

Where v is discharge velocity; k is the coefficient of permeability or Darcy's permeability; i is the hydraulic gradient.

The coefficient of permeability or Darcy's permeability can be expressed as below:

$$k = \frac{K\rho g}{\mu} \qquad \text{Equation (3-10)}$$

where K is intrinsic permeability (m^2 or cm^2), a parameter depending on soil physical properties, such as soil particle shape, diameter and packing; μ is the absolute viscosity of the fluid; ρ is fluid density; g is Earth's gravity.

The hydraulic gradient is defined as the ratio of the total head difference to the distance of the flow path.

$$i = \frac{\Delta H}{\Delta L} \qquad \text{Equation (3-11)}$$

where ΔH is the total head difference along the flow path; ΔL is the distance of the flow path.

The implicit result of Darcy's experiments is that the hydraulic gradient is the driving force of the water seepage. If the hydraulic gradient equals zero, there will be no water seepage.

$$v = ki = \frac{K\rho g}{\mu} \cdot \frac{\Delta H}{\Delta L} = \frac{K}{\mu} \cdot \frac{\rho g \Delta H}{\Delta L} \qquad \text{Equation (3-12)}$$

Based on the principle of the centrifuge modelling test (or dynamic similarity), vertical stress in the model is identical to that in the prototype. Therefore, the water pressure difference in the model $\rho(Ng)\left(\frac{\Delta H}{N}\right)$ is identical to that in the prototype $\rho g \Delta H$.

Based on geometric similarity, the total head difference ΔH in the prototype is N times larger than that in the model $\frac{\Delta H}{N}$. Flow path distance in the prototype ΔL is N times larger than that in the model $\frac{\Delta L}{N}$.

Therefore, the discharge velocity in the model can be expressed as below:

$$v_m = \frac{K}{\mu} \cdot \frac{\rho(Ng)\left(\frac{\Delta H}{N}\right)}{\left(\frac{\Delta L}{N}\right)} = \frac{K}{\mu} \cdot \frac{\rho g \Delta H}{\left(\frac{\Delta L}{N}\right)} \qquad \text{Equation (3-13)}$$

The discharge velocity in the prototype can be expressed as below:

$$v_p = \frac{K}{\mu} \cdot \frac{\rho g \Delta H}{\Delta L} \qquad \text{Equation (3-14)}$$

Theoretically, discharge velocity in the model should be identical to that in the prototype. However, the abovementioned analysis points out that discharge velocity in the model is N times larger than that in the prototype. This is the main reason leading to the conflict of the scaling laws.

3.5 Advantages and disadvantages of geotechnical centrifuge modelling

There is no perfect approach to a geotechnical problem from the perspective of quality and reliability of the results, cost and efficiency. This is the major reason why many geotechnical problems are explored through several approaches such as field monitoring, numerical simulation, and geotechnical centrifuge modelling. Results from different approaches are complementary with each other. As shown in Figure 3-3, both the in-situ test and centrifuge modelling can provide calibration for numerical modelling.

It is known that soil behaviour is dependent upon the stress state and stress path, implying that the experimental results from the approaches that can recreate the stress state and stress path are powerful tools in geotechnical engineering. Geotechnical centrifuge modelling, which is an advanced technique for tackling complex geotechnical problems, is the most efficient way to recreate stress conditions that exist in a prototype.

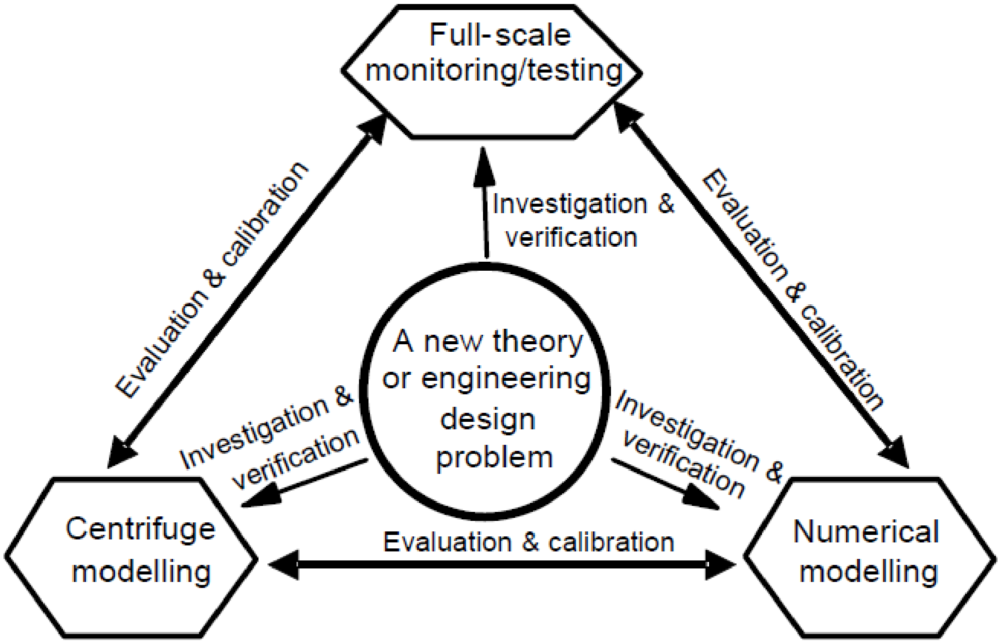

Figure 3-3 Relationship between in-situ test, numerical modelling and centrifuge modelling (Ng, 2014)

Several advantages of this technique have made it widely accepted by geotechnical engineers:

- Compared with a conventional method such as the triaxial test, geotechnical centrifuge modelling test adopts large-scale samples.
- Compared with full-scale field monitoring, geotechnical centrifuge modelling test is cost effective and efficient. Most importantly, it could take into account the major factors affecting geotechnical problems and to eliminate those possible uncertainties encountered in the field.
- The material properties, boundary conditions and ground conditions of the geotechnical centrifuge modelling tests are known, indicating that the experimental results can be used with confidence to calibrate numerical modelling results.

Over the past few decades, numerous cases have proven that this technique is a valuable tool to complement numerical analysis and field monitoring. At the same time, the rapid development of technologies in the centrifuge equipment and the data acquisition system has made it possible to explore more complex geotechnical systems such as the caprock failure process, earth structures, and geoenvironmental studies.

However, as described previously, there is no perfect universal approach to studying geotechnical problems. The geotechnical centrifuge creates an artificial gravity field that is many times stronger than the Earth's gravity. Theoretically, the artificial gravity field should be as close to the Earth's gravity field as possible, and the magnitude should keep unchanged while the direction should be normal to the model surface. However, the artificial gravity field of the geotechnical centrifuge is created based on the theory of the uniform circular motion, indicating that the magnitude and the direction of the artificial gravity changes with position.

Based on the principle of the geotechnical centrifuge, the centripetal acceleration is a function of the angular velocity ω and the radius r, and r is the distance between the element and the rotation shaft. As shown in Figure 3-4, the rectangle $C_1B_1B_2C_2$ represents the model placed in the swing cradle. The model is spun in the centrifuge facility with an angular velocity of ω. For a random arc in the model such as $\widehat{BC}$, the elements on the arc have the same magnitude of the centrifugal force, but the direction of the force points to the point O. Based on the relationship between the vertical stress in the model and the centrifugal force, it is evident that the equipotential line of the vertical stress is not a horizontal line as that in the prototype. Instead, it is a circle with the centre at the rotation shaft. Therefore, the vertical stress distribution through the model depth is not linear but rather a parabolic curve. The vertical stress in the prototype can be expressed as below:

$$\sigma_{vp} = \rho g h_p = \rho N g h_m \qquad \text{Equation (3-15)}$$

The vertical stress in the model can be expressed as below:

$$\sigma_{vm} = \int_0^z \rho\omega^2 (R_t + z)\, dz = \rho\omega^2 z \left(R_t + \frac{z}{2}\right) \qquad \text{Equation (3-16)}$$

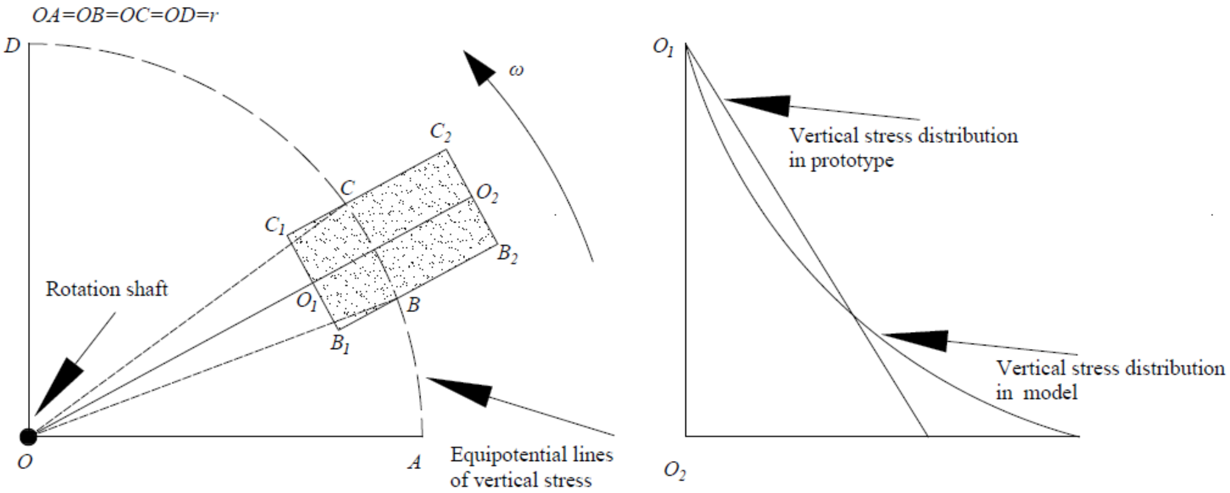

Figure 3-4 The vertical stress variation in the centrifuge model

A few points can be obtained from Figure 3-4:

1. At the topmost surface, the vertical stress is zero.
2. With the increase of the buried depth, the vertical stress in the sample as well as that in the prototype increase. However, the vertical stress in the model is clearly smaller than that in the prototype.
3. At a critical point, the vertical stress in the model equals exactly to the vertical stress in the prototype. This point corresponds to the two-thirds model depth.
4. Below this critical point, the vertical stress in the model is greater than that in the prototype.

In order to minimize the error in stress distribution, an effective centrifuge radius (R_e) is used to calculate the vertical stress. Taylor (2005) gives the derivation of the effective radius and concludes that the effective radius is equal to the distance from the rotation shaft to one-third of the model depth.

$$R_e = R_t + \frac{h_m}{3} \qquad \text{Equation (3-17)}$$

where R_e is the effective radius; R_t is the distance from the rotation shaft to the top of the model.

In general, if the ratio of the model height to the effective radius is less than 0.2, the error induced by the curvilinear stress distribution is minor, less than 3% of the in-situ stress. The effective radius of the centrifuge facility adopted in this study is 1.7 m, while the model height is 0.2 m. Thus, the ratio of the model height to the effective radius is 0.1176, far less than the limit.

3.6 The GT50/1.7 Geotechnical Beam Centrifuge

The centrifuge facility utilized in the study was provided by Thomas Broadbent and Sons Ltd and located in the lowermost floor in the Natural Resources Engineering Facility (NREF) at the University of Alberta. The capacity of the beam centrifuge, as shown in Figure 3-5, is 50 g-tonnes, indicating that the product of the weight of the payload and the centrifugal acceleration (in terms of the number of gravities) should be less than 50. For instance, if the weight of the payload is 500 kg and the corresponding effective radius is 1.7 m, then the centrifugal acceleration should not exceed 100. The centrifugal acceleration G is defined as below:

$$\mathrm{G} = \frac{\omega^2 r}{g} = \left(\frac{2\pi N}{60}\right)^2 \frac{r}{g} = \frac{N^2 r}{895} \qquad \text{Equation (3-18)}$$

where G is centrifugal acceleration (number of gravities); ω is angular velocity (radians per second); r is horizontal distance between the centre of gravity of the payload in the swing cradle and the rotational shaft; g is Earth's gravity, 9.81 m/s^2.

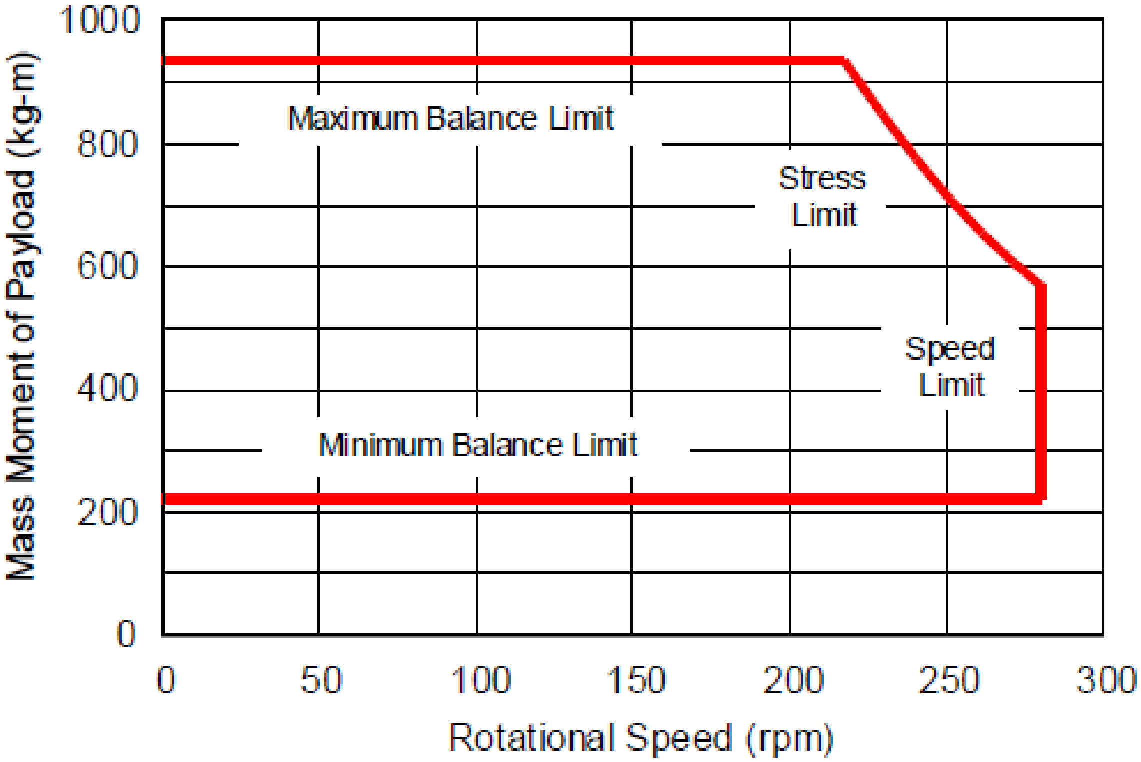

Figure 3-5 The centrifuge capacity of the GT50/1.7 Geotechnical Beam Centrifuge

In general, the rotational speed instead of the angular velocity is used to determine the parameters needed for the adjustment of the centrifuge velocity. The relationship between the rotational speed, in revolutions per minute, and the angular velocity, in radians per second, is expressed as below.

$$\omega = \frac{2\pi N}{60} \qquad \text{Equation (3-19)}$$

Where N is rotational speed (revolutions per minute).

In practice, the experimental package has many components. The location of the centre of gravity of these components is therefore different. To guarantee that the mass moment of the payload does not exceed the capacity of the centrifuge, it is essential to get the total mass moment of these components:

$$\mathrm{MR} = \sum mr \qquad \text{Equation (3-20)}$$

Where *m* is the mass of each component of the experimental package, in *kg*; *r* is the horizontal distance between the rotational shaft and the centre of gravity of each component of the experimental package, in *m*; *M* is the total mass of the experimental package, in *kg*; *R* is the horizontal distance between the rotational shaft and the centre of gravity of the experimental package, in *m*; *MR* is the total mass moment of the experimental package, in *kg-m*.

Thus, based on the principle of the uniform circular motion, the centrifugal force exerted by the experimental package can be expressed as below:

$$F = MR\omega^2 \qquad \text{Equation (3-21)}$$

Therefore, the total centrifugal force GT (G-Tonnes) can be expressed as below:

$$GT = \frac{F}{g} = \frac{MR\omega^2}{g} \qquad \text{Equation (3-22)}$$

Prior to the centrifuge spinning, it is essential to get the weight and the effective radius of the experimental package so that the mass moment can be calculated. The mass moment of the payloads in the swing cradle is coarsely balanced by repositioning the counterweight. When the centrifuge is spinning, the in-flight balancing system monitors the balance of the system and automatically adjusts the balance.

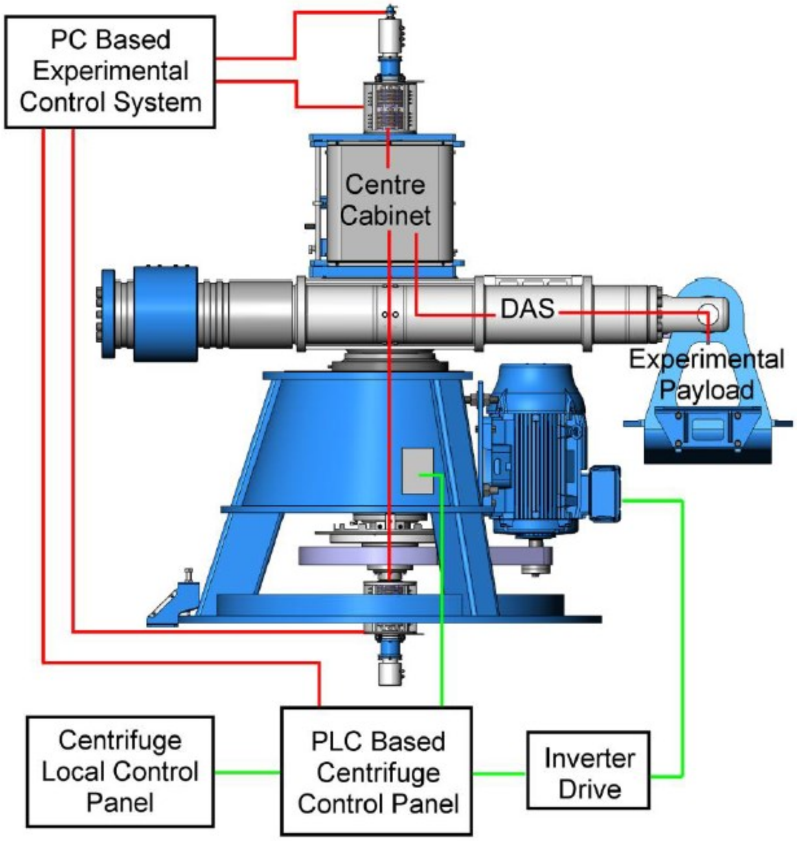

Figure 3-6 Schematic diagram of the GT50/1.5 Geotechnical Beam Centrifuge

Figure 3-6 shows the schematic diagram of the control scheme. The centrifuge speed, automatic balancing and other safety-related machine functions are controlled through a computer control system based on an industrial programmable logic controller (PLC). In the control room, two remote-accessed computers are used to memorize data from the data acquisition system (DAS) and the high-resolution camera.

3.7 The general overview on the experimental package

This general overview briefly introduces the experimental package. In general, the geotechnical centrifuge modelling should at least include the three components:

1. The container, which is used to contain the model.

2. The system that is used to recreate the in-situ condition, including the water level and the external forces.
3. The system that is used to monitor the change that occurs in the model and to acquire the corresponding data generated when the change happens.

Table 3-2 describes the major components of the experimental package. Generally, the plane strain box (PSB) is used to contain the model. The GeoCDM is used to mimic the expansion of the steam chamber beneath the shale barrier while the lead bars are used to mimic the overburden on the shale barrier.

Table 3-2 Major components of the centrifuge modelling test

Components	Function
Plane Strain Box	Contain sample
GeoCDM	Mimic the expanding steam chamber
Parker Servo motor	Control uplifting velocity of the GeoCDM
Mariotte bottle	Control water level inside the sample
Lead bars	Mimic the overburden pressure on the shale barrier
Kulite pore pressure transducer	Monitor pore pressure change
External pore pressure transducer	Monitor water level change
Perspex glass	Visualize soil particle movements
IDS UI-6280RE-C-HQ camera	Record soil particle movements
LED Illumination Towers	Provide LED illumination

The Perspex glass window, the IDS UI-6280RE-C-HQ camera, which can capture images with a resolution of 2448 × 2048 pixels, and the LED Illumination Towers are used to control image quantities and to memorize the soil deformation behaviour under uplift forces. The Mariotte bottle is used to control water level in the PSB.

3.7.1 Plane Strain Box

The plane strain box (PSB), having inside dimensions of 700 mm × 200 mm in plane and 400 mm in height, is an open-topped container for the prismatic samples. It comprises a stainless-steel U-shaped body, an aluminium alloy back plate, an aluminium alloy front plate, and a transparent acrylic front window with an aluminium alloy frame, as shown in Figure 3-7.

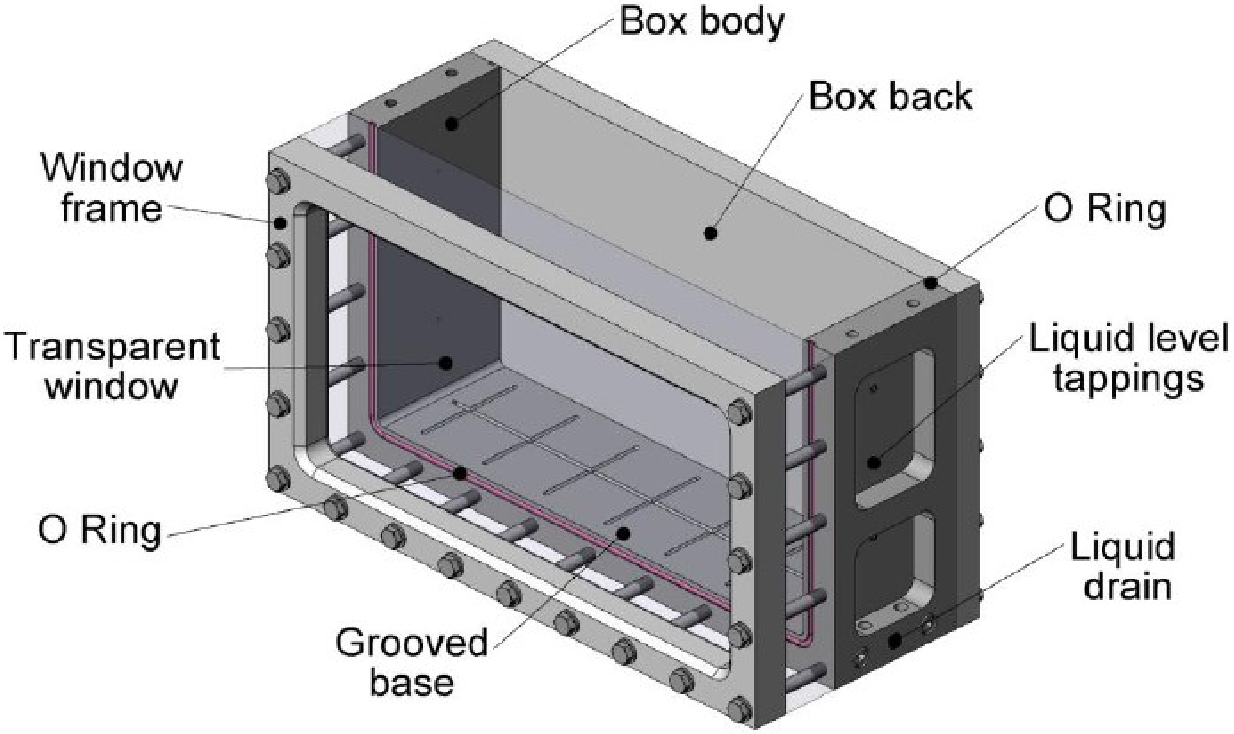

Figure 3-7 General arrangement of the plane strain box

Figure 3-8 shows the modified PSB. The GeoCDM is placed in the PSB. The engineer in the lab manufactured a hole in the aluminium alloy back plate so that the shaft of the driving system can control the GeoCDM. Similarly, three holes that are at the same level as the top surface of the GeoCDM are manufactured to allow the water from the Mariotte bottle to flow into the PSB. Ten centimeters above the holes for the Mariotte bottle, there are two holes which are manufactured for the installation of the pore water pressure transducers.

Well-mixed soil slurry is transferred from the mixing pot of the vacuum mixer to the PSB for curing. After 28 days, the aluminium alloy front plate is then replaced by the transparent acrylic front window. The inside wall of the transparent acrylic window is attached with a layer of transparency to reduce any boundary effects caused by the friction between the model and the walls.

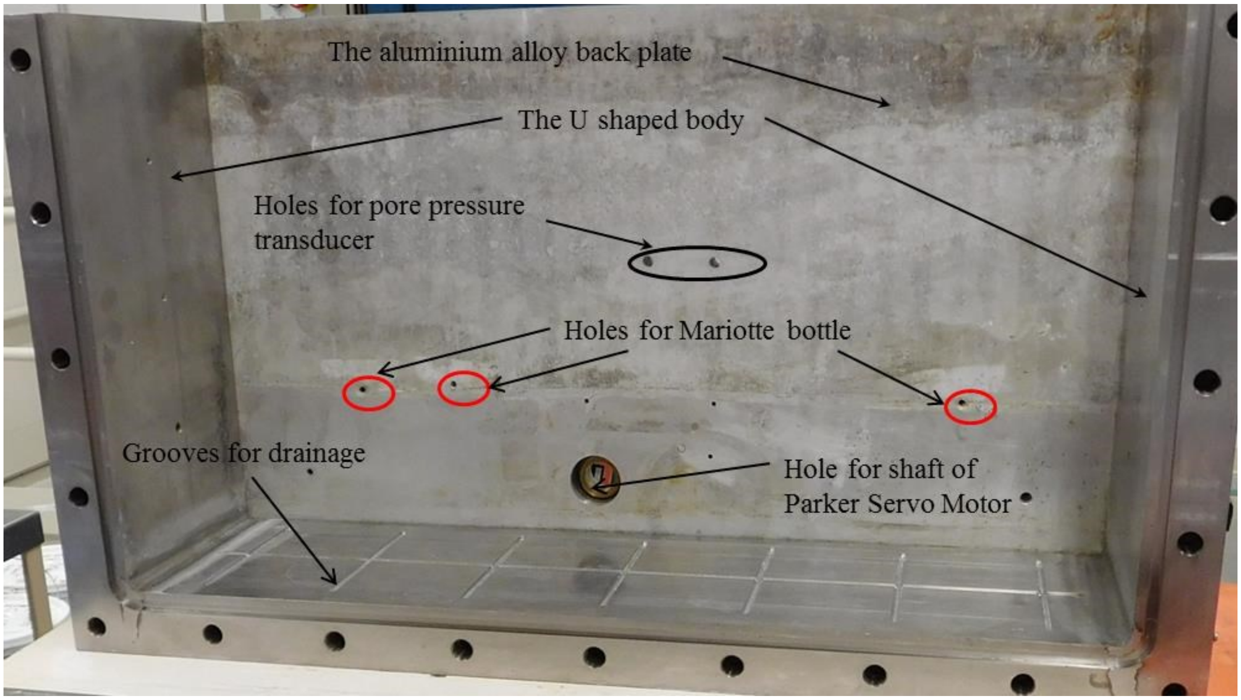

Figure 3-8 The modified plane strain box

3.7.2 Geomechanical Caprock Deflection Mechanism (GeoCDM)

The GeoCDM is a custom-designed device to mimic the expansion of the steam chamber beneath the shale barrier. It comprises the driving system and transmission system. The driving system, which comprises a Parker BE233D servo motor controlled by a Parker AR-08CE controller and a Parker RX23-100-S2 gearhead with a reduction ratio of 100:1, provides power to the transmission system. The transmission system comprises a rotation shaft, two sets of worm gears, the centre-lifting table, the left flank, the right flank and two fixed side blocks, as shown in Figure 3-9.

The width of the uplifting table is 10 cm, while that of each flank is 5 cm. The motion of the uplifting table is controlled by the Parker Servo Motor, while the motion of the two flanks is controlled by the uplifting table. When the uplifting table moves upward, it exerts an uplifting force on each flank. The joint between the flank and the uplifting table is sealed with O-rings to prevent water and soil slurry flowing down to the inner space of the GeoCDM.

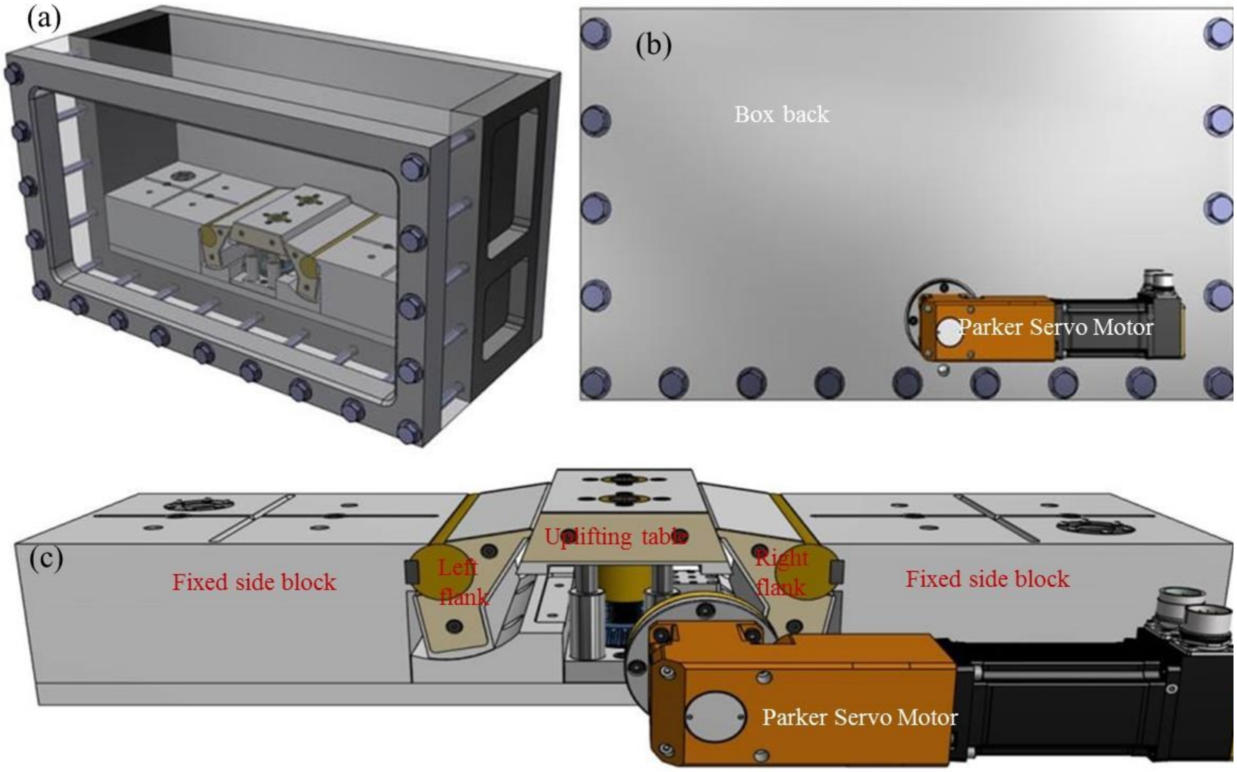

Figure 3-9 Schematic diagram of the GeoCDM (a) isometric view; (b) back view; (c) the major components

3.7.3 Mariotte bottle

To consider the effect of the pore-water pressure, the water level in the PSB is required to keep constant during the centrifuge modelling test. This goal can be achieved through the application of a simple closed system called the Mariotte bottle, which was created by Edme Mariotte (1620-1684).

The biggest advantage of such a device is that it can supply water to a system with a constant pressure head if the water level in the Mariotte bottle is above the bottom of the steel tube inserted into the Mariotte bottle.

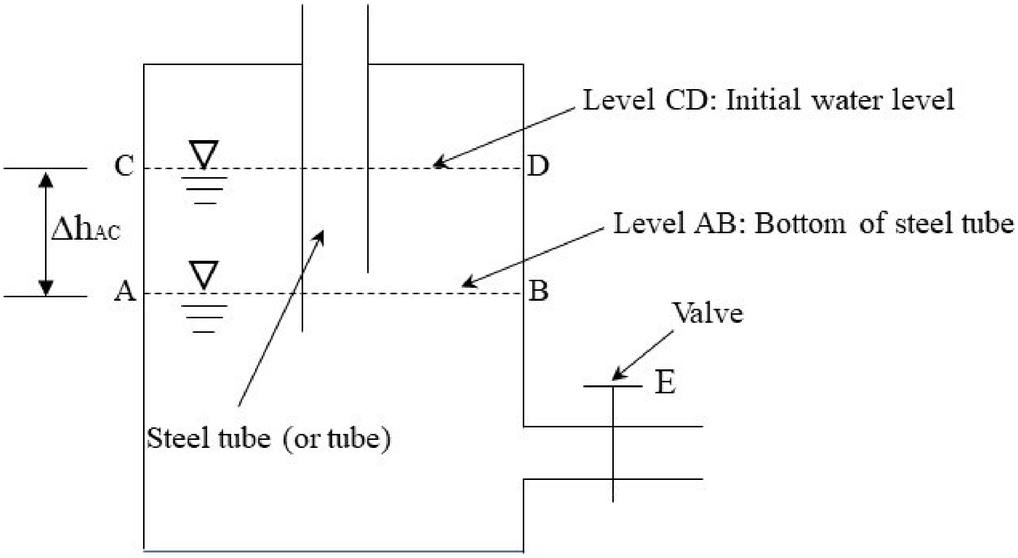

Note: When water level in the Mariotte bottle is below level AB, Mariotte bottle becomes a communicating vessel.

Figure 3-10 Schematic illustration of the Mariotte bottle

Prior to opening valve E, the water level in the Mariotte bottle (CD) is the same as that in the steel tube. Pressure on the top of the water column in the steel tube is equal to the atmospheric pressure. Even though the air in the Mariotte bottle is separated from the atmosphere, it is still equal to the atmospheric pressure because the water volume in the Mariotte bottle does not change. Pressure on level AB is equal to the sum of the atmospheric pressure and the pressure resulting from water column AC or BD.

$$P = p_{atm} + \Delta h_{AC} g \rho_w \qquad \text{Equation (3-23)}$$

where ρ_w is the water density; g is the Earth gravity; Δh_{AC} is the height of the water column AC or BD; p_{atm} is the atmospheric pressure.

Immediately after opening valve E, water flows into the PSB. At the same time, the water level in the Mariotte bottle and the steel tube drops. However, before the water level in the steel tube drops to the bottom of the steel tube, the water level in the Mariotte bottle keeps almost constant.

The decrease of the water pressure at the bottom of the steel tube is equal to $\rho_w g \Delta h$. At the same time, the decrease of the water pressure at the level AB is equal to $p_{atm}-\frac{h_0}{h_1}p_{atm}+\rho_w g(h_1-h_0)$. Since the decrease of the water pressure in the steel tube should be equal to that in the Mariotte bottle, it is straightforward to derive the following equations:

$$p_{atm}-\frac{h_0}{h_1}p_{atm}+\rho_w g(h_1-h_0)=\rho_w g\Delta h \qquad \text{Equation (3-24)}$$

$$\left(1-\frac{h_0}{h_1}\right)\times 10.3+(h_1-h_0)=\Delta h \qquad \text{Equation (3-25)}$$

$$\left(\frac{h_1-h_0}{h_1}\right)\times 10.3+(h_1-h_0)=\Delta h \qquad \text{Equation (3-26)}$$

where h_0 is the distance between the water level in the Mariotte bottle and the top of the Mariotte bottle prior to opening valve E; h_1 is the distance between the water level in the Mariotte bottle to the top of the Mariotte bottle when the water level in the steel tube drops to the tube tip; Δh is the change of the water level in the steel tube; (h_1-h_0) is the head loss due to the decrease of the water level in the Mariotte bottle; $\left(\frac{h_1-h_0}{h_1}\right)\times 10.3$ is the head loss due to depressurization.

Immediately after the water level in the steel tube drops to the bottom of the steel tube, air flows into the Mariotte bottle through the steel tube so that the pressure at level AB can stay the same as the atmospheric pressure.

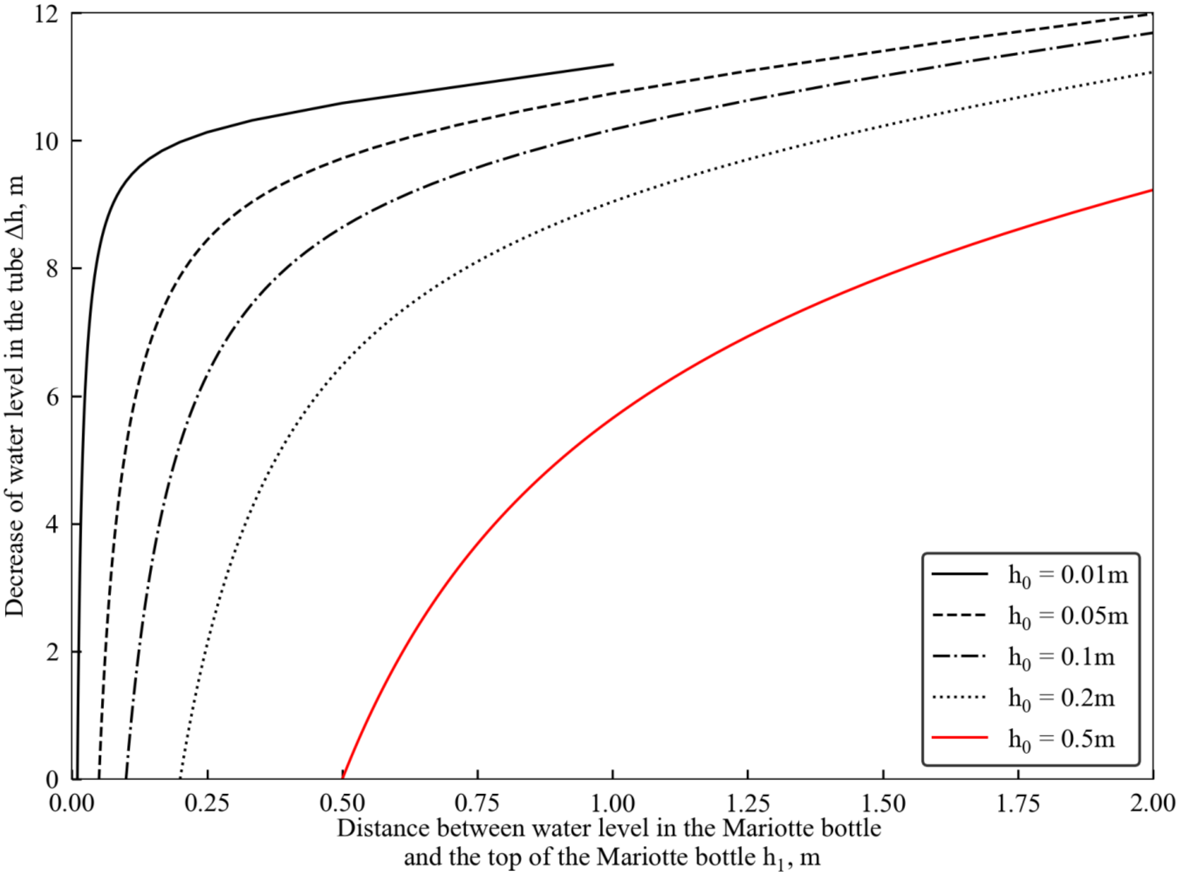

Figure 3-11 Relationship between water level in the Mariotte bottle and that in the steel tube at 1 g

To intuitively understand the relationship between the water level in the tube and that in the Mariotte bottle, Figure 3-11 describes the relationship between the two variables. When the water level in the tube drops a few meters, the water level in the Mariotte bottle only drops a few centimeters. The initial distance between the water level in the Mariotte bottle and the top of the Mariotte bottle is assumed to be 0.01, 0.05, 0.1, 0.2 and 0.5 m, respectively. Obviously, with the increase of h_0, the impact of the decrease of the water level in the tube on the decrease of the water level in the Mariotte bottle becomes great.

The above discussion describes the variation of the water level in the Mariotte bottle before the water level in the steel tube drops to level AB. Immediately after valve E opens, the water level in the steel tube quickly reaches the bottom of the steel tube, and this process takes only a few seconds. Immediately after the water level in the tube drops to the level AB, the water in the Mariotte bottle works as the water reservoir to supply water to the container. When the water level in the PSB is at the same level as AB, the Mariotte bottle stops supplying water for the PSB. Under this condition, the water levels in the PSB and the Mariotte bottle keep constant. It is impossible for the water level in the PSB to be higher than that in the Mariotte bottle.

However, when the centrifuge is spinning at 100 g, it is the water pressure of column AC rather than the atmospheric pressure that plays the dominant role in the water-supply system.

$$P_{atm}\text{-}\frac{h_0}{h_1}p_{atm}+\rho_w\times 100g\times(h_1\text{-}h_0)=\rho_w\times 100g\times \Delta h \qquad \text{Equation (3-27)}$$

$$\left(1\text{-}\frac{h_0}{h_1}\right)\times\frac{10.3}{100}+(h_1\text{-}h_0)=\Delta h \qquad \text{Equation (3-28)}$$

$$\left(\frac{h_1\text{-}h_0}{h_1}\right)\times\frac{10.3}{100}+(h_1\text{-}h_0)=\Delta h \qquad \text{Equation (3-29)}$$

Therefore, based on Equation (3-29), it is easy to derive the relationship between the water level in the steel tube and that in the Mariotte bottle, as shown in Figure 3-12. In practice, the E valve is opened prior to starting the centrifuge facility, indicating that the Mariotte bottle works as a communicating vessel when the centrifuge is spinning.

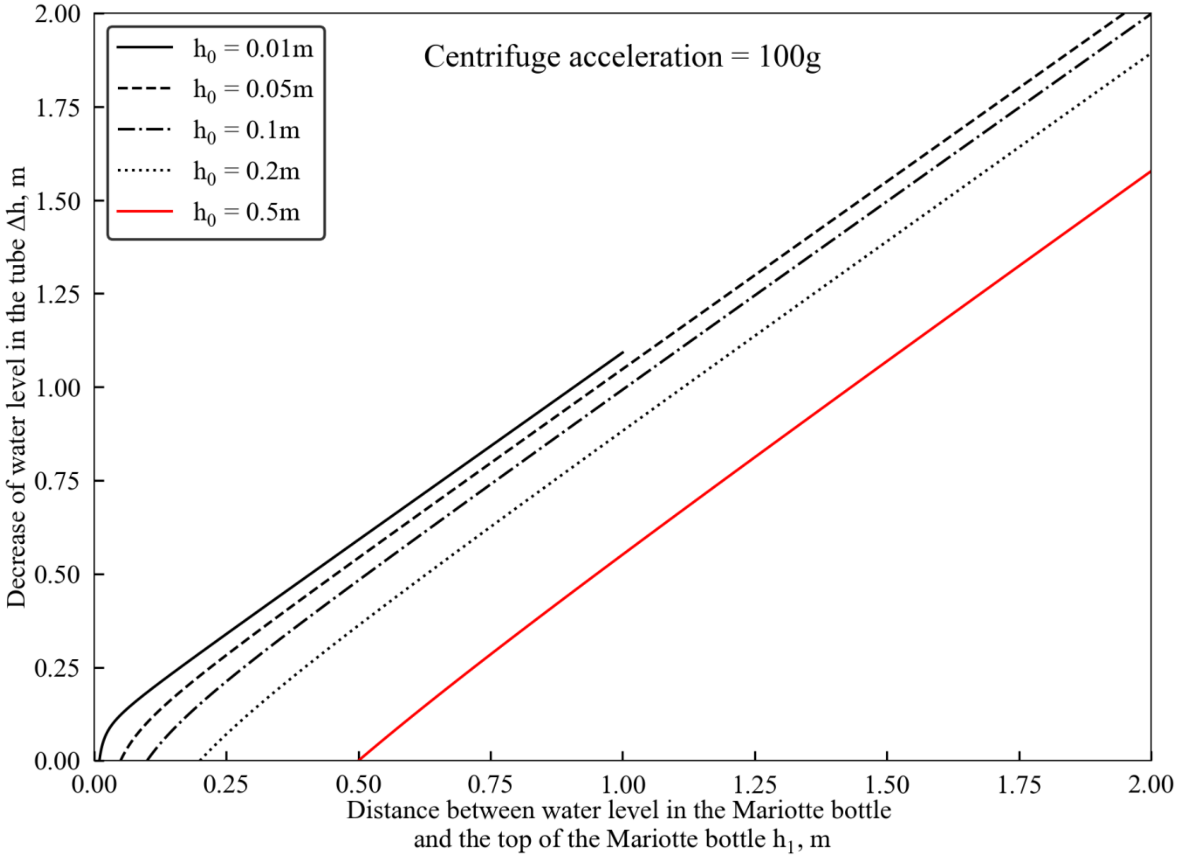

Figure 3-12 Relationship between water level in the Mariotte bottle and that in the steel tube at 100 g

3.8 Experimental procedure of centrifuge modelling test

Compared with the specimen size for triaxial tests, the size of the geotechnical centrifuge model in this study is very large. The width and the length are 20 cm and 70 cm, respectively. The height is approximately 20 cm to mimic the behaviour of the prototype with 20 m thickness. Therefore, the model preparation involves a large quantity of soil and distilled water, indicating that the commonly used mixer cannot satisfy the requirement of the test. Moreover, it is essential to remember that the model is used for the centrifuge modelling test, indicating that the sample will spin around the rotational shaft at over 200 revolutions per minute. Therefore, great care should be taken when preparing the experimental package.

The objective of this section is to present the experimental procedure of the geotechnical centrifuge modelling test. It includes the assemblage of the plane strain box (PSB), consolidation of the Speswhite kaolin clay slurry, and sample preparation for the centrifuge modelling test.

3.8.1 Assemblage of the Plane Strain Box (PSB)

This section describes the procedure of assembling the PSB. The PSB mainly consists of the aluminum alloy front plate, the aluminum alloy back plate, the stainless-steel U-shaped body, a transparent acrylic front window with an aluminum alloy frame and the GeoCDM.

Before assembling the PSB, it is essential to clean the U-shaped body and to check the workability of the drainage lines and ports. The pressurized air is used to remove those residual materials adhered to the grooves of the grooved base and the drainage lines to make sure that the water can flow through these channels without any restrictions. The maintenance of the GeoCDM and the PSB will ensure the device works properly during the centrifuge modelling test.

The first step is the assemblage of the GeoCDM. The components are submerged in the Varsol for 24 hours, and then cleaned by the brush to remove any residual material such as clay, metal oxide and other unnecessary material out of the surface, followed by the drying process during which the components are cleaned with the paper tower. The dried components are then smeared with a layer of grease to prevent corrosion and oxidation. These well-prepared components are then put together for the assemblage of the GeoCDM.

The second step is the installation of the aluminum alloy back plate. To reduce the friction between the aluminum alloy back plate and the sample, the surface of the plate is cleaned by the sandpaper to remove any residual material. The soap water is then thoroughly sprayed onto the surface. A layer of transparent film is then prepared and placed onto the aluminum plate to prevent corrosion and oxidation. A wiper is used to squeeze out the water and air trapped in between the transparency and the aluminum plate. The redundant transparency at the left, right, bottom side as well as that which covers the aluminum plate's holes are removed with a sharp knife. It is essential to make sure that there is enough transparency left at the top side of the plate so that it can be folded onto the top of the plate to prevent slurry invasion in between the transparency and the aluminum plate. Then the aluminum plate is screwed to the U-shaped body with O-ring cord seals.

The third step involves the placement of the GeoCDM into the PSB. Due to the weight of the GeoCDM (about 100 kg), it is preferred to push the GeoCDM into the U-shaped body. To achieve this goal, the PSB is placed on an adjustable cart to make sure that the top surface of the PSB's base is at the same level as the GeoCDM's bottom. The U-shaped body is then aligned to the GeoCDM through the adjustment of the cart's position. The GeoCDM is then pushed into the U-shaped body with the O-rings cord seals, as shown in Figure 3-13.

It is essential to check the workability of GeoCDM prior to starting the next step because the assemblage of the PSB and the GeoCDM is very troublesome. If the GeoCDM does not work properly after the completion of the installation or in the process of the centrifuge spinning, the whole system must be dismantled to troubleshoot the problem, indicating that the previous efforts are in vain.

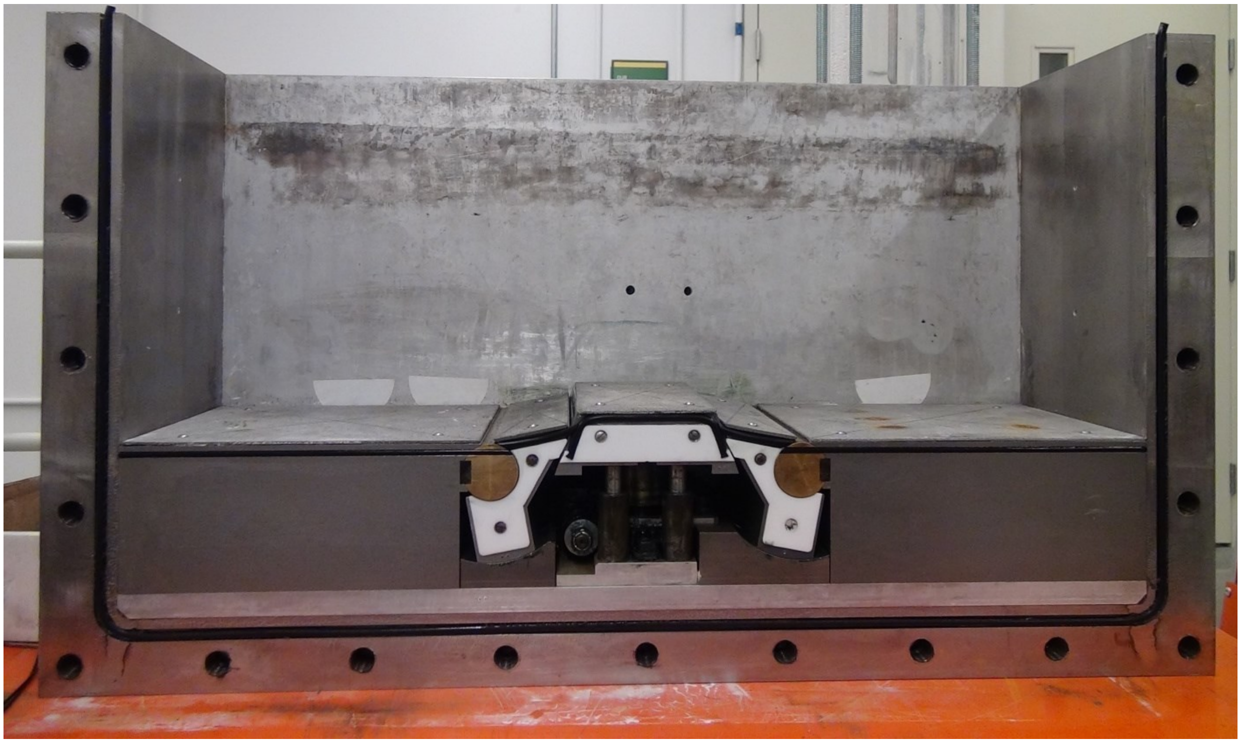

Figure 3-13 The installation of the GeoCDM

The fourth step is the installation of the aluminum alloy front plate, and the procedure is the same as that for the aluminum alloy back plate.

The last step is the installation of the porous stones. The porous stones should be soaked in the distilled water for at least 24 hours before the installation. It is essential to check the gap between the porous stone and both the aluminum alloy back plate and the aluminum alloy front plate to make sure that there is enough space left to avoid scratching as the uplifting table of the GeoCDM moves up, as shown in Figure 3-14. After that, the porous stones are screwed to the top of the GeoCDM.

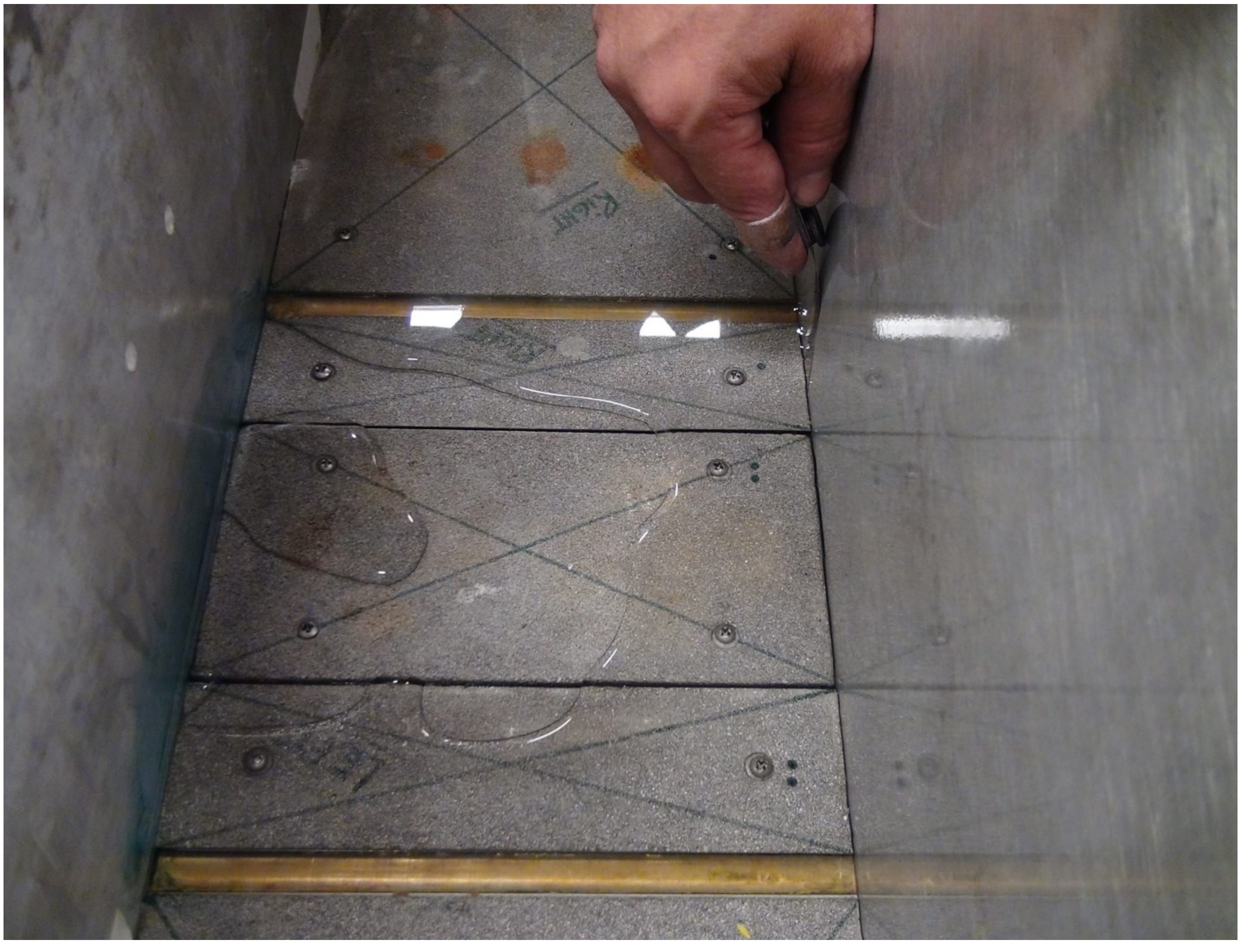

Figure 3-14 The installation of the porous stones

3.8.2 Preparation of soil-water slurry

The first step is to connect the PSB with the standpipe. Water level in the standpipe is higher than the top of the GeoCDM. When the water submerges the porous stones, the PSB is then disconnected with the standpipe. The porous stones are then submerged into the water for a few hours to ensure full saturation. Three layers of filter papers are placed on top of the porous stones, followed by the geotextile, as shown in Figure 3-15. The system is then transported to the soil preparation lab for the next step.

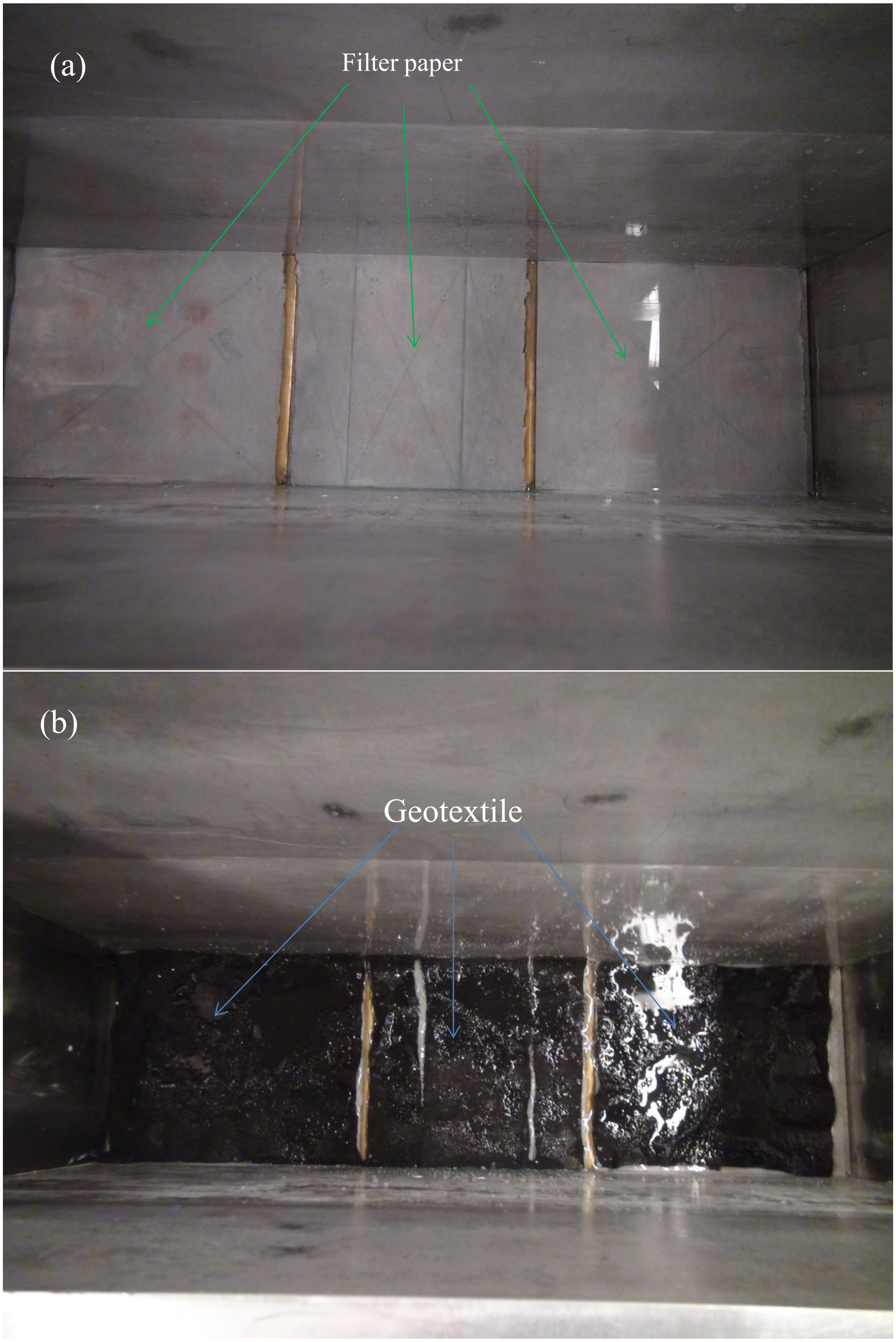

Figure 3-15 Saturation of the (a) filter paper and (b) geotextile

Based on the requirements of the geotechnical centrifuge modelling test, the final height of the model after consolidation should be approximately 20 cm. Thus, it is essential to calculate the weight of the Speswhite kaolin clay and the distilled water for the test. The specific gravity of the Speswhite kaolin is 2.61, and the total soil-water content is 100%. According to the experimental results of the consolidation test, the weight of the Speswhite kaolin powder is 37.8 kg.

The distilled water is then added into the vacuum mixer, followed by the Speswhite kaolin powder. Immediately after the vacuum pressure of the GS1500 vacuum mixer is up to -60 kPa, the mixing procedure starts.The mixing process lasts for 2 hours. Due to the long mixing time, it is essential to check the workability of the vacuum mixer and the ventilation system prior to starting the GS1500 vacuum mixer. Moreover, this vacuum mixer is powered electrically; therefore, it is essential to make sure that all parts of the machine are dry, the vacuum hoses are properly secured and the vacuum pump works properly. In order to make sure the soil water is thoroughly mixed, the mixing is intercepted at a 1-hour time interval to clean the soil slurry adhered to the blade to the mixing pot.

After being well mixed, the soil-water slurry is then transferred to the PSB in five separate layers. After filling each layer, the trapped air bubbles are then removed by tapping the PSB with a rubber hammer. Immediately after completing the soil-filling process, a layer of filter paper is placed on the sample, followed by the geotextile and the porous stone. A level is placed on the porous stone to make sure that the surface of the soil-slurry is not inclined. Then the loading plate which will exert an equivalent consolidation pressure of 1.9 kPa is gently positioned on top of the porous stone. The loading plate is left on the kaolin block overnight for stabilization. To shorten the consolidation time, double drainage is maintained during consolidation. To guarantee that the model is fully saturated during the consolidation stage, the water level in the PSB is above the top of the kaolin block, and the drainage channels are connected to the standpipe**.**

After 24 hours, the PSB should be placed on the loading platform for successive consolidation. Prior to pushing the PSB onto the loading platform, it is necessary to sprinkle mineral oil to the platform to minimize the friction between the PSB and the platform.

The settlement is recorded through the linear variable differential transformer (LVDT) while the load is recorded through the load cell, as shown in Figure 3-16. The consolidation pressure is successively doubled until the required maximum consolidation pressure is achieved (2 kPa, 5 kPa, 10 kPa, 20 kPa, 40 kPa, 80 kPa, 160 kPa, 320 kPa, 640 kPa, 1000 kPa, 1450 kPa). It typically takes 2 to 3 days to complete one consolidation stage.

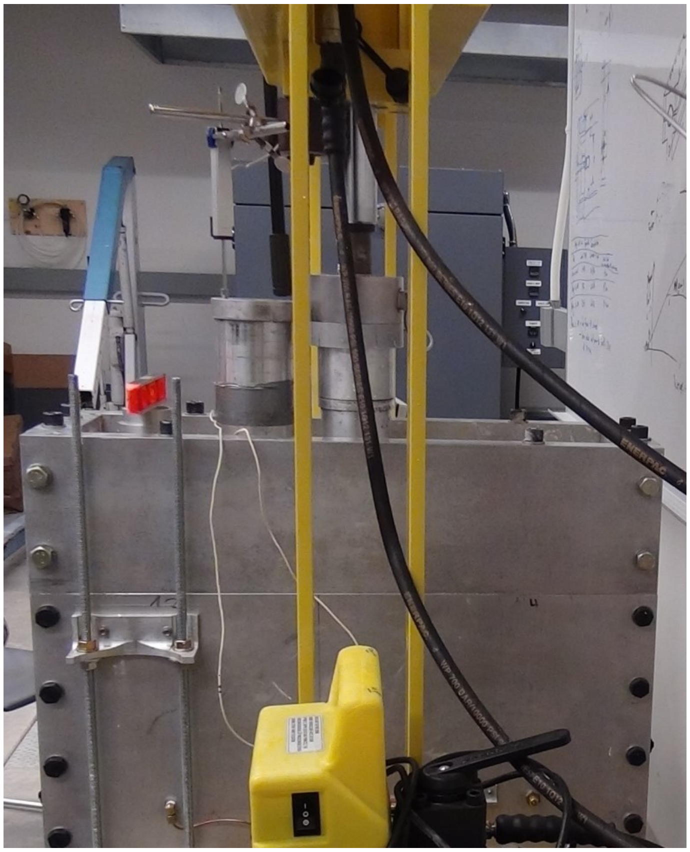

Figure 3-16 The consolidation procedure of the sample

3.8.3 Model preparation for geotechnical centrifuge modelling test

The final consolidation pressure is 100 kPa. After the completion of the consolidation, it is essential to close the bottom drainage valves and remove the free water on top of the kaolin block prior to unloading the vertical pressure from 100 kPa to 0 kPa. The major purpose of this step is to isolate the kaolin block from free water and thus prevent the possible elastic swell caused by the suction of the free water.

After the completion of consolidation, the sample is then processed for the geotechnical centrifuge modelling test. Before removing the front aluminum plate from the PSB, it is necessary to remove the water/soil mixture on top of the sample by using a vacuum cleaner. Otherwise, the front surface of the sample may be polluted by the mixture, which can affect the image quality, as shown in Figure 3-17. If the front surface is polluted, great care should be taken to remove the polluted area and to smooth the surface.

Figure 3-17 The front surface of the model polluted by the soil-water mixture

Immediately after being exposed to the air, the front surface is trimmed, levelled, and cleaned with a wet paper towel. The oxidized and polluted clay on the top of the kaolin block may migrate to the lower parts of the block when the centrifuge is spinning at 100 g and thus pollutes the front surface of the model, and eventually affects the experimental results. Therefore, removing these materials and smoothing the top surface of the block are essential parts of this step.

Concurrently, it is essential to check if there are tiny holes on the front surface of the model. These tiny holes are the result of the trapped air bubbles when transferring the soil-water slurry into the PSB. They may result in strain concentration superficially during the deformation of the model, and therefore affect the analysis of the experimental results. This study uses the residual material from the block to fill these tiny holes.

Before installing the transparent acrylic front window, it is necessary to clean the O-ring and the front surface of the PSB to make sure that there is no clay or other materials that could affect the seal-ability of the PSB, as shown in Figure 3-18.

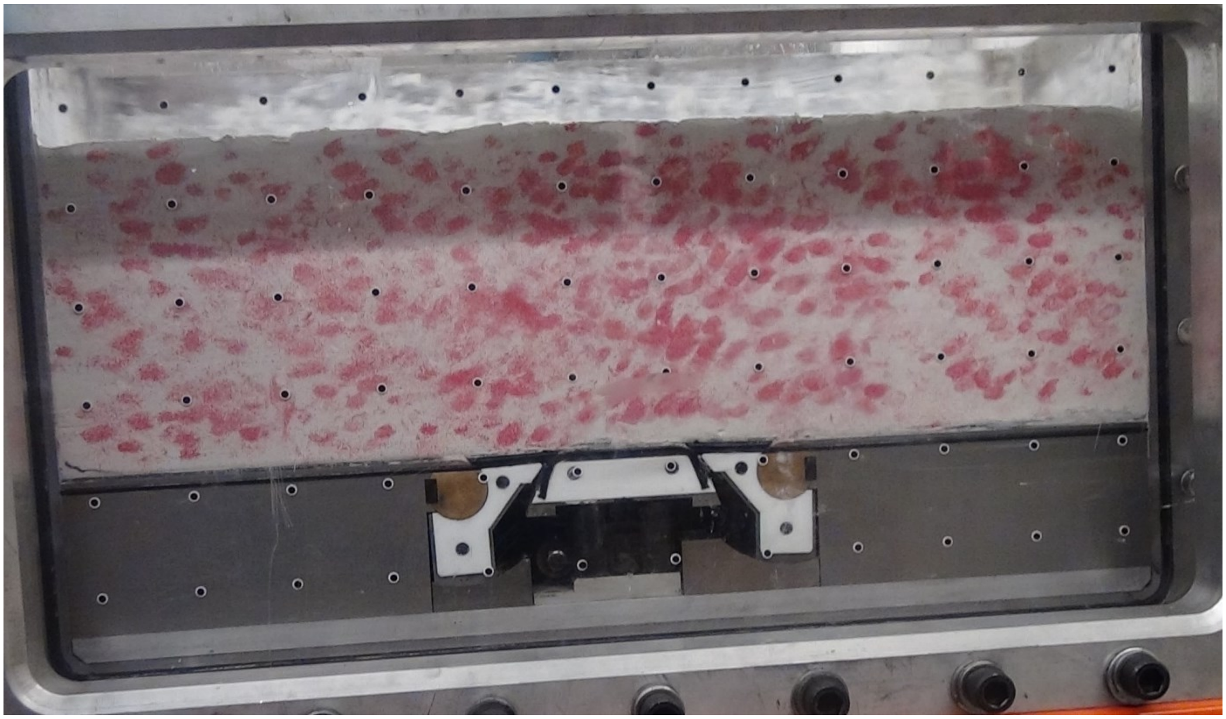

Figure 3-18 The well-prepared model for the geotechnical centrifuge modelling test

3.8.4 Texture of sand

Many techniques have been previously adopted by different researchers to measure the displacements in physical modelling tests. Being a velocity-measuring technique, particle image velocimetry (PIV) is initially used in the field of experimental fluid mechanics to get instantaneous velocity measurements and corresponding fluid properties (Adrian, 1991). To examine flow field of a fluid, the flow is firstly seeded with marker particles which can be tracked as the fluid flows. There are two methods for examining flow field of a fluid: particle tracking velocimetry (PTV) and high image density PIV. The first method uses low seeding density so that individual particles can be tracked. In contrast, the second method, which has been adopted by GeoPIV, uses high seeding density so that every small patch within those images contains several particles. Normally, natural soil does not need to be seeded with particles to create features for image processing. Their colourful grains are the good features upon which image processing can operate. However, coloured powder or fine sand needs to be added to the exposed surface of clay samples to create features for tracking soil deformation.

A deformation measurement system based on close-range photogrammetry and PIV is adopted by this study to measure planar soil deformation under a high gravitational field. Sample deformation can be obtained through analyzing digital images captured by a digital camera. The application of GeoPIV to solve geotechnical problems was first proposed by White et al. (White et al., 2003). The following section will discuss the basic principle of the software.

The principle of PIV has been described in detail by some researchers (White, 2002). The reference image, which in general is the image prior to soil deformation, is divided into a user-defined mesh of test patches that have a certain number of pixels, such as $L \times L$ pixels. Each test patch has a unique texture expressed by intensity matrices I(U), where U = (u,v) represents coordinates of each pixel of the test patch. Patch size and image pixel coordinates (u,v) of corresponding patch in the first image are used to determine the centroid position of each patch.

To find the displacement of the test patch in the following images, a user-defined search patch $I_{search}(U+s)$ that extends beyond the test patch by a value of s_{max} in the u and v directions, respectively, is extracted from the second image. The cross-section of the test patch $I_{test}(U)$ and search patch $I_{search}(U+s)$ is evaluated through the below expressions:

$$\mathrm{R(s)} = \sum_{\mathrm{U}} I_{test}(U)\cdot I_{search}(U+s) \qquad \text{Equation (3-30)}$$

However, this equation alone may not be able to find the best match position of the test patch in the second image. This is because the size of $I_{test}U$ and $I_{search}(U+s)$ may be different, and brightness or intensity matrices of the two areas may have different variations. Under this condition, the following methods are used to find the "best match" of the test patch over the search zone:

$$\mathrm{N(s)} = \sum_{\mathrm{U}} [I_{search}(U+s)\cdot I_{search}(U+s)]\cdot M(U) \qquad \text{Equation (3-31)}$$

$$R_n(s) = \frac{R(s)}{N(s)} \qquad \text{Equation (3-32)}$$

where *N(s)* is a normalization matrix that can be determined by obtaining the cross-correlation of the square of the search zone matrix with a dummy mask test patch, *M(U)*, of uniform amplitude.

To create sufficient texture for the Speswhite kaolin block, a thin layer of uniform fine red sand is sprinkled on the front surface of the specimen. After the front surface of the model has been processed, the next step is the preparation of the transparent acrylic front window. The surface of the window is cleaned with soft paper towel to remove any unnecessary material. Soapy water is then thoroughly sprayed onto the surface. To prevent the window from the scratch caused by the soil particles, a piece of transparency is placed onto the surface. A wiper is used to squeeze out the water and air trapped in the space between the transparency and the aluminum plate. The redundant transparency at the left, right, top and bottom side as well as that which covers the window's holes are removed with a sharp knife. The window and the aluminum alloy frame are then screwed to the U-shaped body with O-ring cord seals.

After completing the installation of the window, three layers of filter paper should be placed on top of the sample to prevent the materials adhered to the lead bars from polluting the model. The weight of lead bars depends on the requirement of the experiment. The Mariotte bottle which is used to control water level in the PSB is installed, followed by the Parker Servo Motor which is used to control the movement of the uplifting table of the GeoCDM.

After completing the assembly, it is necessary to measure the weight of the experimental package before putting it into the centrifuge pit. The body of the PSB is provided with holes at the bottom so that it can be bolted down to the centrifuge swing. The quality of images captured by the camera can significantly affect results of GeoPIV, and therefore should be checked prior to starting the centrifuge facility. The next step is the adjustment of the counterbalance based on the weight in the swing cradle.

3.8.5 Centrifuge test procedure

In general, the G-level increases step by step. The average time required to spin up the centrifuge to the 100 g is about 10 minutes. After reaching the desired acceleration field, the centrifuge acceleration keeps constant to consolidate the sample for at least 8 hours. Water level in the PSB is maintained through the Mariotte bottle. After the consolidation is approximately completed, the uplifting table of the GeoCDM is simulated. The camera is used to take images of soil deformation before and during the upward movement of the GeoCDM. After reaching the desired vertical displacement, the GeoCDM is stopped. Samples are then removed out of the centrifuge pit for post-experiment observations.

3.9 Properties of Speswhite kaolin clay

The Speswhite kaolin clay used in this study is supplied by IMERYS Minerals Ltd. As shown in Table 3-3, the liquid limit and plastic limit of the material are approximately 65% and 35%, respectively. The specific gravity is 2.61, and the main chemical composition is SiO_2 (47%) and Al_2O_3 (38%). The grain size distribution of the material, which is obtained from the data sheet supplied by IMERYS Minerals Ltd, is shown in Figure 3-19. It is evident that the Speswhite kaolin clay is composed of 20% silt and 80% clay.

Table 3-3 Properties of Speswhite kaolin clay

Properties of Speswhite kaolin clay (Spk)[a]	Characteristics value
Liquid limit, LL (%)	65
Plastic limit, PL (%)	35
Grain size distribution	
+ 300 mesh (mass % max.)	0.02
+ 10 μm (mass % max.)	0.5
- 2 μm (mass %)	76 – 83
Specific gravity	2.61
Surface area (BET; m^2/g)	14
Chemical composition	
Silicon Dioxide (SiO_2) (mass %)	47
Aluminum Oxide (Al_2O_3) (mass %)	38

Note: [a]Imerys Minerals Co.

As required by the physical modelling test, the final height of the model after the completion of the consolidation should be 20 cm. To achieve this goal, a few consolidation tests are needed to determine the weight of the Speswhite kaolin clay and the distilled water. Previous studies performed by Cao (2003) and Wu (2015) not only provide extensive information about the material's properties but also illustrate the experimental results of the consolidation test, which is of great value for establishing the relationship between the weight of the Speswhite kaolin clay and the thickness of the model at certain consolidation pressures. The experimental results presented by these researchers show that the void ratio of the Speswhite kaolin clay and water mixture decreases sharply with the increase of the vertical consolidation pressure. However, when the vertical consolidation pressure is higher than 200 kPa, with the increase of the vertical consolidation pressure, the change rate of the void ratio with respect to the consolidation pressure gradually decreases.

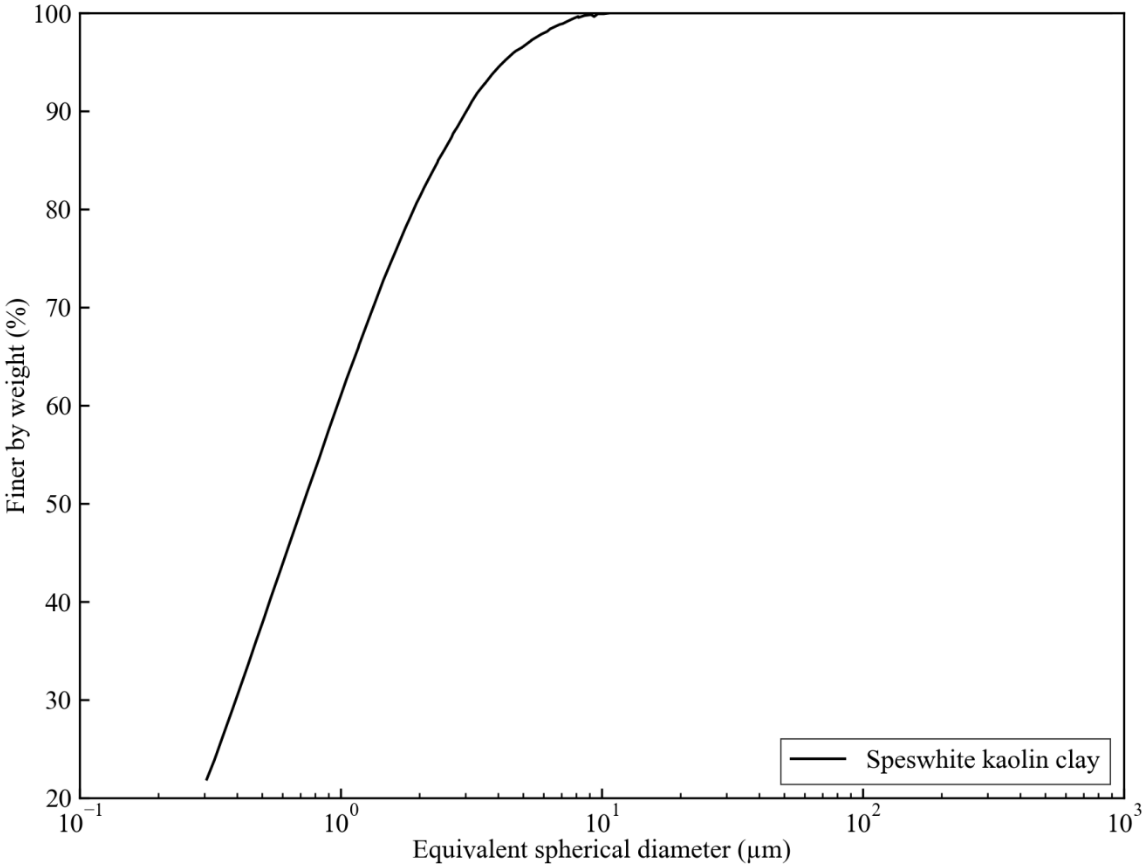

Figure 3-19 Grain-size distribution of Speswhite kaolin clay (from the Imerys Minerals Co.)

Figure 3-19 demonstrates the experimental results of the consolidation test of the Speswhite kaolin clay performed by this study. The x-axis is the time in normal coordinates while the y-axis is the settlement of the material under the vertical consolidation pressure shown in the corresponding subplot. From the perspective of simplicity, the settlement of each consolidation stage is processed so that the value ranges from zero to the maximum settlement.

The initial void ratio of the soil-water slurry is solely a function of the total soil-water content and the specific gravity of the soil, as shown below:

$$\mathrm{w}(\%) = \frac{W_w}{W_s} \times 100 \qquad \text{Equation (3-33)}$$

$$e = \frac{V_v}{V_s} \qquad \text{Equation (3-34)}$$

$$G_s = \frac{\rho_s}{\rho_w} \Rightarrow \rho_s = 2.61\rho_w \qquad \text{Equation (3-35)}$$

$$\mathrm{w}(\%) = \frac{\rho_w \times V_w}{\rho_s \times V_s} \times 100 \qquad \text{Equation (3-36)}$$

$$\mathrm{e} = \frac{2.61 \times w(\%)}{100} \qquad \text{Equation (3-37)}$$

where w is the water content; W_w is the water quantity in the soil slurry; W_s is the solid quantity in the soil slurry; V_v is the water or void volume in the soil slurry; V_s is the solid volume in the soil slurry; ρ_s is the density of the soil solid; ρ_w is the water density; e is the void ratio.

To derive the change of the void ratio induced by the consolidation pressure, it is essential to have the following assumptions:

1. There is no chemical reaction in the soil-water mixture, or the chemical reaction does not affect the change of the void ratio.
2. The solid volume does not change during the whole process of the consolidation.

$$\Delta e=\frac{\left(H_0\text{-}H_f\right)\times W\times L}{\left(\frac{W_s}{G_s}\right)} \qquad \text{Equation (3-38)}$$

where H_0 is initial height of the model; H_f is final height of the model; W is the width of the model; L is length of the model; G_s is the specific gravity of the Speswhite kaolin clay.

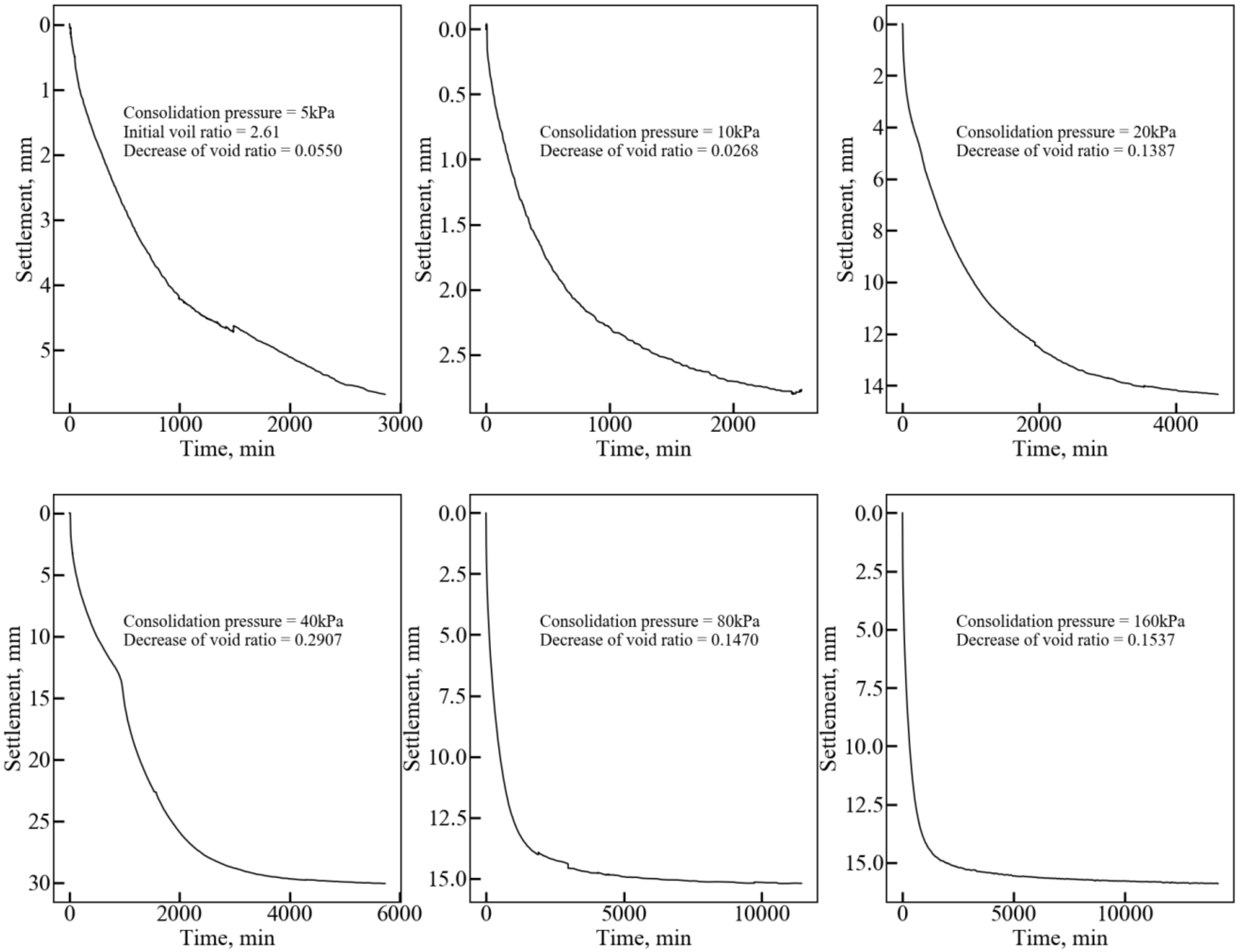

Figure 3-20a Relationship between the settlement of the Speswhite kaolin clay and the consolidation pressure

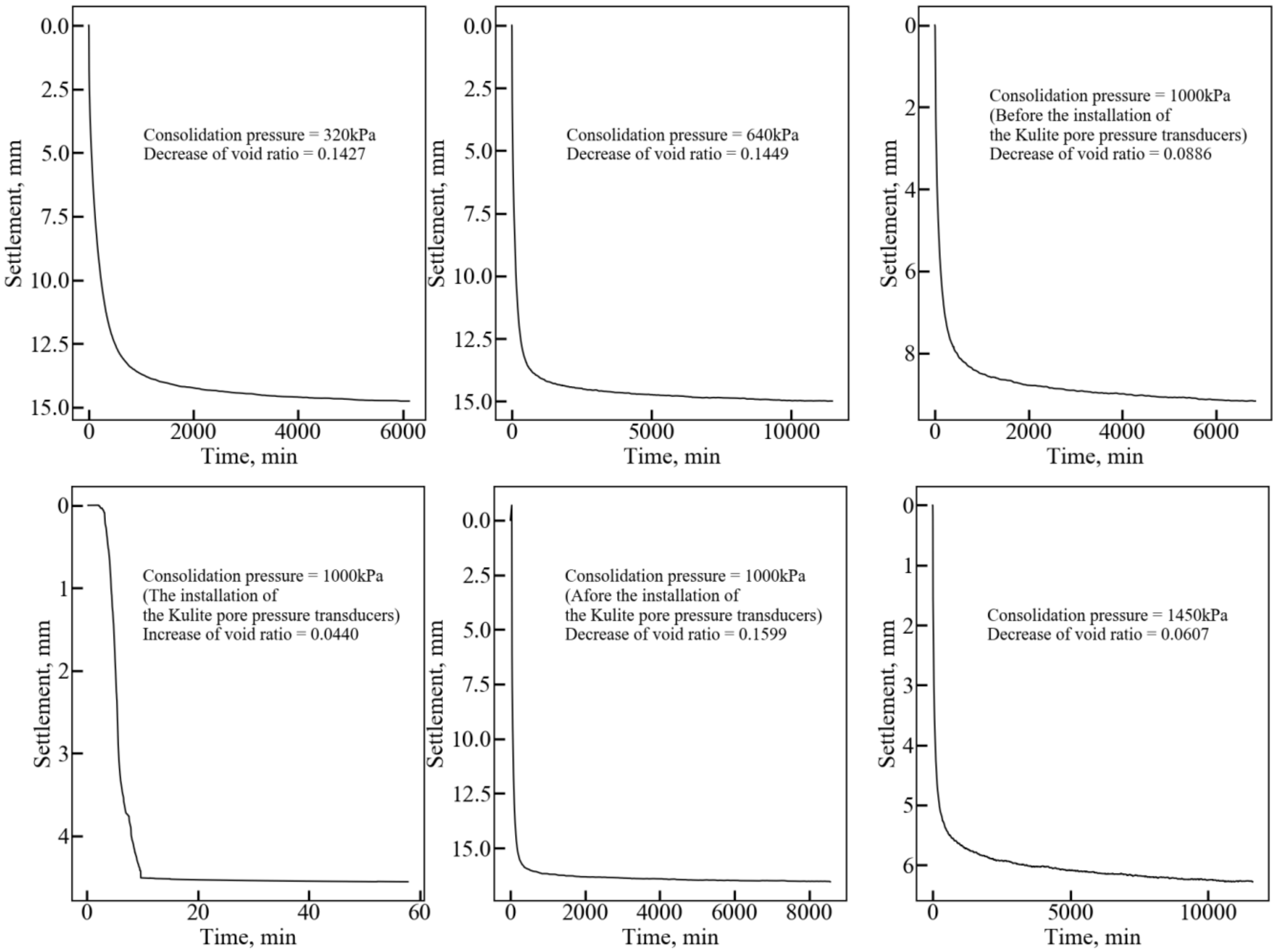

Figure 3-20b Relationship between the settlement of the Speswhite kaolin clay and the consolidation pressure

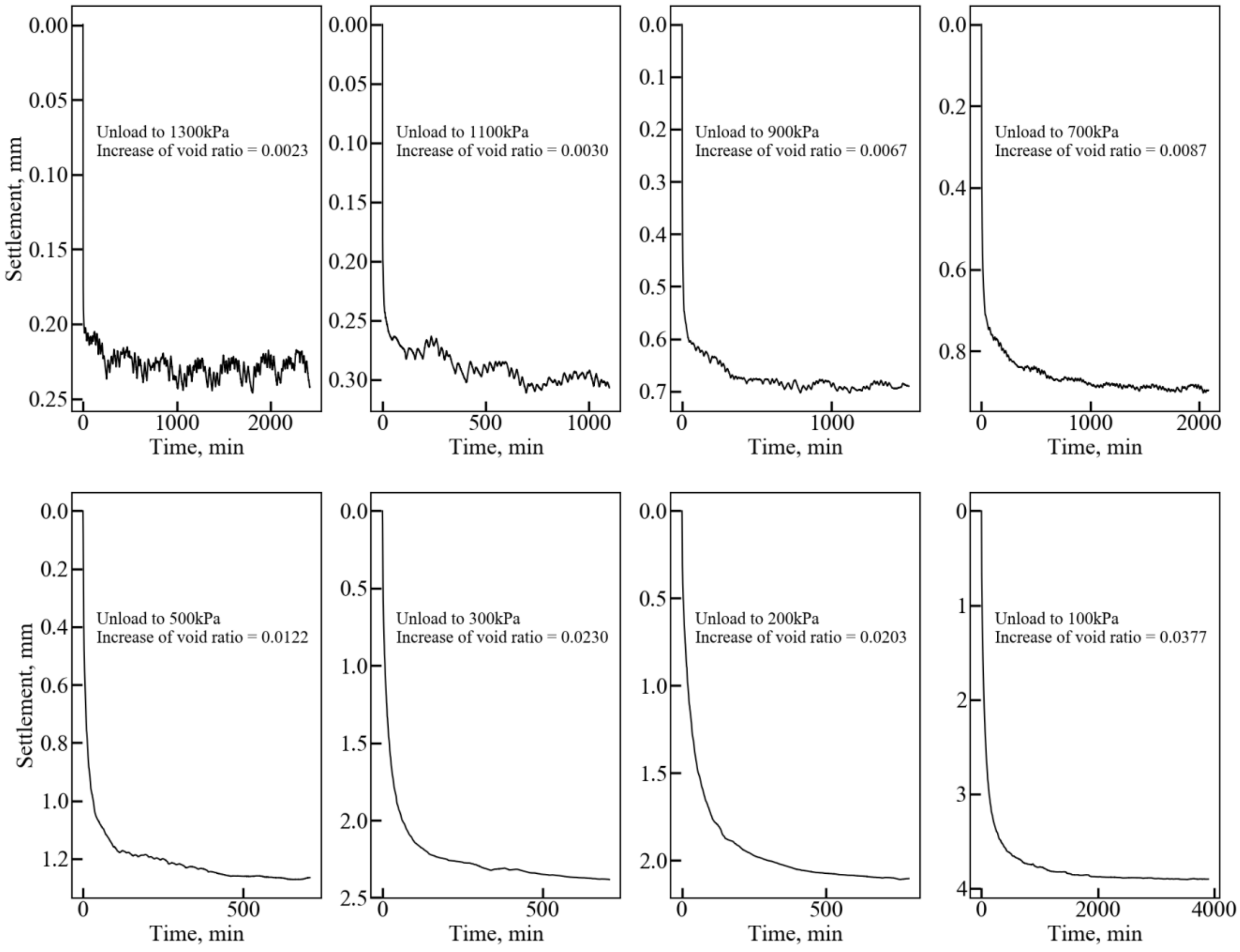

Figure 3-20 Relationship between the settlement of the Speswhite kaolin clay and the consolidation pressure

Based on the settlement of each consolidation stage, the relationship between the void ratio and the vertical consolidation pressure is shown in Figure 3-21. The maximum consolidation pressure, which is 1450 kPa, is the upper limit of the consolidation system. The high consolidation pressure is intended to achieve two goals: 1) making samples with strengths that are very close to those of the Clearwater shales and 2) making sure that the stress state of the model is very similar to that of the in-situ condition.

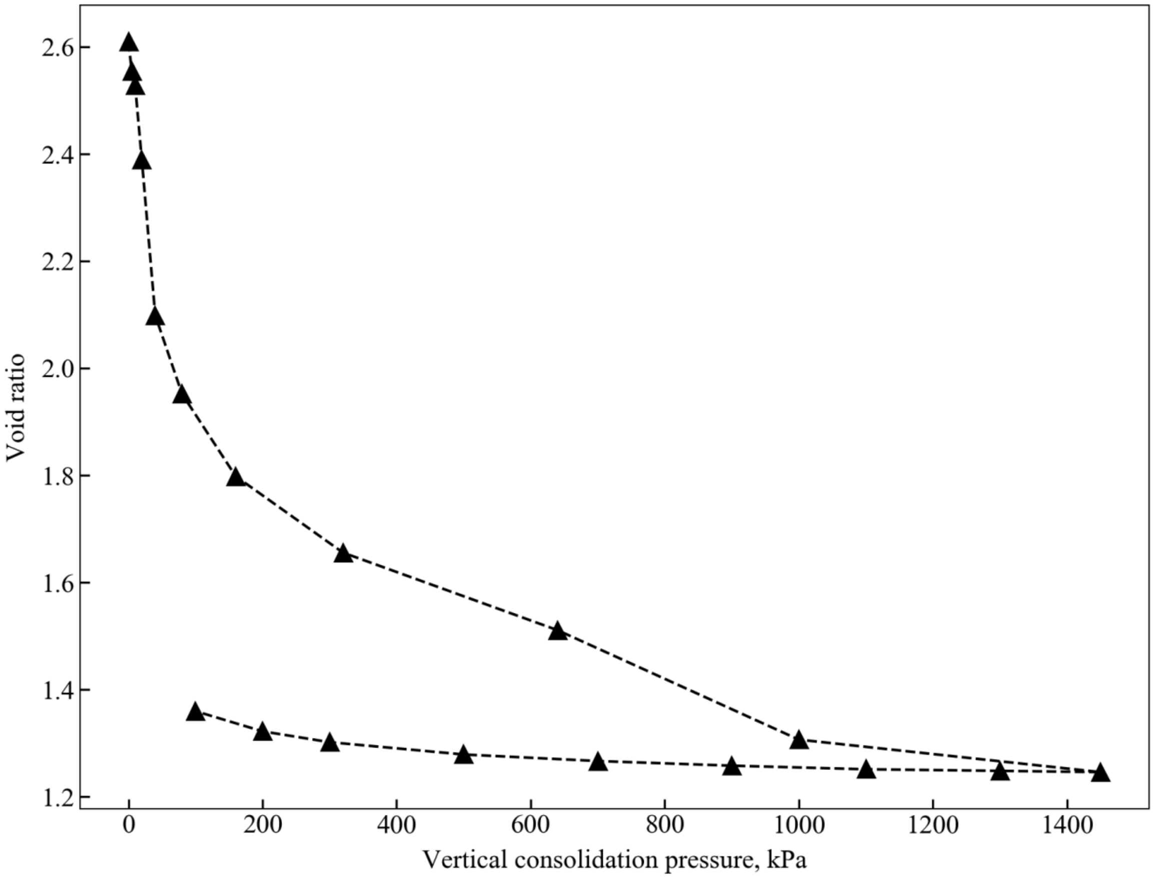

Figure 3-21 Variation of the void ratio after completing each consolidation stage

Figure 3-21 clearly demonstrates that when the vertical consolidation pressure is lower than 200 kPa, the void ratio of the model decreases sharply with the increase of the vertical consolidation pressure. However, when the vertical consolidation pressure is higher than 200 kPa, the change rate of the void ratio with respect to the vertical consolidation pressure gradually decreases.

After completing the 1450 kPa consolidation, the void ratio is about 1.2. Based on the definition of the plastic limit and the void ratio, it is easy to have the relationship as shown below:

$$\frac{PL}{100} = \frac{m_{w\text{-}PL}}{m_s} = \frac{\rho_w \times V_{w\text{-}PL}}{\rho_s \times V_s} = \frac{1}{2.61} \times e_{PL} \qquad \text{Equation (3-39)}$$

where PL is the plastic limit; $m_{w\text{-}PL}$ is the water quantity in the soil at the plastic limit; m_s is the quantity of soil particles;$\rho_w$and$\rho_s$are the density of water and soil particles, respectively; $V_{w\text{-}PL}$ and V_s are the volume of water and soil particles, respectively; e_{PL} is the void ratio of the soil at the plastic limit.

The void space is assumed to be fully filled with water during the consolidation stage. Therefore, when the water content is at the plastic limit, the corresponding void ratio is 0.9135, which is lower than 1.2, indicating that the model after 1450 kPa consolidation is very soft and that the consolidated Speswhite kaolin clay may not be suitable to represent Clearwater shale for the physical modelling test. Regardless of this assessment, a test using the kaolin clay was conducted to examine its behaviour as well as provide an initial scoping test for the caprock testing workflow.

3.10 Geotechnical centrifuge modelling test using Speswhite kaolin clay

This geotechnical centrifuge modelling test uses the consolidated Speswhite kaolin clay to model the behaviour of the Clearwater shales. As shown in Table 3-4, the initial water content of the soil slurry is 100%. The initial height of the soil-water mixture in the PSB is approximately 37.5 cm. After completing consolidation (maximum consolidation pressure = 1450 kPa), the final height is approximately 20 cm. Based on the scaling law of the geotechnical centrifuge, the model can be used to model the behaviour of the caprock with 20 m thickness when the centrifuge is spinning at 100 g.

The overburden pressure on the caprock, which is a function of the buried depth, the Earth's gravity and the overburden density, is simulated through an appropriate thickness of lead bars. The relationship between the weight of lead bars and the corresponding thickness of in situ overburden is calculated based on the following derivation:

Table 3-4 Sample information of the geotechnical centrifuge modelling test

Slurry preparation					
Soil	Speswhite kaolin clay				
Liquid limit, %	65				
Plastic limit, %	35				
Initial water content, %	100				
Weight of Speswhite kaolin clay, kg	37.8				
Sample preparation					
Initial height, cm	37.5	37.3	37.1	37.2	37.4
Final height, cm	19.9	20.2	19.5	19.9	20.0
Weight of lead bars, kg	86.2				
Vertical pressure at 100g, kPa	604				
Overburden height, m	28.64				
Parameters for GeoCDM					
Jog velocity	1.67				
Jog acceleration	2				
Jog distance	24000				
Shearing time, hr	4				
The corresponding prototype time, yr	4.63				

The total force, F, applied on the model can be expressed as below:

$$F = ma$$ Equation (3-40)

The corresponding vertical pressure, P, on the model is a function of the total force, F, and the horizontal cross-sectional area of the model, A.

$$P = \frac{F}{A} \qquad \text{Equation (3-41)}$$

In this study, the overburden density is assumed to be 2150 kg/m^3.

As shown in Table 3-4, the weight of lead bars on the model is 86.2 kg, and the corresponding buried depth is 28.64 m.

The expansion of the steam chamber is mimicked through the GeoCDM. As shown in Table 3-4, the jog velocity and the jog acceleration are 1.67 and 2, respectively. The jog distance is 24000 which correspond to 20 mm uplift displacement. Because 1200 rotations of the Parker Servo Motor can displace the uplifting table by 1 mm, the corresponding uplifting velocity of the uplifting table is therefore equal to 0.000139 mm/s. The corresponding shearing time in the centrifuge is about 4 hours, which corresponds to 4.63 years prototype time.

To track the progressive development of deformations within the model, images were captured with a camera mounted on the swing platform and focussed on the transparent face of the PSB. Figure 3-22 shows the relationship between the uplift displacement and the image number, captured during the test flight. In general, the images are recorded at constant time intervals, indicating that the relationship shown in the figure should be a linear line. However, a few images are recorded manually during the test to check the workability of the GeoCDM, resulting in the non-linear line shown in the figure. The redundant images do not affect the analysis of the caprock deformation behaviour. To present the results at specific uplift displacement, it is essential to get the corresponding image number based on Figure 3-22. Horizontal and vertical displacement contours and maximum total shear strain contours, which are crucial for understanding deformation within the model and the development of failure surfaces, can be extracted at selected uplift displacements of the GeoCDM.

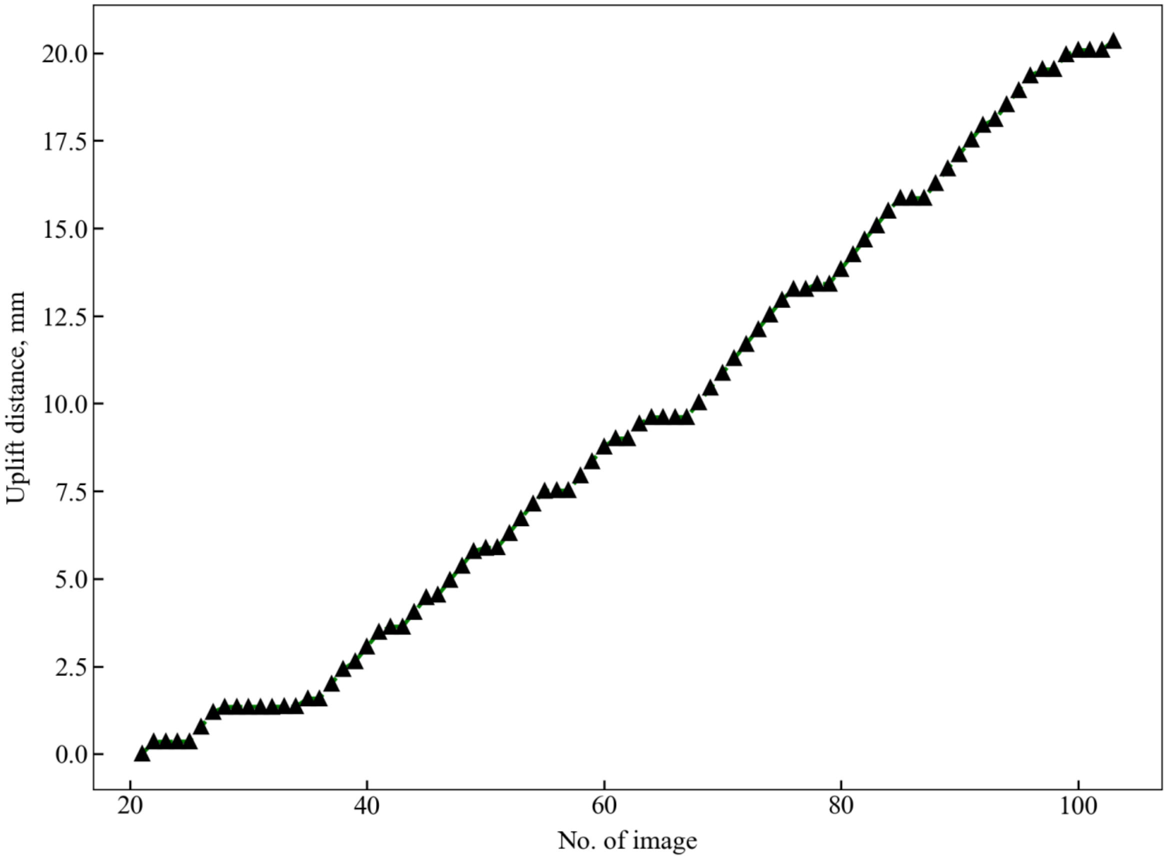

Figure 3-22 The variation of the uplift displacement with the image No.

3.11 Discussion

The analyses discussed above have indicated that the final water content of the model after consolidation at 1450 kPa may be higher than the plastic limit. To assess the potential for this condition, immediately after the physical modelling test, a quick Atterberg plastic limit test was conducted by rolling a mass of test soil on the ground glass plate. When the diameter of the thread was approximately 3.2 mm, it did not crumble, providing qualitative proof that the water content of the soil mass was higher than the plastic limit.

Through the analysis of the images recorded during the centrifuge modelling test, it was clear that the lead bars settled into the model, as shown in Figure 3.23. Prior to starting the centrifuge facility, the lead bars on top of the model do not penetrate into the model. However, immediately after starting the centrifuge facility, the lead bars penetrate into the model in a relatively short time, thus occupying the model space, and changing the level of the model's top surface.

Because of the large settlement of the lead bars, the front surface of the model enlarges. Therefore, the surface density of red sand on the front surface of the model decreases, leading to the phenomenon that some regions of the front surface of the model does not have enough red sand to track the model deformation behavior, which can significantly affect the analysis of the model deformation behaviour.

As the test progresses, the material "flows" into the GeoCDM, which can also affect the experimental results. Compared with the volume of the model, the volume of the soil that leaks into the GeoCDM is very small.

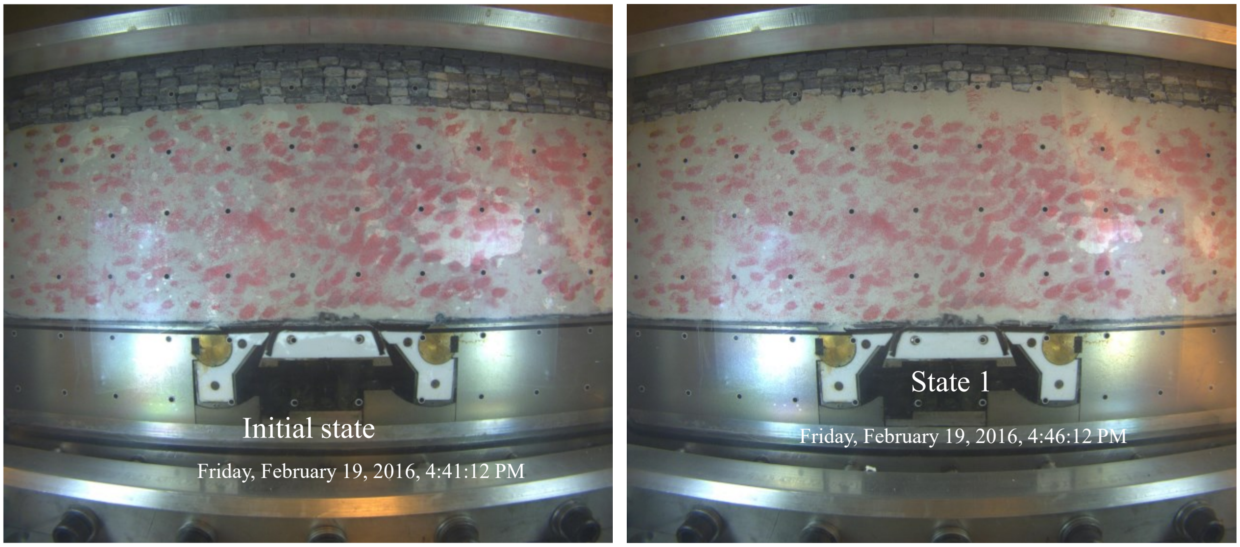

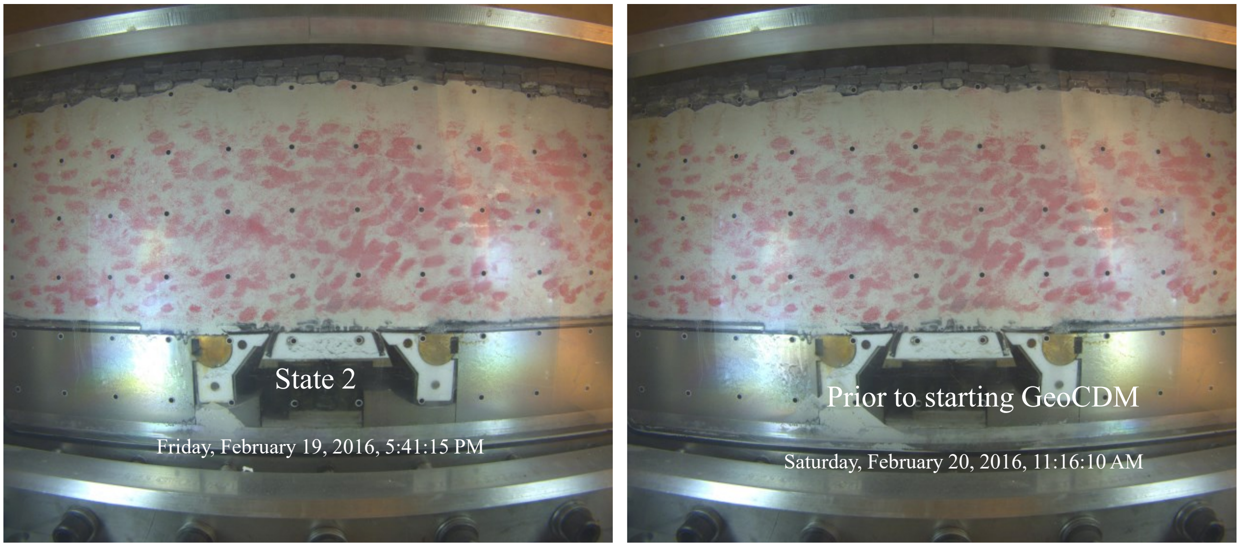

Figure 3-23 Subsidence of the lead bars

The evolution of the horizontal displacement contours, the vertical displacement contours, the resultant displacement contours and the maximum total shear strains are shown in Figure 3-24, Figure 3-25, Figure 3-26 and Figure 3-27, respectively, for cumulative GeoCDM uplift displacements of nominally 1, 5, 10, 15 and 20 mm. The horizontal displacement contour with positive value indicates that the soil particles move towards the +X direction while that with negative value demonstrates that the soil particles move towards the –X direction.

3.11.1 Evolution of the horizontal displacement contours

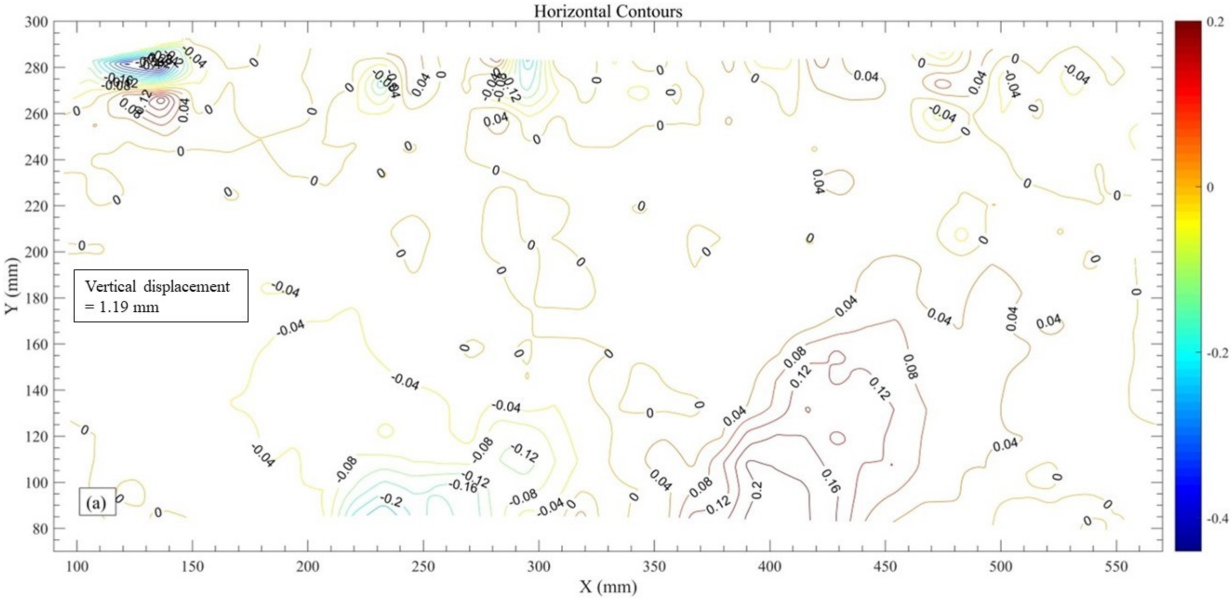

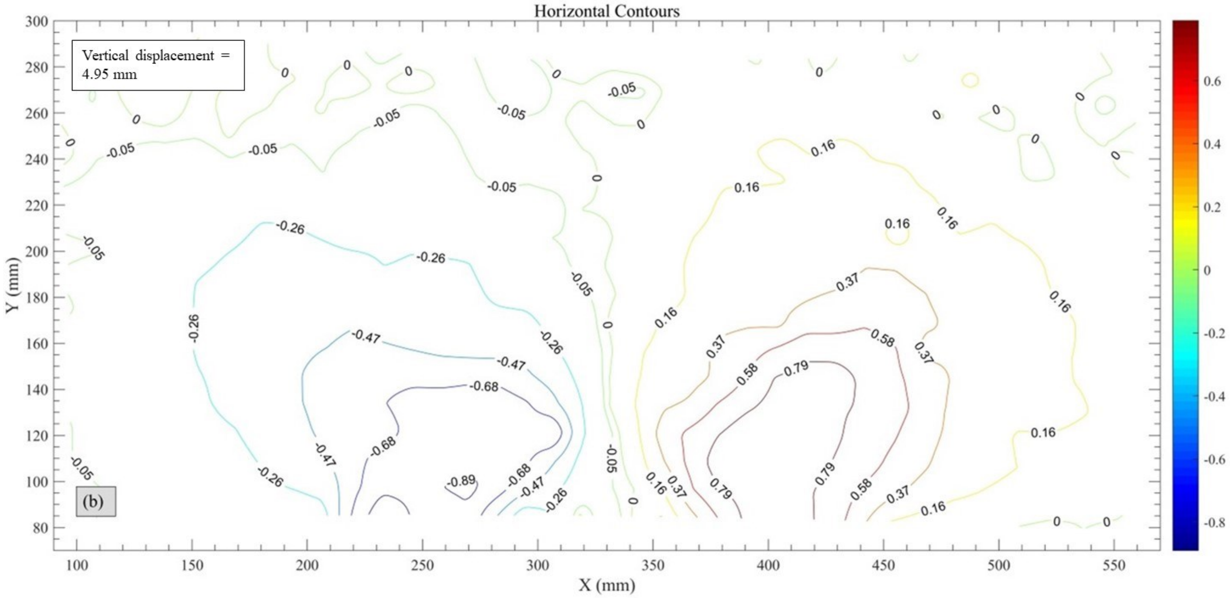

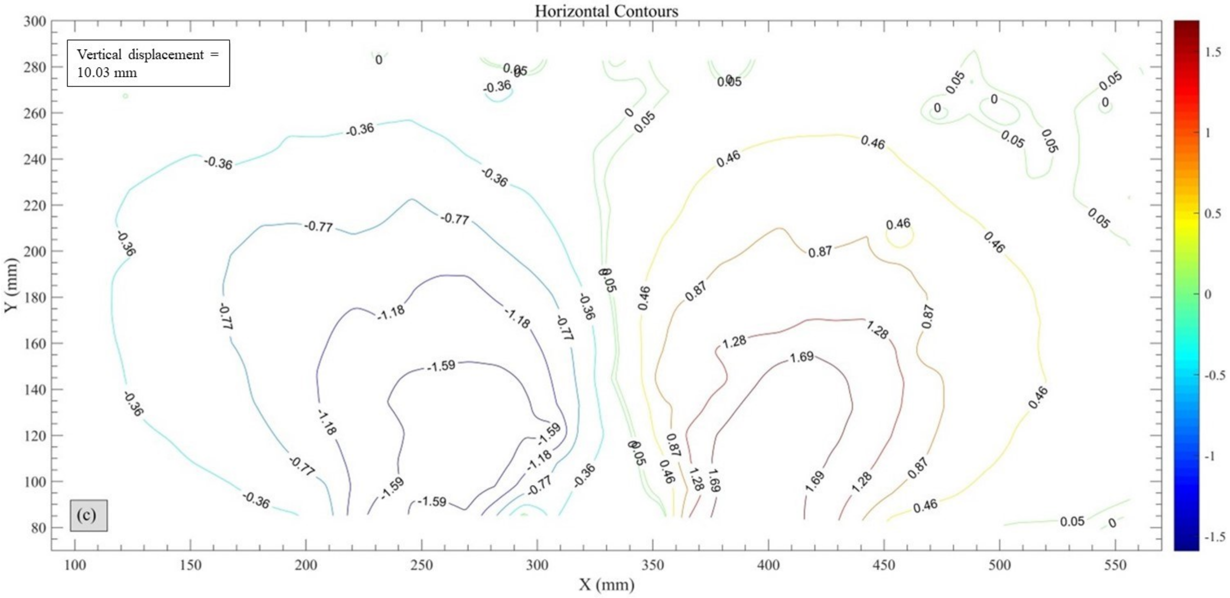
Horizontal Contours
Vertical displacement = 10.03 mm
(c)
Y (mm)
X (mm)
-0.36
-0.77
-1.18
-1.59
0
0.05
0.46
0.87
1.28
1.69
1.5
1
0.5
0
-0.5
-1
-1.5
300
280
260
240
220
200
180
160
140
120
100
80
100
150
200
250
300
350
400
450
500
550

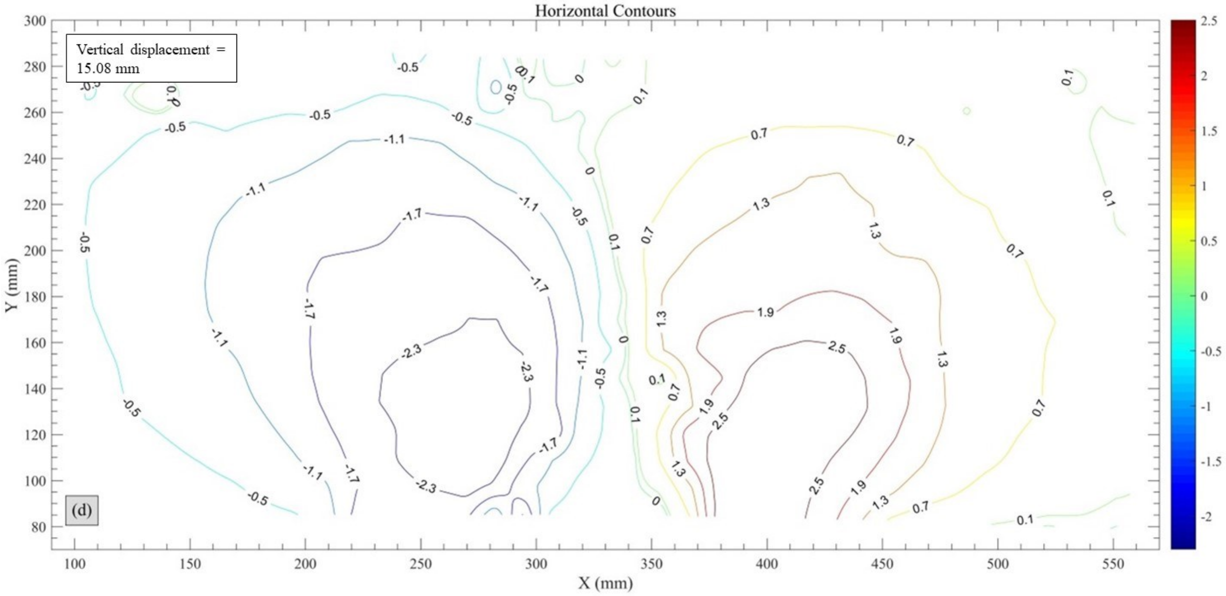
Horizontal Contours
Vertical displacement = 15.08 mm
(d)
Y (mm)
X (mm)
-0.5
-1.1
-1.7
-2.3
0
0.1
0.7
1.3
1.9
2.5
2.5
2
1.5
1
0.5
0
-0.5
-1
-1.5
-2
300
280
260
240
220
200
180
160
140
120
100
80
100
150
200
250
300
350
400
450
500
550

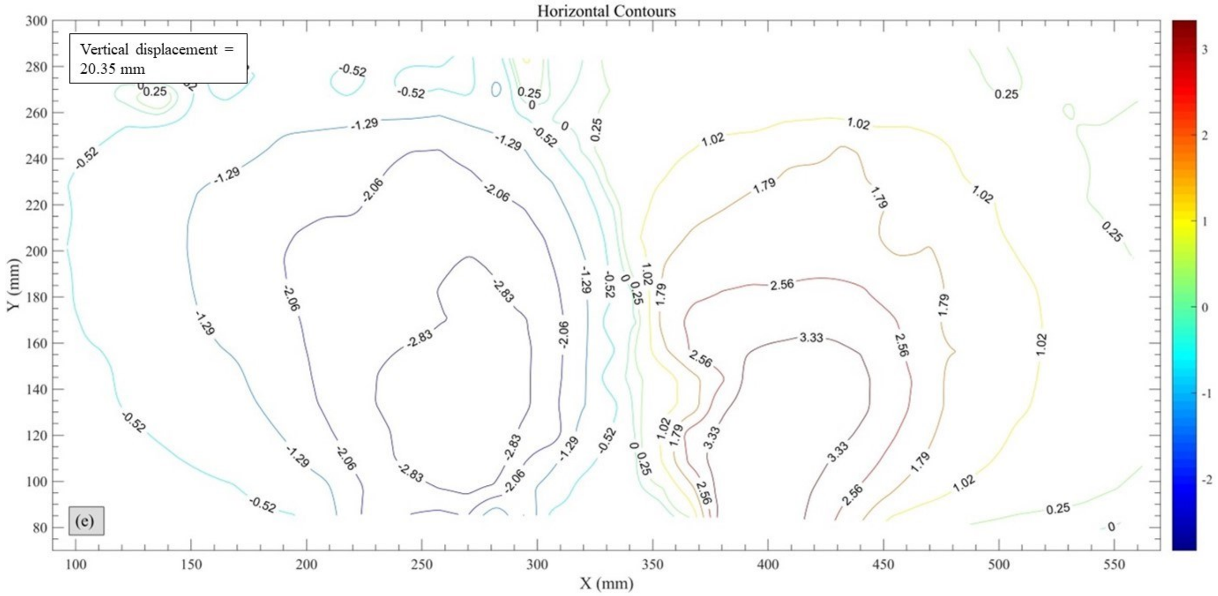

Figure 3-24 Evolution of the horizontal displacement contours. Vertical displacement noted in the grey box is the uplift of the GeoCDM. Contour magnitudes are in mm

3.11.2 Evolution of the vertical displacement contours

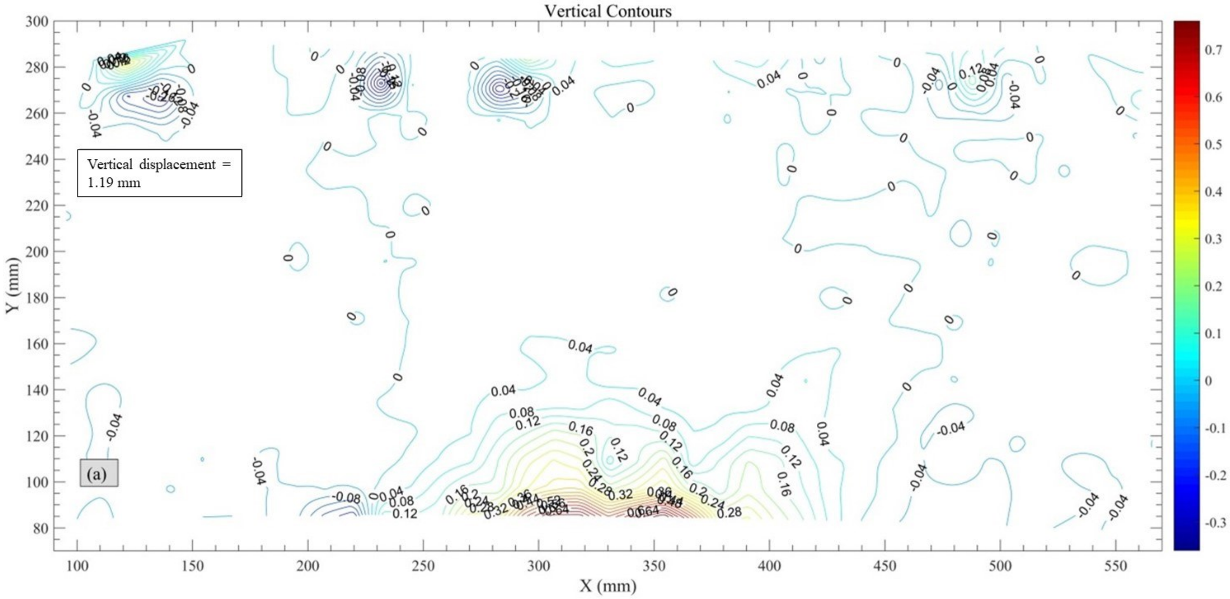

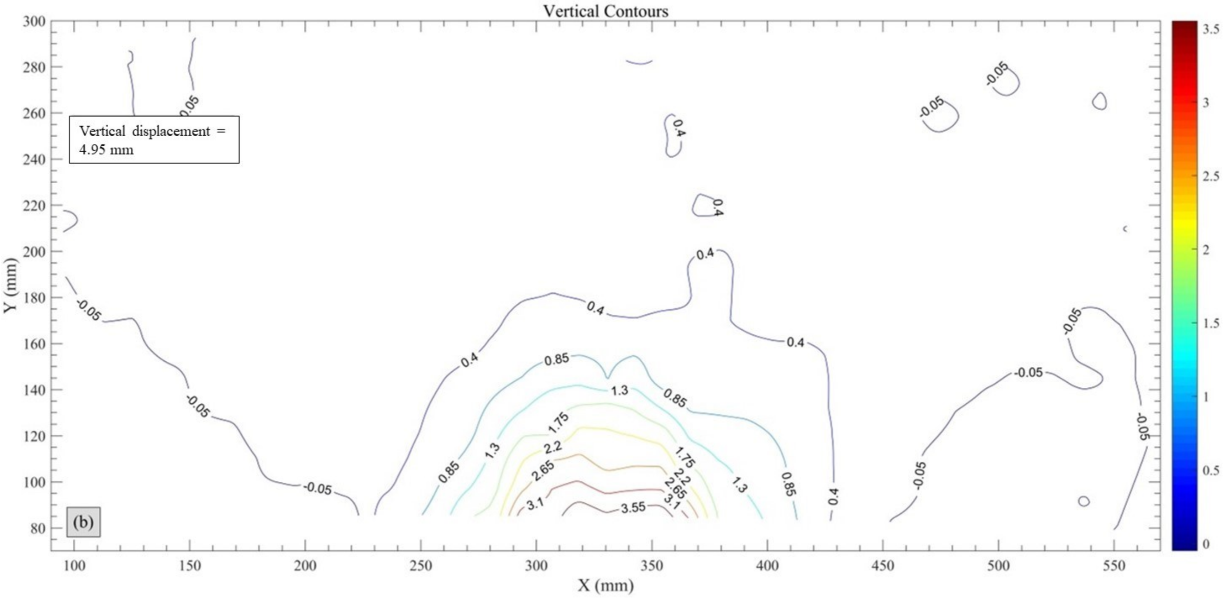
Vertical Contours
Vertical displacement = 4.95 mm
(b)
Y (mm)
X (mm)
300
280
260
240
220
200
180
160
140
120
100
80
100
150
200
250
300
350
400
450
500
550
-0.05
0.4
0.85
1.3
1.75
2.2
2.65
3.1
3.55
3.5
3
2.5
2
1.5
1
0.5
0

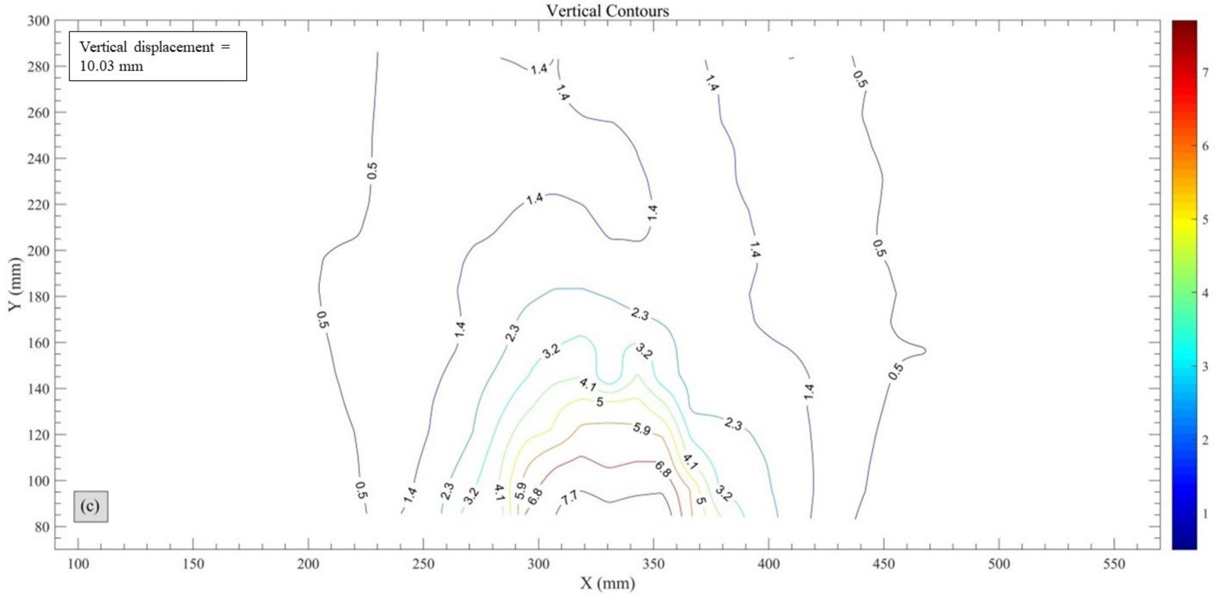
Vertical Contours
Vertical displacement = 10.03 mm
(c)
Y (mm)
X (mm)
300
280
260
240
220
200
180
160
140
120
100
80
100
150
200
250
300
350
400
450
500
550
0.5
1.4
2.3
3.2
4.1
5
5.9
6.8
7.7
7
6
5
4
3
2
1

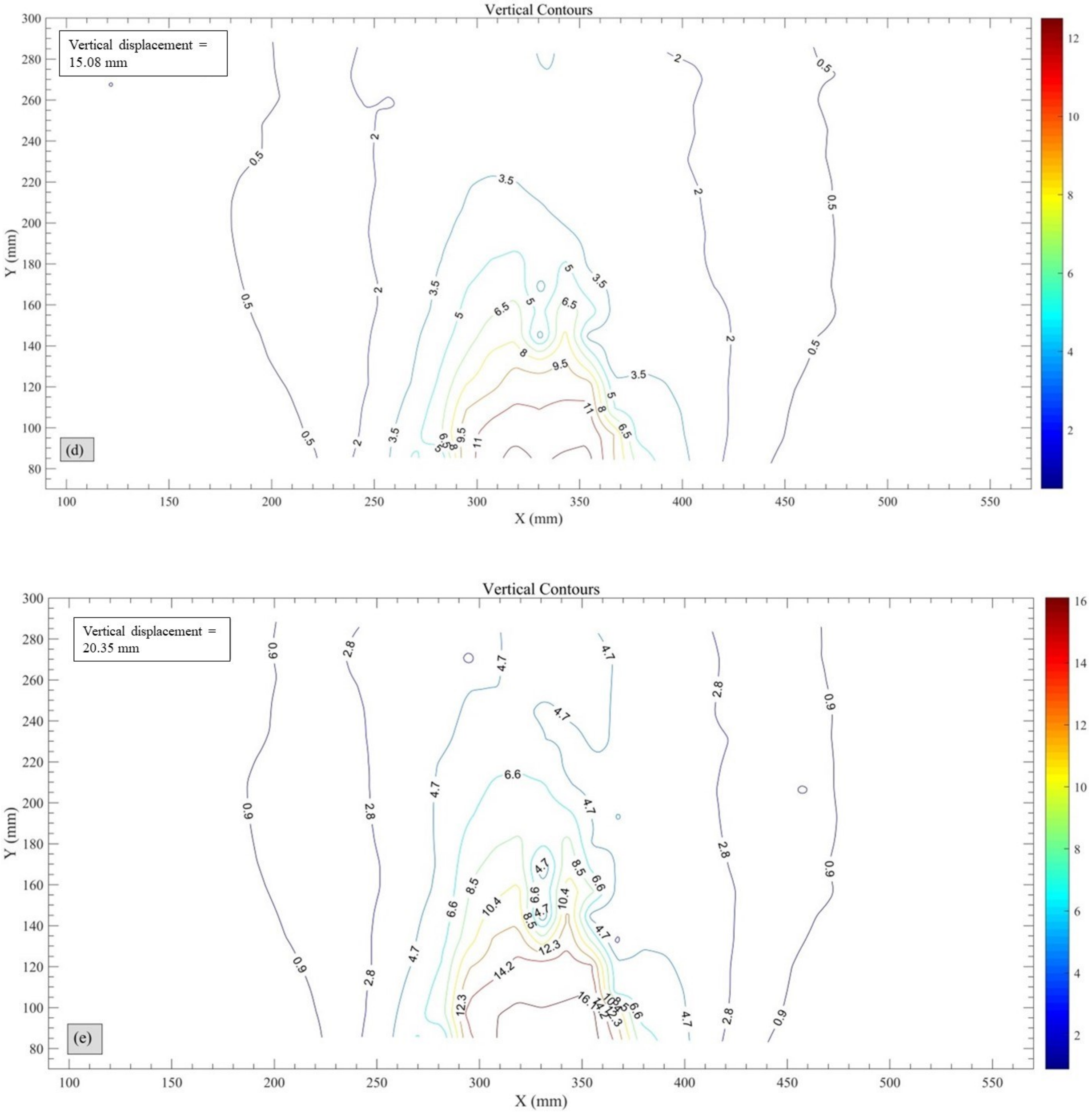

Figure 3-25 Evolution of the vertical displacement contours. Vertical displacement noted in the grey box is the uplift of the GeoCDM. Contour magnitudes are in mm.

3.11.3 Evolution of the resultant displacement contours

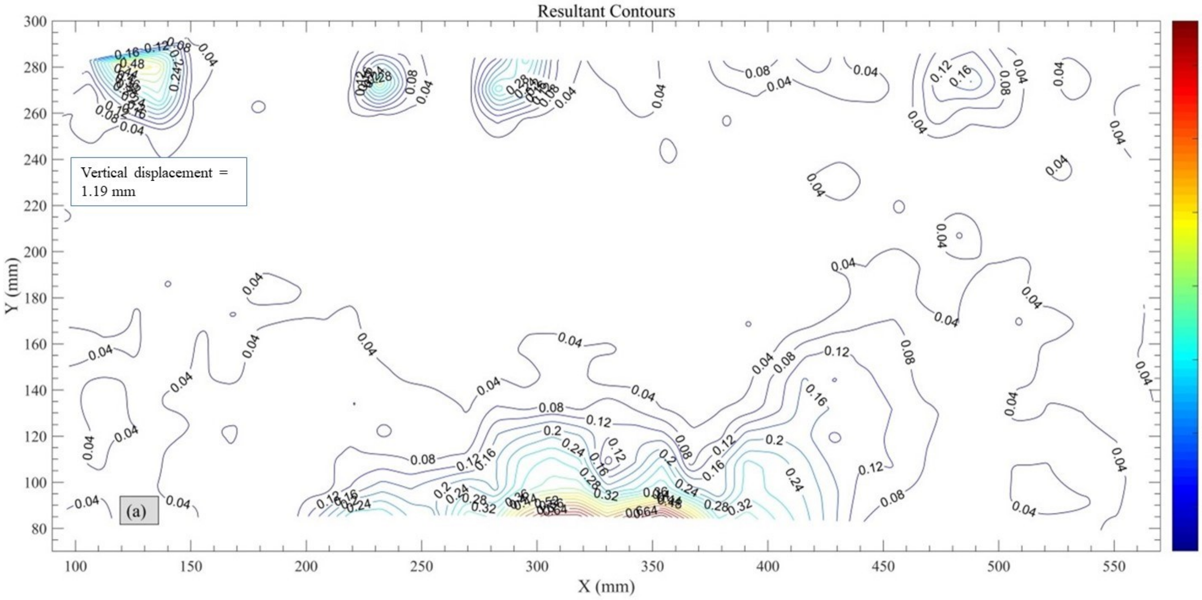

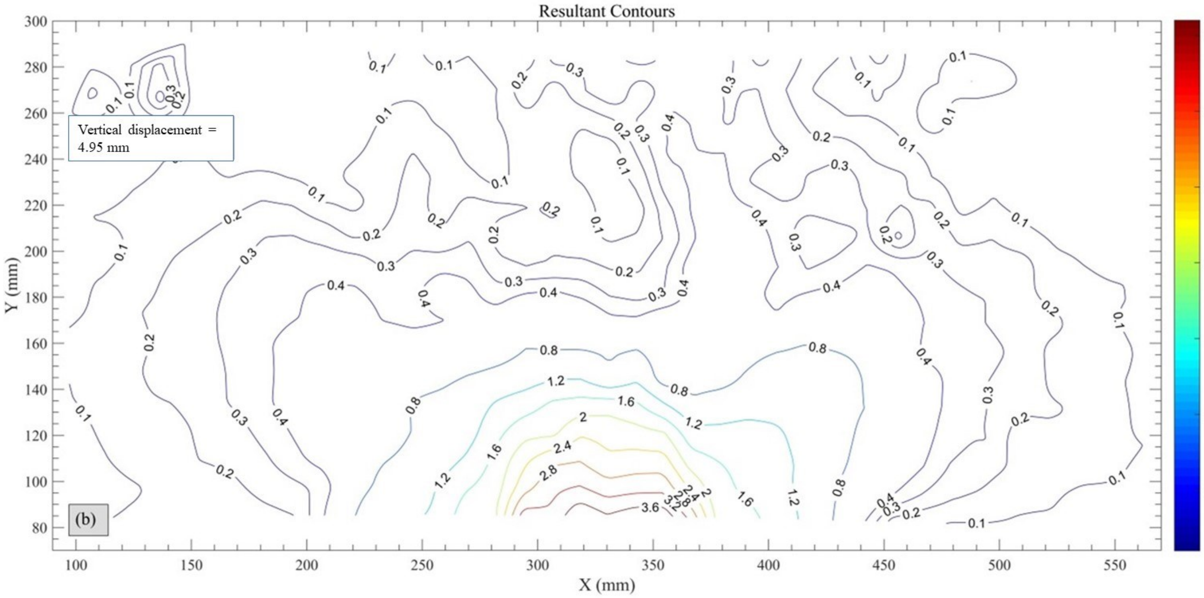

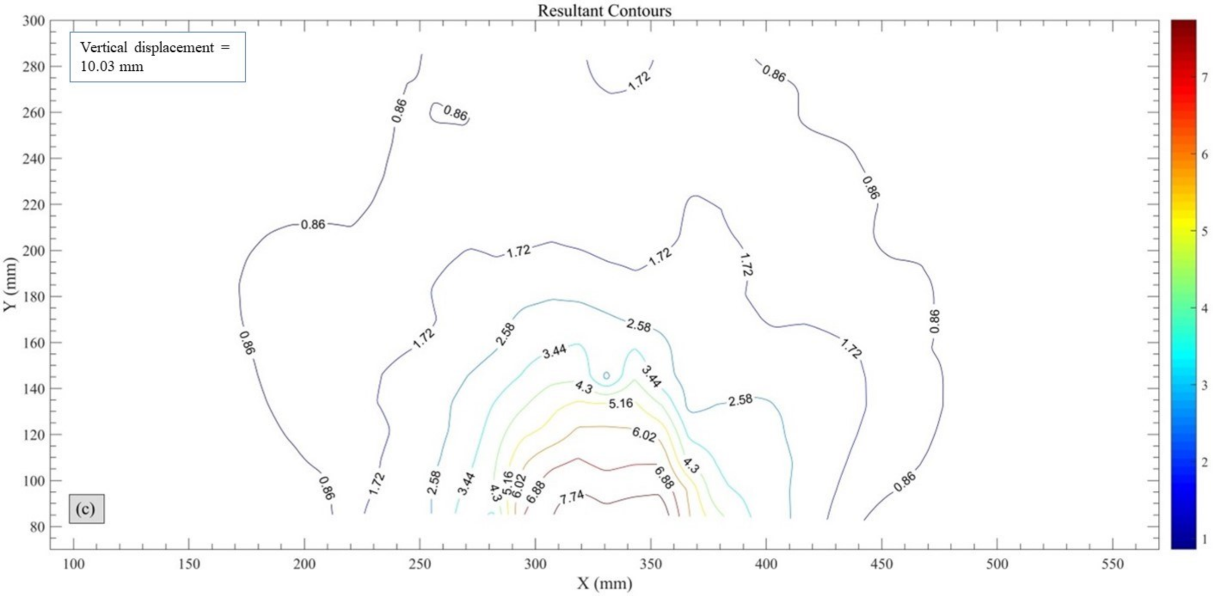
Resultant Contours
Vertical displacement = 10.03 mm
(c)
Y (mm)
X (mm)
0.86
1.72
2.58
3.44
4.3
5.16
6.02
6.88
7.74
100
150
200
250
300
350
400
450
500
550
80
100
120
140
160
180
200
220
240
260
280
300
1
2
3
4
5
6
7

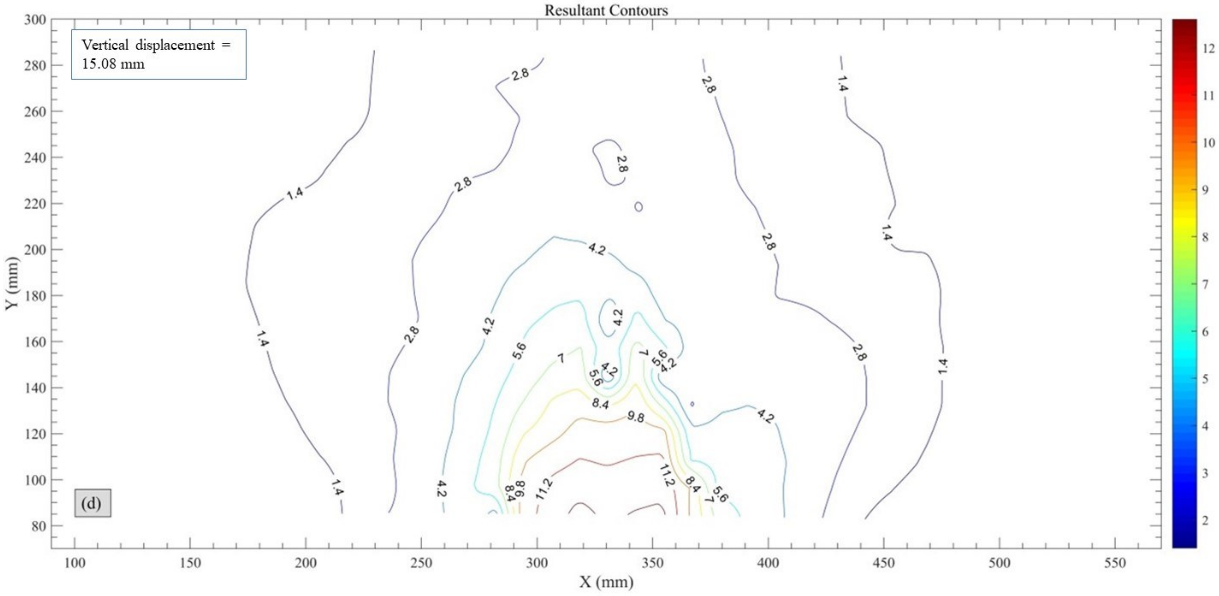
Resultant Contours
Vertical displacement = 15.08 mm
(d)
Y (mm)
X (mm)
1.4
2.8
4.2
5.6
7
8.4
9.8
11.2
100
150
200
250
300
350
400
450
500
550
80
100
120
140
160
180
200
220
240
260
280
300
2
3
4
5
6
7
8
9
10
11
12

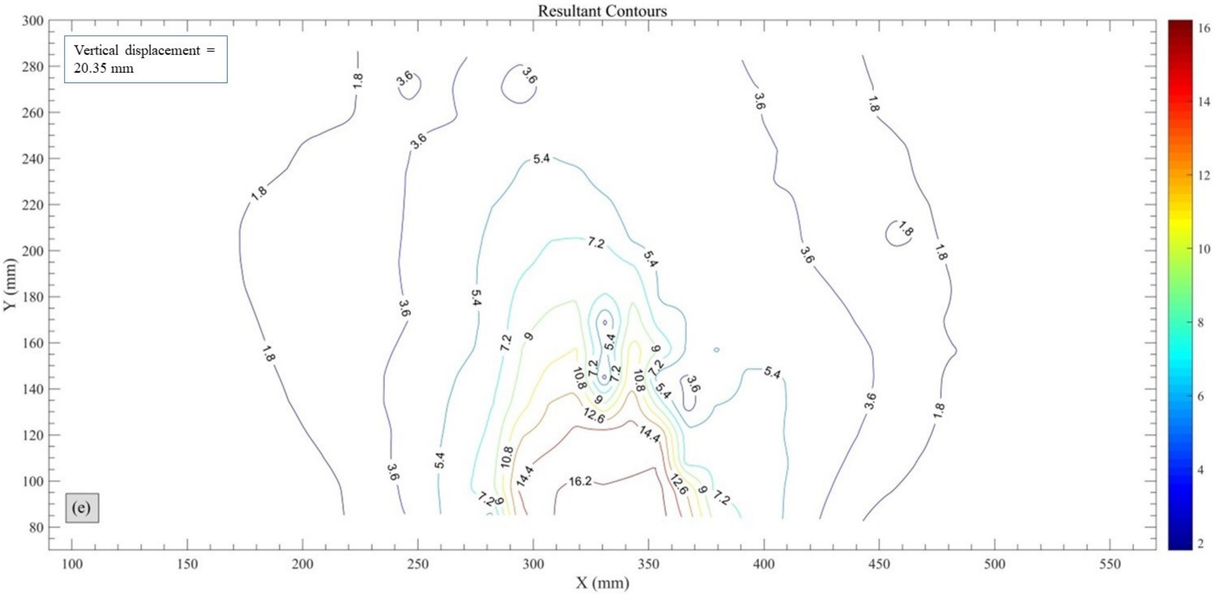

Figure 3-26 Evolution of the resultant (total) displacement contours. Vertical displacement noted in the grey box is the uplift of the GeoCDM. Contour magnitudes are in mm.

3.11.4 Evolution of the maximum total shear strain

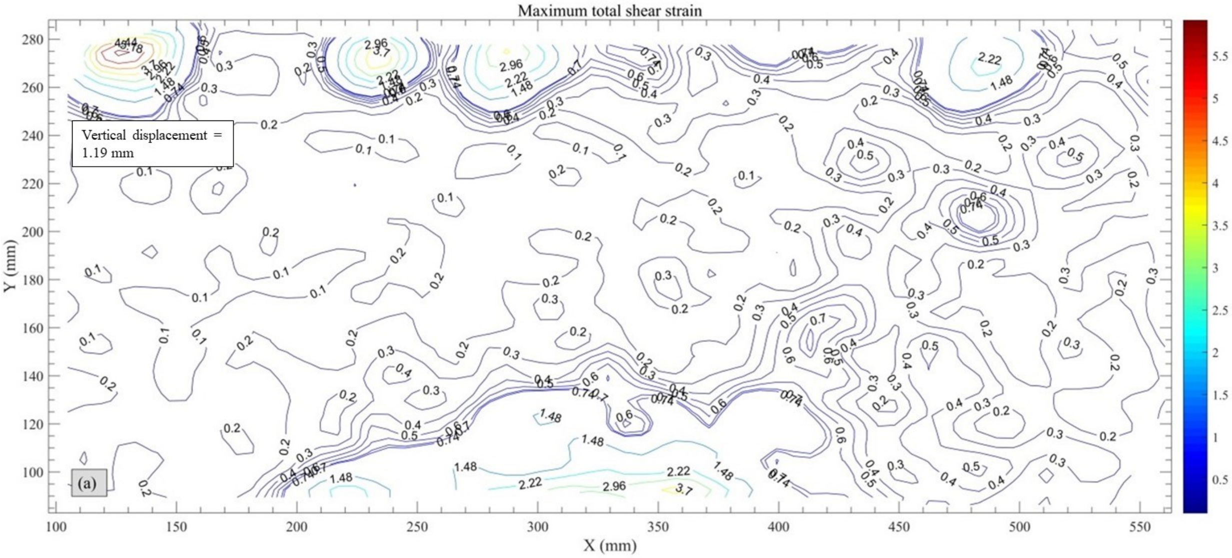

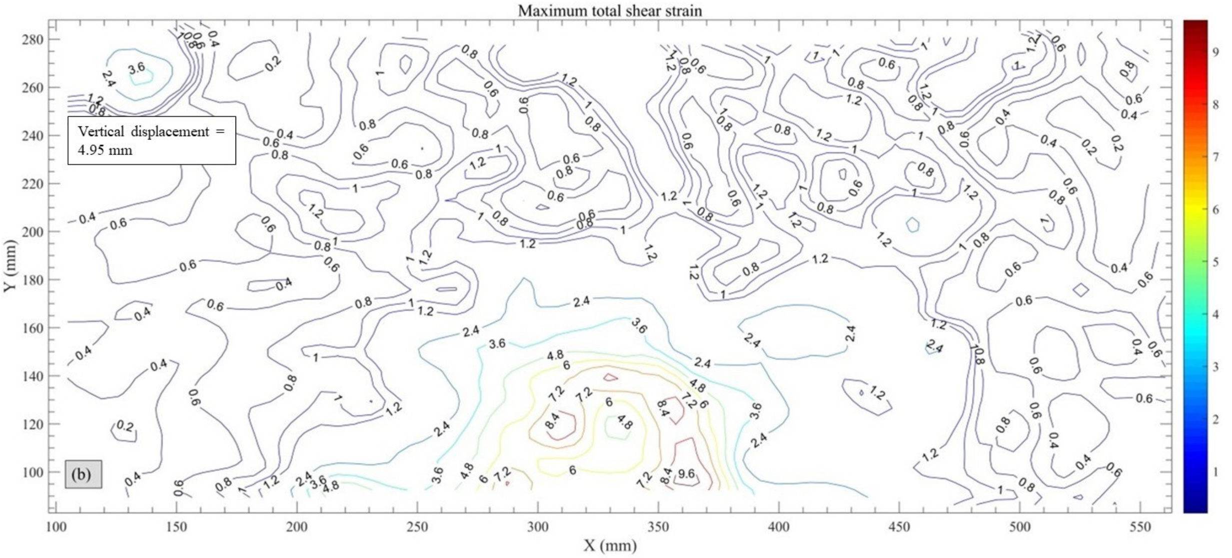

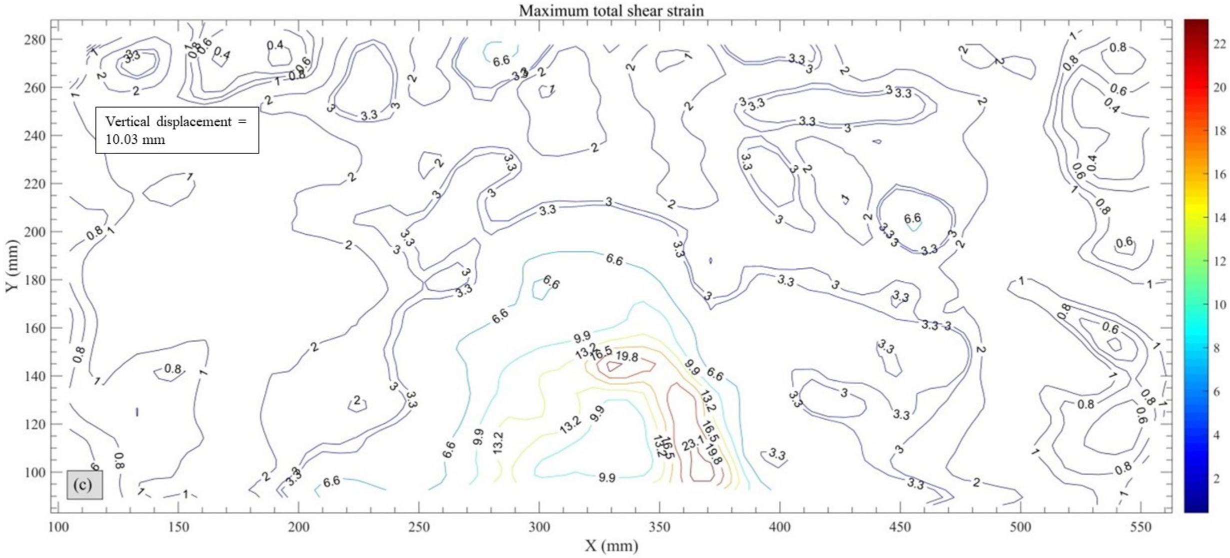
Maximum total shear strain
Vertical displacement = 10.03 mm
(c)
Y (mm)
X (mm)
100
120
140
160
180
200
220
240
260
280
100
150
200
250
300
350
400
450
500
550
2
4
6
8
10
12
14
16
18
20
22

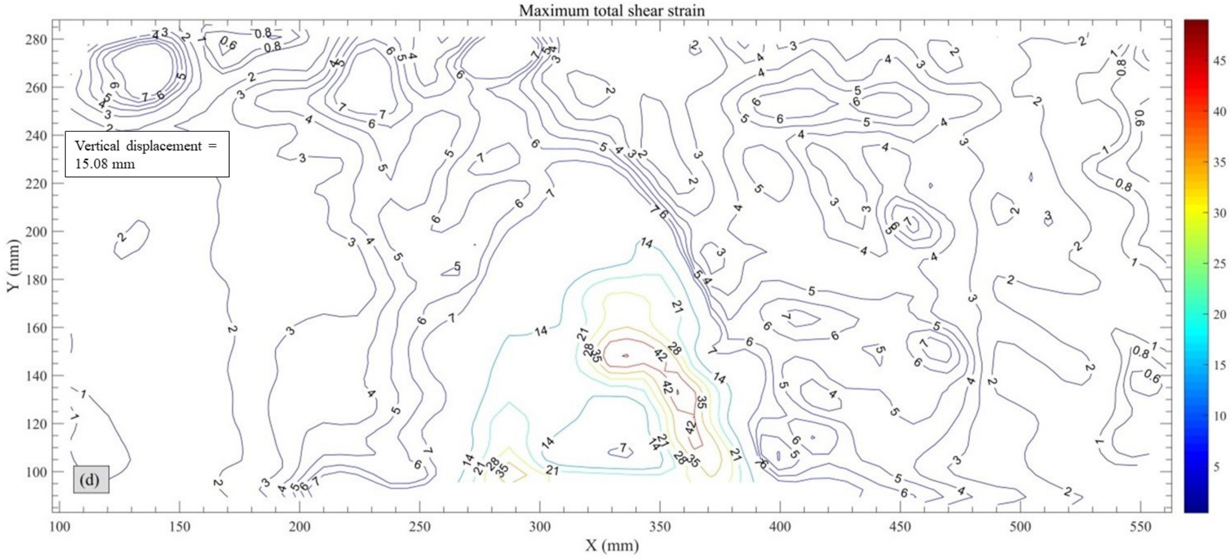
Maximum total shear strain
Vertical displacement = 15.08 mm
(d)
Y (mm)
X (mm)
100
120
140
160
180
200
220
240
260
280
100
150
200
250
300
350
400
450
500
550
5
10
15
20
25
30
35
40
45

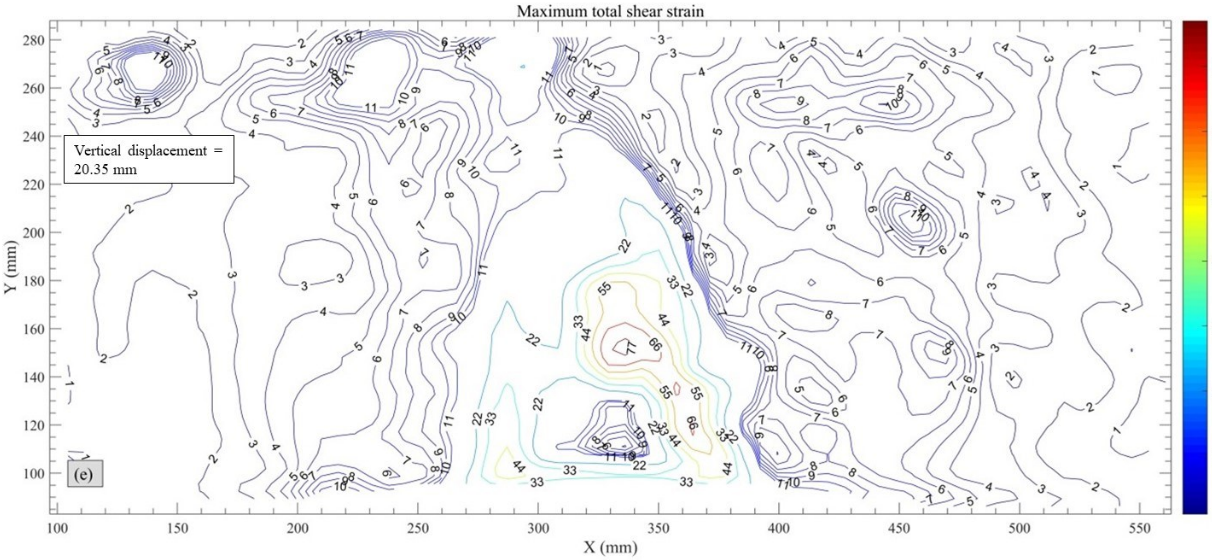

Figure 3-27 Evolution of the maximum total shear strain. Vertical displacement noted in the grey box is the uplift of the GeoCDM.

The analysis of the five subplots in Figure 3-24 demonstrates that the horizontal displacement contours are symmetrical with reference to the centreline of the model. The horizontal displacement contours concentrate at the vertices of the uplifting table, indicating that the gradient of the horizontal displacement contours changes rapidly at the two points. This observation concludes that the vertices of the uplifting table may be the most highly strained area. Moreover, these horizontal displacement contours form balloon-shaped curves with the lip at the vertices of the uplifting table. With the increase of the uplifting displacement, the horizontal displacement contour enlarges, as if the balloon is being blown up. But it seems that the “balloons” never cross over the centreline of the model.

From the analysis of the five subplots in Figure 3-25, it is evident that the evolution of the vertical displacement initializes at the uplifting table. The contour forms an ellipse curve with the major axis coinciding with the uplifting table. However, with the increase of the uplifting table distance, the ellipse expands and turns into a bowl-shaped curve. As the uplifting table moves up, the bowl-shaped curve expands and eventually reaches the top surface of the model. After that, the two edges of the bowl-shaped curve gradually turn into two vertically straight lines.

The vertical displacement of these soil particles decreases from the centreline of the model. Moreover, the vertical displacement contours are also symmetrical with reference to the centreline of the model. With the increase of the uplifting table distance, this phenomenon becomes more obvious. Because the horizontal displacement is relatively small when compared with the vertical displacement, the resultant displacement contours are very similar to those of the vertical displacement contours.

The analysis of the five subplots in Figure 3-27 provides the evolution of the maximum total shear strain. Obviously, at the initial stage, the vertices of the uplifting table or the uplifting table itself are the most highly strained area. At the same time, there are a few highly strained areas at the top of the model, which are induced by the subsidence of the lead bars.

The most highly strained area forms a cone-shaped curve and expands as the test goes on. The bottom of the highly strained area coincides with the uplifting table and the flanks and seems to be unchanged as the uplifting table moves up. In contrast, its height enlarges and eventually reaches the top surface of the model and may induce the caprock failure. However, no fracture can be detected in the model. This is mainly because the material is very soft and exerts ductile behaviour during the test.

Based on the above analysis, the value of the vertical displacement contours decreases toward the model surface. The same conclusion can also be obtained when analyzing the value of the maximum total shear strain contours. Therefore, it may be concluded that the soil directly above the uplifting table is compressed.

In summary, the centrifuge modelling test provides valuable information for the identification of the caprock failure process. However, due to the weak strength of the material, it cannot be used to represent the Clearwater shale for future tests.

3.12 Consolidation behaviour of the synthetic Clearwater shale-I

Table 3-5 Sample preparation of the synthetic Clearwater shale-I

Slurry preparation					
Speswhite kaolin clay: Sil325 (38-75µm)	55:45				
Total soil-water content, %	100				
Total soil-water to cement ratio	7.5				
Wt. of Speswhite kaolin clay, kg	14.9905				
Wt. of Sil325 (38-75µm), kg	12.2702				
Wt. of cement, kg	3.6349				
Wt. of water, kg	27.2894				
Initial height, cm	26.7	26.5	26.6	26.1	26.8

As discussed previously, the consolidated Speswhite kaolin clay is too soft to represent the Clearwater shale for the physical modelling test. This next test utilized a mixture of Speswhite kaolin clay, Sil325(38-75µm), cement and water to prepare the synthetic Clearwater shale known as the synthetic Clearwater shale-I for the physical modelling test.

Table 3-5 describes the parameters for the preparation of the soil-water-cement mixture. The Speswhite kaolin clay to Sil325 (38-75µm) proportion is 55:45, and the total soil-water to cement ratio is 7.5. The curing period takes almost two months, leaving enough time for the hydration and pozzolanic reactions.

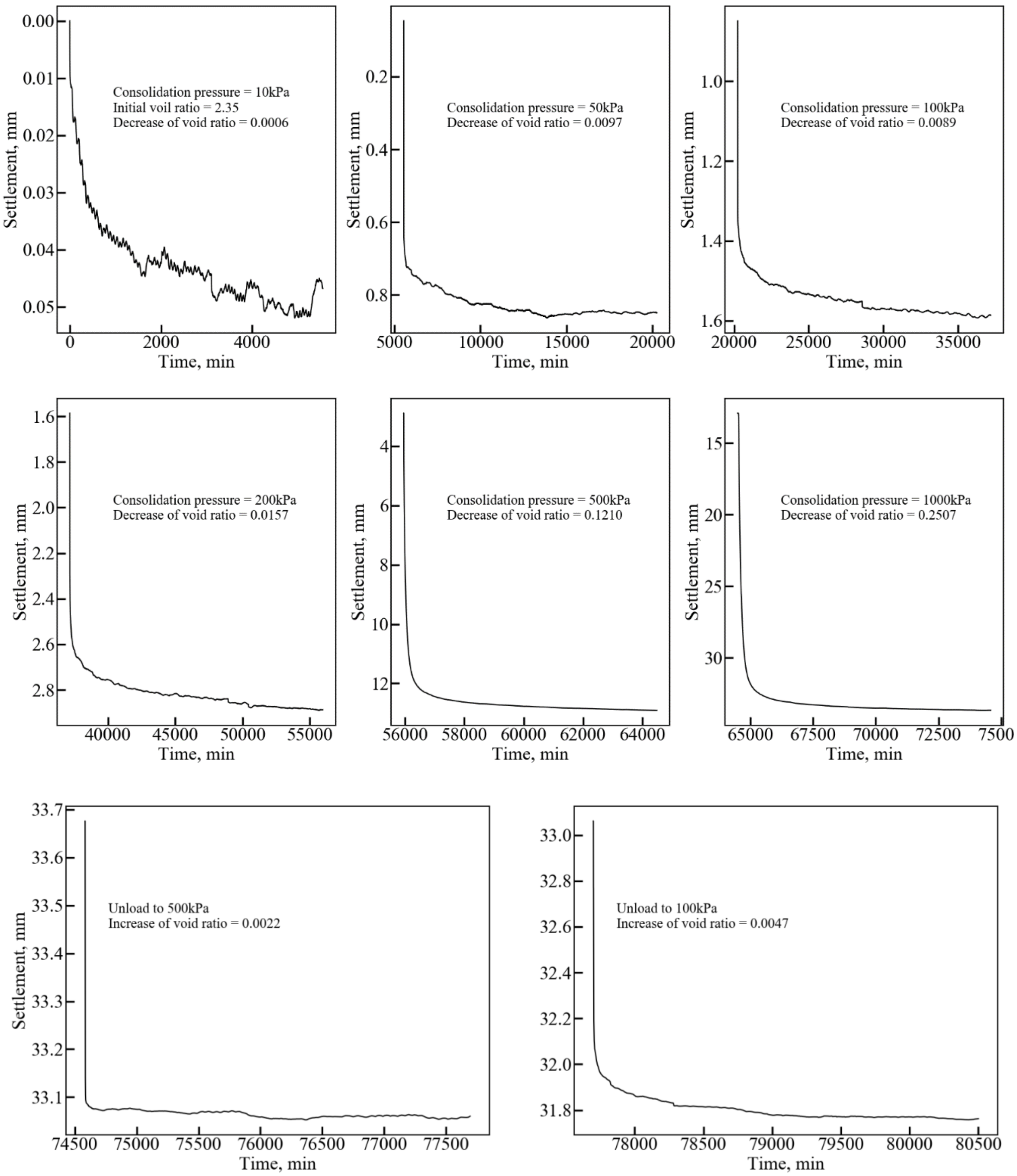
Consolidation pressure = 10kPa
Initial voil ratio = 2.35
Decrease of void ratio = 0.0006
Settlement, mm
0.00
0.01
0.02
0.03
0.04
0.05
0
2000
4000
Time, min
Consolidation pressure = 50kPa
Decrease of void ratio = 0.0097
Settlement, mm
0.2
0.4
0.6
0.8
5000
10000
15000
20000
Time, min
Consolidation pressure = 100kPa
Decrease of void ratio = 0.0089
Settlement, mm
1.0
1.2
1.4
1.6
20000
25000
30000
35000
Time, min
Consolidation pressure = 200kPa
Decrease of void ratio = 0.0157
Settlement, mm
1.6
1.8
2.0
2.2
2.4
2.6
2.8
40000
45000
50000
55000
Time, min
Consolidation pressure = 500kPa
Decrease of void ratio = 0.1210
Settlement, mm
4
6
8
10
12
56000
58000
60000
62000
64000
Time, min
Consolidation pressure = 1000kPa
Decrease of void ratio = 0.2507
Settlement, mm
15
20
25
30
65000
67500
70000
72500
7500
Time, min
Unload to 500kPa
Increase of void ratio = 0.0022
Settlement, mm
33.7
33.6
33.5
33.4
33.3
33.2
33.1
74500
75000
75500
76000
76500
77000
77500
Time, min
Unload to 100kPa
Increase of void ratio = 0.0047
33.0
32.8
32.6
32.4
32.2
32.0
31.8
78000
78500
79000
79500
80000
80500
Time, min

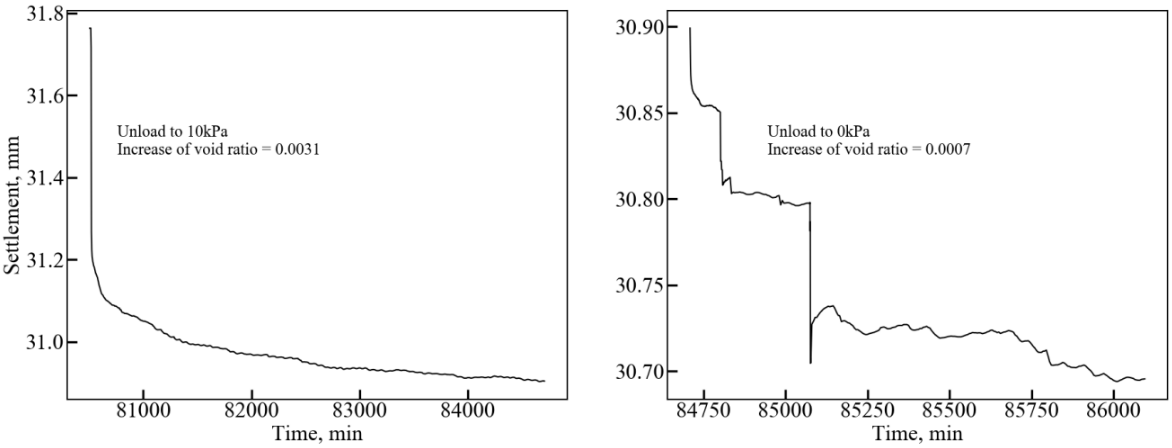

Figure 3-28 Consolidation behaviour of the synthetic Clearwater water-I

Figure 3-28 demonstrates the variation of the settlement at different consolidation pressures. Each subplot also illustrates the change of the void ratio. The initial void ratio of the soil-water-cement slurry is calculated based on the following equation:

$$V_s = \frac{m_{sp}}{G_{sp}} + \frac{m_{silt}}{G_{silt}} + \frac{m_{cement}}{G_{cement}}$$ Equation (3-42)

$$V_w = \frac{m_w}{G_w}$$ Equation (3-43)

$$e = \frac{V_w}{V_s}$$ Equation (3-44)

Where m_{sp}, m_{silt}, m_{cement} and m_w are the weights of Speswhite kaolin clay, Sil325 (38-75 μm), cement and distilled water, respectively; G_{sp}, G_{silt}, G_{cement} and G_w are the specific gravity of Speswhite kaolin clay, Sil325 (38-75 μm), cement and distilled water, respectively; V_w and V_s are the volumes of water and solid, respectively; e is the void ratio.

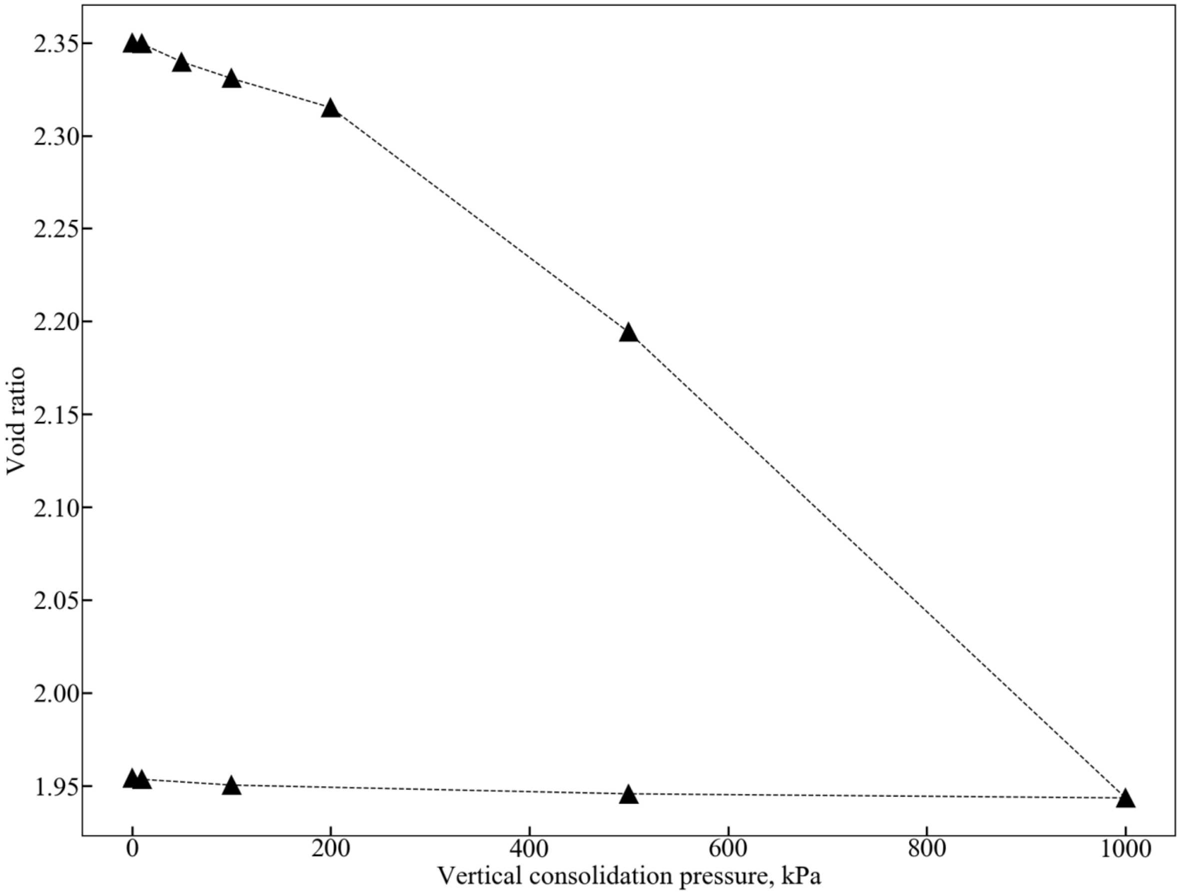

Figure 3-29 The relationship between the void ratio and consolidation pressure

The total settlement is about 30 mm based on the settlement of each consolidation stage. The change of void ratio versus the vertical consolidation pressure is shown in Figure 3-29. A few assumptions are made when calculating the void ratio:

1. The void ratio change is solely induced by the reduction of the void spaces.
2. The chemical reaction between the soil, water and cement does not contribute to the change of the void spaces. However, in practice, specific gravity of the soil-water-cement mixture decreases with the curing period, indicating that the solid volume expands.

3.13 Comparison between Clearwater shale and synthetic Clearwater shale-I

Immediately after completing the consolidation phase on the block, cylindrical samples are extracted from the block for the determination of the unconfined compressive strength, as shown in Figure 3-30. The unconfined compressive strength of the material is approximately 450 kPa. Unfortunately, previous UCS testing conducted on relatively undisturbed Clearwater Formation clay shale showed UCS typically in the range of 1200 to 1300 kPa(Shafie Zadeh & Chalaturnyk, 2015). Based in UCS values, it was concluded that the synthetic Clearwater shale-I was also likely going to be too weak to appropriately represent in situ clay shale behavior, but it clearly showed improved characteristics over Speswhite kaolin clay.

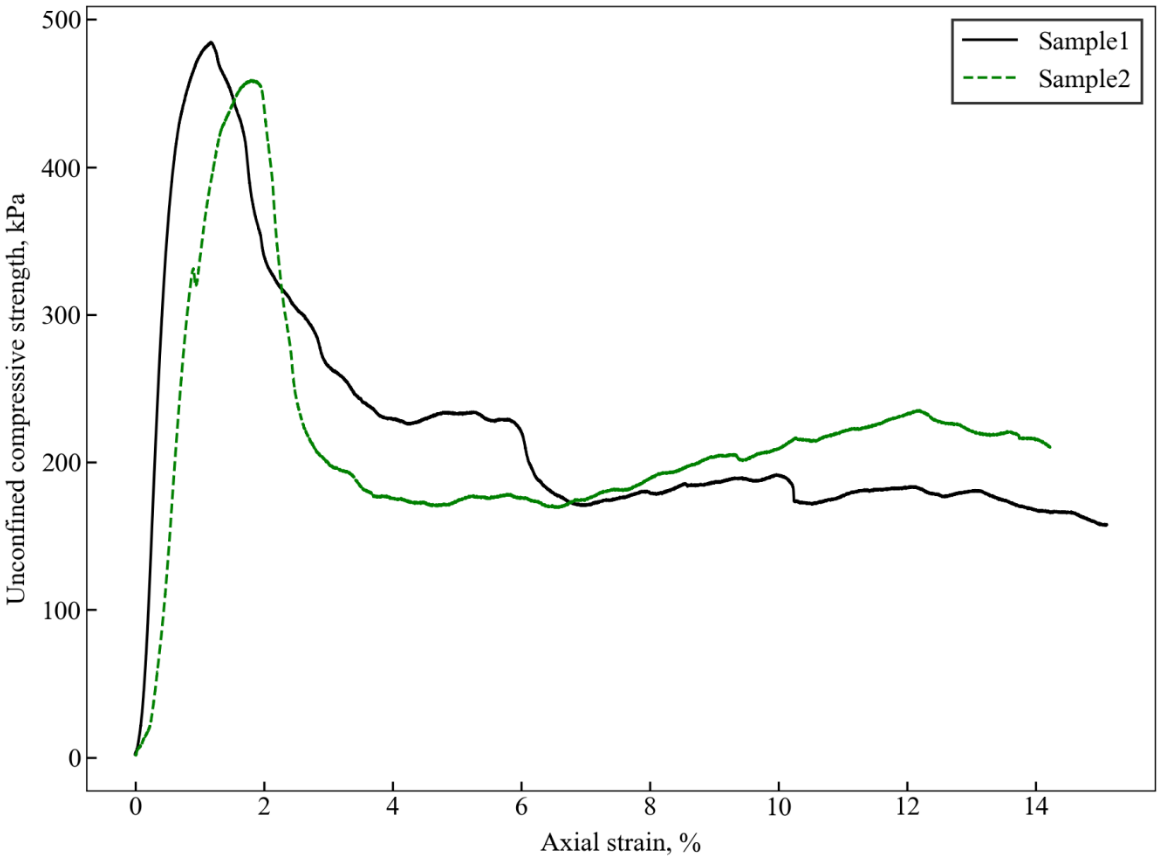

Figure 3-30 Unconfined compressive strength of the synthetic Clearwater shale-I

3.14 The first centrifuge modelling test using the synthetic Clearwater shale-I

Table 3-6 Sample preparation of the centrifuge modelling test using synthetic Clearwater shale-I

Slurry preparation					
Speswhite kaolin clay: Sil325 (38-75μm)	55:45				
Total soil-water content	100				
Total soil-water to cement ratio	7.5				
Wt. of Speswhite kaolin clay, kg	17.00				
Wt. of Sil325 (38-75μm), kg	13.92				
Wt. of cement, kg	4.12				
Wt. of water, kg	30.29				
Sample preparation					
Initial height, cm	29.619	29.62	29.617	29.581	29.893
Final height, cm	24.30	24.40	24.40	24.50	-
Weight of lead bars, kg	73.1				
Vertical pressure at 100g, kPa	512.22				
Overburden height, m	24.29				
Parameters for GeoCDM					
Jog velocity	1.67				
Jog accelerating	2				
Jog distance	24000				
Shearing time, hr	4				
The corresponding prototype time, yr	4.63				

Experimental results showed that the synthetic Clearwater shale-I was stronger than the consolidated Speswhite kaolin clay. However, compared with the in-situ Clearwater clay shale, it was still relatively weak. With an assumption that this material would represent a caprock with low strength, a few geotechnical centrifuge modelling tests were performed by using the synthetic Clearwater shale-I to obtain the deformation behaviour of the caprock with low strength. As shown in Table 3-6, the proportion of Speswhite kaolin clay to Sil325(38-75 μm) is 55 to 45, the total soil-water content is 100% and the total soil-water to cement ratio is 7.5.

The preparation of the soil-water-cement mixture involves two steps:

1. Preparation of the soil-water mixture. The mixing process is the same as that described in section 3.8 and
2. Mixing process of the soil-water-cement mixture. The water-cement mixture is first mixed by hand in a container. Here, it is important to know that the cement powder cannot be added to the soil-water slurry directly because the cement powder can form tiny lumps in the mixture.

Immediately after being prepared, the cement slurry is then added to the soil-water mixture and mixed for another 30 minutes. The well-mixed soil-water-cement mixture is then transferred to the PSB for consolidation and curing. After 28 days, the sample is then processed for the physical modelling test.

Figure 3-31 describes the settlement of the synthetic Clearwater shale-I during the consolidation period. In contrast to the consolidation behaviour of the Speswhite kaolin clay, the settlement of the synthetic Clearwater shale-I at relatively low consolidation pressure is not so obvious. Figure 3-32, which describes the relationship between the void ratio and consolidation pressure, also demonstrates this point. This is mainly because the synthetic Clearwater shale-I is a mixture of soil, water and cement, indicating that the material has relatively high cohesive strength. At relatively low consolidation pressure, the cementitious bonds formed during the hydration and pozzolanic reaction offset the consolidation pressure.

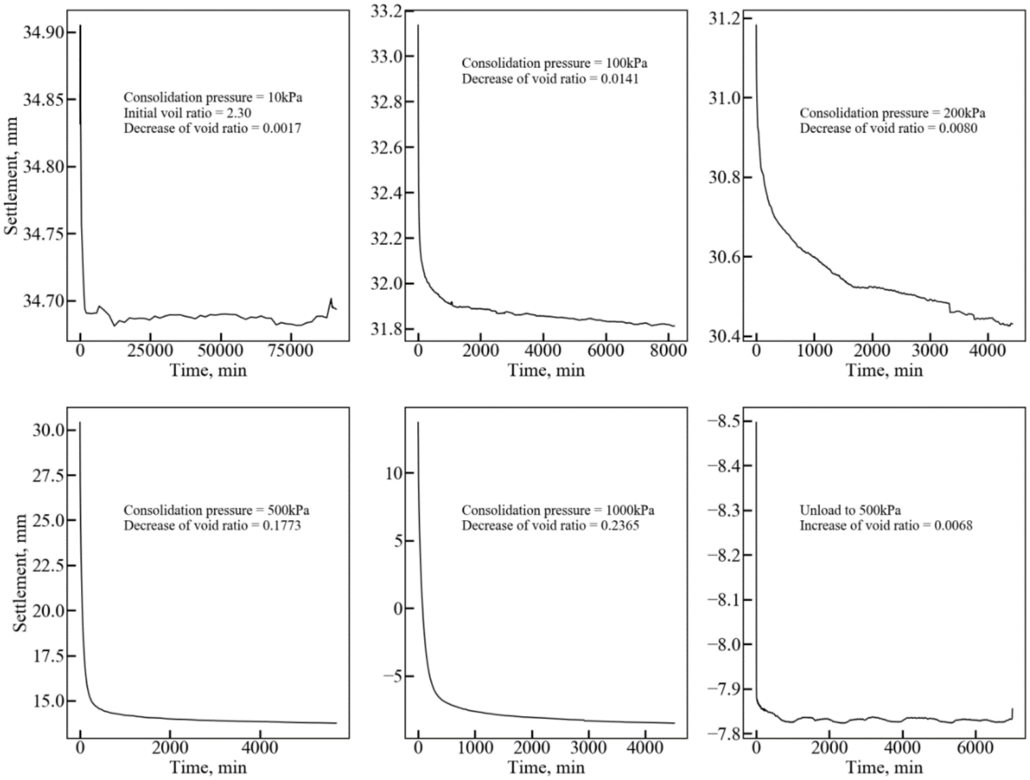

Figure 3-31 Consolidation behaviour of the synthetic Clearwater shale-I

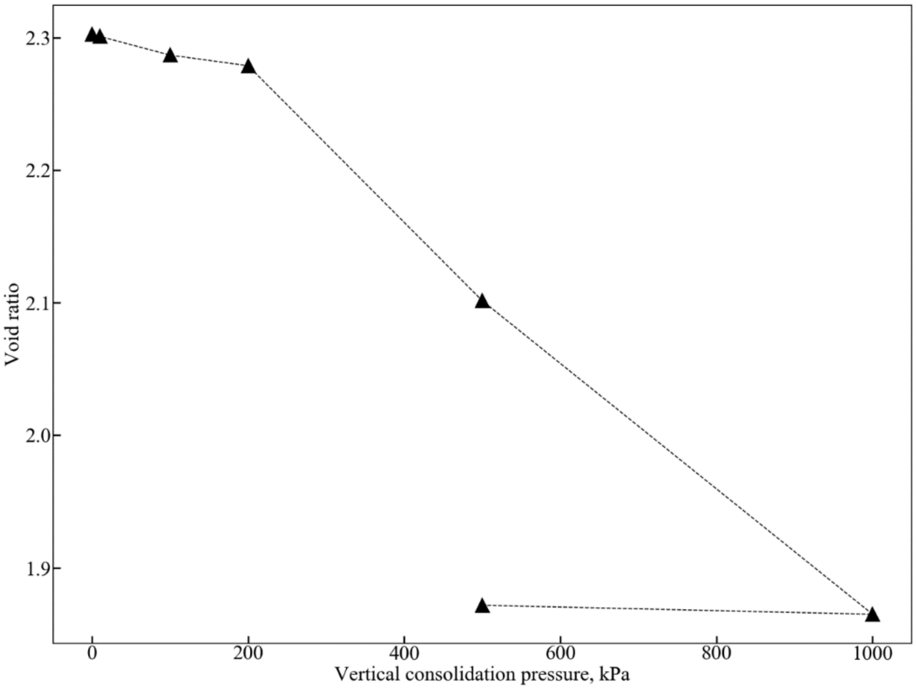

Figure 3-32 The relationship between the void ratio and the consolidation pressure

Due to the problem of the illumination light used on the swing platform of the centrifuge, the quality of the images captured during the first test are very poor. Consequently, a second geotechnical centrifuge modelling test was performed. For this test, only the consolidation behaviour is presented.

3.15 The second centrifuge modelling test using the synthetic Clearwater shale-I

The second geotechnical centrifuge modelling test adopts the same synthetic Clearwater shale formula used in the first centrifuge modelling test discussed above. As shown in Table 3-7, the weights of the Speswhite kaolin clay and Sil325 (38-75 μm) are 15.18 kg and 12.32 kg, respectively. The total soil-water content is 100%, and the weight of the distilled water is 29.54 kg. The total soil-water to cement ratio is 7.5, and the weight of the cement is 3.76 kg.

The mixing process is the same as that in the first geotechnical centrifuge modelling test. After 28 days, the model is then processed for the physical modelling test. The overburden is also simulated through an appropriate thickness of lead bars. For this test, the weight of lead bars is 90.0 kg, which corresponds to 29.90 m buried depth. It takes about 6 hours to complete the test, and the corresponding prototype time is about 7 years.

Figure 3-33 demonstrates the variation of the settlement at different consolidation pressures while Figure 3-34 illustrates the void ratio versus the vertical consolidation pressure. The initial void ratio is about 2.5, which is higher than the void ratio of previous consolidation tests. This is mainly because more water is used to rinse the bucket than is used by the previous test, and thus the total soil-water content of this test is slightly higher than 100%. However, after the completion of the

1000 kPa consolidation, the final void ratio is about 1.9, which is quite close to the final void ratio of the previous test.

Table 3-7 Sample preparation of the centrifuge modelling test using synthetic Clearwater shale-I

Slurry preparation					
Speswhite kaolin clay: Sil325 (38-75 µm)	55:45				
Total soil-water content, %	100				
Total soil-water to cement ratio	7.5				
Wt. of Speswhite kaolin clay, kg	15.18				
Wt. of Sil325 (38-75 µm), kg	12.32				
Wt. of cement, kg	3.76				
Wt. of water, kg	29.54				
Sample preparation					
Initial height, cm	31.15	30.94	30.23	29.842	30.893
Final height, cm	23.50	23.50	23.30	23.20	-
Weight of lead bars, kg	90.0				
Vertical pressure at 100 g, kPa	630.64				
Overburden height, m	29.90				
Parameters for GeoCDM					
Jog velocity	1.1221				
Jog accelerating	2				
Jog distance	24000				
Shearing time, hr	5.94				
The corresponding prototype time, yr	6.876				

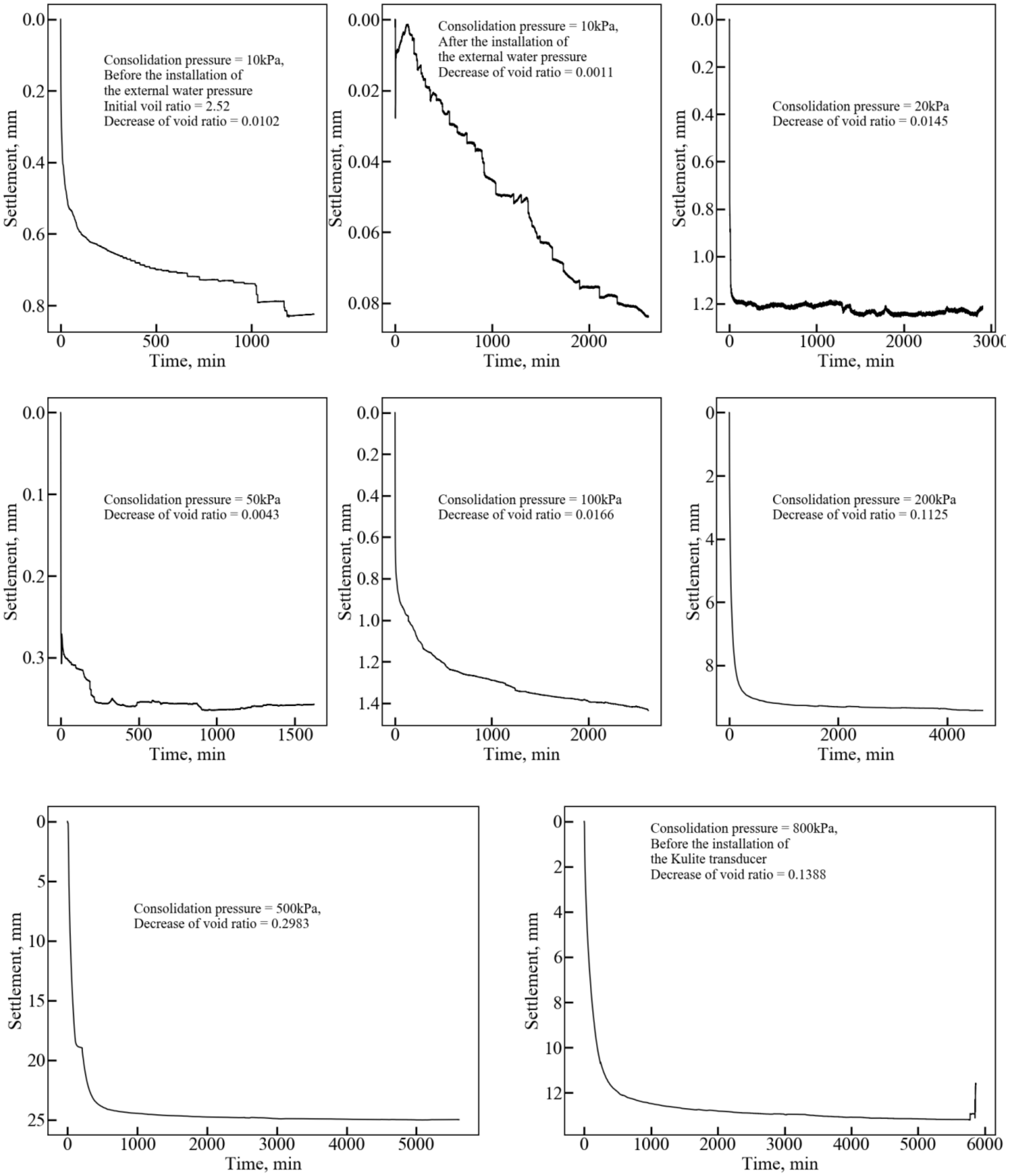
Consolidation pressure = 10kPa,
Before the installation of
the external water pressure
Initial voil ratio = 2.52
Decrease of void ratio = 0.0102
Settlement, mm
0.0
0.2
0.4
0.6
0.8
0
500
1000
Time, min
Consolidation pressure = 10kPa,
After the installation of
the external water pressure
Decrease of void ratio = 0.0011
Settlement, mm
0.00
0.02
0.04
0.06
0.08
0
1000
2000
Time, min
Consolidation pressure = 20kPa
Decrease of void ratio = 0.0145
Settlement, mm
0.0
0.2
0.4
0.6
0.8
1.0
1.2
0
1000
2000
3000
Time, min
Consolidation pressure = 50kPa
Decrease of void ratio = 0.0043
Settlement, mm
0.0
0.1
0.2
0.3
0
500
1000
1500
Time, min
Consolidation pressure = 100kPa
Decrease of void ratio = 0.0166
Settlement, mm
0.0
0.2
0.4
0.6
0.8
1.0
1.2
1.4
0
1000
2000
Time, min
Consolidation pressure = 200kPa
Decrease of void ratio = 0.1125
Settlement, mm
0
2
4
6
8
0
2000
4000
Time, min
Consolidation pressure = 500kPa,
Decrease of void ratio = 0.2983
Settlement, mm
0
5
10
15
20
25
0
1000
2000
3000
4000
5000
Time, min
Consolidation pressure = 800kPa,
Before the installation of
the Kulite transducer
Decrease of void ratio = 0.1388
Settlement, mm
0
2
4
6
8
10
12
0
1000
2000
3000
4000
5000
6000
Time, min

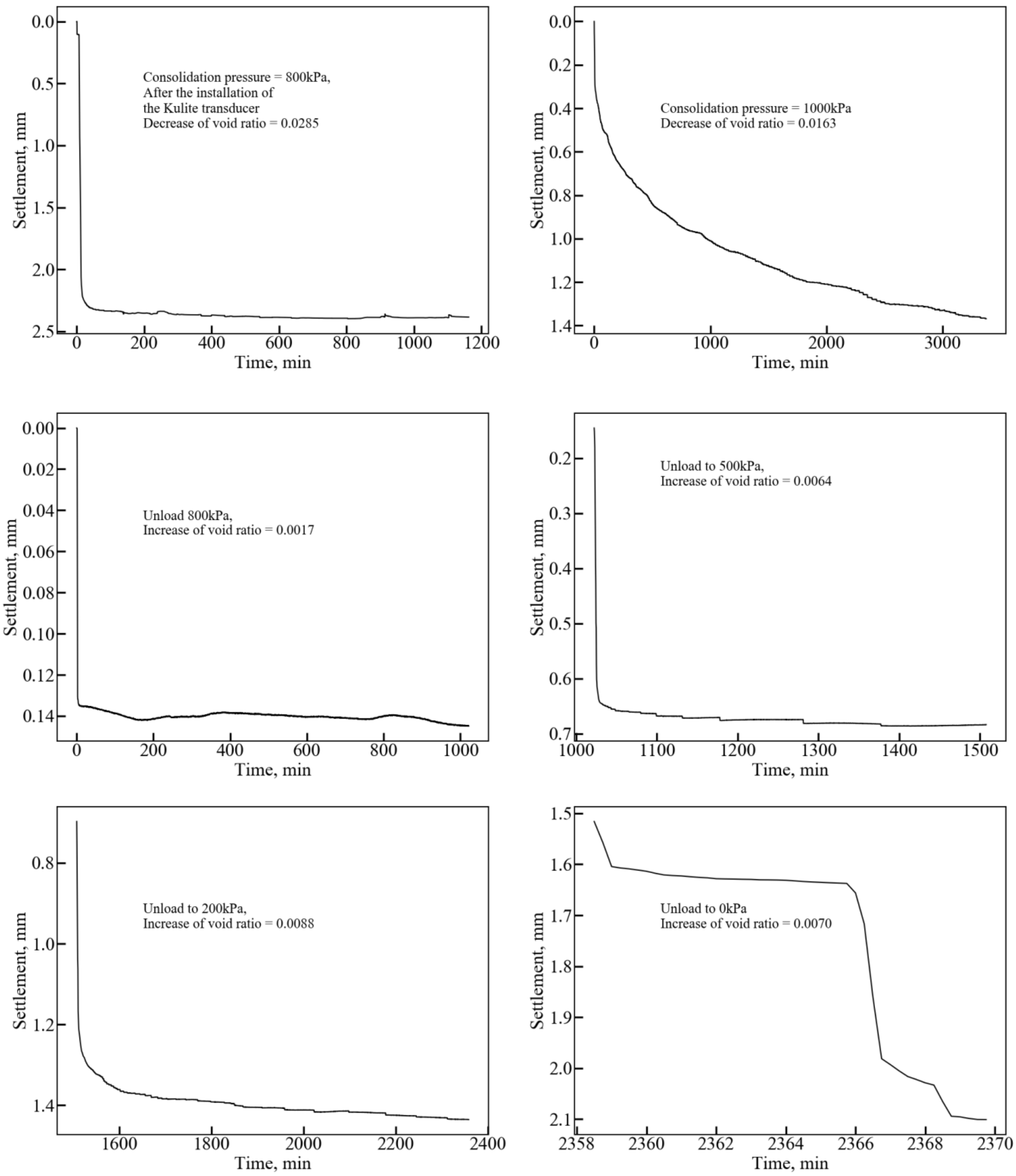

Figure 3-33 The consolidation behaviour of the synthetic Clearwater shale-I in second centrifuge test

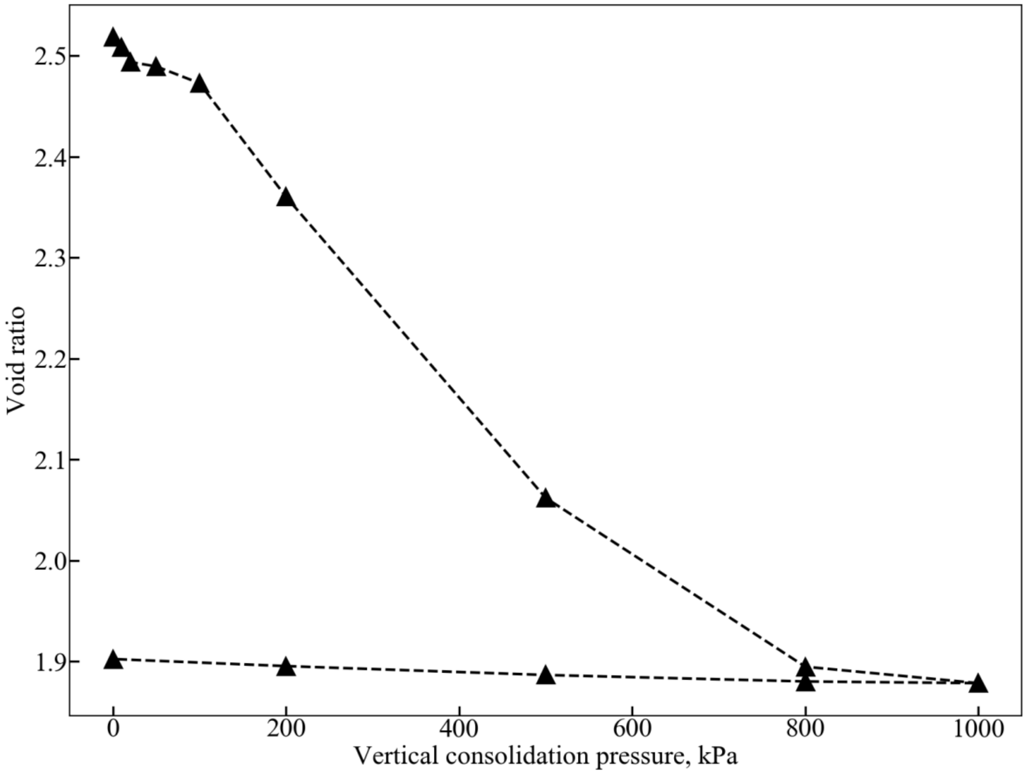

Figure 3-34 The relationship between the void ratio and the consolidation pressure in second centrifuge test

3.15.1 Discussion

The evolution of the horizontal displacement contour, vertical displacement contour, resultant (total) displacement contour and the maximum total shear strain contour are shown in Figures 3-35, 3-36, 3-37 and 3-38, respectively. From the evolution of horizontal displacement illustrated in Figure 3-35, the symmetry of negative (to the left) and positive (to the right) displacements around the centreline of the model can be seen. Near the boundary of the GeoCDM, some artifacts in horizontal displacement can be seen as the symmetry boundary moves to the left of the GeoCDM centre.

At the initial stage, such as 1.0 mm uplift displacement, it is hard to see the horizontal displacement concentration in the model. However, with the increase of the uplift displacement, the horizontal displacement contours form a series of ellipses with the same minor axis coinciding with the uplifting table. Even though the contours expand as the GeoCDM moves up, the contour does not cross the boundary.

Through the analysis of the evolution of the vertical displacement contours, there is no doubt that the uplifting table is the origin of these contours. With the increase of the distance between the uplifting table and the soil particle, the vertical displacement decreases, indicating that the soil above the uplifting table is compressed during the whole process. Moreover, the gradient of the vertical displacement increases with the decrease of the distance between the contour and the uplifting table. This observation indicates that the compression propagates from the uplifting table to the top surface of the model gradually. The vertical displacement of these soil particles on the same horizontal plane above the uplifting table decreases from the centreline of the model in the radial direction. The gradient decreases as the distance from the centreline of the model increases.

Figure 3-38 illustrates the evolution of the maximum total shear strain which is deduced from the soil deformation. From the analysis of the five subplots, it is evident that the uplifting table, the left flank and the right flank are the highly strained areas. At the initial stage, such as at 1.0 mm uplift displacement, the highly strained area is confined within the limited space above the uplifting table and forms an ellipse with the major axis coinciding with the uplifting table. As the uplifting table moves up, the ellipse expands. However, when the uplift displacement is 15 mm, it seems that the strained area above the flanks keeps almost unchanged, while that above the uplifting table still expands upwards. As the uplifting table continues moving up, a new highly strained area develops along the centreline of the model and forms a condit connecting the top of the previous highly strained area with the top surface of the model.

3.15.2 Evolution of the horizontal displacement contours

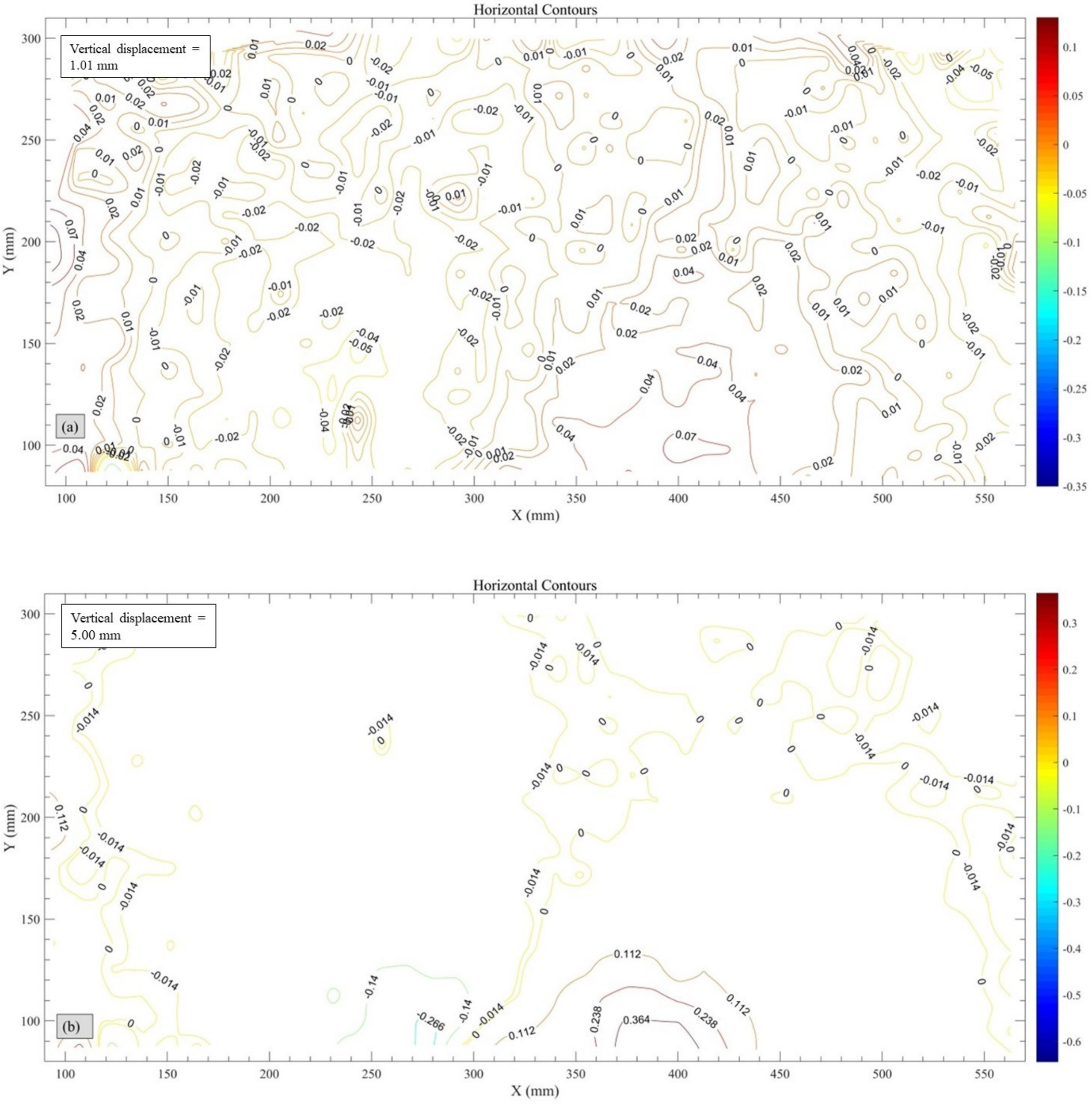

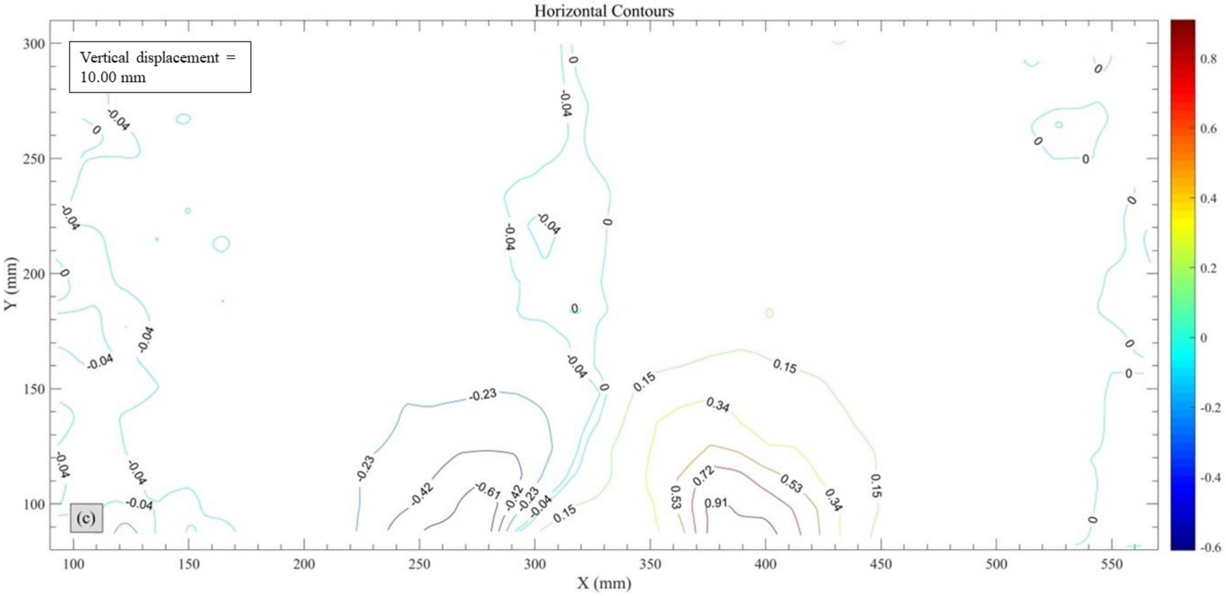
Horizontal Contours
Vertical displacement = 10.00 mm
(c)
Y (mm)
X (mm)
100
150
200
250
300
350
400
450
500
550
-0.04
0
-0.23
-0.42
-0.61
0.15
0.34
0.53
0.72
0.91
0.8
0.6
0.4
0.2
-0.2
-0.4
-0.6

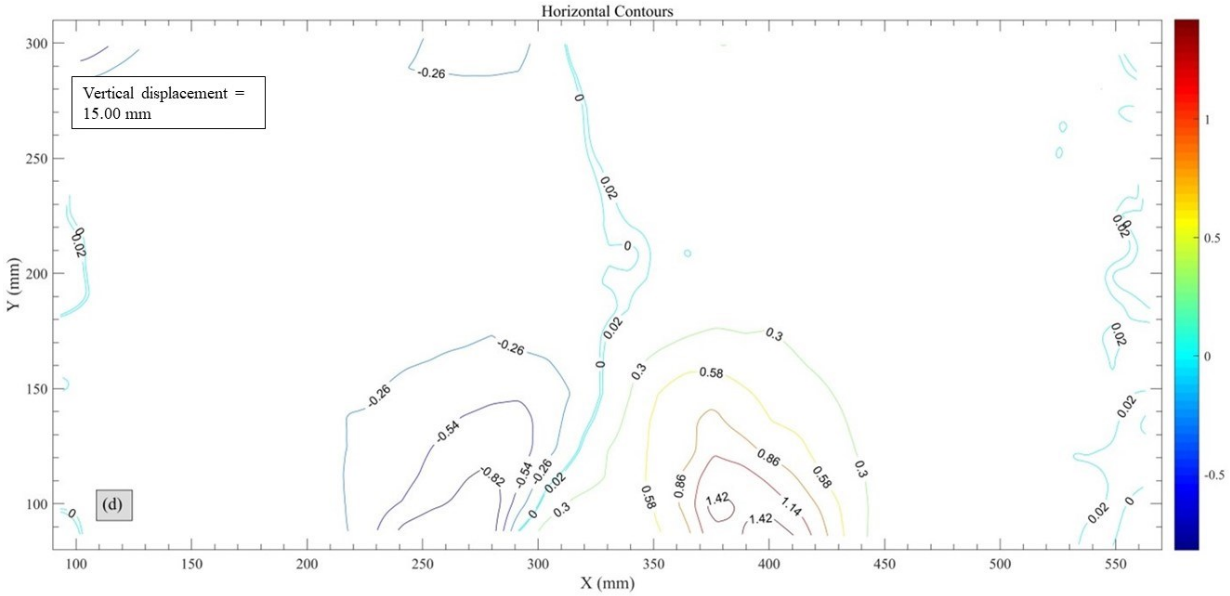
Horizontal Contours
Vertical displacement = 15.00 mm
(d)
Y (mm)
X (mm)
100
150
200
250
300
350
400
450
500
550
0
0.02
-0.26
-0.54
-0.82
0.3
0.58
0.86
1.14
1.42
1
0.5
-0.5

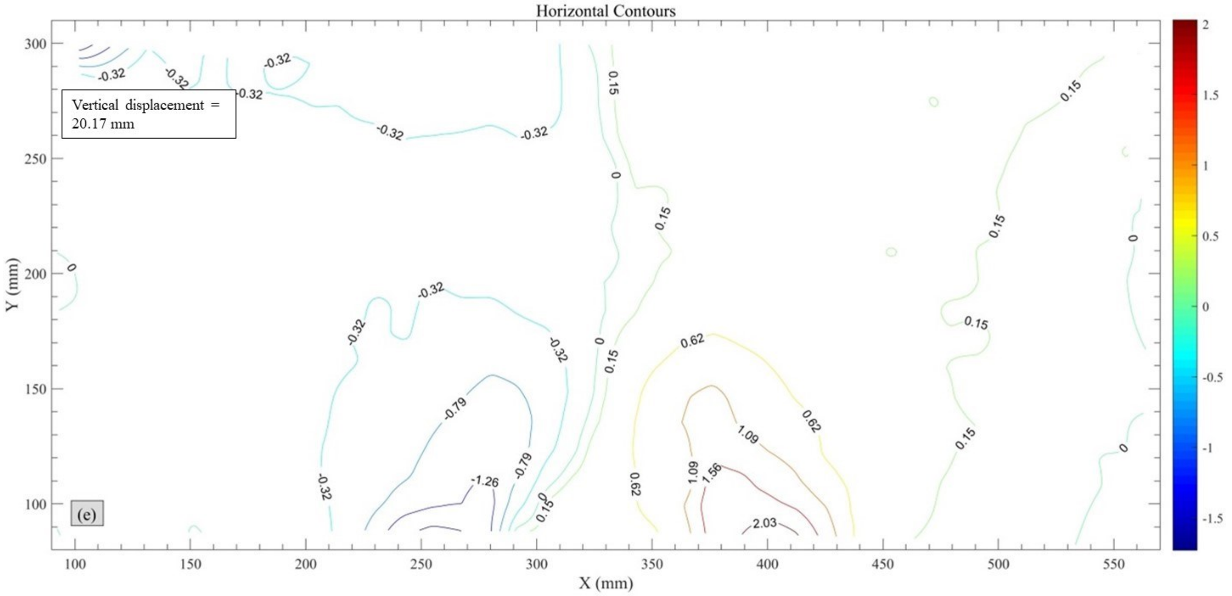

Figure 3-35 Evolution of the horizontal displacement contours

3.15.3 Evolution of the vertical displacement contours

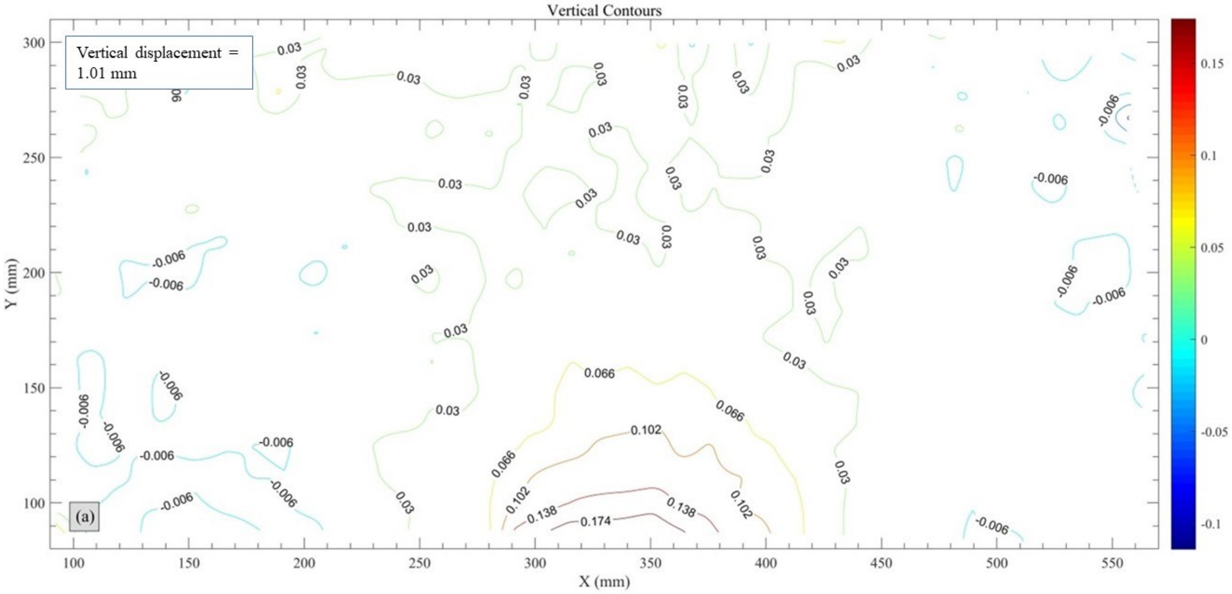

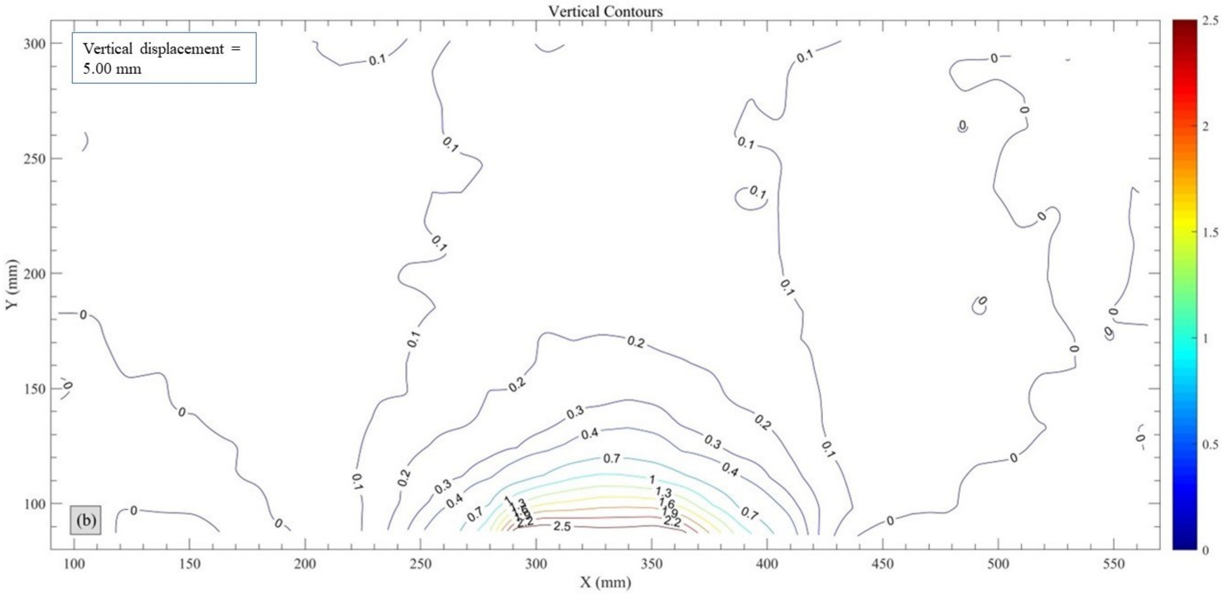
Vertical Contours
Vertical displacement = 5.00 mm
(b)
Y (mm)
X (mm)
0
0.1
0.2
0.3
0.4
0.7
1
1.3
1.6
1.9
2.2
2.5
100
150
200
250
300
350
400
450
500
550
0
0.5
1
1.5
2
2.5

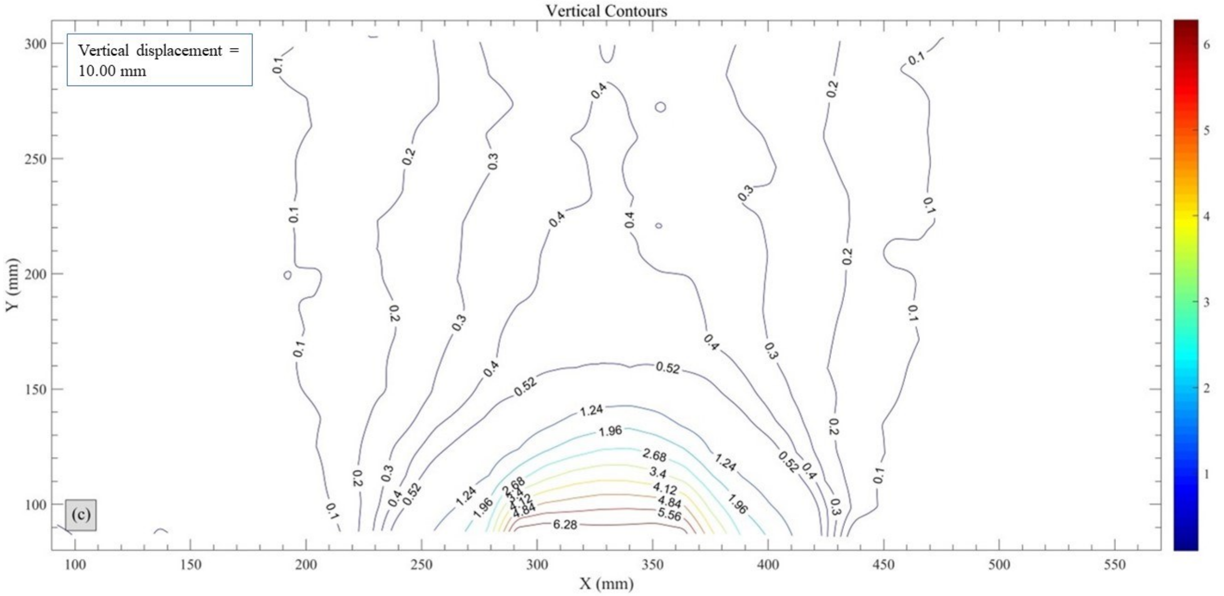
Vertical Contours
Vertical displacement = 10.00 mm
(c)
Y (mm)
X (mm)
0.1
0.2
0.3
0.4
0.52
1.24
1.96
2.68
3.4
4.12
4.84
5.56
6.28
100
150
200
250
300
350
400
450
500
550
1
2
3
4
5
6

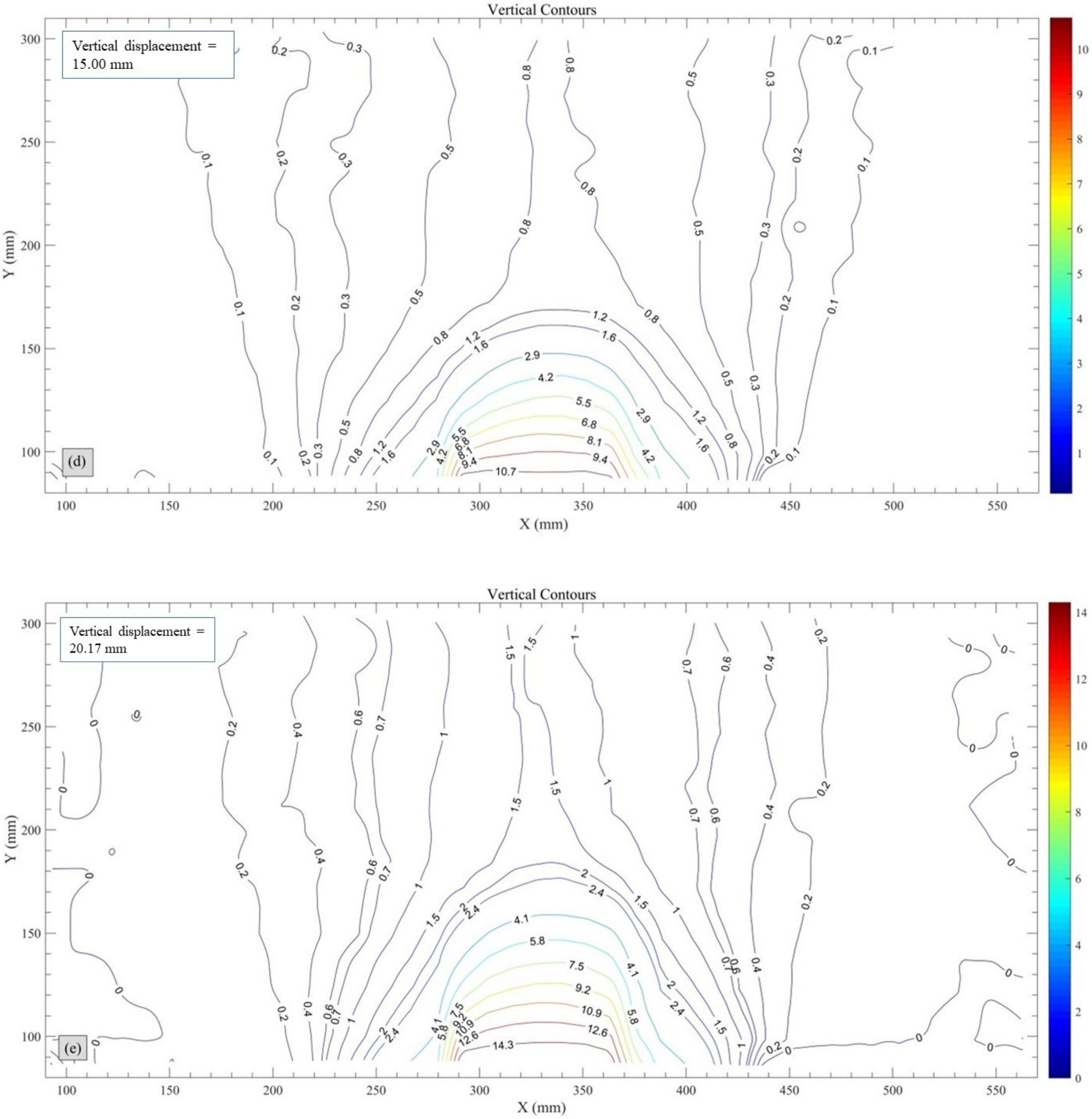

Figure 3-36 Evolution of the vertical displacement contours

3.15.4 Evolution of the resultant displacement contours

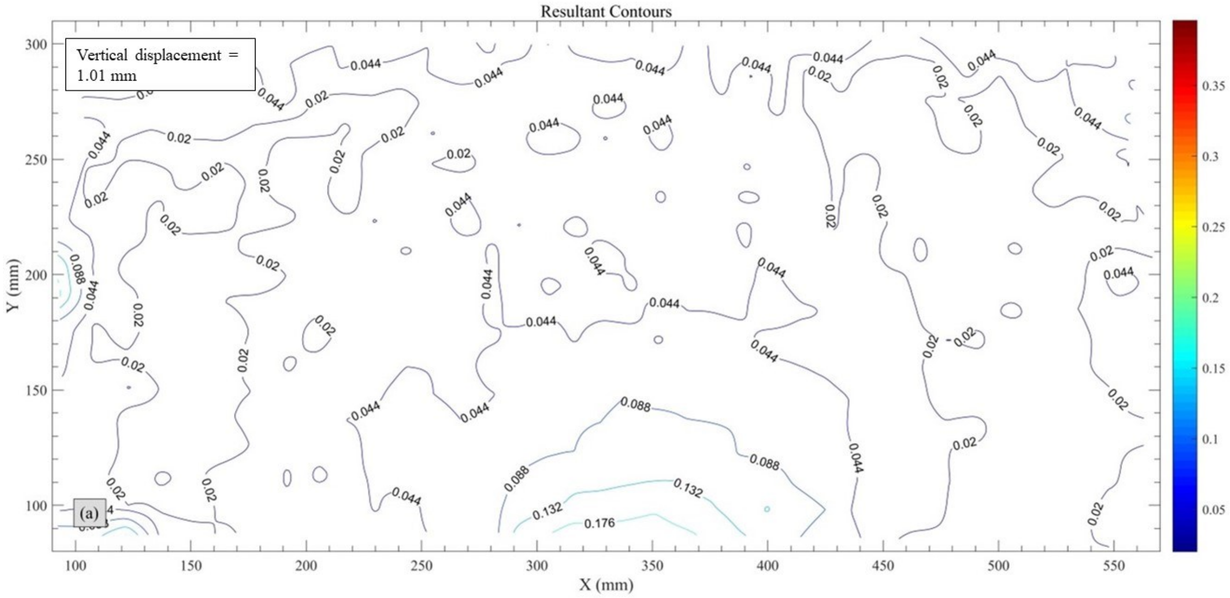

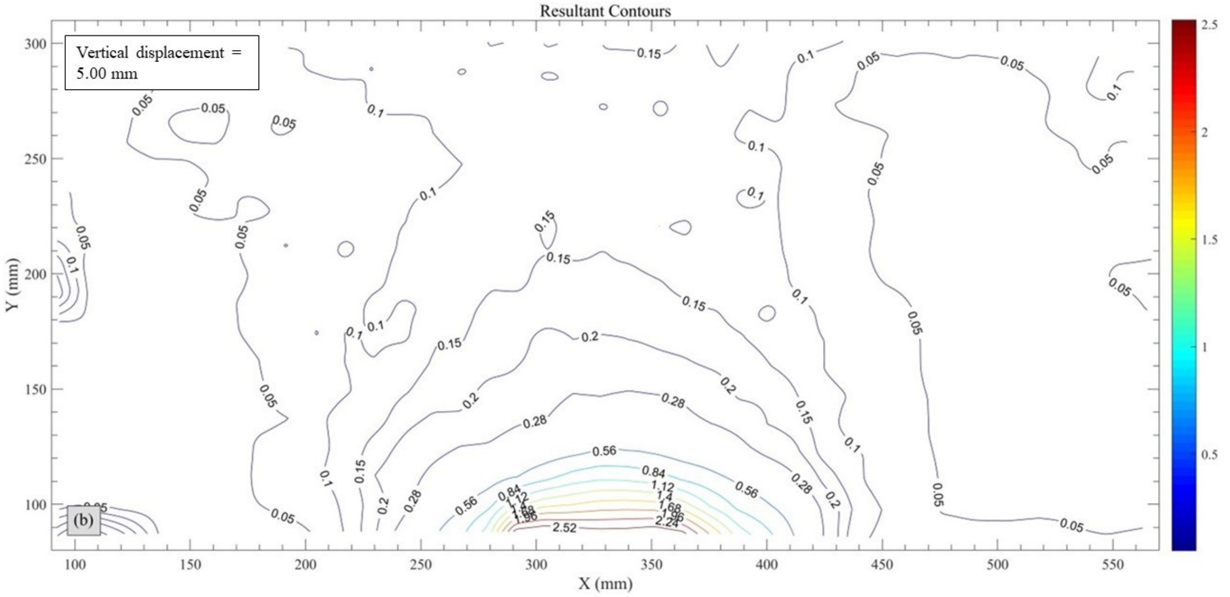

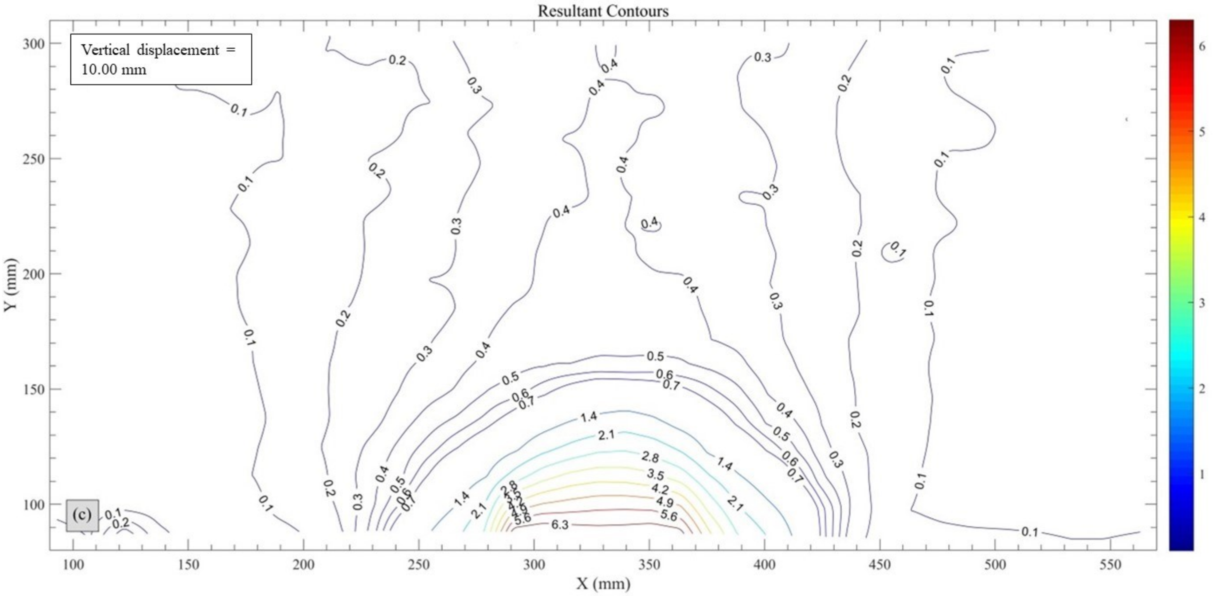
Resultant Contours
Vertical displacement = 10.00 mm
(c)
Y (mm)
X (mm)
100
150
200
250
300
350
400
450
500
550
1
2
3
4
5
6
0.1
0.2
0.3
0.4
0.5
0.6
0.7
1.4
2.1
2.8
3.5
4.2
4.9
5.6
6.3

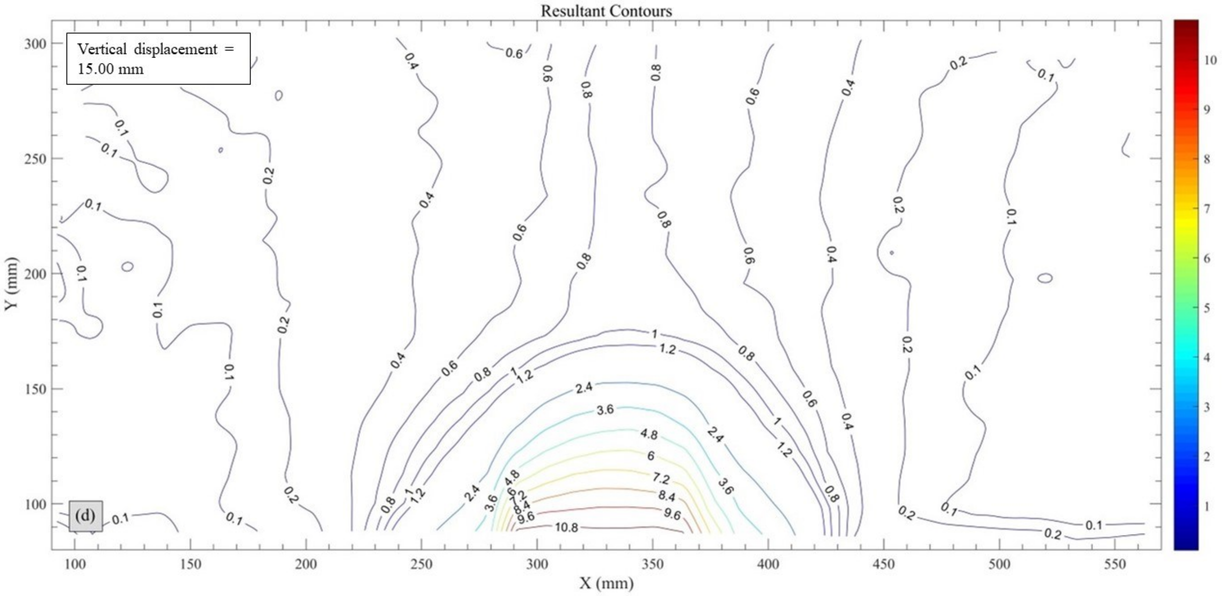
Resultant Contours
Vertical displacement = 15.00 mm
(d)
Y (mm)
X (mm)
100
150
200
250
300
350
400
450
500
550
1
2
3
4
5
6
7
8
9
10
0.1
0.2
0.4
0.6
0.8
1
1.2
2.4
3.6
4.8
6
7.2
8.4
9.6
10.8

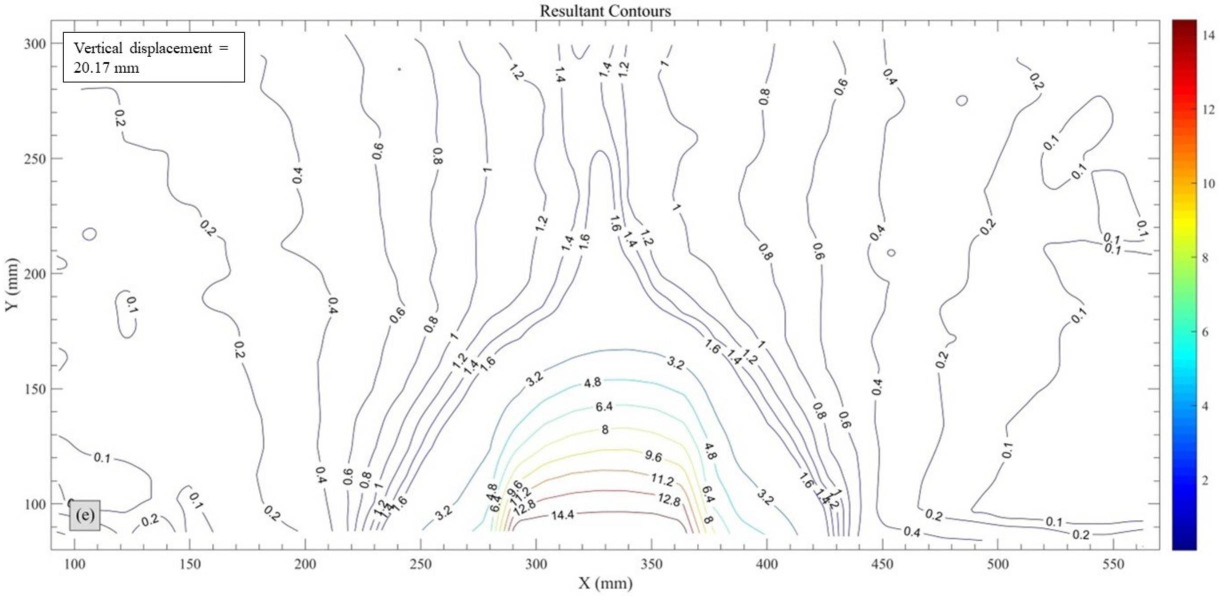

Figure 3-37 Evolution of the resultant displacement contours

3.15.5 Evolution of the maximum total shear strains

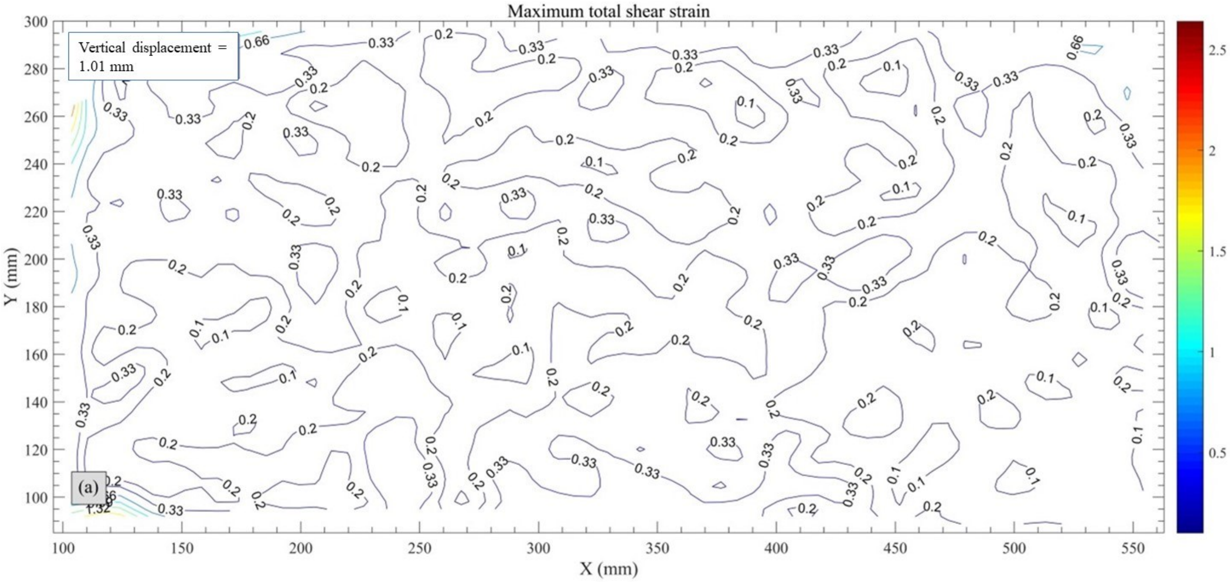

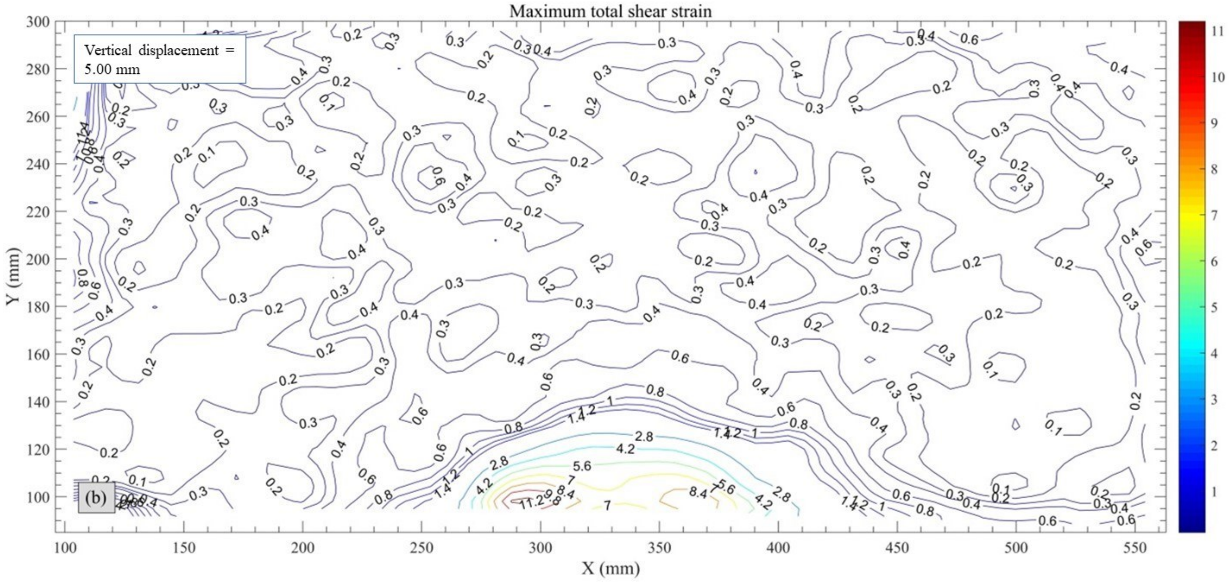
Maximum total shear strain
Vertical displacement = 5.00 mm
(b)
Y (mm)
X (mm)
300
280
260
240
220
200
180
160
140
120
100
150
250
350
400
450
500
550
11
10
9
8
7
6
5
4
3
2
1
11.2
8.4
7
5.6
4.2
2.8
1.4
1.2
1
0.8
0.6
0.4
0.3
0.2
0.1

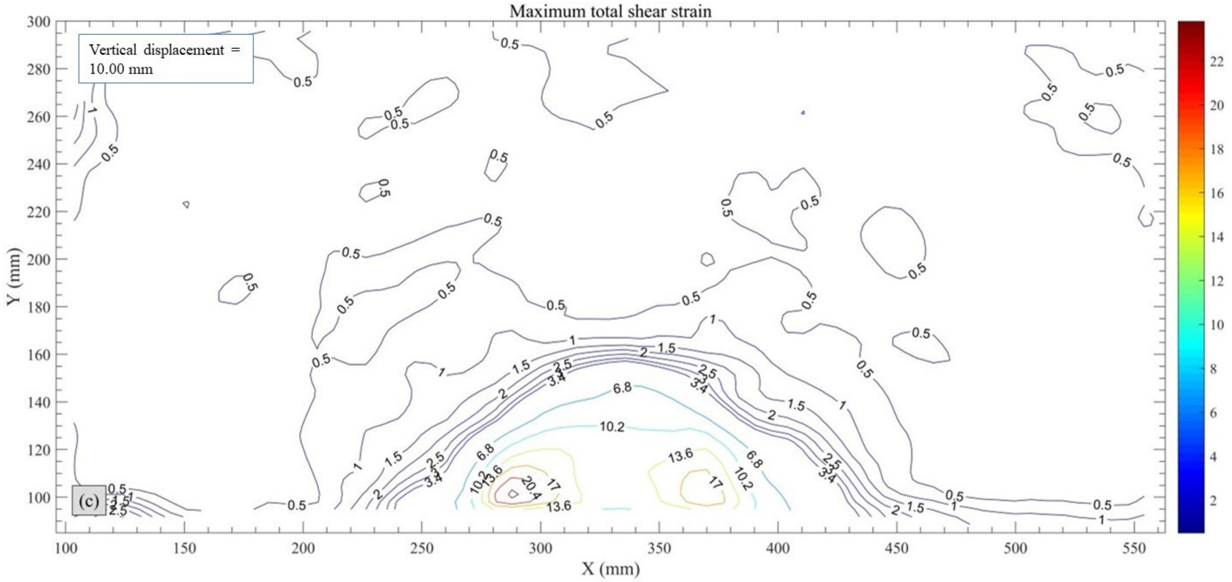
Maximum total shear strain
Vertical displacement = 10.00 mm
(c)
Y (mm)
X (mm)
300
280
260
240
220
200
180
160
140
120
100
150
250
350
400
450
500
550
22
20
18
16
14
12
10
8
6
4
2
20.4
17
13.6
10.2
6.8
3.4
2.5
2
1.5
1
0.5

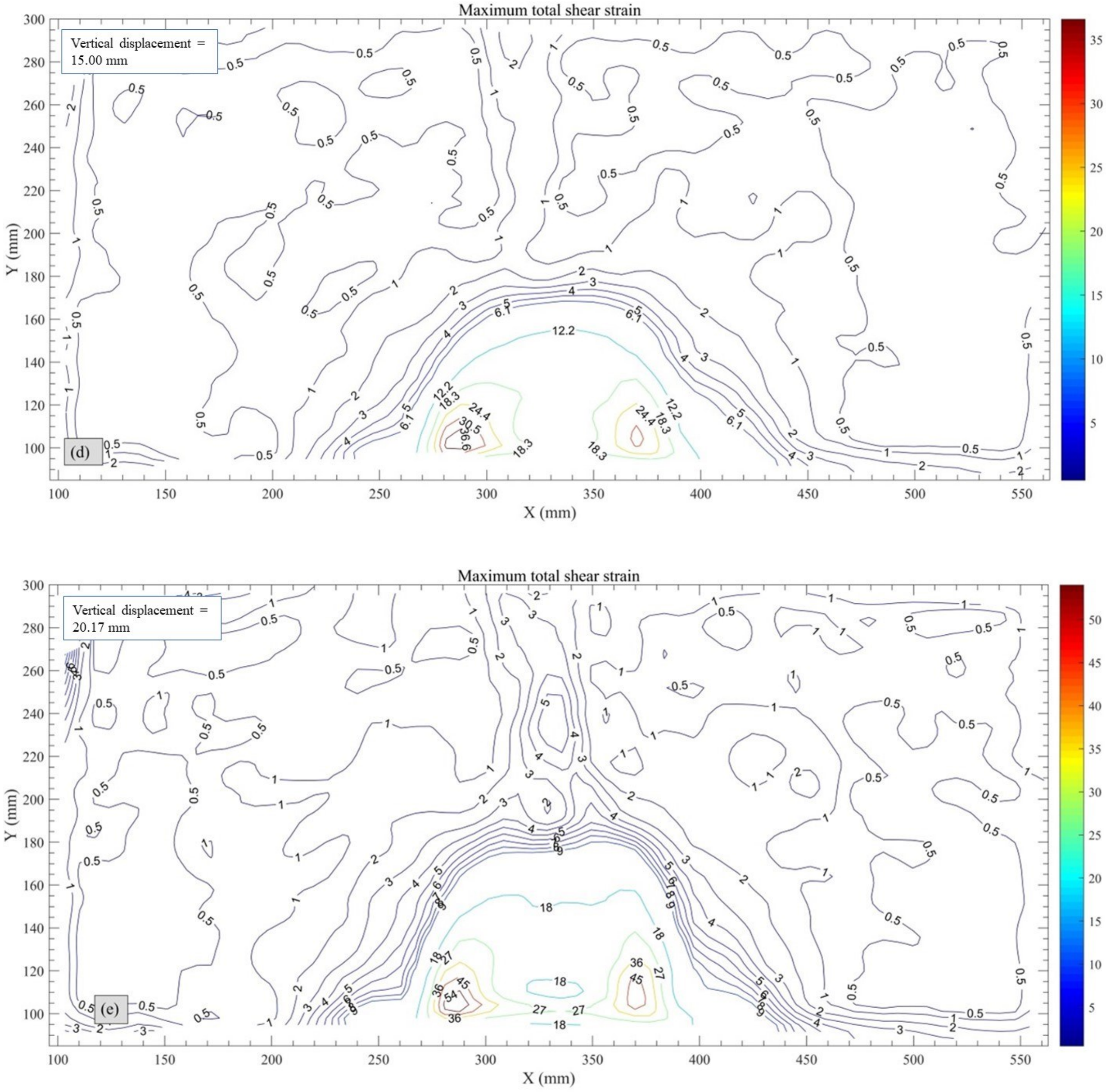

Figure 3-38 Evolution of the maximum total shear strains

3.16 Summary

This chapter presented the basic information of the geotechnical centrifuge facility and its application in the identification of the caprock failure process. The experimental results show that a more detailed plan is needed to make the synthetic Clearwater shale.

The geotechnical centrifuge can create the stress state of the prototype in a small-scale sample, and this ability has led to its wide use in geotechnical engineering. However, the basic principle of the technique is the uniform circular motion, and the direction of the vertical stress created by the technique points to the rotational shaft. Studies show that the error can be neglected as long as the ratio of the model height to the effective radius is less than 0.2.

The preparation of the experimental package and the model takes time and effort. It involves the assemblage of the PSB, the placement of the GeoCDM and so on. During the mixing process of the soil-water slurry, great care should be taken to make sure that the material is homogeneous and isotropic.

The consolidation behaviour of the Speswhite kaolin clay implies that the material may be too soft. This conclusion is verified by the centrifuge modelling test, during which the lead bars subside into the model. Moreover, there is no clear fracture in the model after the centrifuge modeling test.

The mixture of the Speswhite kaolin clay, Sil325 (38-75μm), cement and water is used for the physical modelling test. The mixture material is stronger than the consolidated Speswhite kaolin clay. But, when compared with the Clearwater shale, the mixture material is too soft. The experimental results of the geotechnical centrifuge modelling test reveal that the failure plane does not extend to the ground surface.

The two centrifuge modelling tests point out that the vertices of the uplifting table are the most highly strained areas. The failure plane emerges at the two points and then propagates towards the model surface.

Chapter 4 Development of an alternative material for Clearwater shale

4.1 Introduction

Based on the results presented in the previous two chapters, a greater effort is required to formulate a “recipe” for a synthetic material that will serve as an appropriate analogue for in situ Clearwater clay shale. Consequently, this chapter reports on research undertaken to conduct an extensive series of tests to establish a database for the determination of an appropriate synthetic Clearwater shale material suitable for use in centrifuge caprock studies.

A total of 160 formulations of a reconstituted soil are investigated using unconfined compressive tests as the primary test for comparison of the formulations. Unlike most previous studies, which are discussed below, that considered one type of soil, this study develops an experimental plan considering 10 types of synthetic soils. For each synthetic soil, 16 formulations with total soil-water contents ranging from 1.1 to 2.5 times the liquid limit and soil water to cement ratios ranging from 3 to 5 are tested.

Initial structuring of the testing results is based on the after-curing moisture content to establish the relationship between the initial parameters such as the cement content, total soil-water content, liquid limit and unconfined compressive strength of the synthetic soils. The experimental results reveal that the total soil-water content and cement content are the major factors controlling the after-curing moisture content irrespective of the silt content.

4.2 Literature review of artificial soil mixtures

Researchers in geotechnical engineering have gradually recognized the advantages of geotechnical centrifuge modelling in tackling complex geotechnical problems. However, the centrifuge modelling test requires large-scale samples for experimental laboratory investigations. Due to the inherent geological variability, it is almost impossible to find large block samples that have both homogeneous and isotropic properties from the field. A commonly adopted method to overcome the shortage of prototype samples is to use artificial soil mixtures (Cheney et al., 1991; Tavenas et al., 1973). Kaolin, bentonite, illite and other commercially available products have been used to provide active clay fractions for artificial soil mixtures. Among those industrial products, kaolin clay is preferred by numerous researchers due to its high permeability and the existing database of tests on the material's physical and mechanical properties (Rossato et al., 1992). However, kaolin clay, which consists of 80% clay-sized particles (particle size < 2 μm) and 20% silt-sized particles (2 μm < particle size < 75 μm), is to some extent atypical of natural soils, which always consist of more silt and sand fractions.

Previous studies found that the behaviour of the mixture of kaolin clay and granular soils such as silt can more closely reflect the behaviour of the "destructured" natural soils (Al-Tabbaa & Wood, 1987; Rossato et al., 1992). With the increase of the silt content, the physical and mechanical properties of the mixture change, and the plasticity expressed by the plasticity index (PI) and Skempton's activity coefficient reduces (Lupini et al., 1981; Seed et al., 1964), both the effective friction angle and residual friction angle increase (Lupini et al., 1981; Nocilla & Coop, 2006; Stark, T. D. et al., 1994; Stark & Eid, 1994; Yin, 2002), and the drained and undrained shear strength and the stiffness increase (Anantanasakul et al., 2012).

The variation of the cohesive soil strength (critical friction angle and residual friction angle) with the clay fraction forms an S-shaped curve in normal coordinates (M. D. Liu et al., 2013; Lupini et al., 1981). The S-shaped relationship, although largely ignored by geotechnical engineers, widely exists in the natural world such as in soil consolidation behaviour, population growth, drug dose response and physicochemical reactions. The consolidation behaviour of both the cement-treated soils and untreated soils show that the relationship between the vertical effective pressure and the void ratio are S-shaped in the semi-logarithmic scale (Kamruzzaman et al., 2009). The variation of the unconfined compressive strength of cement-admixed Ariake clay with the cement content forms an S-shaped curve in normal coordinates (Horpibulsuk et al., 2003). The study divides the cement content into four different zones: the inactive zone (Zone I) in which the cement content is too low to clearly improve the soil strength, the clay-cement interaction zone (Zone II) in which the cement content is high enough to bring about a high strength increase rate, the transition zone (Zone III) in which the strength increase rate is many times lower than that in Zone II, and the cement-clay interaction zone (Zone IV) in which the clay fabric loses its identity and is far beyond the scope of the strength improvement of cement-treated soil. The three zones—inactive zone, active zone and inert zone—are also observed with the strength improvement of cement-treated Singapore marine clay under different curing periods and water contents (Chew et al., 2004b; Kamruzzaman et al., 2009). Zhang, Santoso, Tan, & Phoon (2013) provided detailed discussion on the strength behaviour of cement-admixed soils in both Zone I and Zone II, and proposed an empirical formula applicable to the two zones for the prediction of soil strength.

The Clearwater shale, which is a major component of the caprock units overlying a bitumen reservoir, plays a major role in caprock integrity. It is extremely difficult to obtain large-size prismatic samples of Clearwater shale for the physical modelling tests. And since previous trials using just Speswhite kaolin clay and a simple mixture of clay, silt and cement were unable to appropriately replicate the important characteristics of in situ Clearwater clay shale, it becomes apparent that a model material should be developed to overcome the inability to use in-situ Clearwater shale samples. Critically, the model material is required to display a relatively high cohesive strength and so it is essential to choose the suitable bonding agent to replace the natural cohesion of the prototype materials. The literature review by Stimpson (1970) summarizes the components and manufacturing methods of different model materials. However, due to dissimilar engineering properties, these model materials and corresponding recipes are only suitable for specific projects. Johnston & Choi (1986) developed a synthetic soft rock to predict the behaviour of the Melbourne mudstone under external forces or displacement. The principal component of the synthetic soft rock is the reconstituted mudstone, while ordinary Portland cement is chosen as the cementing agent. Tavenas, Roy, & Rochelle (1973) developed a synthetic material to simulate Champlain clay. This synthetic soil is a mixture of kaolinite, bentonite, Portland cement and water.

The cement content (A_w), which is defined as the percentage ratio of the weight of cement powder to the dry weight of the soil, is widely accepted as the major parameter controlling the strength development of cement-admixed soils (Bergado et al., 1999; Uddin et al., 1997). Meanwhile, some studies point out that there exists an optimum total clay-water content at which the strength of cement-admixed soil reaches the highest value. The optimum clay water content is between the liquid limit and 1.1 times the liquid limit irrespective of the cement content (Bergado & Lorenzo, 2005). Miura et al. (2001) propose that the clay-water to cement ratio ($\frac{C_w}{A_w}$), defined as the ratio of the weight of water in the clay-water-cement mixture to the dry weight of cement, is a prime parameter reflecting the combined effect of the water content and the cement content.

In this study, cement is used to create cementitious bonds between soil grains while the silt soil is added to the Speswhite kaolin clay to make model materials much closer to the Clearwater shale. The total soil-water content is defined as a percentage ratio of the water weight in the soil-water-cement mixture to the dry weight of the synthetic soil. The normalized water content is defined as the ratio of the water content of the soil-water-cement mixture to the liquid limit of the synthetic soils ($\frac{C_w}{LL}$).

4.3 Basic information of the Clearwater shale

Geotechnical experience has indicated that shale poses a serious challenge to coal mining, slope stability, tunnel settlement and other engineering activities (Skempton & Brown, 1961; Tiwari & Ajmera, 2011). These incidents cannot be solely attributed to the lack of good knowledge of the physical and mechanical properties of the shales. It is also essential to realize that the shale mechanical properties can drop to the same level as those of the reconstituted shale after being exposed to water for a few hours. This is mainly because the shale can transition to slurry type conditions very quickly after being exposed to water (i.e. slaking), resulting in serious practical problems.

In practice, the definition of a shale is not straightforward, and many terminologies have been used to describe the material, such as mudrock, argillaceous material, weak rock and shale. However, it is worth noting that these terminologies represent the shale at different conditions. For example, mudrock is used by geologists to represent the shale that has been extremely weathered and has no cementation. Engineers in different fields may work at different depths and thus prefer to use different names to describe the shale. Asef and Farrokhrouz (2013) describe the reason the shale has so many names, as shown in Table 4-1.

Table 4-1 Terminologies used to describe the shale (modified from Asef & Farrokhrouz, 2013)

Definer	Terminology	Reason
Geologist	Claystone or mudrock	1. Working at the ground surface → Extremely weathered material 2. From the perspective of chemical composition and/or grain size classification
Geotechnical engineer	Argillaceous material or soft rock	Working on shallow depth → seriously weathered material, weak cementation
Petroleum engineer	Weak rock or shale	Working at different depths → natural weathering may not exist, relative strong cementation, rock characteristics

Through the adoption of the X-ray diffraction techniques at AGAT Laboratories Ltd, the engineers in the RG^2 group concluded that the Clearwater shale is mainly composed of sand/clay (quartz, plagioclase feldspar, pyrite, kaolinite, chlorite, and illite) in general. The amounts of potassium feldspar, dolomite, corrensite, and smectite are minor. Smectite (montmorillonite), the swelling clay, only exists in the bulk samples extracted from 26 to 39 m below the ground surface, and the amount is only about 2-3%.

The particle size distribution of the Clearwater shale is shown in Figure 4-1. The content of materials passing through the No. 200 sieve (75 μm) ranges from 45% to 95%. The clay content ranges from 5% to 55%. The Clearwater shale is therefore categorized as silty clay material.

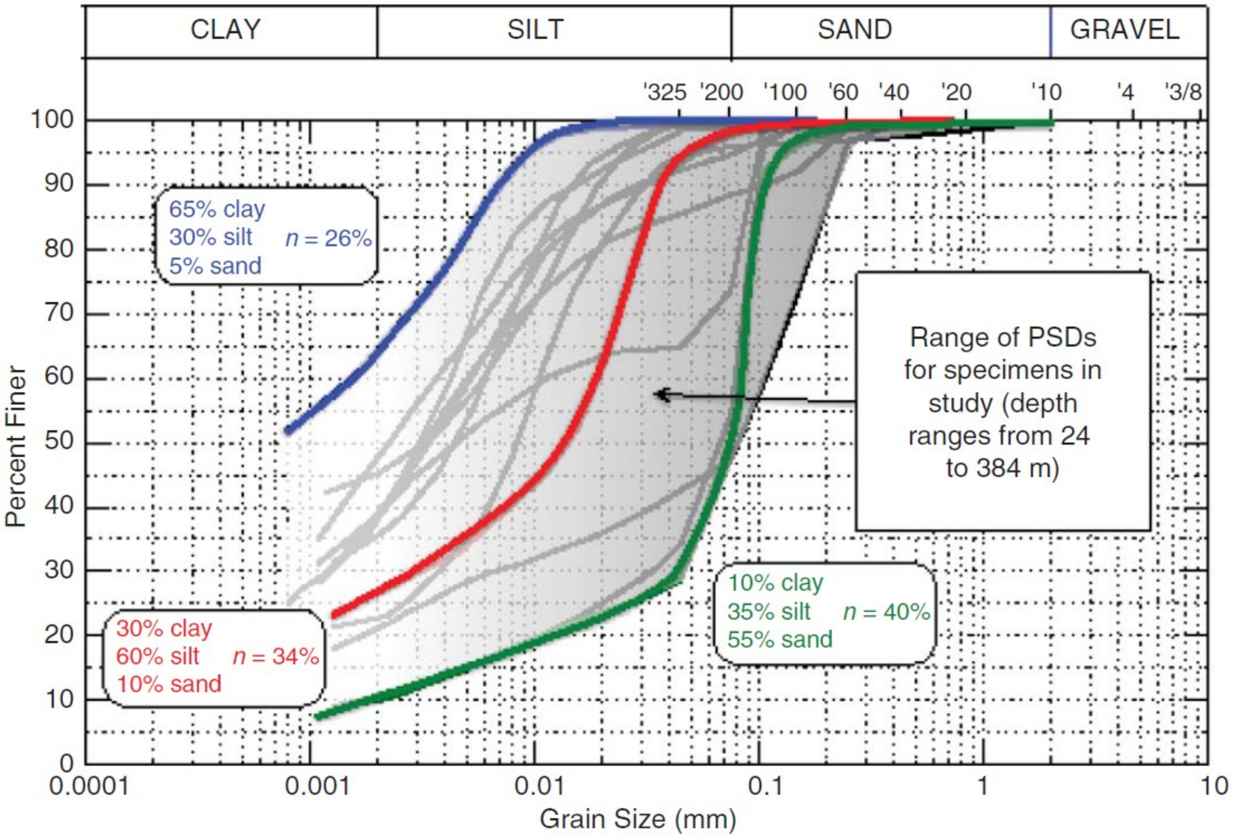

Figure 4-1 Grain size distribution of the Clearwater shales (Shafie Zadeh & Chalaturnyk, 2015)

4.4 Components of the synthetic Clearwater shale

The guiding principles for the selection of the components of the synthetic soils are listed as below:

1. The minerology of the synthetic soil should be as close to that of the Clearwater shale as possible, indicating that quartz, kaolinite, chlorite and illite should be the dominant minerals of the synthetic soils.
2. The grain size distribution should be as close to that of the Clearwater shale as possible.
3. The components of the synthetic soils should be easy access, commercially available and low cost.
4. The components of the synthetic soils should be inert. This implies that the components can be kept in the lab for a long time without changing their chemical properties.

Table 4-2 Properties of Speswhite kaolin clay and Sil325

Properties of Speswhite kaolin clay (Spk)[a]	Characteristics value	Properties Sil325 (S325)	Characteristics value
Liquid limit, LL (%)	65	Grain size distribution[b]	
Plastic limit, PL (%)	35	+ 300 mesh (mass % max.)	10.6
Grain size distribution		-325 mesh (mass % max.)	73.6
+ 300 mesh (mass % max.)	0.02	D50[b]	20 μm
+ 10 μm (mass % max.)	0.5	Specific gravity[c]	2.63
- 2 μm (mass %)	76 - 83	Chemical composition[c]	
Specific gravity	2.6	Silicon Dioxide (SiO2) (mass %)	97.10
Surface area (BET; m^2/g)	14	Iron Oxide (Fe2O3) (mass %)	0.49
Chemical composition		Aluminum Oxide (Al2O3) (mass %)	1.31
Silicon Dioxide (SiO_2) (mass %)	47	Potassium Oxide (K2O) (mass %)	0.41
Aluminum Oxide (Al_2O_3) (mass %)	38	Sodium Oxide (Na2O) (mass %)	0.37

Note: [a]Imerys Minerals Co.; [b]Based on Saadat (2014); [c]Sil Industrial Minerals

The principal components of the synthetic soils utilized by this study are Speswhite kaolin clay supplied by IMERYS Minerals Ltd. and Sil325 supplied by Sil Industrial Minerals. The grain size distribution of Speswhite kaolin clay was obtained from IMERYS Minerals Ltd., while that of Sil325 was obtained from the thesis by Saadat (2014). Figure 4-2 shows that the Speswhite kaolin clay is composed of 20% silt and 80% clay, while the Sil325 is composed of approximately 4% sand, 93% silt and 3% clay. The specific gravity of Speswhite kaolin clay and Sil325 are 2.61 and 2.63, respectively. The liquid limit and plastic limit of Speswhite kaolin clay are approximately 65% and 35%, respectively. The main chemical composition of Speswhite kaolin clay is SiO_2 (47%) and Al_2O_3 (38%). For Sil325, the main composition is SiO_2, which is approximately 97.10%

by weight. Table 4-2 illustrates the properties of Speswhite kaolin clay and Sil325 used in this study. From the perspective of simplification, Speswhite kaolin clay and Sil325 are hereinafter referred to as Spk and S325, respectively.

Ten fine-grained synthetic soils with the following Spk-to-S325 proportions are used in the study: 100:0, 90:10, 80:20, 70:30, 60:40, 50:50, 40:60, 30:70, 20:80, 10:90. The grain size distribution of the 10 synthetic soils and S325 is given in Figure 4-2.

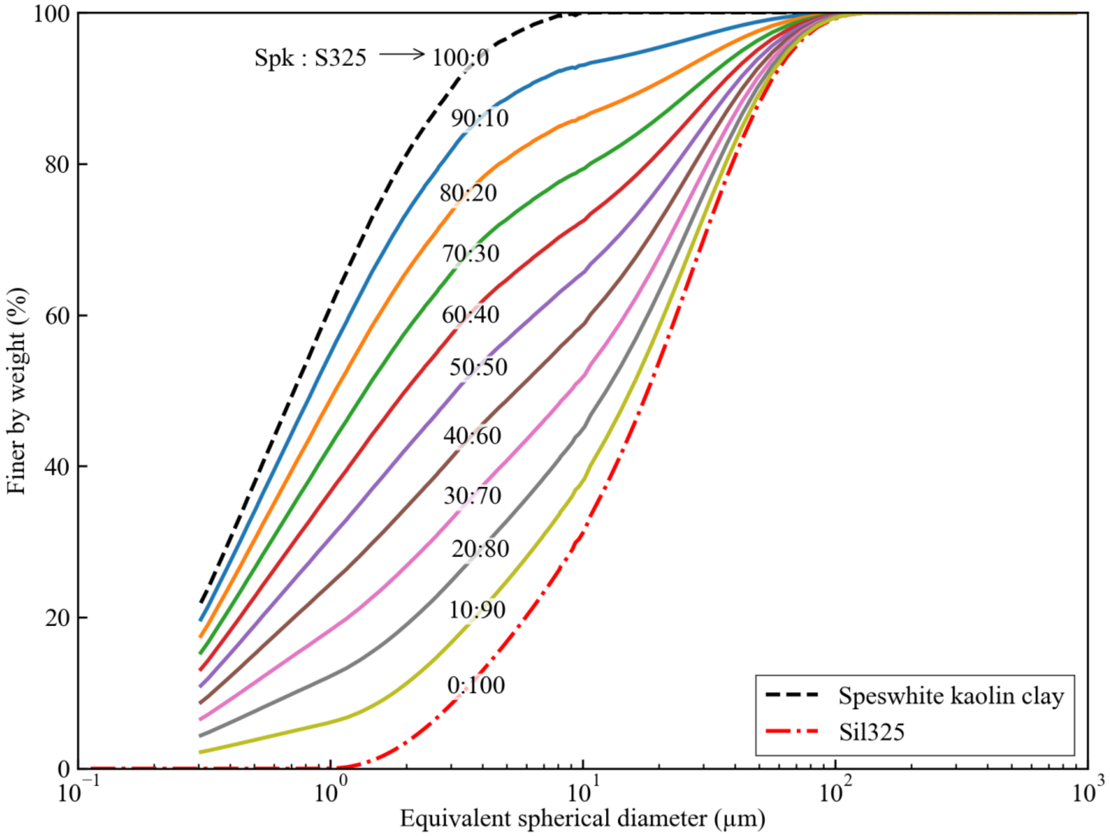

Figure 4-2 Grain size distribution of Spk, S325 and synthetic soils

The proportions of clay, silt and sand of these soils are shown in Figure 4-3(a). The clay content decreases while both the silt and sand content increase with increasing S325 content. The liquid limit and plastic limit of the 10 synthetic soils are shown in Figure 4-3(b). It is evident that the liquid limit increases with increasing Spk content. However, the plastic limit keeps almost constant when the S325 content is higher than 70% by weight. This phenomenon is mainly because the synthetic soils with high S325 content are easier to be crumbled prior to being rolled into threads of 3.2 mm diameter. Therefore, the thread crumbled at a diameter of 3.2 mm may have moisture content higher than the plastic limit. In this study, it is the liquid limit rather than the plastic limit that is used for the calculation of the water weight for the soil-water-cement slurry. Quikrete® Type GU General Use Type 10 Portland Cement is utilized in this study for the experimental program to create cementitious bonds between soil particles.

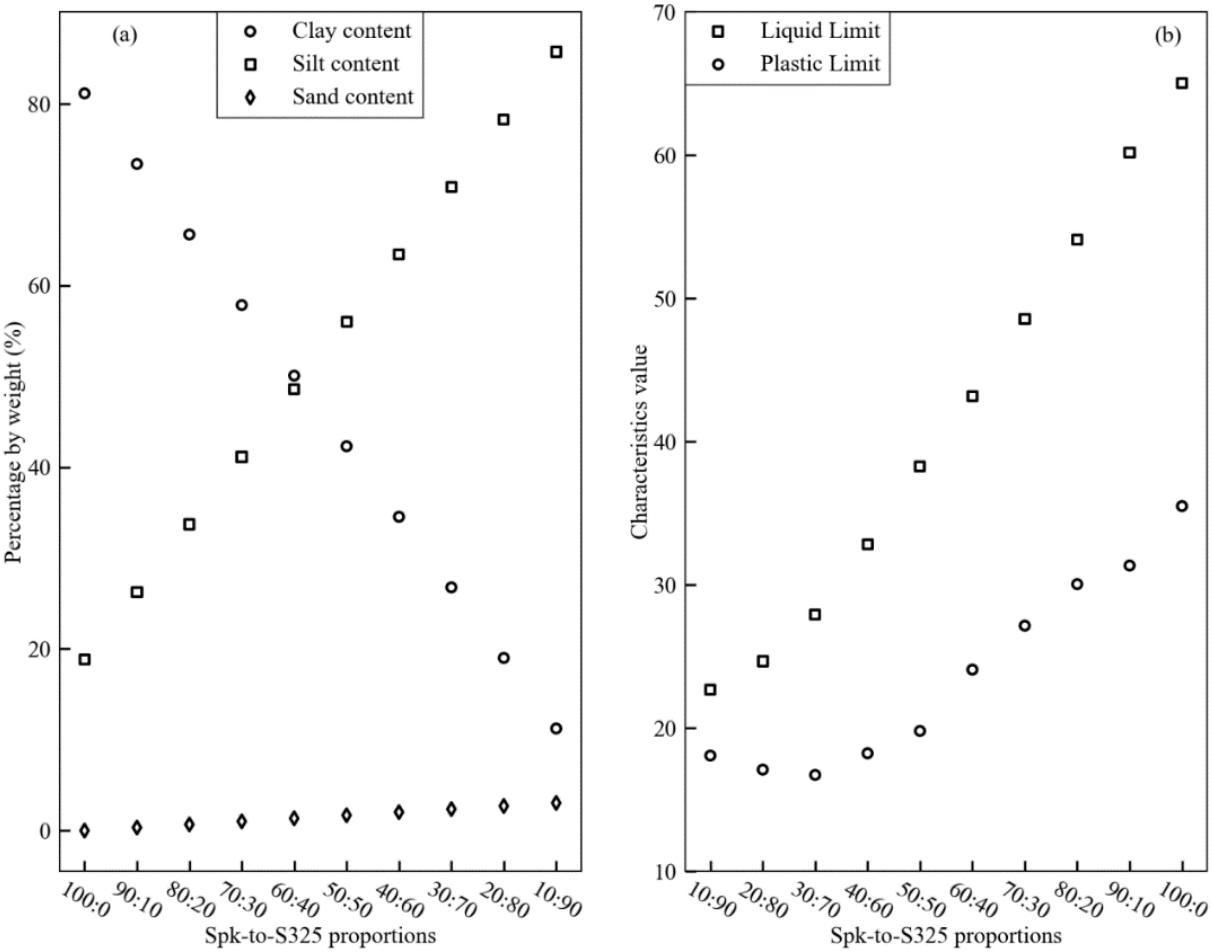

Figure 4-3 Properties of the synthetic soil: (a) Clay, silt and sand content, (b) Variation of liquid limit (LL) and plastic limit (PL) of the synthetic soils

4.5 Experimental procedure

In general, an experimental plan should consider two different types of variables: 1) the independent variables, which are silt content, cement content and the total soil-water content in this study, and 2) the dependent variables, which are the after-curing moisture content, the unconfined compressive strength, the after-curing void ratio and the degree of saturation of the cement-treated synthetic soils, etc.

Table 4-3 Experimental program for the synthetic Clearwater shale

Group No.	Spk-to-S325 proportions (%)	Total soil-water to cement ratio, C_w/A_w	Total soil-water content (initial moisture content), C_w	Curing period (days)	Type of test
G1	100 : 0	3, 5, 7, 8	1.1, 1.5, 2.0, 2.5 × liquid limit	28	UCS
G2	90 : 10	3, 5, 7, 8	1.1, 1.5, 2.0, 2.5 × liquid limit	28	UCS
G3	80 : 20	3, 5, 7, 8	1.1, 1.5, 2.0, 2.5 × liquid limit	28	UCS
G4	70 : 30	3, 5, 7, 8	1.1, 1.5, 2.0, 2.5 × liquid limit	28	UCS
G5	60 : 40	3, 5, 7, 8	1.1, 1.5, 2.0, 2.5 × liquid limit	28	UCS
G6	50 : 50	3, 5, 7, 8	1.1, 1.5, 2.0, 2.5 × liquid limit	28	UCS
G7	40 : 60	3, 5, 7, 8	1.1, 1.5, 2.0, 2.5 × liquid limit	28	UCS
G8	30 : 70	3, 5, 7, 8	1.1, 1.5, 2.0, 2.5 × liquid limit	28	UCS
G9	20 : 80	3, 5, 7, 8	1.1, 1.5, 2.0, 2.5 × liquid limit	28	UCS
G10	10 : 90	3, 5, 7, 8	1.1, 1.5, 2.0, 2.5 × liquid limit	28	UCS

To study the impact of these independent variables on the dependent variables, the concept of a controlled experiment is adopted in this study, indicating that only one variable changes at a specific time while the other keeps constant. There are 10 groups of synthetic soils to investigate the role of the major factors. Each group has 16 recipes, each of which has different normalized water content and cement content. Table 4-3 summarizes the experimental program. The silt content increases from 0% in G1 to 90% in G10. The total soil-water content (C_w) varies from 1.1 to 2.5 times the liquid limit. The total soil-water to cement ratio ranges from 3 to 8.

The schematic diagram shown in Figure 4-4 outlines the experimental program of this study. In Figure 4-4(b), the x-axis is the normalized water content, the y-axis is the total soil-water to cement ratio, and the z-axis is the group No., which also indicates the Spk-to-S325 proportions. The red dots, 160 in total, represent the recipes used for making the soil-water-cement mixture. To intuitively understand the parameters for each recipe, Figure 4-4(a) demonstrates the location of each recipe in a 2-D plot. It is evident that the soil-water-cement mixture is prepared in different water contents ranging from 1.1 to 2.5 times the liquid limit and with different total soil-water to cement ratios ranging from 3 to 8.

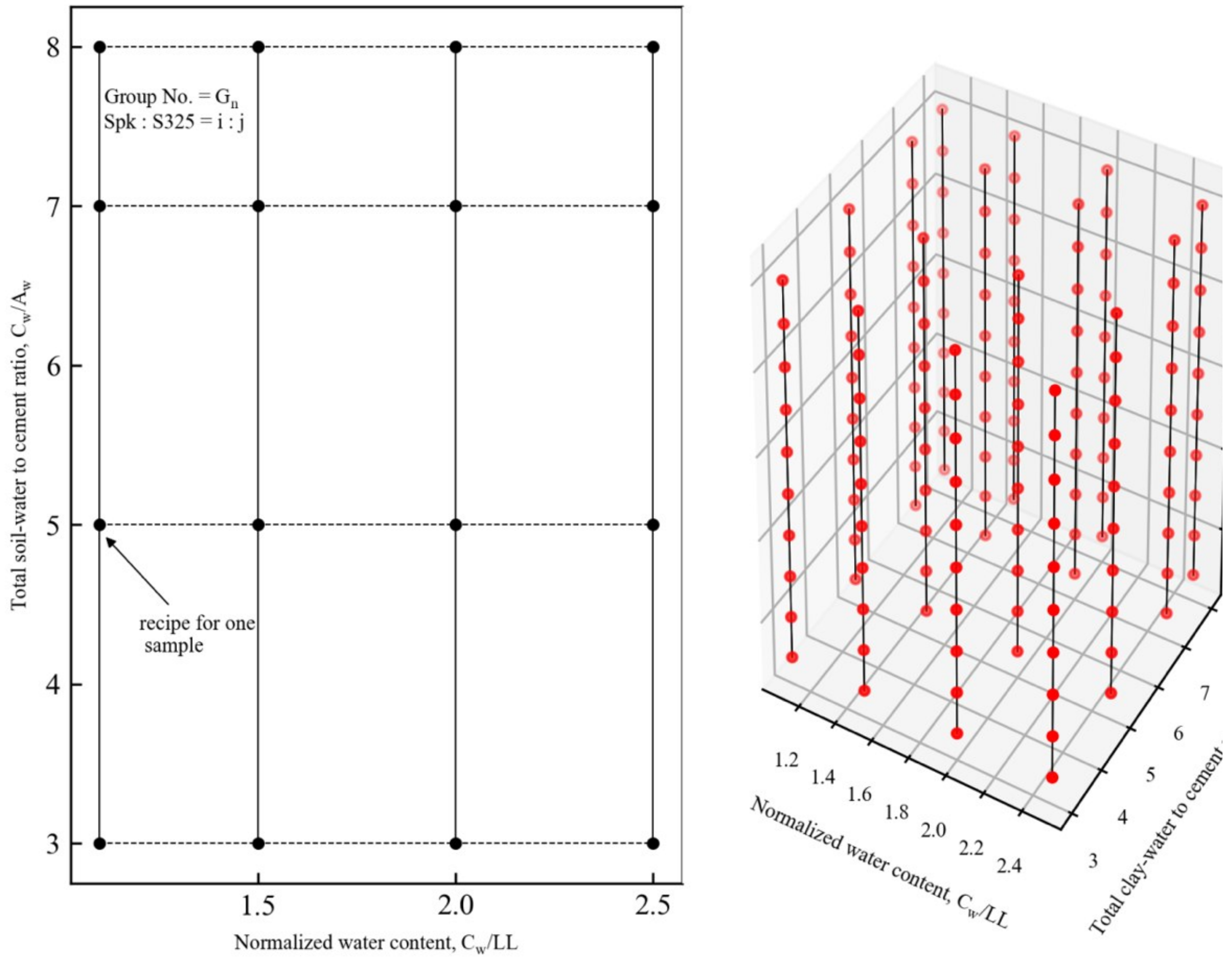

Figure 4-4 Experimental plan for the synthetic Clearwater shale

4.6 Specimen preparation

A total of 10 groups, each of which has 16 recipes, are mixed based on information shown in Table 4-3. Before preparing the soil-water-cement slurry, a plastic tube, which is 45 mm in diameter, is sawed into molds 120 mm in length to assure sufficient specimen height for the unconfined compression tests. A thin layer of petroleum jelly is applied on the inner surface of the mold so that the samples can be easily protruded from the mold after the desired curing period.

In preparing the specimens, quantities of soil, distilled water and cement for at least two specimens are calculated and weighed. Distilled water is then stored in three different beakers, Bk1, Bk2 and Bk3. The water in Bk2 is used to make cement slurry with a water-cement ratio of 0.6. The water in Bk3 is about 20 grams and used to rinse Bk2 after the cement slurry is transferred to the well-mixed soil slurry. The rest of the water is then stored in Bk1 and used for making the soil-water slurry.

After the soil, cement and water are well prepared, the soil and the distilled water in Bk1 are added to the KitchenAid Stand Mixer and mixed until a homogeneous paste is created. Cement powder is then added to Bk2 and mixed with the distilled water by hand until a homogeneous water-cement mixture is attained. Immediately after being well mixed, the cement slurry is added to the well-mixed soil slurry. The cement slurry that adhered to the inside wall of the Bk2 is cleaned using water in Bk3 and then added to the soil slurry. The soil-water-cement mixture is then mixed for another 10 minutes until a homogeneous paste is created. The mixing procedure is performed under room temperature (20±2 °C).

The well-mixed soil-water-cement mixture is then poured into the mold in three separate layers. After filling each layer, the trapped air bubbles are removed by subjecting the mold to vibrations until no air bubbles erupt from the sample. Immediately after completing the soil-filling process, the specimen together with the mold is sealed with plastic film to prevent moisture loss. After 24 hours, the cylindrical sample is protruded from the mold, wrapped with plastic film, and then carefully stored in a custom-built humidity container which is then placed in the laboratory at a constant temperature (20±2ºC).

After 28 days, these samples are trimmed to 45 mm (diameter) by 90 mm (height) for the unconfined compression tests. The rate of the vertical displacement is chosen to produce an axial deformation rate of approximately 0.5% per minute. The axial strain measurements are made using a linear variable differential transformer (LVDT). The circumferential displacement is measured by the radial chain. Immediately after the unconfined compression test, the sample is weighed using digital balance and then dried in the oven at a temperature of 110±5 ºC until a constant mass is attained for the measurement of the moisture content. If strength difference of the two samples for each recipe is very large, samples are then made again based on the procedure described above until the strength difference is within a tolerable amount.

4.7 Results and discussions

4.7.1 The variation of the after-curing moisture content

Figure 4-5 demonstrates the variation of the after-curing moisture content (C_{wf}) of the synthetic soils treated with 3, 5, 7 and 8 total soil-water to cement ratios, respectively. Regardless of the Spk-to-S325 proportions, the after-curing moisture content of the specimens treated with the same total soil-water to cement ratio forms a smooth curve with both the total soil-water content and the cement content, indicating that the soil grain size distribution may not be a major factor affecting the after-curing moisture content.

As shown in Figure 4-5(a), the after-curing moisture content increases with the total soil-water content but the increase rate clearly decreases as the total soil water content increases. This phenomenon is notable for samples with a total soil-water to cement ratio of 3. When the total soil-water content is about 150%, the gradient approaches to zero. However, at a high total soil-water to cement ratio such as 5, 7 and 8, the after-curing moisture content increases almost linearly within the range of total soil-water content being considered. Through the analysis of the four types of symbols, a quadratic function fits well to the relationship between the total soil-water content and the after-curing moisture content.

The vertical offset between any two adjacent regression lines decreases with the increase of the total soil-water to cement ratio. For instance, when the total soil-water to cement ratio is 7 and 8, the vertical offset between the two regression lines is almost equal to zero. However, the vertical offset between the regression curve with a total soil-water to cement ratio of 3 and that of 5 is quite clear.

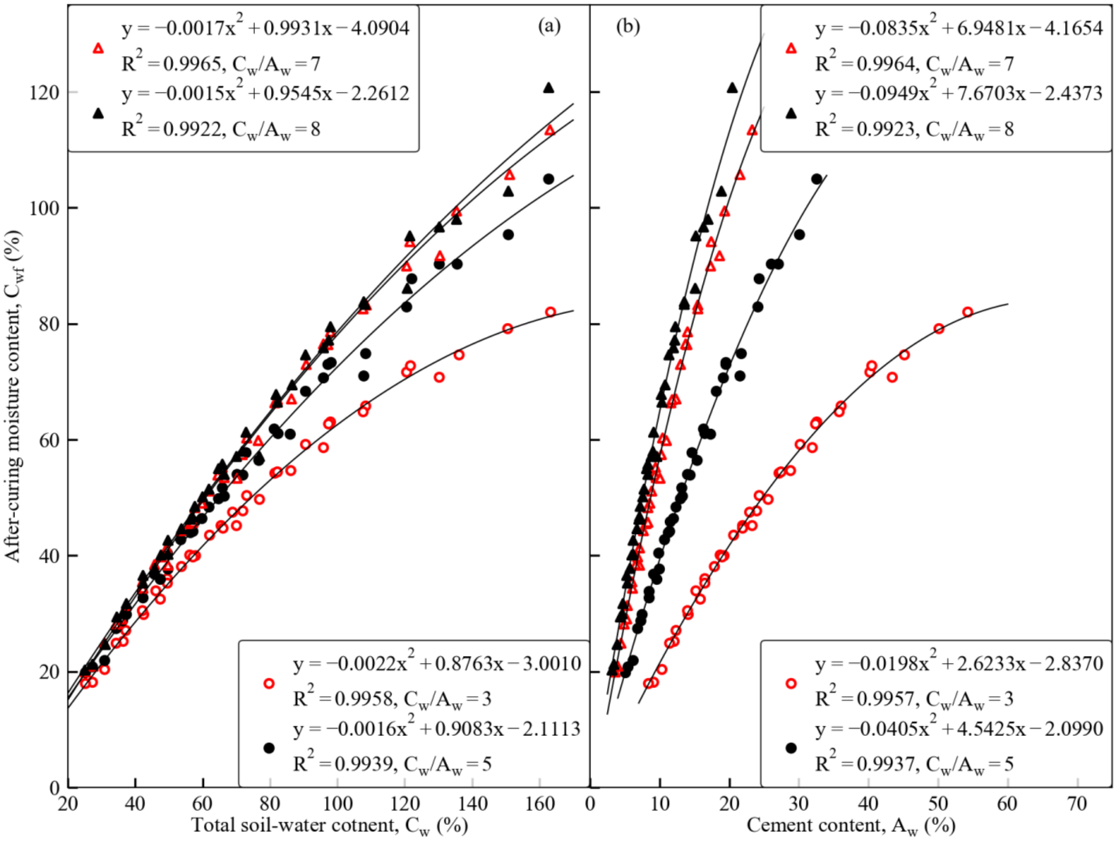

Figure 4-5 Relationship between total soil water content, cement and after-curing moisture content: (a) after-curing moisture content versus total soil-water content; (b) after-curing moisture content versus cement content

Figure 4-5(b) illustrates the relationship between the after-curing moisture content and the cement content. As shown in the figure, the after-curing moisture content increases gradually with the cement content but the experimental result is opposite to that presented by other researchers (Lorenzo & Bergado, 2004). The major reason leading to the conflict between the previous studies and the results presented in this study is that the symbols with the same type in Figure 4-5(b) represent specimens treated with the same total soil-water to cement ratio, indicating that the total soil-water content also increases with the cement content. Whereas in the Lorenzo & Bergado (2004) study, the total soil-water content is adjusted to ensure it does not change with increasing cement content.

At a low total soil-water to cement ratio such as 3, the relationship between the after-curing moisture content and the cement content forms a quadratic function with a positive gradient decreasing gradually. At a high total soil-water to cement ratio such as 7 and 8, the after-curing moisture content almost increases linearly within the range of cement content being considered. A quadratic function fits well to the relationship between the cement content and the after-curing moisture content. Through the analysis of the four regression curves, it is evident that the vertical offset between any two adjacent regression lines decreases with the total soil-water to cement ratio.

This study finds that the modified total soil-water to cement ratio (C_w^M) is more acceptable when investigating the after-curing properties of cement-treated synthetic soils.

$$C_w^M = \frac{C_w}{e^{\frac{A_w}{100}}} \qquad \text{Equation (4-1)}$$

As shown in Figure 4-6(a), there exists a linear relationship between the after-curing moisture content and the modified total soil-water to cement ratio. It is worth noting that the figure includes the specimens of the 10 subgroups, and the soil grain size distributions of the 10 types of synthetic soils are quite different. It once again indicates that the soil grain size distribution does not play a major role in the after-curing moisture content.

A closer look at the relation C_{wf} - C_w^M, as shown in Equation (4-2), indicates that the after-curing moisture content is a continuous function of the modified total soil-water to cement ratio, as shown in Figure 4-6(a).

$$C_{wf} = 0.897 \times C_w^M - 1.228 \qquad \text{Equation (4-2)}$$

Based on Equation (4-1) and Equation (4-2), the partial derivative of after-curing moisture content with respect to the total soil water content can be expressed as below:

$$\frac{\partial C_{wf}}{\partial C_w} = \frac{0.897}{e^{\frac{A_w}{100}}}$$ Equation (4-3)

Similarly, the partial derivative of after-curing moisture content with respect to the cement content can be expressed as below:

$$\frac{\partial C_{wf}}{\partial A_w} = -\frac{0.00897 \times C_w}{e^{\frac{A_w}{100}}}$$ Equation (4-4)

It is evident that the after-curing moisture content is a continuous function of both the total soil-water content and the cement content in the three-dimensional space. That is because: 1) the partial derivative of after-curing moisture content with respect to the total soil-water content is continuous; 2) the partial derivative of after-curing moisture content with respect to the cement content is continuous. Figure 4-6(b) illustrates the 3-D plot of the after-curing moisture content with the cement content and the total soil-water content. The four types of symbols in the subplot represent samples with the total soil-water to cement ratio of 3, 5, 7 and 8, respectively.

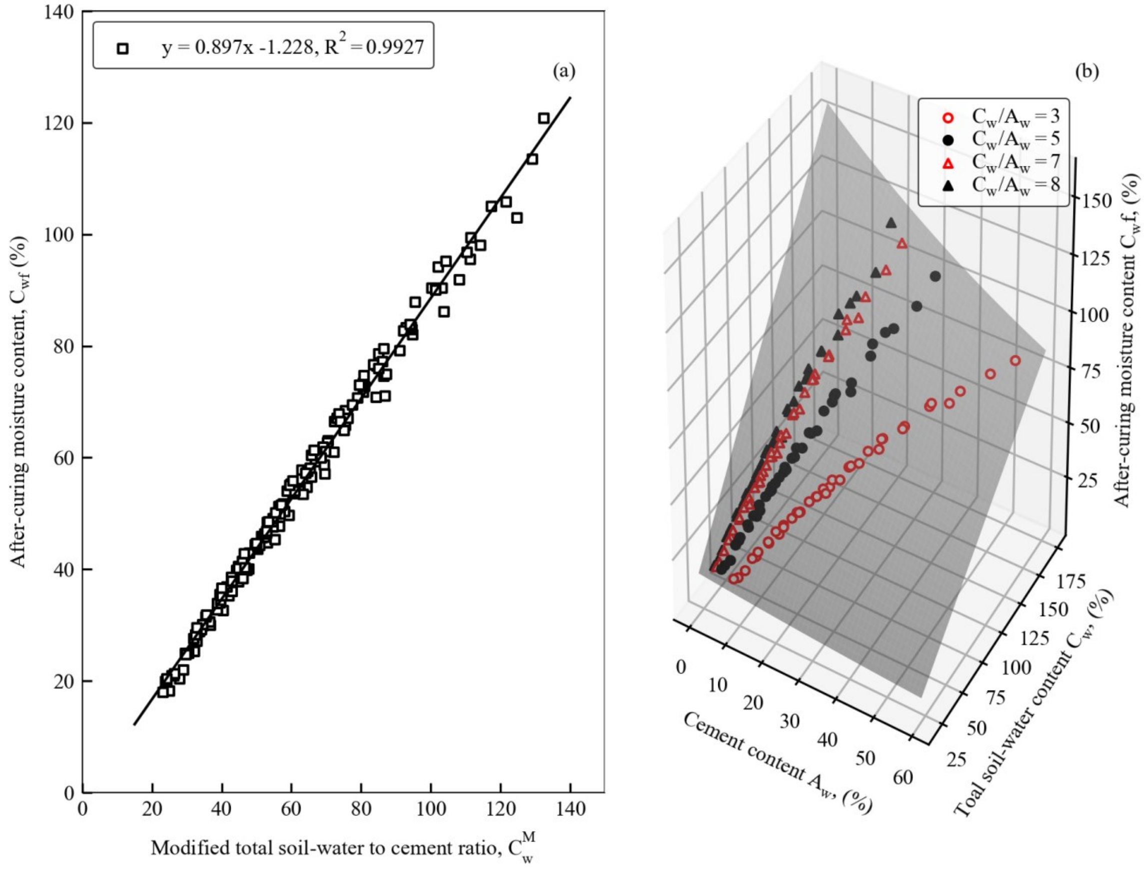

Figure 4-6 The relationship between total soil-water moisture content, cement content and after-curing moisture content

From the analysis of Equation (4-3), it is evident that the partial derivative of after-curing moisture content with respect to the total soil-water content ($\frac{\partial C_{wf}}{\partial C_w}$) is dependent upon the cement content. The analysis of Equation (4-4) indicates that for specimens with the same total soil-water content, the magnitude of the partial derivative of the after-curing moisture content with respect to the cement content ($\frac{\partial C_{wf}}{\partial A_w}$) increases with the decrease of the cement content. If the cement content in the soil-water-cement mixture is too high, there may be a critical point at which the gradient is close to zero, indicating that the cement content is very high and the water in the soil-water-cement mixture has been totally consumed by the hydration and pozzonlanic reaction.

Figure 4-7 compares the predicted after-curing moisture content based on Equation (4-2) to the measured after-curing moisture content. It is worth noting that the predicted after-curing moisture content is developed from the relationship between the measured after-curing moisture content and the total soil-water content and the cement content. The major purpose of the comparison is to make sure that the difference between the predicted after-curing moisture content and the measured after-curing moisture content is very small.

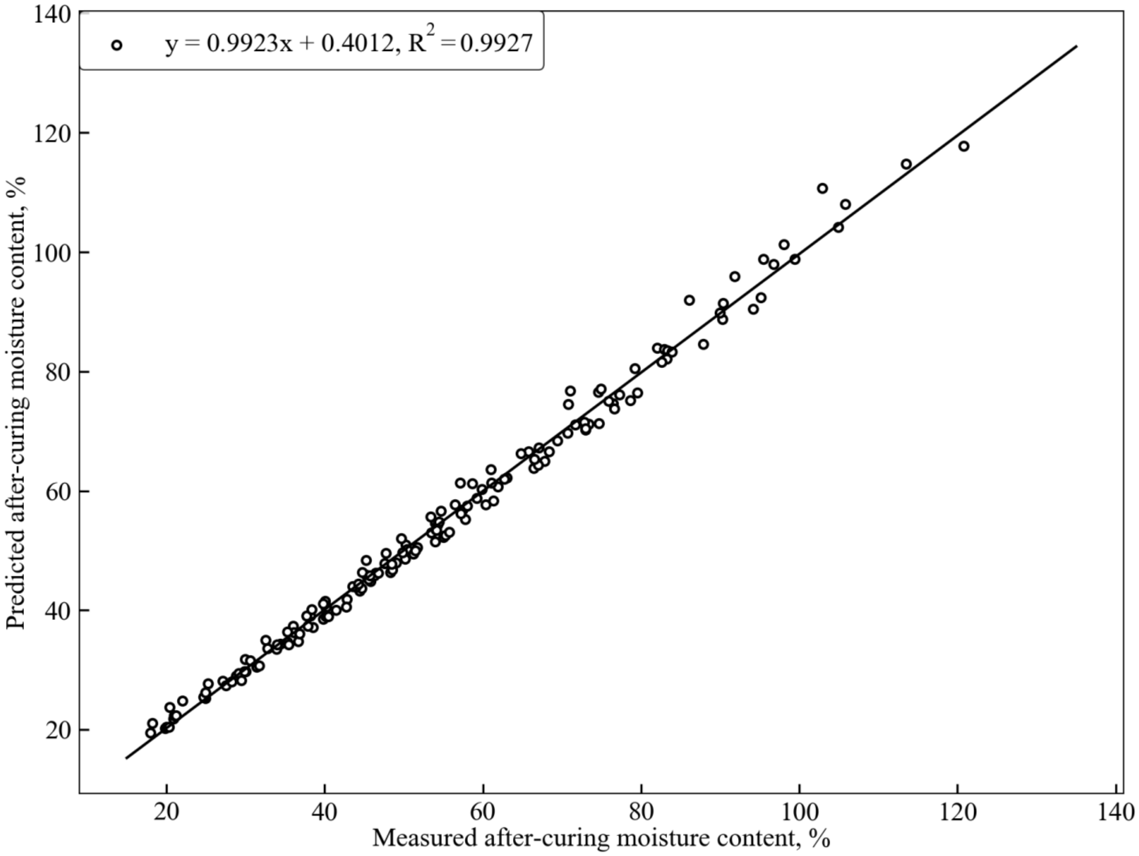

Figure 4-7 A comparison between the measured after-curing moisture content and the predicted after-curing moisture content

Under this condition, the equation for the predicted after-curing moisture content can be used to obtain the after-curing moisture content of those formulas not included in the experimental plan. Obviously, the coefficient of the linear regression line is 0.9923, which is almost equal to 1, indicating that these points are symmetrical around the 45° line of the square. The y-intercept is only about 0.4, which almost has no effect on the predicted after-curing moisture content.

Equation (4-2) and Figure 4-7 are of great value for predicting the after-curing moisture content of these formulas not included in the experimental plan. As discussed previously, the study only considers the selected 160 formulas. The total soil-water to cement ratios such as 3, 5, 7 and 8 and the total soil-water contents, which are 1.1, 1.5, 2.0 and 2.5 times the liquid limit, are only a few isolated points. The prediction, which uses the total soil-water content and the cement content as the input parameters, links these isolated points together and forms a continuous surface for the prediction of the after-curing moisture of the points not included in the experimental plan.

4.7.2 Unconfined compressive strength versus after-curing moisture content

The unconfined compressive strength variation with the after-curing moisture content is shown in Figure 4-8. The 10 subplots correspond to synthetic soils with 0, 10, 20, 30, 40, 50, 60, 70, 80 and 90% S325 by weight, respectively. In each subplot, there are four types of symbols, each of which corresponding to specimens treated with 3, 5, 7 and 8 total soil-water to cement ratios, respectively. Through the analysis of Figure 4-8, the following results can be drawn:

First, the unconfined compressive strength (q_u) decreases with the increase of the after-curing moisture content (C_{wf}). A linear function fits well to the relation q_u - C_{wf}.

$$q_u = k_f\left(C_{wf} - C_{wf_0}\right) \qquad \text{Equation (4-5)}$$

When the after-curing moisture content is higher than the maximum after-curing moisture content (C_{wf_0}), the unconfined compressive strength is less than zero, which is impossible in practice.

Second, through the comparison of the four linear regression lines in each subplot, it is evident that the magnitude of the strength coefficient decreases with the total soil-water to cement ratio.

For instance, when Spk-to-S325 proportions are 100:0, the strength coefficient with total soil-water to cement ratios of 3, 5, 7 and 8 are -32.266, -14.216, -8.464 and -6.750, respectively. The same observation can also be drawn from the other nine subplots.

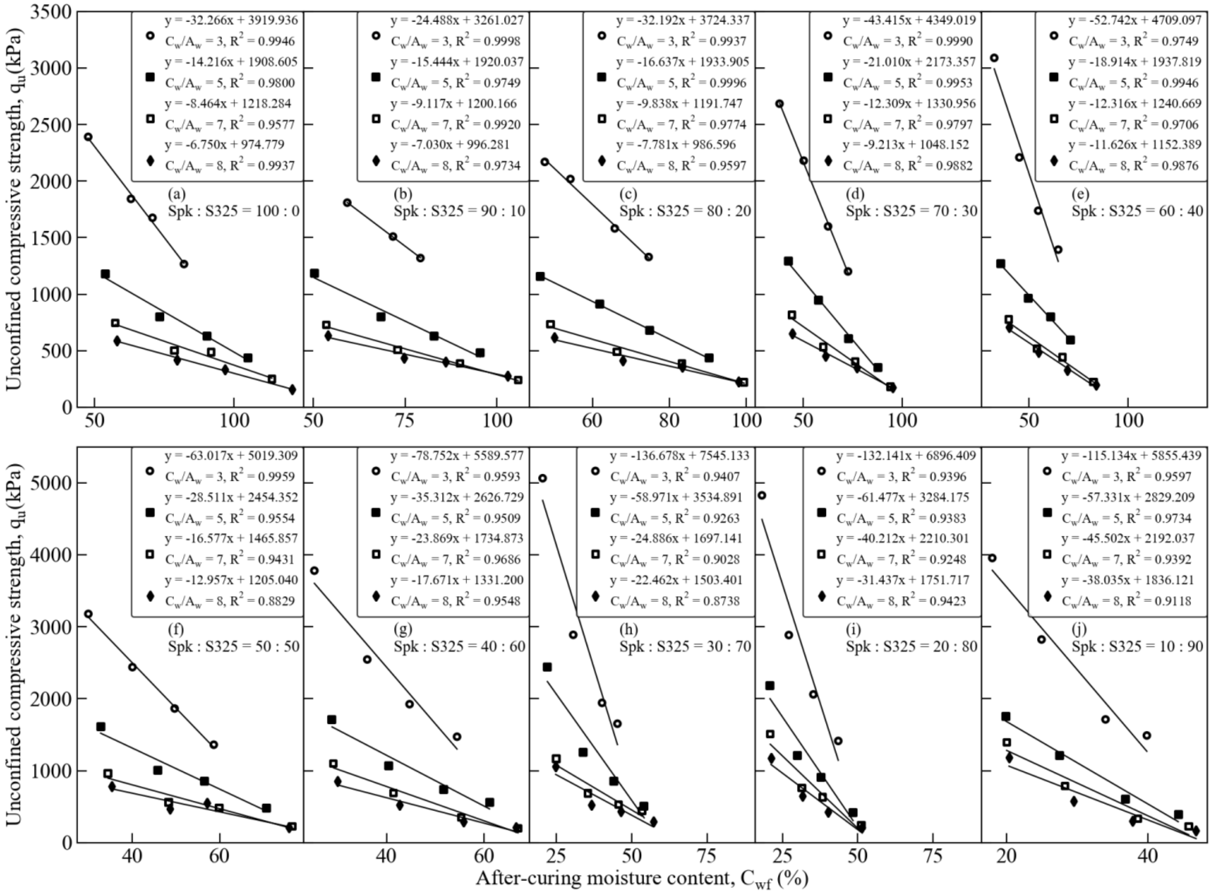

Figure 4-8 Relationship between after-curing moisture content and unconfined compressive strength

Third, through the comparison of the strength coefficient with the same total soil-water to cement ratio, the strength coefficient changes with the Spk-to-S325 proportions, as shown in Figure 4-9(a). For total soil-water to cement ratios of 3 and 5, the magnitude of the strength coefficient reaches the highest value when the S325 content is 70%. For a total soil-water to cement ratio of 7 and 8, the magnitude of the strength coefficient keeps increasing with the S325 content.

The variation of the maximum after-curing moisture content with Spk-to-S325 proportions is illustrated in Figure 4-9(b): it almost decreases linearly with the Spk-to-S325 proportions. Future analysis demonstrates that the maximum after-curing moisture content is highly dependent upon the liquid limit of the synthetic soils, as shown in Figure 4-10. The figure demonstrates the variation of the normalized maximum after-curing moisture content, which is defined as the ratio of the maximum after-curing moisture content to the liquid limit of the corresponding synthetic soils, with the Spk-to-S325 proportions and most of the data fall in the range of 2.0 to 2.4.

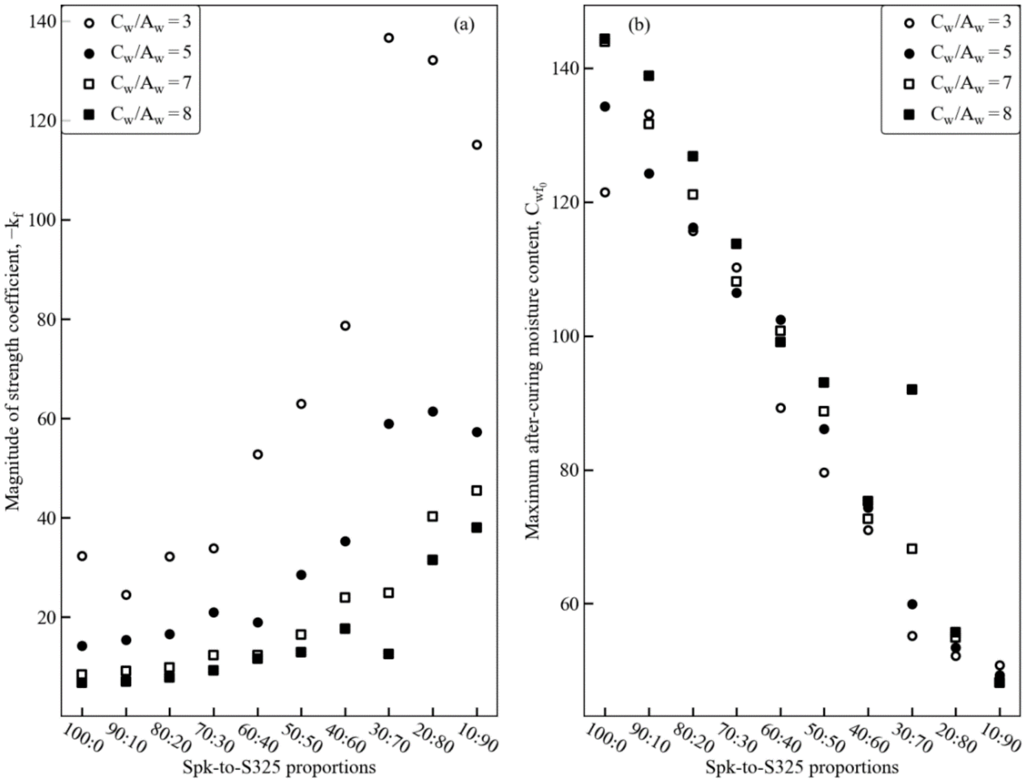

Figure 4-9 Variation of the (a) magnitude of the strength coefficient and (b) maximum after-curing moisture content with Spk-to-S325 proportions

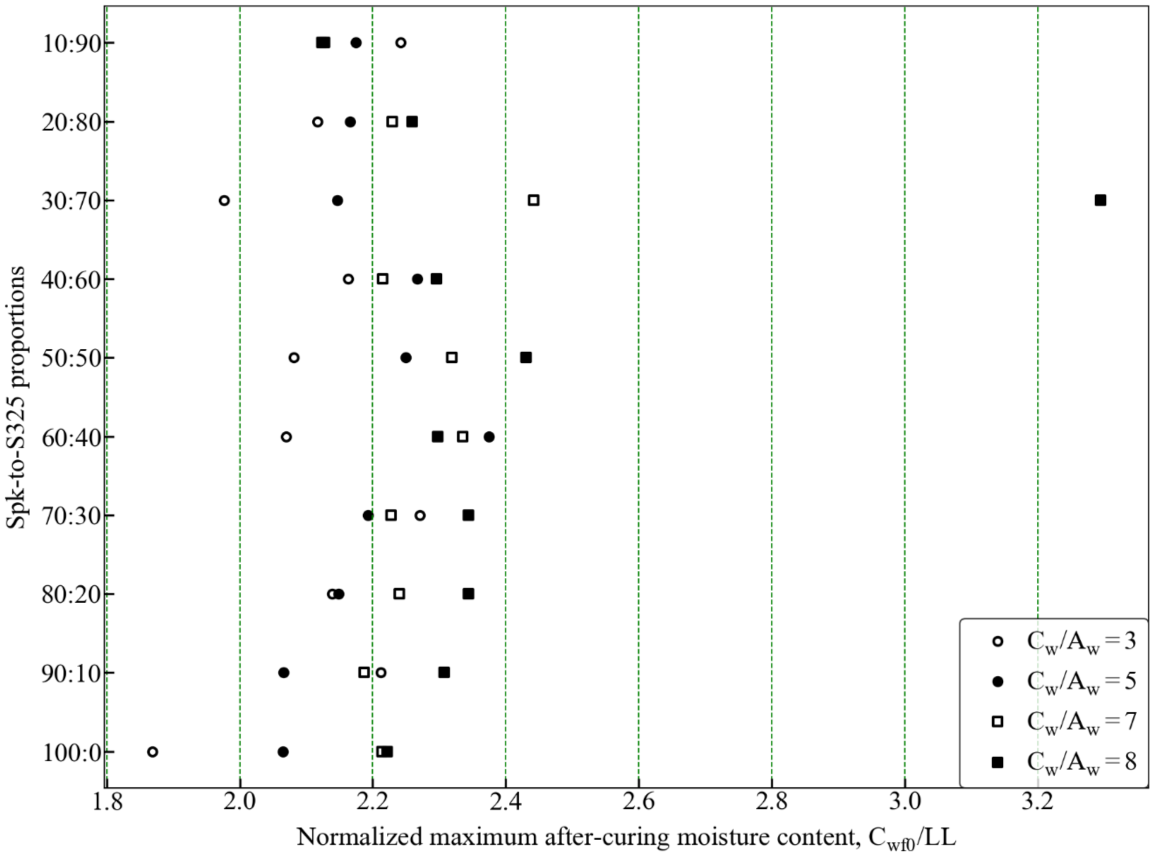

Figure 4-10 Relationship between normalized maximum after-curing moisture content and Spk-to-S325 proportions

Through the analysis of the relationship between the strength coefficient, the maximum after-curing moisture content and the total soil-water to cement ratio, this study finds that there exists a linear relationship between the modified strength coefficient ($k_f^M = ln\left[\frac{-k_f}{\left(\frac{C_w}{A_w}\right)}^{1.5}\right]$) and the modified maximum after-curing moisture content ($C_{wf_0}^M = ln\left[C_{wf0} \times \left(\frac{C_w}{A_w}\right)^2\right]$), as shown in Figure 4-11(a). A linear function fits well to the relation k_f^M-C_{wf0}^M.

$$ln\left[C_{wf_0} \times \left(\frac{C_w}{A_w}\right)^2\right] = -0.6794 \times ln\left[\frac{-k_f}{\left(\frac{C_w}{A_w}\right)^{1.5}}\right] + 8.297 \qquad \text{Equation (4-6)}$$

Figure 4-11(b) demonstrates that the maximum after-curing moisture content is a continuous function of the total soil-water to cement ratio and the magnitude of the strength coefficient. For a certain total soil-water to cement ratio, the maximum after-curing moisture content almost increases exponentially with the decrease of the magnitude of the strength coefficient. For a certain magnitude of the strength coefficient, the maximum after-curing moisture content decreases with the increase of the total soil-water to cement ratio. Figure 4-11(b) illustrates the surface based on Equation (4-6), which once again proves that the after-curing moisture content is a continuous function of the total soil-water to cement ratio and the magnitude of the strength coefficient in the 3-D space.

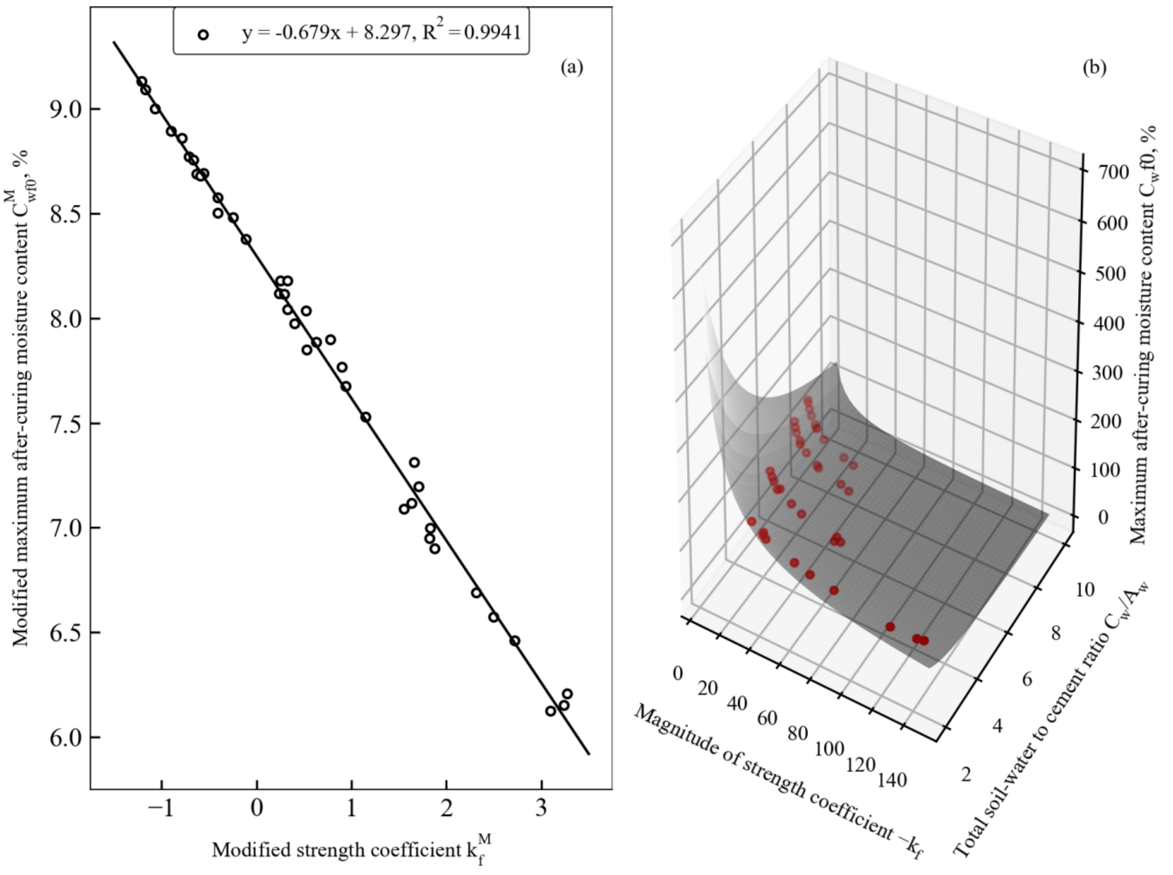

Figure 4-11 Relationship between the modified strength coefficient and modified maximum after-curing moisture content shown in (a) 2-D plot and (b) 3-D plot

Based on Equation (4-6), the relationship between the maximum after-curing moisture content, the strength coefficient and total soil-water to cement ratio can be expressed as below:

$$ln\left(C_{wf_0}\right) + 0.9809\, ln\left(\frac{C_w}{A_w}\right) = -0.6794 \times ln\left(-k_f\right) + 8.297 \qquad \text{Equation (4-7)}$$

Based on Equation (4-7), the strength coefficient can be expressed as below:

$$\left[C_{wf_0} \times \left(\frac{C_w}{A_w}\right)^{0.9809} \times e^{-8.297}\right]^{\frac{-1}{0.6794}} = -k_f \qquad \text{Equation (4-8)}$$

Therefore, the unconfined compressive strength of the cement-treated synthetic soils can be expressed as below:

$$q_u = -\left[C_{wf_0} \times \left(\frac{C_w}{A_w}\right)^{0.9809} \times e^{-8.297}\right]^{\frac{-1}{0.6794}} \times \left(C_{wf} - C_{wf_0}\right) \qquad \text{Equation (4-9)}$$

For simplicity, Equation (4-9) is expressed as below:

$$q_u = -\left(C_{wf_0}\right)^{-1.4719} \times \left(\frac{C_w}{A_w}\right)^{-1.444} \times e^{12.2122} \times \left(0.897 \times \frac{C_w}{\frac{A_w}{e100}} - 1.228 - C_{wf_0}\right) \qquad \text{Equation (4-10)}$$

Figure 4-12 makes the comparison between the predicted unconfined compressive strength based on Equation (4-10) and the measured unconfined compressive strength. The physical meaning of these parameters is quite clear. For the maximum after-curing moisture content, the value is deduced from Figure 4-10 and equals 2.2 times the liquid limit of the corresponding synthetic soils. The coefficient of the linear regression line is 1.0006, indicating that these points are symmetrical around the 45° line of the square. Meanwhile, the high value of the coefficient of determination (R^2) demonstrates that the points are very close to the fitted regression line. The y-intercept has a small magnitude, approximately 2.75, which has a limited influence on the predicted value. Equation (4-10) and Figure 4-12 are of great value for predicting the unconfined compressive strength of these formulas not included in the experimental plan.

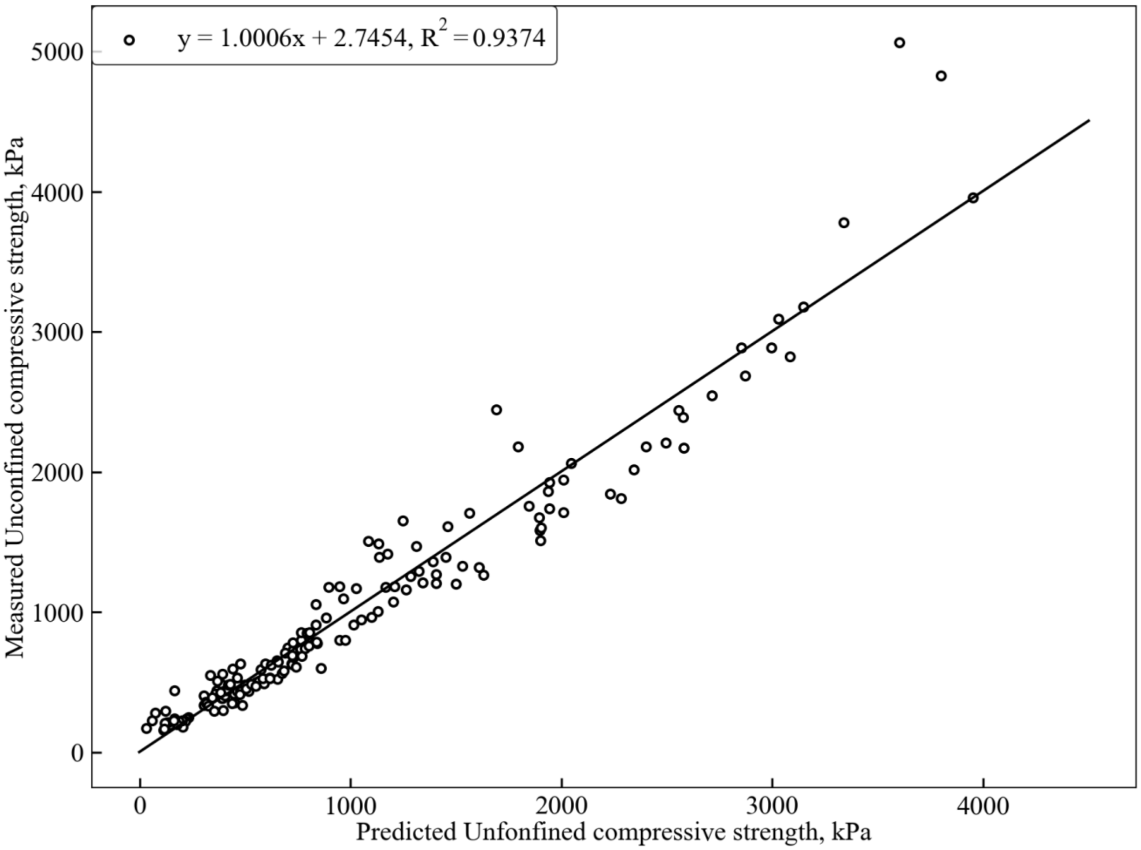

Figure 4-12 Measured unconfined compressive strength versus the predicted unconfined compressive strength

4.7.3 Assessment of degree of saturation and after-curing void ratio (e_f)

In this study, the after-curing specific gravity of cement-admixed soil is also considered an important index to qualitatively investigate the degree of saturation or the after-curing void ratio. The specific gravity of the soil-cement mixture can be determined through the following equation:

$$G_s = \frac{\sum_{i=1}^{n} m_i}{\sum_{i=1}^{n} \frac{m_i}{G_i}} \qquad \text{Equation (4-11)}$$

where m_i is the quantity of the specific soil or cement in the soil-cement mixture; G_i is the specific gravity of the specific soil or cement in the soil-cement mixture.

An element of the soil-water-cement mixture of volume V is shown in Figure 4-13. Sasanian (2011) found that the total pore volume of the cured soils remained the same as before the curing period. The study also revealed that the volume of the macro-pores in the cement-treated soils decreased, leading to a reduction in permeability. Similarly, Locat, Trembaly, and Leroueil (1996) found that there existed a certain lime content above which the pozzolanic reactions could be provoked and produced cementitious material filling the pore space, leading to a reduction in hydraulic conductivity. Uddin et al. (1997) found that the after-curing specific gravity of those cement-admixed specimens was lower than those of the untreated soil, whatever the curing time was. Meanwhile, the after-curing specific gravity decreases with the curing time but keeps almost constant after 8-12 weeks. Other studies have also shown that the after-curing specific gravity decreases with curing time (Q. Li et al., 2014; Lorenzo & Bergado, 2004; Xiao & Lee, 2008). Some studies have presented that the after-curing void ratio also decreases with curing time (Jongpradist et al., 2009). The decrease of after-curing specific gravity or void ratio indicates that the solid volume of cement-treated soils increases with curing time.

Based on these previous studies, it is evident that the solid volume of the cured samples is not less than the solid volume of the soil-water-cement mixture. For instance, the volume of the soil solids, cement solids and water before the hydration and pozzolanic reactions are V_{ss}, V_{cs} and V_w, respectively. After 28 days curing, the solid volume is not less than $V_{ss}+V_{cs}$.

Water in the soil-water-cement mixture can be classified into three different types: water for hydration and pozzolanic reactions; double-layer water or bound water, which is electrically attracted toward the surface of the soil particles; and free water, which can flow through the interconnected pore spaces (Das, 2013; Zhu et al., 2007). Prior to the chemical reactions in the soil-water-cement mixture, there are only free water and bound water. The chemical reactions consume part of the pore water, leading to the formation of hydrates and the transfer of part of the pore water to the bound water. The water consumed by the chemical reactions becomes an integral part of the hydrates, leading to a strength increase (Chew et al., 2004a; S. N. Rao & Rajasekaran, 1996). Meanwhile, there may be moisture loss due to the evaporation caused by the heat that is generated during the chemical reactions. Zhu et al. (2007) estimated that the moisture loss due to evaporation is approximately 13 kg per unit volume of the cement-admixed soil. This value is adopted by this study for the calculation of the degree of saturation and the after-curing void ratio. After curing the specimens for 28 days, only the bound water and pore water can be measured by the drying oven method.

The following section intends to explore the degree of saturation using three different methods:

1. The first method follows the experimental results presented in the study by Sasanian (2011), which describes that the total pore volume of the cement-admixed samples remains the same as before the hydration and pozzolanic reactions.
2. The second method is deduced from the fact that the after-curing specific gravity decreases with curing time, indicating that the solid volume of the cured sample is larger than before the hydration and pozzolanic reactions. Therefore, the solid volume of the cured specimen is no less than $(V_{ss}+V_{cs})$.
3. The third method assumes that the solid volume of the cement-admixed specimen is no more than $(V_{ss}+V_{cs}+V_{wr})$, indicating that the volume of the water consumed by hydration and pozzolanic reactions totally contributes to the solid volume of the cured sample.

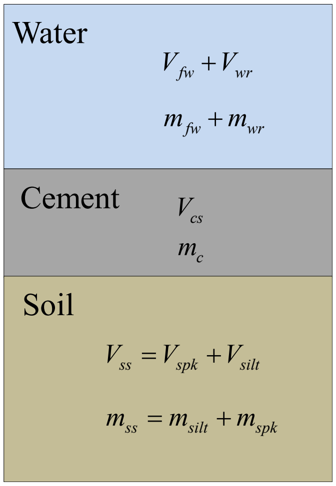

Figure 4-13 Phase diagram for cement-admixed soils

The total soil-water content of the soil-water-cement mixture can be expressed by the relation:

$$w_i = \frac{m_{fw}+m_{wr}}{m_{fss}-m_c} \qquad \text{Equation (4-12)}$$

Moisture loss due to the evaporation caused by the chemical reactions is also considered during the calculation of the total soil-water content. After the desired curing period, the after-curing moisture content can be calculated as follows:

$$w_f = \frac{m_{fw}}{m_{fss}+m_{wr}} \qquad \text{Equation (4-13)}$$

where w_i is the total soil-water content; w_f is the after-curing moisture content; m_{wr} is the quantity of water for hydration and pozzolanic reactions; m_{fw} is the quantity of water left in the voids of the sample after the desired curing period; m_{fss} is the quantity of the soil and cement solid; m_c is the quantity of the cement solid.

The weight of the specimen after curing (m_{ft}) can be calculated as follows:

$$m_{ft} = m_{fss}+m_{wr}+m_{fw} \qquad \text{Equation (4-14)}$$

The relationship between m_c and m_{fss} can be expressed as below:

$$m_{fss} = m_{spk}+m_{silt}+m_c \qquad \text{Equation (4-15)}$$

where m_{silt} is the quantity of Sil325; m_{spk} is the quantity of Speswhite kaolin clay.

From Equation (4-13) and Equation (4-14), m_{fw} can be expressed as below:

$$m_{fw} = \frac{w_f \times m_{ft}}{1+w_f} \qquad \text{Equation (4-16)}$$

From Equation (4-12) and Equation (4-15), the total soil-water content can be rewritten as below:

$$w_i = \frac{m_{fw}+m_{wr}}{m_{spk}+m_{silt}} \qquad \text{Equation (4-17)}$$

The cement content can be calculated as below:

$$A_w = \frac{m_c}{m_{spk}+m_{silt}} \qquad \text{Equation (4-18)}$$

Therefore, based on Equation (4-12) to Equation (4-18), the weight of water consumed during the hydration and pozzolanic reactions (m_{wr}) and the weight of the soil and cement solid (m_{fss}) can be expressed as below:

$$m_{wr} = \frac{m_{fw} \times \left(w_i - w_f - A_w \times w_f\right)}{w_f \times (1+w_i+A_w)} \qquad \text{Equation (4-19)}$$

$$m_{fss} = \frac{m_{fw} \times \left(1+w_f\right)(1+A_w)}{w_f \times (1+w_i+A_w)} \qquad \text{Equation (4-20)}$$

Thus, the weight of Speswhite kaolin clay (m_{spk}), Sil325 (m_{silt}) and cement (m_c) in the soil and cement solid (m_{fss}) can be calculated as follows:

$$k_1 = \frac{m_{silt}}{m_{spk}} \qquad \text{Equation (4-21)}$$

$$k_2 = \frac{m_c}{m_{spk}} \qquad \text{Equation (4-22)}$$

From Equation (4-15), Equation (4-21) and Equation (4-22),

$$m_{spk}+k_1 \times m_{spk}+k_2 \times m_{spk} = m_{fss} \qquad \text{Equation (4-23)}$$

$$m_{spk} = \frac{m_{fss}}{1+k_1+k_2} \qquad \text{Equation (4-24)}$$

$$m_{silt} = k_1 \times \frac{m_{fss}}{1+k_1+k_2} \qquad \text{Equation (4-25)}$$

$$m_c = k_2 \times \frac{m_{fss}}{1+k_1+k_2} \qquad \text{Equation (4-26)}$$

Thus, the degree of saturation based on the second method, which is hereinafter referred to as lower limit (WL), can be expressed as below:

$$S_r = \frac{V_{fw}}{V_{ft}\text{-}V_{spk}\text{-}V_{silt}\text{-}V_c} \qquad \text{Equation (4-27)}$$

where V_{fw} is the volume of the water left in the voids of the sample after the desired curing period; V_{ft} is the volume of the sample after the desired curing period; V_{spk} is the volume of Speswhite kaolin clay; V_{silt} is the volume of Sil325; V_c is the volume of cement.

The lower limit of the degree of saturation assumes that the solid volume is only composed of the volume of Speswhite kaolin clay, Sil325 and cement. The water for the chemical reaction does not contribute to the solid volume.

The third method assumes that the water for the reaction also contributes to the solid volume of the cement-admixed samples. It implies that the solid volume is equal to the volume of Speswhite kaolin clay, cement, Sil325 and water for the reaction. The degree of saturation based on the third method, which is hereinafter referred to as the upper limit (UL), can be expressed as below:

$$S_r = \frac{V_{fw}}{V_{ft}\text{-}V_{spk}\text{-}V_{silt}\text{-}V_c\text{-}V_{wr}} \qquad \text{Equation (4-28)}$$

Figure 4-14 illustrates the degree of saturation based on the three methods. It is evident that the third method (UL) overestimates the degree of saturation due to the presence of the degree of saturation over 100%. The first method assumes that the void ratio of the cured soil is the same as that of the untreated soils. This assumption does not coincide well with the fact that the cement-treated soil shrinks during the curing period, indicating that the degree of saturation based on the first method may be conservative. The fact that the after-curing specific gravity decreases with curing times implies that the solid volume of cured soils is larger than the volume of the soil solid and the cement solid. However, it is difficult to accurately determine the after-curing solid volume. Based on the above analysis, it is reasonable to deduce that the solid volume of the cured samples is larger than the sum of the soil solid volume and the cement solid volume, but smaller than the sum of the soil solid volume, the cement solid volume and the volume of the water for the chemical reactions:

$$V_{soil}+V_{cement} \le V_{solid} \le V_{soil}+V_{cement}+V_{wr} \qquad \text{Equation (4-29)}$$

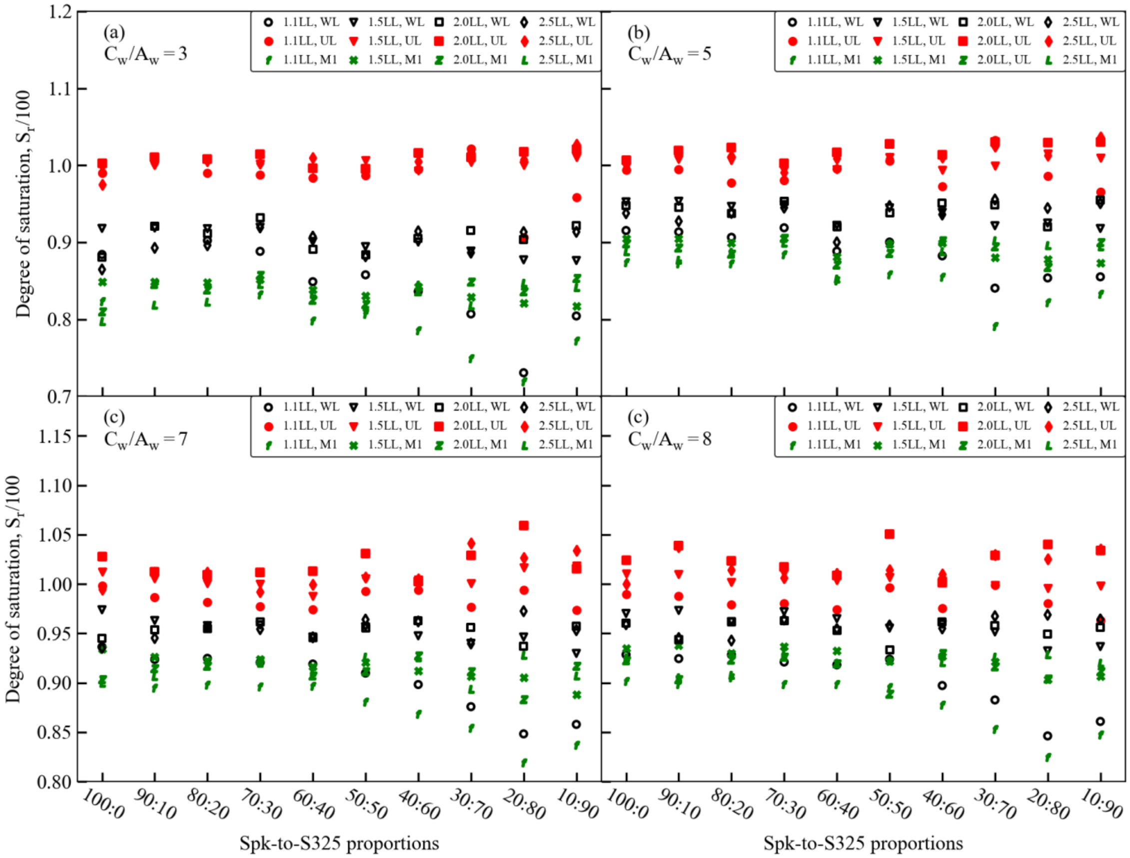

Figure 4-14 Degree of saturation of the synthetic soils

4.7.4 Unconfined compressive strength versus after-curing void ratio

The total soil-water to cement ratio ($\frac{C_w}{A_w}$) has been considered as the prime parameter governing the engineering behaviour of the cement-treated soils (Miura et al., 2001). However, it is worth noting that the after-curing properties of the cement-treated soils are affected by many factors. Some studies adopt the after-curing void ratio as the major parameter for the assessment of the unconfined compressive strength of cement-treated soils (Lorenzo & Bergado, 2004). The after-curing void ratio not only considers the effect of commonly seen factors, such as the total soil-water content and the cement content, but also factors neglected by most researchers, such as chemical composition of soil and cement, liquid limit, etc.

Based on the assessment of the after-curing void ratio in the previous section, this study proposes that the modified after-curing void ratio (M_e) can be used to supersede the total soil-water to cement ratio. The parameter takes into account the total soil-water content, the cement content, the liquid limit of the synthetic soils and the after-curing void ratio.

$$M_e = \frac{A_w}{\sqrt{\left(\frac{C_w}{LL}\right)} \times \left(e_f\right)^{1.5}} \qquad \text{Equation (4-30)}$$

Figure 4-12 illutrates that there exists a quadratic relationship between the unconfined compressive strength (q_u) and the modified after-curing void ratio:

$$q_u = A \times (M_e)^2 + B \times M_e + C \qquad \text{Equation (4-31)}$$

where A, B and C are constants.

The unconfined compressive strength is well correlated with the modified after-curing void ratio irrespective of the method calculating the after-curing void ratio. Therefore, the after-curing void ratio may also be another parameter used for the prediction of the unconfined compressive strength. Compared with the initial parameters of the soil-water-cement mixture, the application of the after-curing void ratio for the prediction of the unconfined compressive strength is more complex.

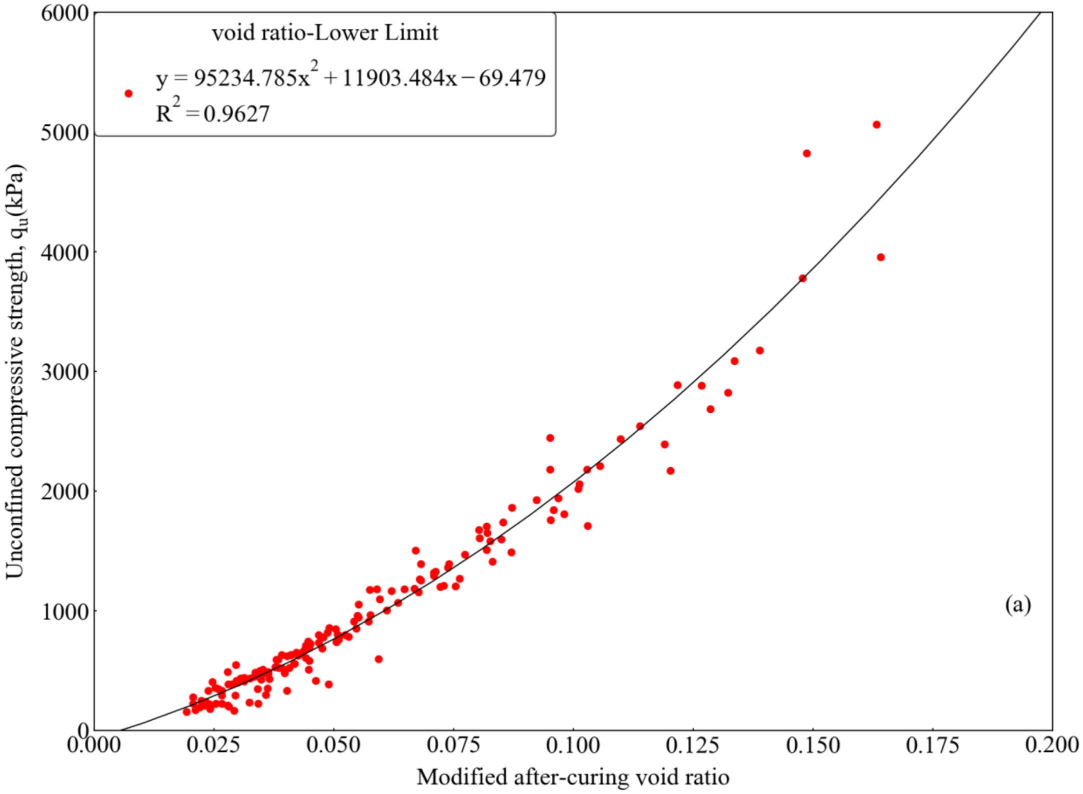

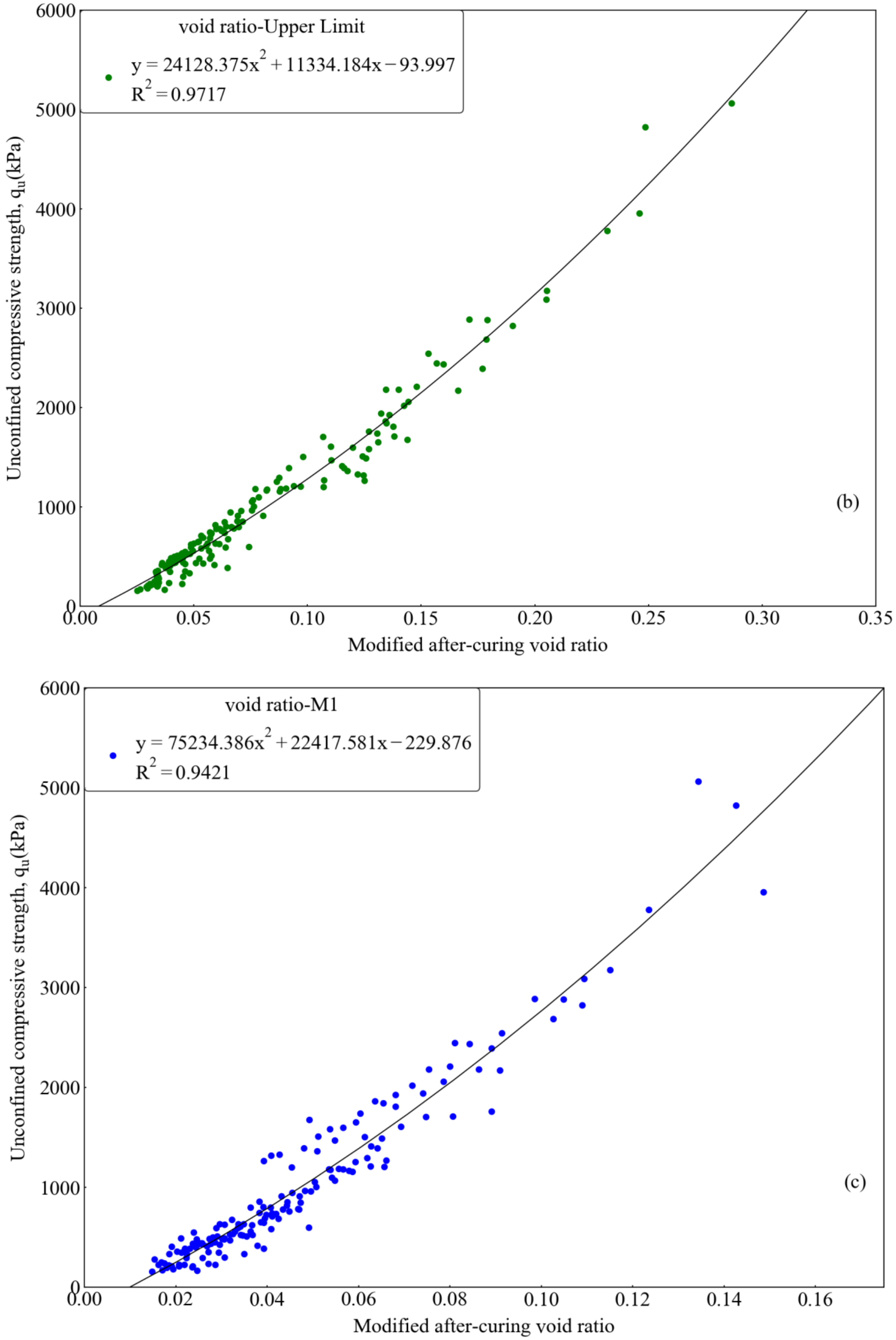

Figure 4-15 Variation of the unconfined compressive strength with the modified after-curing void ratio

4.8 Interaction of silt and cement on the unconfined compressive strength

Figure 4-16 demonstrates the variation of the unconfined compressive strength of the cement-admixed synthetic soils against the Spk-to-S325 proportions. The y-axis represents the unconfined compressive strength (q_u), while the x-axis represents the Spk-to-S325 proportions. The plot has four subplots, each of which has four types of symbols corresponding to specimens with the normalized water content of 1.1, 1.5, 2.0 and 2.5, respectively.

When the total soil-water to cement ratio is equal to 3 and 5, for specimens with a normalized water content of 1.1, the unconfined compressive strength increases significantly with Spk-to-S325 proportions as the S325 content is lower than 70% by weight. However, as S325 content continues increasing, the unconfined compressive strength slightly drops. On the other hand, when the total soil-water to cement ratio is 7 and 8, for specimens with a normalized water content of 1.1, the unconfined compressive strength increases with the Spk-to-S325 proportions as the S325 content is less than 80% by weight, which then keeps almost constant with the increase of the S325 content. This study summarizes three possible reasons for the drop of the unconfined compressive strength at high S325 content. The first possible reason may be the low water content. The synthetic soils with high S325 content have a relatively low liquid limit, and the lack of water can block the dispensing of ions, thus hindering the hydration and pozzolanic reactions. The redundant cement powder not reacting with water can be left in the cemented soil mass to fill soil voids (Bergado & Lorenzo, 2005). The second possible reason may be the air bubbles trapped in the soil-water-cement mixture. At a relatively low normalized water content, for example 1.1 and 1.5, the low consistency of the soil-water-cement mixture makes it hard to remove air bubbles through vibration. Therefore, the high void ratio leads to the strength decrease. The third possible reason may be the vibration experienced by the mold during the slurry filling procedure. The vibration and the mixing procedure by the electrical mixer may separate soil particles from the slurry-form binder, especially for samples with high S325 content. This separation between soil particles and binder can also lead to the strength decrease, but this condition usually happens when water content is relatively high, for example 2.0 and 2.5 times the liquid limit. This can be seen in Figure 4-16, in which the strength of samples with 2.0 normalized water content decreases slightly as the S325 content is higher than 80% by weight.

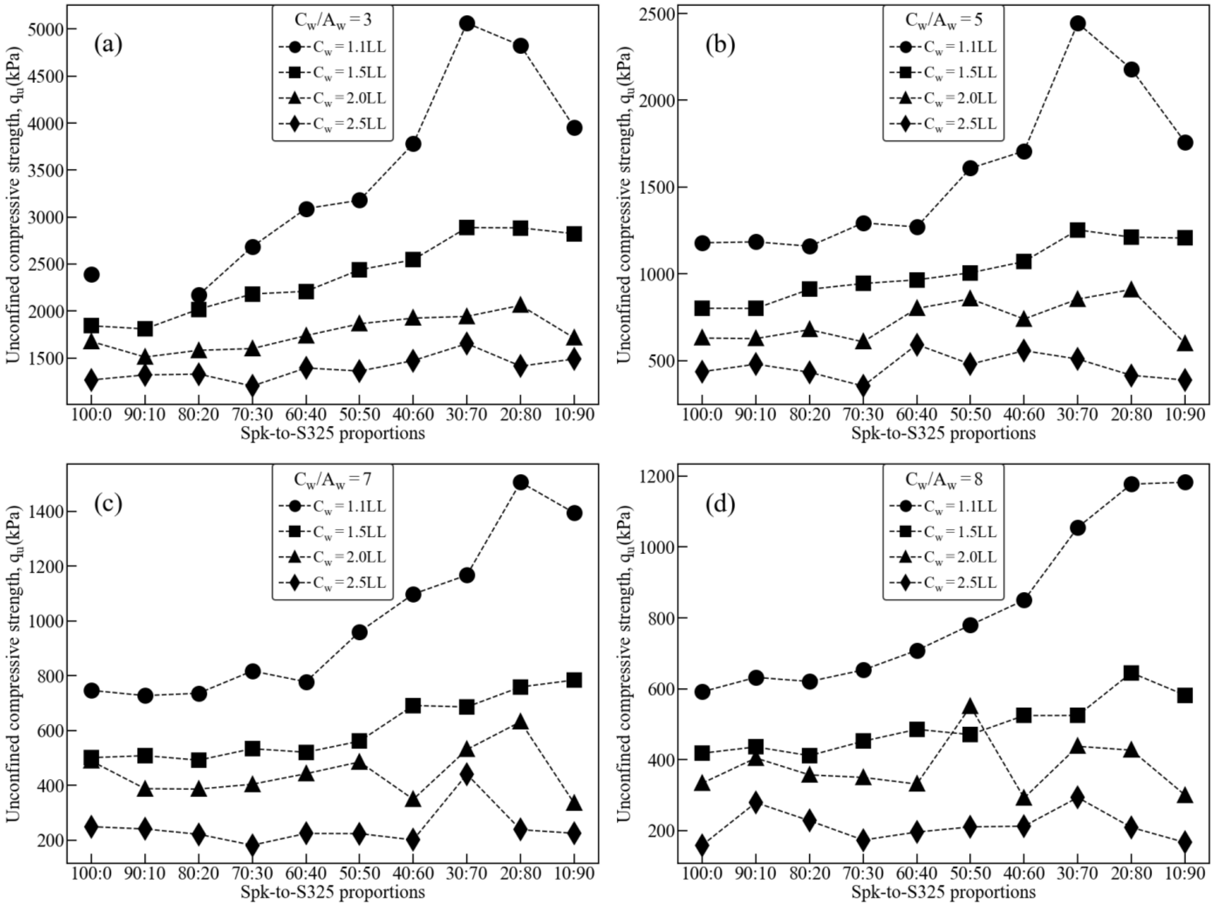

Figure 4-16 Variation of unconfined compressive strength with Spk-to-S325 proportions

For samples with a normalized water content of 1.5 in the four subplots, the strength increases smoothly with Spk-to-S325 proportions. A similar trend is also observed in samples with a normalized water content of 2.0, but the increase rate is clearly lower than that of samples with a normalized water content of 1.1 and 1.5. When the normalized water content is 2.5, the increase rate shown in the four subplots is subtle.

Previous studies showed the total soil-water to cement ratio ($\frac{C_w}{A_w}$) as the sole parameter governing the strength development of cement-treated soil (Horpibulsuk et al., 2003; Horpibulsuk & Miura, 2001; Miura et al., 2001). However, in this study, within the range of the total soil-water to cement ratio ($\frac{C_w}{A_w}$) being considered, the unconfined compressive strength (q_u) decreases with increasing total soil-water content. Zhang et al. (2013) proves that the total soil-water to cement ratio ($\frac{C_w}{A_w}$) as the sole parameter controlling the unconfined compressive strength is only applicable to some special cases.

The above discussion reveals that the unconfined compressive strength changes with the Spk-to-S325 proportions, indicating that the existence of silt in the synthetic soils can affect strength improvement. However, it is almost not possible to quantitatively analyze the strength variation with the silt content from Figure 4-16. Under this condition, this study proposes a new parameter referred to as unconfined compressive strength per unit cement content (U_c) to describe the interaction of the silt and cement.

$$U_c = \frac{q_u}{A_w} \qquad \text{Equation (4-32)}$$

where q_u represents the unconfined compressive strength, while A_w represents the cement content, only the nominator of cement content is used in this equation. From the perspective of simplicity, the unconfined compressive strength per unit cement content is hereinafter referred to as the strength per unit cement content.

The variation of the strength per unit cement content versus the silt-to-clay proportions is shown in Figure 4-17 (a-d). The four subplots correspond to specimens with total soil-water to cement ratios of 3, 5, 7 and 8, respectively. In each subplot, there are four types of symbols, each of which corresponds to specimens with normalized water contents of 1.1, 1.5, 2.0 and 2.5, respectively. The trends presented by the four types of symbols in each subplot show a similar phenomenon:

1. At the initial stage or low silt-to-clay proportion, the strength per unit cement content shows exponential growth. This zone is designated as the inactive zone.
2. As the silt content continues increasing, the incremental gradient of the strength per unit cement content keeps almost constant, indicating that the strength per unit cement content uniformly increases. This zone is designated as the active zone.
3. Beyond this active zone, the incremental gradient of the strength per unit cement content gradually decreases and eventually reaches zero. This zone is referred to as the inert zone or stabilized zone.

Fitting attempts indicate that the trends presented by the experimental data can be adequately described by a logistic curve with the following form:

$$U_c = \frac{a_1}{b_1 + c_1 \times e^{S_{s\text{-}c}}} + d_1 \qquad \text{Equation (4-33)}$$

where $S_{s\text{-}c}$ represents the silt-to-clay proportions; a_1, b_1, c_1 and d_1 are experimentally fitted values.

The table in Figure 4-17 shows the best fit using Equation (4-33), followed by the R-squared value. As shown in Figure 4-17, the scatter of the data points about the fitted curve is negligible at low normalized water content. However, at high normalized water content, especially when the total soil-water to cement ratio is 7 and 8, the scatter of data points about the fitted curve is high but acceptable.

For a certain silt-to-clay proportion, the strength per unit cement content decreases with increasing the normalized water content. The comparison of the vertical offset between any two adjacent regression curves shows that the offset enlarges as the normalized water content decreases, indicating that the positive influence of the cement on the strength improvement is gradually neutralized with the increase of the normalized water content. However, this phenomenon only exists before the strength per unit cement content reaches the inert zone. Immediately after reaching the inert zone, the strength per unit cement content keeps almost unchanged, indicating that the addition of more silt to the synthetic soil is a waste of material.

It is worth noting that the incremental gradient of the strength per unit cement content keeps increasing in the active zone and decreasing in the inert zone, indicating that there may be an inflection point, which is hereinafter referred to as the critical silt content.

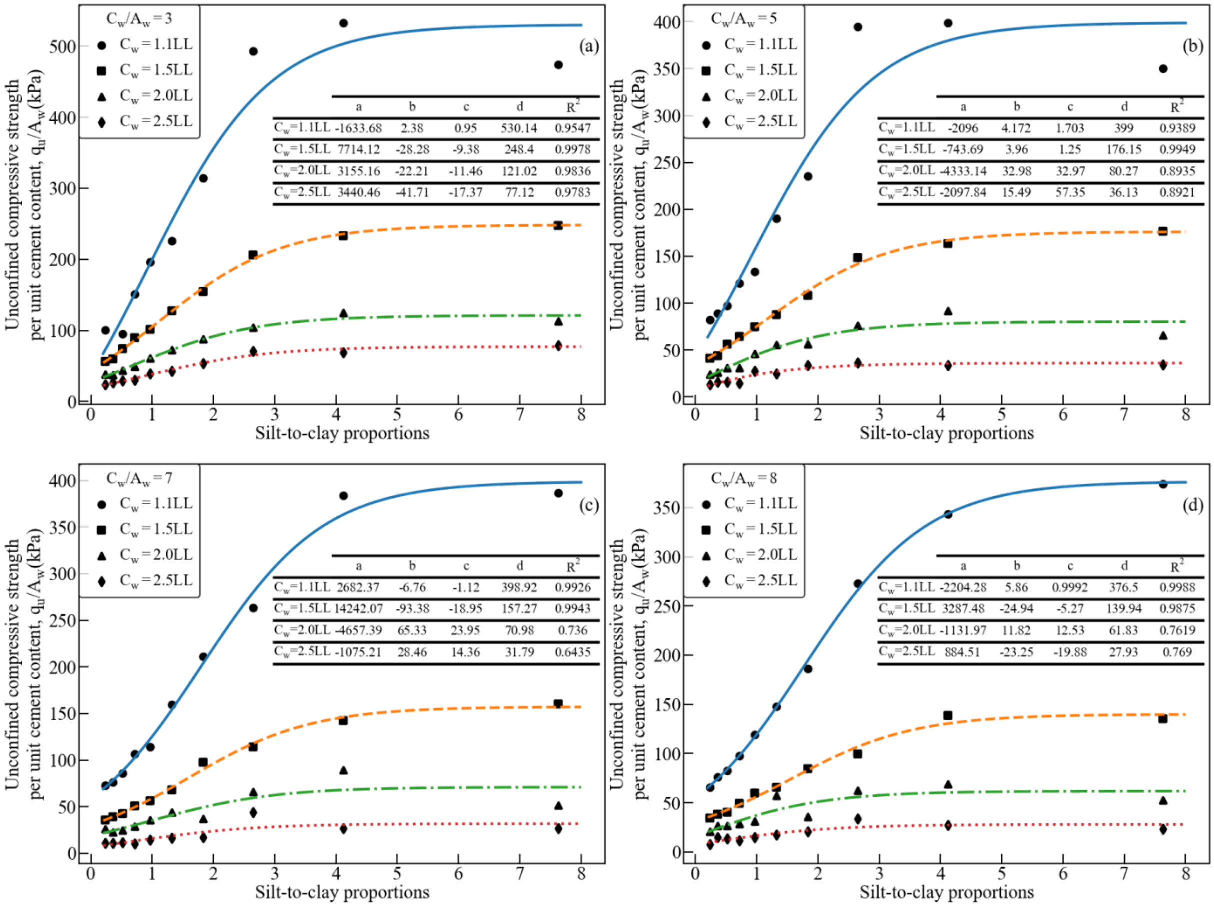

(a)

	a	b	c	d	R^2
C_w=1.1LL	-1633.68	2.38	0.95	530.14	0.9547
C_w=1.5LL	7714.12	-28.28	-9.38	248.4	0.9978
C_w=2.0LL	3155.16	-22.21	-11.46	121.02	0.9836
C_w=2.5LL	3440.46	-41.71	-17.37	77.12	0.9783

(b)

	a	b	c	d	R^2
C_w=1.1LL	-2096	4.172	1.703	399	0.9389
C_w=1.5LL	-743.69	3.96	1.25	176.15	0.9949
C_w=2.0LL	-4333.14	32.98	32.97	80.27	0.8935
C_w=2.5LL	-2097.84	15.49	57.35	36.13	0.8921

(c)

	a	b	c	d	R^2
C_w=1.1LL	2682.37	-6.76	-1.12	398.92	0.9926
C_w=1.5LL	14242.07	-93.38	-18.95	157.27	0.9943
C_w=2.0LL	-4657.39	65.33	23.95	70.98	0.736
C_w=2.5LL	-1075.21	28.46	14.36	31.79	0.6435

(d)

	a	b	c	d	R^2
C_w=1.1LL	-2204.28	5.86	0.9992	376.5	0.9988
C_w=1.5LL	3287.48	-24.94	-5.27	139.94	0.9875
C_w=2.0LL	-1131.97	11.82	12.53	61.83	0.7619
C_w=2.5LL	884.51	-23.25	-19.88	27.93	0.769

Figure 4-17 Unconfined compressive strength per unit cement content versus silt-to-clay proportions

The above analysis shows that the silt promotes the strength improvement of cement-admixed synthetic soils. It is evident that the determination of the critical silt content, if the cement-admixed synthetic soil has such silt content, would yield an optimum improvement in the engineering properties and a high efficiency of the cement. When the silt content is below the critical silt content, the incremental gradient of the strength per unit cement content keeps increasing. Beyond the critical silt content, the incremental gradient decreases. To get this critical silt content, it is essential to perform the quantitative analysis through the derivative of Equation (4-33):

$$\frac{\partial U_c}{\partial S_{s\text{-}c}} = -\frac{a_1 \times c_1 \times e^{S_{s\text{-}c}}}{(b_1 + c_1 \times e^{S_{s\text{-}c}})^2} \qquad \text{Equation (4-34)}$$

Figure 4-18 shows the incremental gradient of the strength per unit cement content against the silt-to-clay proportions. The table in each subplot shows the best fit using Equation (4-34), followed by the x- and y-coordinate of the critical silt content.

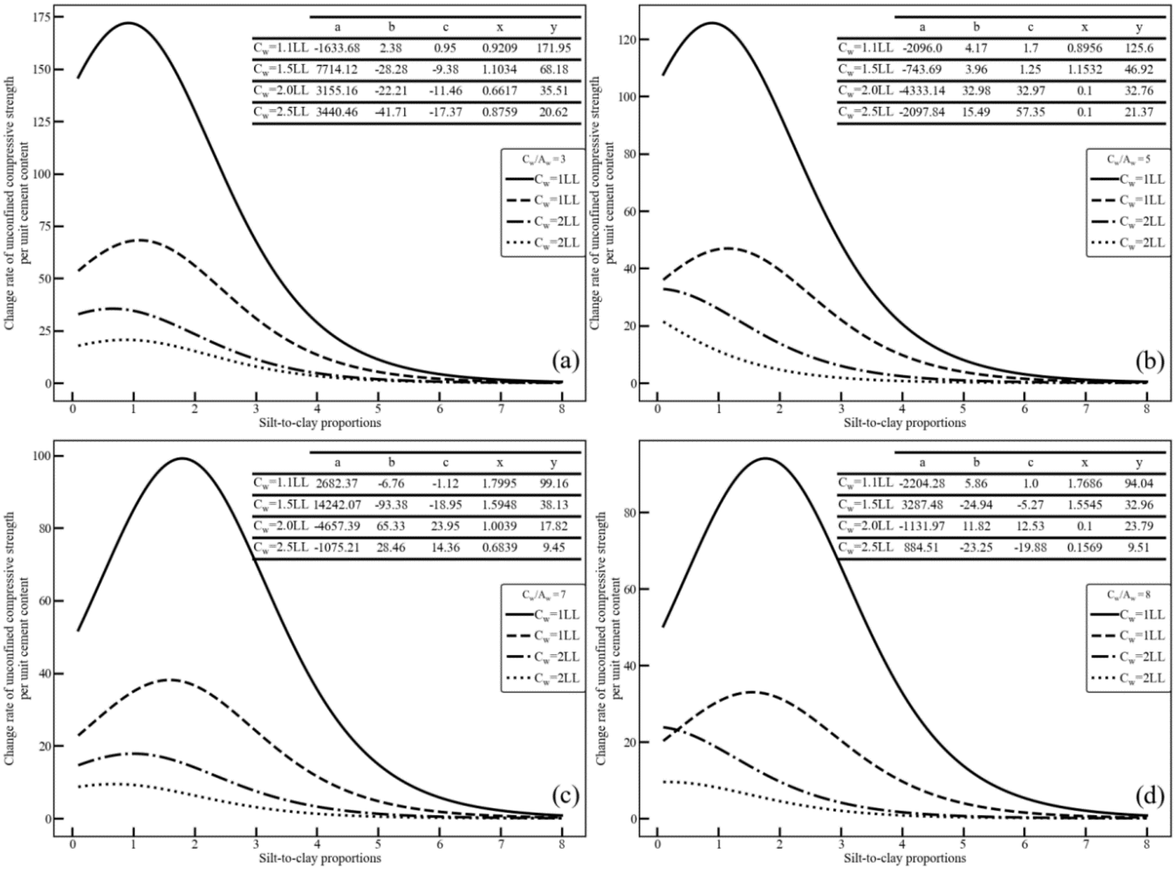

	a	b	c	x	y
C_w=1.1LL	-1633.68	2.38	0.95	0.9209	171.95
C_w=1.5LL	7714.12	-28.28	-9.38	1.1034	68.18
C_w=2.0LL	3155.16	-22.21	-11.46	0.6617	35.51
C_w=2.5LL	3440.46	-41.71	-17.37	0.8759	20.62

	a	b	c	x	y
C_w=1.1LL	-2096.0	4.17	1.7	0.8956	125.6
C_w=1.5LL	-743.69	3.96	1.25	1.1532	46.92
C_w=2.0LL	-4333.14	32.98	32.97	0.1	32.76
C_w=2.5LL	-2097.84	15.49	57.35	0.1	21.37

	a	b	c	x	y
C_w=1.1LL	2682.37	-6.76	-1.12	1.7995	99.16
C_w=1.5LL	14242.07	-93.38	-18.95	1.5948	38.13
C_w=2.0LL	-4657.39	65.33	23.95	1.0039	17.82
C_w=2.5LL	-1075.21	28.46	14.36	0.6839	9.45

	a	b	c	x	y
C_w=1.1LL	-2204.28	5.86	1.0	1.7686	94.04
C_w=1.5LL	3287.48	-24.94	-5.27	1.5545	32.96
C_w=2.0LL	-1131.97	11.82	12.53	0.1	23.79
C_w=2.5LL	884.51	-23.25	-19.88	0.1569	9.51

Figure 4-18 Change rate of unconfined compressive strength per unit cement content versus silt-to-clay proportions

It is evident that there exists the critical silt content at which the incremental gradient of the strength per unit cement content reaches the highest value. This kind of curve has been commonly seen in geotechnical engineering, such as the compaction curve and the variation of unconfined compressive strength of cement-admixed soil versus the normalized water content. Although the application of these curves is different, they have the same purpose, which is to find the extremum.

The critical silt content is more obvious at low normalized water contents such as 1.1 and 1.5. When the total soil-water to cement ratio is 3 and 5, the critical silt content at 1.1 times the liquid limit is about 0.9, but this value increases to 1.1 at 1.5 times the liquid limit. For 7 and 8 total soil-water to cement ratios, the critical silt content at 1.1 times the liquid limit is about 1.8, but this value decreases to 1.6 at 1.5 times the liquid limit. At a high normalized water content, such as 2.0 and 2.5, the critical silt content is around 1.0 when the total soil-water to cement ratio is 7, but the value decreases to 0.1 when the total soil-water to cement ratio is 8.

4.9 Effect of silt on the strength coefficient

The previous section describes the variation of the strength per unit of cement content with the silt-to-clay proportions. It is evident that the silt can increase the strength per unit cement content of cement-treated synthetic soils. This section attempts to answer the question: what is the effect of silt on the strength coefficient of cement-treated synthetic soils?

Tang, Miyazaki, and Tsuchida (2001) suggested that the relationship between the unconfined compressive strength and the cement content can be expressed as below when the water content remains constant:

$$q_u = k_f(C\text{-}C_0) \qquad \text{Equation (4-35)}$$

where k_f is the strength coefficient; C is the cement content defined as the weight of cement powder per unit volume of the treated soil, in $\frac{kg}{m^3}$; C_0 is the minimum cement content for strength mobilization.

Similarly, this study also reveals that there exists a linear relationship between the unconfined compressive strength and the cement content. Previous studies showed that the unconfined compressive strength increased almost linearly with the cement content in Zone II (the active zone) (Zhang, Santoso, Tan, & Phoon, 2013). Therefore, it can be concluded that the cement content being considered in this study may be in the active zone.

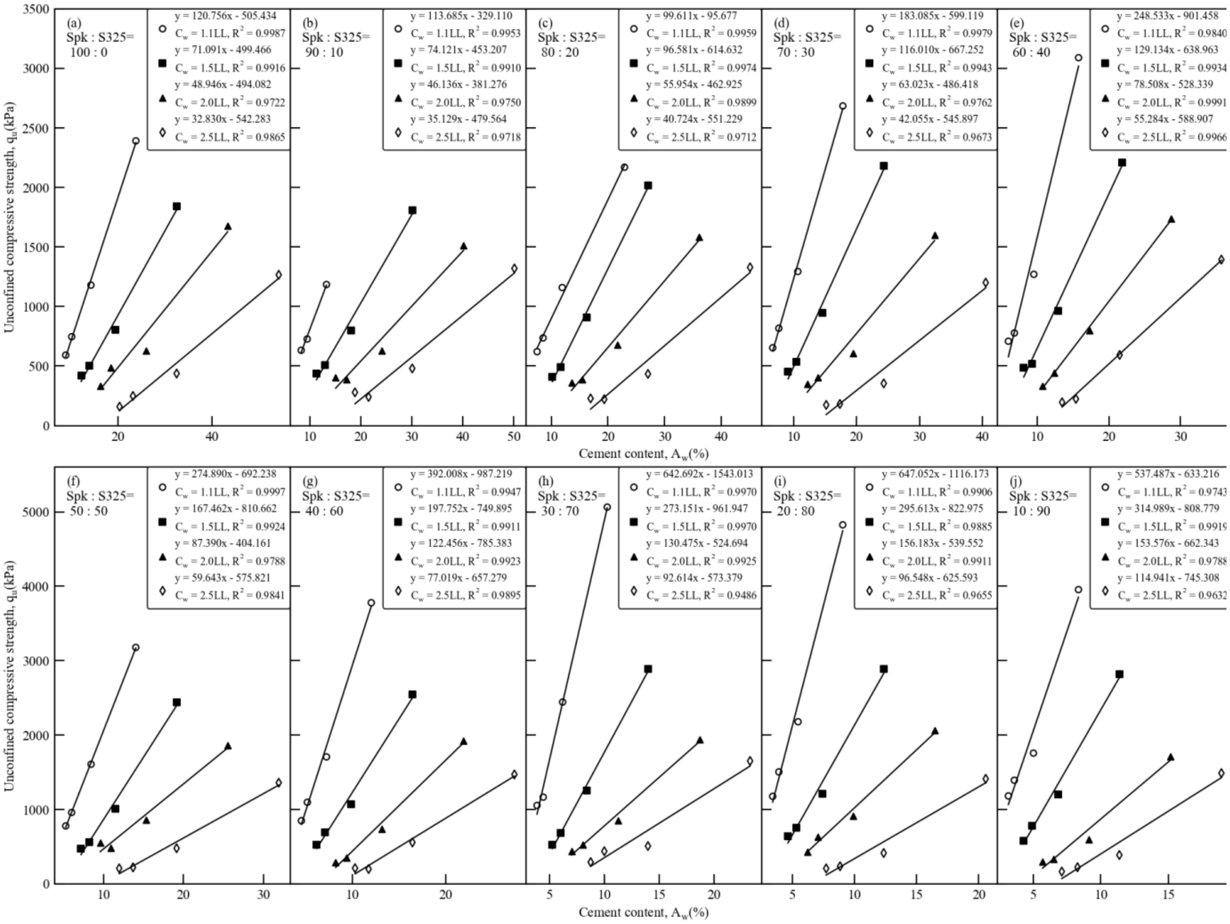

Figure 4-19 Unconfined compressive strength versus cement content

Figure 4-19 illustrates the unconfined compressive strength variation with the cement content. The plot has 10 subplots, each of which has four types of symbols corresponding to specimens with normalized water contents of 1.1, 1.5, 2.0 and 2.5, respectively. The symbols in the same subplot correspond to specimens from the same group, indicating that those specimens have the same synthetic soil.

As expected, at a certain normalized water content, the strength increases with cement content, coinciding with previous studies (Lorenzo & Bergado, 2004). This phenomenon is attributed mainly to the increase in the quantity of cementitious bonds formed during the hydration and pozzolanic reactions as cement content increases. Immediately after adding water to the cement, the hydration reaction starts and produces hydrated calcium silicates (C_2SH_x, $C_3S_2H_x$), hydrated calcium aluminates (C_3AH_x, C_4AH_x) and hydrated lime ($C_a(OH)_2$). These materials dissociating in the water and increasing the water PH value would react with silica and alumina from soil minerals. This process is known as a pozzolanic reaction. The gelatinous and amorphous materials created by the hydration and pozzolanic reaction form inter-aggregate and inter-particle bonds, enclose those un-bonded particles and aggregates and lead to higher soil strength, stiffness and brittleness (Kasama et al., 2000; Sasanian & Newson, 2014).

Through the comparison of the slope of the four linear regression lines in each subplot, it is evident that the magnitude of the strength coefficient decreases with increasing the total soil water content. For instance, when the Spk: S325 proportion is 100:0, the slopes of the four linear regression lines with normalized water contents of 1.1, 1.5, 2.0 and 2.5 are 120.756, 71.091, 48.946 and 32.830, respectively. Similar results can also be obtained from the other nine subplots. The decrease of the strength coefficient with the normalized water content can be attributed to the increase in distance between soil particles. During the hydration and pozzolanic reactions, water is consumed and transformed into pozzolanic products that eventually lead- to the formation of cementitious bonds between soil particles. However, high water content can result in loosely dispensed soil particles, leading to a reduction in the quantity of particle-to-particle contact surfaces, and indicating that more hydrates are needed to bond the soil particles together.

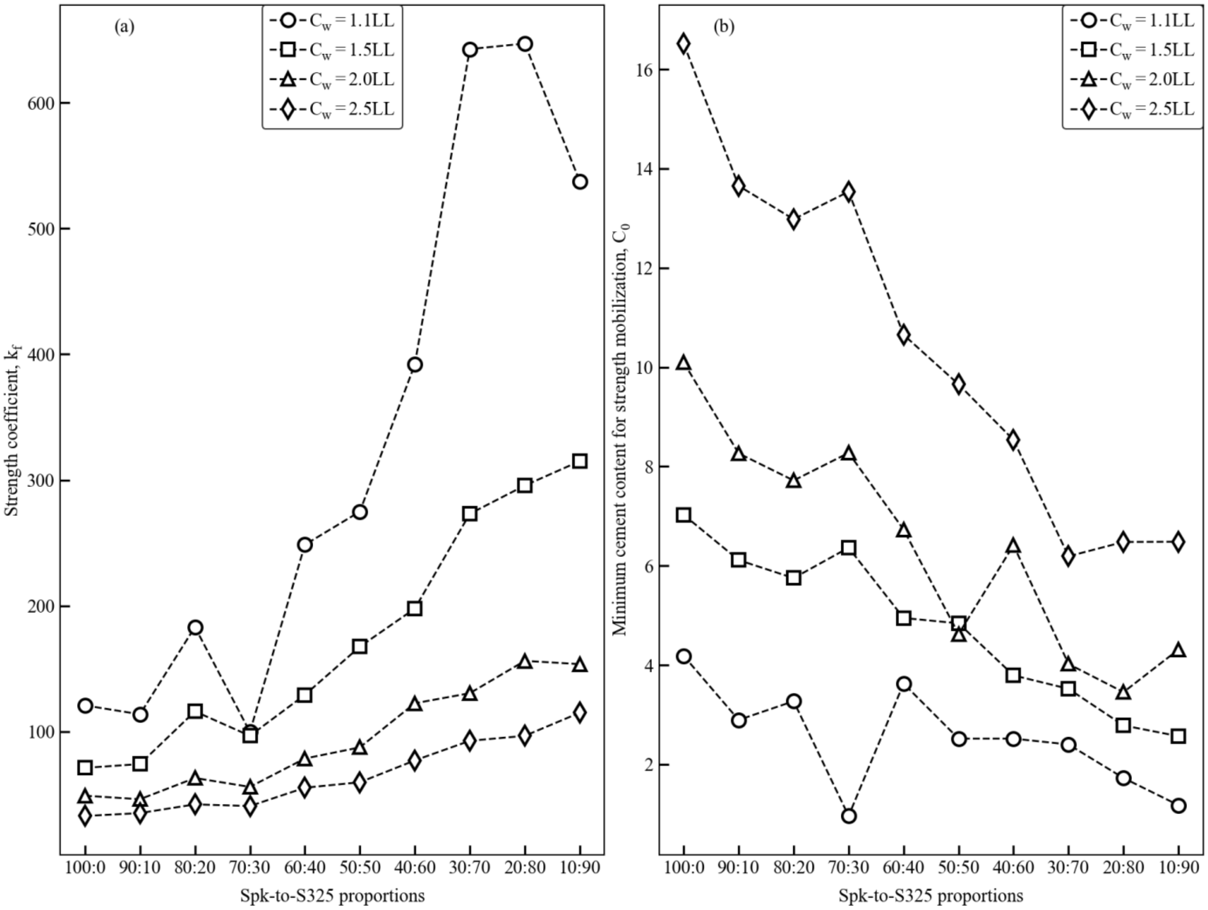

Figure 4-20 Variation of (a) strength coefficient and (b) minimum cement content for strength mobilization with the Spk-to-S325 proportions

Figure 4-20 shows the variation of the strength coefficient and the minimum cement content for strength mobilization with the Spk-to-S325 proportions. For a certain normalized water content, the strength coefficient takes on an ascending trend while the minimum cement content for strength mobilization takes on a descending trend with the Spk-to-S325 proportions. The incremental gradient of the strength coefficient clearly drops down with the increase of the normalized water content. For a certain Spk-to-S325 proportion, the strength coefficient decreases while the minimum cement content for strength mobilization increases with the normalized water content, indicating that the increase of water content has a negative effect on the strength development of cement-treated soil.

The four types of symbols in Figure 4-20(a) show a similar phenomenon that can be classified into three zones: when the S325 content is lower than 30% by weight, the strength coefficient gradually increases. But the incremental gradient of the strength coefficient is too small to be noticed. This zone is designated as the inactive zone. For the S325 content ranging from 30% to 70% by weight, the strength coefficient increases significantly and implies that the physicochemical reactions in the soil-water-cement mixture are quite active. This zone is referred to as the active zone. Beyond this zone, the strength coefficient does not make any significant further improvement. In contrast, the strength coefficient slightly drops for specimens with a normalized water content of 1.1. This zone is designated as the inert zone. The observation explicitly demonstrates that the silt can change the strength coefficient.

The minimum cement content for strength mobilization shown in Figure 4-20(b) almost decreases linearly with the Spk-to-S325 proportions although the data is a bit scattered. It is evident that the magnitude of the incremental gradient increases with the increase of the total soil water content. Moreover, with the increase of the S325 content, the difference of the minimum cement content for strength mobilization between any two different normalized water contents becomes smaller. The observation implies: 1) samples treated with high-water content need more cement for strength mobilization; 2) the increase of silt content can obviously offset the negative effect of water content on minimum cement content for strength mobilization.

By choosing the silt-to-clay proportions as the x-axis, the variation of the strength coefficient and the minimum cement content for strength mobilization is shown in Figure 4-21. In the plot, there are two subplots, each of which has four types of symbols corresponding to specimens with normalized water content of 1.1, 1.5, 2.0 and 2.5, respectively.

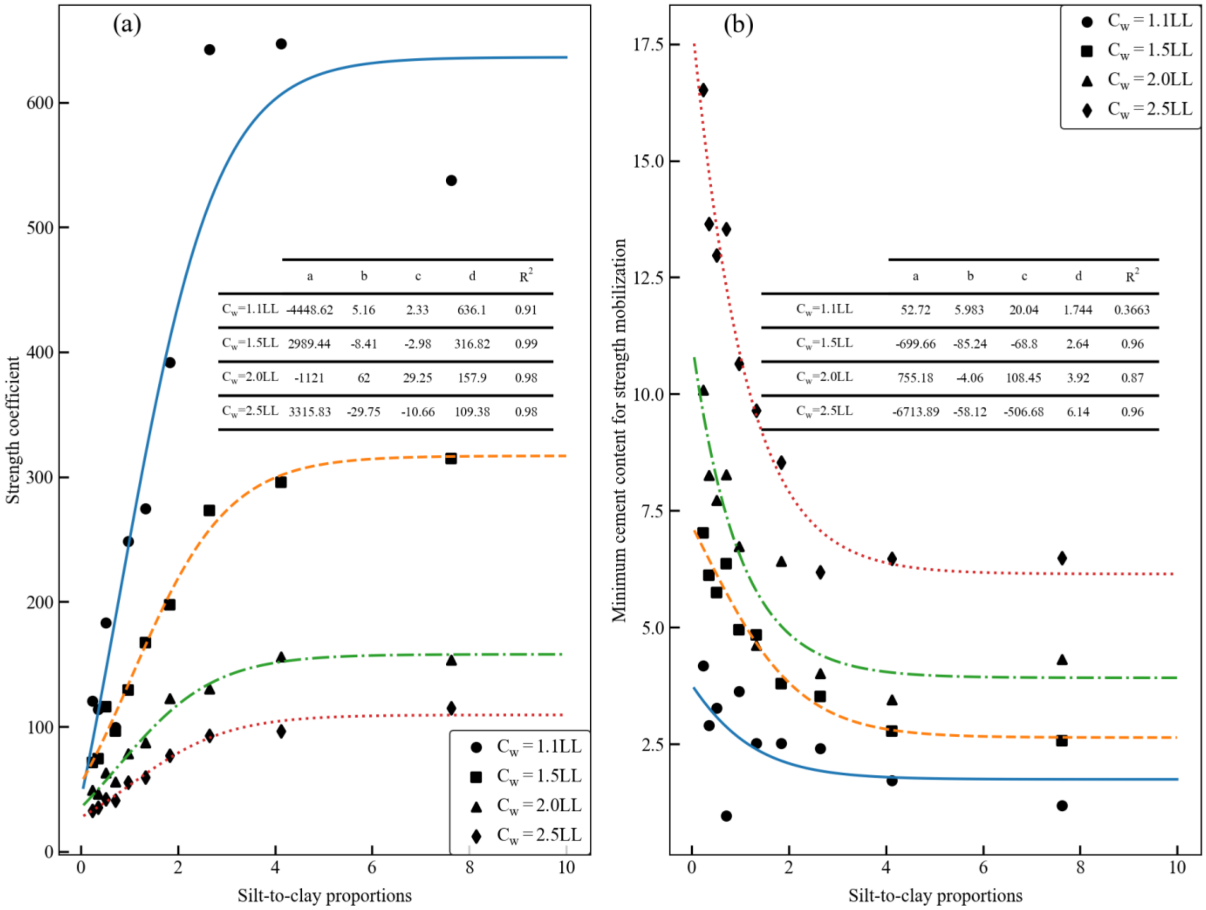

	a	b	c	d	R^2
C_w=1.1LL	-4448.62	5.16	2.33	636.1	0.91
C_w=1.5LL	2989.44	-8.41	-2.98	316.82	0.99
C_w=2.0LL	-1121	62	29.25	157.9	0.98
C_w=2.5LL	3315.83	-29.75	-10.66	109.38	0.98

	a	b	c	d	R^2
C_w=1.1LL	52.72	5.983	20.04	1.744	0.3663
C_w=1.5LL	-699.66	-85.24	-68.8	2.64	0.96
C_w=2.0LL	755.18	-4.06	108.45	3.92	0.87
C_w=2.5LL	-6713.89	-58.12	-506.68	6.14	0.96

Figure 4-21 Variation of (a) strength coefficient and (b) minimum cement content with silt-to-clay proportions

The four types of symbols in Figure 4-21(a) show a similar trend: the dependent variable first increases and then keeps almost unchanged with the independent variable (silt-to-clay proportions). A fitting attempt shows that the trend of the experimental data in Figure 4-21(a) is adequately expressed by the logistic relationship with a high degree of correlation (R^2>= 0.91):

$$k_f = \frac{a_2}{b_2 + c_2 \times e^{S_{s\text{-}c}}} + d_2 \qquad \text{Equation (4-36)}$$

where $S_{s\text{-}c}$ represents the silt-to-clay proportions; a_2, b_2, c_2 and d_2 are experimentally fitted values. The table in Figure 4-21(a) shows the best fit using Equation (4-36), followed by the R-squared value. For a certain silt-to-clay proportion, the strength coefficient increases with the decrease of the normalized water content, coinciding well with the observation from Figure 4-20.

The plot of the minimum cement content for strength mobilization against the silt-to-clay proportions is shown in Figure 4-21(b) even though the data scatter is quite high, especially when the normalized water content is 1.1. A fitting attempt shows that the trend of the experimental data can be adequately expressed by the logistic relationship of the form:

$$C_0 = \frac{a_3}{b_3 + c_3 \times e^{S_{s\text{-}c}}} + d_3 \qquad \text{Equation (4-37)}$$

where $S_{s\text{-}c}$ represents the silt-to-clay proportions; a_3, b_3, c_3 and d_3 are experimentally fitted values. The table in Figure 4-21(b) shows the best fit using Equation (4-37), followed by the R-squared value.

In contrast to the observations from Figure 4-21(a), the minimum cement content for strength mobilization decreases with the S325 content when the silt-to-clay proportion is below a certain limit. Beyond the limit, the minimum cement content for strength mobilization remains almost constant. For a certain silt-to-clay proportion, the minimum cement content for strength mobilization increases with the normalized water content. This observation once again proves that more cement is needed to mobilize the soil strength at high water content. From this perspective, it is evident that the existence of the silt can mobilize the strength of cement-treated soil at relatively low cement content.

Based on the analysis of the logistic regressions shown in Figure 4-21, the variation of the strength coefficient and minimum cement content for strength mobilization can be expressed as below:

$$\begin{cases} \dfrac{\partial k_f}{\partial S_{s\text{-}c}} = \dfrac{\partial^2 q_u}{\partial A_w \times \partial S_{s\text{-}c}} = -\dfrac{a_4 \times c_4 \times e^{S_{s\text{-}c}}}{(b_4 + c_4 \times e^{S_{s\text{-}c}})^2} \\ \dfrac{\partial A_w^m}{\partial S_{s\text{-}c}} = -\dfrac{a_5 \times c_5 \times e^{S_{s\text{-}c}}}{(b_5 + c_5 \times e^{S_{s\text{-}c}})^2} \end{cases} \qquad \text{Equation (4-38)}$$

Figure 4-22(a) shows the variation of the change rate of the strength coefficient with the silt-to-clay proportions. It is evident that there exists an extreme point. Before reaching the extreme point, the change rate of the strength coefficient monotonically increases with the silt content. Beyond the extreme point, the change rate drops sharply and eventually decreases to almost zero. The table in Figure 4-22(a) shows the best fit using Equation (4-38), followed by the x-coordinate, which is the silt-to-clay proportion at which the change rate reaches the highest value, and the y-coordinate, which is the extreme value of the change rate of the strength coefficient. When the silt-to-clay proportion ranges from 0.7 to 1.1, the change rate reaches the highest value.

Figure 4-22(b) shows the change rate of the minimum cement content for strength mobilization against the silt-to-clay proportions. The change rate of minimum cement content for strength mobilization increases with the silt-to-clay proportions. The table in this subplot shows the best fit using Equation (4-38), followed by the x- and y-coordinate of the point at which the change rate is considered to be zero. Figure 4-22(b) indicates that the addition of silt can absolutely improve the productivity of the cement. However, too much silt could be a waste of material.

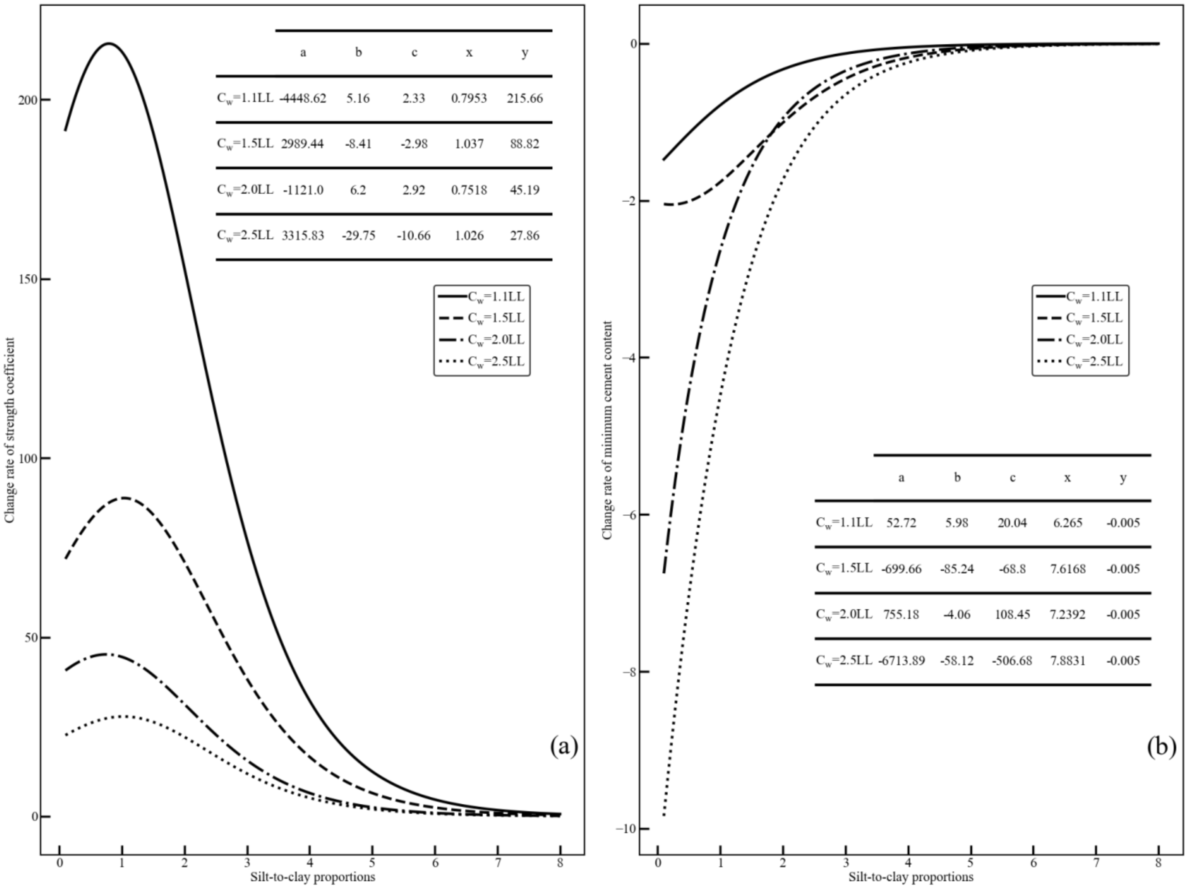

	a	b	c	x	y
C_w=1.1LL	-4448.62	5.16	2.33	0.7953	215.66
C_w=1.5LL	2989.44	-8.41	-2.98	1.037	88.82
C_w=2.0LL	-1121.0	6.2	2.92	0.7518	45.19
C_w=2.5LL	3315.83	-29.75	-10.66	1.026	27.86

	a	b	c	x	y
C_w=1.1LL	52.72	5.98	20.04	6.265	-0.005
C_w=1.5LL	-699.66	-85.24	-68.8	7.6168	-0.005
C_w=2.0LL	755.18	-4.06	108.45	7.2392	-0.005
C_w=2.5LL	-6713.89	-58.12	-506.68	7.8831	-0.005

Figure 4-22 Variation of (a) strength coefficient and (b) minimum cement content for strength mobilization with silt-to-clay proportions

4.10 Review of the water/cement ratio on unconfined compressive strength

Many factors such as cement, water, curing time and soil type can contribute to the strength development of cement-mixed soil (Kitazume & Terashi, 2013). Numerous studies have been performed to establish the relationship between the quantities of the reactants and the unconfined compressive strength. However, due to the complexity of soil characteristics, no general formula is available for the prediction of the unconfined compressive strength.

The experimental results presented in this study have indicated the dependence of the strength on the water content, cement content and silt content. The strength increases with the cement content but decreases with the water content. The addition of silt to the synthetic soils can evidently strengthen the cement-treated soils.

Through the analysis of the experimental results, it is evident that the commonly adopted parameter, the total soil-water to cement ratio, is not the prime factor controlling the strength development of cement-treated soils. In this background, the strength development is analyzed using a new parameter referred to as the improved water-cement ratio (I_c^w) to predict the unconfined compressive strength of cement-admixed synthetic soils.

$$I_c^w = \frac{{C_w}^{2.5}}{{A_w}^{1.5}} \qquad \text{Equation (4-39)}$$

The logistic function of the following form is used to convert the improved water-cement ratio to the combined water-cement ratio (C_c^w), which is also a new parameter proposed in this study.

$$C_c^w = \frac{1}{I_c^w}\left[2+(I_c^w\text{-}1)\cdot e^{-I_c^w}\right] \qquad \text{Equation (4-40)}$$

Figure 4-23 illustrates the variation of the unconfined compressive strength of the 10 groups of cement-admixed synthetic soils against the combined water-cement ratio. The water content varies from 1.1 to 2.5 times the liquid limit, and the total soil-water to cement ratio varies from 3 to 8. The S325 content varies from 0 to 90% by weight. The linear function of the following form is used to predict the strength development of cement-treated synthetic soils.

$$q_u = A\cdot C_c^w + B \qquad \text{Equation (4-41)}$$

where q_u is unconfined compressive strength; A and B are empirical constants.

It is evident that the scatter of the data points about the fitted linear regression line is quite considerable. This phenomenon is unlikely to be induced by the experimental procedure because the parameters such as water content, cement content, etc. are closely controlled during the process of sample preparation. Moreover, the analysis in the previous sections shows a high correlation between the unconfined compressive strength and the corresponding parameters, indicating that the scatter of the data points may not be induced by the experimental procedure.

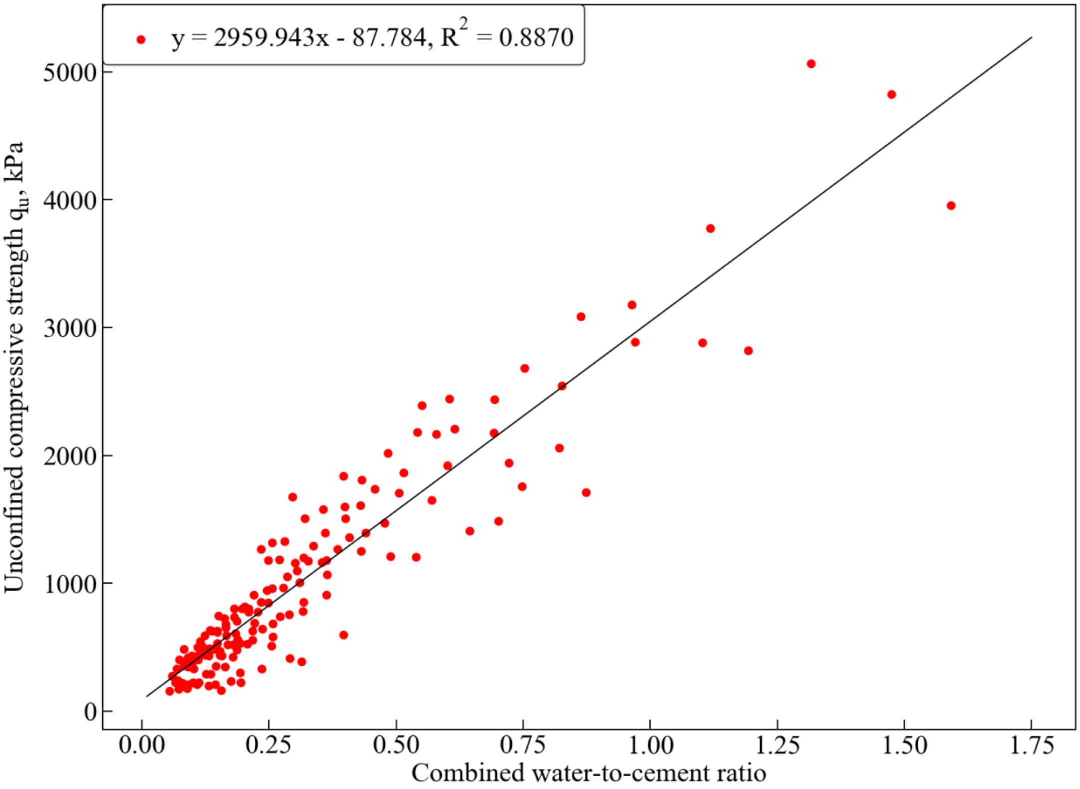

Figure 4-23 Unconfined compressive strength versus combined water-to-cement ratio

To find the possible reason leading to the weak relationship, the data are plotted separately based on the soil type, as shown in Figure 4-24. There are 10 subplots which correspond to specimens with 100:0, 90:10, 80:20, 70:30, 60:40, 50:50, 40:60, 30:70, 20:80 and 10:90 Spk-to-S325 proportions, respectively. It is evident that for a given synthetic soil, the unconfined compressive strength of the cement-treated soil increases linearly with the combined water-to-cement ratio.

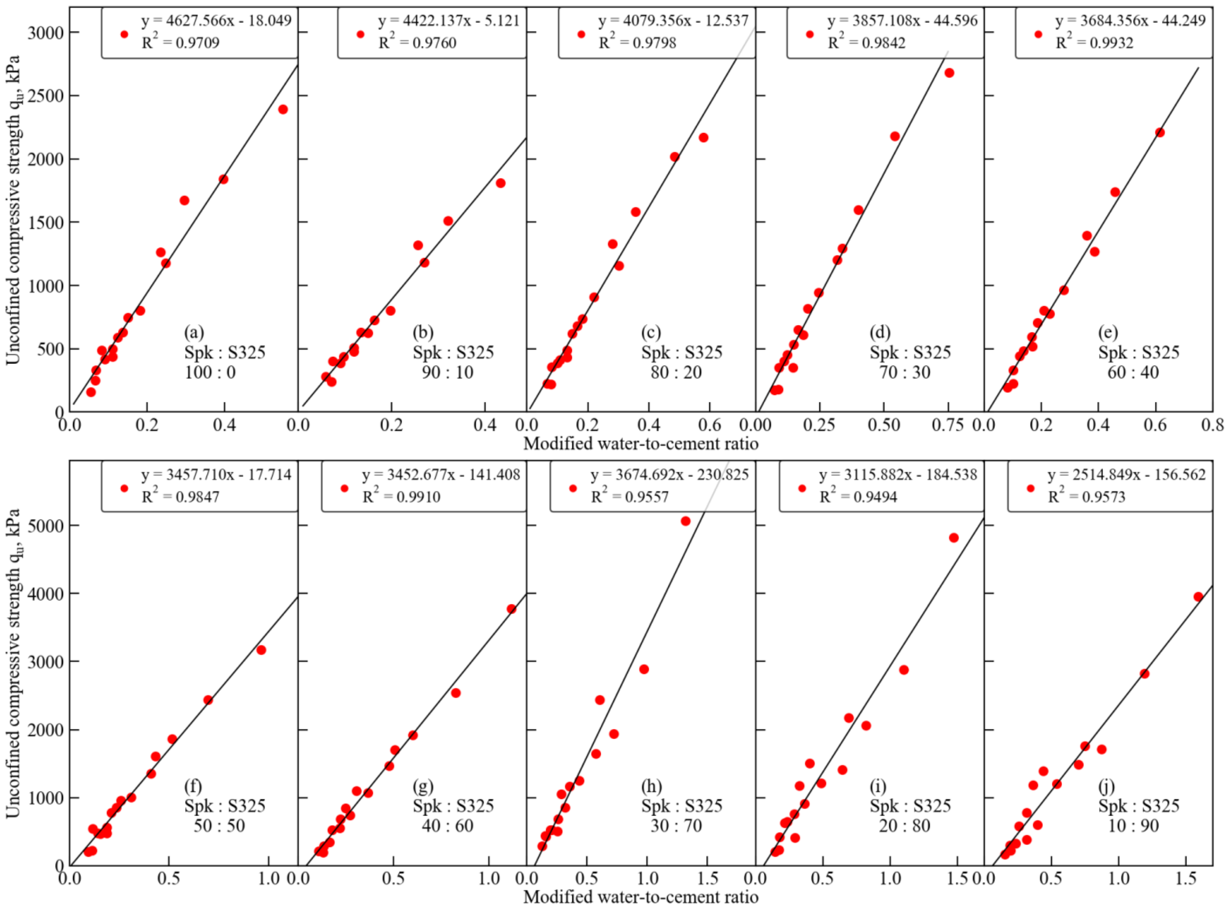

Figure 4-24 Unconfined compressive strength versus combined water-to-cement ratio based on soil type

As shown in Figure 4-24, the unconfined compressive strength increases linearly with the combined water-cement ratio. The rate of increase, which is the slope of the linear regression line, decreases with the Spk-to-S325 proportions. For each subplot, there are 16 red dots corresponding to 16 specimens that are made with different total soil water content and cement content. The high value of the coefficient of determination shown in the 10 subplots indicates that soil type should be the major reason leading to the data points scatter shown in Figure 4-23.

4.11 Young's modulus and Poisson's ratio of the synthetic soils

Young's modulus, also known as the modulus of elasticity, plays an important role in engineering projects. A few methods are available for the determination of this parameter, such as tangent modulus, average slope of the straight-line proportion and so on. Santi, Holschen, and Stephenson (2000) summarize the available methods and the corresponding definition, as shown in Figure 4-25. Young's modulus is equal to the slope between points A and B.

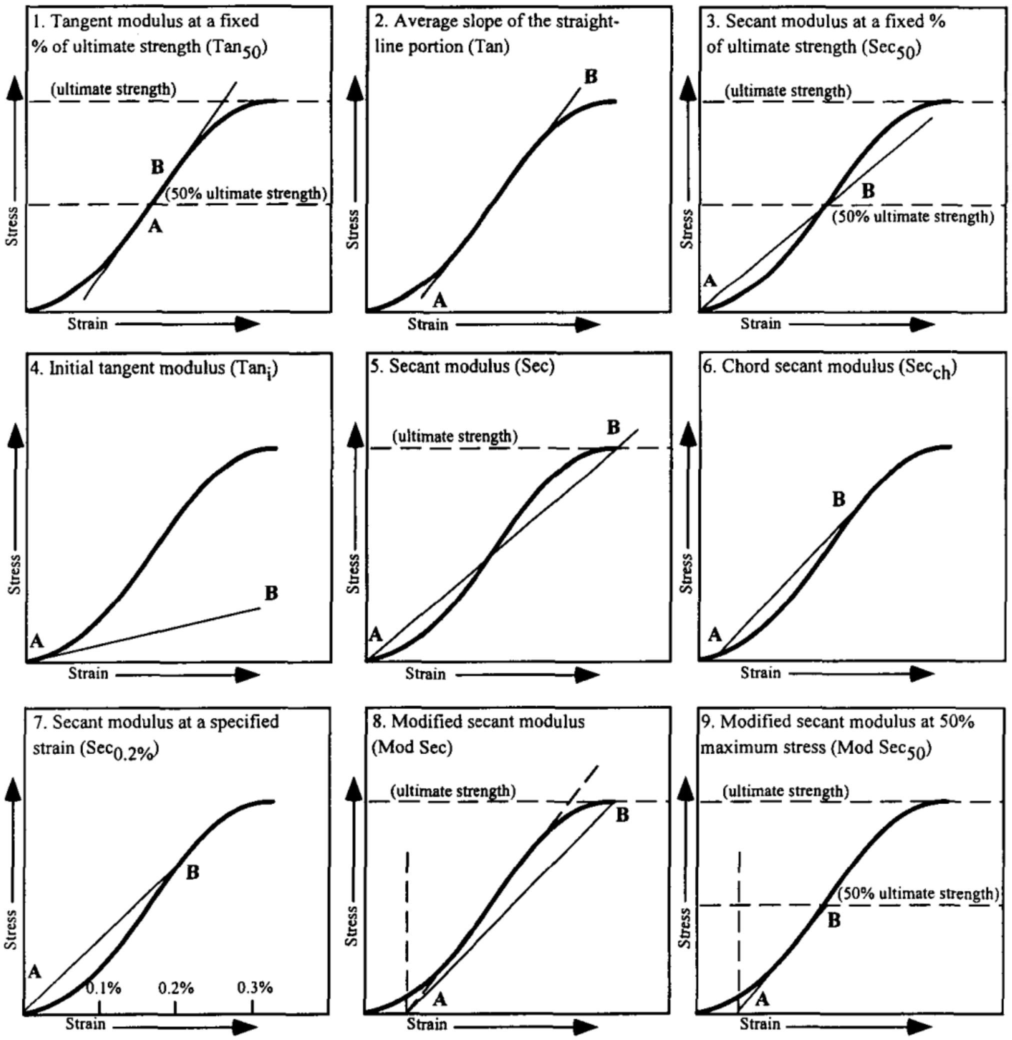

Figure 4-25 Different methods for the determination of the modulus of elasticity (Santi et al., 2000)

In this study, Young's modulus is calculated based on the average slope of the straight-line proportion. As in the discussion of the specimen preparation, the axial displacement and the radial displacement are recorded during the unconfined compression tests. These values are then used to obtain Young's modulus and Poisson's ratio of the synthetic soils.

Figure 4-26 demonstrates the relationship between the unconfined compressive strength and Young's modulus of the synthetic soils. There seems to be a linear relationship between the unconfined compressive strength and the Young's modulus. When the unconfined compressive strength is relatively low, the scatter of the data points is not so obvious. However, when the unconfined compressive strength is higher than 1000 kPa, it seems that the scatter of the data points is obvious. The major reason for this phenomenon is that the specimens with low unconfined compressive strength are made with high water content or low cement content, and therefore the stress-strain curve is always very smooth. However, for these specimens with high unconfined compressive strength, the soil-water-cement mixture is made with low water content or high cement content, and therefore the stress-strain curve is quite steep and very sensitive to the external factors.

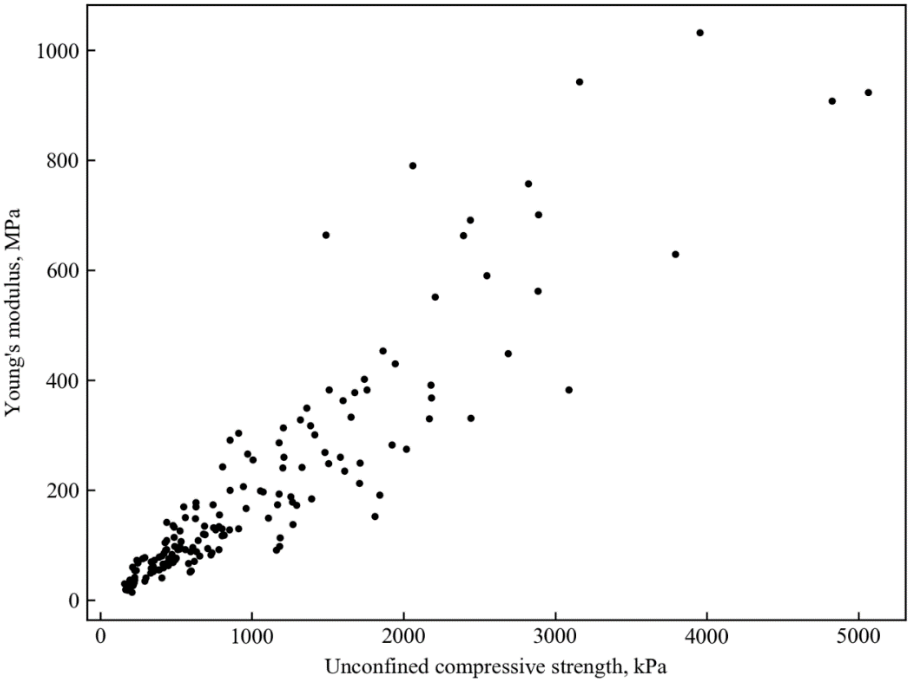

Figure 4-26 Relationship between Young's modulus and unconfined compressive strength of the synthetic soils

Figure 4-27 demonstrates the variation of the Poisson's ratio with the unconfined compressive strength. The overall trend shows that the Poisson's ratio decreases with the increase of the unconfined compressive strength. Poisson's ratio of most of the specimens is around 0.05, which is relatively low. The low value of the Poisson's ratio indicates that the synthetic Clearwater shale is a quite brittle material. The experimental results of the Clearwater shale also illustrate the same. However, the strain at which the strength reaches the highest value for the Clearwater shale is higher than that of the synthetic Clearwater shale.

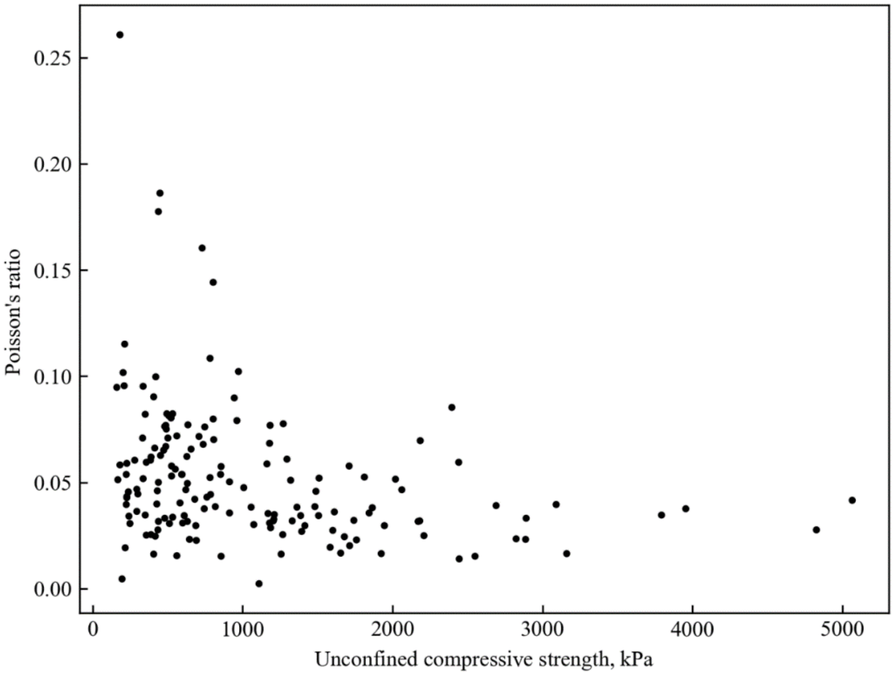

Figure 4-27 Relationship between Poisson's ratio and unconfined compressive strength of the synthetic soils

4.12 Selection of the formula for the synthetic Clearwater shales

Experimental programs conducted on in situ Clearwater clay shale specimens used a total of 24 samples extracted from 30 m and 380 m depth to investigate the unconfined compressive strength of the Clearwater shale. As shown in Figure 4-28, the average UCS of these samples extracted from 30 m depth is about 1292 kPa, while that from 380 m depth is about 1276 kPa. The overall average unconfined compressive shear strength is about 1284 kPa.

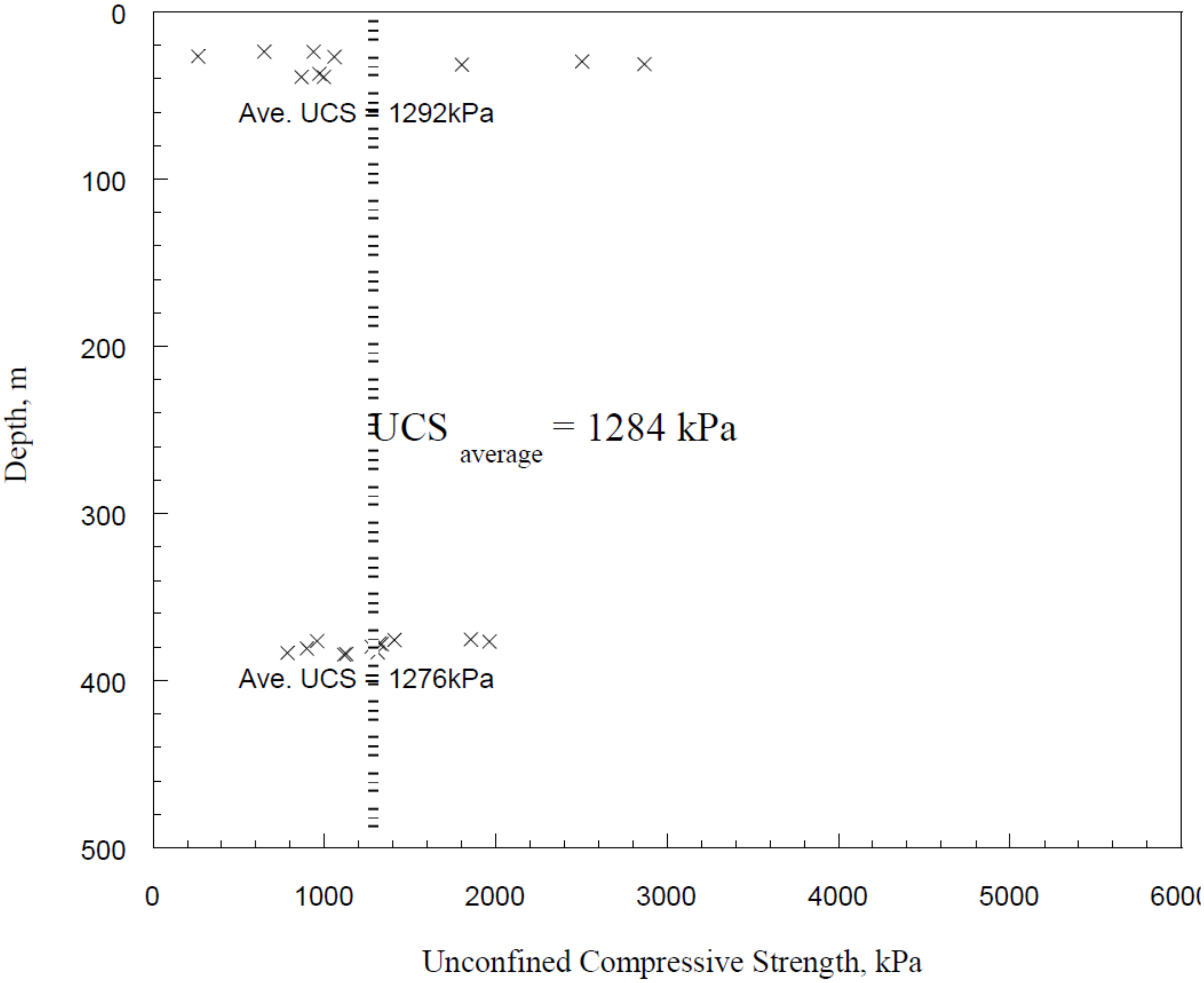

Figure 4-28 The unconfined compressive strength of the Clearwater shales (Wong, 2007)

For the experimental plan described in this chapter, there are 160 formulas in total. Under this condition, a criterion is needed for the selection of the formula for the synthetic Clearwater shale. Tavenas et al. (1973) used the unconfined compressive strength as the criterion because the test is relatively easy, and the undrained shear behaviour played an important role in the project. In this study, the unconfined compressive strength was also selected as the criterion, not only because of the simplicity but also because the uplifting velocity could induce the partially drained or fully undrained condition.

Table 4-4 Possible formulas for the synthetic Clearwater shale

Formula	Axial stress, kPa	Young’s modulus, MPa	Poisson’s ratio
F1,14	1266.34	178.87	0.0255
F1,21-2	1179.17	286.58	0.0684
F2,14	1318.95	328.34	0.0511
F2,21	1184.53	113.86	0.0289
F3,14	1328.86	241.80	0.0320
F3,21	1159.18	90.98	0.0588
F4,14	1201.19	240.57	0.0320
F4,21-2	1295.23	172.95	0.0610
F5,14	1384.15	317.22	0.0345
F5,21	1268.04	138.19	0.0776
F6,14	1360.30	349.48	0.0386
F6,22-2	1007.53	255.34	0.0476
F7,14	1479.93	269.14	0.0386
F7,22-2	1071.54	196.66	0.0303
F7,31	1107.58	149.85	0.00257
F8,22	1254.73	188.46	0.0164
F8,31	1169.14	173.82	0.0354
F8,41	1054.05	199.35	0.0385
F9,14-2	1413.12	300.89	0.0297
F9,22	1211.19	260.41	0.0349
F9,41-2	1177.37	193.51	0.0310
F10,14-2	1488.96	664.02	0.0460
F10,22	1206.29	313.38	0.0329
F10,31	1393.78	184.61	0.0270
F10,41-2	1182.68	98.39	0.0770
F10,22	1206.29	313.38	0.0329
F10,31	1393.78	184.61	0.0270
F10,41-2	1182.68	98.39	0.0770

It is worth noting that the selection of the formula for the synthetic Clearwater shales should follow the rules below:

1. The total soil-water content of the soil-water-cement mixture should not be less than 1.5 times the liquid limit. After completing the mixing procedure, the soil-water-cement mixture should

be transferred to the PSB by hand. If the water content of the mixture is too low, the low consistency makes it hard for the mixture to flow smoothly, thus entrapping air bubbles in the sample.

2. The unconfined compressive strength, Young's modulus and Poisson's ratio of the synthetic Clearwater shales should be as close to those of the Clearwater shale as possible.

The average strength of the Clearwater shale is about 1284 kPa. Therefore, those formulas with strength ranges from 1000 kPa to 1500 kPa are shown in Table 4-4. Based on the rules that should be followed, it is obvious that only a few formulas are left.

In this study, formula F7,14 is the primary choice as the most suitable formula for synthetic soils because of three reasons: 1) the strength of the synthetic Clearwater shale, 1479.93 kPa, is very close to that of the Clearwater shale; 2) the particle size distribution of the synthetic soil is within the range of the particle size distribution of the Clearwater shale; 3) the total soil-water content of the formula is 2.5 times the liquid limit. Under this condition, it is quite easy to transfer the slurry to the PSB; 4) the Young's modulus of the Clearwater shale ranges from a few hundred kPa to over 1 GPa. The Young's modulus of the formula is 269.14 MPa and locates within that range.

4.13 Properties of the synthetic Clearwater shale

As discussed in the previous section, a suitable formula for the synthetic Clearwater shale is selected from 160 formulas. To make a comparison of the mechanical properties between the synthetic Clearwater shale and the real Clearwater shale, a series of triaxial tests and Brazilian tests are performed.

Three undrained triaxial tests are performed at different effective confining stresses at 200 kPa, 500 kPa, and 1000 kPa. Three drained triaxial tests are also conducted at 200 kPa, 500 kPa and

1000 kPa effective confining stresses. During the consolidation stage, the specimen is allowed to reach equilibrium in a drained state at the corresponding effective consolidation pressure.

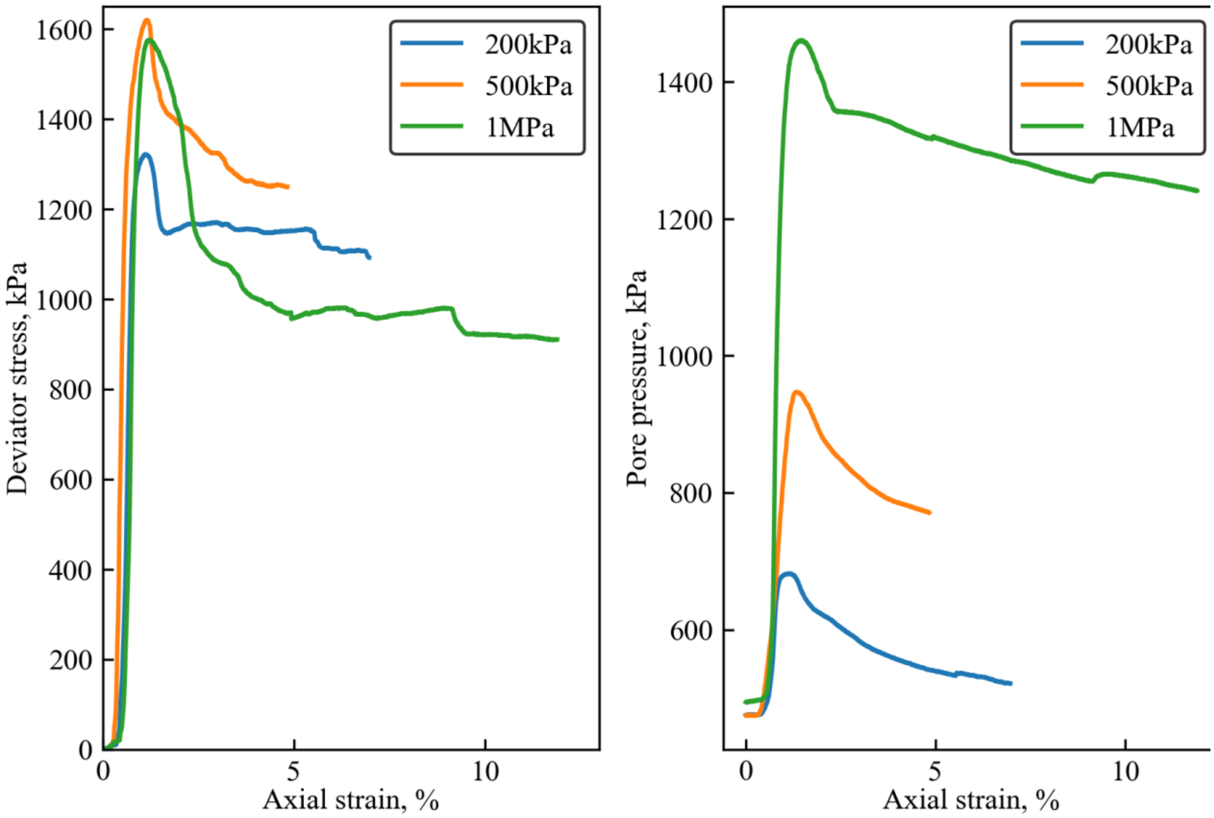

Figure 4-29 Consolidated undrained triaxial tests in synthetic Clearwater shale

At the saturation stage, the back pressure is 500 kPa while the cell pressure is 550 kPa. After the B-test, the consolidation stage commences and consists of a load increment ratio (LIR) of one, which is achieved by adjusting the cell pressure to obtain effective consolidation pressures of about 100, 200, 500, 1000 kPa. After reaching the maximum effective consolidation pressure (1000 kPa), the cell pressure is then reduced to achieve the desired effective consolidation pressure at which the strength determination is performed.

Figure 4-29 describes the variation of the undrained shear strength of the synthetic Clearwater shale with the axial strain. In general, the strength should increase with the effective confining pressure. However, the peak strength at 1 MPa effective confining pressure is lower than at 500 kPa. The most likely reason for the phenomenon is that this study uses two GDS devices for the triaxial tests. Therefore, after a 28-day curing period, the sample used for the test with 1MPa effective confining pressure is preserved in the freezer compartment. After a few weeks, the sample is then used for the test. However, there are a few tiny cracks at the surface of the sample after the sample has been thawed.

Because the test is undrained, the volume of the specimen does not change during the application of the deviator stress. Meanwhile, before the strength reaches the peak value, the pore water pressure increases with the axial strain. When the axial strain is very low, the pore pressure increases, indicating that the sample is under contraction. After the axial strain reaches the peak strain, the pore pressure goes "negative," meaning the specimens are dilating.

From the perspective of the stress analysis, the s′-t′ curve is adopted in this study.

$$s' = \frac{\left(\sigma_1' + \sigma_3'\right)}{2} \qquad \text{Equation (4-42)}$$

$$t' = \frac{\left(\sigma_1' - \sigma_3'\right)}{2} \qquad \text{Equation (4-43)}$$

The slope of the K_f line is known as *tan θ*. There exists a relationship between the magnitude of the slope and the effective friction angle:

$$\tan\theta = \sin\varphi' \tan\theta = \sin\varphi' \qquad \text{Equation (4-44)}$$

The y-intercept of the K_f line and the cohesive strength satisfy the following relationship:

$$t_0 = c' \cos\varphi' \qquad \text{Equation (4-45)}$$

Based on the above information, the s′ versus t′ is shown in Figure 4-30. The friction angle is about 45° and the cohesive strength is 256 kPa.

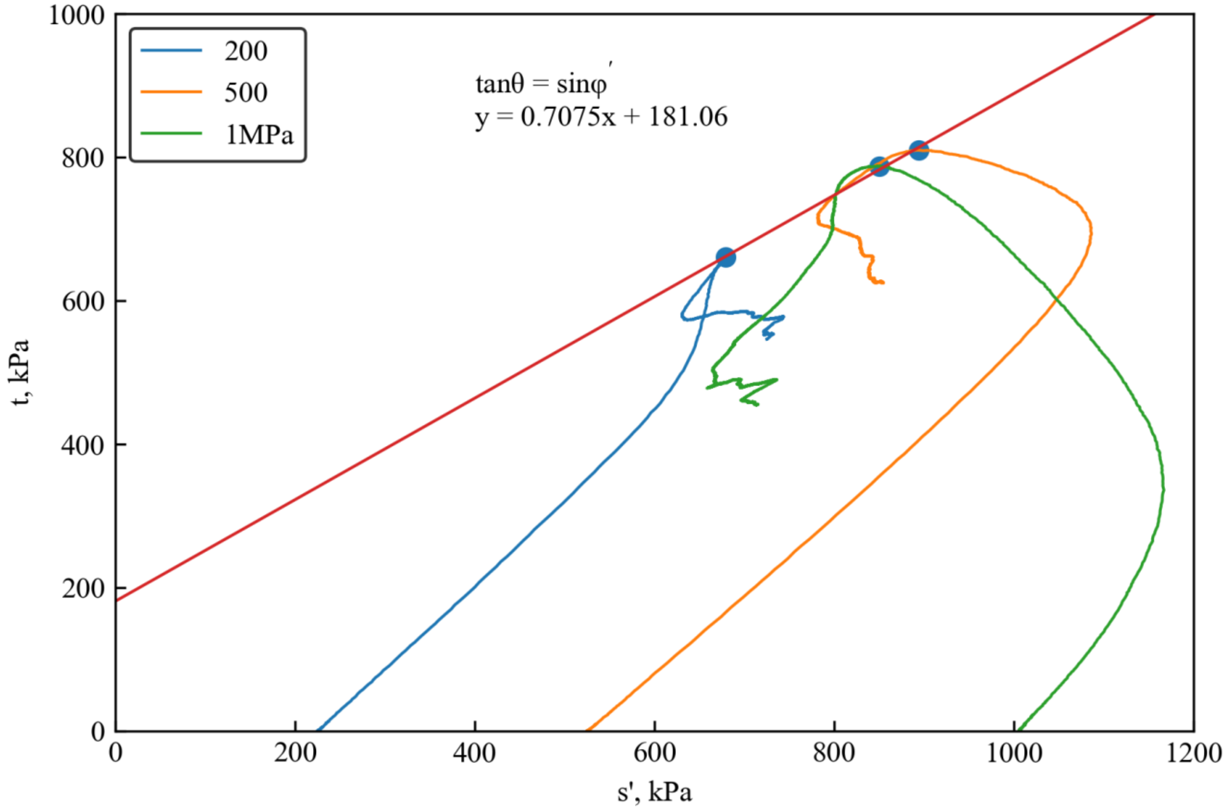

Figure 4-30 Failure envelope of effective stress path from consolidated undrained triaxial tests

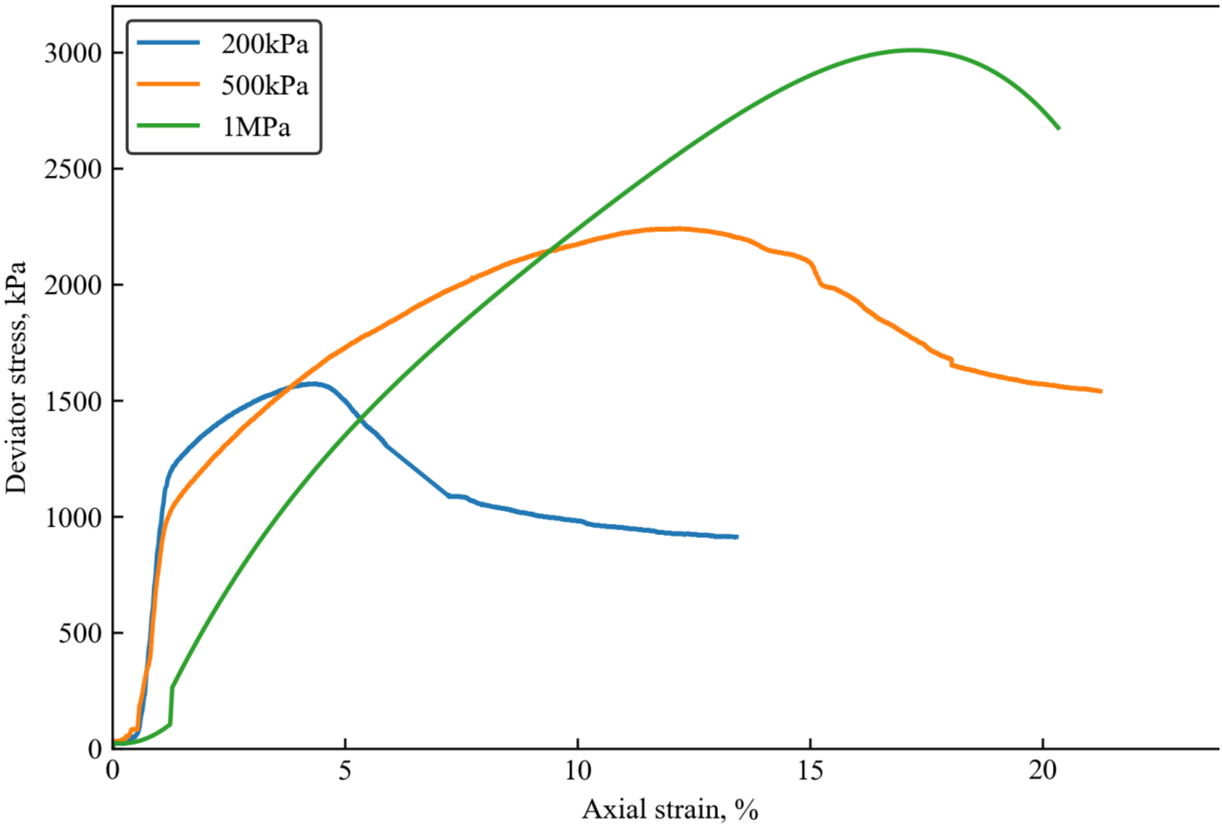

Figure 4-31 Consolidated drained triaxial tests in the synthetic Clearwater shale

Figure 4-31 describes the drained stress-strain curves of the synthetic Clearwater shale. During the process of applying the deviator stress, the volume change of the specimen, pore pressure, cell pressure, load and the axial displacement are monitored through the sensors. However, due to the limitation of the device, the change of the specimen's diameter cannot be directly recorded. Based on the elastic theory, the relationship between the volumetric strain, axial strain and lateral strain satisfies the following equation:

$$\varepsilon_v = \varepsilon_a + 2\varepsilon_r \qquad \text{Equation (4-46)}$$

where ε_v is the volumetric strain, ε_r is the lateral strain.

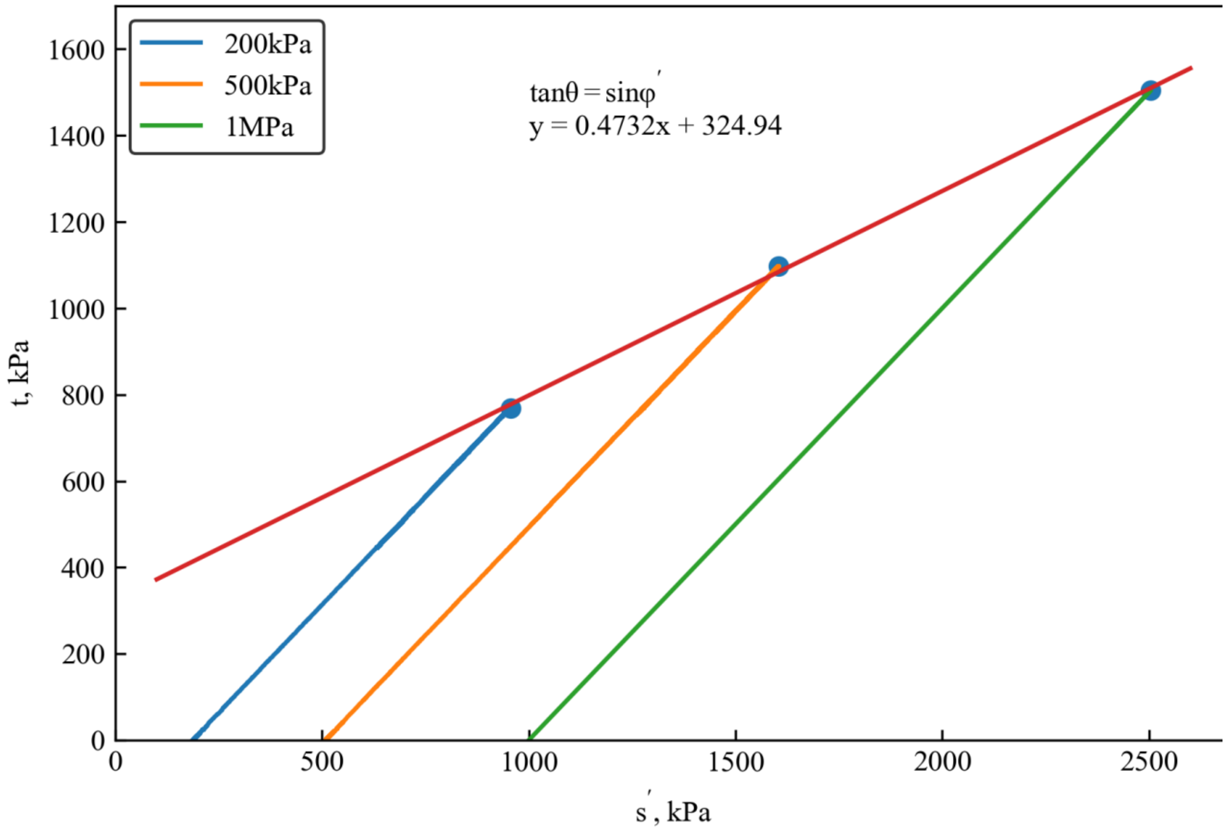

Figure 4-32 Failure envelope of the effective stress path from consolidated drained triaxial tests

The s′ versus t is shown in Figure 4-32. Based on the information shown in the plot, the friction angle is 28º, while the cohesion of the synthetic Clearwater shale is 368 kPa.

For the undrained tests, the axial strain at which the strength reaches the peak value ranges from 1% to 2%. The shear strength drops rapidly after reaching the peak value. For the drained triaxial test, the peak strain increases with the effective confining pressure. At 200 kPa, the peak strain is less than 5% while that for 1000 kPa is over 15%. Based on the analysis of the experimental results of these triaxial tests, Table 4-5 summarizes the mechanical properties of the synthetic Clearwater shale. For the Poisson’s ratio, due to the problem of the triaxial device, the value is higher than 0.5, which is impossible. Under this condition, after completing the triaxial test and dismantling the triaxial device, the diameter of the sample is measured to derive the Poisson’s ratio.

Table 4-5 Mechanical properties of the synthetic Clearwater shale

Triaxial test	Effective confining pressure, kPa	Young's modulus, MPa	Poisson's ratio	Mechanical properties
Drained	200	227.8	0.25	c′ = 368kPa φ′ = 28º
	500	216.4	0.25	
	1000	-	-	
Undrained	200	423.61	0.25	c′ = 256kPa φ′ = 45º
	500	419.03	0.25	
	1000	405.5	0.25	

To get the permeability of the material, the water flow with constant flow rate is injected into the sample. As shown in Figure 4-33, the pore pressure (also known as the base pressure) increases while the back pressure keeps constant during the permeability test. Based on the information shown in the plot, the permeability of the synthetic Clearwater shale is 1.6e^{-6} m/s.

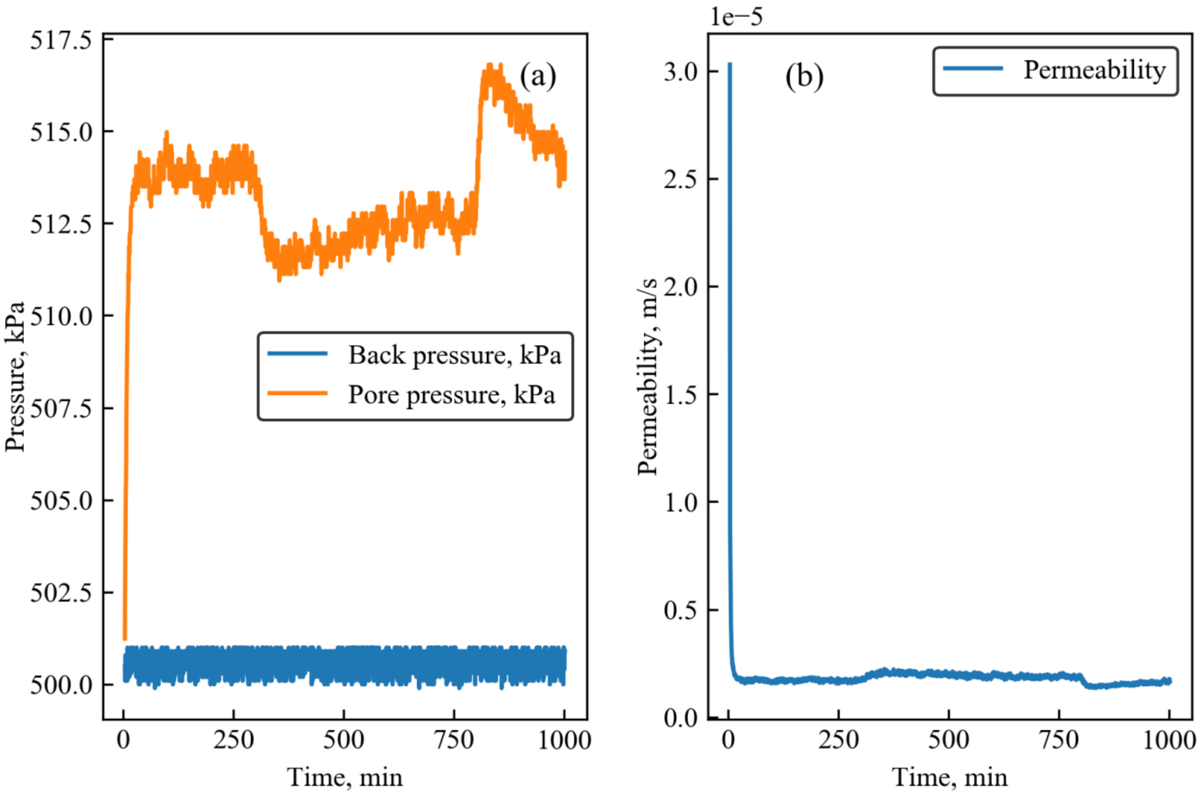

Figure 4-33 Permeability of the synthetic Clearwater shale

After completing the permeability test, the sample is used to determine the tensile strength of the synthetic Clearwater shale, and a few Brazilian tests are conducted, as shown in Figure 4-34. The average tensile strength of the material is 380 kPa. However, it is worth noting that the samples used for the Brazilian tests are preserved in the refrigerator for over 30 days after being cured at room temperature for 28 days.

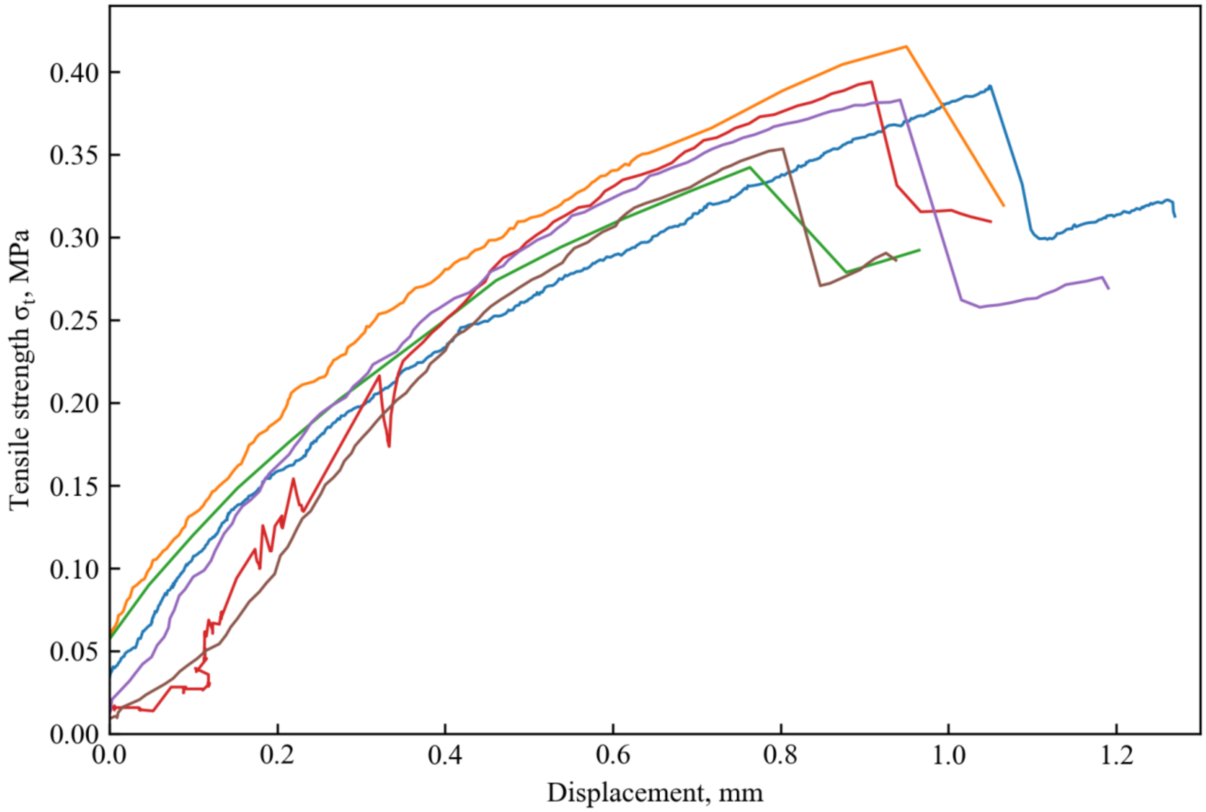

Figure 4-34 Tensile strength of the synthetic Clearwater shale

4.14 Comparison between the Clearwater shale and the synthetic Clearwater shale

Based on the experimental results of the Clearwater shale performed by the reservoir geomechanics research group, as shown Figure 4-35 (Wong, 2007), the effective stress parameters are c′ = 304 kPa and φ′ = 31.9º, as shown in Figure 4-36. By considering the experimental results from both the triaxial test and direct shear test, the Clearwater shale has a cohesive strength of 205 kPa and the friction angle ranges from 26.8º to 33.2º.

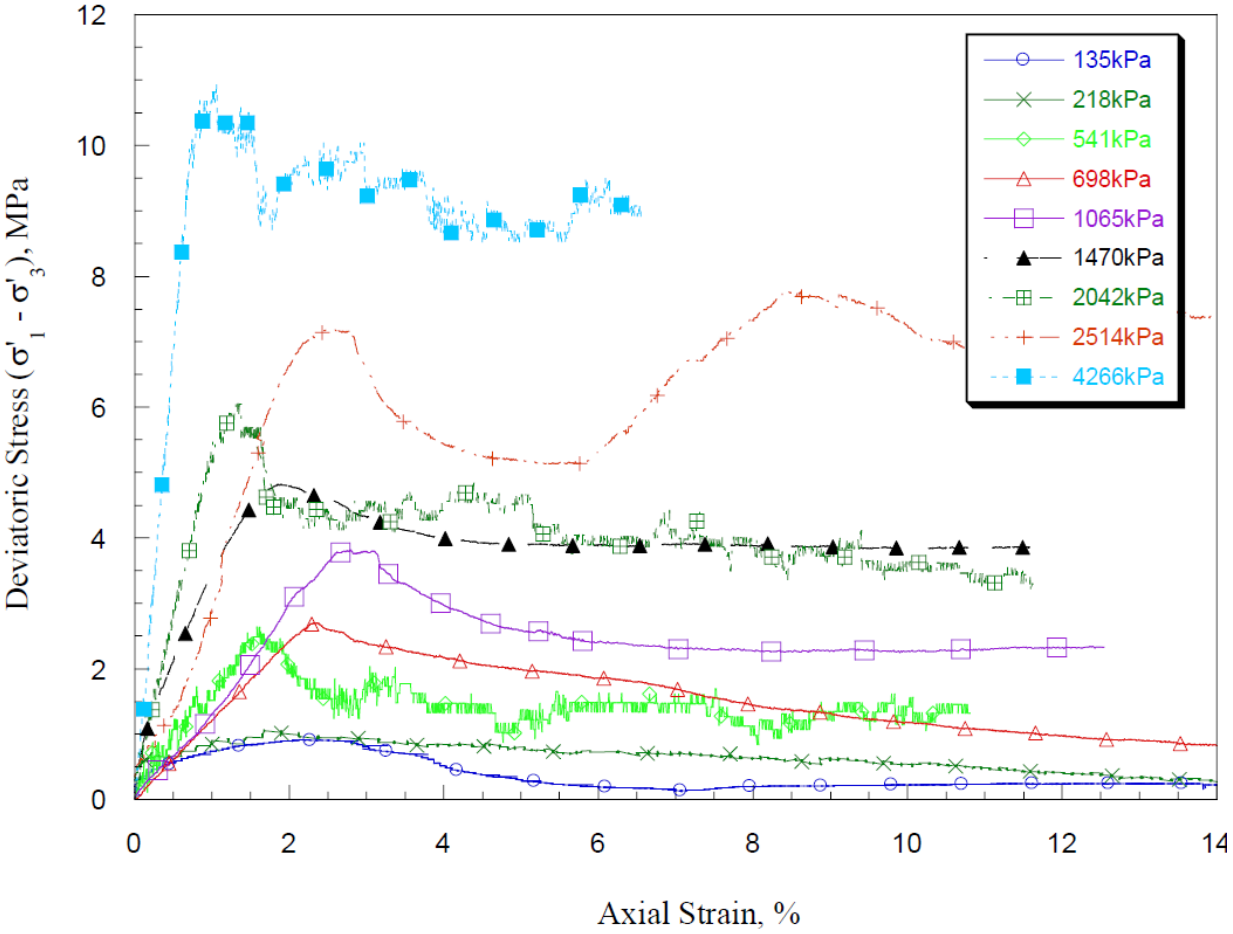

Figure 4-35 Drained Triaxial Stress-Strain curves of Clearwater shale (Wong, 2007)

As shown in Table 4-5, the friction angle of the synthetic Clearwater shale from the drained triaxial tests is 28°, and the cohesive strength is 368 kPa. The mechanical properties of the synthetic Clearwater shale are quite close to those of the Clearwater shale from the perspective of effective stress parameters.

However, the permeability of the in-situ Clearwater shale is around 0.02 md, which is many times lower than the permeability of the synthetic Clearwater shale. In this study, the major requirement of the synthetic Clearwater shale is that the mechanical properties of the material should be as close to the Clearwater shale as possible.

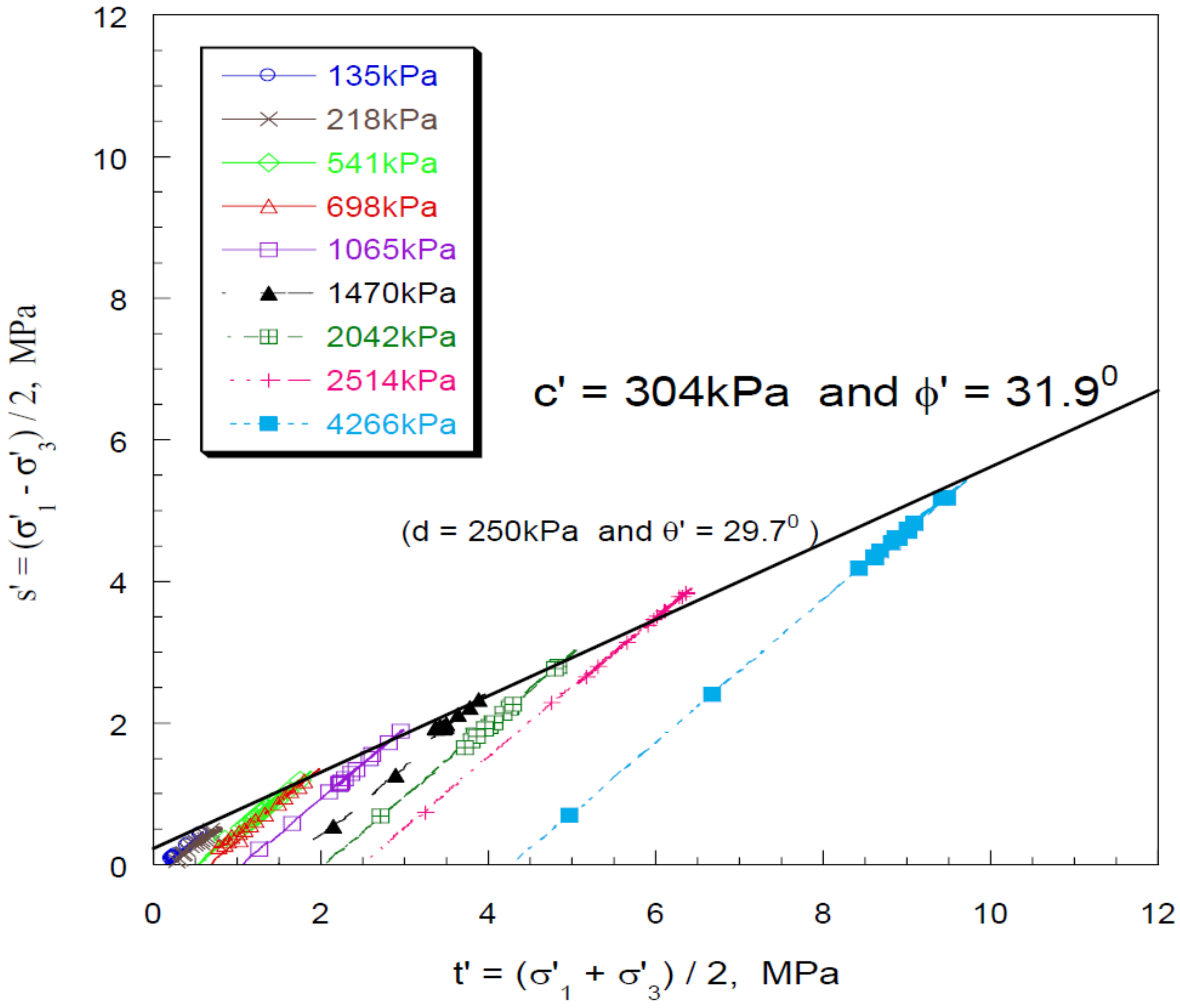

Figure 4-36 Failure envelope of Clearwater shale (Wong, 2007)

4.15 Summary of the synthetic soils

Ten groups of synthetic soils with 0, 10, 20, 30, 40, 50, 60, 70, 80 and 90% S325 by weight, respectively, are used. Each group has 16 recipes, each of which has different normalized water content and cement content. The total soil-water content ranges from 1.1 times the liquid limit to

2.5 times the liquid limit, and the total soil-water to cement ratio varies from 3 to 8. The curing time is 28 days. From the analysis of the experimental results, the following conclusions are made:

A parameter referred to as the modified total soil-water to cement ratio (C_w^M) is proposed to establish the relationship between the after-curing moisture content (C_{wf}) and the total soil-water content and the cement content. A linear function fits well to the relation $C_{wf} - C_w^M$ regardless of the grain size distribution of the synthetic soils.

There exists a linear relationship between the unconfined compressive strength and the after-curing moisture content. Under this condition, the after-curing moisture content is used as the intermediate parameter to establish the relationship between the unconfined compressive strength and the initial parameters such as the total soil-water content, the cement content and the liquid limit of the synthetic soils.

Three different methods are used to derive the after-curing void ratio: the first method considers that the total pore volume of the cured samples remains the same as before the hydration and pozzolanic reactions, the second method considers that the volumes of the soil solid and the cement solid do not change during the curing period, and the third method considers that the volume of the water consumed by the hydration and pozzolanic reactions totally contributes to the solid volume of the cured sample. Based on this analysis, it is believed that the accurate value of the after-curing void ratio is between the lower limit and the upper limit.

A new parameter referred to as the modified after-curing void ratio (M_e), which combines together the effect of the total soil-water content, the cement content, the liquid limit and the after-curing void ratio, is proposed as the prime parameter for the prediction of strength. The quadratic relationship between the strength and the modified after-curing void ratio shows a good correlation, indicating that the after-curing void ratio is of great value for the prediction of the unconfined compressive strength.

A new parameter referred to as the unconfined compressive strength per unit cement content (U_c) is proposed for the quantitative analysis of the unconfined compressive strength variation with the silt-to-clay proportions. It is found that the variation of the strength per unit cement content with the silt-to-clay proportions forms a logistic curve in normal coordinates.

The strength coefficient in this study describes the change rate of the unconfined compressive strength with respect to the cement content at certain water contents. Obviously, the strength coefficient increases with the decreases of the total soil water content. The effect of silt on the strength coefficient can be categorized into three zones: the inactive zone, in which the strength coefficient increases gradually with the silt content; the active content, in which the change rate of the strength coefficients accelerates; and the inert zone, in which the change rate of the strength coefficient gradually reduces to almost zero with the silt content. In short, the variation of the strength coefficient with the silt-to-clay proportions forms a logistic curve in normal coordinates. The same conclusion can also be obtained when analyzing the relationship between the minimum cement content for strength mobilization and the silt-to-clay proportions.

A new parameter referred to as the combined water-cement ratio is proposed for the investigation of the unconfined compressive strength. A linear relationship exists between the combined water-cement ratio and the unconfined compressive strength. Moreover, the soil type is found to be another factor affecting the soil strength. After plotting the data separately based on the soil type, a linear relationship with a high correlation fits well between the combined water-cement ratio and the unconfined compressive strength.

The physical and mechanical properties of the Clearwater shale, which are determined by the engineers in the RG2 group, provide valuable information for the selection of the formula for the synthetic Clearwater shale. A series of tests are performed to determine the properties of the synthetic Clearwater shale. Experimental results show that the mechanical properties of the synthetic Clearwater shale are very close to those of the Clearwater shale. However, the permeability of the synthetic Clearwater shale is many times higher than that of the Clearwater shale. In this study, the major requirement of the synthetic Clearwater shale is that the mechanical properties of the material should be as close to the Clearwater shale as possible.

Chapter 5 Centrifuge modelling test using synthetic Clearwater shale

5.1 Introduction

Previous caprock integrity studies adopted either numerical modelling or analytical methods to investigate caprock failure mechanisms, both of which require simplifying assumptions in the model. The disadvantages of these methods have been discussed in the previous chapters. This study adopts advanced geotechnical centrifuge modelling technology for the investigation of the failure evolution of caprock during SAGD process. One significant advantage of geotechnical centrifuge modelling is the transparent Perspex glass window and the high-resolution camera which enable capturing a visual record of the soil (caprock) deformation process.

As discussed in Chapter 2, numerous studies have been performed to research the interaction between a buried object and surrounding soils. These studies provide valuable guidance for the study of the caprock deformation behaviour. The primary objective of this chapter is to present the experimental results of a series of three geotechnical centrifuge modelling tests utilizing the specific synthetic Clearwater shale determined from the extensive testing discussed in Chapter 4.

Ideally, the experimental research would be conducted over a range of model variables including overburden weight (i.e., depth of caprock), the model thickness, the water level in the plane strain box (PSB), the width of the uplifting table and the uplifting velocity. An investigation of these five variables on the model caprock deformation behaviour would require many centrifuge tests, which is impractical. To refine the testing matrix, the following assumptions have been made:

- The overburden weight, which serves as a proxy for depth of caprock, and the caprock thickness are constant since the testing program is related to one particular location (e.g., Joslyn project area) and these variables would not be expected to change during a SAGD project.
- The groundwater level, which may seasonally fluctuate generally does not communicate directly with the water beneath the shale barrier if the caprock integrity is maintained; and
- Adjusting the width of the uplifting table, which serves as a proxy for the size of the steam chamber below the caprock, would require extensive modifications to the GeoCDM and was beyond the budget allocated for this research.

Consequently, this research focuses on the impact of the uplifting velocities on the caprock deformation behaviour, which serves as a proxy for the rate at which the steam chamber develops below a caprock interval. To ensure the consistency of the material properties, the centrifuge model utilized in the three tests is prepared using the same preparation procedure described in Chapter 3 but the synthetic Clearwater shale is a mixture of water, soil and cement using the formulation established in Chapter 4.

Table 5-1 Experimental program of the geotechnical centrifuge modelling test

Test	Overburden, kPa	GeoCDM uplifting velocity, m/s	Model thickness, cm	Prototype time, yr
1	509	6.43004×10^{-7}	20	10
2	527	2.14335×10^{-6}	20	3
3	510	4.28669×10^{-7}	20	15

The experimental program is summarized in Table 5-1, along with the parameters utilized in the tests. Detailed information on each of the experimental parameters will be discussed in the subsequent sections.

This chapter is divided into two sections: the first section briefly introduces the coordinates of the control markers while the second section introduces the experimental results of the three tests.

5.2 Control Markers on PSB Test Models

The control markers are indispensable for converting the soil deformation behaviour from the image-space to the object-space. As shown in Figure 5-1, the black dots on the Persplex glass window are the control markers manufactured with GeoCERF. The horizontal direction is the X-axis while the vertical direction is the Y-axis. The control marker at the lower left corner is used as the coordinate origin. The diameter of the control marker is 4.5 mm. The centre-to-centre distance of the adjacent control markers on the same vertical line or horizontal line is 60 mm.

The coordinates of these control markers for x=0 and y=0 are shown in Figure 5-1. The six uniformly distributed control markers on the vertical direction covers a height of over 300 mm. The 12 control markers on the horizontal direction cover a length of over 660 mm. Based on the experimental results that will be discussed later, the area covered by these control markers is sufficient for the analysis of the soil deformation behaviour.

Despite the coordinates of the control markers, the position of the uplifting table (GeoCDM) is also of great importance for the analysis of the caprock deformation behaviour. First, the uplifting table provides the uplift force, which is used to mimic the expansion of the steam chamber. Second, based on previous studies on the horizontal plate anchor, the initialization of the failure plane may initiate at the edge of the uplifting table. Third, the vertical displacement of the soil particles along any vertical lines or horizontal lines may provide information of the soil failure mode. Therefore, it can be deduced that the uplifting table may be the most highly strained area and getting the coordinates of the uplifting table becomes essential for an analysis of the failure mode.

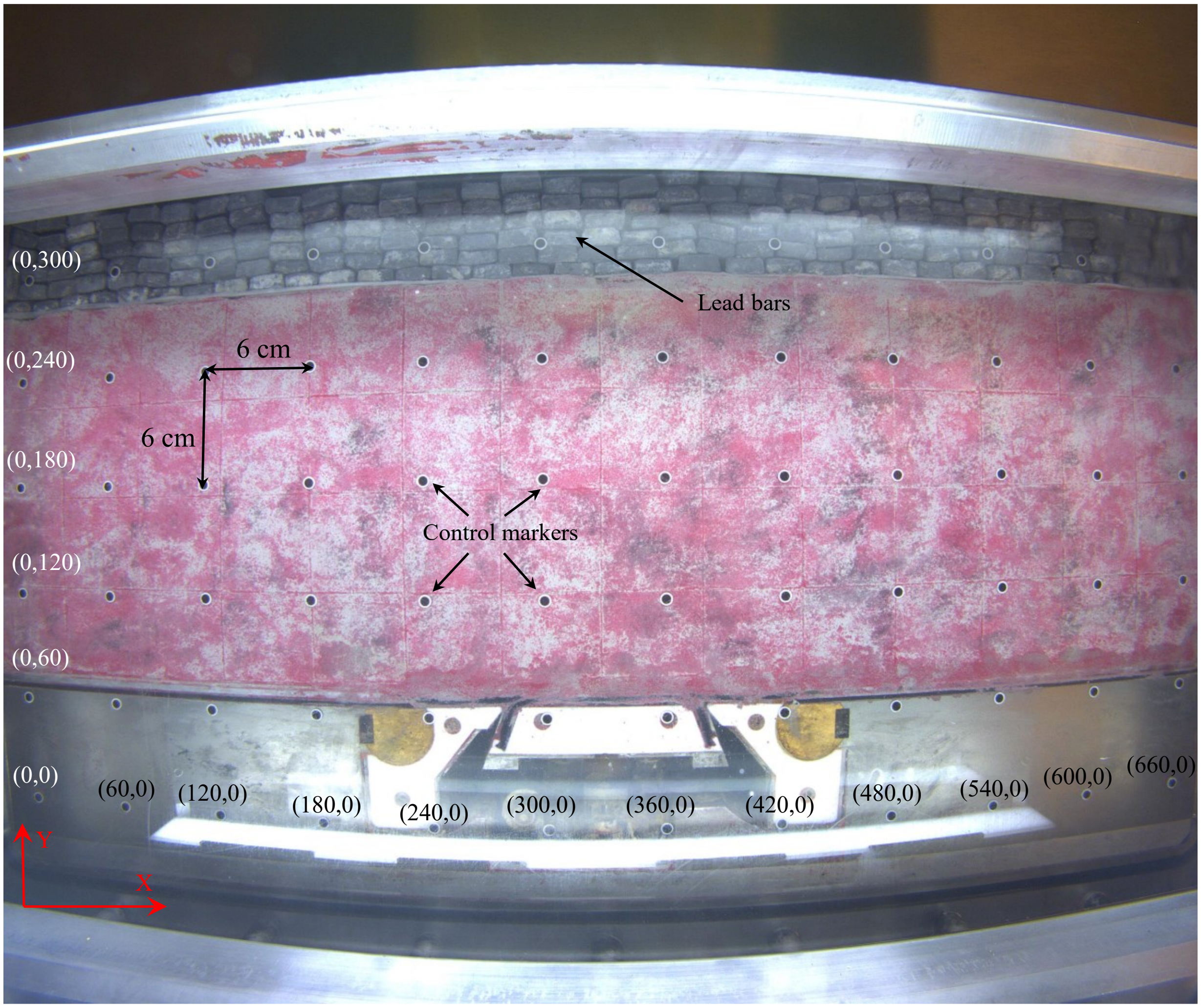

Figure 5-1 The coordinates of control markers

Figure 5-2 illustrates the sketch of the PSB obtained from Thomas Broadbent & Sons Ltd. The dimension of each component is quite clear: the thickness of the side wall is 50 mm, the inner length is 70 mm and the width is 20 mm. To deduce the position of the uplifting table, it is essential to obtain the position of the GeoCDM.

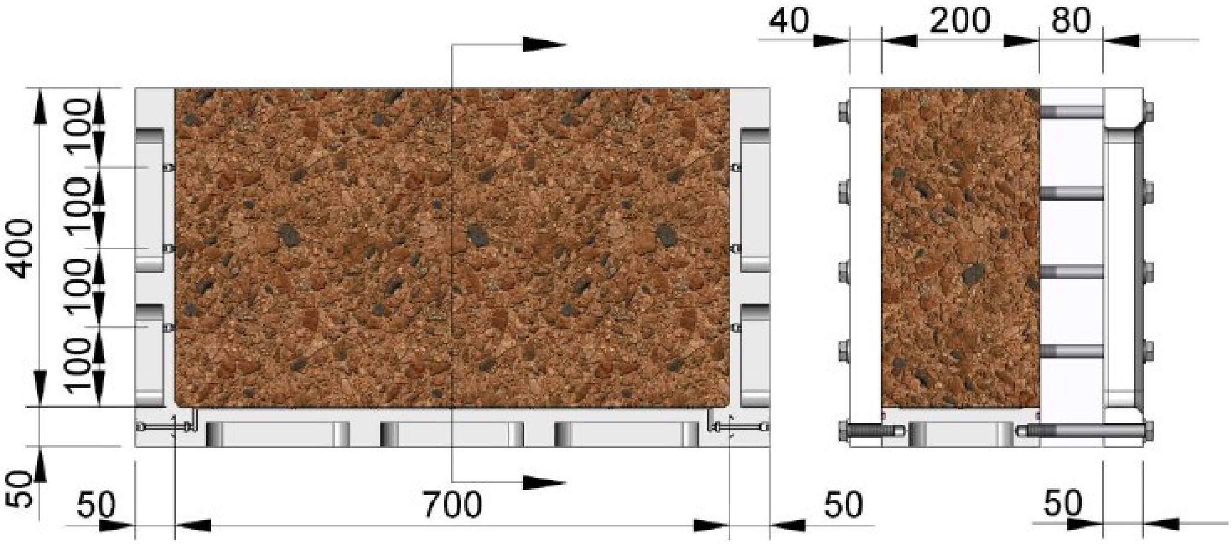

Figure 5-2 Sketch of plane strain box (unit in mm) (TBS, 2012)

As shown in Figure 5-3 (a), the vertical distance between the bottom of the PSB and the top of the uplifting Table is 16.5 cm which gives a height of the GeoCDM of 11.5 cm. However, it is worth noting that a layer of porous stone and three layers of filter paper are placed on top of the GeoCDM when assembling the PSB, indicating that the actual position of the uplifting table may be slightly different from that deduced from the sketch. Under this condition, the vertical distance between the bottom of the sample and the control markers directly above the GeoCDM is measured after the whole system is well prepared, as shown in Figure 5-3 (b).

By using the coordinate system shown in Figure 5-1, the y-coordinate of the top surface of the GeoCDM is 75 mm. The vertical position of the uplifting table may be adjusted based on the requirements of the experiments, indicating that the y-coordinate of the top surface of the uplifting table may be slightly higher or lower than 75 mm. However, in practice, the actual position of the uplifting table is strictly controlled for the purpose of protecting the gears. If the position is too low, a very small downward movement of the uplifting table may reach the limit, stuck the gears and result in irreversible damage. When assembling the PSB, a magnetic torpedo level is used to check the position of the uplifting table to make sure that it is at the same level as that of the two flanks.

To obtain the x-coordinate of the GeoCDM, the priority is to find the distance between the centre of the first column of control markers on the left side and the left edge of the PSB, as shown in Figure 5-4(a). It is evident that the distance between the left edge of the PSB and the centre of the control marker is 6.8 cm. Based on the information shown in Figure 5-2, the distance between the centre of these control markers and the left inner wall of the PSB is 18 mm.

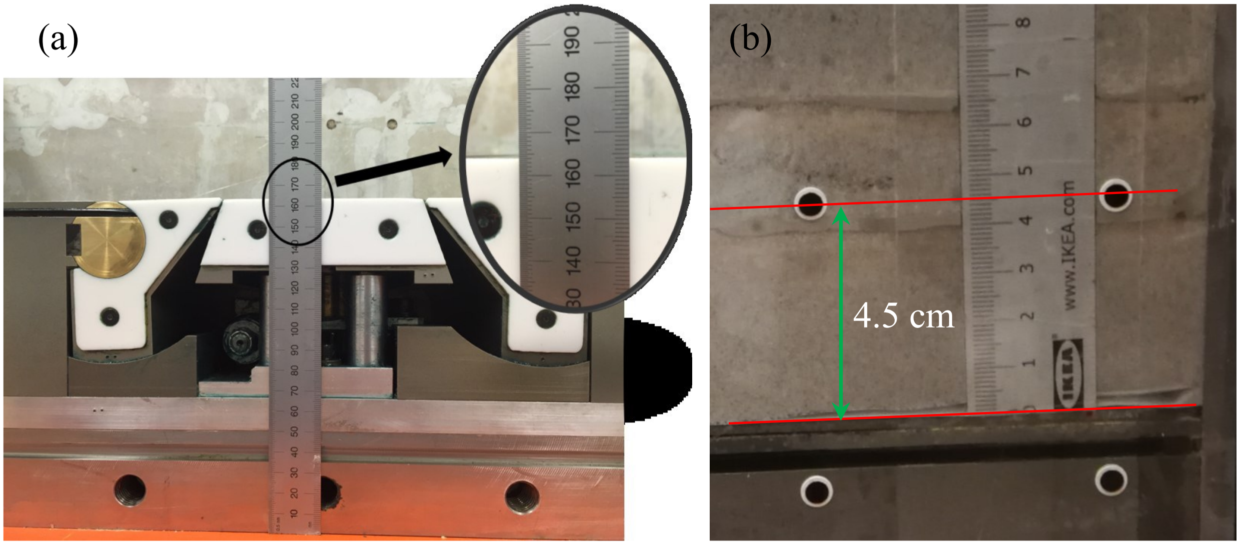

Figure 5-3 Determination of the y-coordinate of the GeoCDM

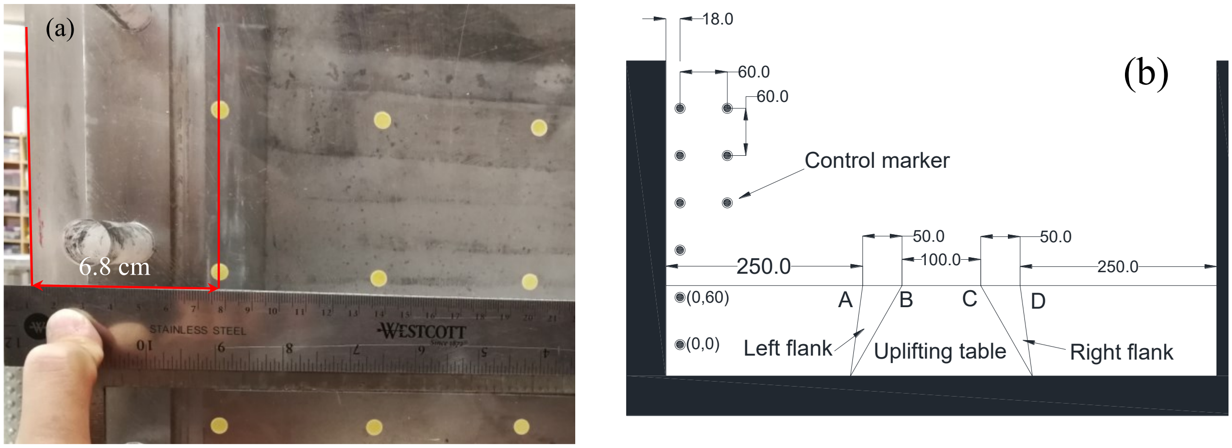

Figure 5-4 Determination of the x-coordinate of the GeoCDM

Figure 5-4(b) illustrates the coordinates of the GeoCDM while Table 5-2 provides the coordinates of the critical points of the GeoCDM, such as the start point and end point of the uplifting table and the flanks.

Table 5-2 Coordinates of the critical points of the GeoCDM

Point	X-coordinate, mm	Y-coordinate, mm	Note
A	232	75	Left vertex of the left flank
B	282	75	Right vertex of the left flank, or left vertex of the uplifting table
C	382	75	Right vertex of the uplifting table, or left vertex of the right flank
D	432	75	Right vertex of the right flank

5.3 The GeoPIV_RG program

The patch size (*L*) is of great importance for the analysis of these images. Small patches result in a finer mesh of the displacement fields while large patches increase the precision of the PIV. White, Take, & Bolton (2003), Stanier & White (2013) and Kelly (2014) performed a series of experiments to assess the influence of patch size on the precision of PIV. The experimental results showed that the precision of the PIV was strongly dependent upon the patch size, as shown in Figure 5-5. White et al. (2003) presented the following equation for the estimation of the precision error.

$$\rho_{pixel} = \frac{0.6}{L} + \frac{150000}{L^8} \qquad \text{Equation (5-1)}$$

Although the error obtained from the equation may be conservative, it provides valuable information for the estimation of a suitable patch size.

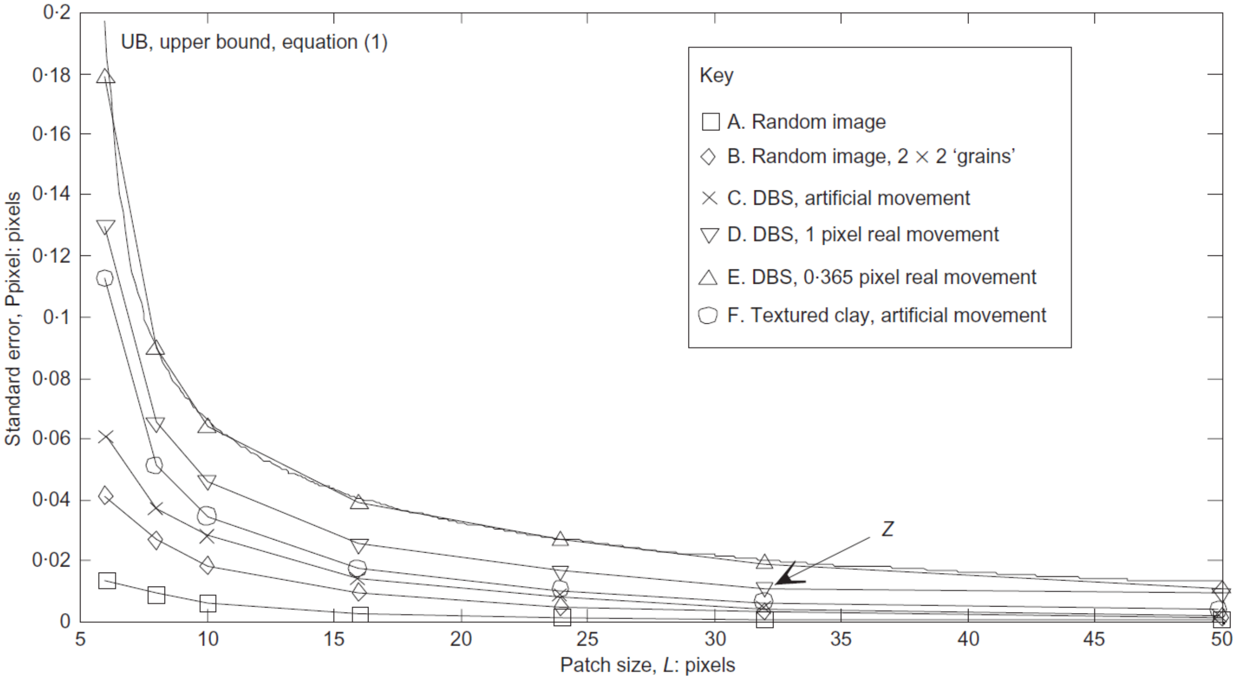

Figure 5-5 Relationship between the precision of the PIV and the patch size (White et al., 2003)

As shown in Figure 5-5, the standard error for patches of size 50×50 pixels is approximately 0.0007 pixels. Similar results were also obtained by Kelly (2014), who determined the standard tracking errors in both the vertical direction and the horizontal direction. When the patch size was 50 pixels, the standard error vector sum was less than 0.02 pixels. Based on the analysis of the previous studies, this study adopts patches of size 50×50 pixels for the PIV analysis.

5.4 Test No. 1 with prototype time of 10 years

5.4.1 Experimental Results – 10 years

Table 5-3 provides the details for the first geotechnical centrifuge modelling test, Test No. 1, using the synthetic Clearwater shale. The proportion of the Speswhite kaolin clay to the Sil325 is 40:60. The total soil-water content is 2.5 times the liquid limit while the total soil-water to cement ratio is 3. After being well mixed, the soil-water-cement mixture is transferred to the PSB. The initial height of the soil-water-cement mixture is approximately 21.5 cm. After 28 days curing, due to the shrinkage, the model height is about 20 cm. The weight of the lead bars is 72.7 kg, which corresponds to 509.42 kPa overburden pressure when the centrifuge is spinning at 100 g.

Table 5-3 Sample information of the first centrifuge modelling test

Slurry preparation					
Speswhite kaolin clay: Sil325	40:60				
Liquid limit	32.81				
Plastic limit	18.23				
Normalized water content	2.5				
Total soil-water to cement ratio	3				
Sample preparation					
Initial height, cm	21.30	21.00	20.90	21.50	21.10
Final height, cm	19.60	19.80	19.60	19.90	19.90
Weight of lead bars, kg	72.7				
Vertical pressure at 100 g, kPa	509.42				
Overburden height, m	24.15				
Parameters for GeoCDM					
Jog velocity (revolutions/min)	0.7716				
Jog accelerating	2				
Jog distance (mm)	24000				
Shearing time, hr	8.64				
The corresponding prototype time, yr	10				

Prior to starting the GeoCDM, the model is consolidated in the centrifuge facility for at least 8 hours. During this process, the performance of the system is monitored to make sure that experimental conditions are achieved, for instance the water level in the PSB, the balance, etc. The jog velocity of the Parker Servo Motor is 0.7716 revolutions per minute. Under this condition, it takes 8.64 hours for the uplifting table to move 20 mm, and the corresponding prototype time is 10 years.

The following figures provide the interpreted response of the centrifuge model at the end of the prototype time of 10 years. Figures of early responses (1 yrs, 2 yrs, 5 yrs, 7.5 yrs and 10 yrs) are provided in Appendix B.

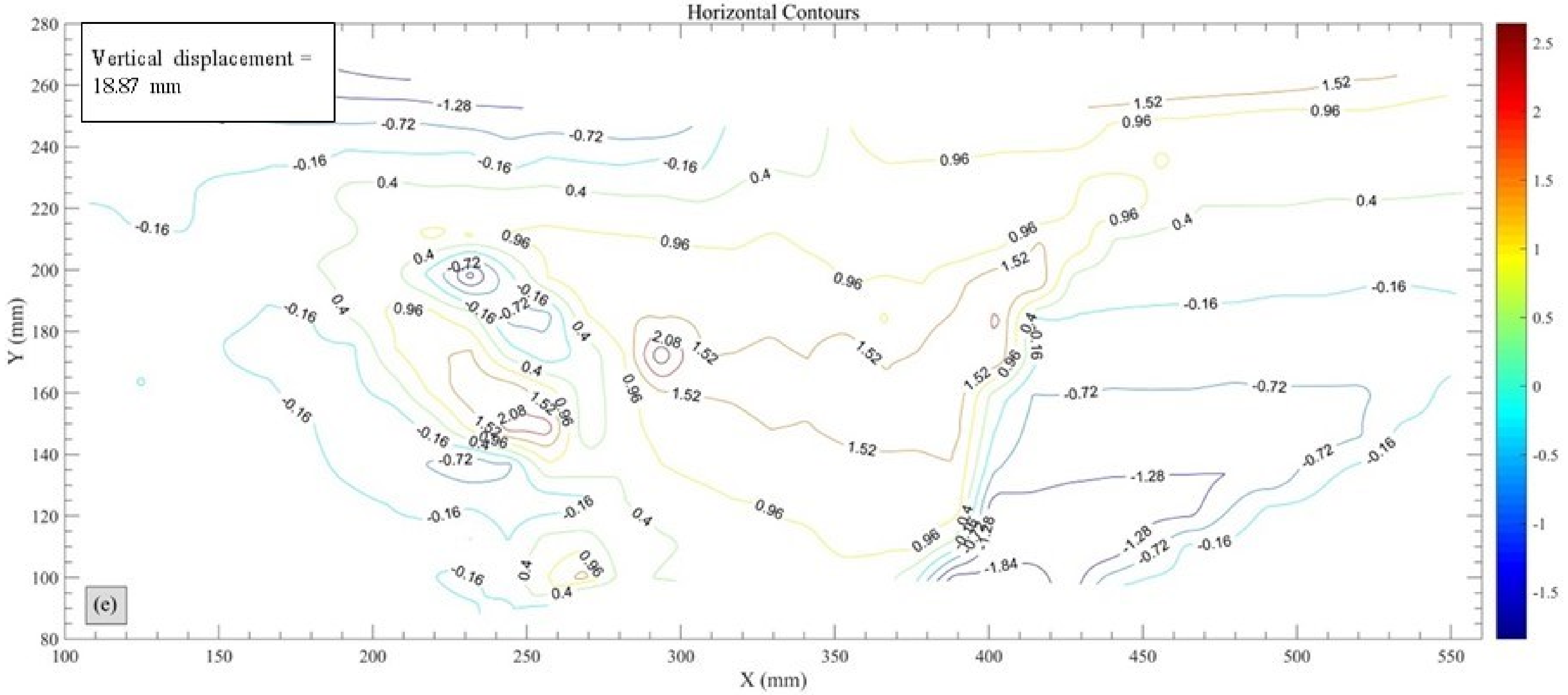

Figure 5-6 Evolution of horizontal displacements – t = 10 yrs

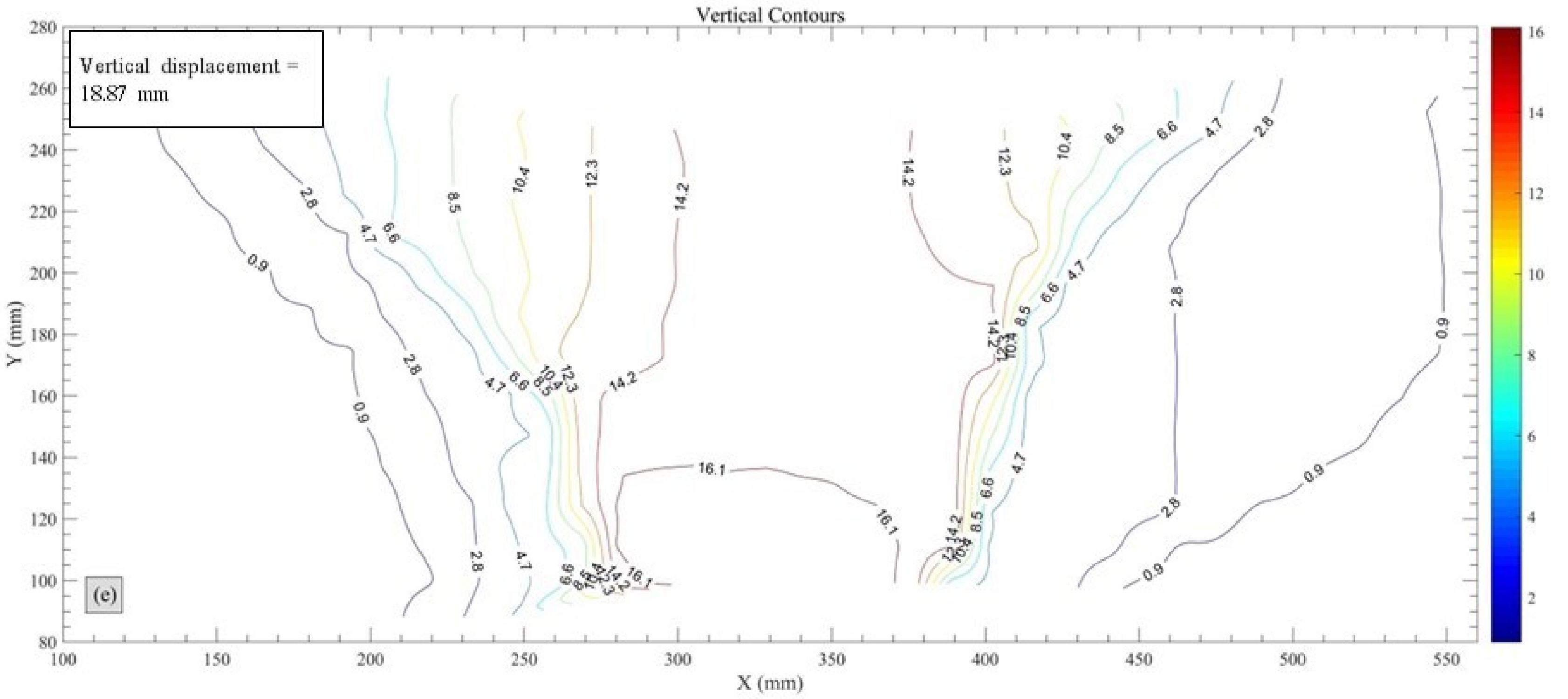

Figure 5-7 Evolution of vertical displacements – t = 10 yrs

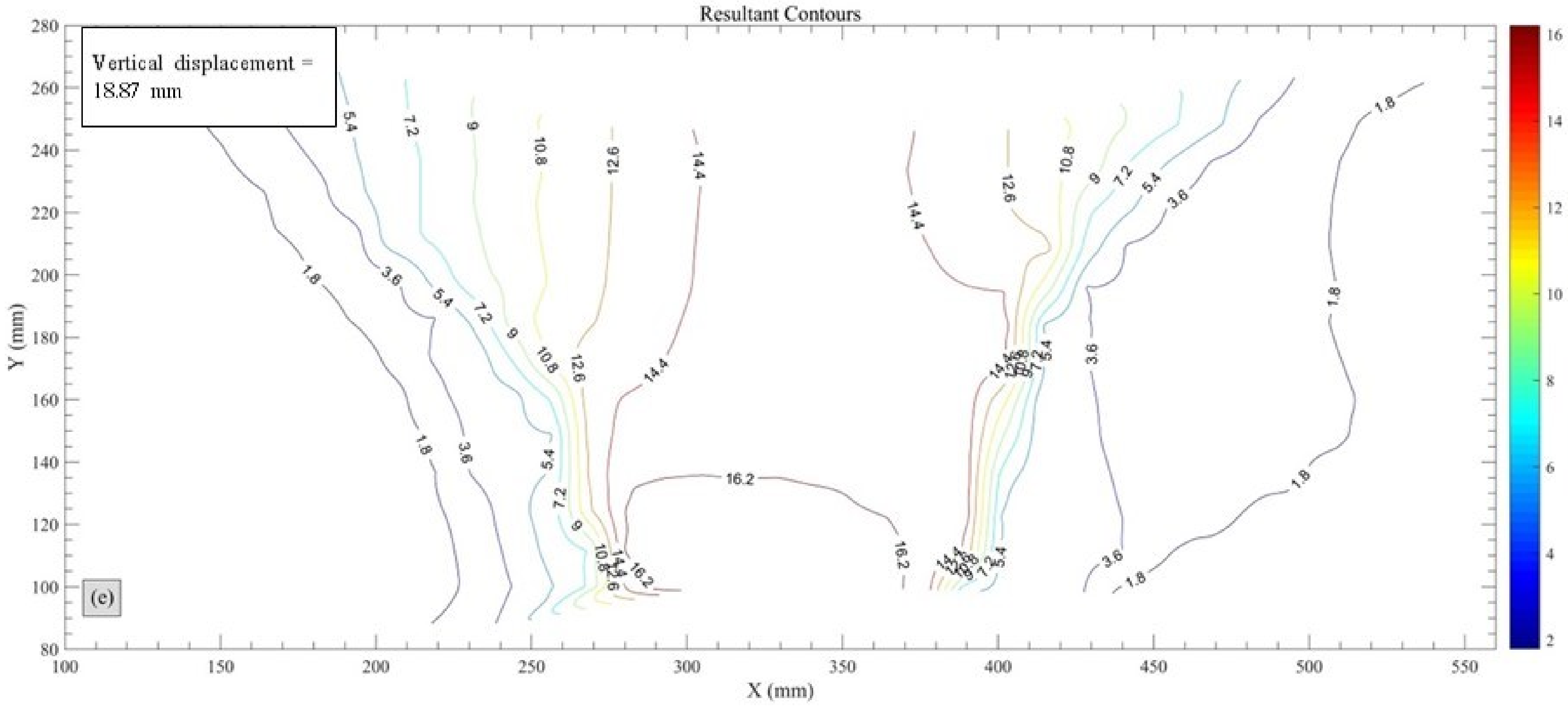

Figure 5-8 Evolution of resultant (total) displacements – t = 10 yrs

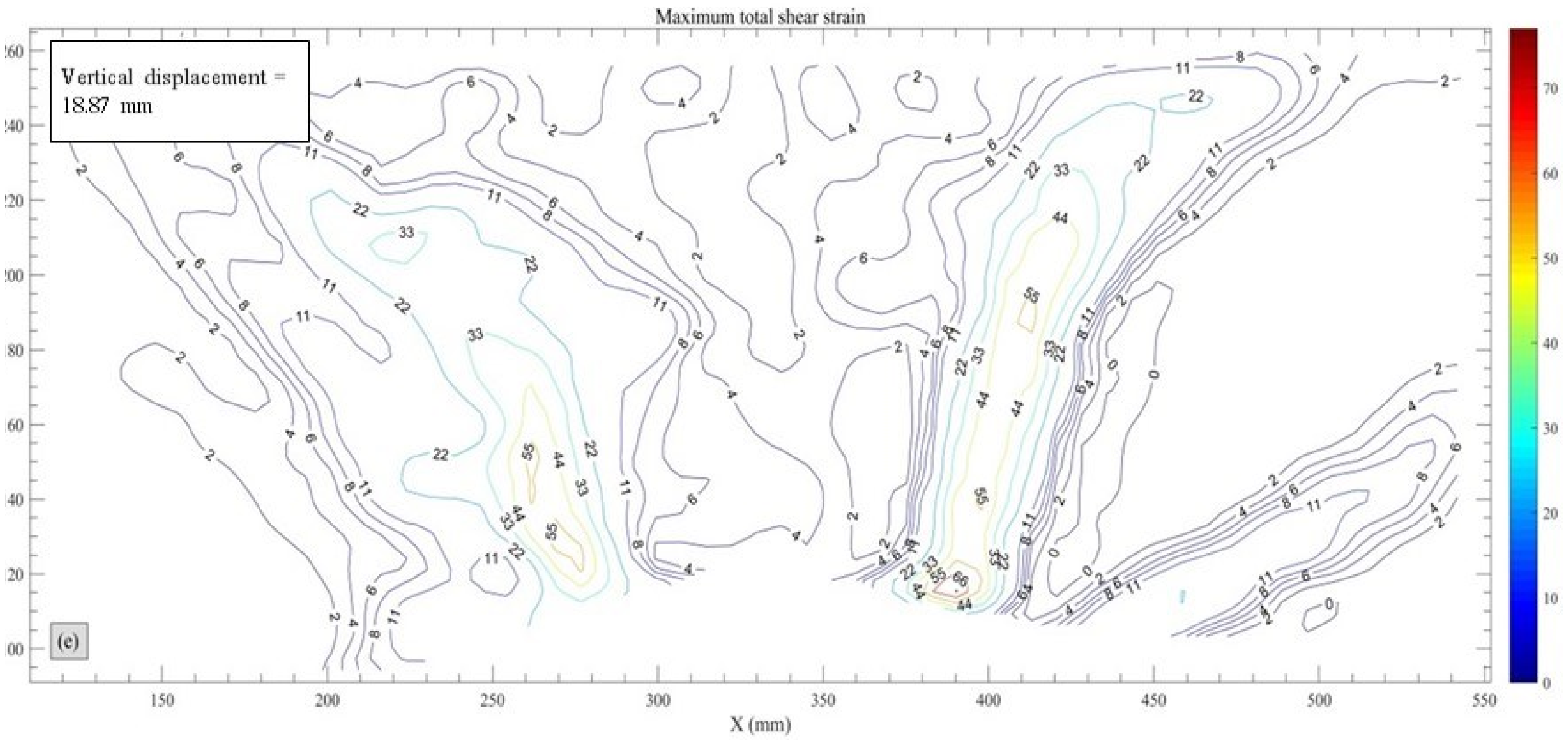

Figure 5-9 Evolution of maximum shear strain – t = 10 yrs

5.4.2 Experimental Observations – 10 years

During the centrifuge modelling test, a few fractures at the top of the model are first observed. However, these fractures only propagate downwards for a few centimeters. As the test continues, a few fractures emerge from the middle height of the model and then propagate towards the model surface and the model bottom. In previous "trap-door" type experiments, marking samples with a few thin layers of colored sand adjacent to the glass wall of the container, Tanaka and Sakai (1993) and Mcnulty (1965) revealed that the shear band gradually increased to the ground surface and curved toward horizontal as the trap door moved up. Similarly, Vardoulakis, Graf, and Gudehus (1981) observed that a small upward deflection of the trap door in the dense sand can clearly result in the occurrence of the shear bands extending from the edge of the trap door. For loose sand with a small embedment ratio, the shear bands were almost vertical. For loose sand with a large embedment ratio, the shear bands were not observed in the sample.

This type of behaviour was not evident in the centrifuge test. A major reason for the conflict of the shear band development between this study and the abovementioned literature is that the horizontal stress increases with depth. Therefore, at the bottom of the model, the high horizontal stress prohibits the horizontal expansion of the fractures, making it very hard to visually document the fractures especially when the front surface of the model is uniformly marked with a layer of colored sand.

5.5 Test No. 2 with prototype time of 3 years

5.5.1 Experimental Results – 3 years

As shown in the Table 5-4, formula F7-14 (Spk: S325 = 40: 60, total soil-water content = 2.5 times the liquid limit, the total soil-water to cement ratio = 3) is used to make the synthetic Clearwater shale. The initial height of the soil-water-cement mixture in the PSB is approximately 21.5 cm. Due to the shrinkage, the final height of the sample after curing is about 20 cm. At 100 g, the model can be used to mimic the behaviour of the caprock with 20 m thickness. The overburden on the caprock is simulated through an appropriate thickness of lead bars. In this study, the weight of lead bars is about 75.3 kg, which corresponds to the in-situ overburden with 25 m thickness. The model of the second geotechnical centrifuge modelling test was made November 19, 2018. After 28 days curing period, the centrifuge test with the model should have conducted. However, due to the schedule demands of the centrifuge facility, the test was performed January 21, 2019. Under this condition, the strength of the model may be slightly higher than these models cured for 28 days. From the perspective of Mohr-Coulomb failure criteria, shear failure or shear fracture of the model may occur at higher principal stresses when compared with those models cured for 28 days. This test intends to mimic the deformation behaviour of the caprock that is continuously uplifted by the steam chamber for up to 3 years. The corresponding shearing time in the centrifuge is about 2.592 hours. To achieve this goal, the jog velocity, which is an important parameter controlling the velocity of the GeoCDM, is 2.5720 revolutions per second.

The corresponding uplifting velocity of the uplifting table is 0.002143 mm/s. Image of the model deformation behavior is taken at 15-seconds intervals. Based on the relationship between the uplifting velocity and the corresponding displacement, the incremental vertical displacement between the two adjacent images is 0.0322 mm.

The following figures provide the interpreted response of the centrifuge model at the end of the prototype time of 3 years. Figures of early responses (0.25 yrs, 0.5 yrs, 1 yrs, 2 yrs and 3 yrs) are provided in Appendix C.

Table 5-4 Sample information of the second centrifuge modelling test

Slurry preparation					
Speswhite kaolin clay: Sil325	40:60				
Liquid limit	32.81				
Plastic limit	18.23				
Normalized water content	2.5				
Total soil-water to cement ratio	3				
Date of sample preparation	November 19， 2018				
Date of centrifuge spinning	January 21， 2019				
Sample preparation					
Initial height, cm	20.91	20.94	21.23	21.18	20.92
Final height, cm	20.00	21.10	19.90	20.10	20.20
Weight of lead bars, kg	75.3				
Vertical pressure at 100 g, kPa	527.64				
Overburden height, m	25.02				
Parameters for GeoCDM					
Jog velocity (revolutions/min)	2.5720				
Jog accelerating	2				
Jog distance (mm)	24000				
Shearing time, hr	2.59				
The corresponding prototype time, yr	3				

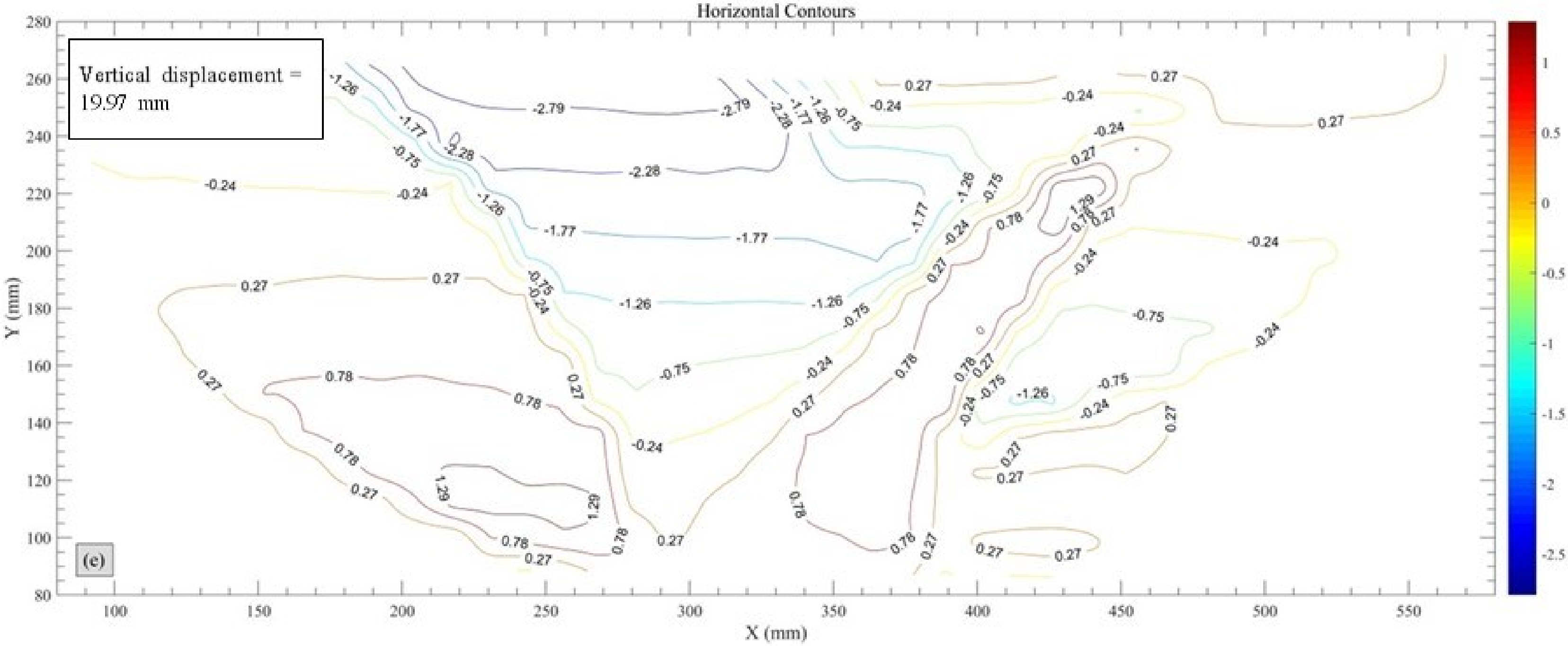

Figure 5-10 Evolution of horizontal displacements – t = 3 yrs

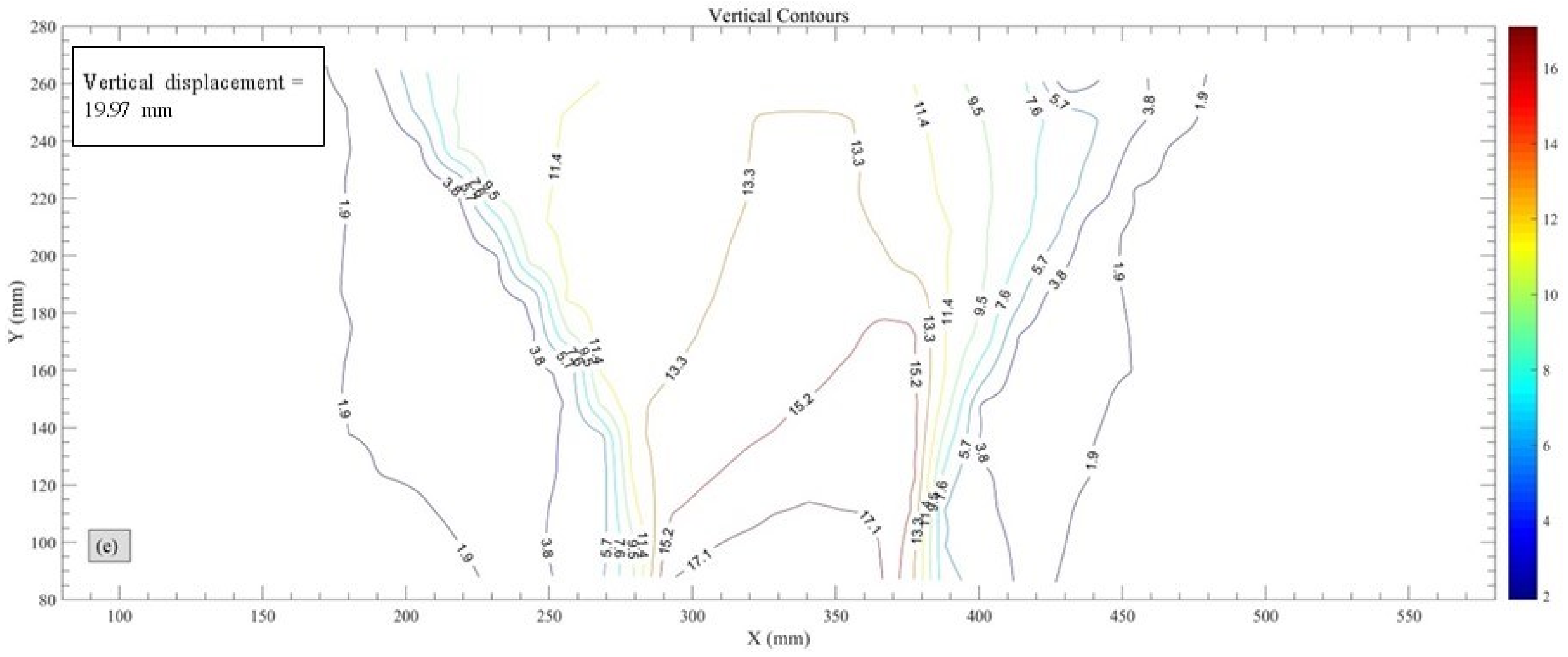

Figure 5-11 Evolution of vertical displacements – t = 3 yrs

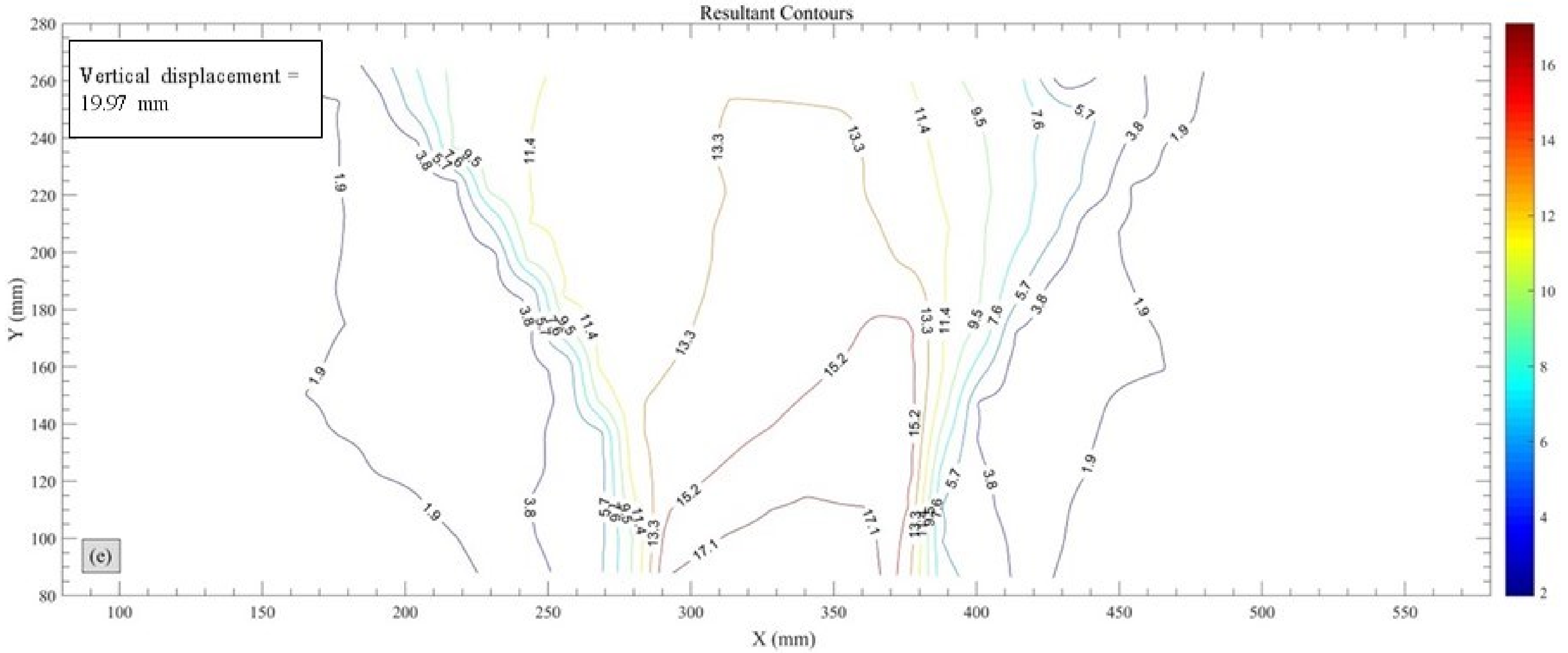

Figure 5-12 Evolution of resultant (total) displacements – t = 3 yrs

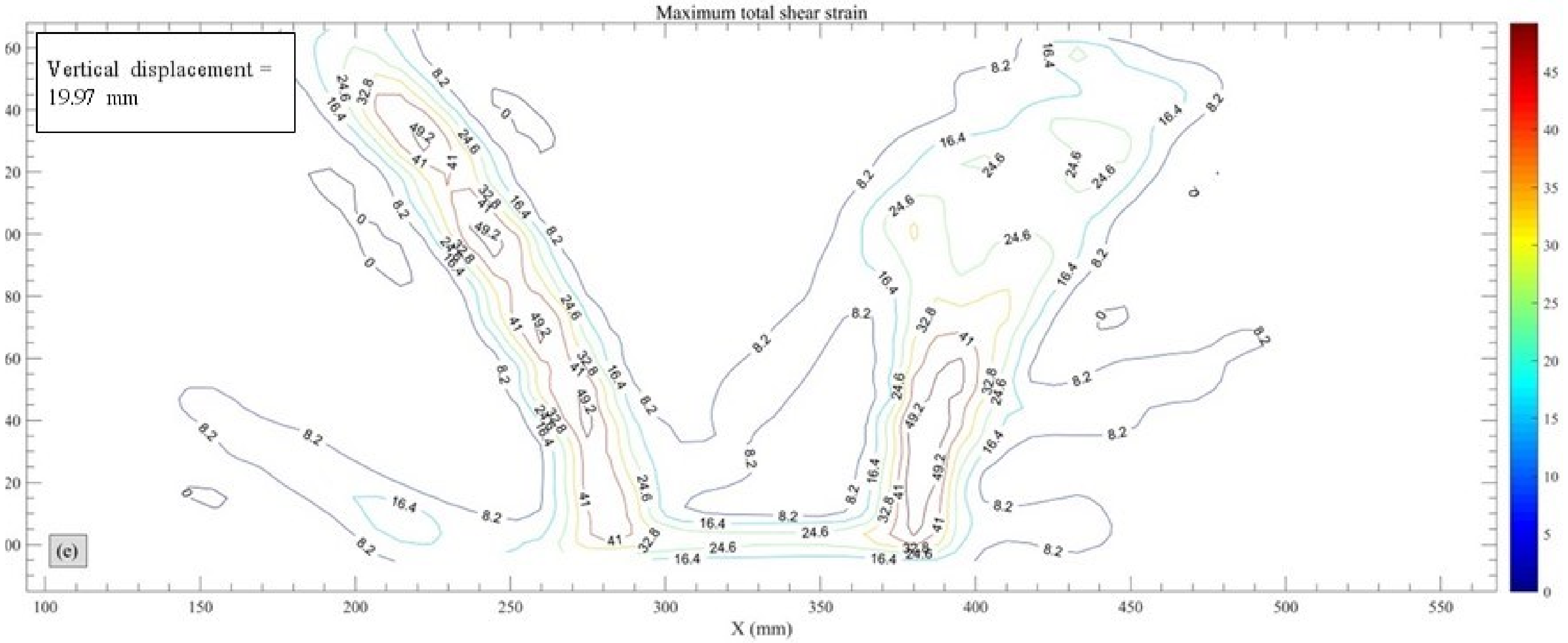

Figure 5-13 Evolution of maximum shear strain – t = 3 yrs

5.5.2 Experimental Observations – 3 years

A few fractures at the top of the model are first observed in the model but these fractures only extend down toward the base of the model for a few centimeters and then stop developing. During the centrifuge modelling test, it seems that the fractures also emerge from the middle height of the model and then propagate towards the model surface and the model bottom. The previous studies performed by Tanaka and Sakai (1993) and McNulty (1965) marked the samples by a few thin layers of colored sand adjacent to the glass wall of the container so that very tiny deflection of the horizontal line can be observed. Therefore, very tiny deflection of these horizontal lines can be observed, and these studies concluded that the shear bands extended from the edge of the trap door. However, no evidence to prove that these fractures are induced by either shear forces or tensile forces.

Intuitively, the soil particles at the left side of the centreline move towards the –X direction, while those at the right side move towards the +X direction.

5.6 Test No. 3 with prototype time of 15 years

5.6.1 Experimental Results – 15 years

The third test is prepared and tested using a slightly more sophisticated method which was informed by experience accumulated from the first two tests regarding construction methodology and the experimental procedure. Therefore, the surface density of the red sand sprinkled on the front surface of the model is more uniform when compared with the previous two tests. The experimental package was assembled in a much shorter time and the time that the model is exposed to air was therefore reduced. The illumination system was updated allowing higher-quality images to be captured during the centrifuge modelling test.

The model utilized in this centrifuge test was prepared March 6, 2019. After a 28-day curing period, the sample was processed for centrifuge spinning. Table 5-5 demonstrates the basic information of the sample and the parameters used for the centrifuge test. As mentioned previously, formula F7-14 (Spk: S325 = 40: 60, total soil-water content = 2.5 times the liquid limit, the total soil-water to cement ratio = 3) is used to make the synthetic Clearwater shale. The initial height of the soil-water-cement mixture in the PSB is approximately 22 cm. After a 28-day curing period, due to the shrinkage of the mixture, the final height is 20 cm. At 100 g, the model can be used to mimic the behaviour of a caprock of 20 m thickness. The overburden on the caprock is simulated through an appropriate thickness of lead bars. In this study, the weight of lead bars is about 72.9 kg, which corresponds to a 24 m thick in-situ overburden.

The expansion of the steam chamber is mimicked through the custom-built device known as the GeoCDM. Detailed information of this device has been shown in the previous chapter. It is worth noting that this test intends to mimic the deformation behaviour of the caprock that is continuously uplifted by the steam chamber for up to 15 years. The corresponding shearing time in the centrifuge is about 13 hours. To achieve this goal, the jog velocity, which is an important parameter controlling the velocity of the GeoCDM, is 0.514403292. The corresponding uplifting velocity of the uplifting table is 0.000428669 mm/s. The image is taken at 60-second intervals. Based on the relationship between the uplifting velocity and the corresponding displacement:

$$v = \frac{L \times 1200}{t} \qquad \text{Equation (5-2)}$$

where L = Uplift displacement, in mm

v = Uplifting velocity, in mm/s

t = Elapsed time, in s

Based on the values provided above, the incremental vertical displacement of the GeoCDM lifting table between two adjacent images is 0.0257 mm.

Table 5-5 Sample information of the third centrifuge modelling test

Slurry preparation					
Speswhite kaolin clay: Sil325	40:60				
Liquid limit	32.81				
Plastic limit	18.23				
Normalized water content	2.5				
Total soil-water to cement ratio	3				
Sample preparation					
Initial height, cm	22.00	21.70	21.50	21.80	22.30
Final height, cm	20.00	20.10	19.90	20.10	20.20
Weight of lead bars, kg	72.9				
Vertical pressure at 100 g, kPa	510.82				
Overburden height, m	24.22				
Parameters for GeoCDM					
Jog velocity	0.5144				
Jog accelerating	2				
Jog distance (mm)	24000				
Shearing time, hr	12.96				
The corresponding prototype time, yr	15				

Initially, it was planned that the plots could be generated for every 1 mm of the uplifting table displacement. However, the analysis indicates that the cumulative uplifting table displacement of 0, 1, 5, 10, 15 and 20 mm is sufficient to describe the failure process of the caprock. The following figures provide the interpreted response of the centrifuge model at the end of the prototype time period of 15 years. Figures of early responses (1 yrs, 3 yrs, 5 yrs, 10 yrs and 15 yrs) are provided in Appendix D.

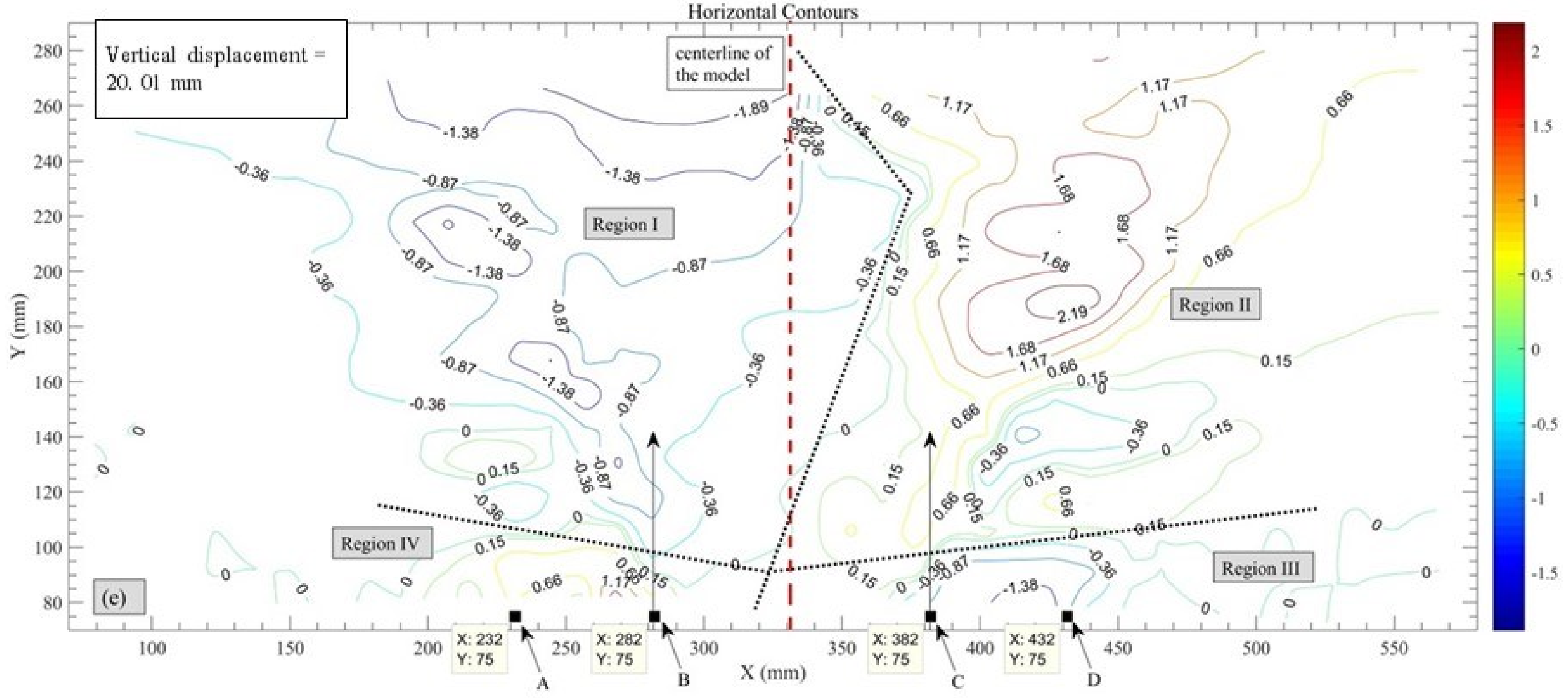

Figure 5-14 Evolution of horizontal displacements – t = 15 yrs

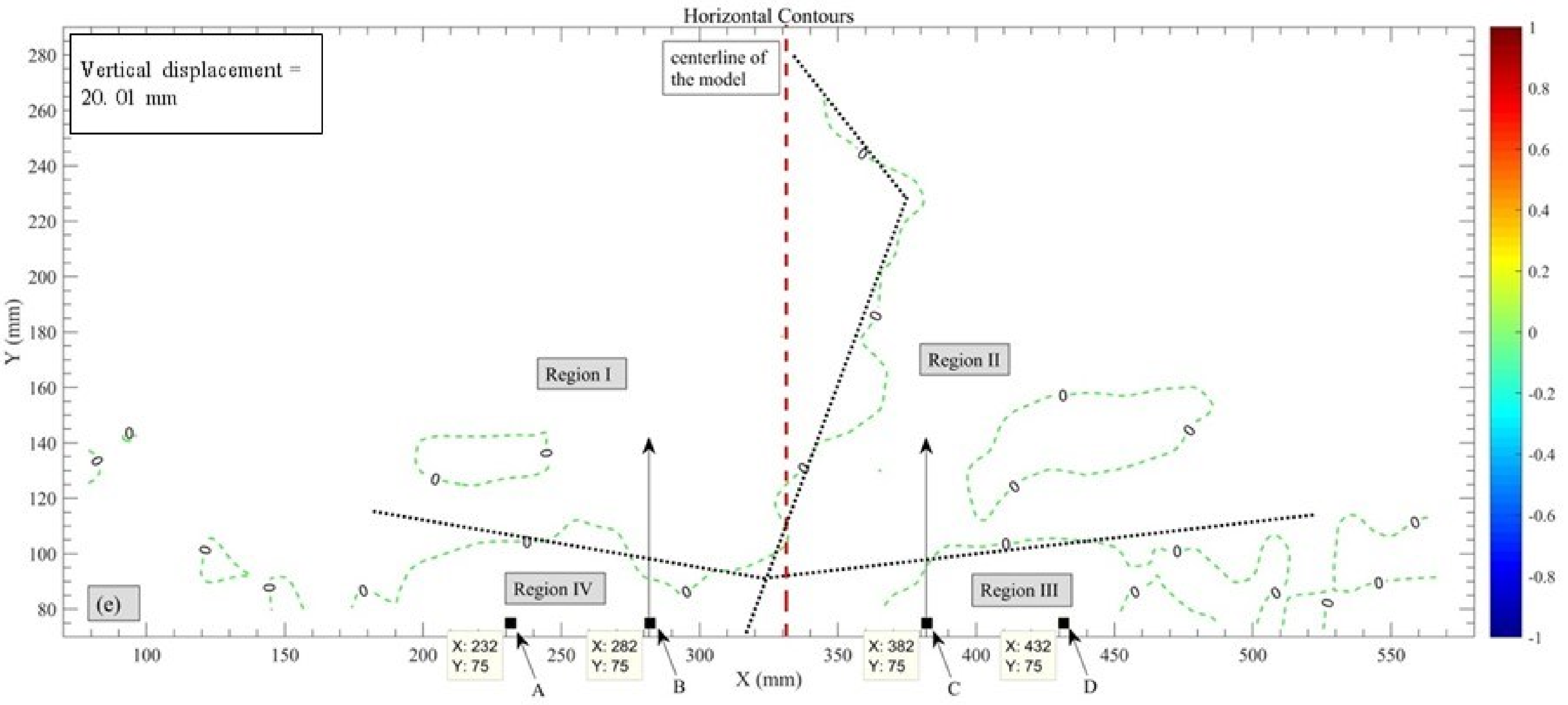

Figure 5-15 Evolution of boundary zones in the model – t = 15 yrs

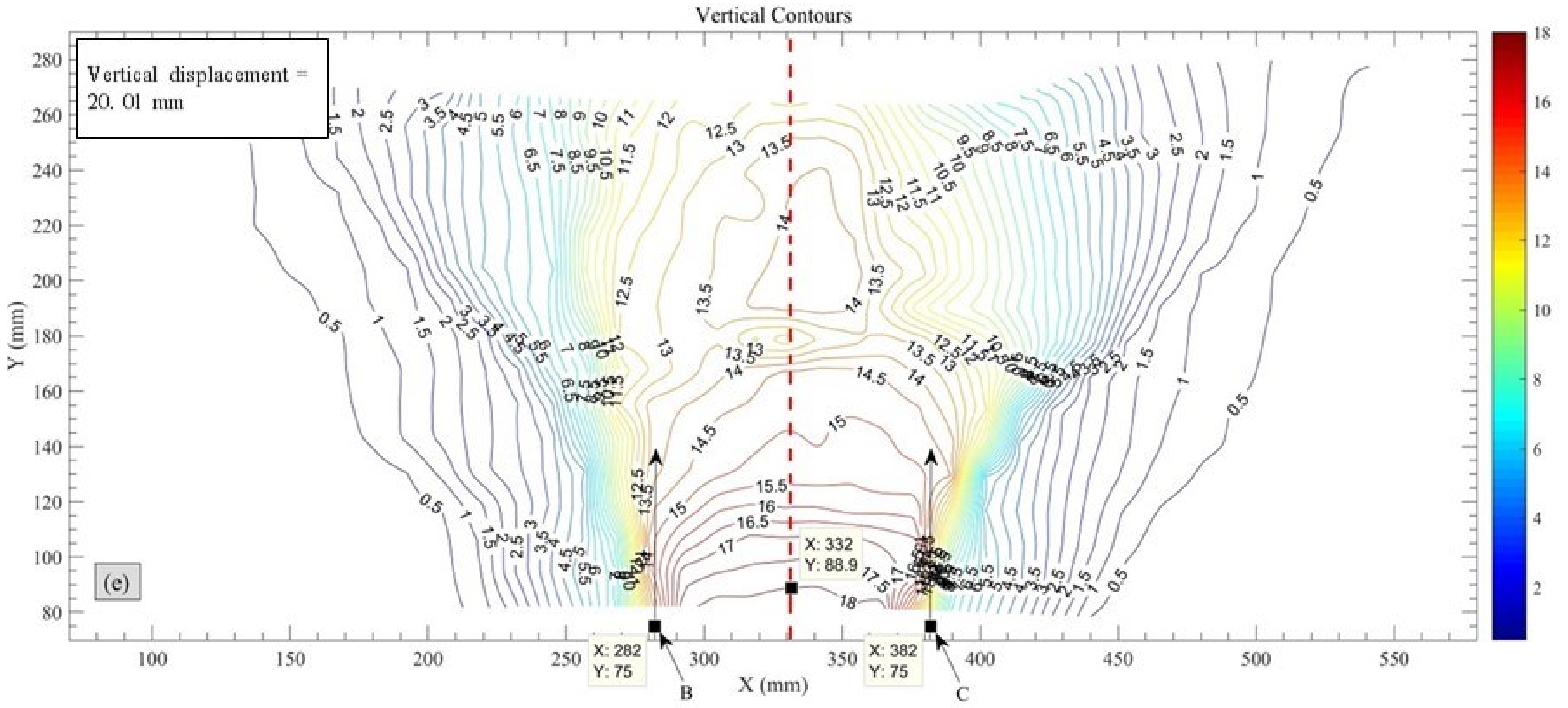

Figure 5-16 Evolution of vertical displacements – t = 15 yrs

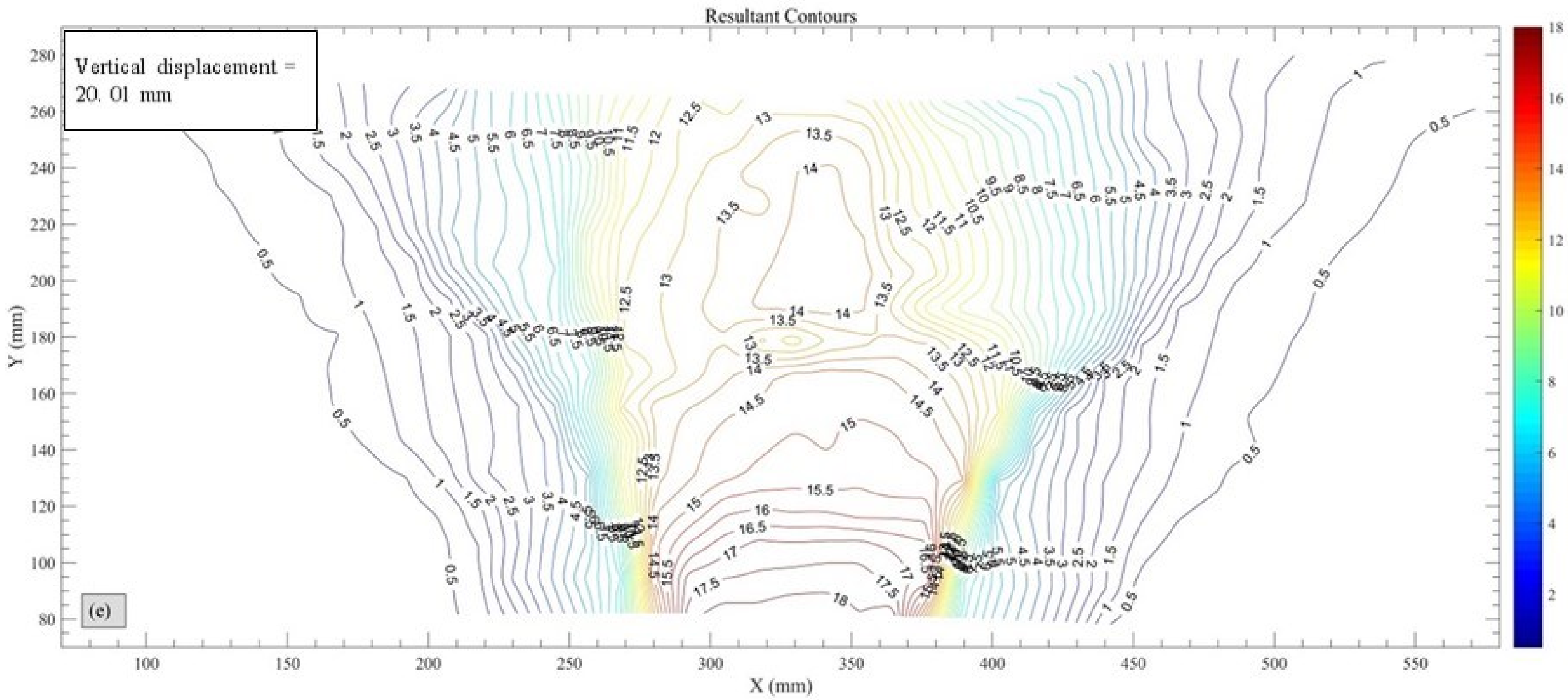

Figure 5-17 Evolution of resultant (total) displacements – t = 15 yrs

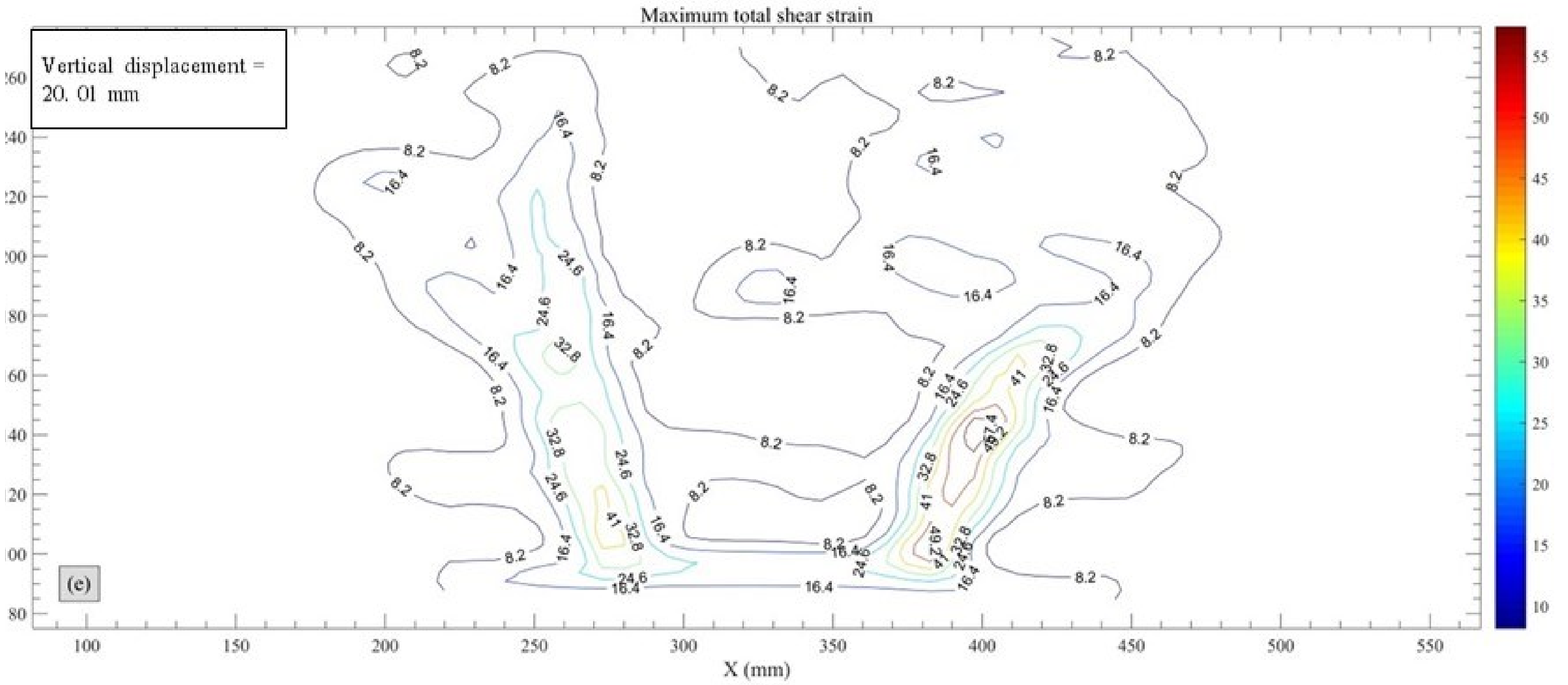

Figure 5-18 Evolution of maximum shear strain – t = 15 yrs

5.6.2 Experimental Observations – 15 years

During the centrifuge modeling test, a few fractures at the top of the model develop in the vertical direction but these cracks only extend downward in the model for a few centimeters and then stop developing. A few tiny cracks are observed at the middle height of the model as the test proceeds, similar to what was observed during the previous two centrifuge modelling tests. However, based on the direction that these cracks developed; these fractures can be divided into three parts. As the fracture propagate towards the model's top surface, it tends to bend toward the horizontal as the GeoCDM moves up. However, the dip angle of the fractures close to the bottom of the model becomes steeper compared with that at the middle height of the model.

As the GeoCDM continues pushing the model up, the width of these cracks enlarges, making it clear to track the direction. Meanwhile, a few tiny cracks can also be observed at the bottom of the model. However, it is difficult to detect the forces that lead to these fractures based on the geotechnical centrifuge modelling test.

Intuitively, the soil particles at the left side of the centreline move towards the –X direction, while those at the right side move towards the +X direction.

5.7 Summary

This chapter presents the experimental results of the three geotechnical centrifuge modelling tests. These tests were motivated by the conditions surrounding the Joslyn steam release incident and included as assessment of the impact of the steam chamber expansion rate on the caprock deformation behaviour. The GeoCDM is used to mimic the uplift imposed on the base of the caprock because of steam chamber evolution. The prototype time of the three centrifuge modelling tests is 3, 10, and 15 years, respectively.

The coordinates of the control markers are indispensable to transfer the caprock deformation behaviour from the image-space to the object-space. Moreover, obtaining the coordinates of the uplifting table and the flanks are very important for the understanding of the development of the zones of concentrated shear strain within the models.

To ensure the consistency of the material properties, the soil used in the models were based on the formulation described in Chapter 4. The well-mixed slurry is transferred to the PSB for curing and after being cured for 28 days, the sample is then placed in the swing cradle for the centrifuge modelling test. The final height of these models is 20 cm to mimic the behaviour of the caprock with 20 m thickness.

The sample is consolidated in the centrifuge for at least 8 hours prior to activating the GeoCDM. Immediately after GeoCDM uplift table begins moving, the caprock deformation behaviour is recorded through the high-resolution camera at constant time intervals. The GeoPIV_RG program is used to analyze these images. The PIV-interpreted values of the horizontal displacement, vertical displacement, resultant (total) displacement and maximum total shear strain have been illustrated to show how the caprock behaves under the test conditions.

Chapter 6 Analysis of Centrifuge Tests

6.1 Introduction

The experimental results from three high quality centrifuge modelling tests were presented in Chapter 5. This chapter provides more extensive discussion of the evolution of the horizontal displacements, vertical displacements, resultant (total) displacements and maximum total shear strains, interpreted from digital images captured during each centrifuge test.

6.2 Analysis of the caprock failure process

The soil used in the three main physical modelling tests conducted for this research is the synthetic Clearwater shale formulation discussed in Chapter 4. Compared with the consolidated Speswhite kaolin clay and the synthetic Clearwater shale-I, strength of the synthetic Clearwater shale is relatively strong exhibiting an unconfined compressive strength more than 1 MPa. Consequently, the deformation behaviour of the caprock centrifuge models is expected to differ from the early pair of tests discussed in Chapter 3.

6.2.1 Evolution of the vertical displacement contours

Through the analysis of evolution of the vertical displacement contours, it is evident that the uplifting table serves as the origin of vertical displacements, as expected. Through the analysis of the vertical displacement of these soil particles on the same line perpendicular to the uplifting table, soil above the uplifting table is pushed upward. With the increase of distance from the uplifting table, soil particles' vertical displacement decreases. For these soil particles along the centreline of the model, the vertical displacement gradually decreases towards the model surface. This phenomenon does not coincide well with previous studies performed by Ilamparuthi, Dickin,

& Muthukrisnaiah (2002). These researchers find that the displacement of the soil particles up to a certain height is greater than that of the anchor itself. However, when the embedment depth of the anchor is very large, the displacement of the soil particles progressively decreases towards the model surface, indicating that the embedment depth has a significant impact on soil particles' vertical displacement. For instance, when embedment depth reaches a certain height of 691 mm, the displacement of soil particles is confined to a certain height. Liu, Liu, and Zhu (2012) also find that deformation of loose sand occurs within a bulb-shaped zone as the embedment depth enlarges. This bulb-shaped zone emerges from the edge of the anchor and extends to a certain height, which is usually two times the anchor diameter within the sample. Meanwhile, the researchers concludes that the deformation is mainly induced by the compression based on the gradient change of the displacement, indicating that displacement of these soil particles above the anchor is less than that of the anchor itself. For this study, with the increase of vertical distance between the particle and the uplifting table, the vertical displacement decreases, indicating that soil above the uplifting table is compressed as the uplifting table moves up. Therefore, at this stage, it seems that the compromise of caprock integrity may be induced by shear failure.

On any horizontal plane above the uplifting table, the vertical displacement of these soil particles decreases from the centreline of the model in the radial direction. The gradient decreases as the distance from the centreline of the model increases. The vertices of the uplifting table, point B and C as shown in Figure 6-1, seem to be the most highly strained areas. This conclusion is deduced from the phenomenon that the gradient of the vertical displacement contours changes rapidly at the two points. This observation makes sense because the two points (Pt. B and C) mark the boundary of the applied force, indicating that the two points are the place where the stress concentration occurs. The report, "*Summary of Investigations into the Joslyn May 18th 2006 Steam*

Release”, released by Total E&P Canada Ltd. also demonstrates that the vertices of the pressurized zone are the highly strained areas. The development of the areas can eventually provide conduit for the injected steam during SAGD process. As shown in Figure 6-8, these fractures originate from the uplifting table and propagates towards the model surface. Therefore, determining radius of the pressurized zone becomes one of the priorities when operating SAGD projects because vertices of the pressurized zone may be the origin of caprock compromise.

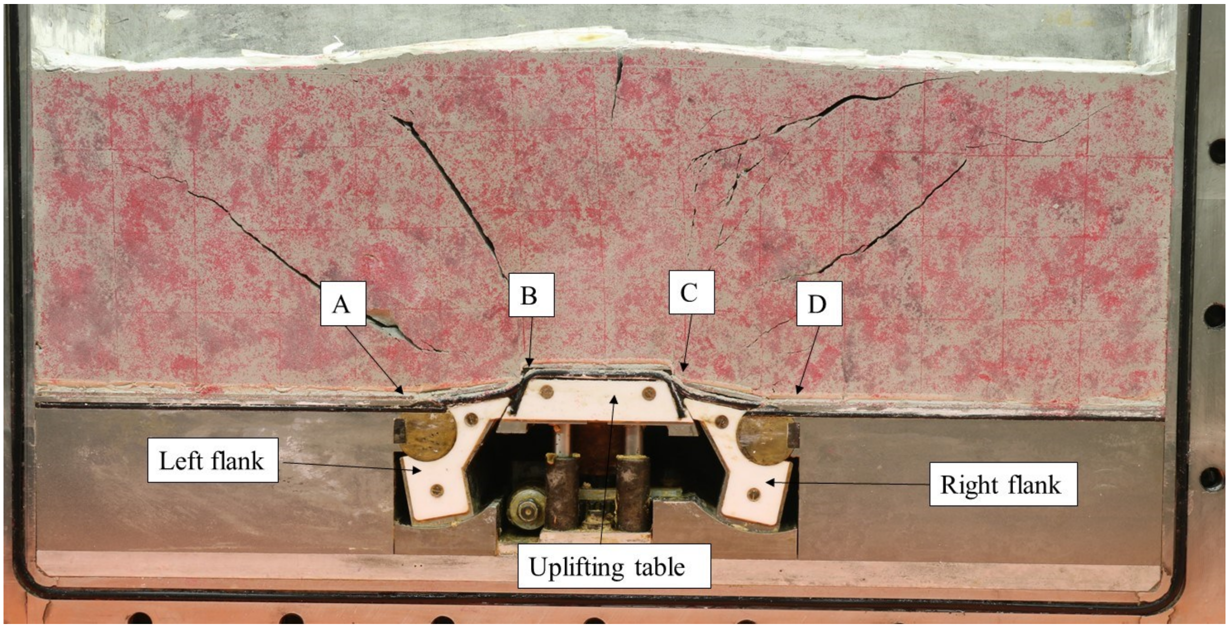

Figure 6-1 Position of flanks and uplifting table

Moreover, the vertical displacement contours seem to be symmetrical with reference to the centreline of the model. This phenomenon is evident when the uplift displacement of the uplifting table is larger than 1 mm. Meanwhile, these contours form concentric ellipses, one after another. For contours with large values, the major axis coincides with the uplifting table. With the decrease of the contour value, the direction of the major axis changes from the horizontal direction to the vertical direction, which coincides with the centreline of the model. As the value of the contour decreases, the ellipse turns to a bowl-shaped curve. Surface heave accompanied by vertical fractures is also observed.

Based on numerical simulation results provided by "*Summary of Investigations into the Joslyn May 18th 2006 Steam Release*", the model focusing on dilation strain around steam injectors demonstrates that the surface heave is only about 12 mm. The geotechnical centrifuge modelling results not only show the surface heave but also the development of vertical fractures at the top surface of the model as the uplifting table moves up.

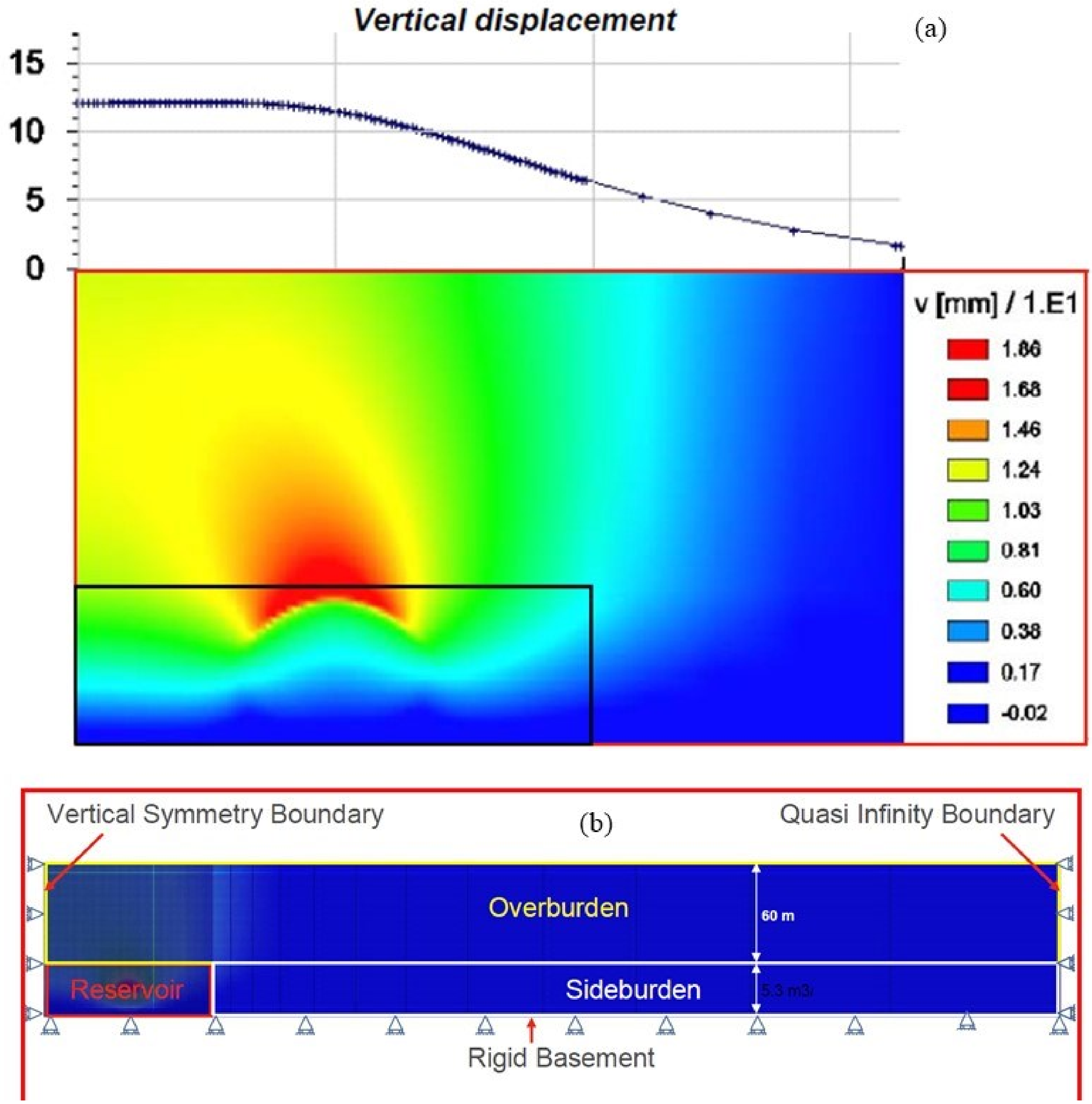

Figure 6-2 Vertical displacement (a) and finite element model (b) for the calculation of dilation strains around steam injectors (Total E&P Canada, 2007)

Figure 6-3 illustrates the vertical displacement contours from a finite model. It shows that the evolution of the vertical displacement contours also emerges from the pressurized zone, and the shape of the contour forms a bowl-shaped curve, which coincides well with the geotechnical centrifuge modeling results presented in this study.

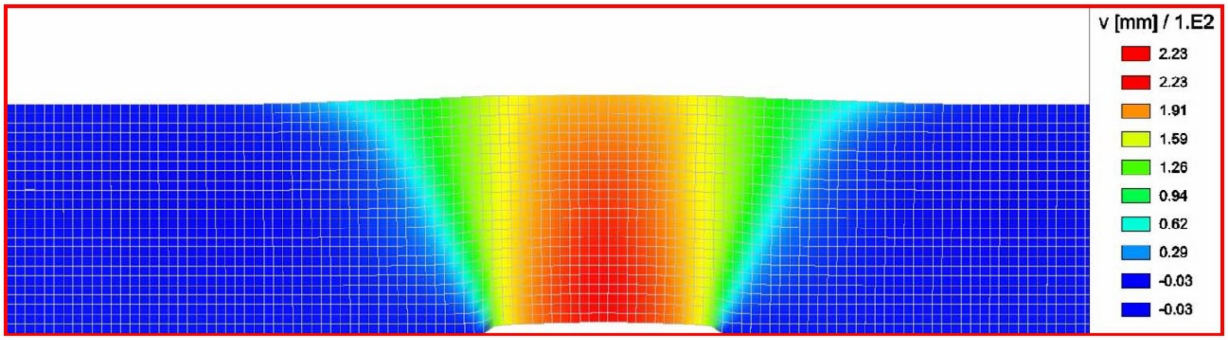

Figure 6-3 Vertical displacement from the finite element model provided by Total E& P Canada Ltd. (Total E&P Canada, 2007)

6.2.2 Evolution of the horizontal displacement contours

The model can be divided into four different regions based on the horizontal displacement. The boundary between different regions therefore becomes the fragile area at which shear or tensile fractures can initiate. As shown in these plots in Appendix D regarding the evolution of the horizontal displacement contours, a positive value indicates that soil particles move towards +X direction, while a negative value implies that direction of the horizontal displacement is towards -X. A, B, C and D mark out the flanks and the uplifting table. Here, the definition of the topographic prominence is used to describe both the positive and negative peak value of the horizontal displacement contours. In this study, the positive peak value is referred to as the positive prominence, while the negative peak value is simplified as the negative prominence. The third test is the last test and prepared with sophisticated construction methodology, thus providing the most representative results of caprock deformation behaviour, this thesis analyzes the experimental results in detail and aims to use them to describe the evolution of the horizontal displacement.

As shown in Appendix D, region I of the third test marks out the negative prominence while Region II marks out the positive prominence. Future analysis shows that the two peaks, which are of the same value, are almost symmetrical with respect to the centreline of the model. As the uplifting table continues to 5 mm displacement, the prominences develop but the location does not change. Meanwhile, there is a positive prominence with the location at the centre of line AB, and a negative prominence with the location at the centre of line CD. However, in general, the soil particles at the left side of the centreline should move towards –X direction, while those at the right side should move towards +X direction. The emergence of the positive prominence at the left side and the negative prominence at the right-side conflicts with intuitive judgement. The horizontal displacement contour with a value of zero separates the positive prominence from the negative prominence. In this study, the contour with a value of zero is used as the boundary of different regions.

Immediately after the formation of the boundary between Region I and Region IV, the location of the boundary does not change with the upward movement of the uplifting table. It is also the same fact for the boundary between Region II and Region III. However, for the boundary between Region I and Region II, the location changes slightly with the development of the upward movement of the uplifting table. For instance, when the upward displacement is about 1 mm, the boundary between Region I and Region II is not so clear. At this stage, only the lower part of the model is affected by the uplift force while other parts keep stationary. However, when the upward displacement is 5 mm, the boundary between Region I and Region II separates the model into two parts. Meanwhile, the boundary does not conincide with the centreline of the model. Instead, the upper part of the boundary is located at the right side of the centreline, while the lower part is located at the left side. Because of low tensile strength of the model material, this boundary may lead to the formation of tensile fracture at the upper part of the model. The lower part of the model may have the potential to form the tensile fracture. However, due to the high horizontal stress, tensile fracture may be prohibited by the high stress.

Similar results are also presented in "*Summary of Investigations into the Joslyn May 18th 2006 Steam Release*" released by Total E&P Canada Ltd., as shown in Figure 6-4. In this model, positive strains indicate stretching which might lead to fracture opening. The model can also be divided into different regions based on the sign of horizontal strains. The boundary between each region is therefore becomes the fragile area at which tensile or shear fractures can initiate. The report points out that the tensile strains at the vertices of the sheared zone may eventually provide conduit for the injected steam.

At the initial stage, the value of the horizontal displacement is very small. As the uplifting table moves up, the soil is displaced laterally, and the horizontal movement of these soil particles enlarges. The concentration of the horizontal displacement contours around the vertices of the uplifting table is clearly seen in each subplot. This phenomenon exists at the five stages for all the three physical modelling tests. As the uplifting table moves up, the uplifting table and the flanks are the most highly strained areas. This makes sense because these areas are the locations where the movement starts. The same phenomenon is also observed in the numerical simulation tests provided by "*Summary of Investigations into the Joslyn May 18th 2006 Steam Release*".

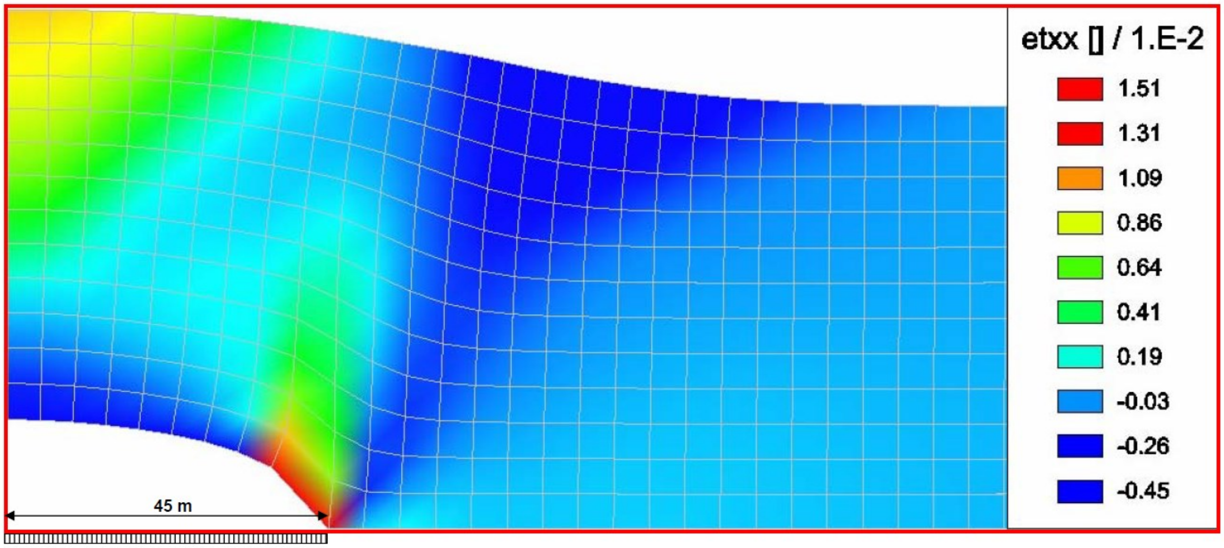

Figure 6-4 Horizontal strains from the finite element model provided by Total E& P Canada Ltd. (Total E&P Canada, 2007)

6.2.3 Evolution of the resultant (total) displacement contours

The resultant displacement contours are very similar to those of the vertical displacement contours. The major reason leading to this phenomenon is that the magnitude of the vertical displacement is many times larger than that of the horizontal displacement. Therefore, the vertical displacement plays a major role in the magnitude and direction of the resultant displacement.

At the initial stage (1.0 mm upward displacement), the resultant displacement contours form an ellipse with the major axis coinciding with the uplifting table. As the uplifting table moves up, soil particles adjacenet to the uplifting table are motivated firstly. The motion then propagates radially towards to the edge of the model. Undoubtedly, with the increase of the radius from the centre of the uplifting table, the resultant displacement decreases. When the contour reaches the top surface of the model, it breaks into two parts which are symmetrical with respect to the centreline of the model. Meanwhile, the gradient of the resultant displacement contour rapidly changes at the vertices of the uplifting table, indicating that the two points are the highly strained areas.

As the upward displacement continues to 5 mm, 10 mm, 15 mm and 20 mm, the above mentioned analysis also exists. It is worth noting that the maximum resultant displacement shown in Appendix D is pretty close to the upward displacement of the uplifting table, indicating that soil particles adjacenet to the uplifting table also have horizontal displacement, even though the value may be very small.

6.2.4 Evolution of the maximum total shear strain

This study adopts maximum total shear strain as the criteria for determining the position of the failure surface since it has been used successfully by other researchers (J. Liu et al., 2012; Yamamoto & Kusuda, 2001). When the uplift displacement is about 1 mm which corresponds to 0.1 m prototype displacement, there is no clear strained area.

As the uplifting table moves up, the highly strained area emerges. From the analysis of the five subplots of each geotechnical centrifuge modelling test, it is evident that there exists two highly strained areas. The first one is at the left vertex of the uplifting table, and the second one is at the right vertex of the uplifting table, which coincides well with the results from the report provided by Total E&P Canada Ltd., as shwon in Figure 6-6. With the increase of the uplift displacement, the highly strained area develops and propagates at a dip angle of approximately 65^{o} to the horizontal line, as shown in Table 6-1. Based on the information provided by Table 6-1, it is quite difficult to identify the effect of the uplifting velocity on the characteristics of the failure planes.

Table 6-1 Dip angle of the failure planes of the three tests

Test No.	Left failure plane	Right failure plane	Prototype time, yr
The first test	61	69	10
The second test	62	63	3
The third test	72	65	15

A comparison between the geotechnical centrifuge modelling results and numerical simulation results provided by "*Summary of Investigations into the Joslyn May 18th 2006 Steam Release*" is made. As shown in Figure 6-5, as the radius of the pressurized zone enlarges, the plastic shear strain (or norm of plastic deviatoric strain) increases. The numerical simulation test shows that vertices of the pressurized zone are the highly strained area whatever the radius of the pressurized zone is, which coincides well with the results of the geotechnical centrifuge modelling tests.

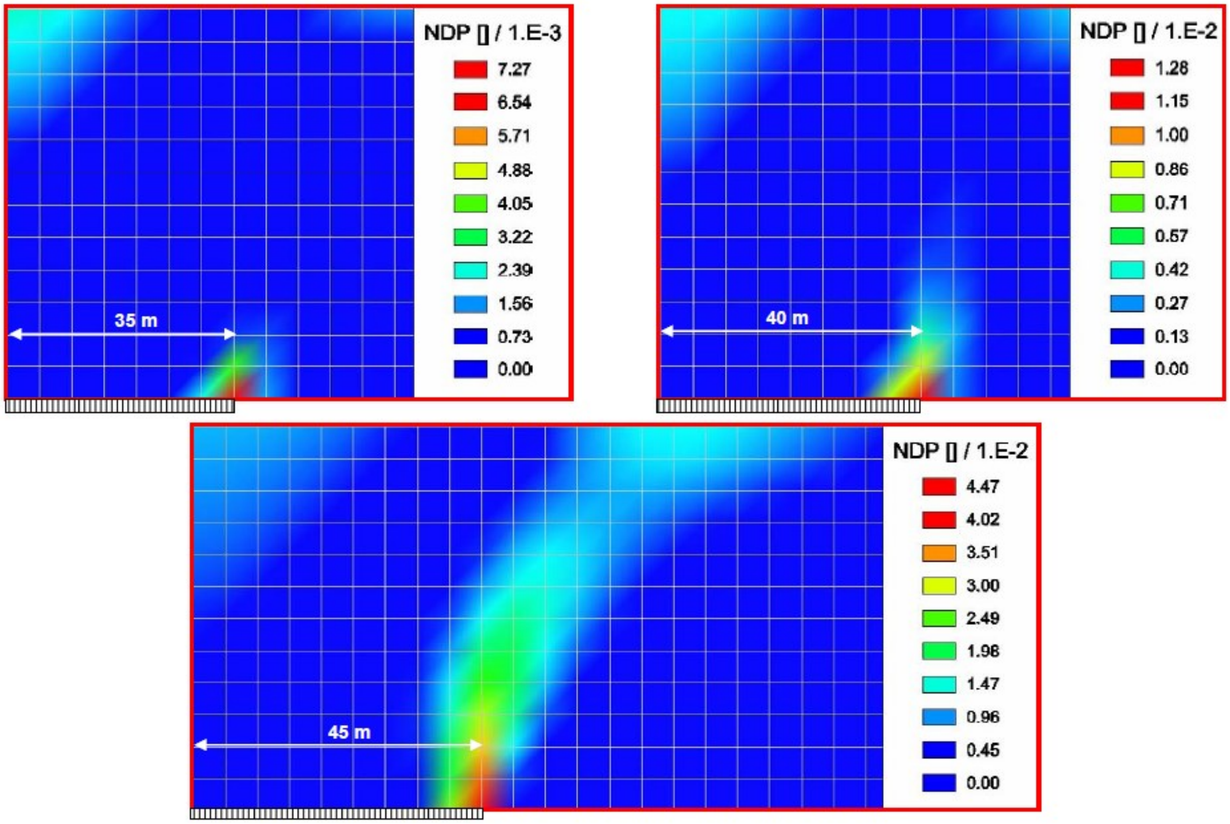

Figure 6-5 Norm of plastic strain versus radius of the pressurized zone (Total E&P Canada, 2007)

As shown in Figure 6-6, the highly strained area is almost vertical at the bottom of the model. With the decrease of model depth, dip angle of the highly strained area decreases. The same phenomenon is also observed in the geotechnical centrifuge modelling tests as shown in Figure 6-7 and Figure 6-8.

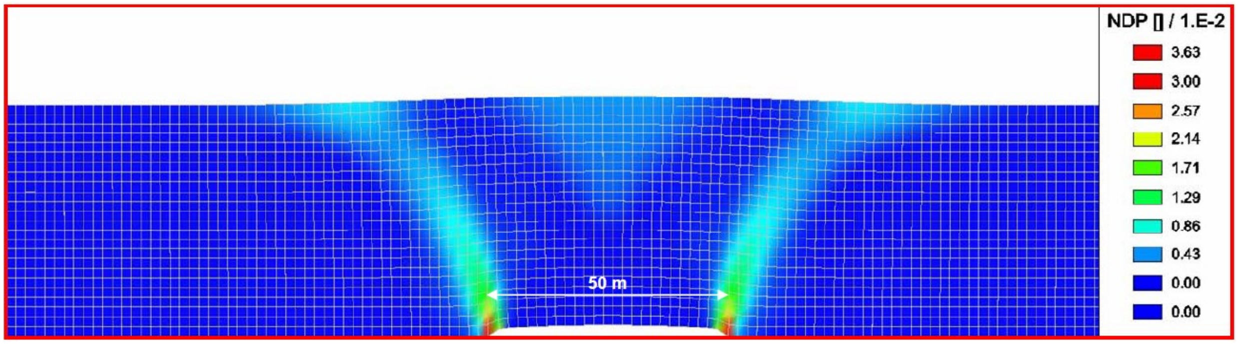

Figure 6-6 Norm of plastic strain from a finite element test provided by Total E&P Canada Ltd. (Total E&P Canada, 2007)

When analyzing the characteristics of these failure planes shown in Figure 6-7, a few interesting points can be obtained:

1. When the prototype time is 3 years, the corresponding failure plane is a curvature. At the bottom of the model, the failure plane is almost perpendicular to the uplifting table. With the decrease of the model depth, the failure plane turns into a straight plane and eventually extends to the model surface. This phenomenon coincides well with the results shown in "*Summary of Investigations into the Joslyn May 18th 2006 Steam Release*", as shwon in Figure 6-6.
2. When the prototype is 10 years and 15 years, the failure plane is a straight plane at the bottom of the model, and then gradually turns into a curvature as the model depth decreases.

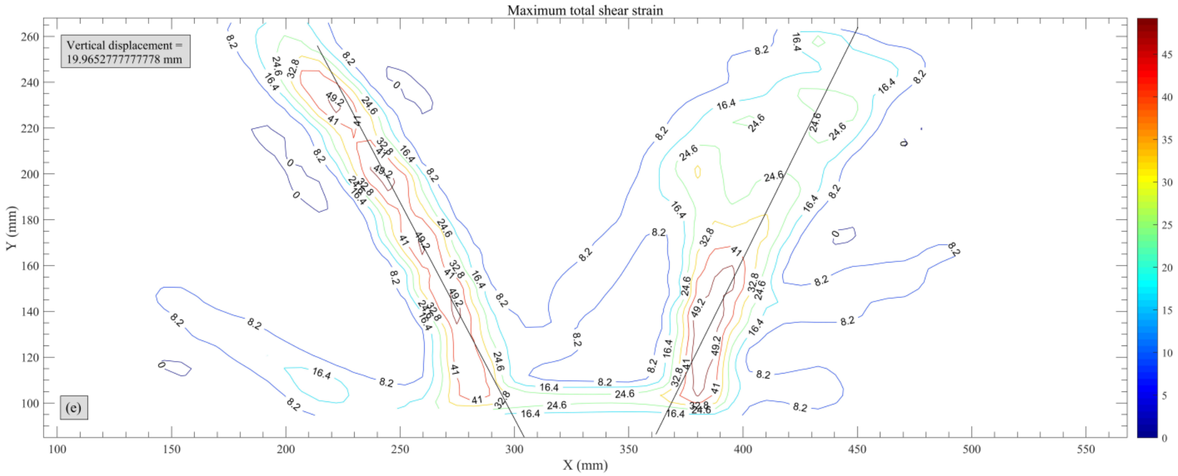

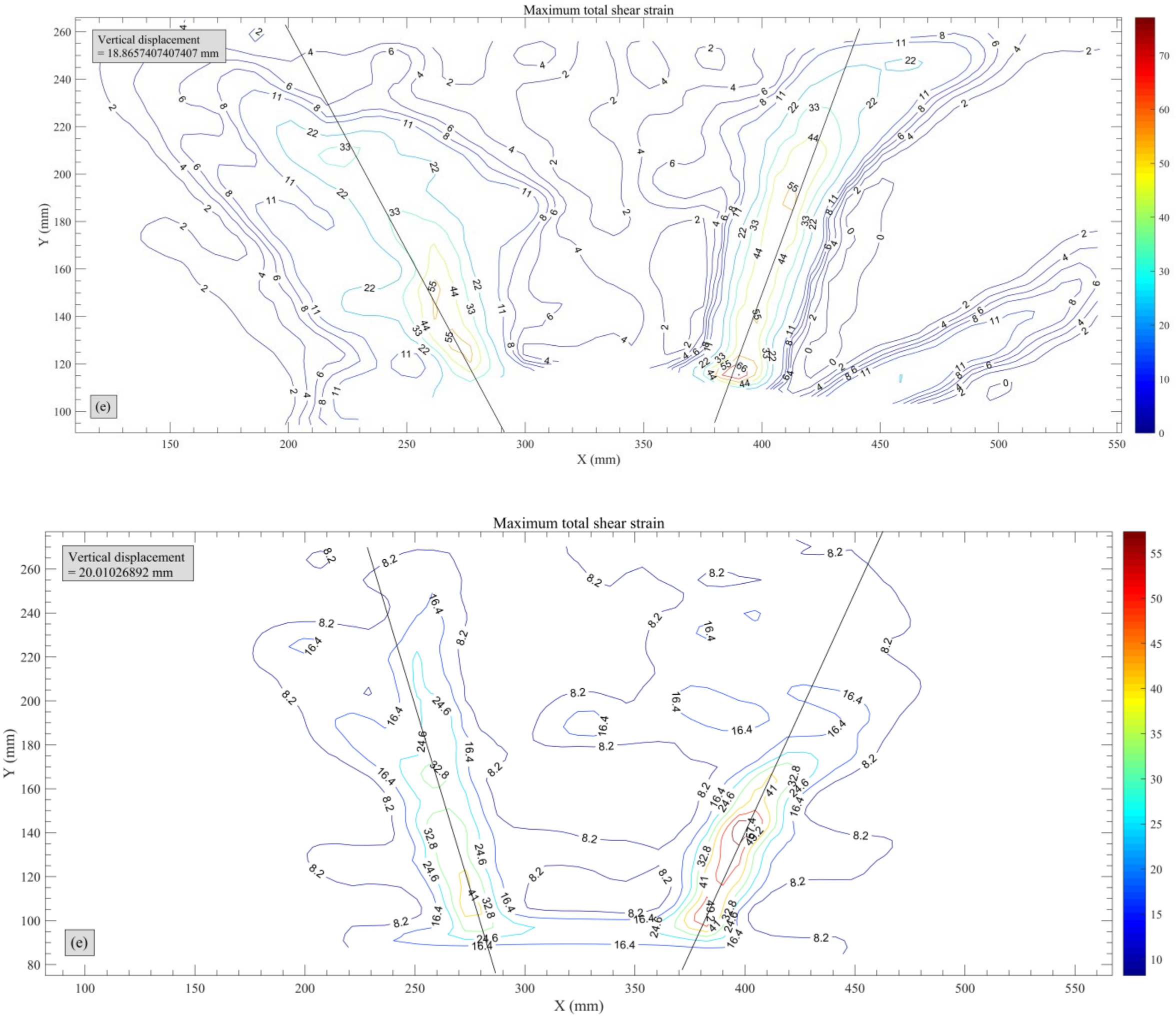

Figure 6-7 The failure planes of the three physical modelling tests: the first test (prototype time = 3 years), the second test (prototype time = 10 years) and the third test (prototype time = 15 years) in sequence

Figure 6-8 demonstrates the fractures in the sample after the physical modelling tests. A few interesting points can be obtained from the analysis of these images:

1. Surface heave is observed in the three geotechnical centrifuge modelling tests.
2. Vertical fractures accompanying surface heave initiate at the top surface of the model and propagate towards mid-height of the model whatever the uplifting velocity is. Based on the analysis of the horizontal displacement contours, the vertical fractures at the top of the model is the combined result of uplift movement of the model and the low tensile strength of the

model material. However, vertical fractures of the three tests only propagate towards the mid-height of the model for a few centimeters and then stops propagating as the uplifting table still moves up. Moreover, with the increase of model depth, the width of these vertical fractures decreases, indicating that high horizontal stress can effectively prohibit the development of tensile fractures. Field data shown in report "*Summary of Investigations into the Joslyn May 18th 2006 Steam Release*" also shows surface heave with the SAGD process. But no clear fractures were observed on the ground surface.

3. The second observation is that the inclined fractures extend to the ground surface when the prototype time is 3 years while those fractures for prototype time of 15 years seem to propagate horizontally when reaching a certain level.
4. Uplifting table and the two flanks are the origin of these inclined fractures. This observation coincides well with the numerical simulation results in "*Summary of Investigations into the Joslyn May 18th 2006 Steam Release*", demonstrating that radius of pressurized zone is also a significant factor affecting caprock integrity. Therefore, when designing a SAGD project, the engineer should not only consider material properties but also the combined effect of material properties, radius of pressurized zone and expansion rate of steam chamber.

To deepen the understanding of caprock deformation behavior, the maximum total shear strain at the four cross-sections as shown in Figure 6-9 is obtained to demonstrate the variation of maximum total shear strain on horizontal planes parallel to the X axis.

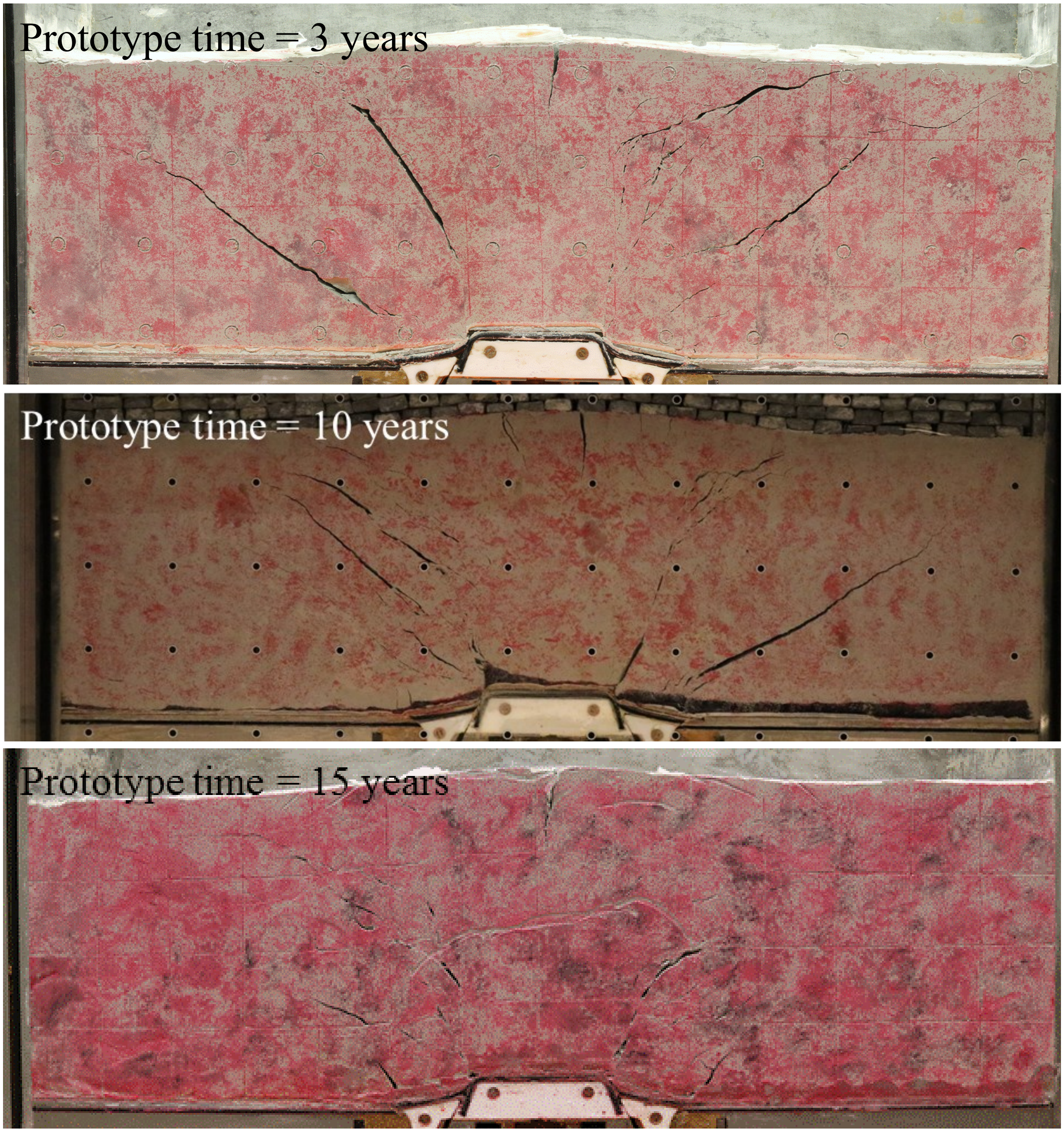

Figure 6-8 The fractures in the model after the physical modelling test: the first test (prototype time = 3 years), the second test (prototype time = 10 years) and the third test (prototype time = 15 years) in sequence

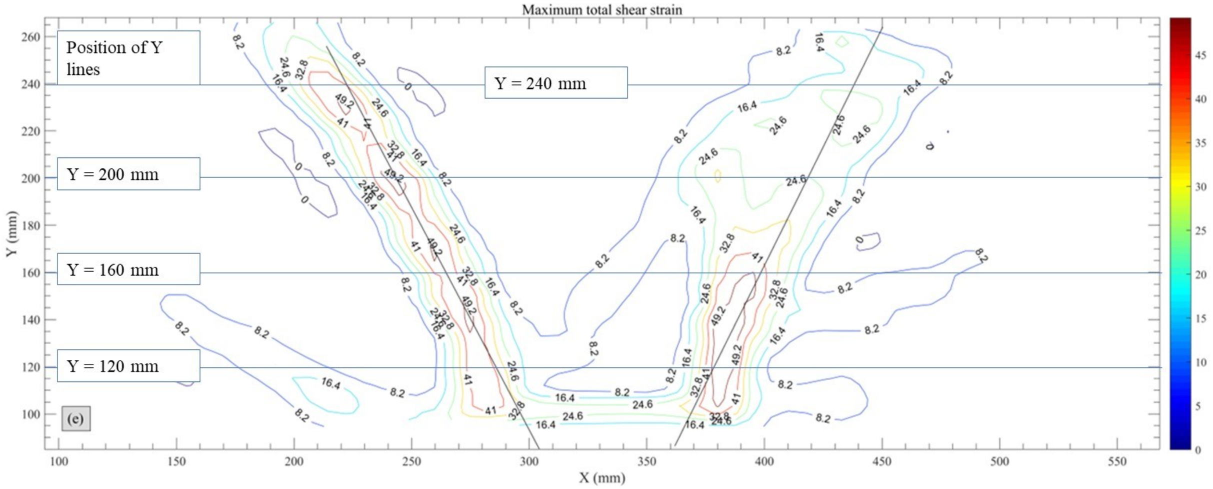

Figure 6-9 Position of different cross-sections

A few interesting points can be obtained through the analysis of Figure 6-10:

1. At the bottom of the model, soils above the flanks experience the largest maximum total shear strain. This phenomenon validates the numerical simulation results in "*Summary of Investigations into the Joslyn May 18th 2006 Steam Release*". In the report, the numerical simulation test shows that vertices of the pressurized zone are the highly strained areas. With the decrease of model depth, strain value decreases.
2. Analysis of Figure 6-10 demonstrates that the highly strained area is not above the uplifting table. It originates from the vertices of the uplifting table and then propagates towards the model surface. This observation coincides well with the numerical simulation test as shown in Figure 6-6. With the increase of Y distance, the highly strained areas move away from the centreline of the model.

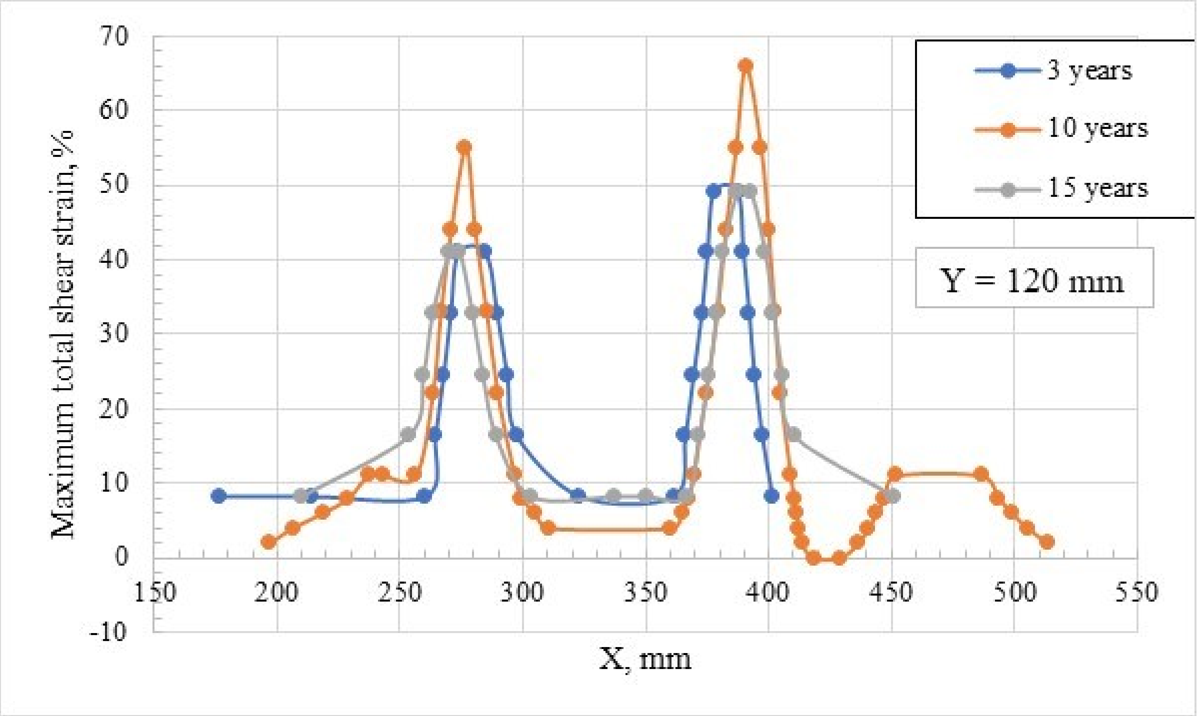

Maximum total shear strain, %
X, mm
3 years
10 years
15 years
Y = 120 mm
70
60
50
40
30
20
10
0
-10
150
200
250
300
350
400
450
500
550

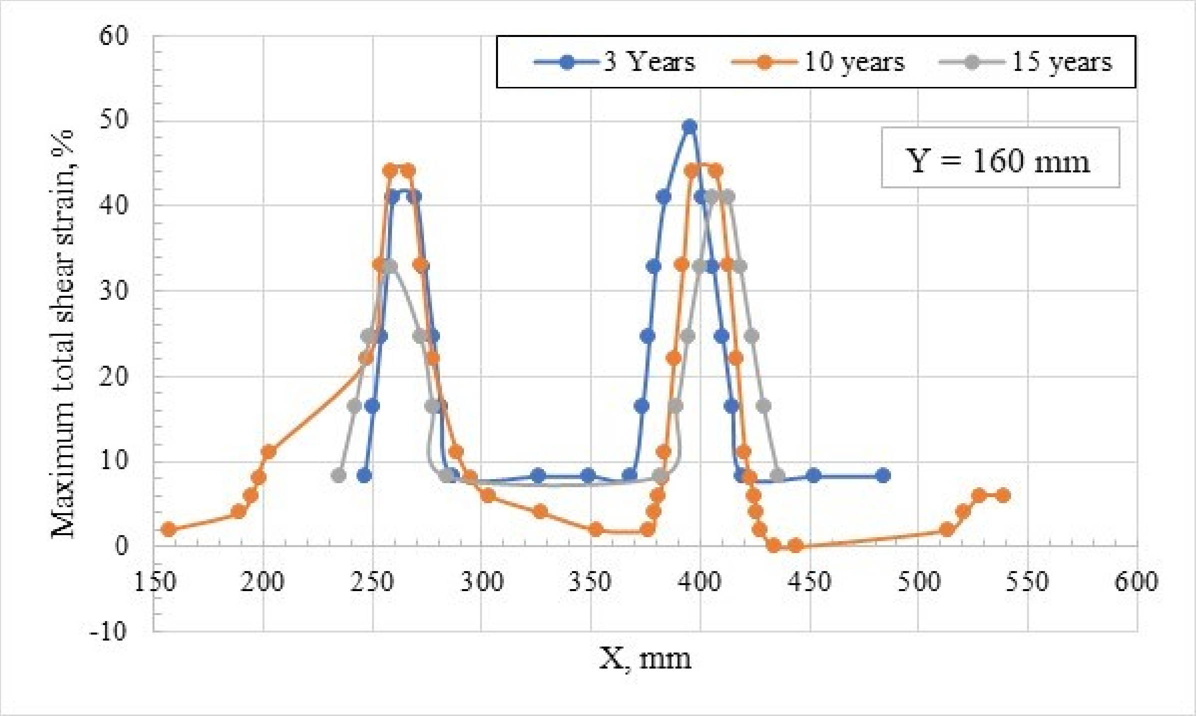

Maximum total shear strain, %
X, mm
3 Years
10 years
15 years
Y = 160 mm
60
50
40
30
20
10
0
-10
150
200
250
300
350
400
450
500
550
600

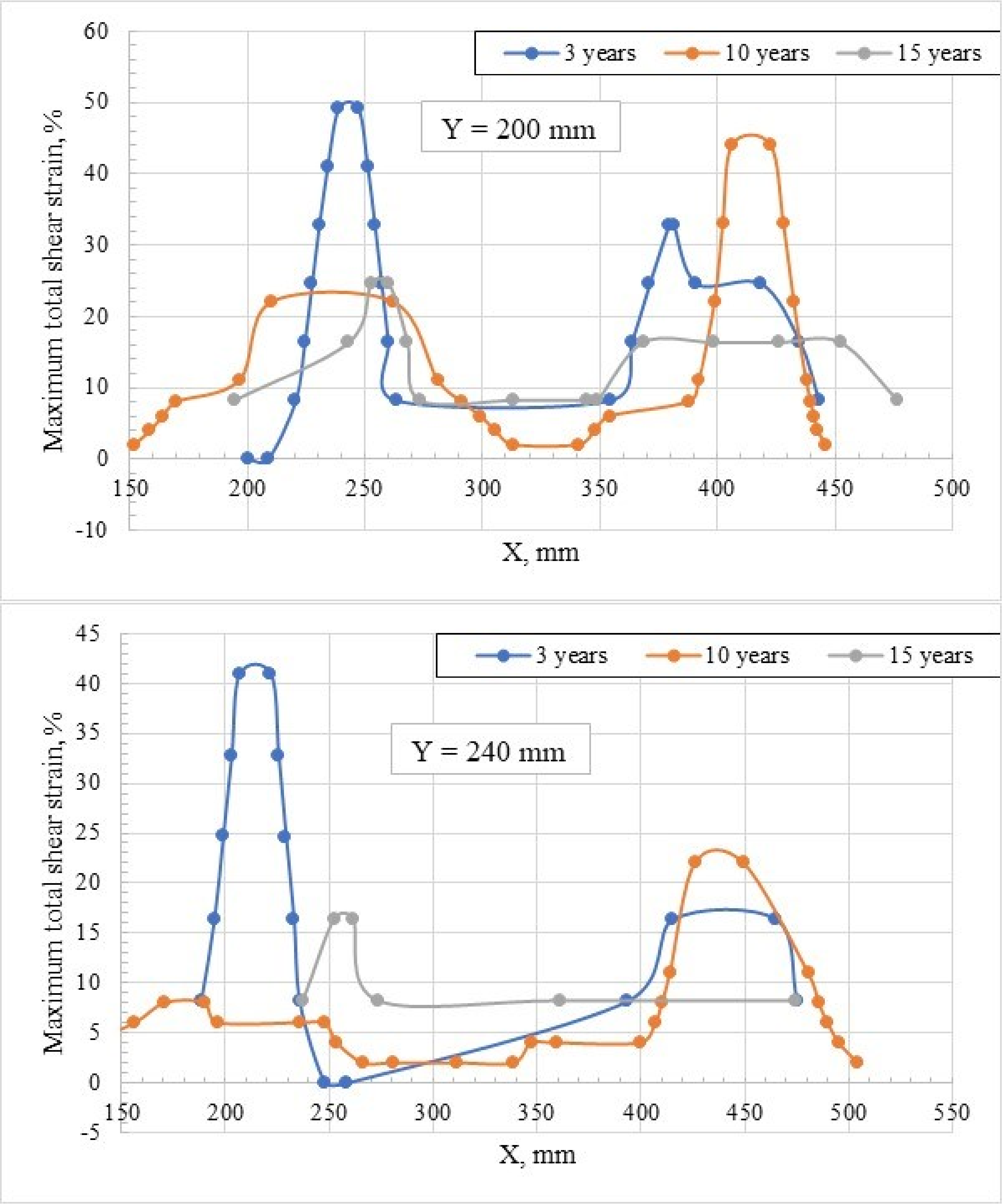

Figure 6-10 Variation of maximum total shear strain with horizontal distance X

6.3 Summary

Vertical displacement decreases with the increase of the vertical distance from the uplifting table, indicating that the soil above the uplifting table is compressed as the uplifting table moves up. On any horizontal plane above the uplifting table, the vertical displacement of the soil particles decreases from the centreline of the model in the radial direction. Moreover, the vertical displacement contours seem to be symmetrical with reference to the centreline of the model. The geotechnical centrifuge modelling results coincide well with the numerical simulation results in "*Summary of Investigations into the Joslyn May 18th 2006 Steam Release*". The three geotechnical centrifuge modelling tests show that vertical fractures initiate at the top surface of the model and then propagate towards the mid-height of the model.

The concentration of the horizontal displacement contours around the vertices of the uplifting table is seen in each subplot. This phenomenon exists at the five stages for all the three physical modelling tests. This phenomenon coincides well with the finite element model provided by Total E& P Canada Ltd. Based on the sign of horizontal displacement contours, the model can be divided into four regions. The boundary between different regions is therefore becomes the fragile area at which tensile or shear fractures can initiate. Region I marks out the negative prominence while Region II marks out the positive prominence. The two peaks, which are of the same value, are almost symmetrical with respect to the centreline of the model. Because of low tensile strength of the model material, tensile fractures may develop at the boundary between Region I and Region II. There exist a few vertical fractures at the top of the model. These vertical fractures only propagate towards the mid-height of the model for a few centimeters. The major reason leading to the short vertical fractures may be the increase of horizontal stress with depth. High horizontal stress can effectively prohibit the development of these vertical fractures.

The resultant displacement contours are very similar to those of the vertical displacement contours. The major reason leading to this phenomenon is that the magnitude of the vertical displacement is many times larger than that of the horizontal displacement. Therefore, the vertical displacement plays a major role in the magnitude and direction of the resultant displacement.

The analysis of the experimental results reveals that the failure plane emerges at the vertices of the uplifting table. However, during the centrifuge modelling test, it seems that the failure planes emerge from the middle height of the model and then propagate towards the model surface and the model bottom. A major reason for the conflict is that the horizontal stress increases with depth. Therefore, at the bottom of the model, the high horizontal stress prohibits the horizontal expansion of the fractures, making it very hard to notice the fractures.

It is quite difficult to detect the effect of uplifting velocity on caprock failure mechanism from the perspective of dip angle of the highly strained area.

Chapter 7 Conclusions and recommendation for future research

7.1 Conclusion

Centrifuge facility has been widely used in geotechnical engineering to solve complex geotechnical problems. One of the biggest advantages of the technique is that it uses small-scale samples to mimic the behaviour of large-size prototype samples. Compared with field test, the geotechnical centrifuge modelling technique is more efficient. Compared with the numerical simulation approach, the geotechnical centrifuge modelling technique can accurately reflect the actual condition.

For quite a long time, the caprock failure mechanism is studied through the numerical simulation method. This study is the first to adopt centrifuge modelling technique to identify caprock failure process.

Chapter 2 is the literature review of this study. It summarizes the basic information of the Joslyn Creek SAGD project area, including geological information, shale barriers and the possible root cause of the steam release incident. The report provided by Total E&P Canada recommends that accumulated water beneath the Clearwater shale barrier is the major reason leading to the incident. Moreover, the numerical simulation test provided by Total E&P Canada also demonstrates that the failure plane eventually reaches the ground surface with the expansion of the pressurized zone. Similarly, Collins (2005) also concludes that the burial depth, dimensions of pressurized zone, caprock thickness and strength, pay zone thickness, and injection pressure of the steam and stress changes induced by the thermal jacking are the major factors controlling caprock integrity.

Geotechnical problems, such as horizontal plate anchor, trap-door test, buried pipe, etc., that are similar to the failure process of caprock widely exist in geotechnical engineering. Numerous studies have been performed to study soil deformation behaviour induced by these “uplifting force providers,” and have provided valuable information for the identification of caprock failure process, including shape of the failure plane, variation of the vertical and horizontal stress during the uplifting process, factors affecting the failure process, and so on.

Some studies have made synthetic soil/rock for different projects. These studies serve as a reference point for this study in making synthetic Clearwater shale for physical modelling tests.

Chapter 3 briefly describes the first set of geotechnical centrifuge modelling tests. The principles, advantages and disadvantages of the geotechnical centrifuge modelling technique are briefly introduced at the beginning of this chapter, followed by the introduction of the centrifuge facility that this study uses. The major components of the experimental package include the PSB, the Mariotte bottle, the camera and so on. The assemblage of these components is described in detail.

At first, the consolidated Speswhite kaolin clay is used for the centrifuge test. However, both the mechanical properties of the material and the experimental results of the geotechnical centrifuge modelling test reveal that the material is too soft to represent the Clearwater shale. Under this condition, the synthetic Clearwater shale-I is developed. Compared with the consolidated Speswhite kaolin clay, the strength of the material is stronger. However, compared with the Clearwater shale, the material is still very weak. Under this condition, this study decides to develop a database for the development of the formula for the synthetic Clearwater shale.

Chapter 4 describes the process of establishing the database for the synthetic Clearwater shales. The experimental plan includes 10 groups, and each group has 16 recipes. The total soil-water content ranges from 1.1 times the liquid limit up to 2.5 times the liquid limit, and the total soil-water to cement ratio varies from 3 to 8. The curing time is 28 days for unconfined compression test specimens.

There exists a linear relationship between the unconfined compressive strength and the after-curing moisture content. By using the after-curing moisture content as the intermediate parameter, this study establishes the relationship between the unconfined compressive strength and the initial parameters such as the total soil-water content, the cement content and the liquid limit.

Three different methods are used to derive the after-curing void ratio: the first method considers that the total pore volume of the cured samples remains the same as before the hydration and pozzolanic reactions, the second method considers that the volume of the soil solid and cement solid does not change during the curing period, and the third method considers that the volume of the water consumed by the hydration and pozzolanic reactions totally contributes to the solid volume of the cured sample. Based on the analysis, it is believed that the accurate value of the after-curing void ratio is between the lower limit and the upper limit.

A new parameter referred to as the unconfined compressive strength per unit cement content is proposed for the quantitative analysis of the unconfined compressive strength variation with the silt-to-clay proportions. It is found that the variation of the strength per unit cement content with the silt-to-clay proportions forms a logistic curve in normal coordinates.

The rate of strength improvement is strongly dependent upon the cement content, water content and silt content. Cement plays a positive role in the strength development of cement-treated soils. But this positive effect can be neutralized by the high-water content. The existence of silt in the synthetic soil can evidently strengthen the positive effect of cement.

Chapter 5 describes the experimental results of the geotechnical centrifuge modelling tests. This chapter first introduces the process of getting the coordinates of the control markers, which are of great importance for the transfer of the information from image-space to object-space.

The information of each geotechnical centrifuge modelling test is first introduced, followed by the evolution of the horizontal displacement contours, vertical displacement contours, resultant displacement contours and the maximum total shear strains.

Chapter 6 analyzes the experimental results shown in Chapter 5. Intuitively, soil particles at the left side of the centreline of the model should move towards the –X direction, while those at the right side should move towards the +X direction. However, near the bottom of the model, the soil particles at the left side move towards the +X direction, while those at the right side move towards the –X direction. Based on the sign of the horizontal displacement contours, the model can be divided into four regions. The boundary between different regions therefore becomes the fragile area at which tensile or shear fractures can initiate. Experimental results of the geotechnical centrifuge modelling test reveal that vertical displacement of the soil particles decreases as the distance from the uplifting table increases.

A comparison is made between results from the geotechnical centrifuge modelling tests and those from the finite element model in "*Summary of investigations into the Joslyn May 18th 2006 Steam Release*". The geotechnical centrifuge modelling results show that the surface heave is accompanied by the development of vertical fractures at the top surface of the model as the uplifting table moves up. Based on the analysis of the horizontal displacement contours, the vertical fracture at the top of the model is the combined result of uplift movement of the model and the low tensile strength of the model material. However, vertical fractures of the three tests only propagate towards the mid-height of the model for a few centimeters and then stops propagating as the uplifting table still moves up. Moreover, with the increase of model depth, the width of these vertical fractures decreases, indicating that high horizontal stress can effectively prohibit the development of vertical fractures.

Both geotechnical centrifuge modelling test and numerical simulation test reveal that vertices of the pressurized zone are the highly strained areas. The failure planes emerge from the uplifting table and propagate towards the model surface. This study finds that it is difficult to find the relationship between uplifting velocity and dip angles of these highly strain areas.

7.2 Recommendations for future research

The caprock failure process is a quite complex geotechnical problem. To fully understand factors affecting the failure process, the following recommends are made for future work:

Although few physical modelling studies pertaining to the caprock failure process are performed, there are numerous studies related to soil deformation behaviour induced by the uplift forces. These studies can provide valuable information for studying the caprock failure process. Therefore, future studies should focus much more attention on collecting this literature.

Synthetic Clearwater shale is an alternative to Clearwater shale. Although a great effort has been made in the preparation of the material, there are still many differences between the synthetic Clearwater shale and the real Clearwater shale. Under this condition, it is necessary to obtain prismatic samples from the field for the centrifuge modelling test.

Permeability of the synthetic Clearwater shale is very high compared with the Clearwater shale. Under this condition, future work should use materials with similar permeability to the Clearwater shale for the physical modelling test to study the caprock deformation process under undrained, partially drained and drained conditions.

Based on the experimental results, it is very difficult to notice the effect of the uplifting velocity on the failure mechanism. Under this condition, for future tests, a load cell may be needed to study the variation of the load under different uplifting velocities.

References

Abdulhadi, N. O. (2009). An experimental investigation into the stress-dependent mechanical behavior of cohesive soil with application to wellbore instability. Ph.D. Thesis, 1–459.

Adrian, R. J. (1991). Particle-image techniques for experimental fluid mechanics. Annual Review of Fluid Mechanics, 23, 261–304. https://doi.org/10.1146/annurev.fl.23.010191.001401

Al-Tabbaa, A., & Wood, D. M. (1987). Some measurements of the permeability of kaolin. Geotechnique, 37(4), 499–514.

Amelung, F., Jónsson, S., Zebker, H., & Segall, P. (2000). Widespread uplift and 'trapdoor' faulting on Galapagos volcanoes observed with radar interferometry. Nature, 407(6807), 993–996.

Anantanasakul, P., Yamamuro, J. A., & Kaliakin, V. N. (2012). Stress-strain and strength characteristics of silt-clay transition soils. Journal of Geotechnical and Geoenvironmental Engineering, 138(10), 1257–1265. https://doi.org/10.1061/(ASCE)GT.1943-5606.0000692.

Asef, M., & Farrokhrouz, M. (2013). Shale engineering: Mechanics and mechanisms (First). Press, CRC.

Azad, A., & Chalaturnyk, R. J. (2011). Numerical Study of SAGD: Geomechanical-Flow Coupling for Athabasca Oil Sands Reservoirs. 45th US Rock Mechanics and Geomechanics Symposium, 1–14.

Babasaki, R., Terashi, M., Suzuki, T., Maekawa, A., Kawamura, M., & Fukazawa, E. (1997). JGS TC Report: Factors Influencing the Strength of improved soil.

Baker, W. H., & Konder, R. L. (1966). Pullout load capacity of a circular earth anchor buried in sand. Highway Research Record, 108, 1–10.

Bergado, D. T., & Lorenzo, G. A. (2005). Economical Mixing Method for Cement Deep Mixing. Proceedings of Geo-Frontiers 2005 Innovations in Grouting and Soil Improvement, 1–10.

Bergado, D. T., Ruenkrairergsa, T., Taesiri, Y., & Balasubramaniam, A. S. (1999). Deep soil mixing used to reduce embankment settlement. Proceedings of the Institution of Civil Engineers-Ground Improvement, 3(4), 145–162. https://doi.org/10.1680/gi.1999.030402

Berghe, J., Cathie, D., & Ballard, J. (2005). Pipeline uplift mechanisms using finite element analysis. In Proceedings of the 16th International Conference on Soil Mechanics and Geotechnical Engineering (pp. 1801–1804). https://doi.org/10.3233/978-1-61499-656-9-1801

Bruno, M. S., Dewolf, G., & Foh, S. (2000). Geomechanical Analysis and Decision Analysis for Delta Pressure Operations in Gas Storage Reservoirs. American Gas Association Operations Conference, 14.

Butler, R. M. (1994). Steam-assisted Gravity Drainage: Concept, Development, Performance And Future. Journal of Canadian Petroleum Technology, 33(02), 44–50. https://doi.org/10.2118/94-02-05

Butler, R. M. (1998). SAGD comes of age! Journal of Canadian Petroleum Technology, 37(7), 9–12. https://doi.org/10.2118/98-07-DA

Butler, R. M. (2004). The Behaviour of Non-Condensible Gas in SAGD - A Rationalization. Journal of Canadian Petroleum Technology, 43(1), 28–34. https://doi.org/10.2118/2002-117

Cao, J. (2003). Centrifuge modeling and numerical analysis of the behaviour of suction caissons in clay. Memorial University of Newfoundland. https://doi.org/10.1017/CBO9781107415324.004

Cheney, J. A., Abghari, A., & Kutter, B. L. (1991). Stability of leaning towers. Journal of Geotechnical Engineering, 117(2), 297–318.

Cheuk, C. Y., White, D. J., & Bolton, M. D. (2008). Uplift Mechanisms of Pipes Buried in Sand. Journal of Geotechnical and Geoenvironmental Engineering, 134(2), 154–163. https://doi.org/10.1061/(ASCE)1090-0241(2008)134:2(154)

Chew, S. H., Kamruzzaman, A. H. M., & Lee, F. H. (2004). Physicochemical and Engineering Behavior of Cement Treated Clays. Journal of Geotechnical and Geoenvironmental Engineering, 130(7), 696–706. https://doi.org/10.1061/(ASCE)1090-0241(2004)130:7(696)

Collins, P. M. (1994). Design of the Monitoring Program For AOSTRA's Underground Test Facility, Phase B Pilot. Journal of Canadian Petroleum Technology, 33(03), 46–53.

Collins, P. M. (2005). Geomechanical Effects on the SAGD Process. In SPE International Thermal Operations and Heavy Oil Symposium. Society of Petroleum Engineers.

Collins, P. M. (2007). Geomechanical Effects on the SAGD Process. In SPE International Thermal Operations and Heavy Oil Symposium (Vol. 10, pp. 367–375). https://doi.org/10.2118/97905-PA

Collins, P. M., Walters, D. A., Perkins, T., Kuhach, J. D., & Veith, E. (2013). Effective caprock determination for SAGD projects. Journal of Canadian Petroleum Technology, 52(2), 112–119. https://doi.org/10.2118/149226-PA

Cuccovillo, T., & Coop, M. R. (1997). Yielding and pre-failure deformation of structured sands. Géotechnique, 47(3), 491–508. https://doi.org/10.1680/geot.1997.47.3.491

Das, B. M. (2013). Advanced soil mechanics. Crc Press.

Das, B. M., & Shukla, S. K. (2013). Earth Anchors (Second Edi). J. Ross Publishing.

Dusseault, M. B. (2007). Monitoring and modelling in coupled geomechanics processes. Journal of Canadian Petroleum Technology, 48(7), 6–14. https://doi.org/10.2118/09-07-06-DA

Dusseault, Maurice B, Media, P., Waterloo, U., Bruno, M. S., & Barrera, J. (2001). Casing Shear: Causes , Cases , Cures, SPE Drilling & Completion, 16(02), 98-107.

El Ganainy, H., Tessari, A., Abdoun, T., & Sasanakul, I. (2013). Tactile pressure sensors in centrifuge testing. Geotechnical Special Publication, 37(1), 151–163. https://doi.org/10.1520/GTJ20120061

Feng, Z., & Yin, Y. (2014). Geotechnical Centrifuge Modelling for Rock Slope Failure: A Brief Overview. Landslide Science for a Safer Geoenvironment, 2(2007), 39–43. https://doi.org/10.1007/978-3-319-04999-1

Garnier, J., Gaudin, C., Springman, S. M., Culligan, P. J., Goodings, D., Konig, D., Thorel, L. (2007). Catalogue of scaling laws and similitude questions in geotechnical centrifuge modelling. International Journal of Physical Modelling in Geotechnics, 7(3), 01–23. https://doi.org/10.1680/ijpmg.2007.7.3.01

Gu, F., Chan, M., & Fryk, R. (2011). Geomechanical-data acquisition, monitoring, and applications in SAGD. Journal of Canadian Petroleum Technology, 50(6), 9–21. https://doi.org/10.2523/30280-MS

Haekes, C. D., McLellan, P. J., & Bachu, S. (2005). Geomechanical factors affecting geological storage of CO2 in depleted oil and gas reservoirs. Journal of Canadian Petroleum Technology, 44(10), 52–61. https://doi.org/10.2118/05-10-05

Han, C., Wang, D., Gaudin, C., O’Loughlin, C. D., & Cassidy, M. J. (2016). Behaviour of vertically loaded plate anchors under sustained uplift. Géotechnique, 66(8), 681–693. https://doi.org/10.1680/jgeot.15.P.232

Haralambos, S. (2009). Compressive Strength of Soil Improved with Cement. 2009 International Foundation Congress and Equipment Expo, 41023(February), 289–296. https://doi.org/10.1061/41023(337)37

Horpibulsk, S., Rachan, R., Suddeepong, A., & Chinkulkijniwat, A. (2011). Strength Development in Cement Admixed Bangkok Clay: Laboratory and Field Investigations. Soils and Foundations, 51(2), 239–251. https://doi.org/10.3208/sandf.51.239

Horpibulsuk, S., & Miura, N. (2001). A new approach for studying behavior of cement stabilized clays. In International Conference on soil mechanics and geotechnical engineering (pp. 1759-1762).

Horpibulsuk, S., Nagaraj, T. S., & Miura, N. (2003). Assessment of strength development in cement-admixed high water content clays with Abrams' law as a basis. Géotechnique. https://doi.org/10.1680/geot.2003.53.4.439

Iglesia, G. R., Einstein, H. H., & Whitman, R. V. (2013). Investigation of Soil Arching with Centrifuge Tests. Journal of Geotechnical and Geoenvironmental Engineering, 140(2), 248–256. https://doi.org/10.1061/(ASCE)GT.1943-5606.0000998.

Ilamparuthi, K., & Muthukrishnaiah, K. (1999). Anchors in sand bed : delineation of rupture surface. Ocean Engineering, 26(12), 1249–1273.

Ilamparuthi, K., Dickin, E. A., & Muthukrisnaiah, K. (2002). Experimental investigation of the uplift behaviour of circular plate anchors embedded in sand. Canadian Geotechnical Journal, 39(3), 648–664. https://doi.org/10.1139/T02-005

Janssen, H. A. (1895). Versuch uber getreidedruck in sillozellen. Zeitschrift Des Vereins Deutscher Ingenieure, 39(35), 1045–1049.

Johnston, I. W., & Choi, S. K. (1986). A synthetic soft rock for laboratory model studies. Géotechnique, 36(2), 251–263. https://doi.org/10.1680/geot.1986.36.2.251

Jongpradist, P., Jumlongrach, N., Youwai, S., & Chucheepsakul, S. (2009). Influence of Fly Ash on Unconfined Compressive Strength of Cement-Admixed Influence of Fly Ash on Unconfined Compressive Strength of Cement-Admixed Clay at High Water Content. Journal of Materials in Civil Engineering, 22(1), 49–58. https://doi.org/10.1061/(ASCE)0899-1561(2010)22

Juran, I., & Riccobono, O. (1991). Reinforcing soft soils with artificially cemented compacted-sand columns, 117(7), 1042–1060.

Kaga, M., & Yonekura, R. (1991). Estimation of strength of silicate grouted sand. Soils and Foundations, 31(3), 43–59.

Kamruzzaman, A. H., Chew, S. H., & Lee, F. H. (2009). Structuration and Destructuration Behavior of Cement-Treated Singapore Marine Clay. Journal of Geotechnical and Geoenvironmental Engineering, 135(4), 573–589.

Kasama, K., Ochiai, H., & Yasufuku, N. (2000). On the stress–strain behaviour of lightly cemented clay based on an extended critical state concept. Soils and Foundations, 40(5), 37–47. https://doi.org/10.1248/cpb.37.3229

Kelly, P. (2014). Soil structure interaction and group mechanics of vibrated stone column foundations. University of Sheffield.

Khan, S., Han, H., Ansari, S. A., & Khosravi, N. (2010). An integrated geomechanics workflow for Caprock-integrity analysis of a potential carbon storage. In SPE International Conference on CO2 Capture, Storage, and Utilization. New Orleans, Louisiana, USA: Society of Petroleum Engineers.

Khan, S., Han, H., Ansari, S., Vishteh, M., & Khosravi, N. (2011). Caprock integrity analysis in thermal operations: an integrated geomechanics approach. In Paper WHOC11-609 presented at the World Heavy Oil Congress (pp. 1–10). Edmonton, Alberta.

Kitazume, M., & Terashi, M. (2013). The Deep Mixing Method. London, UK.

Ko, H., & Craig, W. H. (1988). Summary of the State-of the-Art in Centrifuge Model Testing. In Centrifuges in Soil Mechanics (pp. 11–18).

Lam, S. Y., Ng, C. W. W., Leung, C. F., & Chan, S. H. (2009). Centrifuge and numerical modeling of axial load effects on piles in consolidating ground. Canadian Geotechnical Journal, 46(1), 10–24. https://doi.org/10.1139/T08-095

Langhaar, H. L. (1951). Shales&Other_Degradable_Materials-Trb_Sr247.Pdf. New York, Wiley.

Li, C., Barès, P., & Laloui, L. (2015). A hydromechanical approach to assess CO2 injection-induced surface uplift and caprock deflection. Geomechanics for Energy and the Environment, 4, 51–60. https://doi.org/10.1016/j.gete.2015.06.002

Li, Q., Chen, J., Shi, Q., & Zhao, S. (2014). Macroscopic and microscopic mechanisms of cement-stabilized soft clay mixed with seawater by adding ultrafine silica fume. Advances in Materials Science and Engineering, 1, 1–12.

Ling, H. I., Wu, M.-H., Leshchinsky, D., & Leshchinsky, B. (2009). Centrifuge Modeling of Slope Instability. Journal of Geotechnical and Geoenvironmental Engineering, 135(6), 758–767. https://doi.org/10.1061/(ASCE)GT.1943-5606.0000024

Liu, J., Liu, M., & Zhu, Z. (2012). Sand Deformation around an Uplift Plate Anchor. Journal of Geotechnical and Geoenvironmental Engineering, 138(6), 728–737. https://doi.org/Doi 10.1061/(Asce)Gt.1943-5606.0000633

Liu, M. D., Xu, K. J., & Horpibulsuk, S. (2013). A mathematical function to represent S-shaped relationships for geotechnical applications. In Proceedings of the Institution of Civil Engineers - Geotechnical Engineering (Vol. 166, pp. 321–327).

Locat, J., Trembaly, H., & Leroueil, S. (1996). Mechanical and hydraulic behaviour of a soft inorganic clay treated with lime. Canadian Geotechnical Journal, 33(4), 654–669.

Lorenzo, G. A., & Bergado, D. T. (2004). Fundamental Parameters of Cement-Admixed Clay — A New Approach. Journal of Geotechnical and Geoenvironmental Engineering, 130(10), 1042–1050. https://doi.org/10.1061/(ASCE)1090-0241(2004)130

Lupini, J. F., Skinner, A. E., & Vaughan, P. R. (1981). The drained residual strength of cohesive soils. Géotechnique, 31(2), 181–213.

Matsuo, M. (1967). Study on the uplift resistance of footing (I). Soils and Foundations, 7(4), 1–37.

Mcnulty, J. W. (1965). An experimental study of arching in sand (No. AEWES-TR-1-674).

Meyerhof, G. G., & Adams, J. I. (1968a). The ultimate uplift capacity of foundations. Canadian Geotechnical Journal, 5(4), 225–244.

Mitchell, J. K., & Liang, R. Y. (1986). Centrifuge evaluation of a time dependent numerical model for soft clay deformation. In In Consolidation of Soils: Testing and Evaluation. ASTM International. (pp. 567–592).

Miura, N., Horpibulsuk, S., & Nagaraj, T. S. (2001). Engineering behavior of cement stabilized clay at high water content. Soils and Foundations, 41(5), 33–45.

Moo-young, H., Myers, T., Tardy, B., Ledbetter, R., Vanadit-ellis, W., & Kim, T. (2003). Centrifugal evaluation of a time-dependent numerical model for soft clay deformations. Engineering Geology, 70(3–4), 249–258. https://doi.org/10.1016/S0013-7952(03)00093-0

Moradi, G., & Abbasnejad, A. (2013). The State of the Art Report on Arching Effect. Journal of Civil Engineering Research, 3(5), 148–161. https://doi.org/10.5923/j.jce.20130305.02

Murray, B. E. J., & Asce, F. (1987). Uplift of anchor plates in sand. Journal of Geotechnical Engineering, 113(3), 202–215.

Ng, C. W. (2014). The state-of-the-art centrifuge modelling of geotechnical problems at HKUST. Journal of Zhejiang University SCIENCE A, 15(1), 1–21. https://doi.org/10.1631/jzus.A1300217

Nocilla, A., & Coop, M. (2006). The mechanics of an Italian silt: an example of ‘transitional’ behaviour. Géotechnique, 56(4), 261–271. https://doi.org/10.1680/geot.2006.56.4.261

Nomoto, B. T., Imamura, S., Hagiwara, T., Kusakabe, O., & Fujii, N. (1999). Shield Tunnel Construction in Centrifuge. Journal of Geotechnical and Geoenvironmental Engineering, 125(April), 289–300.

Papamichos, E., Vardoulakis, I., & Heil, L. K. (2001). Overburden modeling above a compacting reservoir using a trap door apparatus. Physics and Chemistry of the Earth, Part A: Solid Earth and Geodesy, 26(1–2), 69–74.

Rahmati, E. (2016). Numerical Assessment of Caprock Integrity in SAGD Operations Considering Mechanical Anisotropic Behavior of Shale Layers. PhD Thesis, University of Alberta, 1-236.

Rahmati, E., Nouri, A., & Fattahpour, V. (2014). Caprock Integrity Analysis during a SAGD Operation Using an Anisotropic Elasto-Plastic Model. In SPE Heavy Oil Conference-Canada (Vol. 2, pp. 1–23). Calgary, Alberta, Canada: Society of Petroleum Engineers. https://doi.org/10.2118/170114-MS

Rao, K. S. S., & Kumar, J. (1994). Vertical uplift capacity of horizontal anchors. Journal of Geotechnical Engineering, 120(7), 1134–1147.

Rao, S. N., & Rajasekaran, G. (1996). Reaction products formed in lime-stabilized marine clays. Journal of Geotechnical Engineering, 122(5), 329–336.

Rossato, G., Ninis, N. L., & Jardine, R. J. (1992). Properties of some kaolin-based model clay soils. Geotechnical Testing Journal, 15(2), 166–179.

Rotta, G. V., Consoli, N. C., Prietto, P. D. M., Coop, M. R., & Graham, J. (2003). Isotropic yielding in an artificially cemented soil cured under stress. Géotechnique, 53(5), 493–501. https://doi.org/10.1680/geot.53.5.493.37508

Rowe, P. W. (1971). Large Scale Laboratory Model Retaining Wall Apparatu.pdf. In In Proc., Roscoe Memorial Symp (pp. 441–449).

Rowe, R. K., & Davis, E. H. (1982). Behaviour of anchor plates in sand. Geotechnique, 32(1), 25–41.

Saadat, M. (2014). Validation of Floc Size Measurements Made with Flow Particle Image Analyzer (FPIA). University of Alberta. Retrieved from http://search.proquest.com/docview/1785357129?accountid=178282

Sadrekarimi, J., & Abbasnejad, A. (2010). Arching effect in fine sand due to base yielding. Canadian Geotechnical Journal, 47(3), 366–374. https://doi.org/10.1139/T09-107

Sakai, T., & Tanaka, T. (2007). Experimental and numerical study of uplift behavior of shallow circular anchor in two-layered sand. Journal of Geotechnical and Geoenvironmental Engineering, 133(4), 469–477.

Santi, P. M., Holschen, J. E., & Stephenson, R. W. (2000). Improving elastic modulus measurements for rock based on geology. Environmental & Engineering Geoscience, 6(4), 333–346.

Sasanian, S. (2011). The Behaviour of Cement Stabilized Clay At High Water Contents. The University of Western Ontario.

Sasanian, S., & Newson, T. A. (2014). Basic parameters governing the behaviour of cement-treated clays. Soils and Foundations, 54(2), 209–224. https://doi.org/10.1016/j.sandf.2014.02.011

Schnaid, F., Prietto, P. D., & Consoli, N. C. (2001). Characterization of Cemented Sand in Triaxial Compression. Journal of Geotechnical and Geoenvironmental Engineering, 127(10), 857–868. https://doi.org/10.1093/bfgp/elp034

Schupp, J., Byrne, B. W., Eacott, N., Martin, C. M., Oliphant, J., Maconochie, A., & Cathie, D. (2016). Pipeline ubburial behaviour in loose sand. In 25th International Conference on Offshore Mechanics and Arctic Engineering (pp. 297–308). Hamburg, Germany.

Scott, G. R. (2002). SPE / Petroleum Society of CIM / CHOA 79020 Comparison of CSS and SAGD Performance in the Clearwater Formation at Cold Lake. In SPE International Thermal Operations and Heavy Oil Symposium and International Horizontal Well Technology Conference. Calgary, Canada: Society of Petroleum Engineers.

Scott, R. F. (1987). Failure. 27th Rankine Lecture. Géotechnique, 37(4), 423–466.

Seed, H. B., Wookward, R. J., & Lundgren, R. (1964). Clay mineralogical aspects of the Atterberg limits. In Journal of the Soil Mechanics and Foundations Division (pp. 107–134).

Selvadurai, A. P. S. (2009). Heave of a surficial rock layer due to pressures generated by injected fluids. Geophysical Research Letters, 36(14), L14302. https://doi.org/10.1029/2009GL038187

Shafie Zadeh, N., & Chalaturnyk, R. (2015). Geotechnical Characterization of Clearwater Clay Shale and Comparison of the Properties with Other Cretaceous Clay Shales in North America. Journal of Canadian Petroleum Technology, 54(6), 394–411.

Spangler, M., & Handy, R. (2007). Geotechnical engineering: soil and foundation principles and practice. (M.-H. Publishing, Ed.) (the 5th ed).

Stanier, S. A., & White, D. J. (2013). Improved image-based deformation measurement in the centrifuge environment. Geotechnical Testing Journal, 36(6), 915–928. https://doi.org/10.1520/GTJ20130044

Stark, T. D., & Eid, H. T. (1994). Drained Residual Strength of Cohesive Soils. Journal of Geotechnical Engineering, 120(5), 856–871. https://doi.org/10.1061/(ASCE)0733-9410(1994)120

Stark, T. D., Ebeling, R. M., & Vettel, J. J. (1994). Hyperbolic Stress-Strain Parameters for Silts. Journal of Geotechnical Engineering, 120(2), 420–441. https://doi.org/10.1061/(ASCE)0733-9410(1994)120

Stimpson, B. (1970). Modelling materials for engineering rock mechanics. International Journal of Rock Mechanics and Mining Sciences And, 7(1), 77–121. https://doi.org/10.1016/0148-9062(70)90029-X

Sutherland, H. B. (1988). Uplift resistance of soils. Geotechnique, 38(4), 493–516.

Tanaka, T., & Sakai, T. (1993). Progressive failure and scale effect of trap-door problems with granular materials. Soils and Foundations, 33(1), 11–22.

Tang, Y. X., Miyazaki, Y., & Tsuchida, T. (2001). Practices of reused dredgings by cement treatment. Soils and Foundations, 41(5), 129–143.

Tavenas, F. A., Roy, M., & Rochelle, P. L. (1973). An Artificial Material for Simulating Champlain Clays. Canadian Geotechnical Journal, 10(3), 489–503. https://doi.org/10.1139/t73-040

Taylor, R. N. (2005). Geotechnical Centrifuge Technology. (CRC Press, Ed.). London: CRC Press.

TBS. (2012). Operating Manual for GT50/1.7 Geotechnical Beam Centrifuge. Thomas Broadbent & Sons Ltd.

Terzaghi, K. (1943). Theoretical soil mechanics. John Wiley & Sons. New York.

Thorne, C. P., Wang, C. X., & Carter, J. P. (2004). Uplift capacity of rapidly loaded strip anchors in uniform strength clay. Géotechnique, 54(8), 507–517. https://doi.org/10.1680/geot.2004.54.8.507

Thusyanthan, N. I., & Madabhushi, S. P. G. (2003). Scaling of seepage flow velocity in centrifuge models. CUED/D-SOILS/TR326.

Thusyanthan, N. I., Mesmar, S., Wang, J., & Haigh, S. K. (2010). Uplift Resistance of Buried Pipelines and DNV-RP-F110 Guidelines. In Proc. Offshore Pipeline and Technology Conference (pp. 1–20). Amsterdam, Netherlands.

Ti, K. S., Gue See, S., Huat, B. B., Noorzaei, J., & Saleh, M. (2009). A Review of Basic Soil Constitutive Models for Geotechnical Application. Electronic Journal of Geotechnical Engineering, 14, 18. Retrieved from http://ejge.com/2009/Ppr0985/Ppr0985ar.pdf

Tien, H. (1996). A Literature Study of the Arching Effect. Massachusetts Institute of Technology.

Total E&P Canada, L. (2007). Summary of investigations into the Joslyn May 18th 2006 Steam Release.

Trautmann, C. H., O'Rourfce, T. D., & Kulhawy, F. H. (1985). Uplift force-displacement response of buried pipe. Journal of Geotechnical Engineering, 111(9), 1061–1076.

Tsuchida, T., & Tang, Y. X. (2015). Estimation of compressive strength of cement-treated marine clays with different initial water contents. Soils and Foundations, 55(2), 359–374. https://doi.org/10.1016/j.sandf.2015.02.011

Uddin, K., Balasubramaniam, A. S., & Bergado, D. T. (1997). Engineering behavior of cement-treated Bangkok soft clay. Geotechnical Engineering, 28(1), 89–119.

Uwiera-Gartner, M. M. E., Carlson, M. R., Walters, D., & Palmgren, C. T. S. (2011). Geomechanical Simulation of Caprock Performance for a Proposed, Low Pressure , Steam-Assisted Gravity Drainage Pilot Project. SPE The Canadian Unconvential Resources Conference, 2011, (November), 1–14.

Vardoulakis, I., Graf, B., & Gudehus, G. (1981). Trap-door problem with dry sand: A statical approach based upon model test kinematics. International Journal for Numerical and Analytical Methods in Geomechanics, 5(1), 57–78.

Vesic, A. S. (1971). Breakout resistance of objects embedded in ocean bottom. Journal of Soil Mechanics & Foundations Div, 97(9), 1183–1205.

Vilarrasa, V., Olivella, S., Carrera, J., & Rutqvist, J. (2014). Long term impacts of cold CO2 injection on the caprock integrity. International Journal of Greenhouse Gas Control, 24, 1–13. https://doi.org/10.1016/j.ijggc.2014.02.016

Walters, D., Wang, J., & Settari, A. (2012). A geomechanical methodology for determining maximum operating pressure in SAGD reservoirs, , SPE Heavy Oil Conference Canada. In Society of Petroleum Engineers, Calgary, Alberta, Canada. (Vol. 2, pp. 1065–1077). https://doi.org/10.2118/157855-MS

White, D. J. (2002). An investigation into the behaviour of pressed-in piles. University of Cambridge, Cambridge, U.K.

White, D. J., Barefoot, A. J., & Bolton, M. D. (2001). Centrifuge modelling of upheaval buckling in sand. International Journal of Physical Modelling in Geotechnics, 1(2), 19–28.

White, D. J., Take, W. A., & Bolton, M. D. (2003). Soil deformation measurement using particle image velocimetry (PIV) and photogrammetry. Geotechnique, 53(7), 619–631. https://doi.org/10.1680/geot.2003.53.7.619

Wood, D. M. (1991). Soil Behaviour and Critical State Soil Mechanics. Soil Behaviour and Critical State Soil Mechanics. https://doi.org/10.1016/0148-9062(92)90570-P

Wu, J. (2015). Feasibility Study of Centrifuge Modeling of SAGD Caprock Integrity. University of Alberta.

Xiao, H. W., & Lee, F. H. (2008). Curing Time Effect on Behavior of Cement Treated Marine Clay. In Proceedings of World Academy of Science, Engineering and Technology (PWASET) (Vol. 33, pp. 2070–3740).

Yamamoto, K., & Kusuda, K. (2001). Failure mechanisms and bearing capacities of reinforced foundations. Geotextiles and Geomembranes, 19(3), 127–162. https://doi.org/10.1016/S0266-1144(01)00003-6

Yin, J. H. (2002). Stress-Strain Strength Characteristics of a Marine Soil with Different Clay Contents. Geotechnical Testing Journal, 25(4), 459–462.

Yuan, Y., Xu, B., & Palmgren, C. (2013). Design of caprock integrity in thermal stimulation of shallow oil-sands reservoirs. Journal of Canadian Petroleum Technology, 52(4), 266–278.

Zhang, R. J., Santoso, A. M., Tan, T. S., & Phoon, K. K. (2013). Strength of High Water-Content Marine Clay Stabilized by Low Amount of Cement. Journal of Geotechnical and Geoenvironmental Engineering, 139(December), 2170–2181. https://doi.org/10.1061/(ASCE)GT.1943-5606.0000951.

Zhu, W., Zhang, C. L., & Chiu, A. C. F. (2007). Soil – Water Transfer Mechanism for Solidified Dredged Materials. Journal of Geotechnical and Geoenvironmental Engineering, 133(5), 588–598.

Appendix A: Code for the 10 years prototype time

```
;10 years
new
config fluid
; --------geometrical model-------, length = 70 m, width = 20 m, height = 20 m.
gen zone brick p0 (0,0,0) p1 (70,0,0) p2 (0,20,0) p3 (0,0,20) size 70 20 20
;--------mechanical model------
model mech mohr
prop bulk = 1.46667e8 shear = 8.8e7 fric = 28
prop coh = 3.68e5 tens = 1.00e5
ini dens 1036.14

fix x range x -0.1 0.1
fix x range x 69.9 70.1
fix y range y -0.1 0.1
fix y range y 19.9 20.1
fix z range z -0.1 0.1
fix y
;--------setting------
apply szz = -5.094192857e5 range z 20; the overburden pressure = 509.419285714286kPa
set gravity 0 0 -9.81
;--------fluid flow model------
model fluid fl_iso
prop perm 1.632e-10 porosity 0.5
ini fmod 2e5 fdensity 1e3 ftens -1e10
;--------water level keeps constant---------
;--------pore pressure fixed at the surface ---
ini pp 8.3385e4 range z 19.9 20.1
fix pp range z 19.9 20.1
```

```
ini pp 2.79585e5 range z -0.1 0.1
fix pp range z -0.1 0.1
;--------Initial state, undrained ---
set fluid off
solve ratio 1e-5
; --- consolidation settlement ---
set mech subs 100 auto
set fluid subs 1000
set fluid on mech on
step 10000
save stage1.sav
;--------Mechanical-fluid copuling------
free z range x 25 45 y 0 20 z 0; release the boundary of the left flank, uplifting table and the right
flank
fix x y z range x 25 30 y 0 20 z 0 ;left flank
fix x y z range x 40 45 y 0 20 z 0 ;right flank
fix x y z range x 30 40 y 0 20 z 0 ; uplifting table
ini disp=(0, 0, 0)
ini zvel 6.43004e-7 range x 30 40 y 0 20 z 0 ;the velocity is 6.43004115226337E-07 m/sec
; --- set mechanical limits ---
set mech subs 100
set fluid subs 1000 auto
set fluid on mech on
set large
step 1321943
```

Appendix B: Test results for a prototype time of 10 years

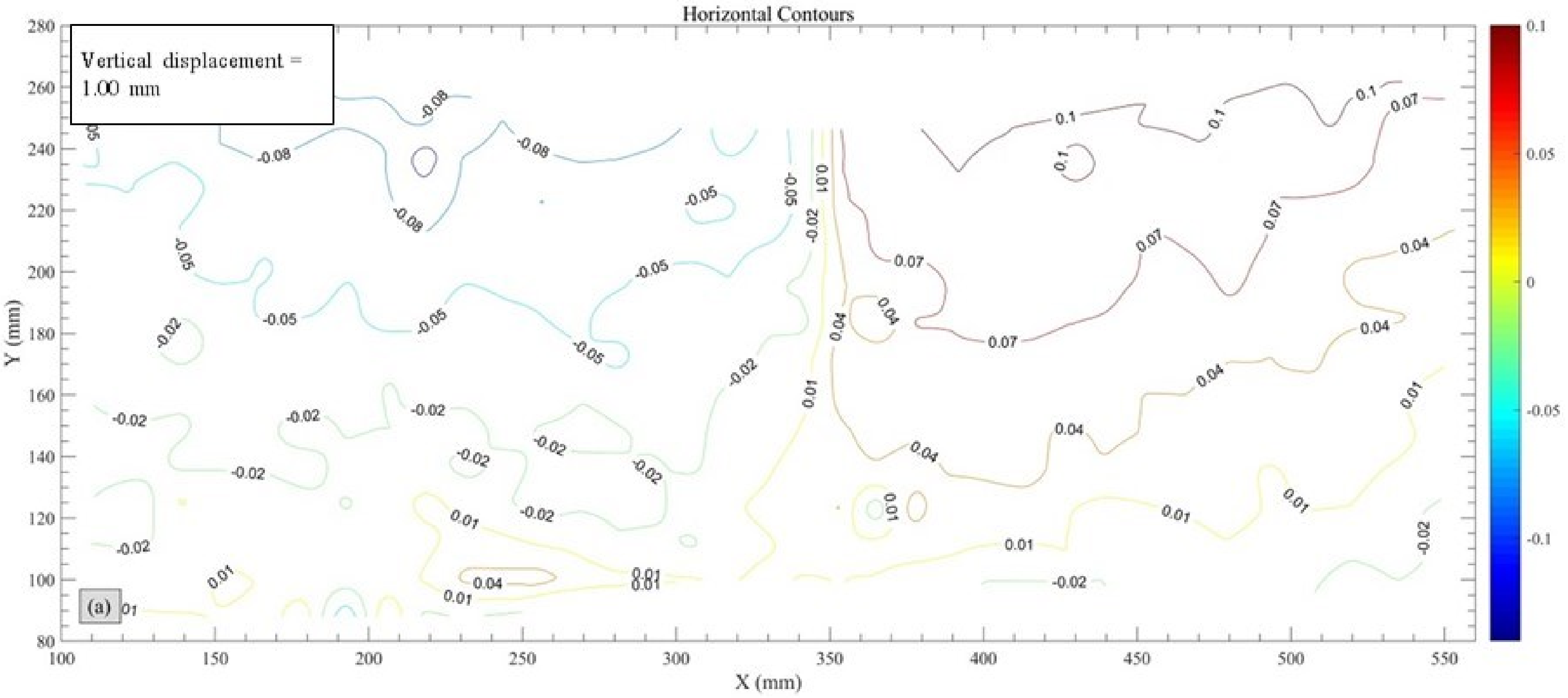

Figure B-0-1 Evolution of horizontal displacements – t = 10 yrs

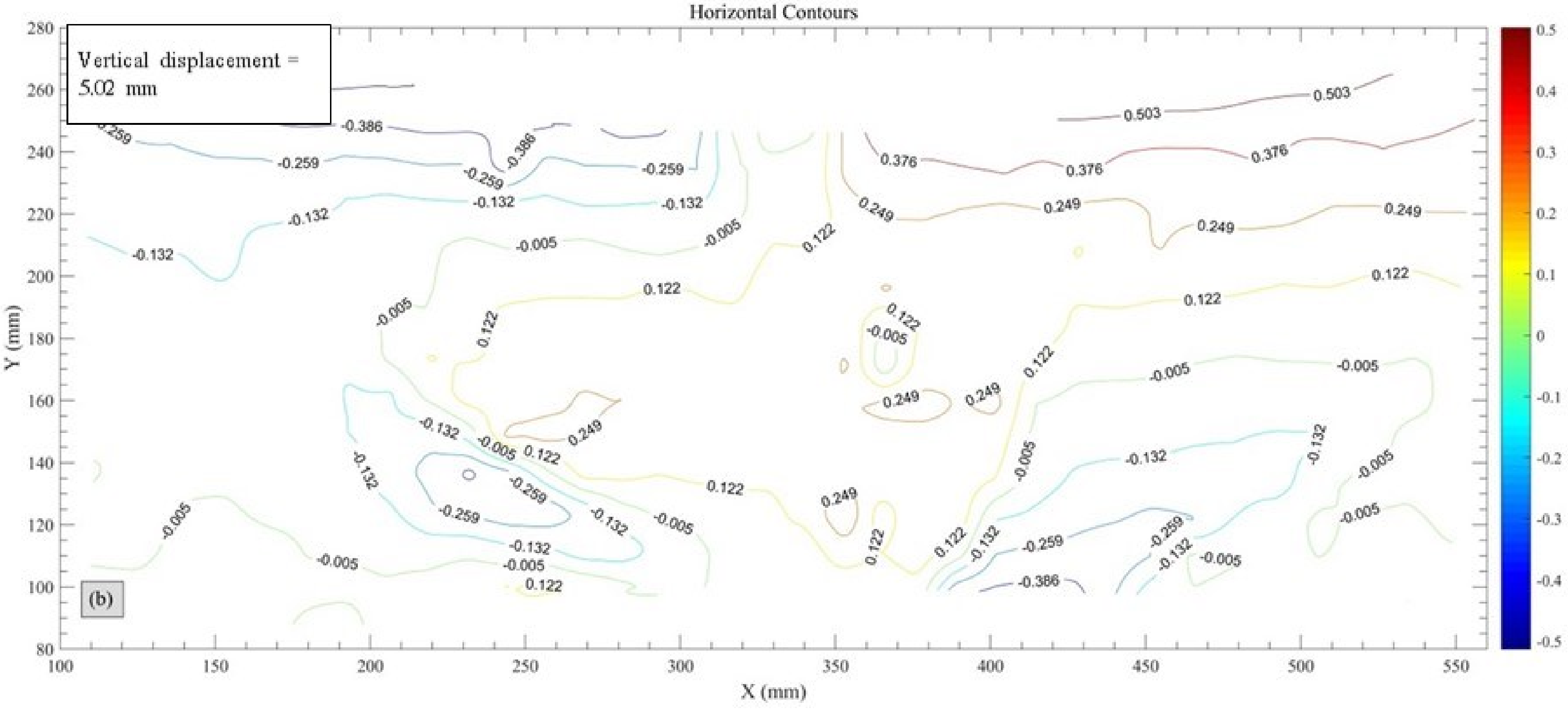

Figure B-0-2 Evolution of horizontal displacements – t = 10 yrs

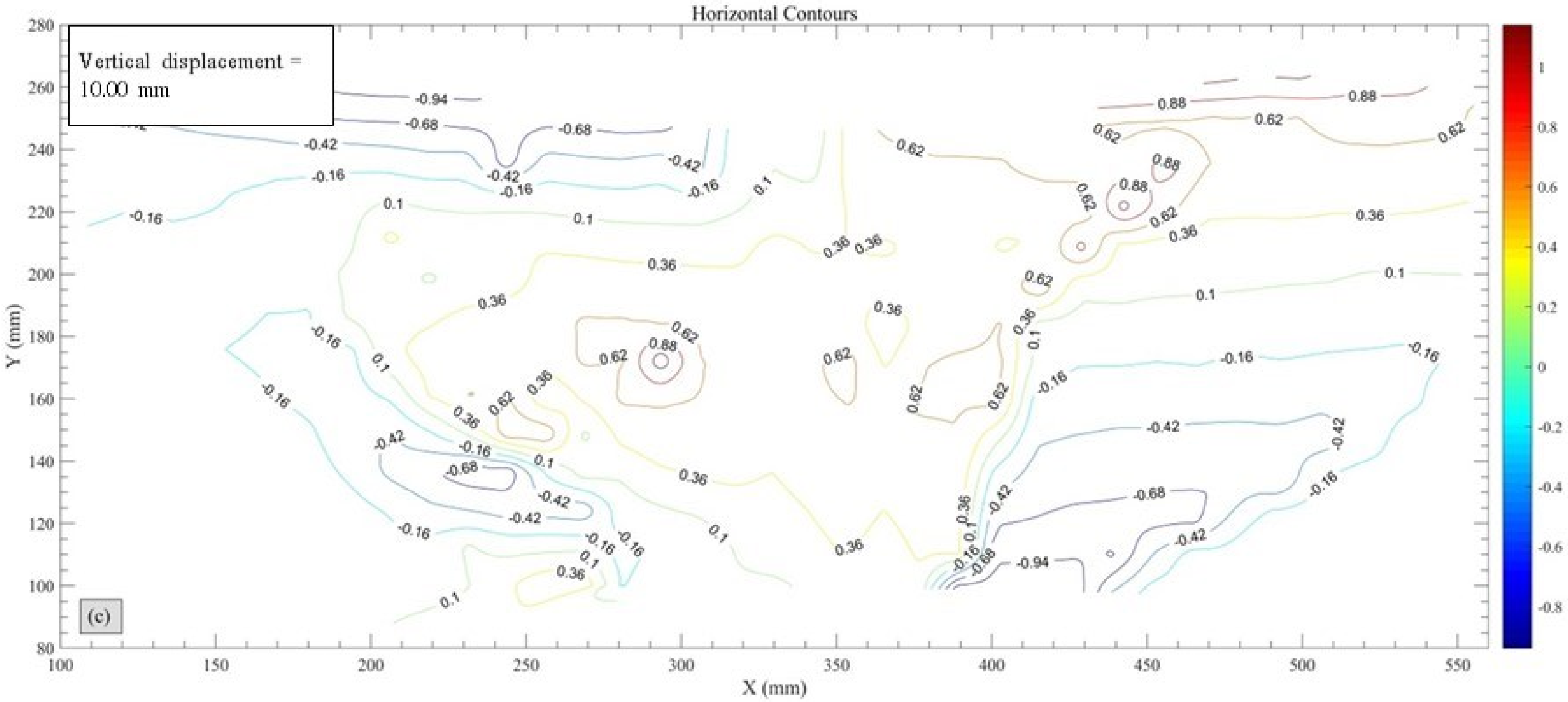

Figure B-0-3 Evolution of horizontal displacements – t = 10 yrs

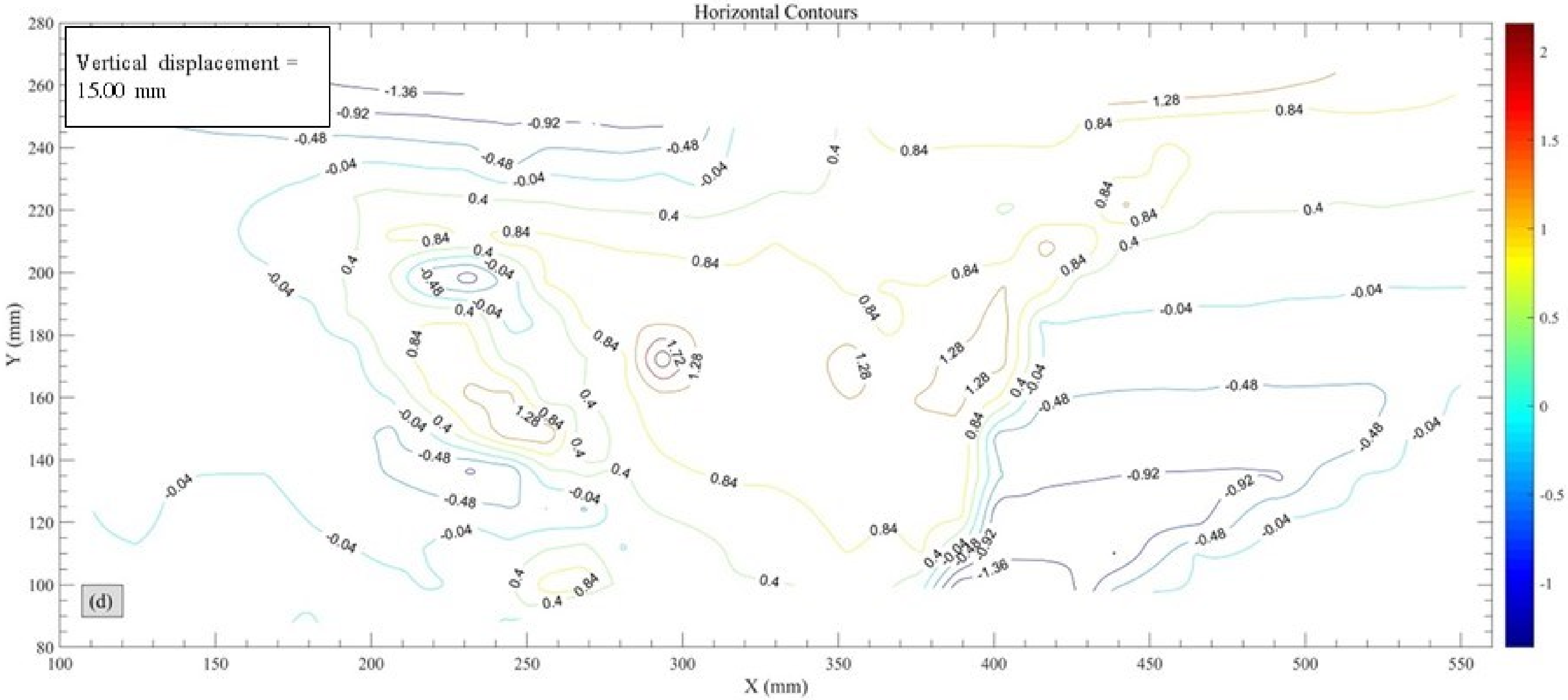

Figure B-0-4 Evolution of horizontal displacements – t = 10 yrs

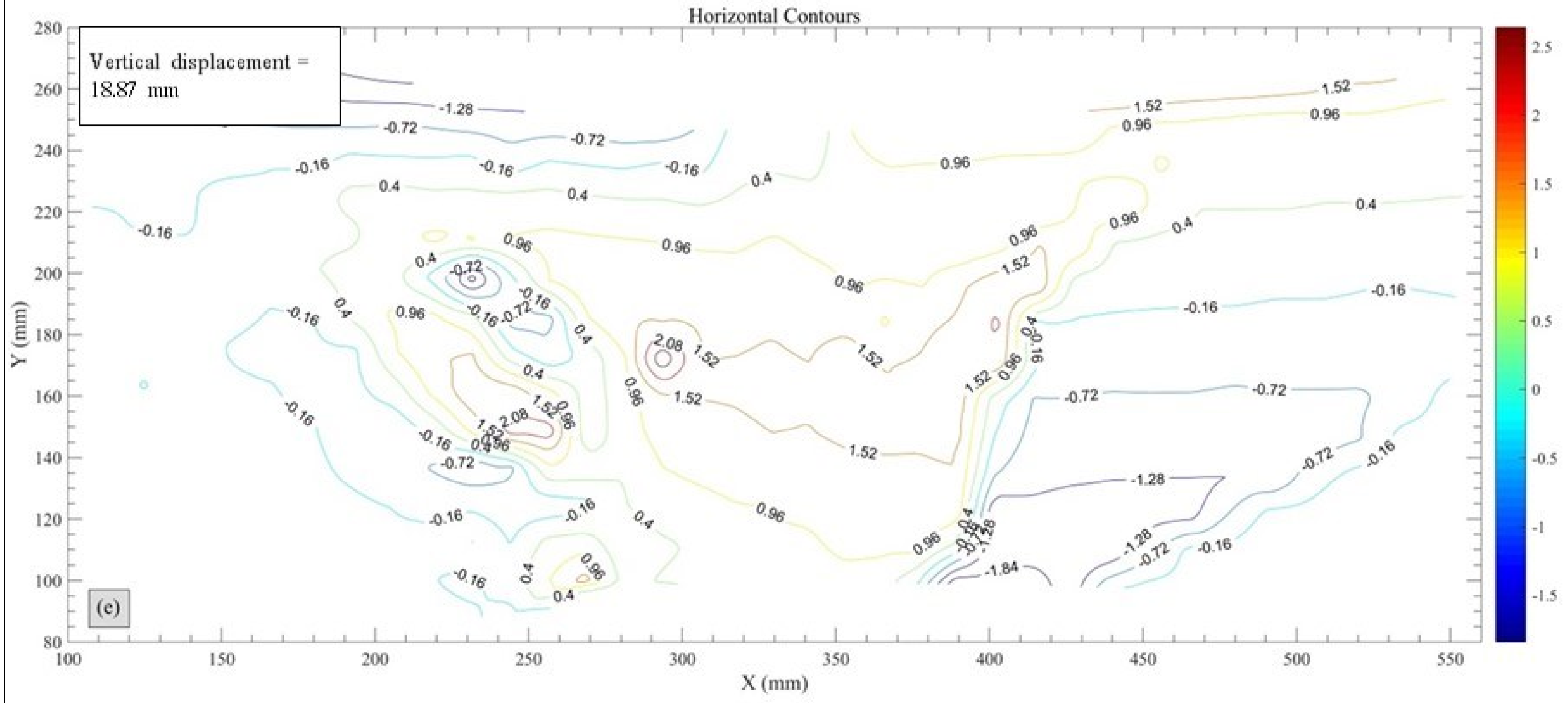

Figure B-0-5 Evolution of horizontal displacements – t = 10 yrs

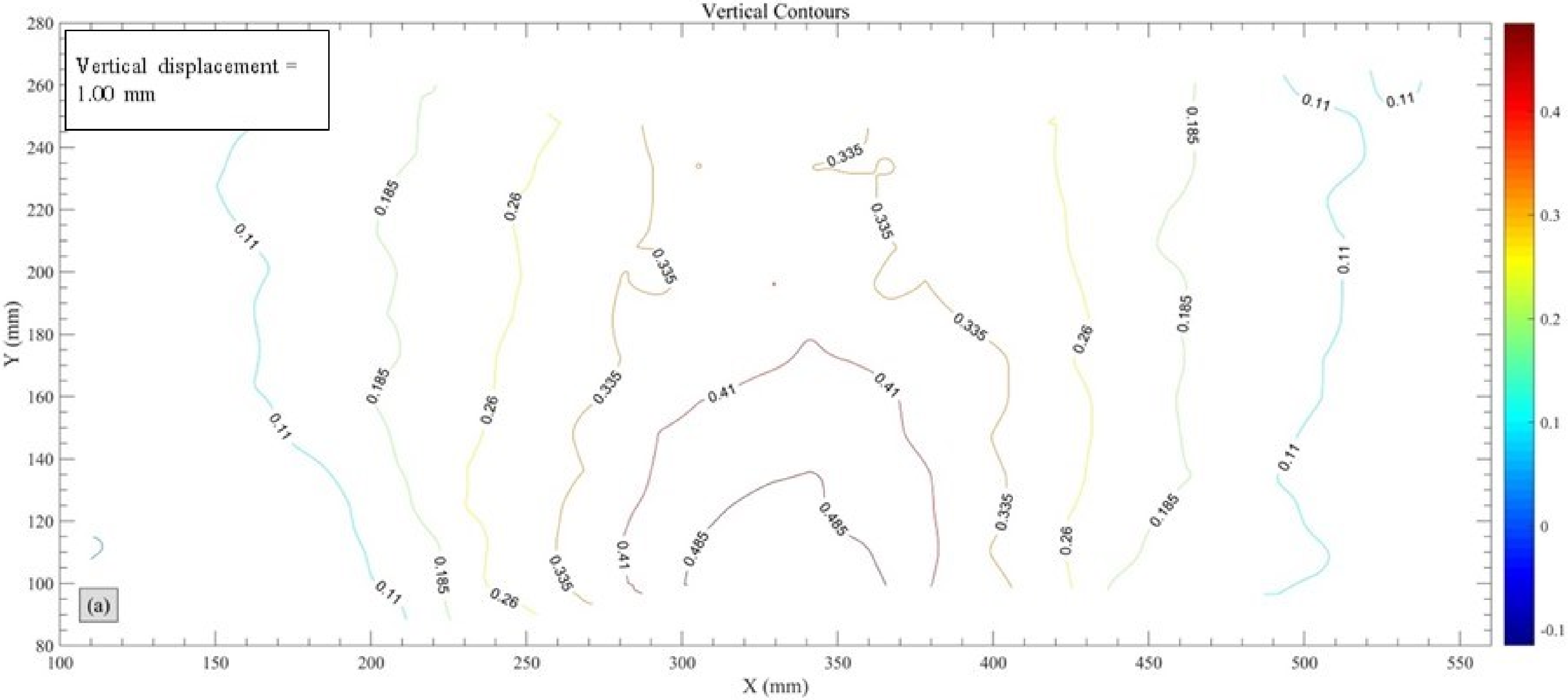

Figure B-0-6 Evolution of vertical displacements – t = 10 yrs

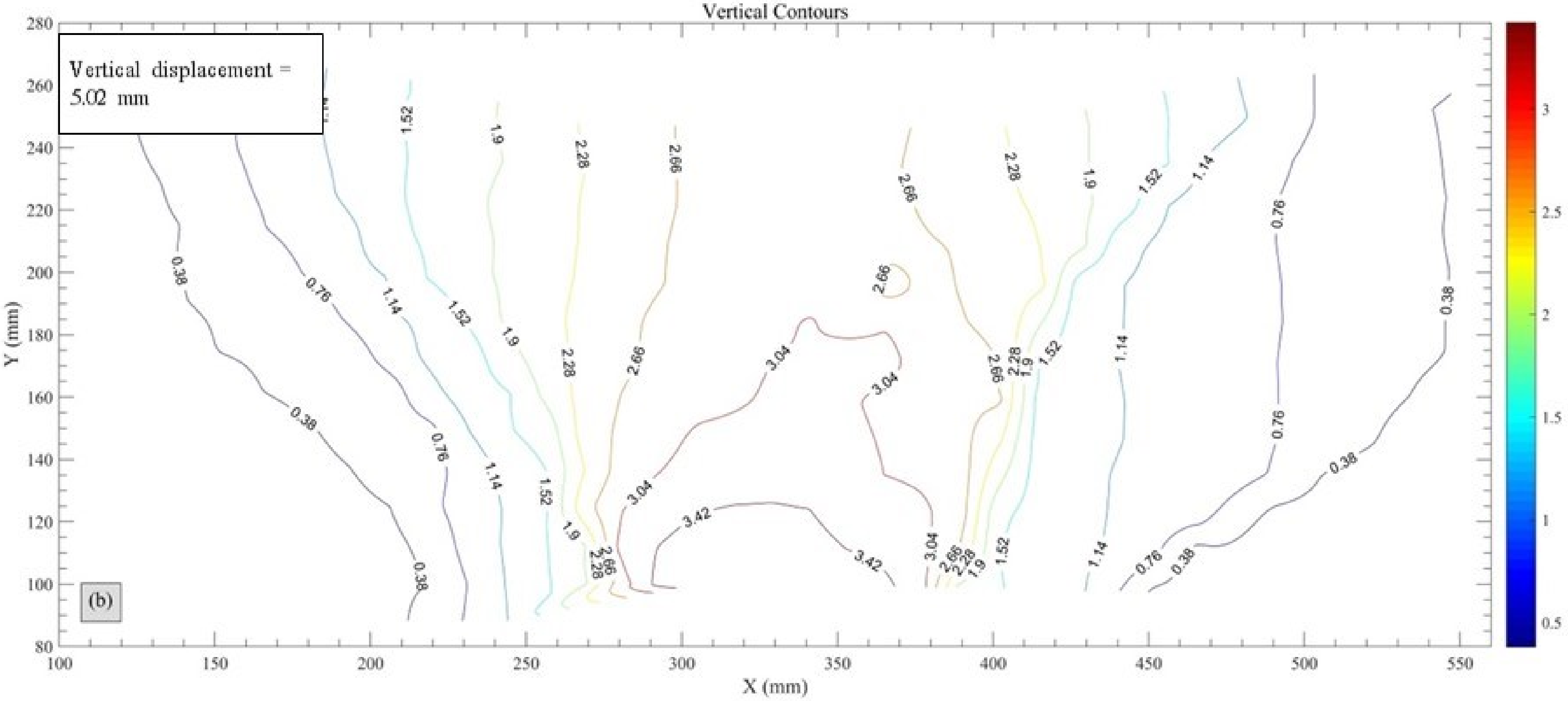

Figure B-0-7 Evolution of vertical displacements – t = 10 yrs

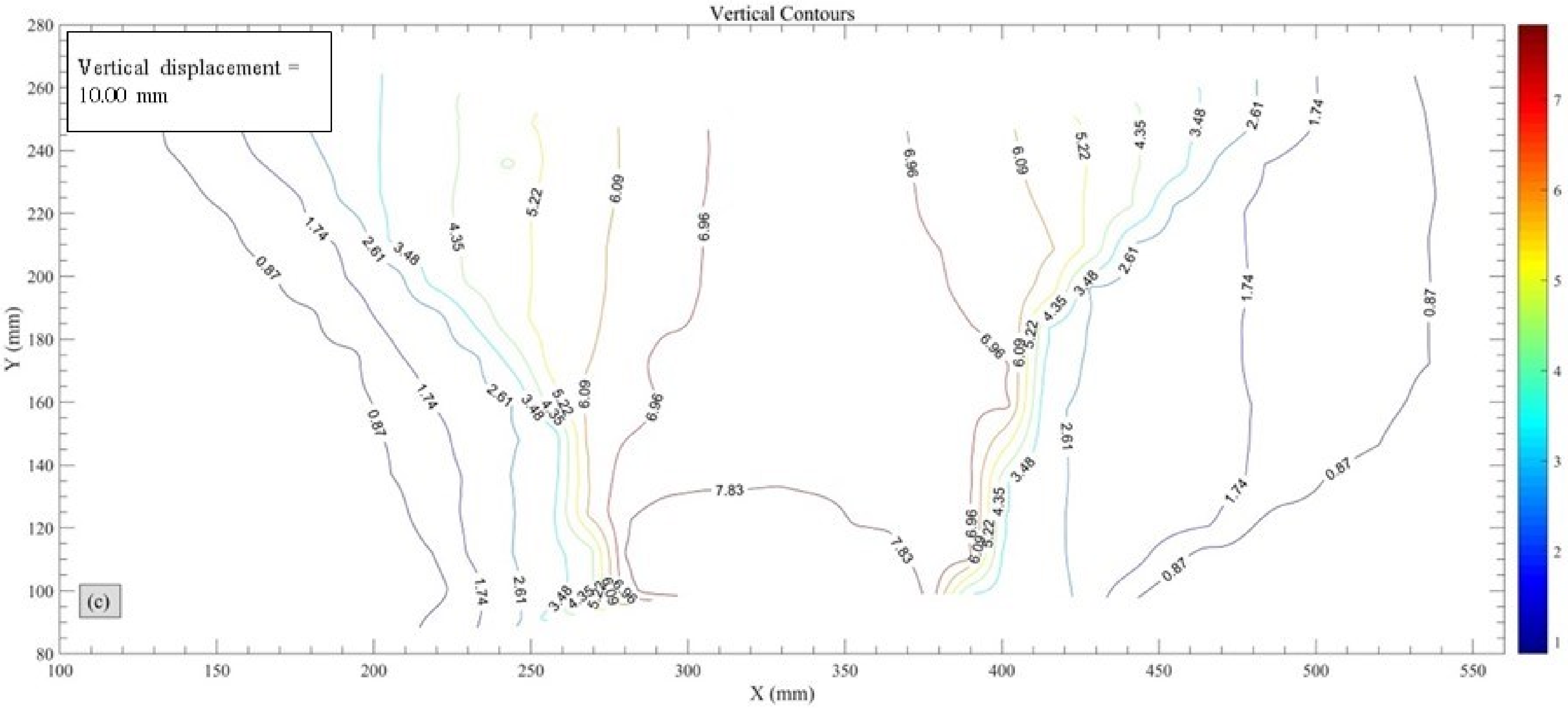

Figure B-0-8 Evolution of vertical displacements – t = 10 yrs

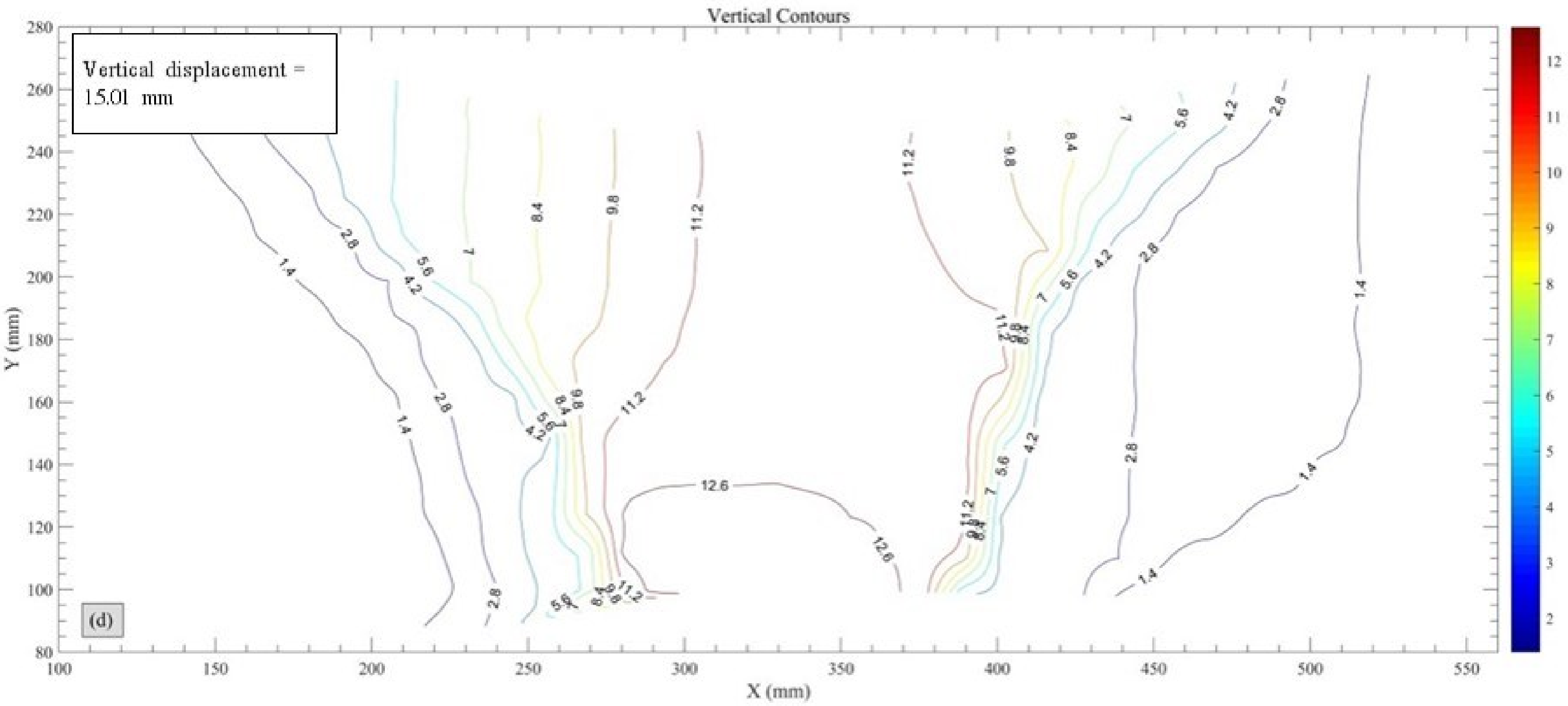

Figure B-0-9 Evolution of vertical displacements – t = 10 yrs

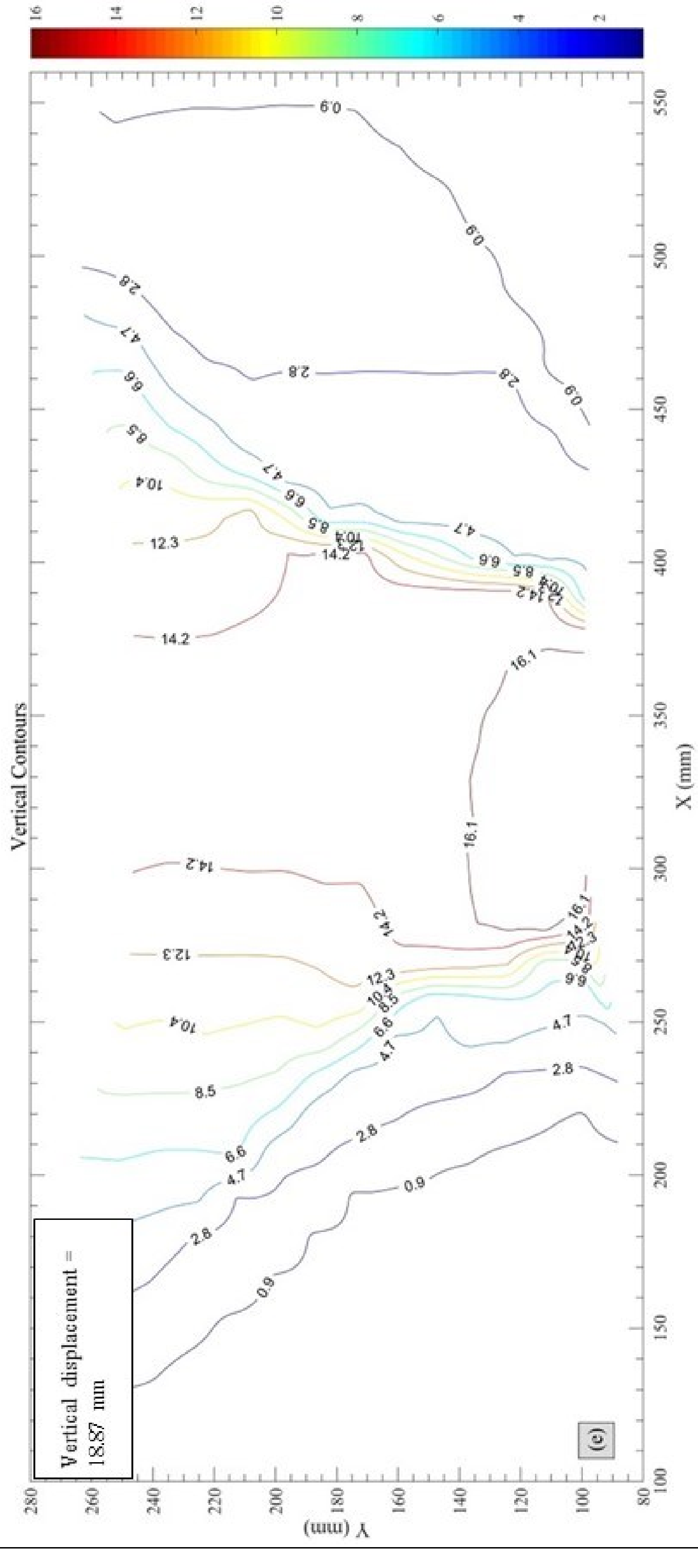

Figure B-0-10 Evolution of vertical displacements – t = 10 yrs

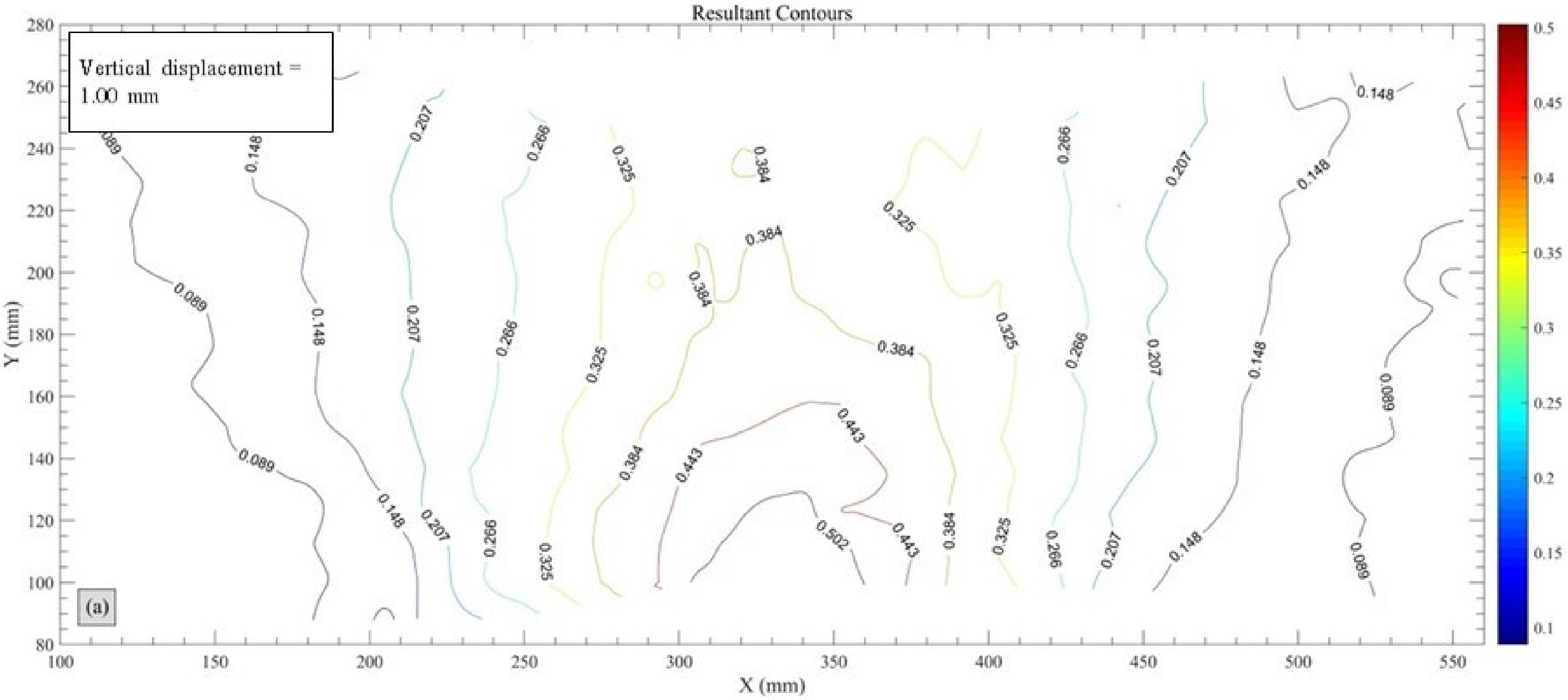

Figure B-0-11 Evolution of resultant (total) displacements – t = 10 yrs

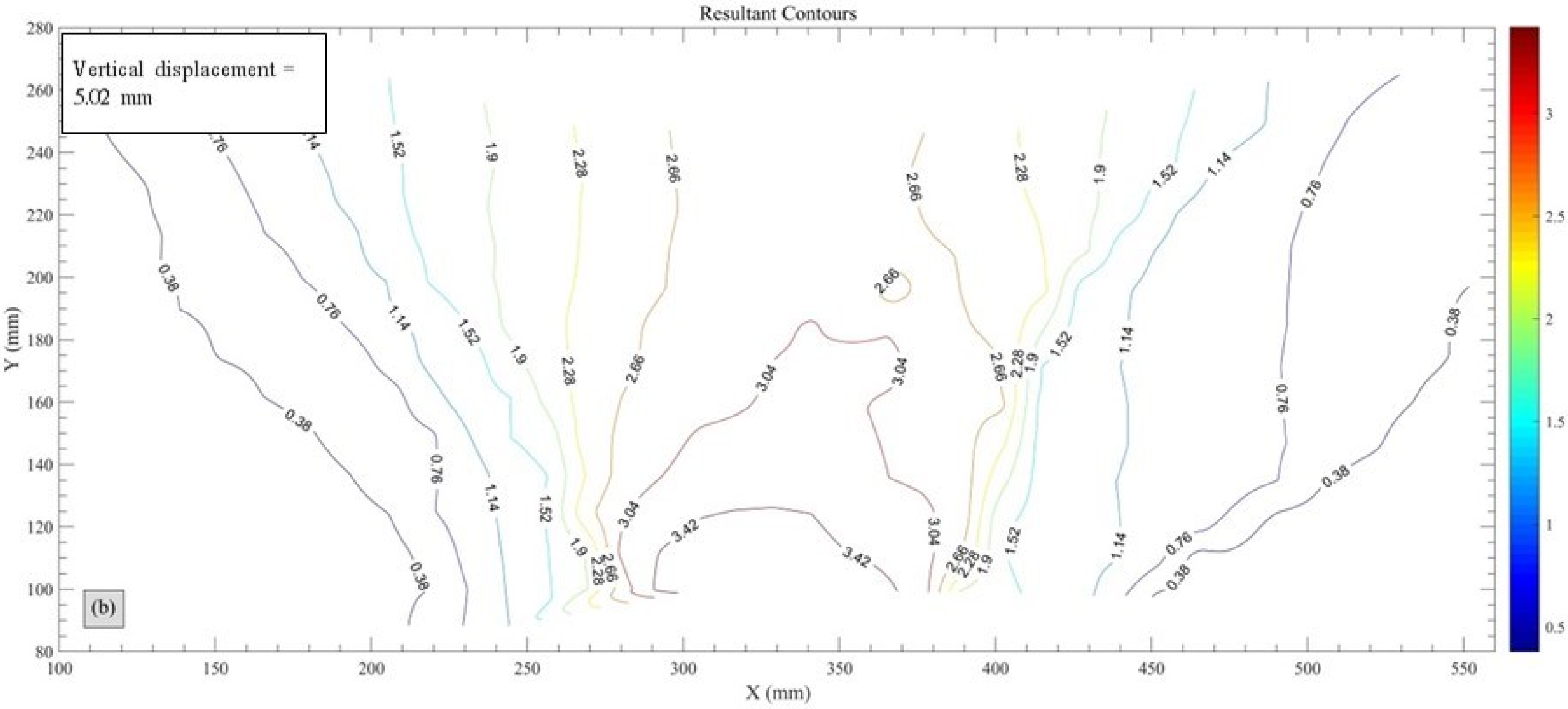

Figure B-0-12 Evolution of resultant (total) displacements – t = 10 yrs

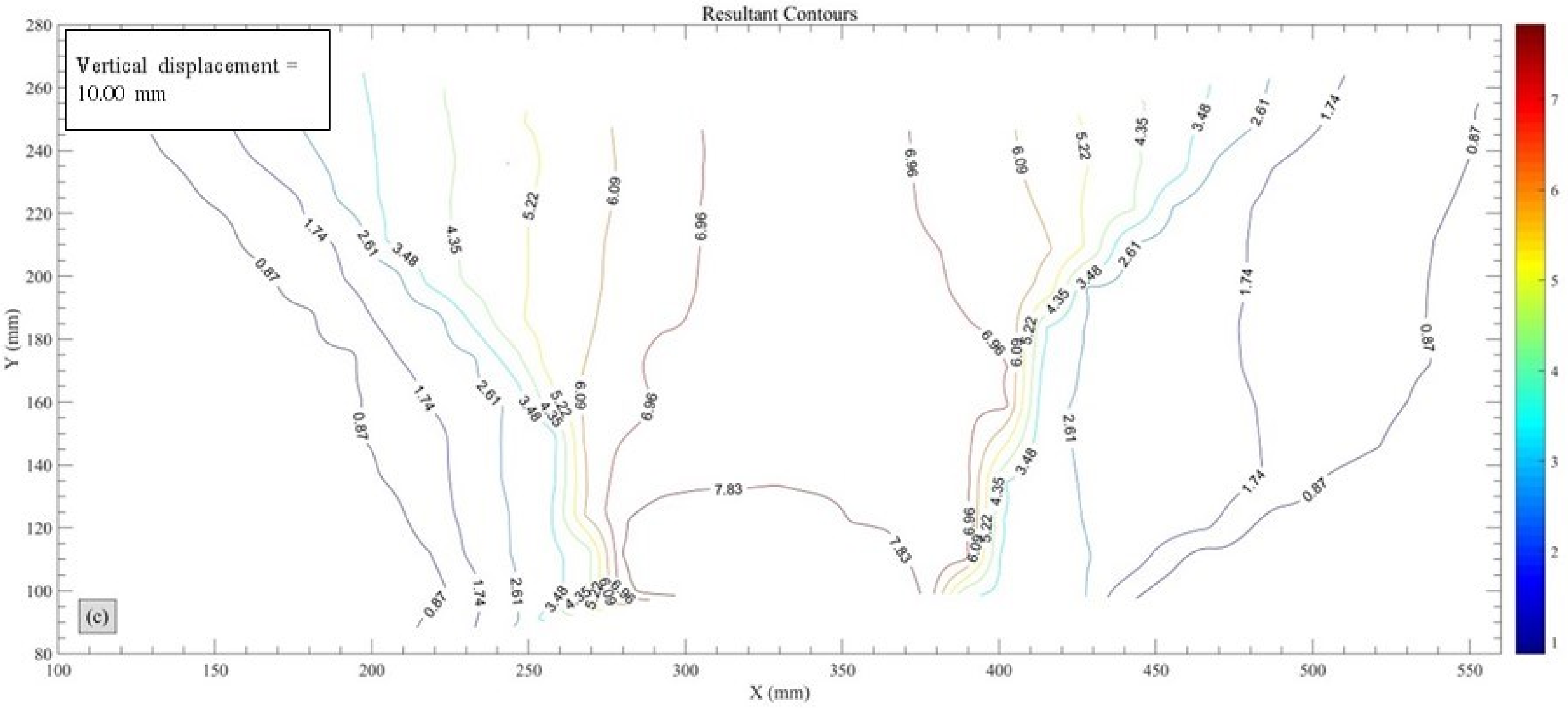

Figure B-0-13 Evolution of resultant (total) displacements – t = 10 yrs

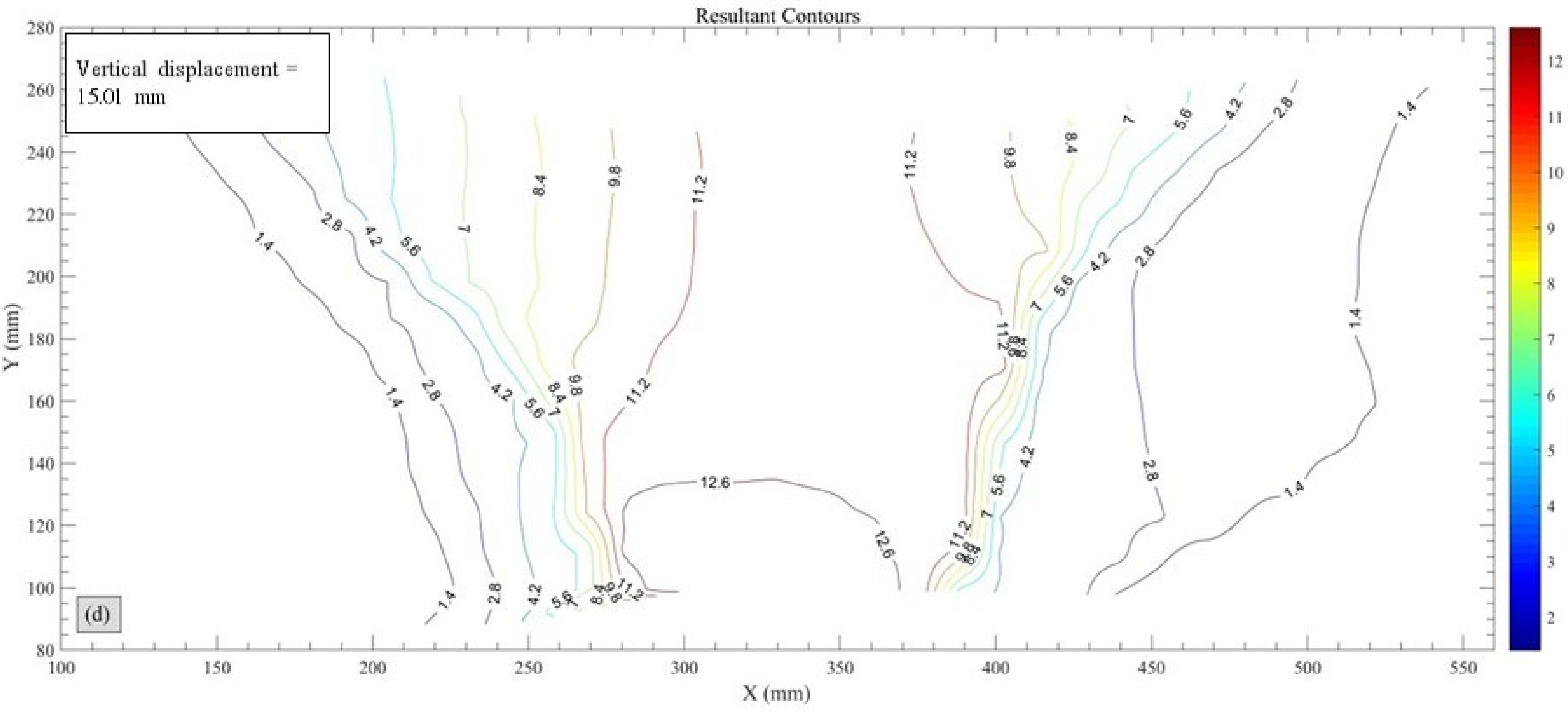

Figure B-0-14 Evolution of resultant (total) displacements – t = 10 yrs

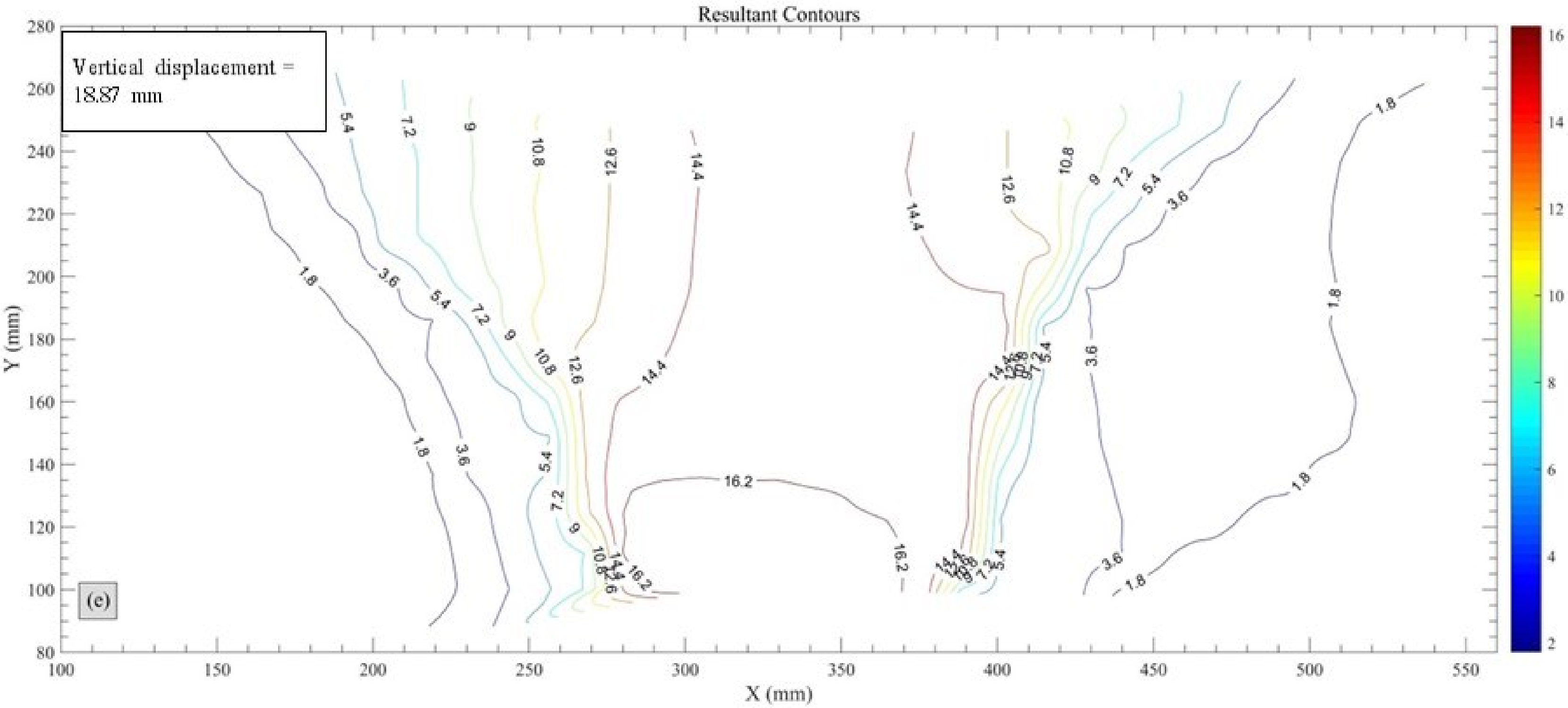

Figure B-0-15 Evolution of resultant (total) displacements – t = 10 yrs

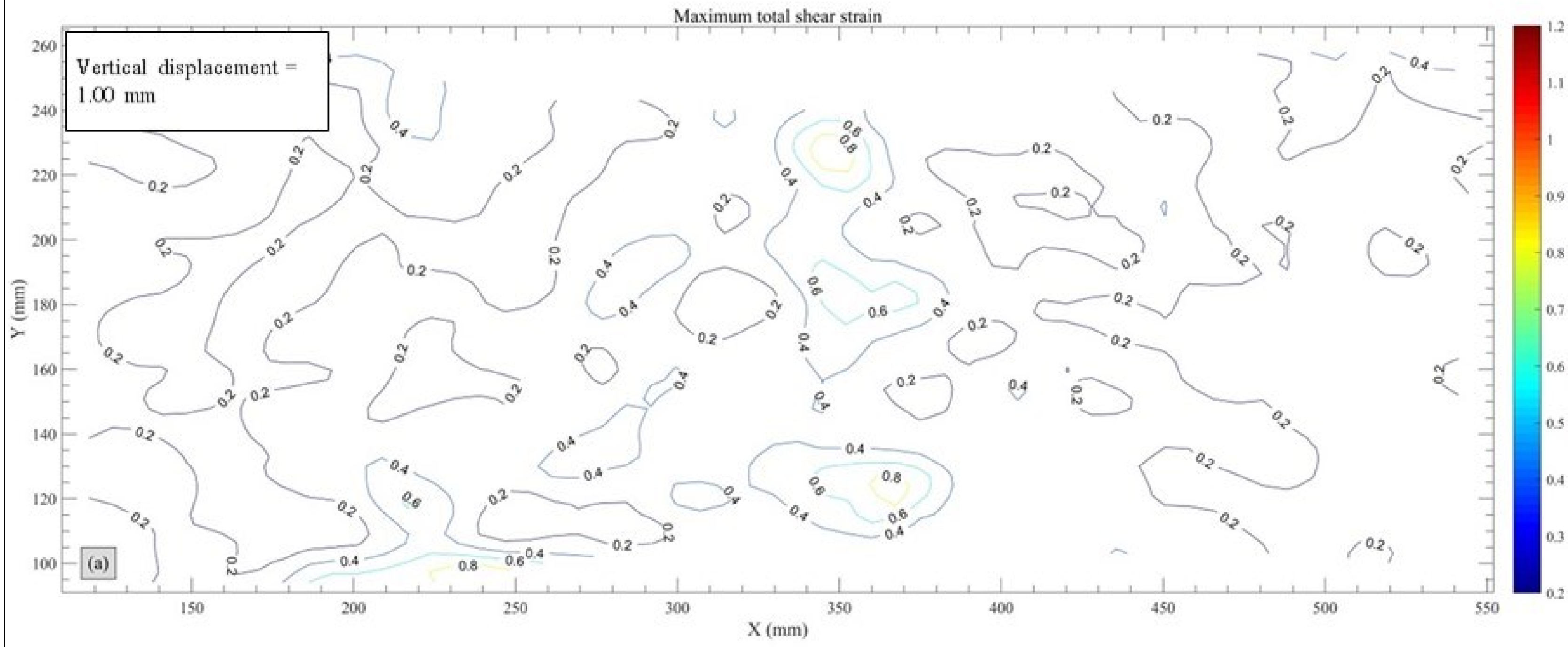

Figure B-0-16 Evolution of maximum shear strains– t = 10 yrs

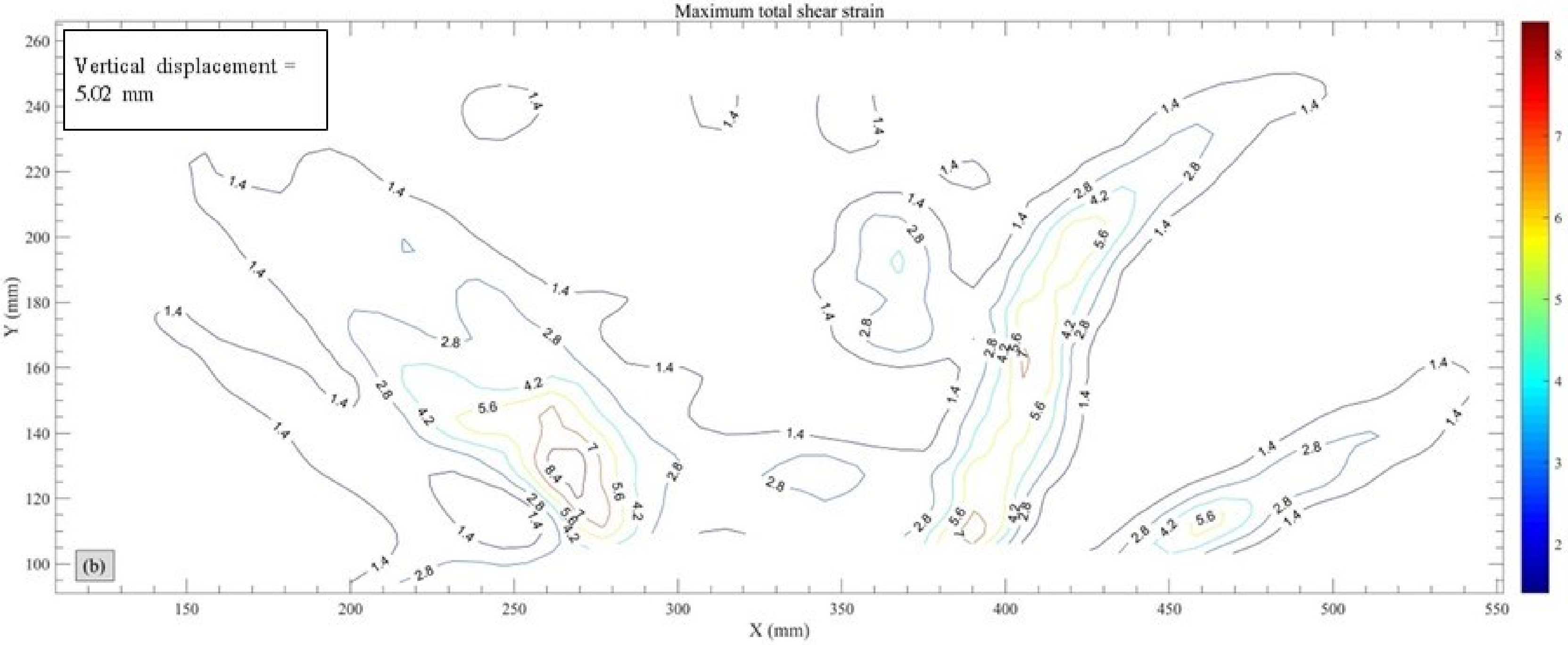

Figure B-0-17 Evolution of maximum shear strains – t = 10 yrs

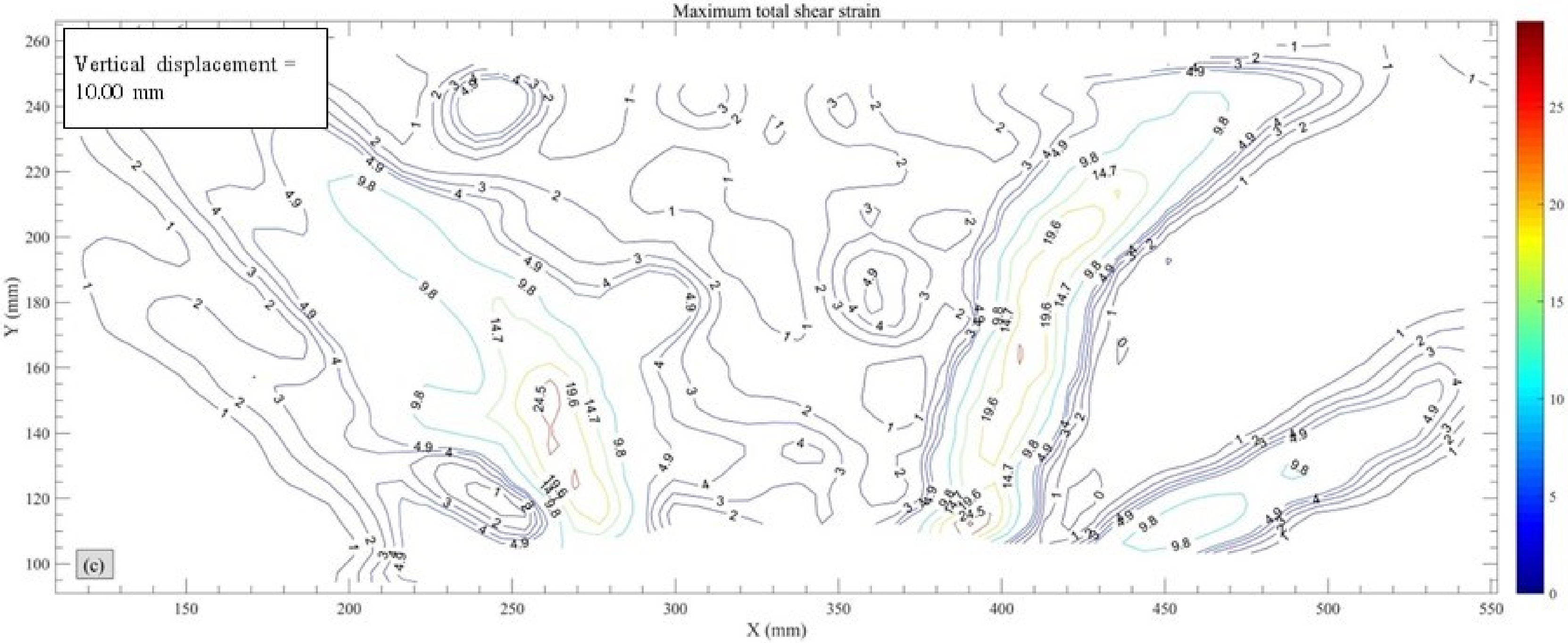

Figure B-0-18 Evolution of maximum shear strains – t = 10 yrs

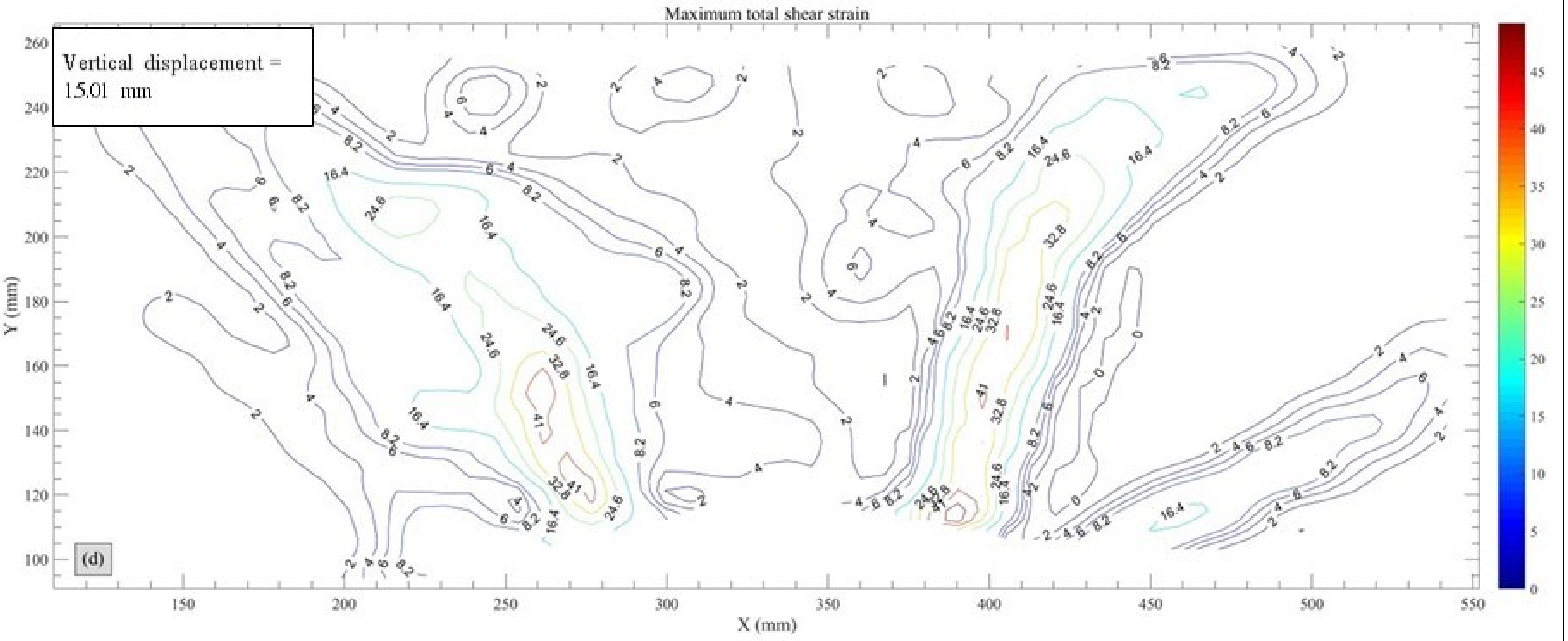

Vertical displacement =
15.01 mm

Figure B-0-19 Evolution of maximum shear strains – t = 10 yrs

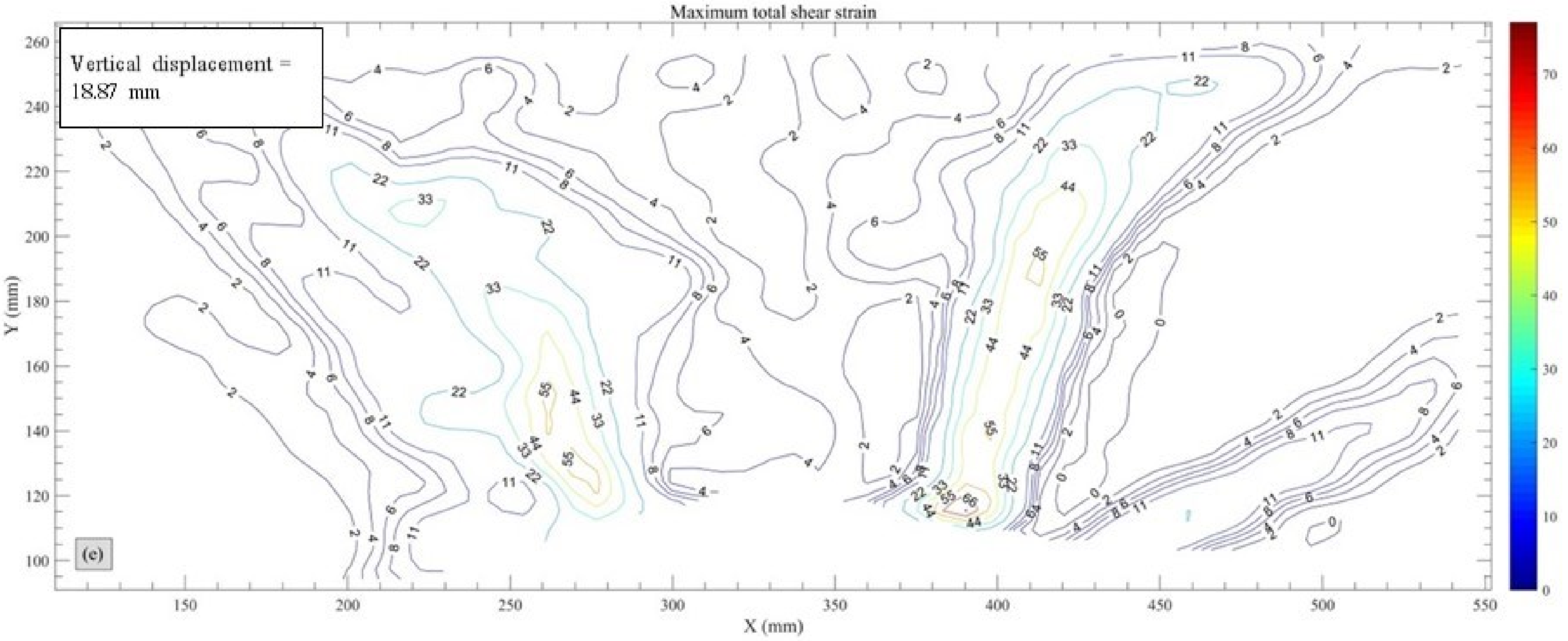

Figure B-0-20 Evolution of maximum shear strains – t = 10 yrs

Appendix C: Test results for a prototype time of 3 years

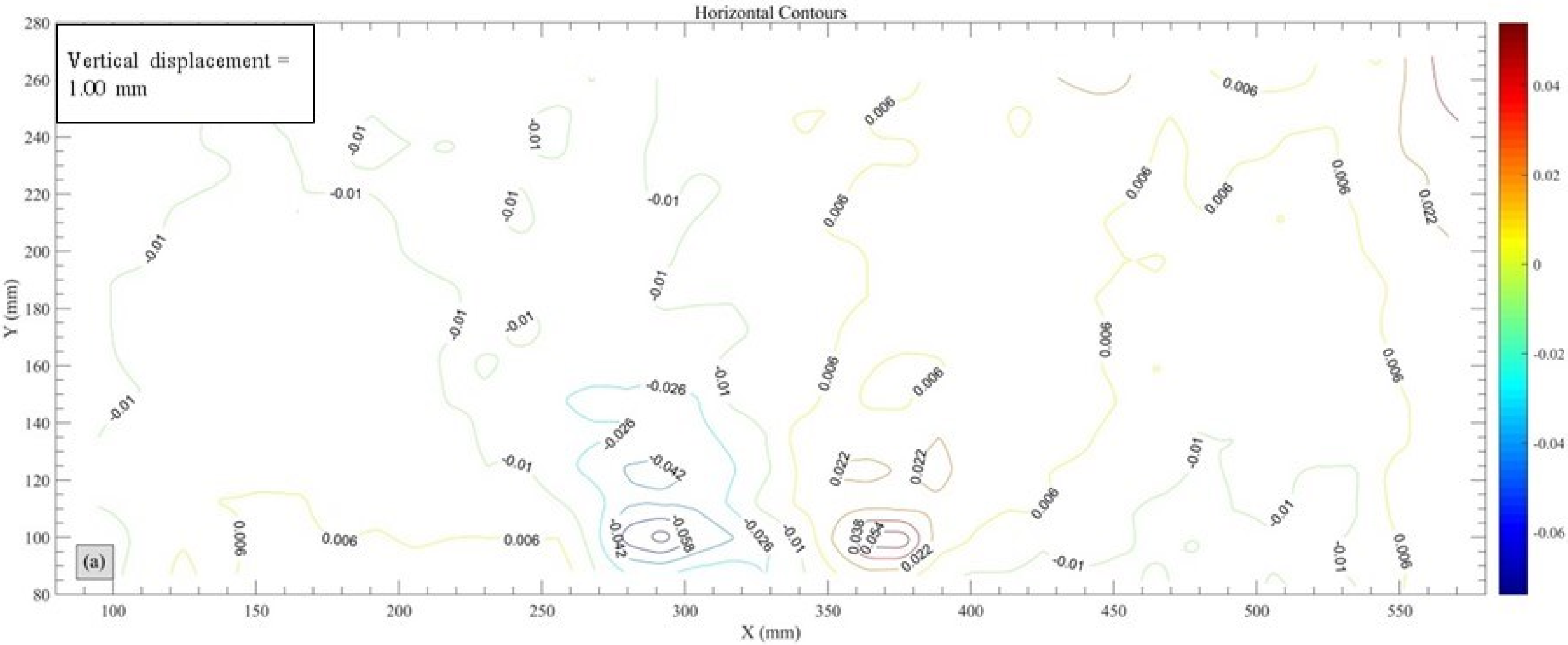

Figure C-0-1 Evolution of horizontal displacements – t = 3 yrs

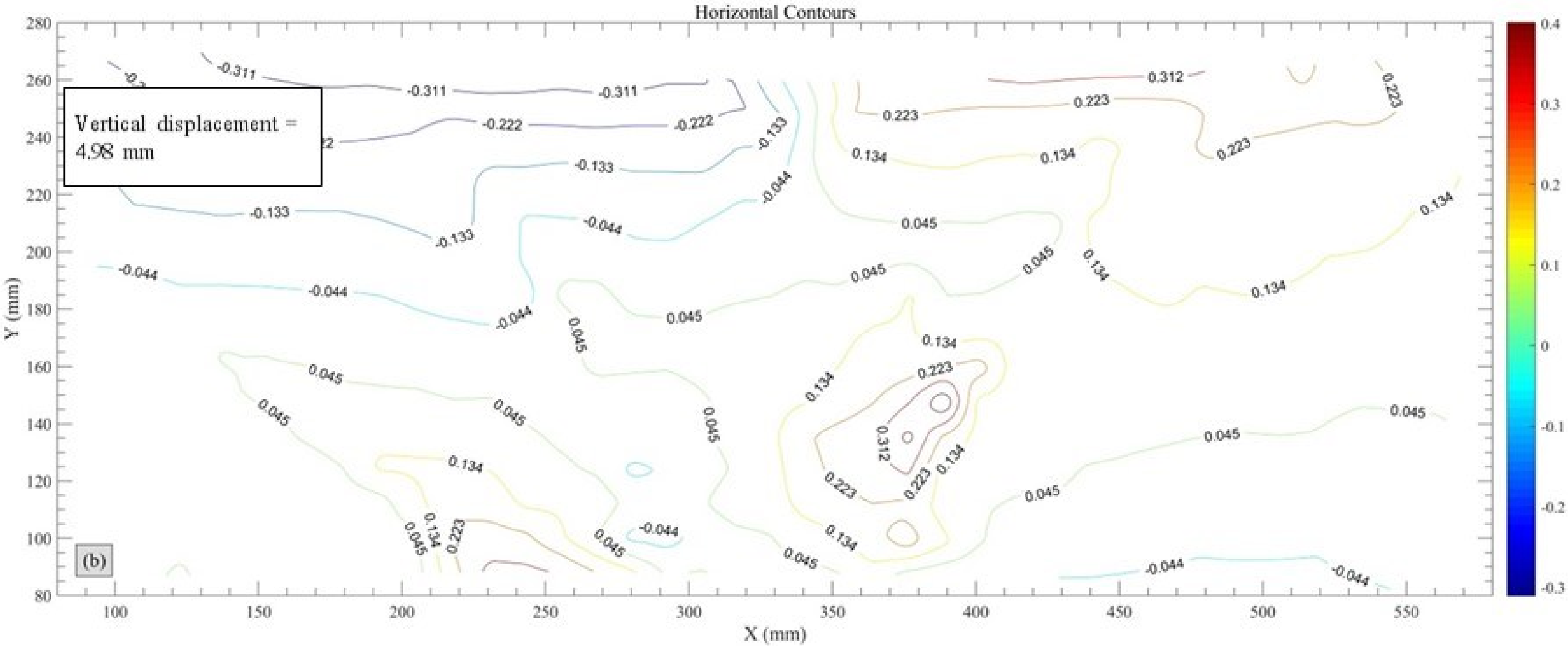

Figure C-0-2 Evolution of horizontal displacements – t = 3 yrs

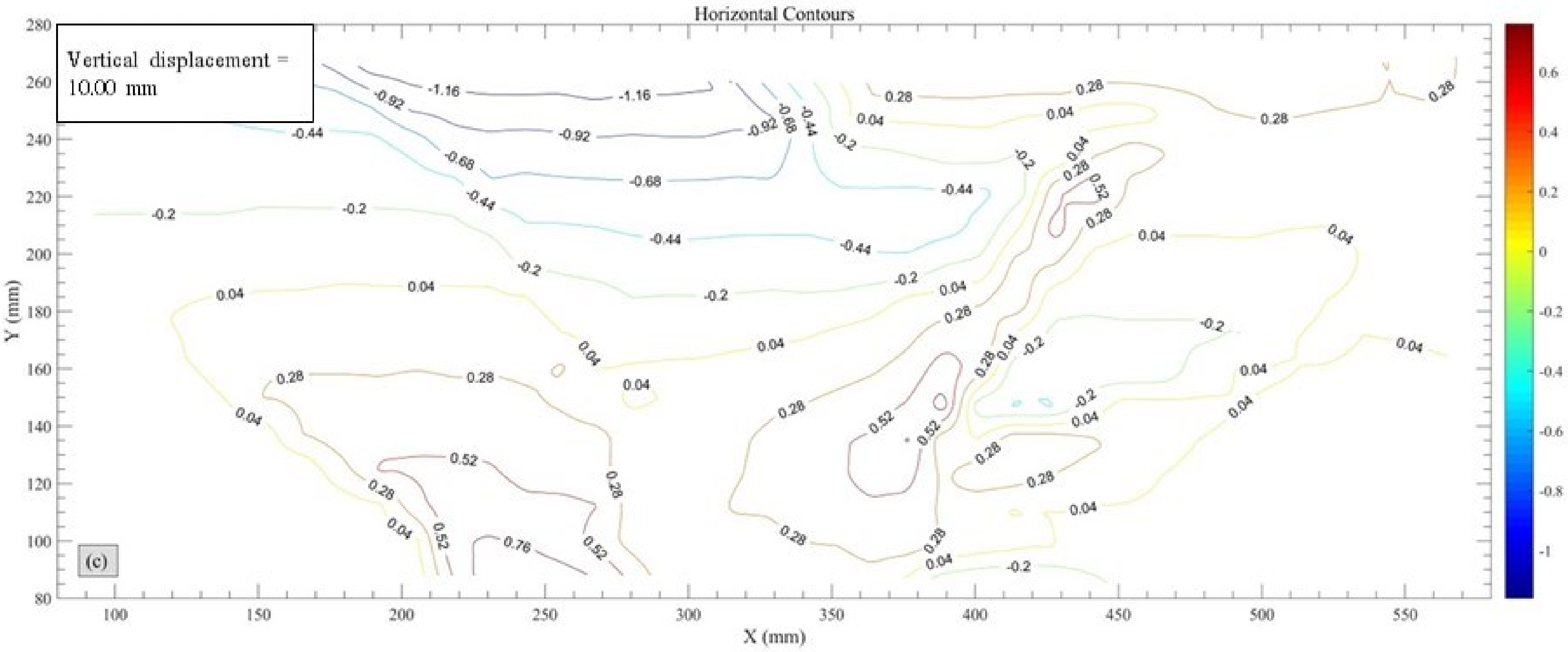

Figure C-0-3 Evolution of horizontal displacements – t = 3 yrs

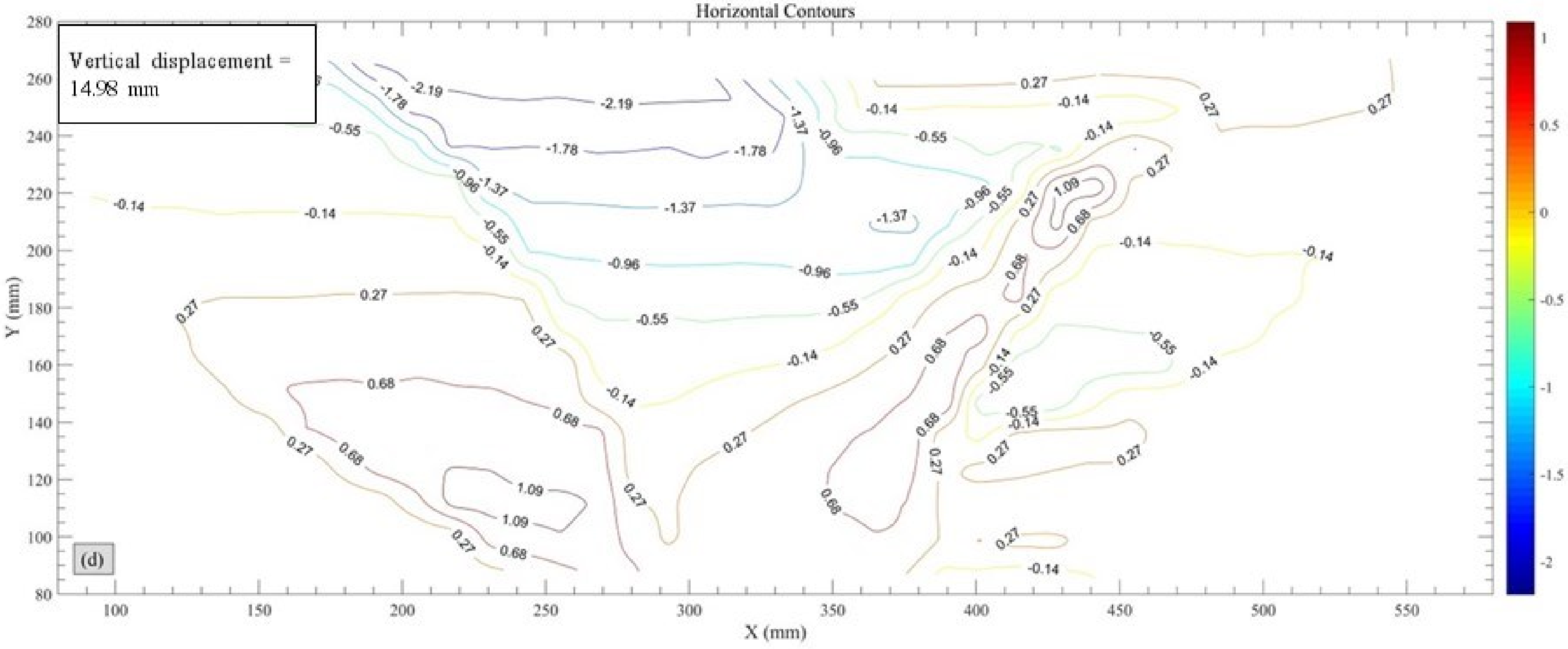

Figure C-0-4 Evolution of horizontal displacements – t = 3 yrs

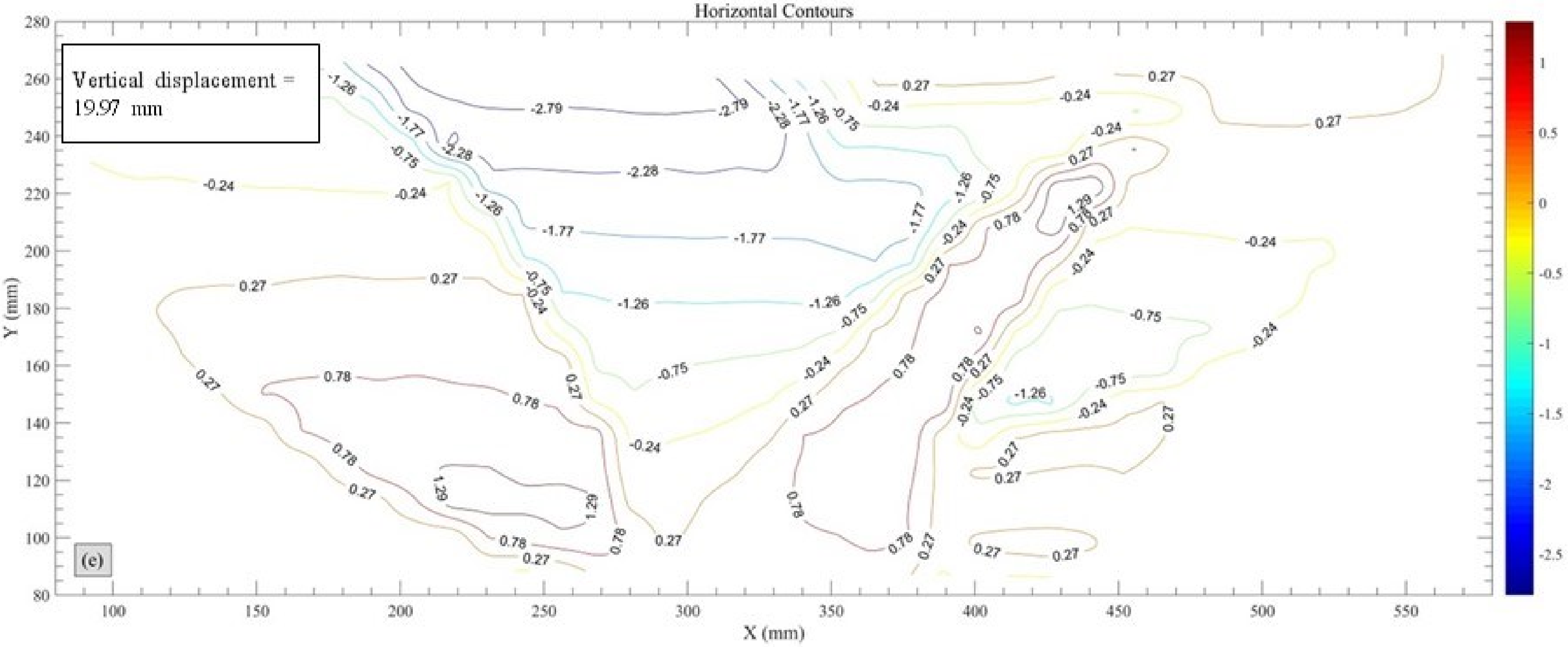

Figure C-0-5 Evolution of horizontal displacements – t = 3 yrs

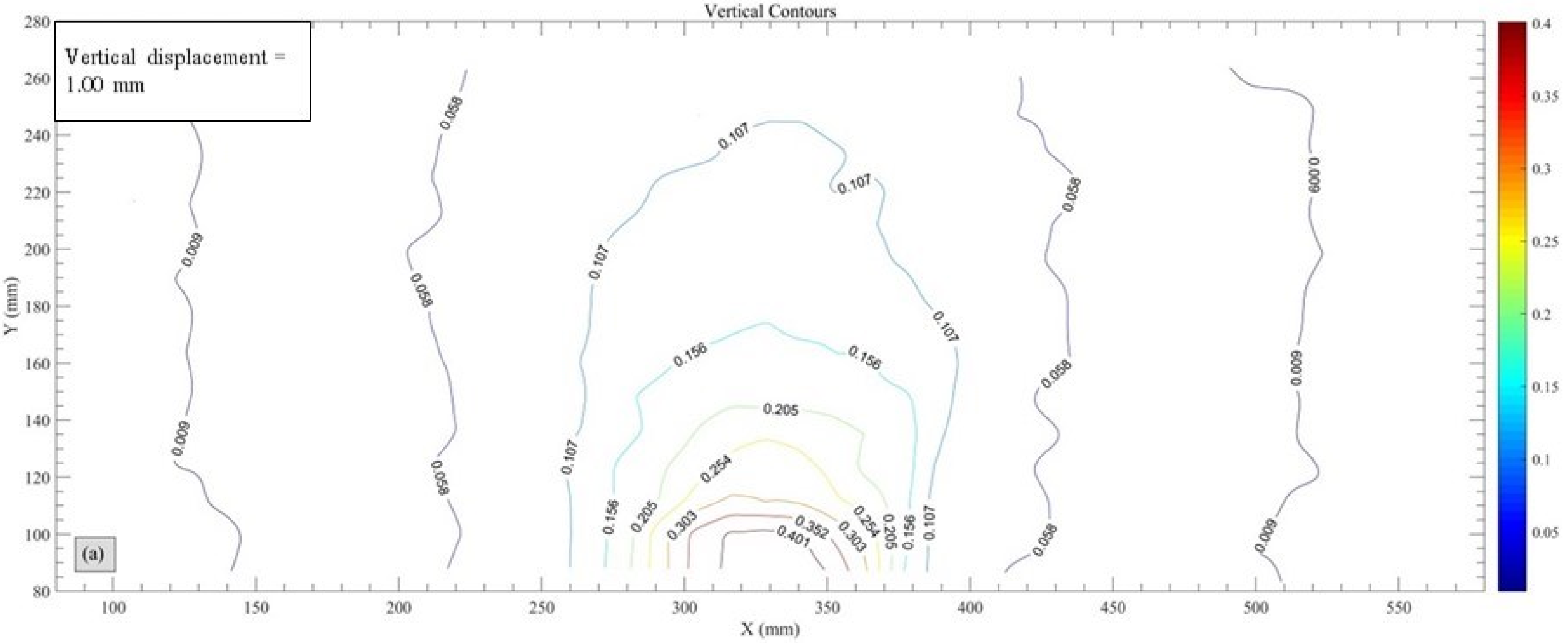

Figure C-0-6 Evolution of vertical displacements – t = 3 yrs

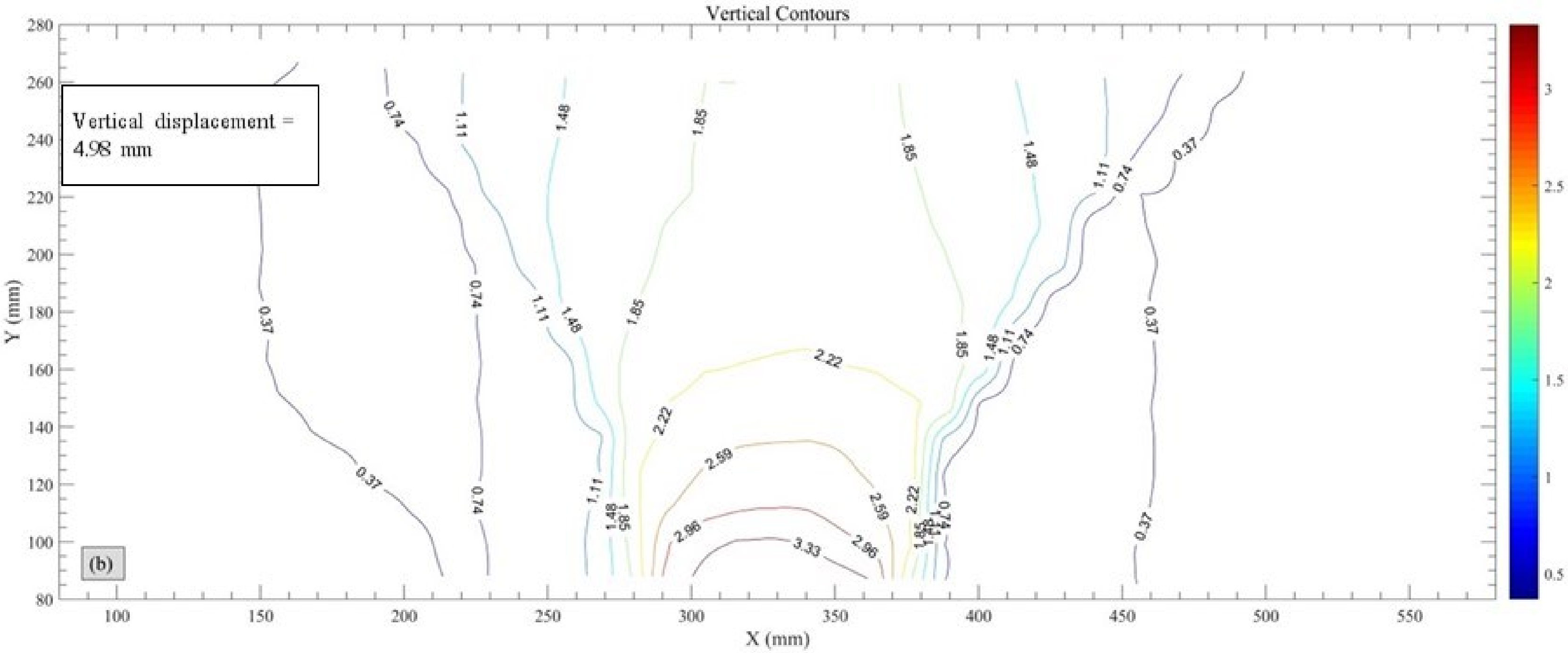

Figure C-0-7 Evolution of vertical displacements – t = 3 yrs

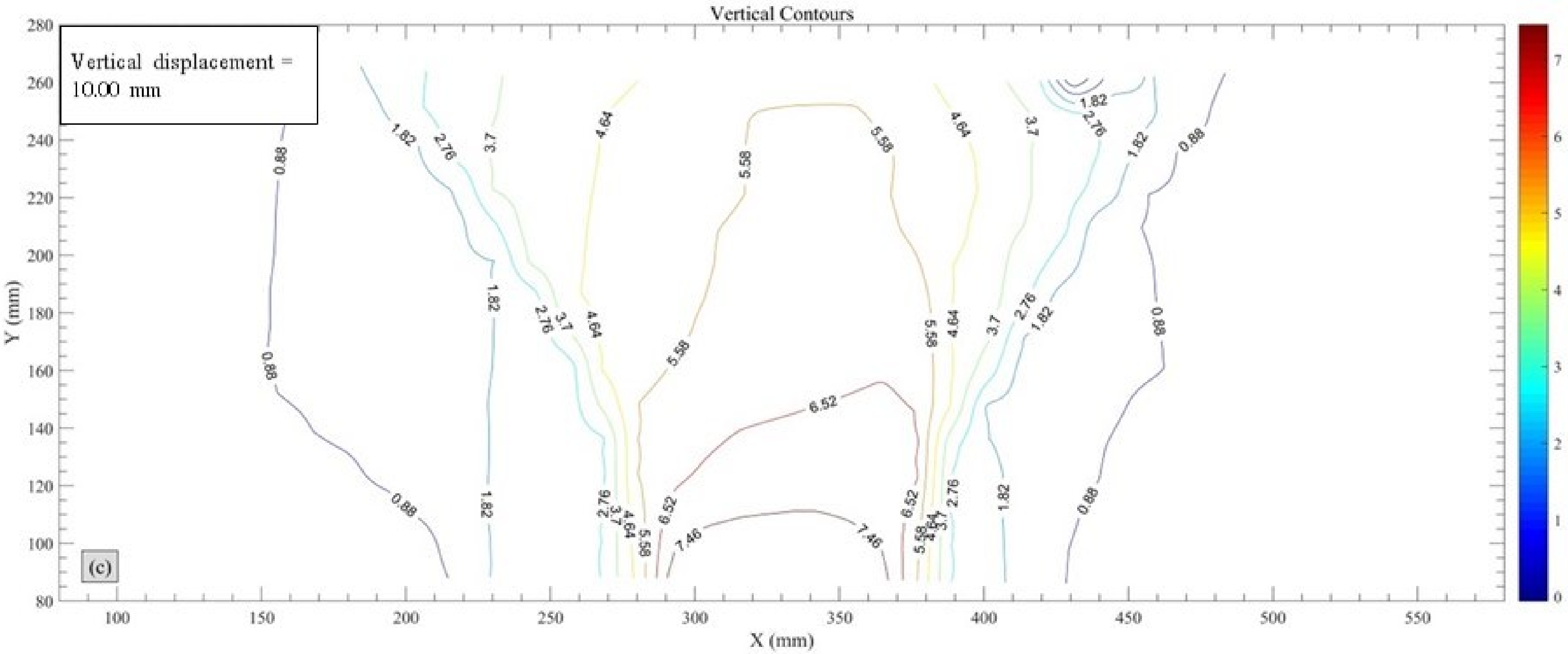

Figure C-0-8 Evolution of vertical displacements – t = 3 yrs

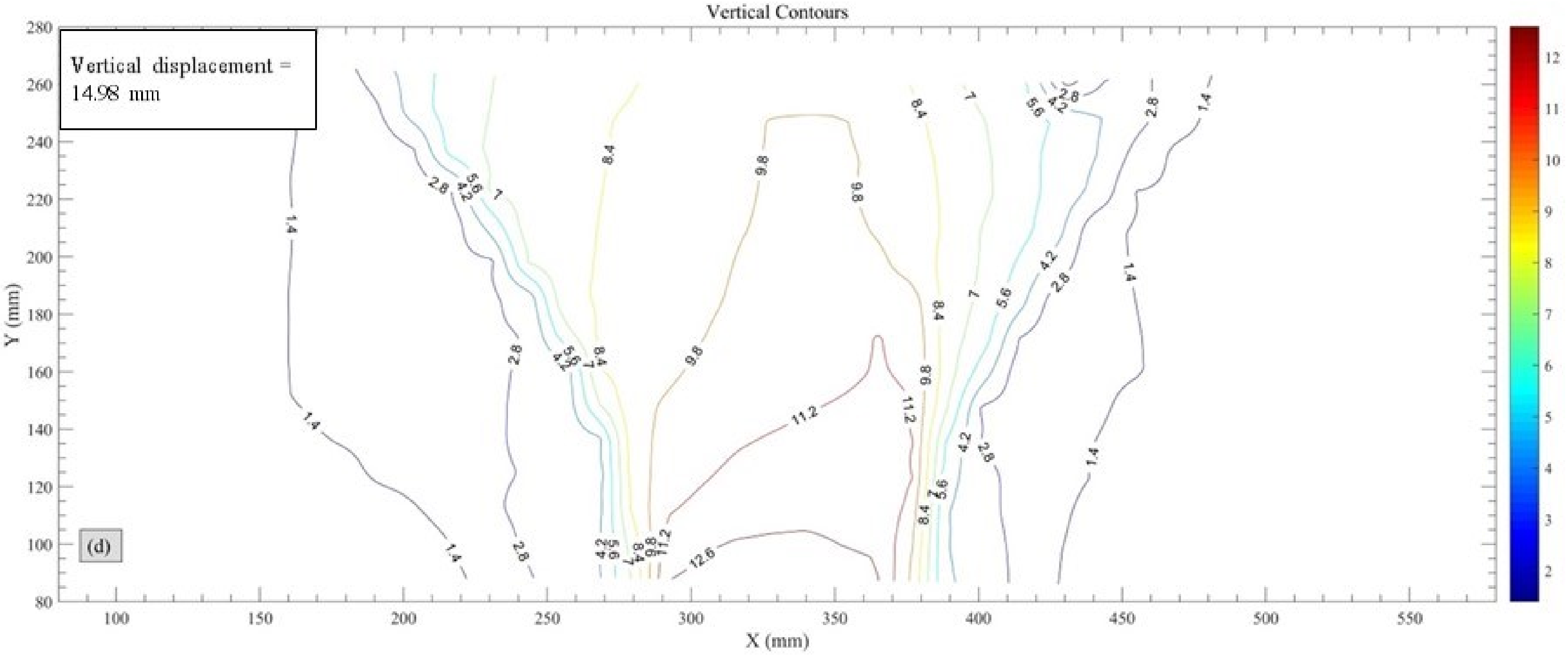

Figure C-0-9 Evolution of vertical displacements – t = 3 yrs

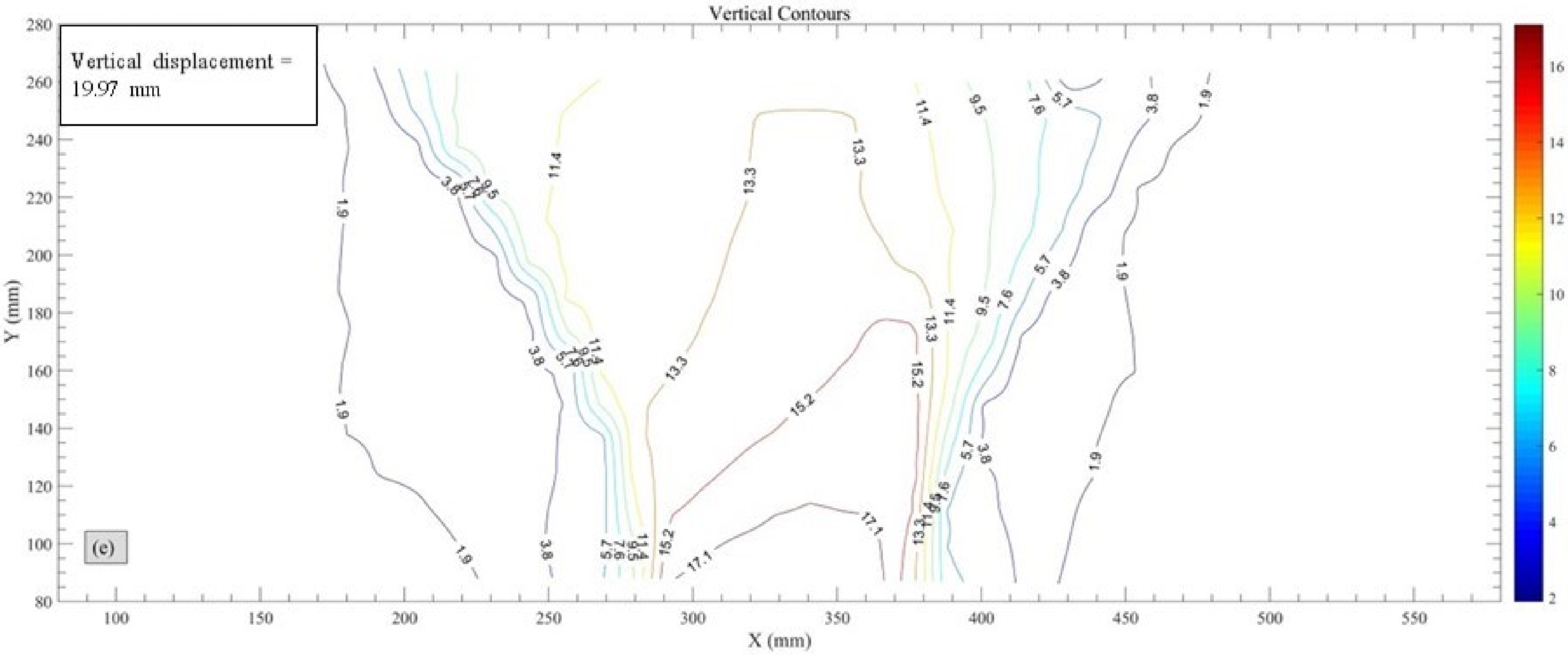

Figure C-0-10 Evolution of vertical displacements – t = 3 yrs

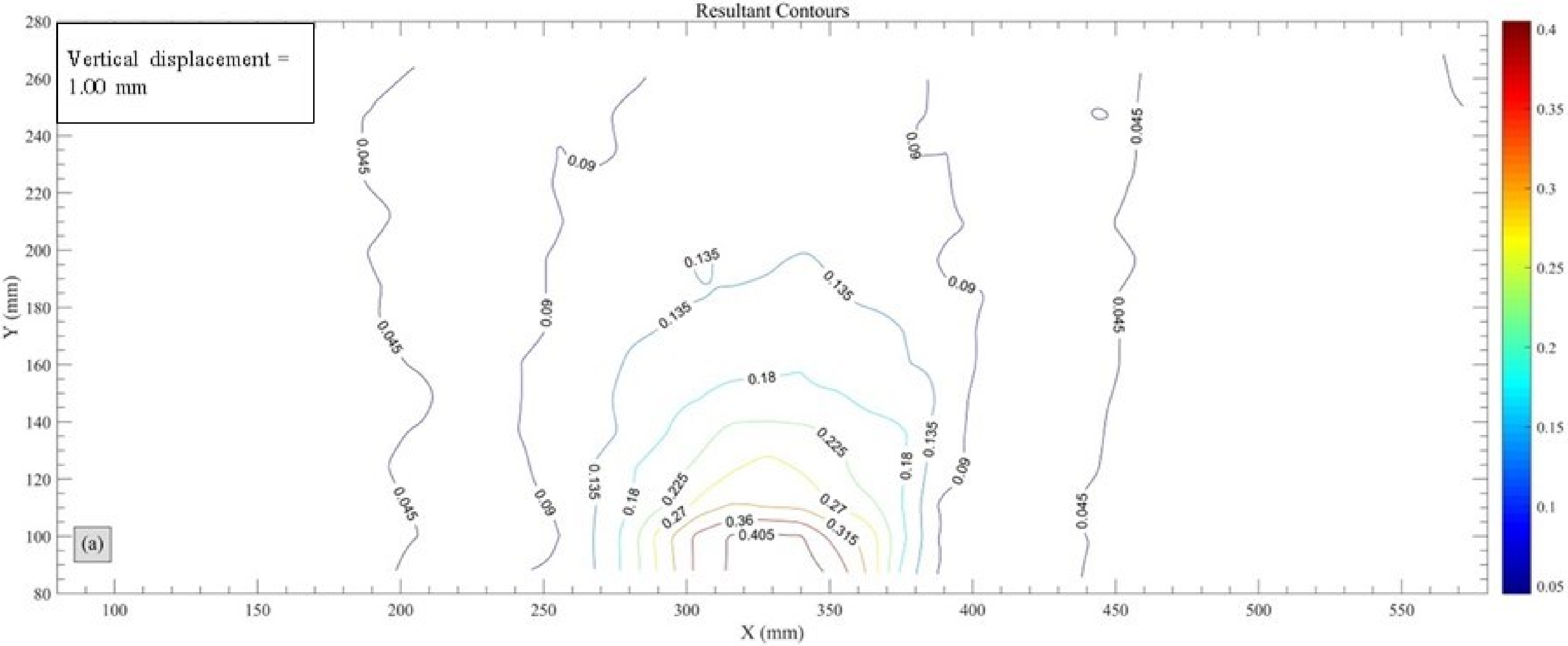

Figure C-0-11 Evolution of resultant (total) displacements – t = 3 yrs

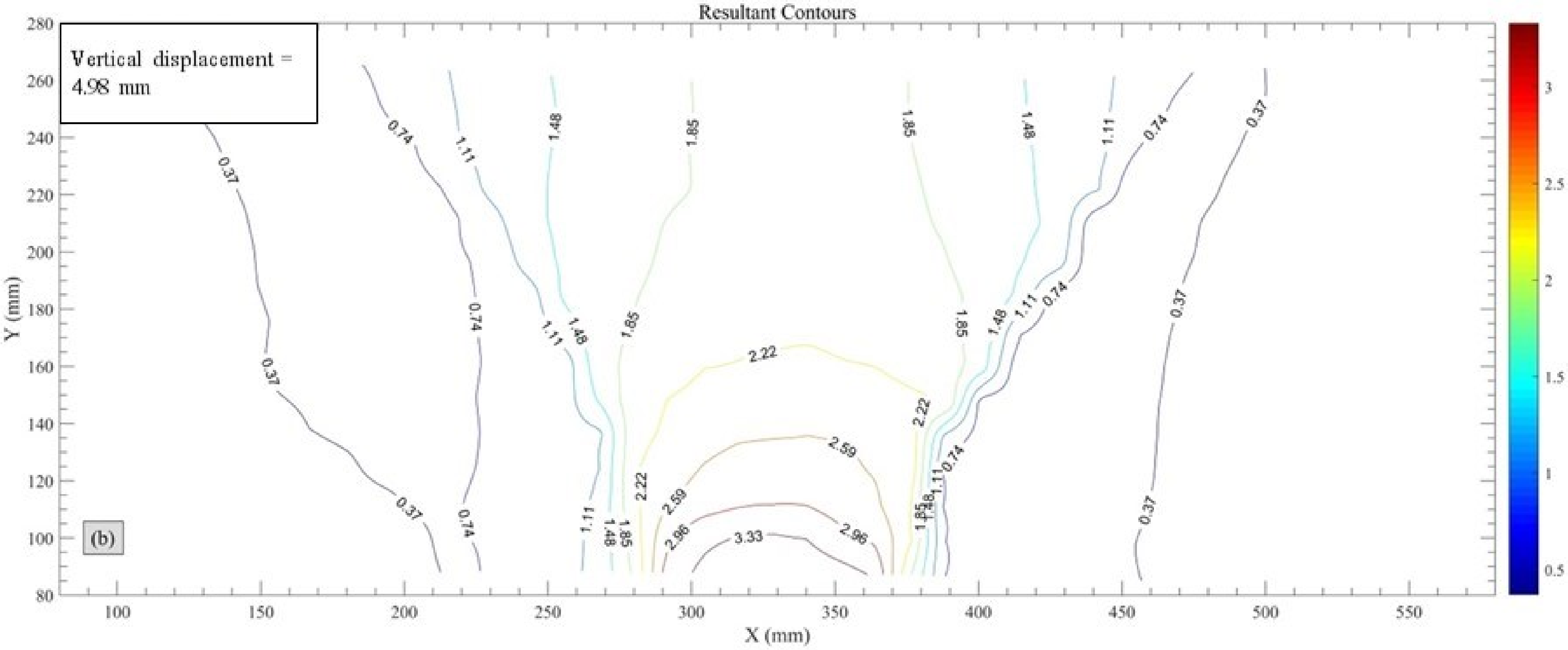

Figure C-0-12 Evolution of resultant (total) displacements – t = 3 yrs

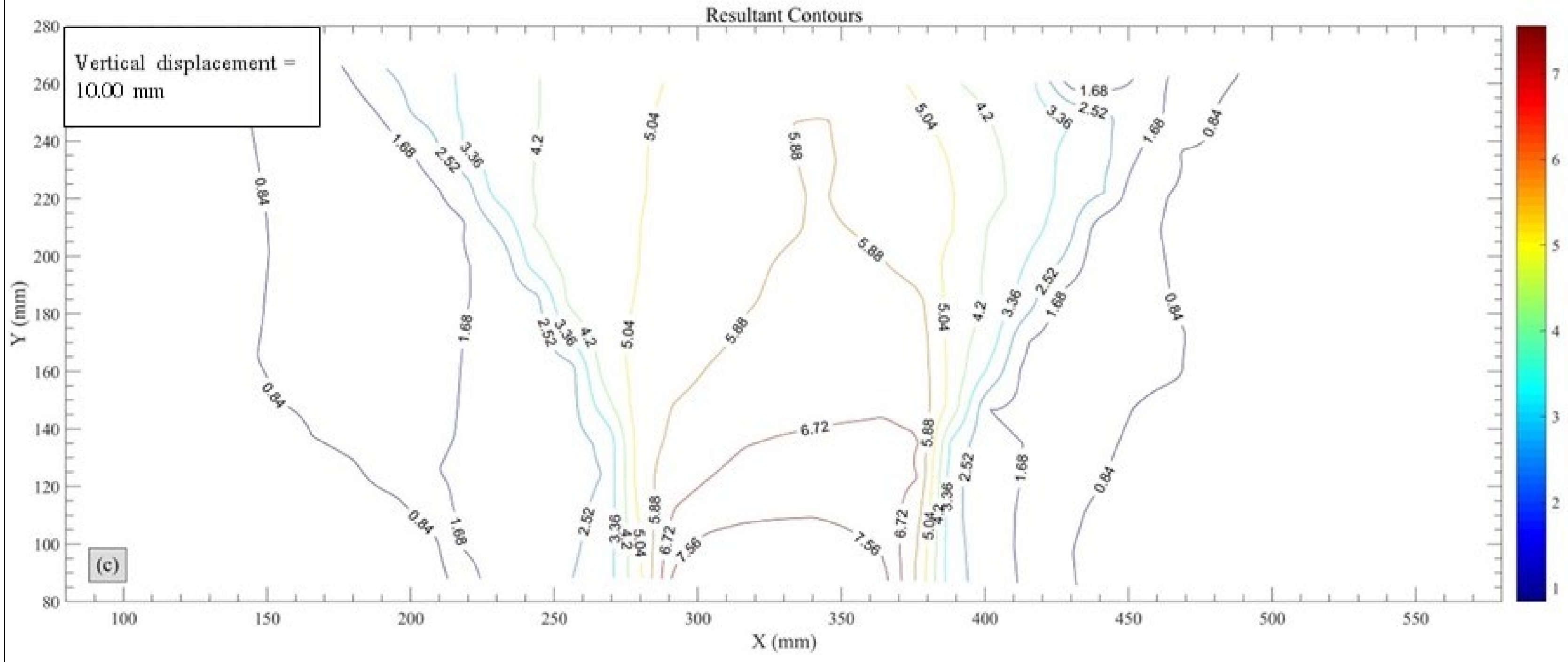

Figure C-0-13 Evolution of resultant (total) displacements – t = 3 yrs

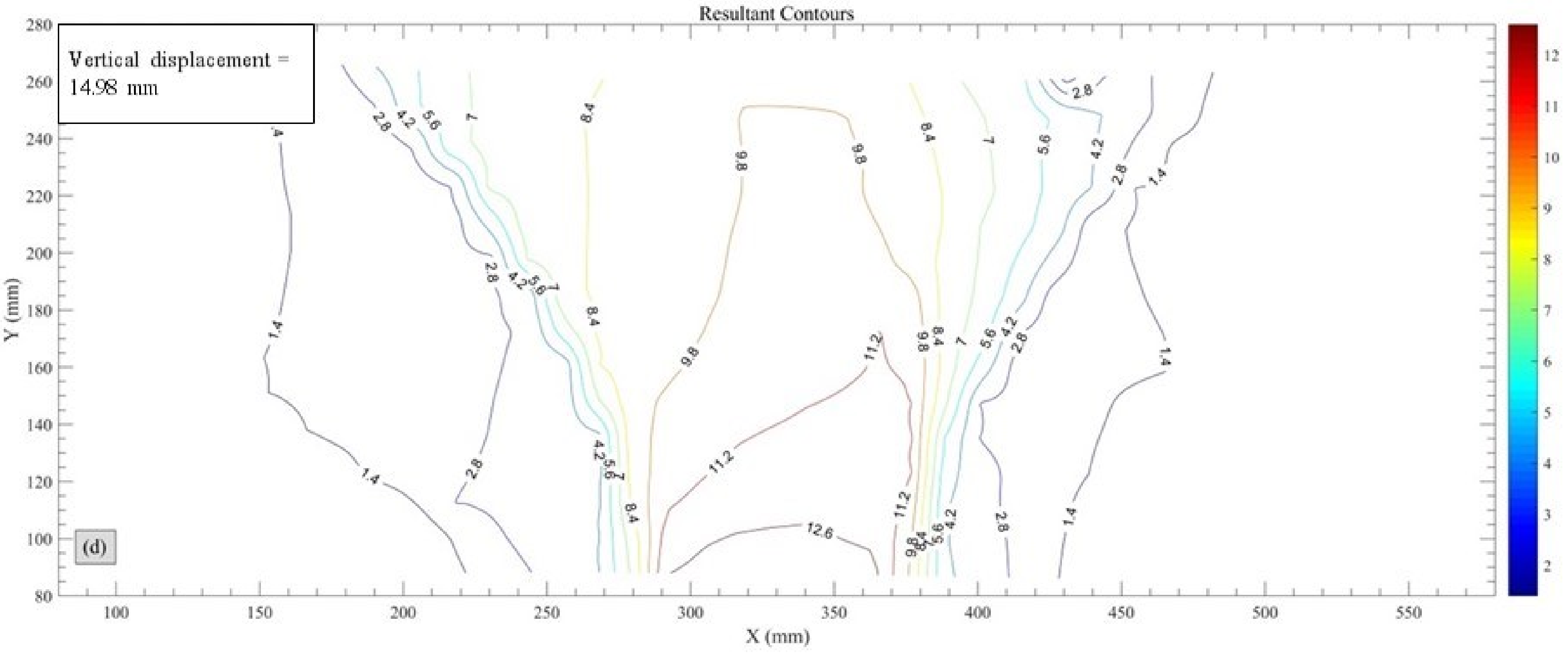

Figure C-0-14 Evolution of resultant (total) displacements – t = 3 yrs

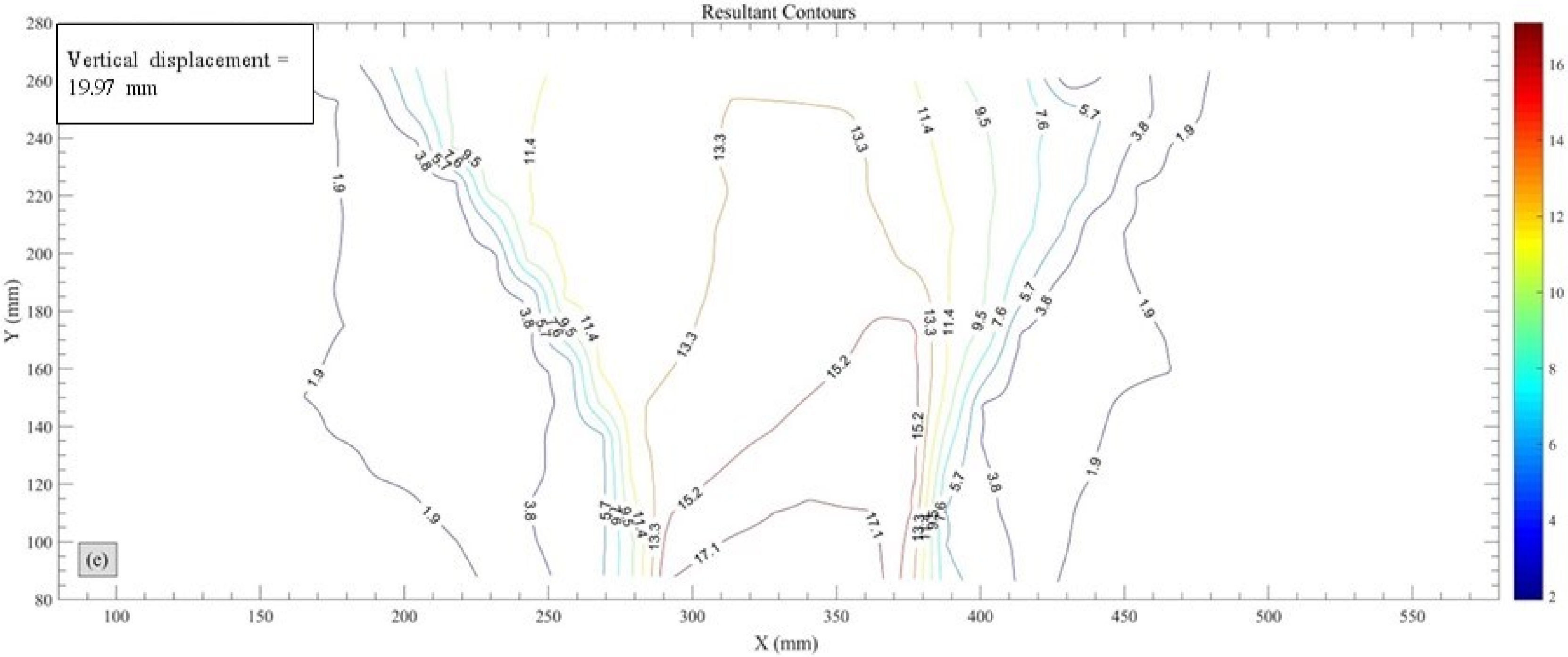

Figure C-0-15 Evolution of resultant (total) displacements – t = 3 yrs

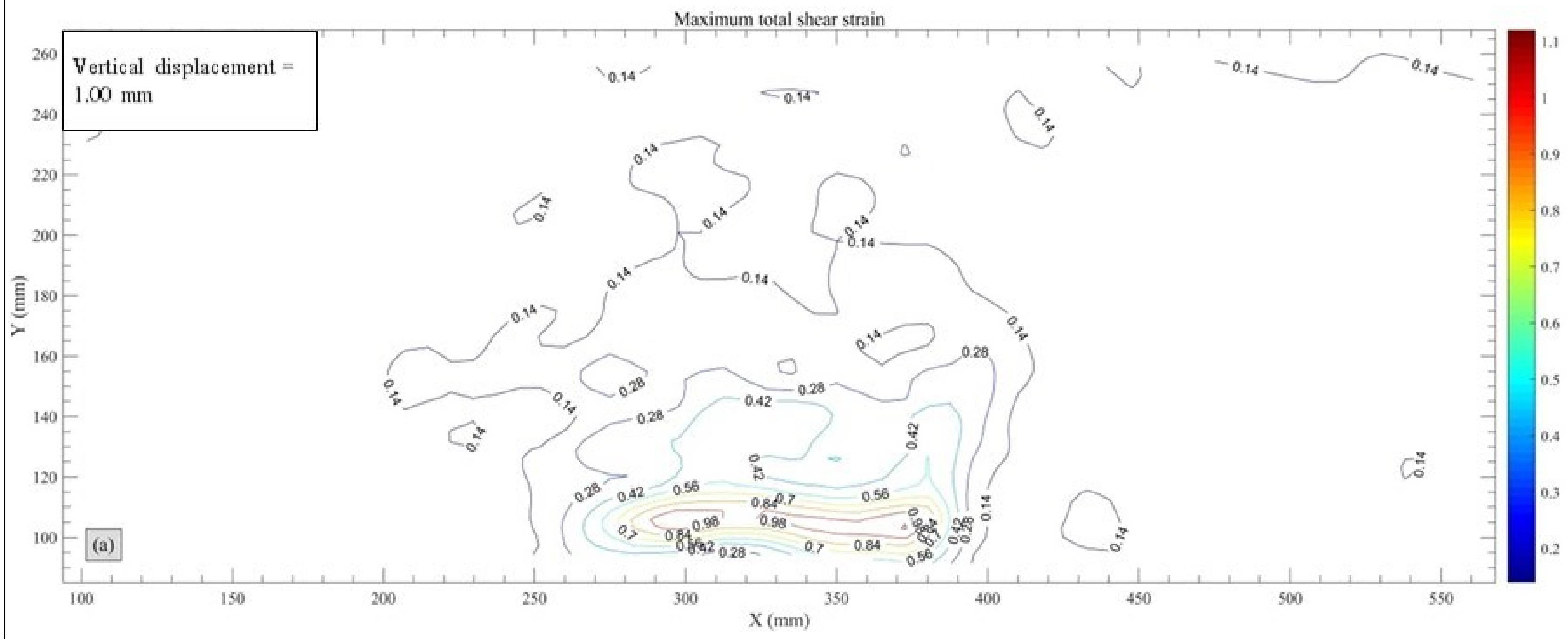

Figure C-0-16 Evolution of maximum shear strains– t = 3 yrs

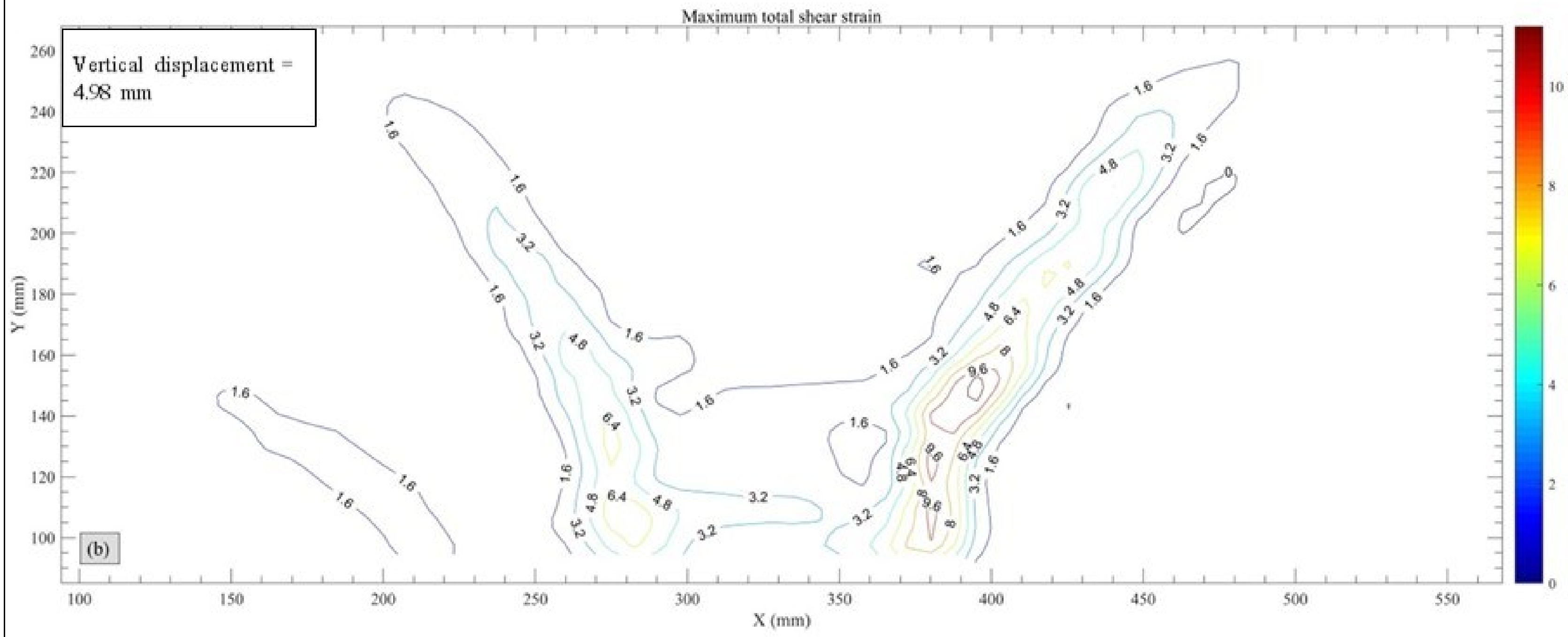

Figure C-0-17 Evolution of maximum shear strains – t = 3 yrs

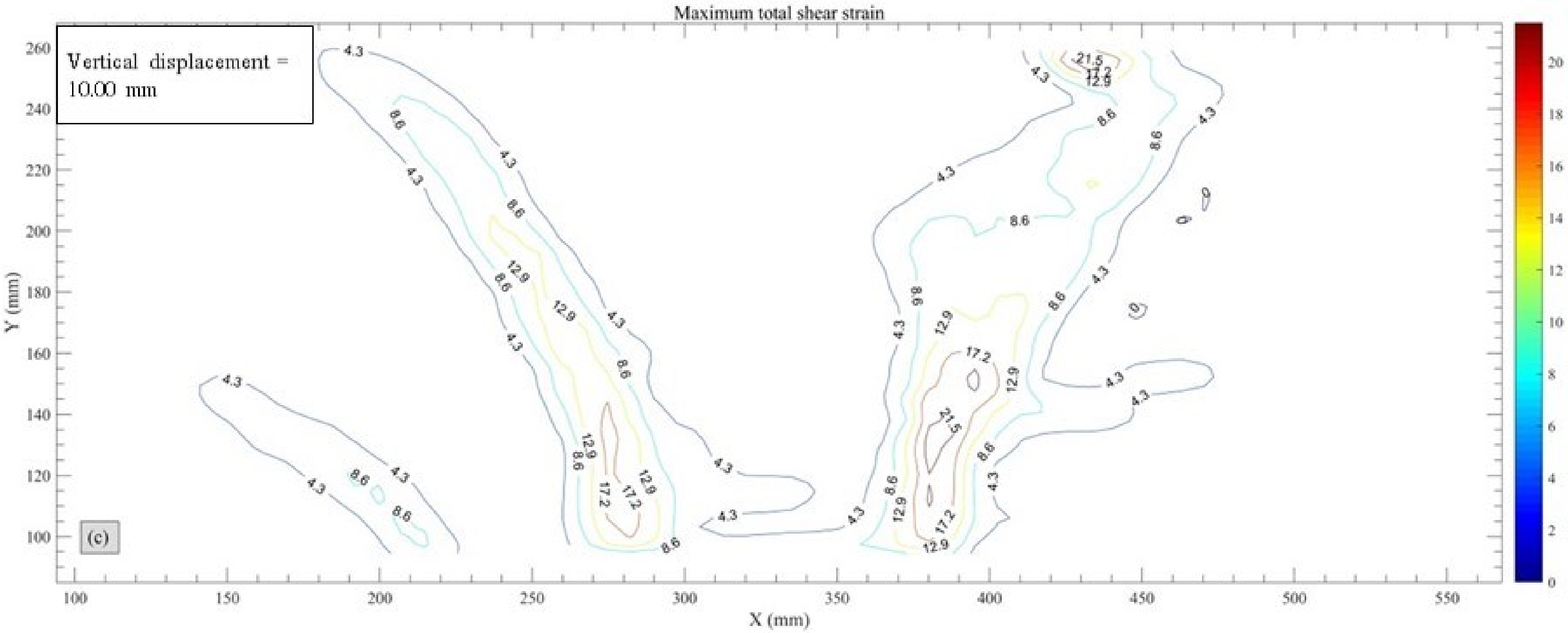

Figure C-0-18 Evolution of maximum shear strains – t = 3 yrs

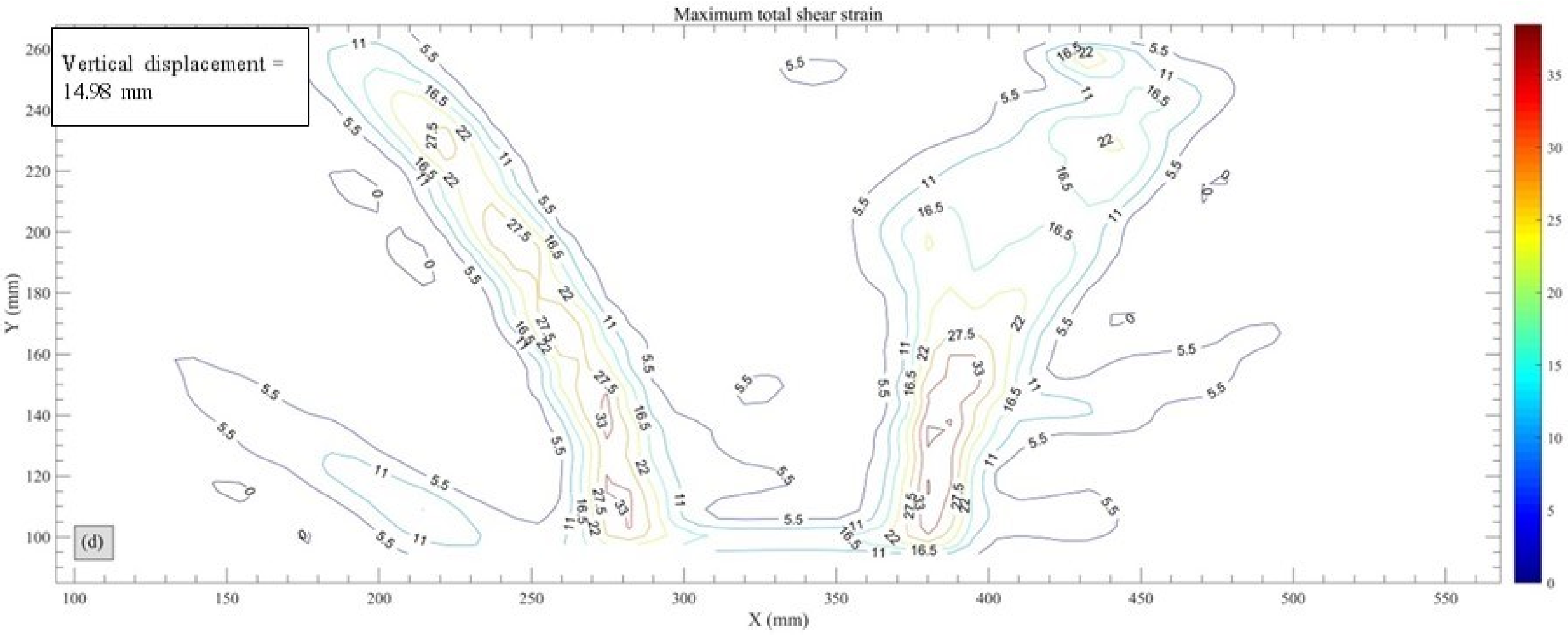

Figure C-0-19 Evolution of maximum shear strains – t = 3 yrs

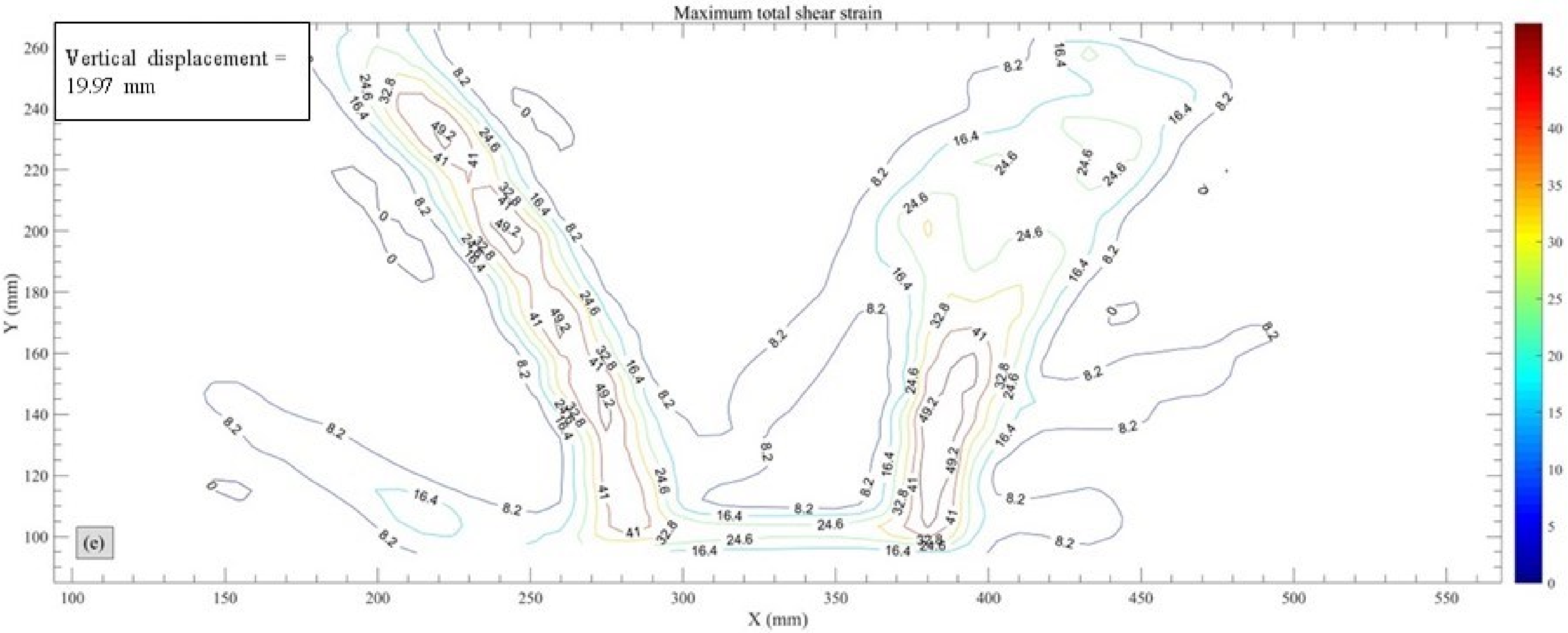

Figure C-0-20 Evolution of maximum shear strains – t = 3 yrs

Appendix D: Test results for a prototype time of 15 years

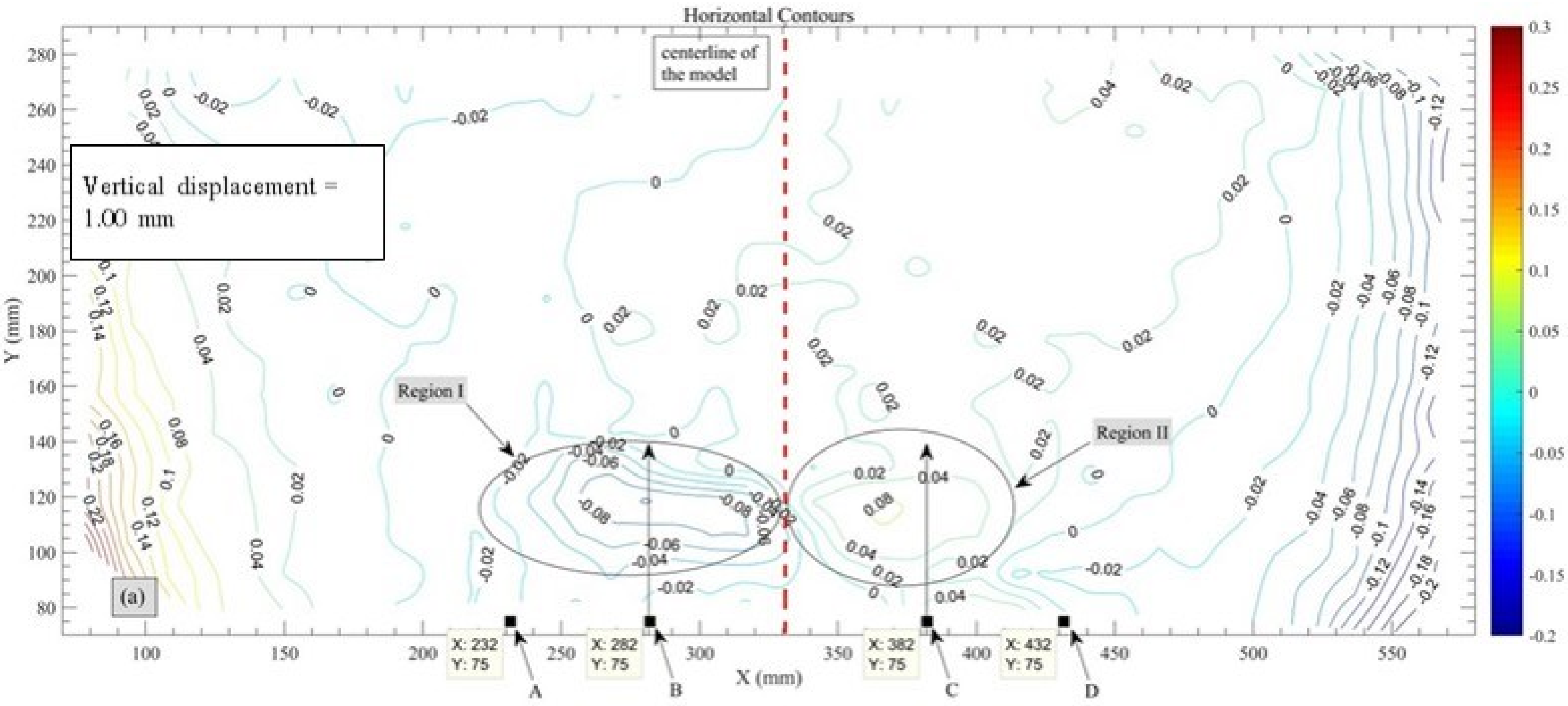

Figure D-0-1 Evolution of horizontal displacements – t = 15 yrs

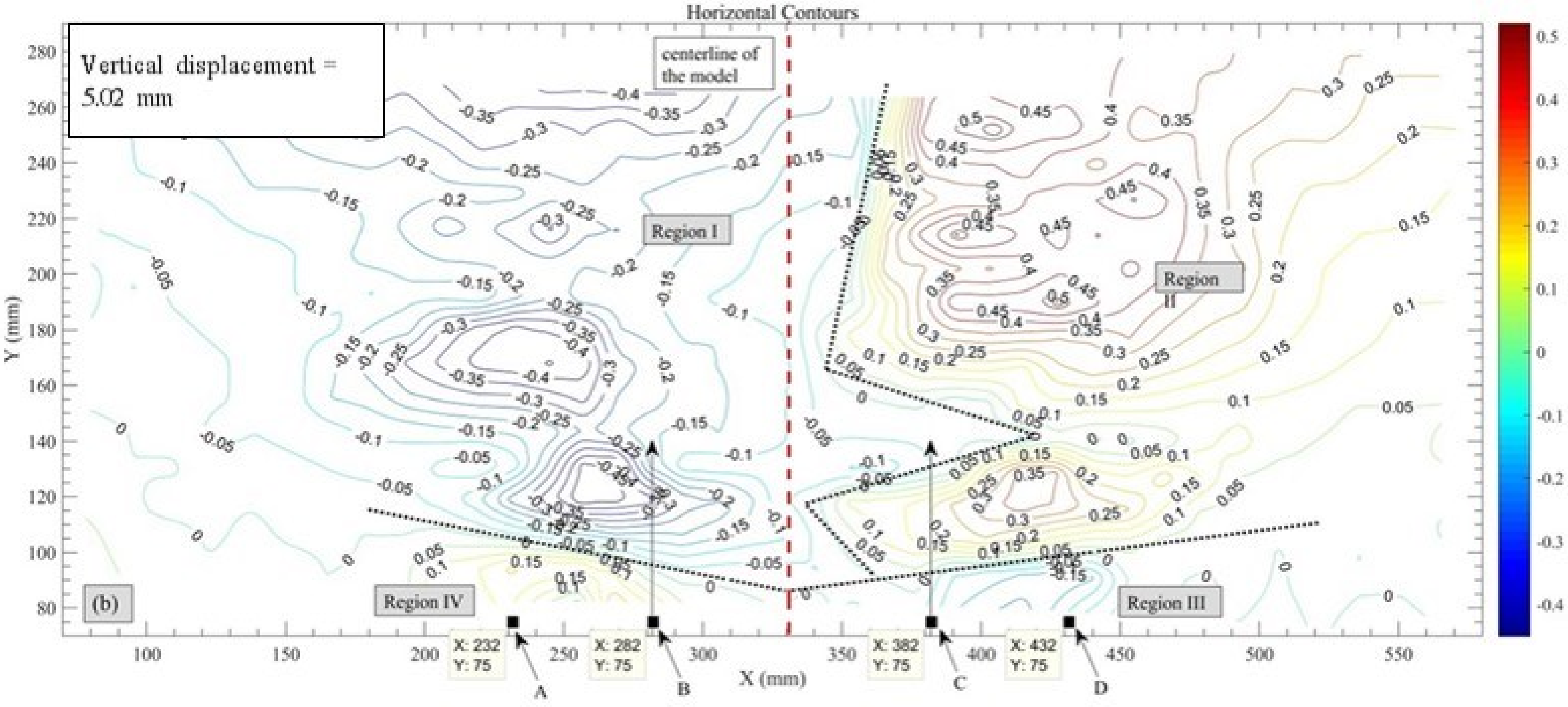

Figure D-0-2 Evolution of horizontal displacements – t = 15 yrs

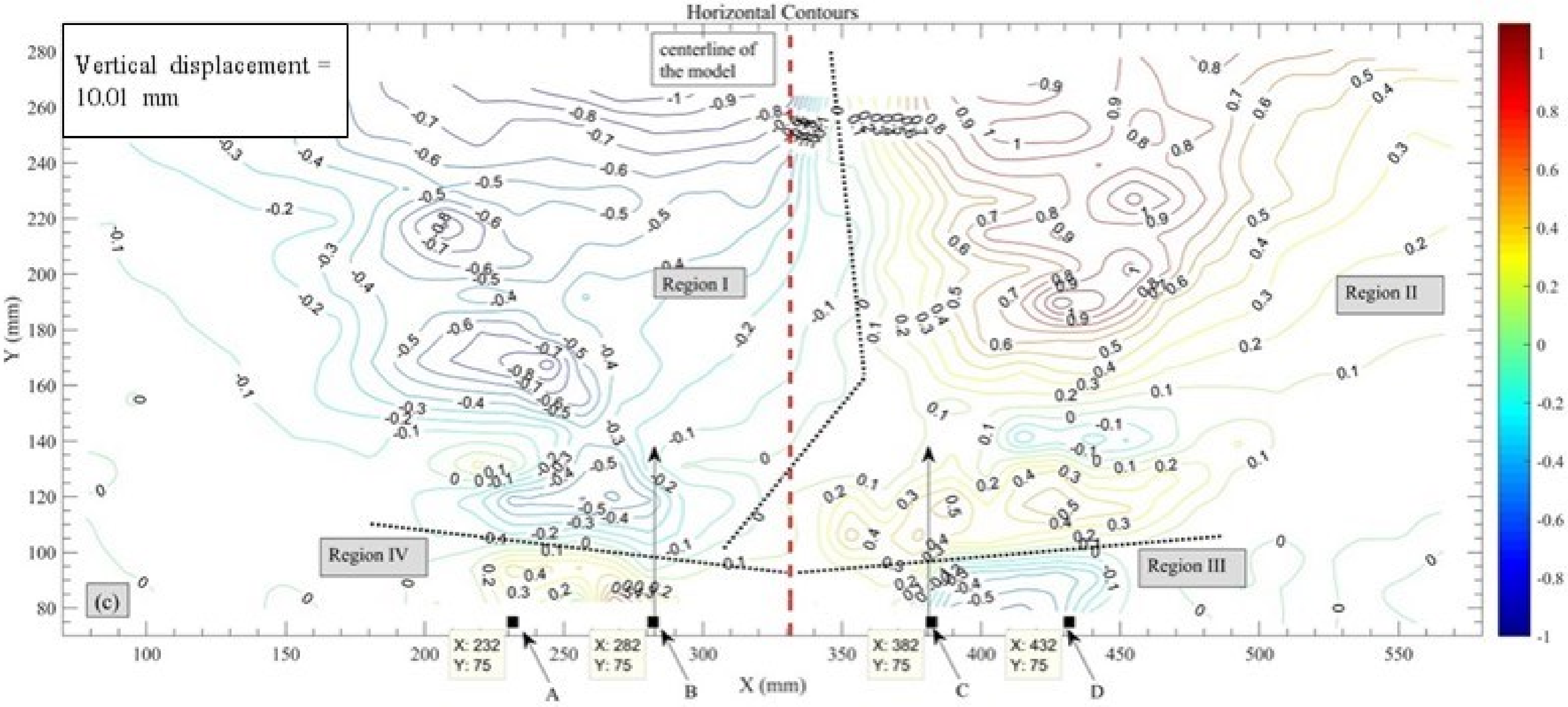

Figure D-0-3 Evolution of horizontal displacements – t = 15 yrs

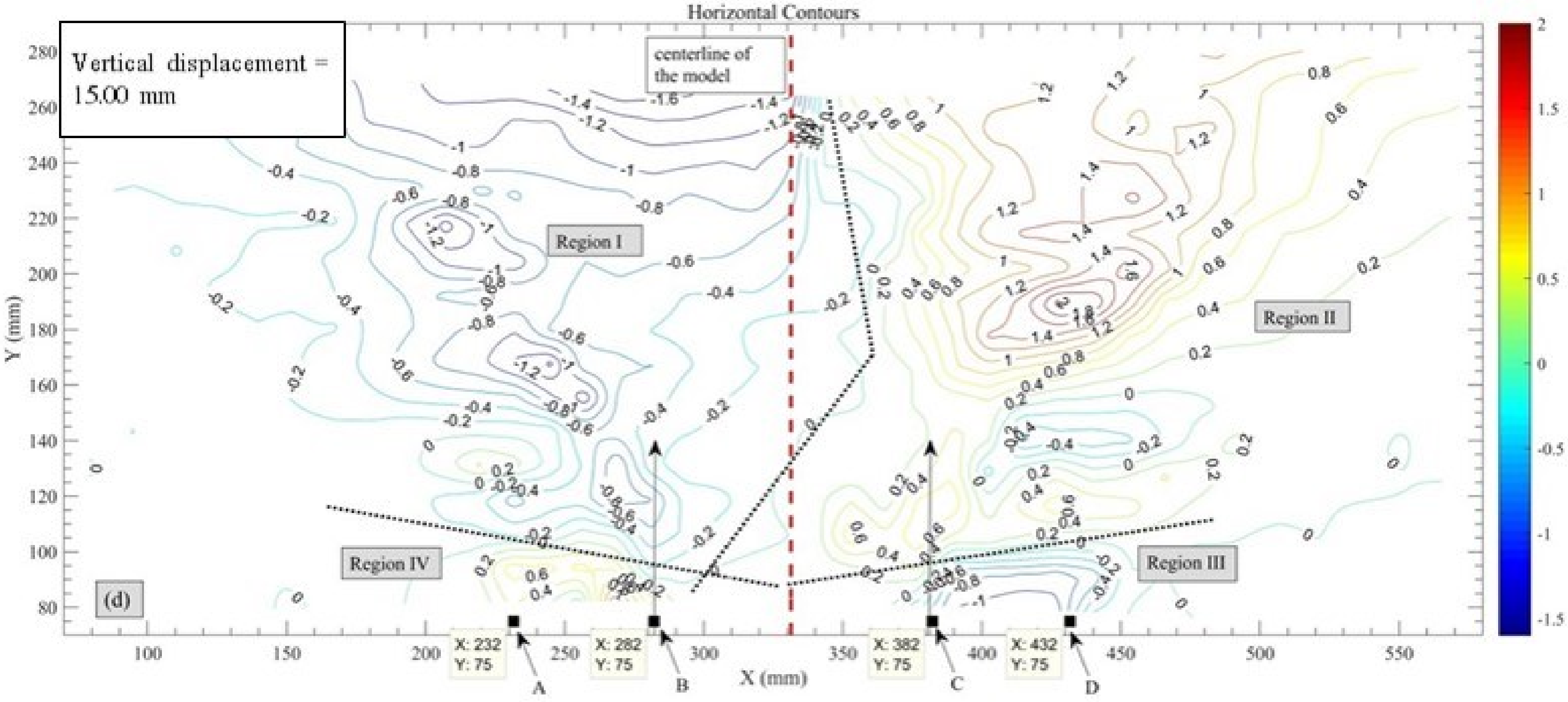

Figure D-0-4 Evolution of horizontal displacements – t = 15 yrs

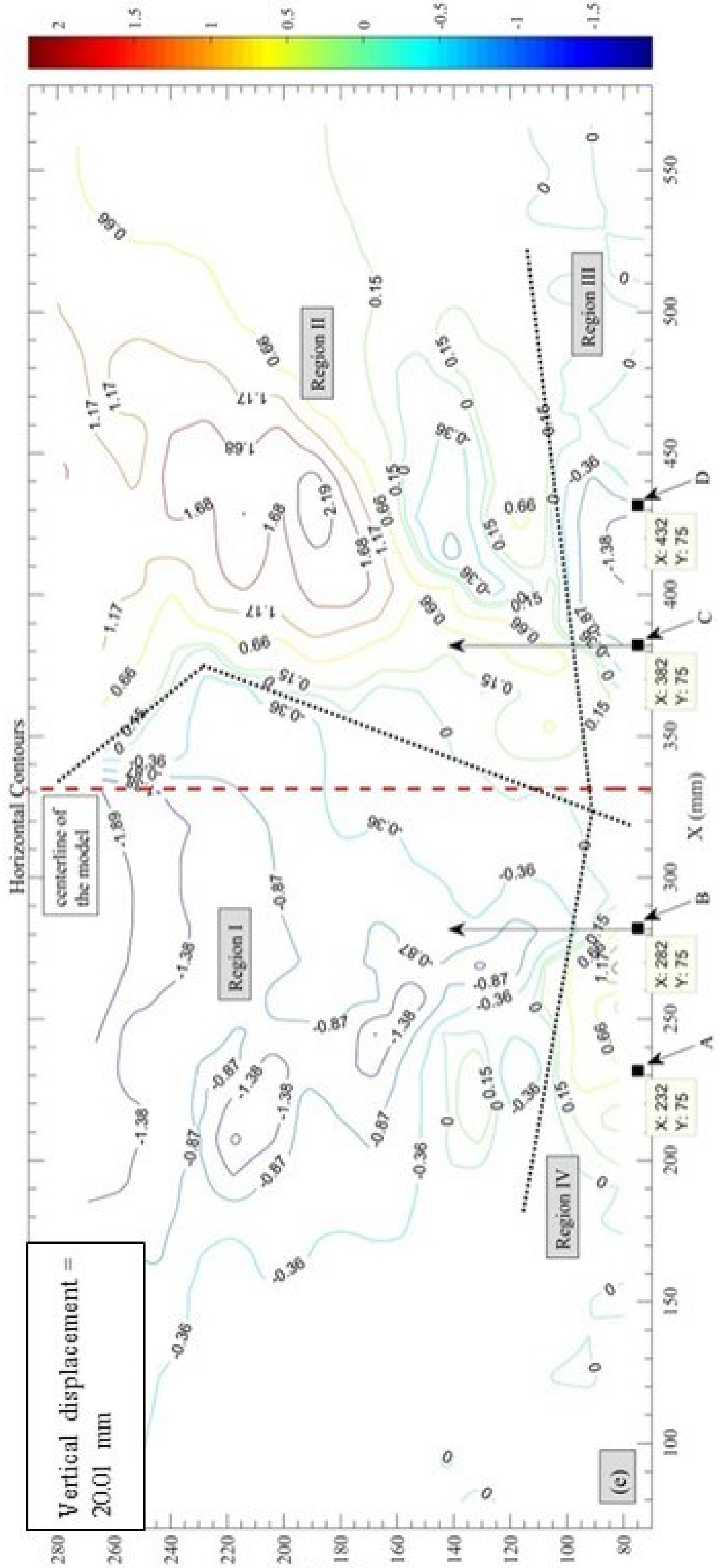

Figure D-0-5 Evolution of horizontal displacements – t = 15 yrs

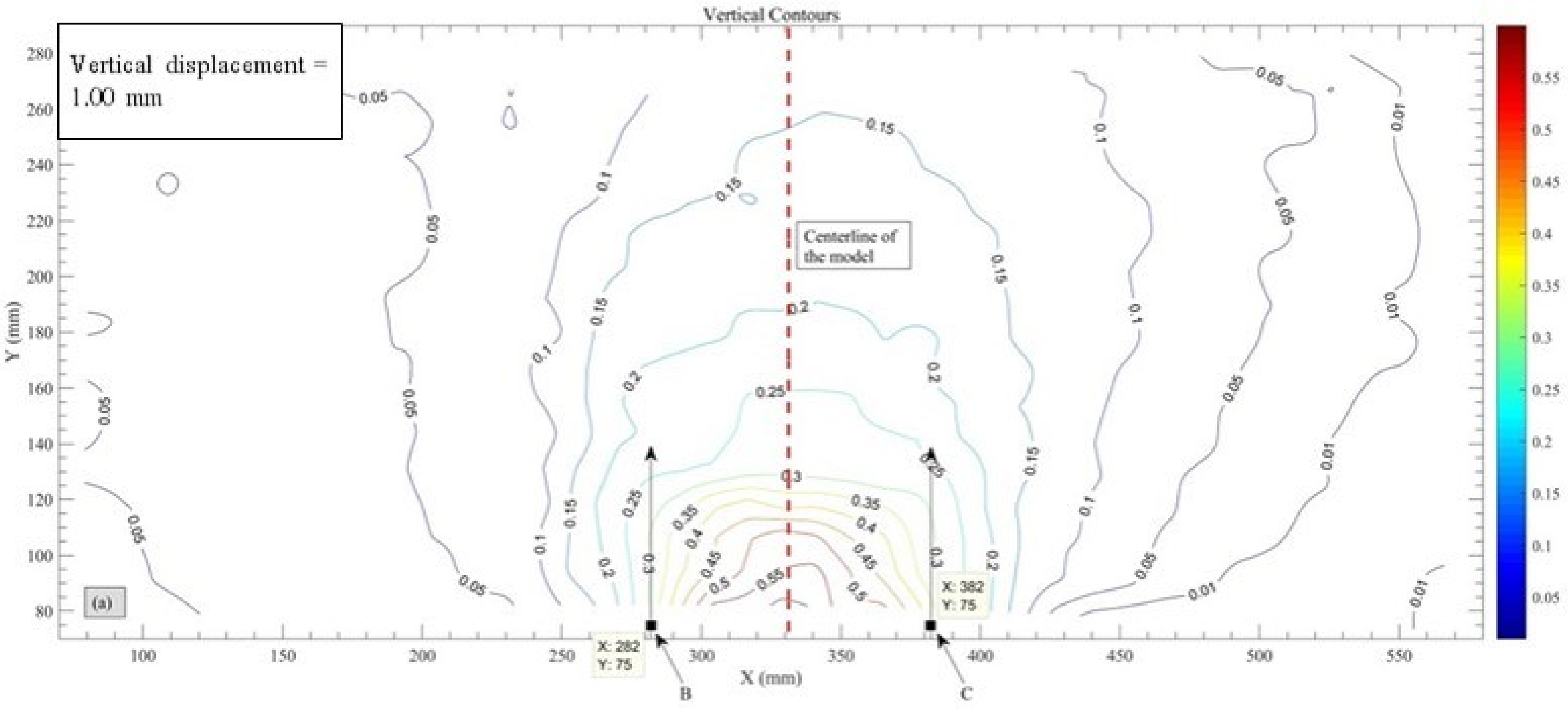

Figure D-0-6 Evolution of vertical displacements – t = 15 yrs

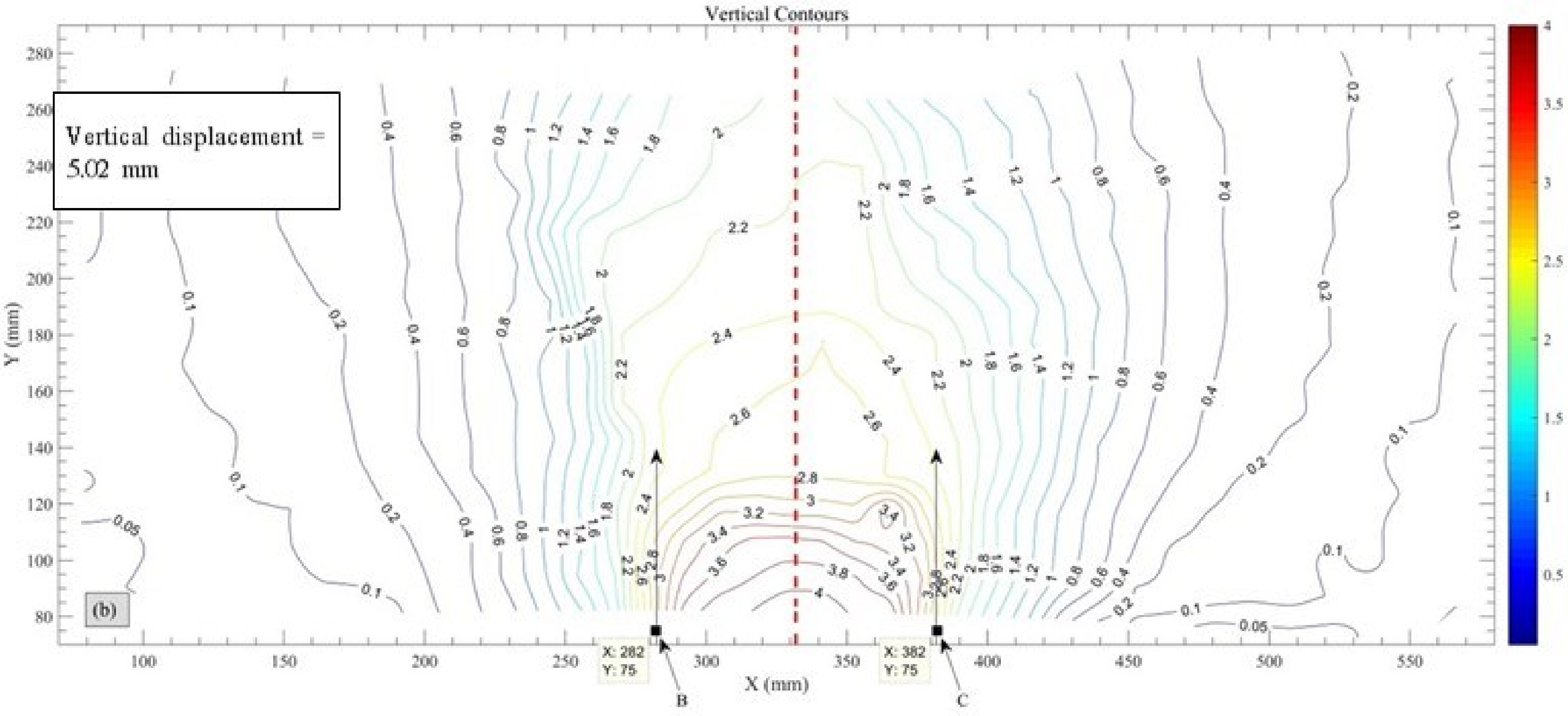
Vertical displacement = 5.02 mm

Figure D-0-7 Evolution of vertical displacements – t = 15 yrs

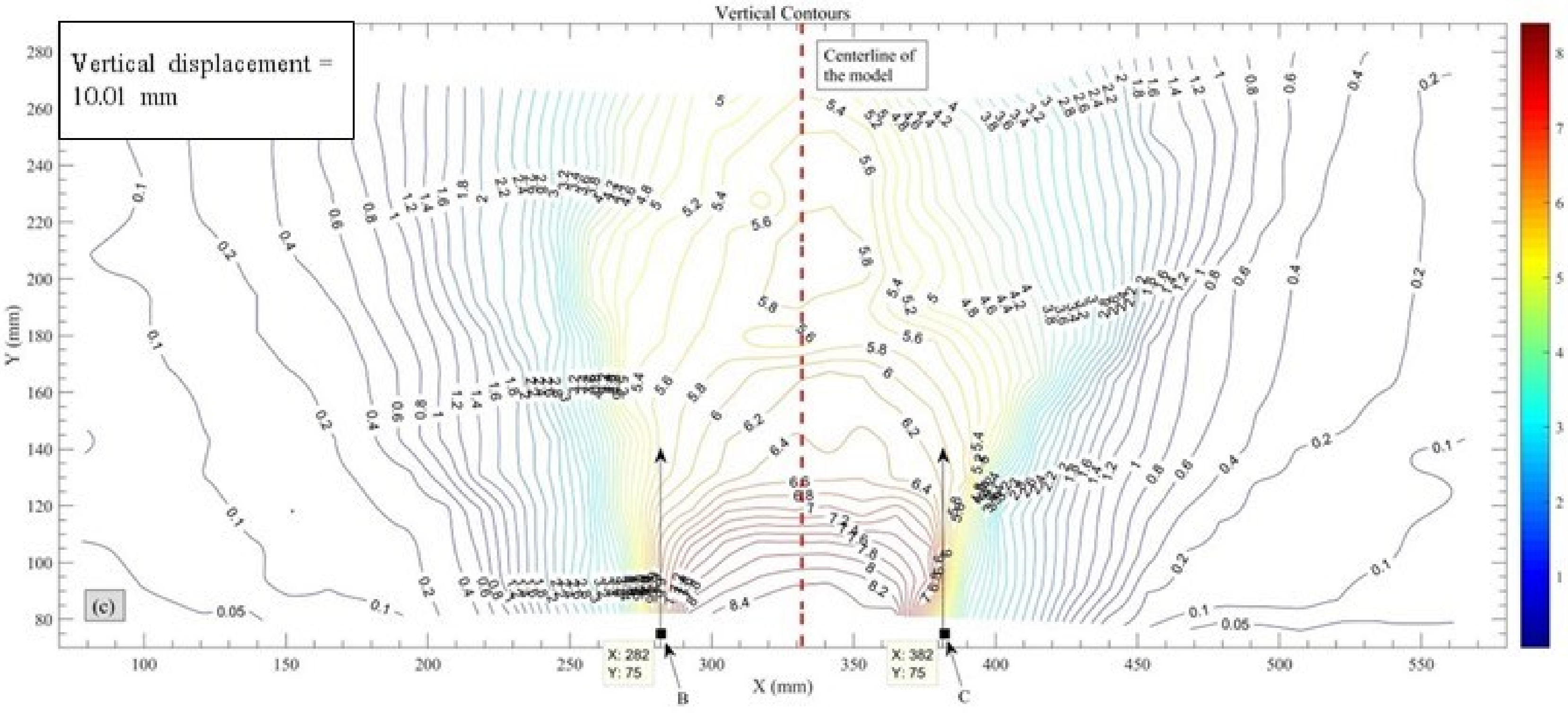

Figure D-0-8 Evolution of vertical displacements – t = 15 yrs

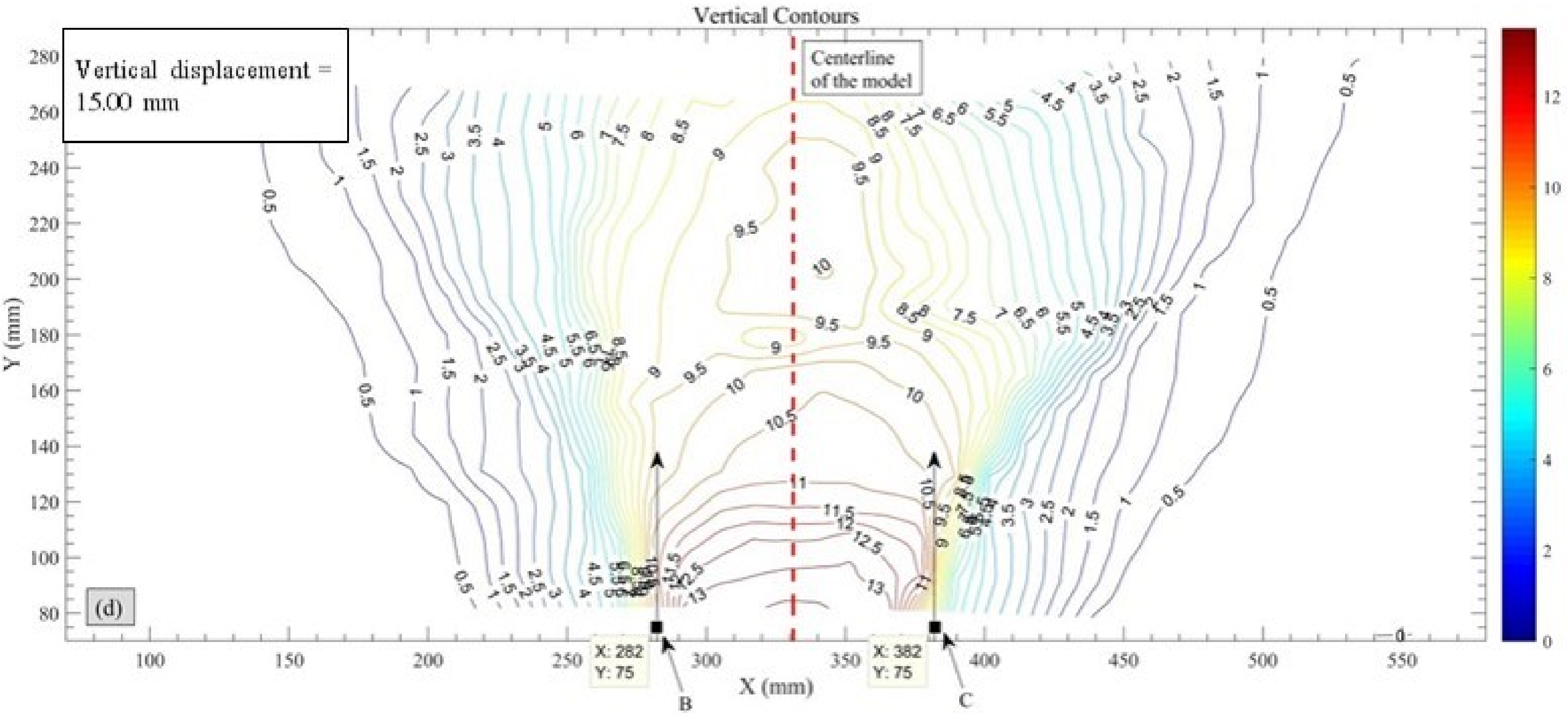

Figure D-0-9 Evolution of vertical displacements – t = 15 yrs

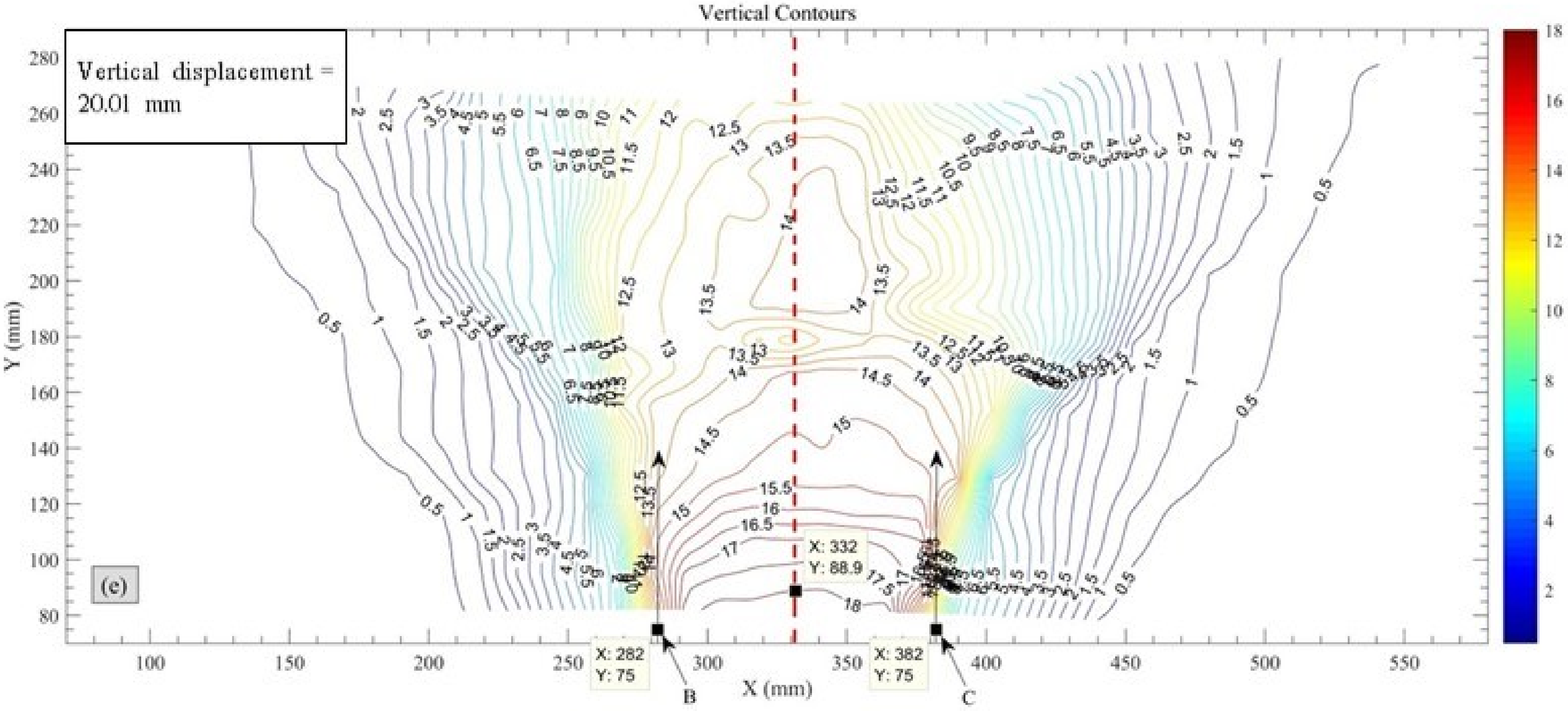

Figure D-0-10 Evolution of vertical displacements – t = 15 yrs

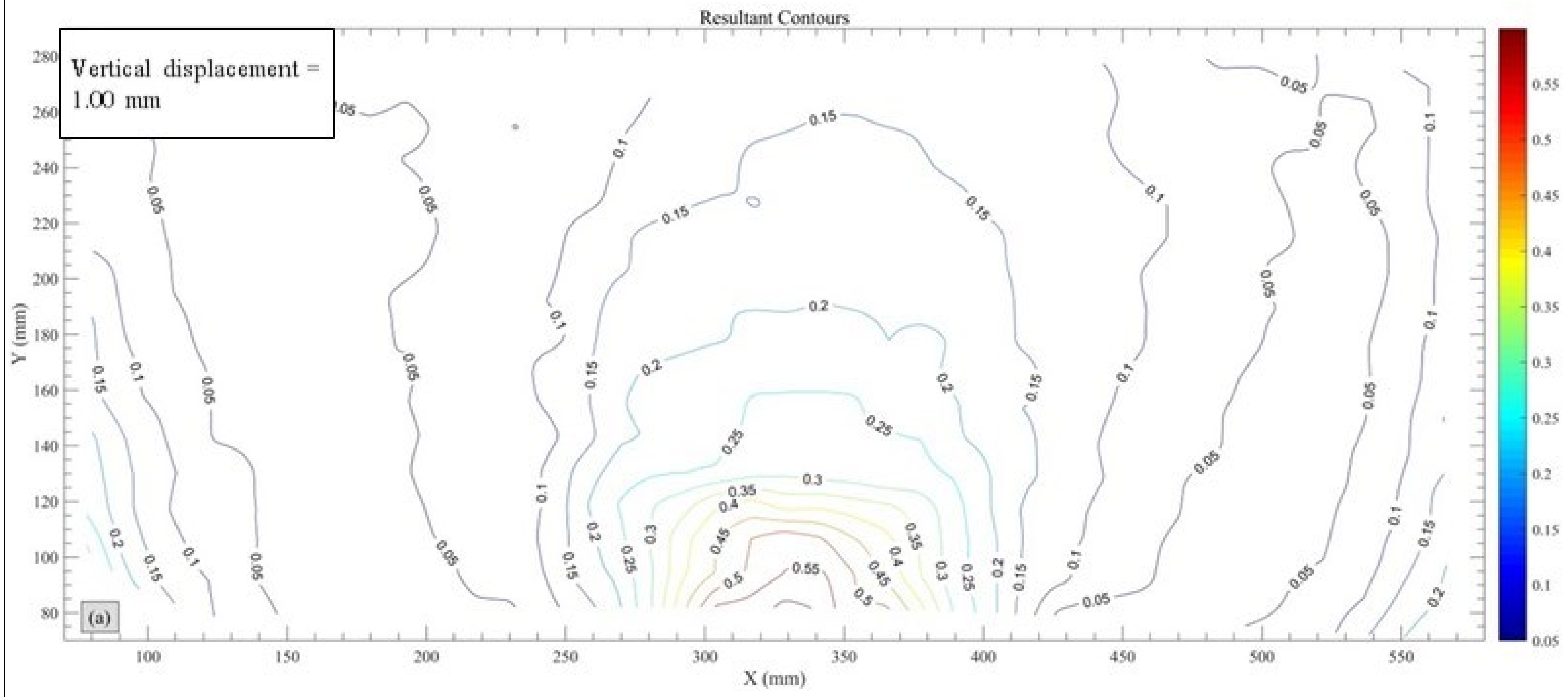

Figure D-0-11 Evolution of resultant (total) displacements – t = 15 yrs

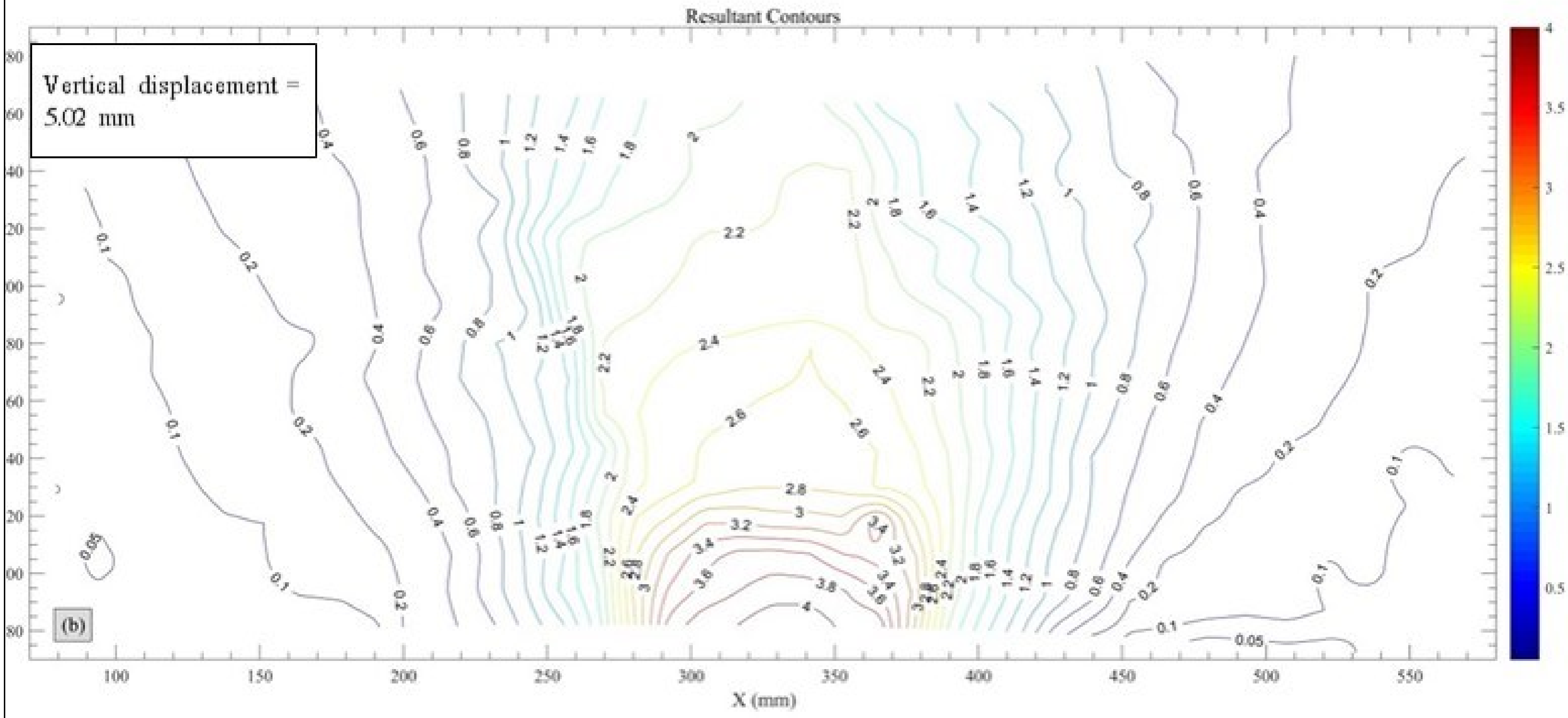

Figure D-0-12 Evolution of resultant (total) displacements – t = 15 yrs

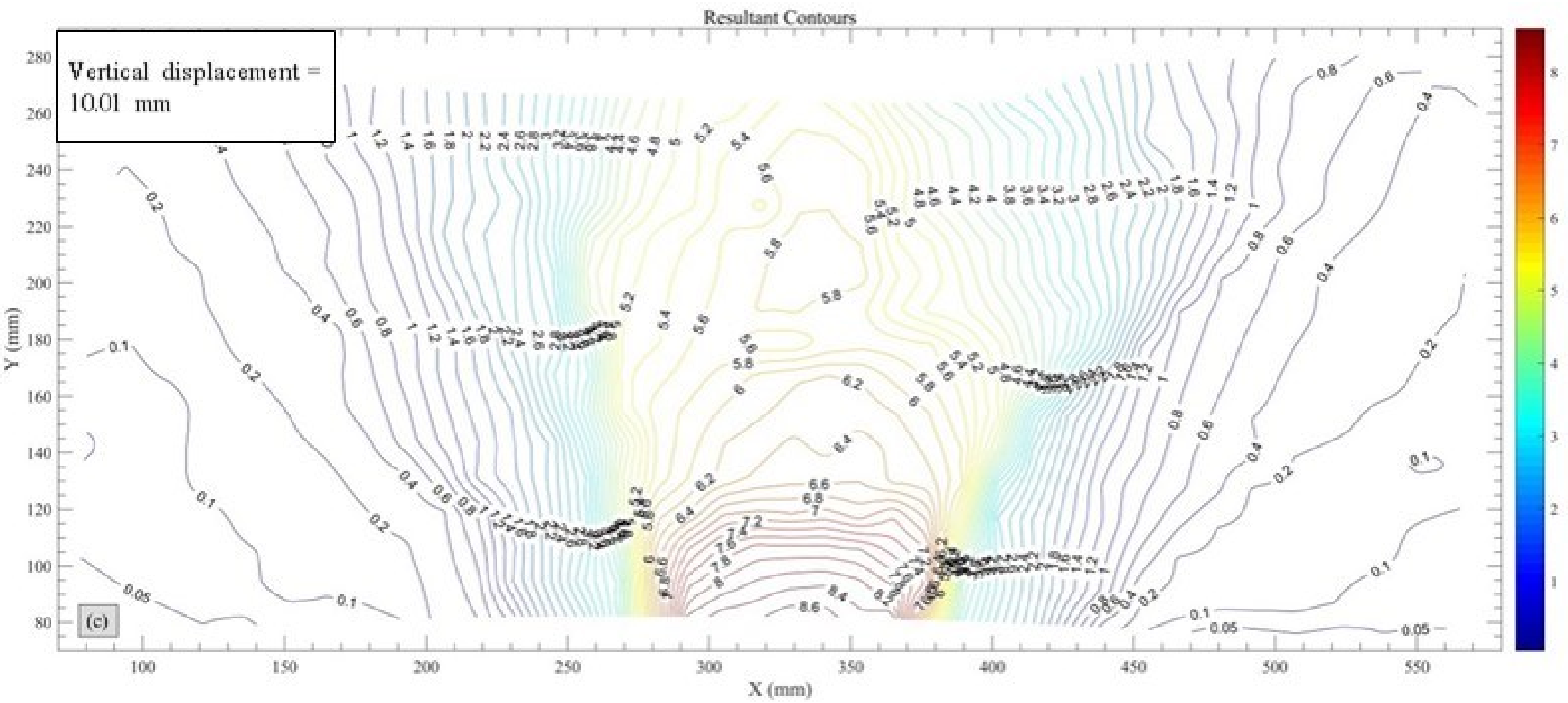

Figure D-0-13 Evolution of resultant (total) displacements – t = 15 yrs

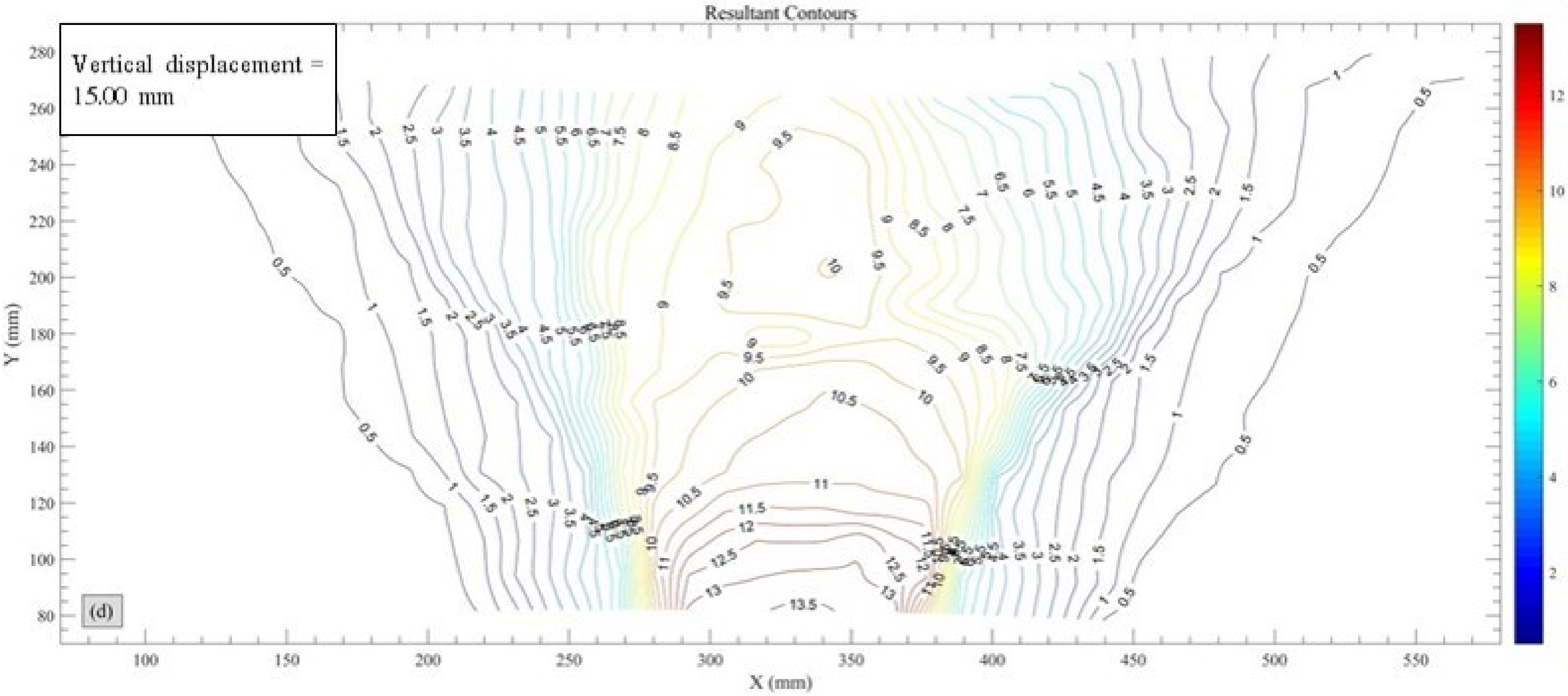

Figure D-0-14 Evolution of resultant (total) displacements – t = 15 yrs

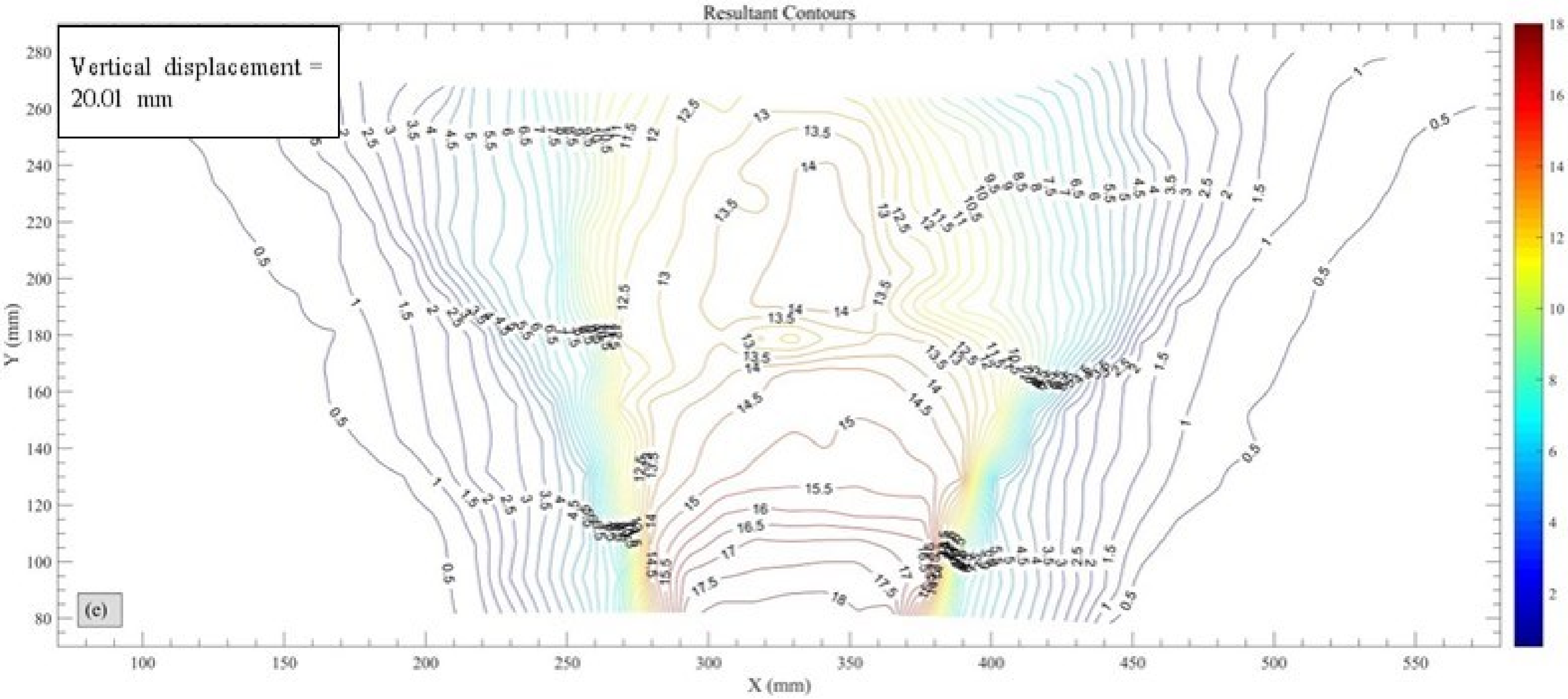

Figure D-0-15 Evolution of resultant (total) displacements – t = 15 yrs

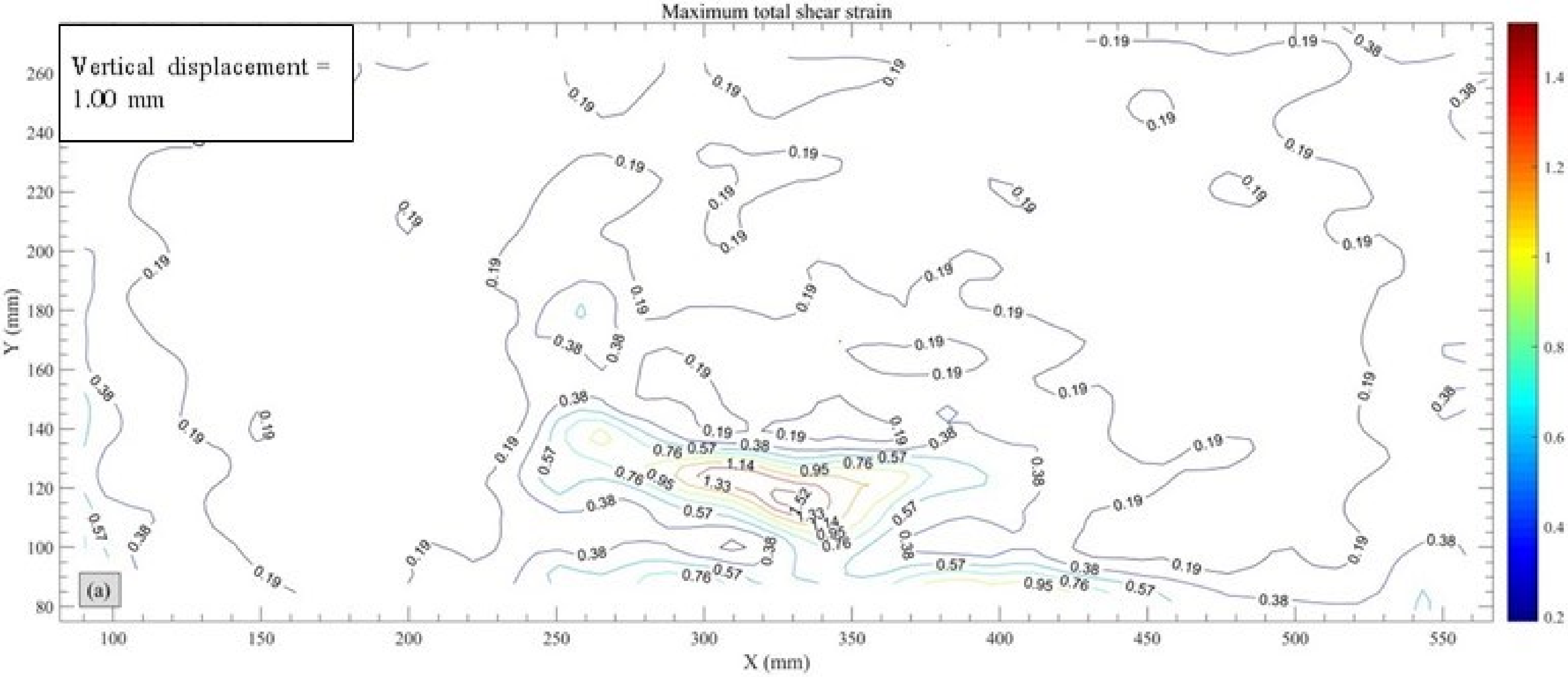

Figure D-0-16 Evolution of maximum shear strains– t = 15 yrs

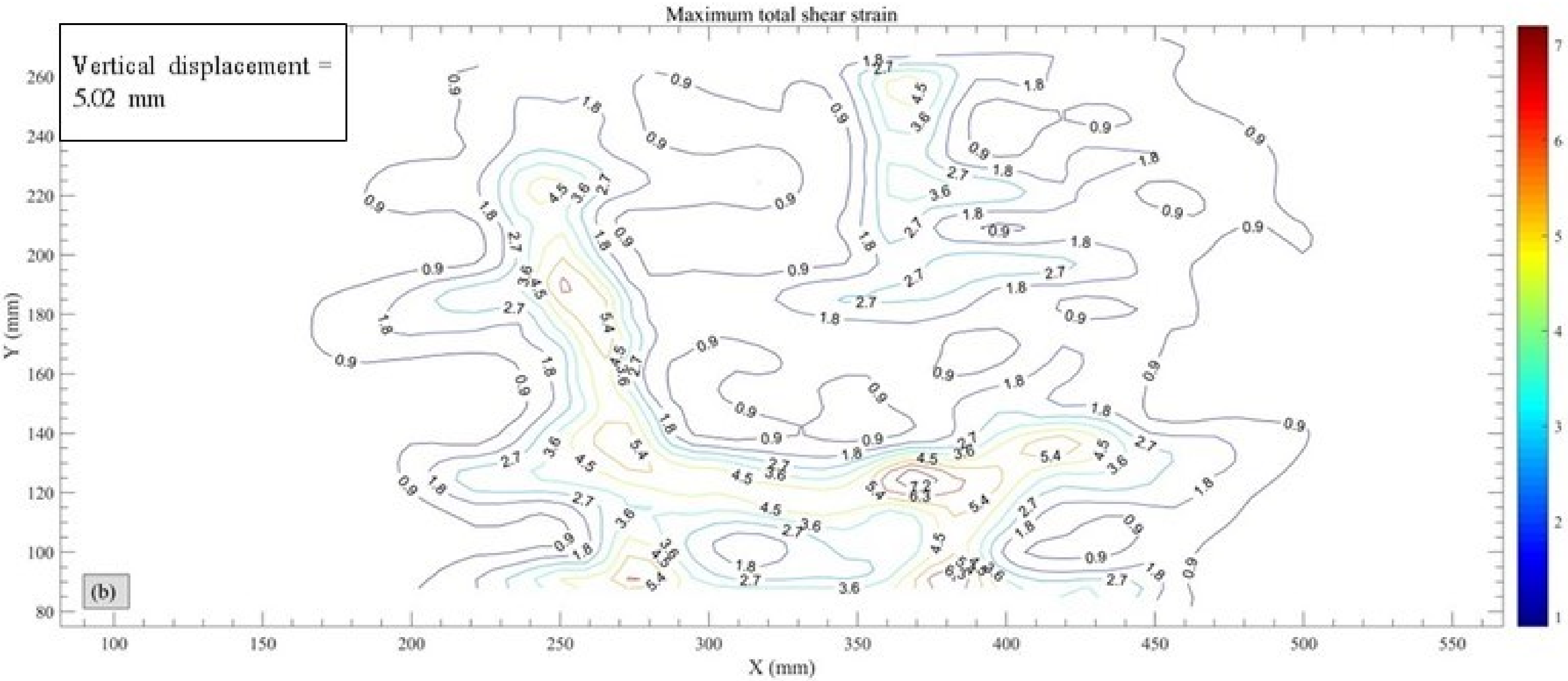

Figure D-0-17 Evolution of maximum shear strains – t = 15 yrs

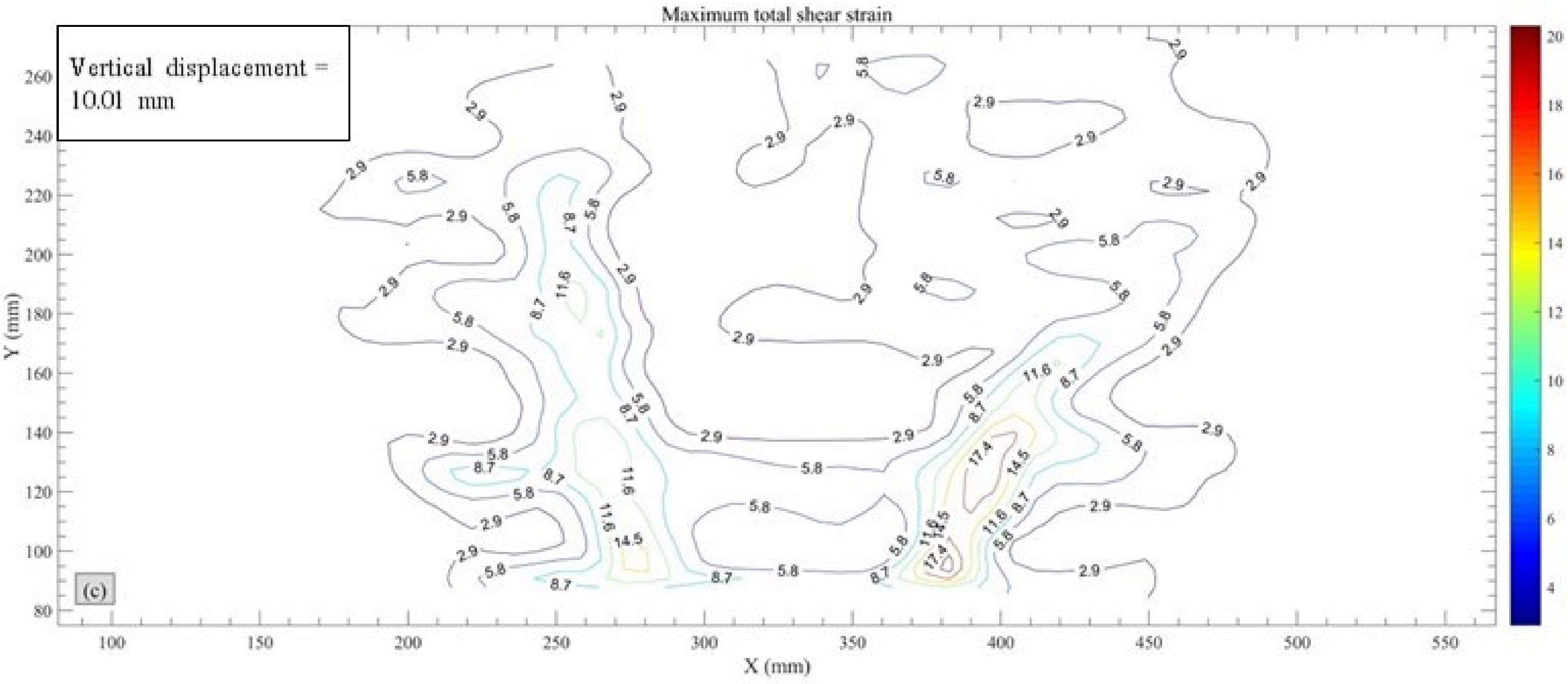

Figure D-0-18 Evolution of maximum shear strains – t = 15 yrs

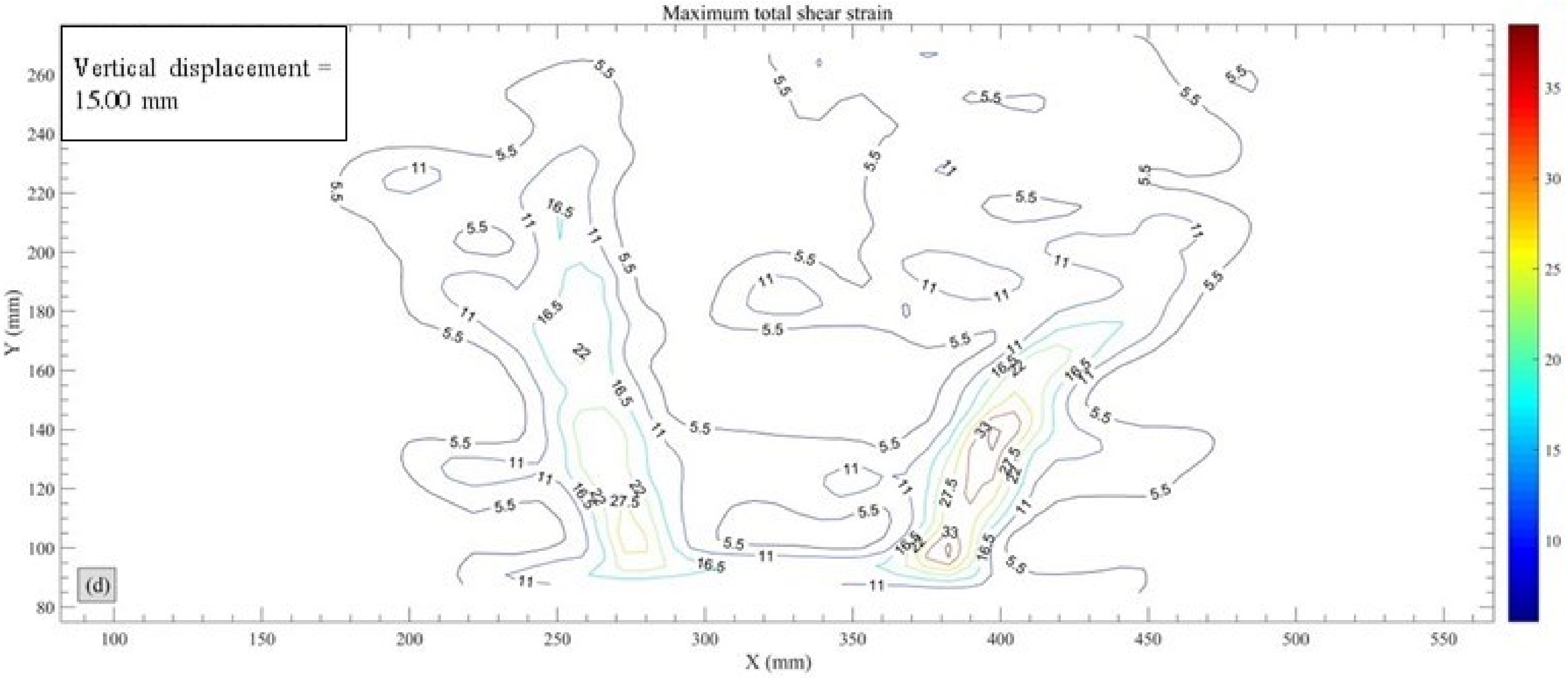

Figure D-0-19 Evolution of maximum shear strains – t = 15 yrs

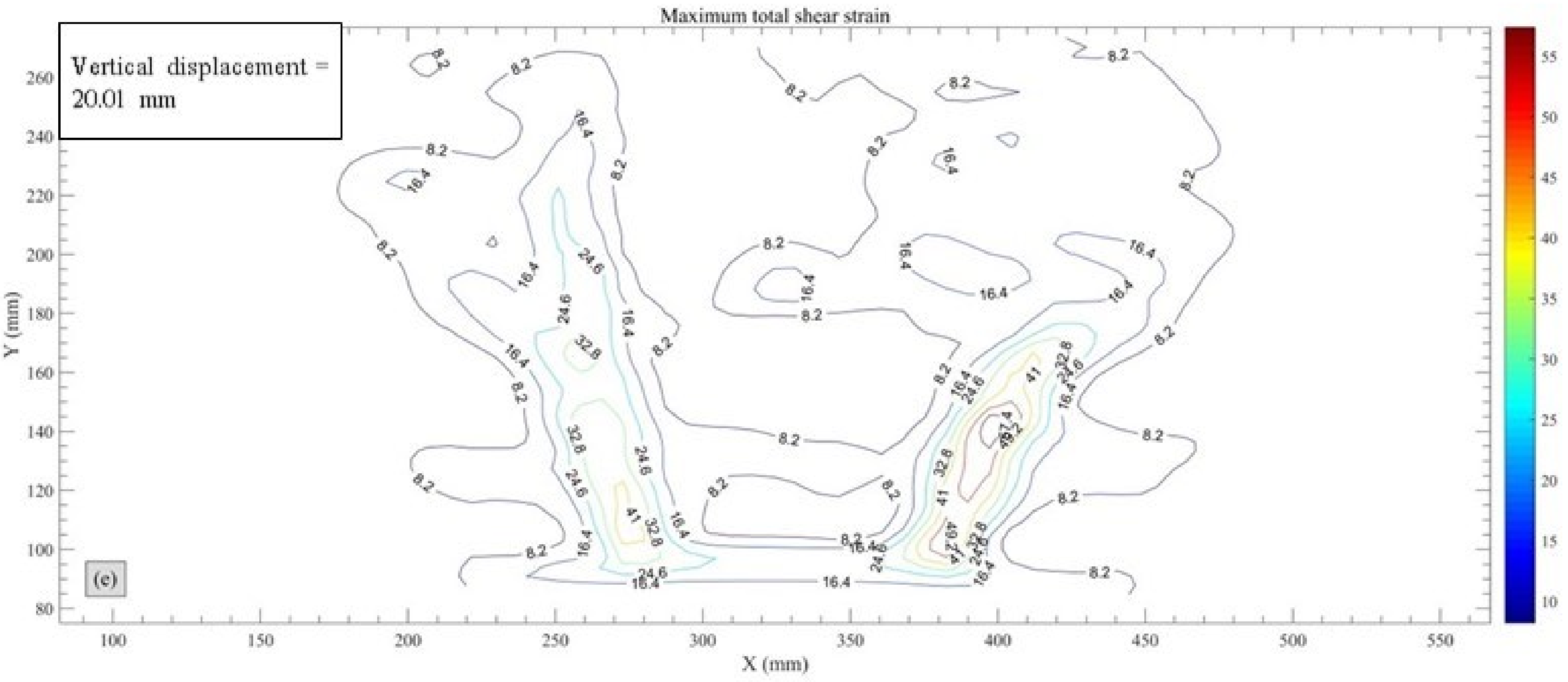

Figure D-0-20 Evolution of maximum shear strains – t = 15 yrs

Appendix E: Application of Numerical Modeling to Centrifuge Tests

E.1 Introduction

This Appendix presents the results of preliminary numerical modelling studies of the caprock behaviour acquired during the centrifuge modelling tests. By using the physical and mechanical properties of the synthetic Clearwater shale determined in Chapter 4 as the input parameters, a series of numerical simulations of the centrifuge tests are compared with the experimental results from the geotechnical centrifuge modelling tests to assess the ability of numerical models to capture the deformation and failure modes seen in the centrifuge tests. As described in Chapter 3, there is no perfect approach to assessing a geotechnical problem from the perspective of quality and reliability of the results, cost and efficiency but comparisons of centrifuge modeling and numerical simulation can provide substantial verification that key mechanisms are being captured for relevant failure mechanisms.

E.2 Input parameters and boundary conditions for numerical model

The input parameters for the numerical simulation are obtained from the physical and mechanical properties of the synthetic Clearwater shale described in Chapter 4, as shown in

Table E- 0-1. The bulk modulus (K) and shear modulus (G) are calculated based on the elasticity theory:

$$\mathrm{K} = \frac{E}{3(1\text{-}2\upsilon)} \qquad \text{Equation (E-1)}$$

$$\mathrm{G} = \frac{E}{2(1+\upsilon)} \qquad \text{Equation (E-2)}$$

The permeability of the model used for the numerical simulation is equal to hydraulic conductivity (in cm/sec) × 1.02 × 10^{-6}. Therefore, the magnitude of the permeability used in the FLAC3D program can be expressed as $1.02\times10^{-6} \times 1.6\times10^{-4}$ (in cm/sec), which is equal to $1.632e^{-10}$. Dry density of the model, which is 1036.14 kg/m^3, is used when FLAC3D is configured for fluid flow. The uplifting distance of the GeoCDM is calculated based on time step, steps and the velocity of the GeoCDM. The initial value of time step is 2.451. This value is then used for the calculation of the steps needed by the GeoCDM to reach the anticipated displacement. However, during the numerical modelling test, the magnitude of time step slightly changes. Therefore, the displacement at specified steps may be slightly different from the anticipated displacement.

Table E- 0-1 Input parameters for numerical modelling test

Parameters	Value
Young's modulus, MPa	220
Poisson's ratio	0.25
Bulk modulus, MPa	146.67
Shear modulus, MPa	88
Hydraulic conductivity, m/s	1.6e-6
Density, kg/m^3	1636
Friction angle, °	28
Cohesive strength, kPa	368
Tensile strength, kPa	100

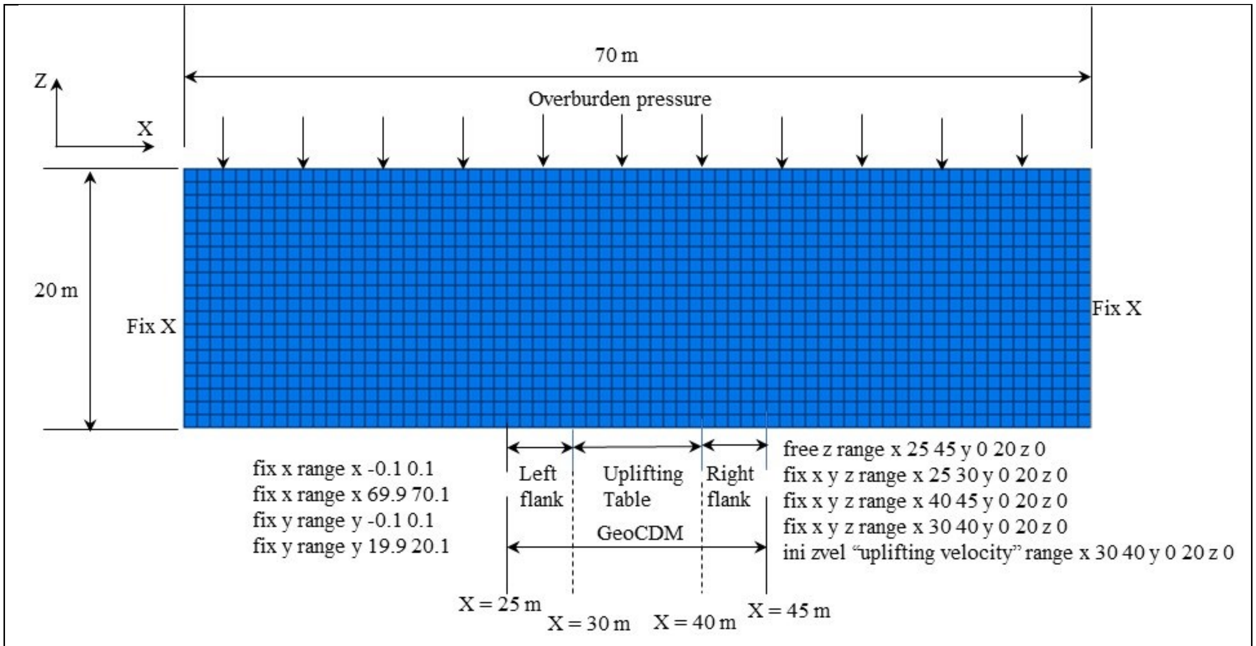

Figure E- 0-1 Schematic view of the numerical simulation model

As shown in Figure E- 0-1, FLAC3D is used to model the deformation behavior of in situ soil. The length, height, width of the model contained in the PSB are 70 cm, 20 cm and 20 cm, respectively. Therefore, the corresponding in situ model length and height are 70 m and 20 m, respectively. The width with a length of 20 m is in the direction perpendicular to the XZ plane. The X-direction movement is constrained at X = 0 m and X = 70 m. The Y-direction movement is constrained at Y = 0 m and Y = 20 m. The X-direction, Y-direction and Z-direction movement are constrained at Z = 0 m except the area representing the uplifting table of the GeoCDM. The area representing the uplifting table is constrained by an uplifting velocity that represents the expansion rate of the steam chamber induced by the SAGD process. The overburden pressure simulated by an appropriate thickness of lead bars in the geotechnical centrifuge modelling test is calculated and applied on top of the in-situ model. The gravitational field used in the model is the Earth's gravity.

E.3 Calibration of the tensile strength

As discussed in Chapter 4, the samples used for the Brazilian test are cured for over 50 days. Therefore, the tensile strength may be higher than that used for the centrifuge modelling test. This section intends to describe the importance of calibrating the input parameters for the numerical modelling test.

As shown in Figure E- 0-2, with the increase of the tensile strength, the dip angle of the failure plane increases. When the tensile strength is higher than 200 kPa, the dip angle is almost equal to 90°, which does not coincide well with the centrifuge modelling test.

Based on the results of the numerical simulation test, we can clearly see the tensile fracture at the top of the model when the tensile strength is relatively low. However, when the tensile strength is over 200 kPa, there is no fracture at the top of the model, which does not coincide well with the centrifuge modelling test. Under this condition, the tensile strength with a value of 100 kPa is used as the input parameter for the numerical modelling test.

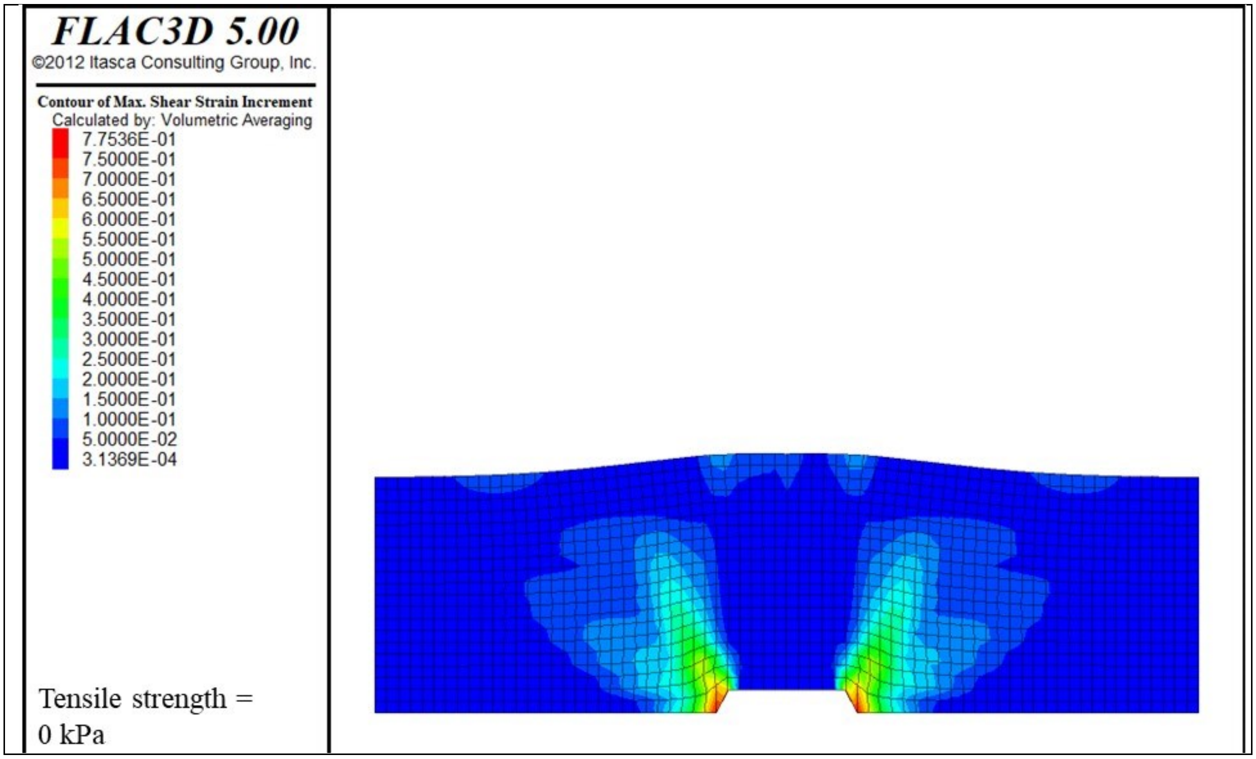

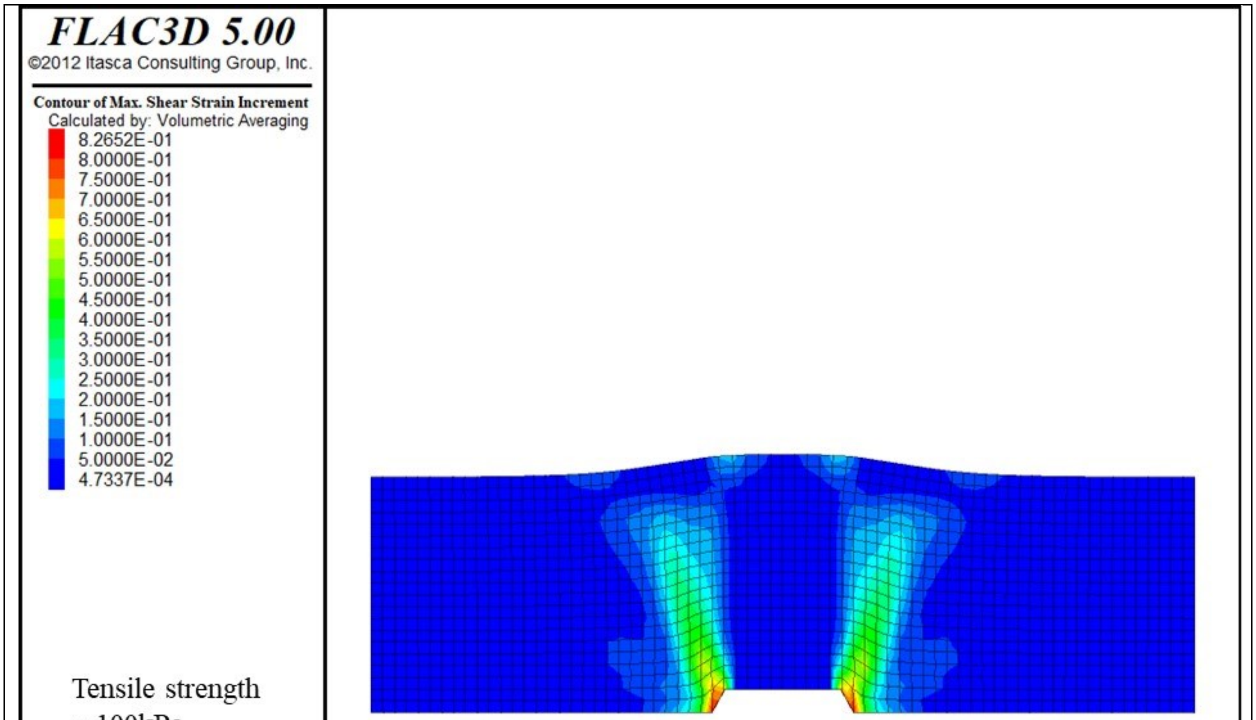

Tensile strength = 100kPa

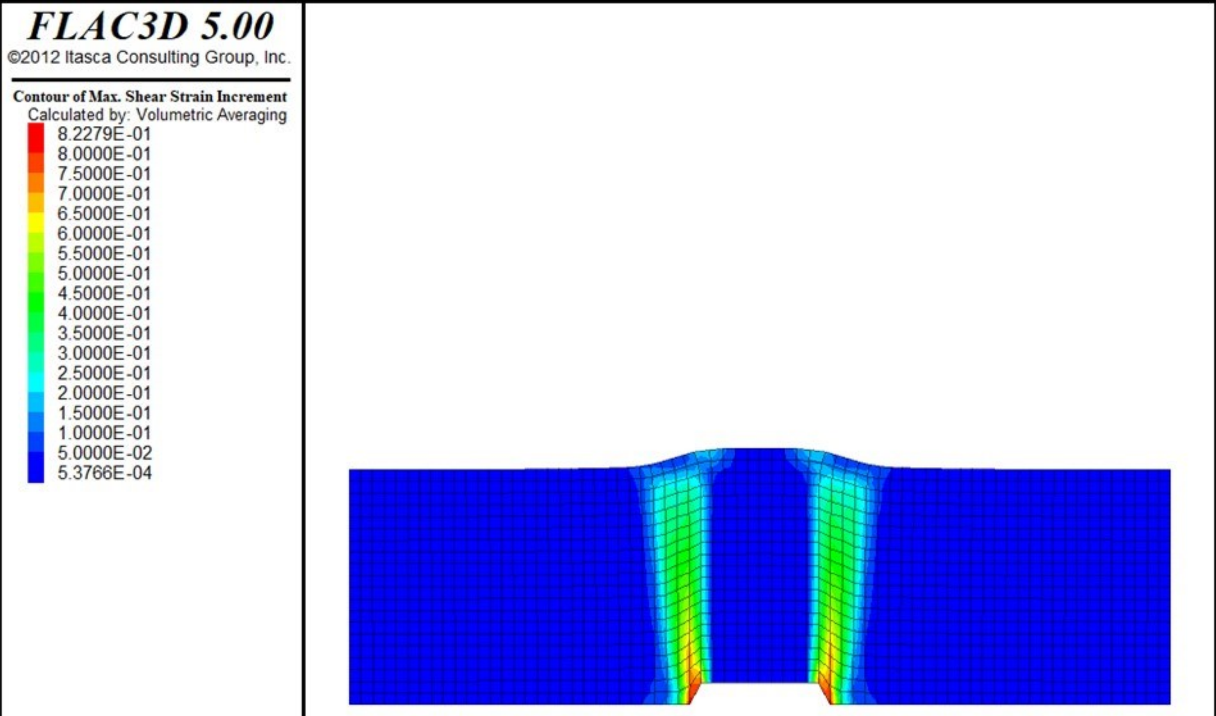

Tensile strength = 200 kPa

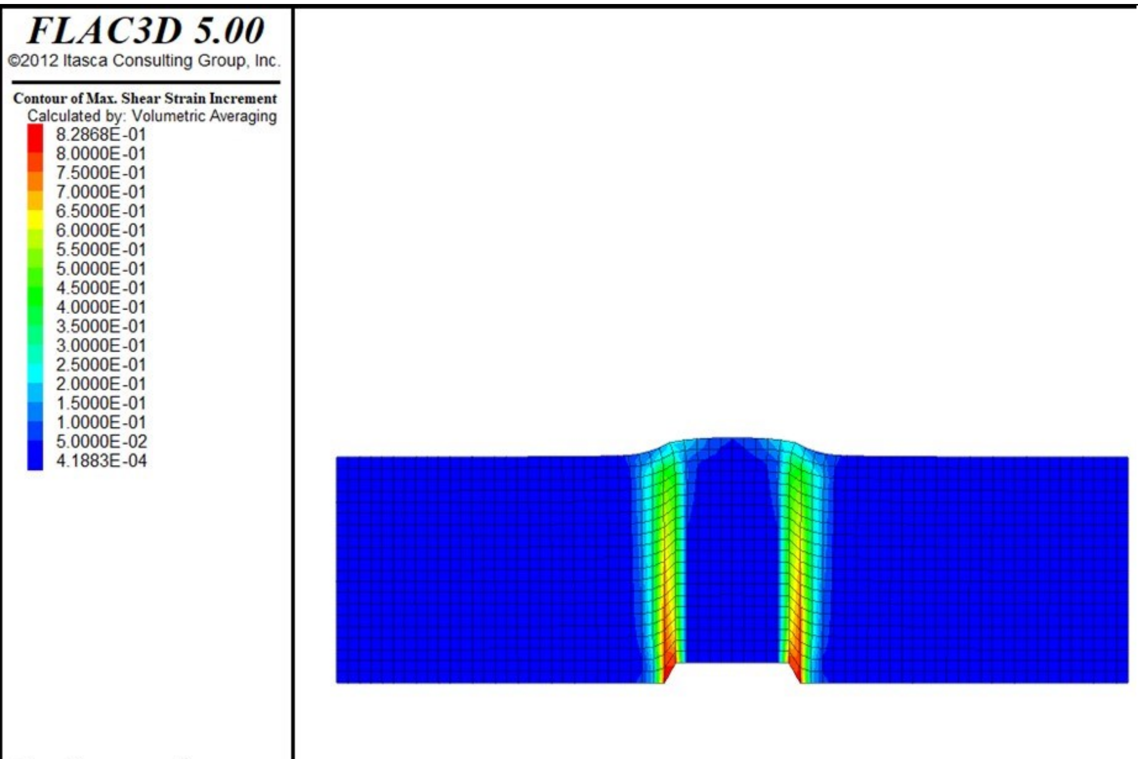

Tensile strength = 300 kPa

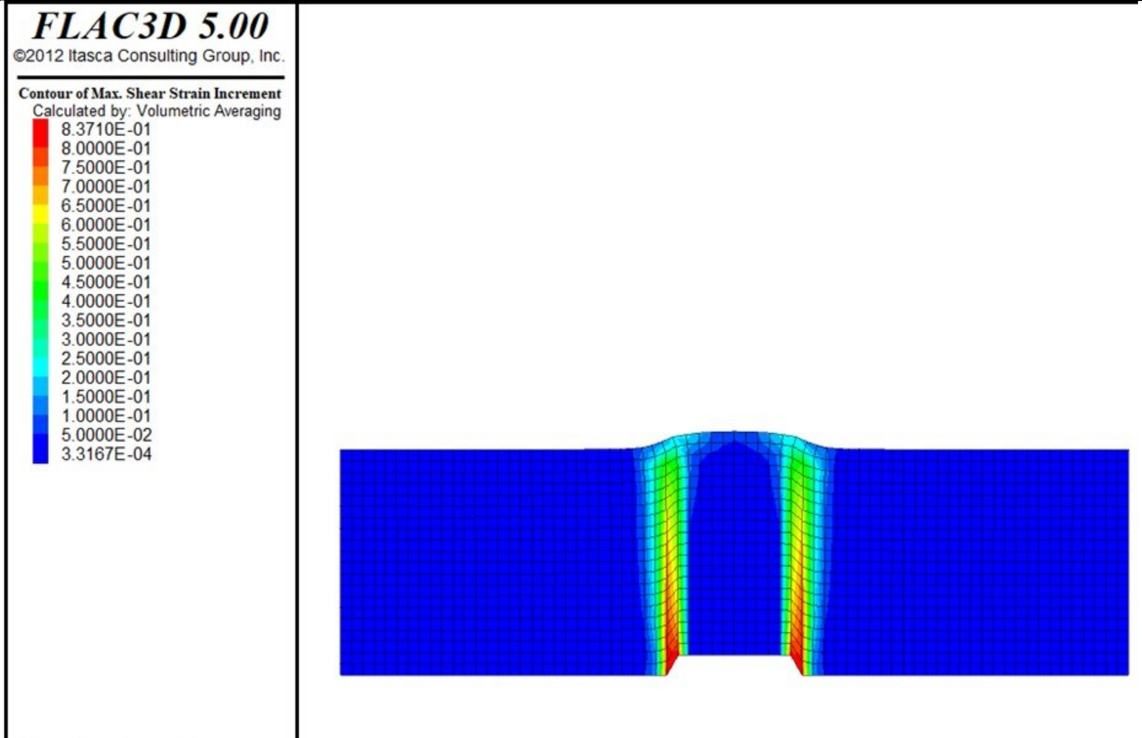

Tensile strength = 380 kPa

Figure E- 0-2 The impact of the tensile strength on the failure planes

E.4 Validation of the numerical modelling test

In general, the soil particles at the left side of the centreline of the model should move towards the –X direction, while those at the right side should move towards the +X direction. However, at the bottom of the model, the soil particles at the left side of the centreline of the model move towards the +X direction, while those at the right side move towards the –X direction.

The same phenomenon happens when analyzing the results of the numerical modelling tests, as shown in Figure E- 0-3. When the uplift displacement of the uplifting table is relatively small, this phenomenon is clear and with the increase of the uplift displacement, the maximum horizontal displacement contours occur at the top of the model. Therefore, the contours at the bottom of the model remain small (e.g., green colour in contours) but nonzero magnitude.

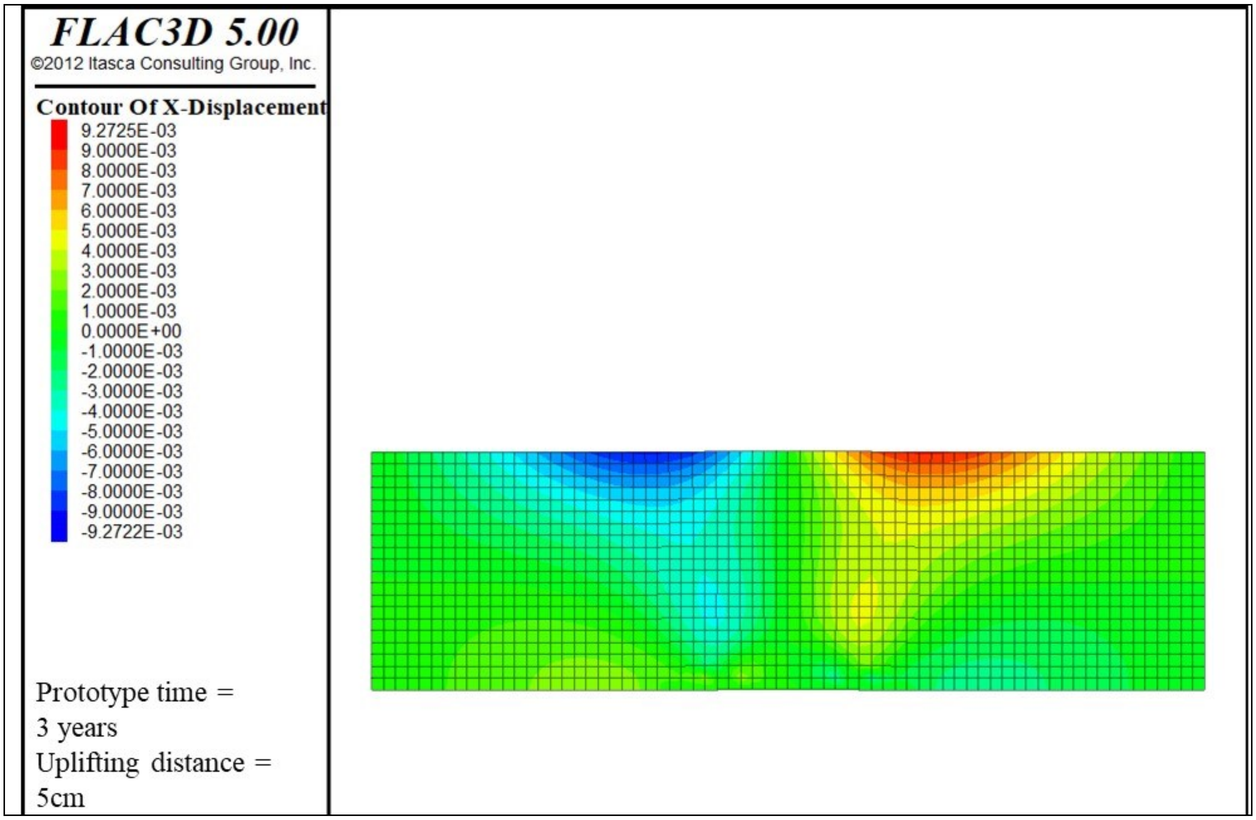

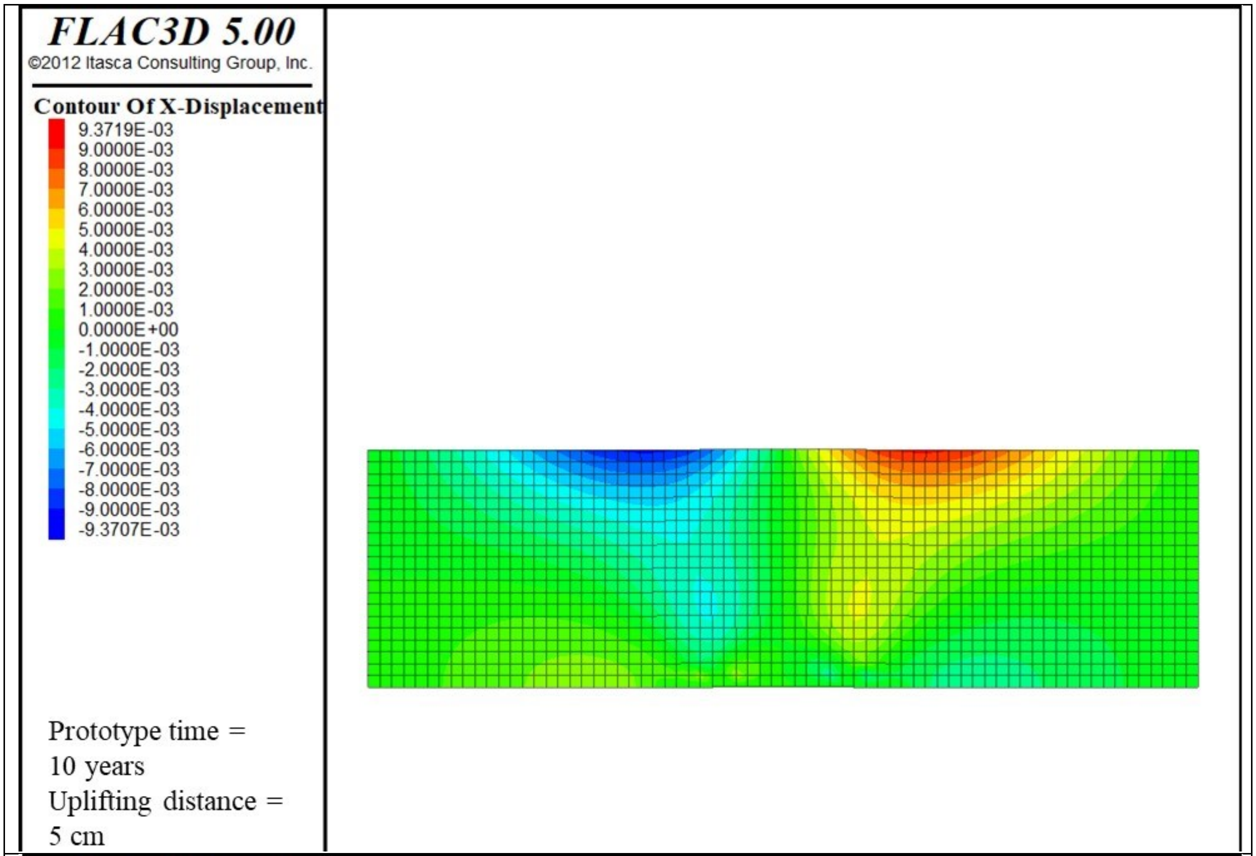

Prototype time = 10 years
Uplifting distance = 5 cm

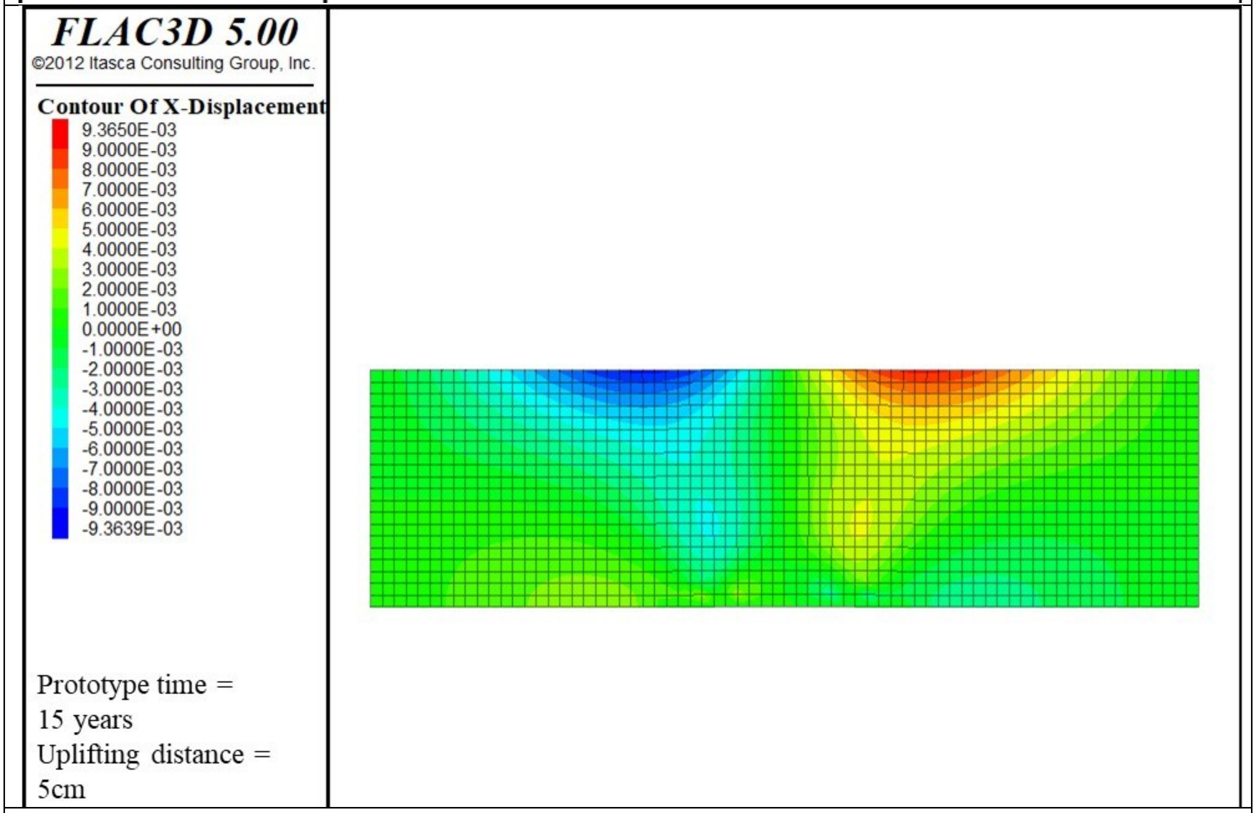

Prototype time = 15 years
Uplifting distance = 5cm

Figure E- 0-3 Horizontal displacement contours from the numerical modelling tests

When the uplift displacement is very small, for instance 20 cm, Figure E- 0-4 demonstrates that the soil above the uplifting table (centreline of model) can be divided into two regions: 1) the soil at the top of the model has yielded due to tensile stresses and 2) soil at the bottom of the model has not yielded at al. Moreover, the tensile force may result in the fracture at the top of the model because the low horizontal stress cannot prevent the fracture's initialization and propagation.

It is evident that only a small proportion of the model is affected by the uplifting table's movement and forms a bell-shaped region. However, the soil at both the left side and the right side of the uplifting table shows that the tensile force plays the dominant role in the affected region. However, the soil along the lines that start from the vertices of the uplifting table and extend to the model surface vertically is affected by the shear force.

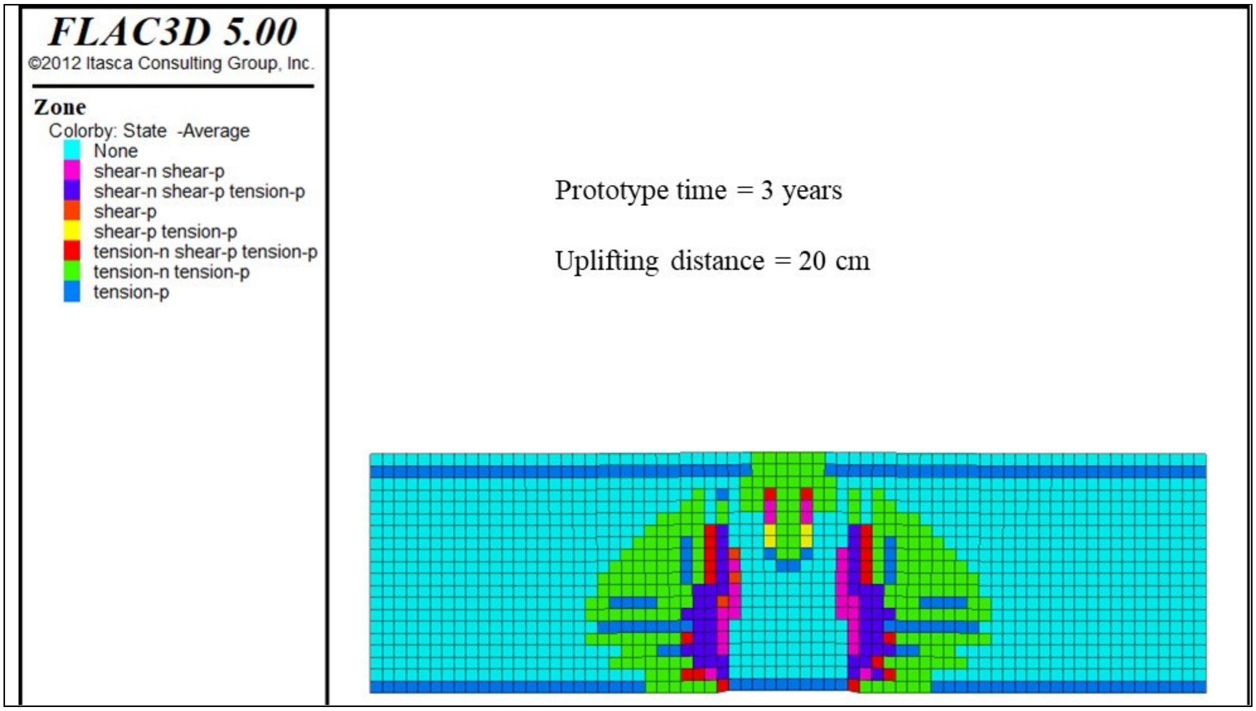

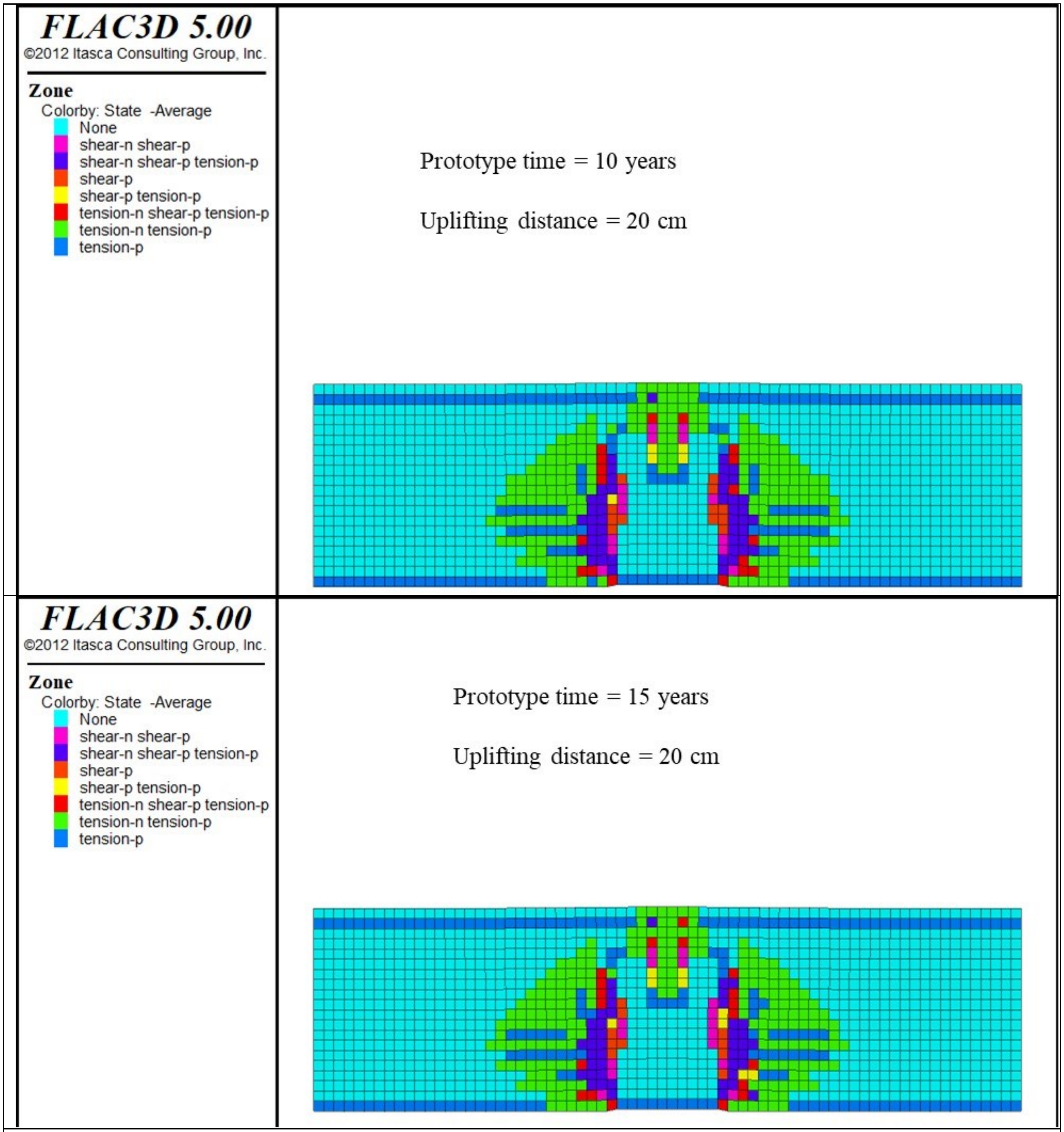

Figure E- 0-4 Zone state when the uplift displacement is 20 cm

To demonstrate the failure process of the caprock, this section presents the zone state of the caprock at different uplift displacements, as shown in Figure E- 0-5, Figure E- 0-6 and Figure E- 0-7.

The following observations are made from the results shown in these figures:

1. The vertical fractures at the top of the model are induced by the tensile force. As shown in Figure E- 0-7, when the uplift displacement is about 50 cm, the tension-p is quite clear at the top of the model. The active plastic zone (indicated by tension-n) expands radially.
2. When the uplift displacement is 1 m, it seems that the area of the plastic zone (indicated by tension-p) at the top of the model does not change, indicating that the vertical fractures at the top of the model may not propagate. At the same time, two regions emerge from the vertices of the flank, expands towards the model surface, and connects with the regions (indicated by shear-n shear-p) at the model surface. This phenomenon may indicate that the failure plane has already reached the ground surface.
3. When the uplift displacement is 2 m, the failure planes obviously have reached the ground surface. It is quite difficult to notice the effect of the uplifting velocity on the dip angle of these failure planes. Moreover, these failure planes are the result of both the shear force and the tensile force. However, for the failure plane near the ground surface, those zones are the result of the shear force only. The ground surface heaves due to the uplifting movement of the uplifting table.

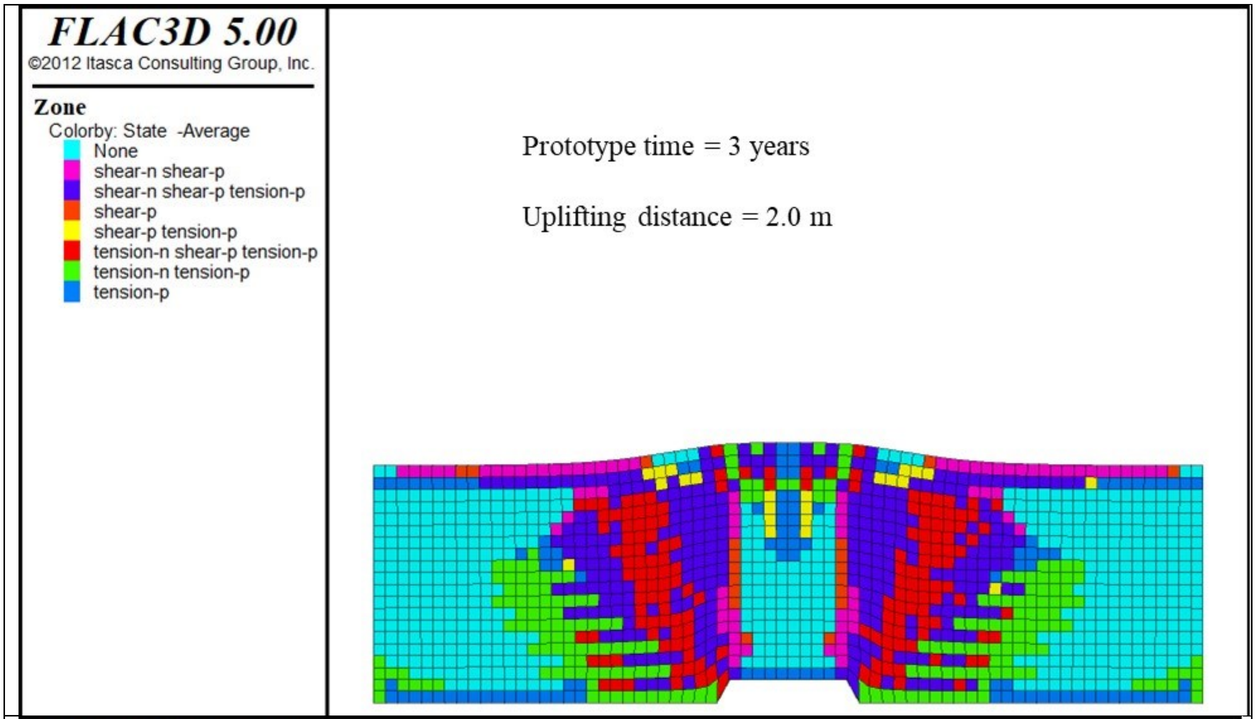

Prototype time = 3 years

Uplifting distance = 2.0 m

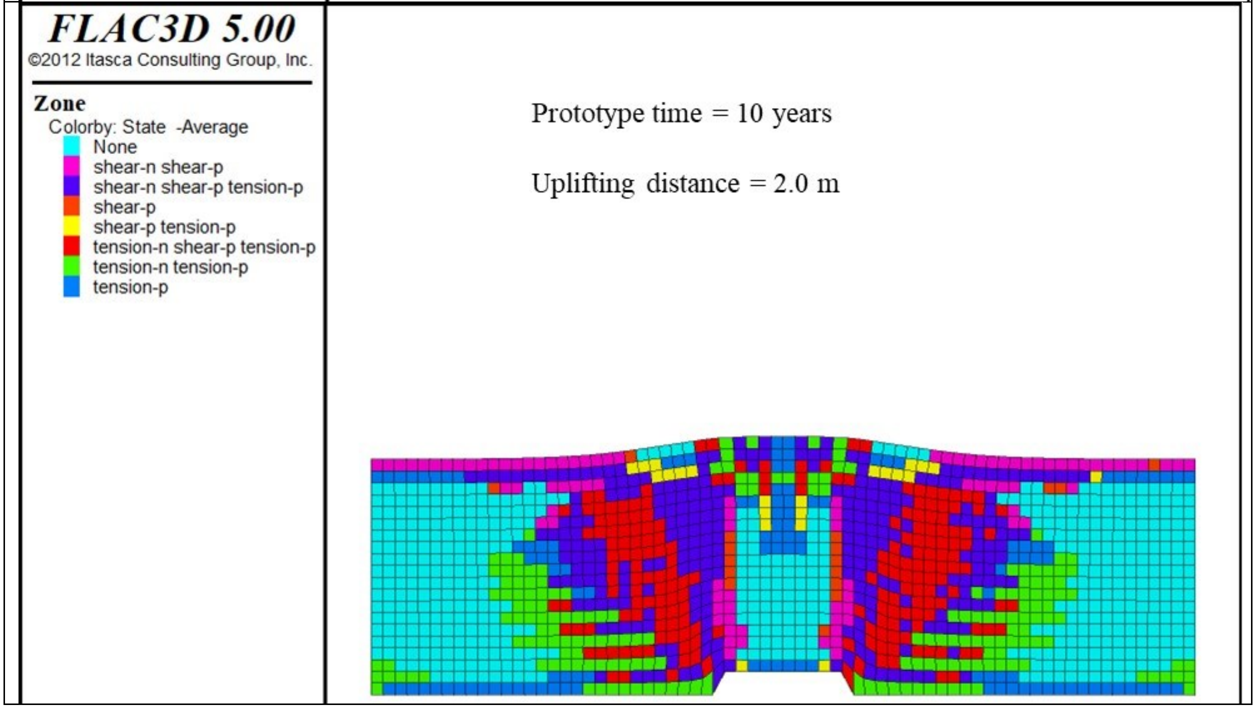

Prototype time = 10 years

Uplifting distance = 2.0 m

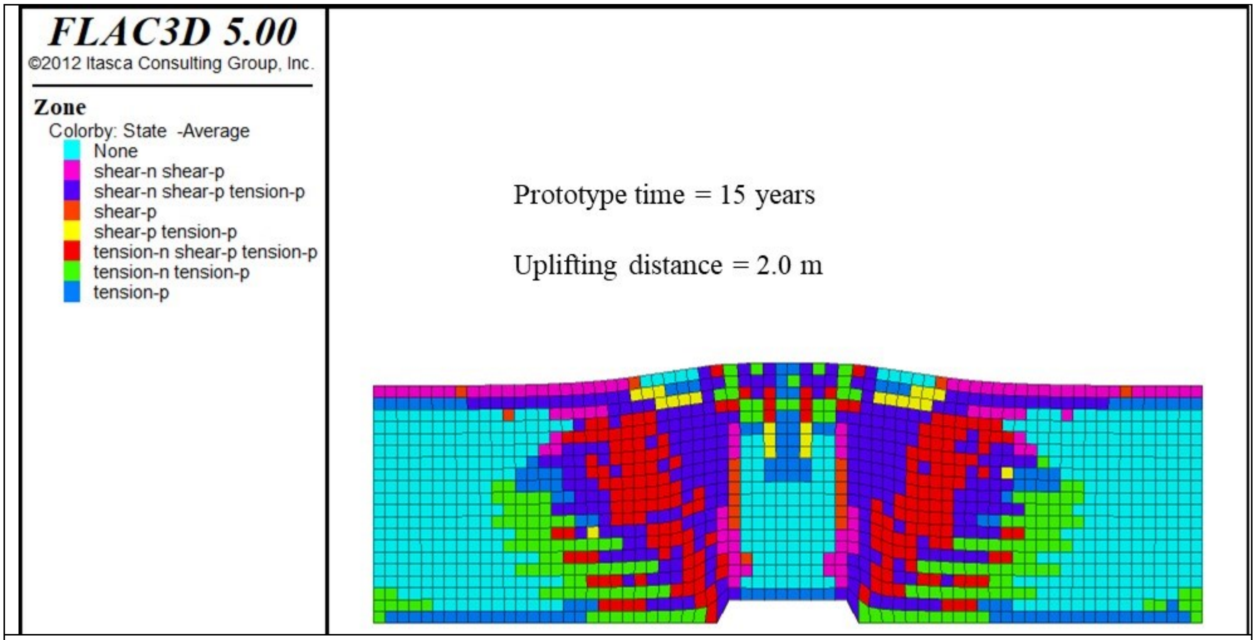

Figure E- 0-5 Zone state when the uplift displacement is 2 m

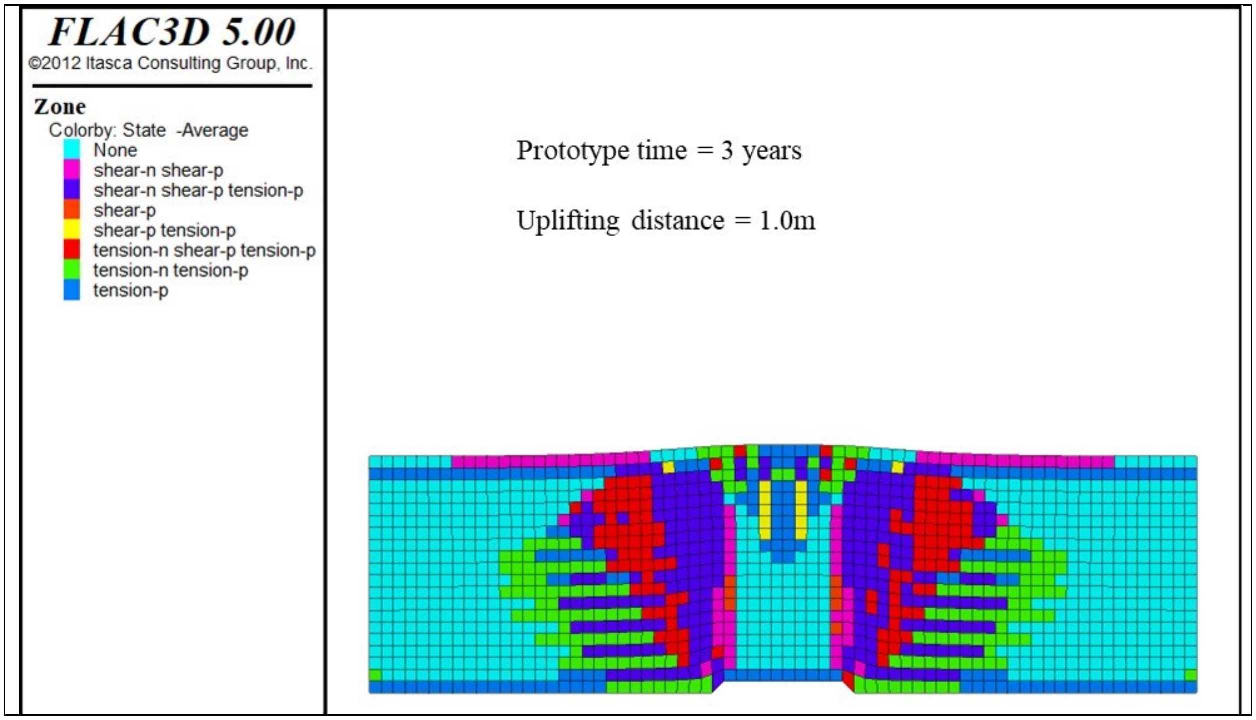

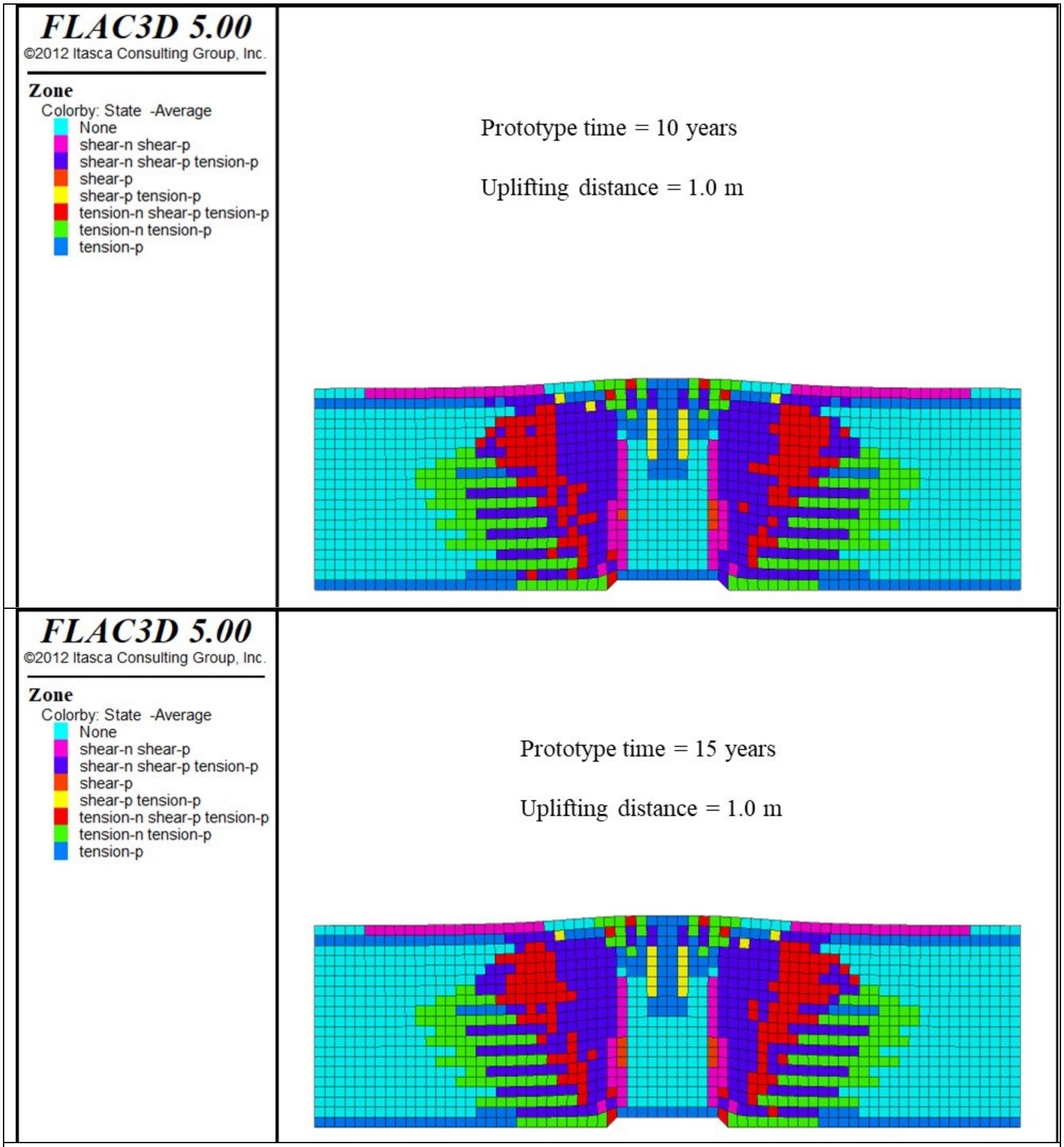

Figure E- 0-6 Zone state when the uplift displacement is 1 m

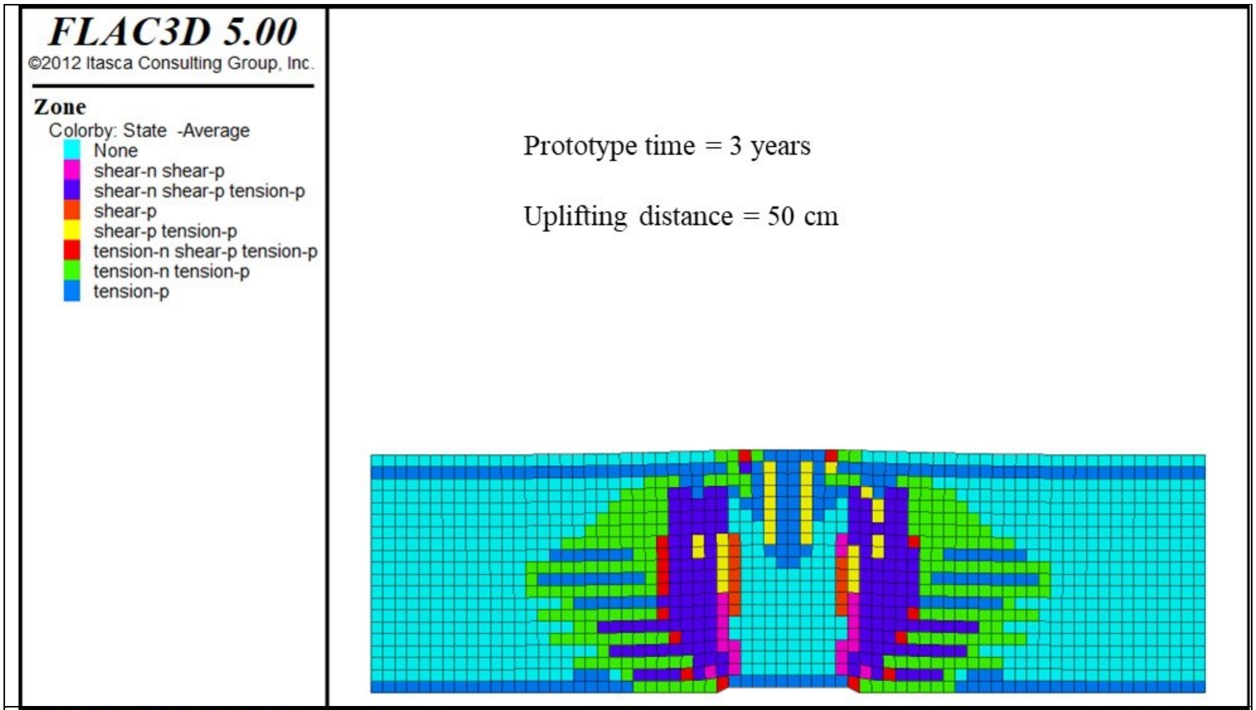

Prototype time = 3 years

Uplifting distance = 50 cm

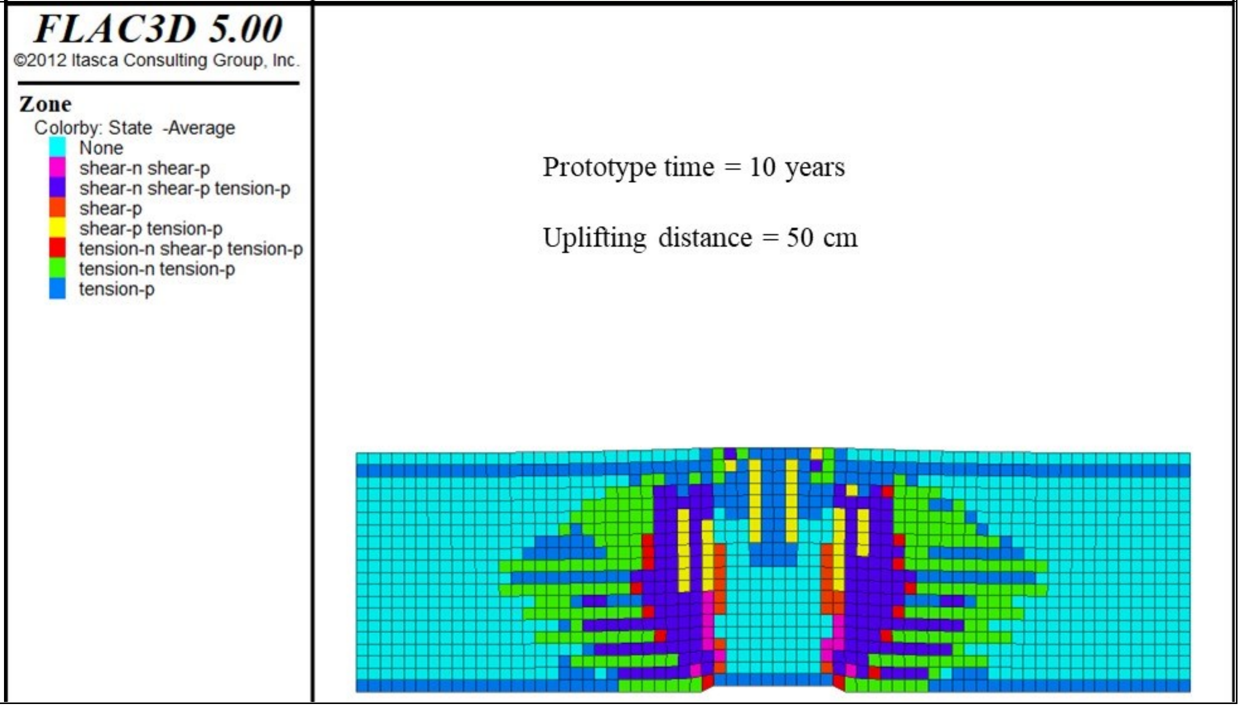

Prototype time = 10 years

Uplifting distance = 50 cm

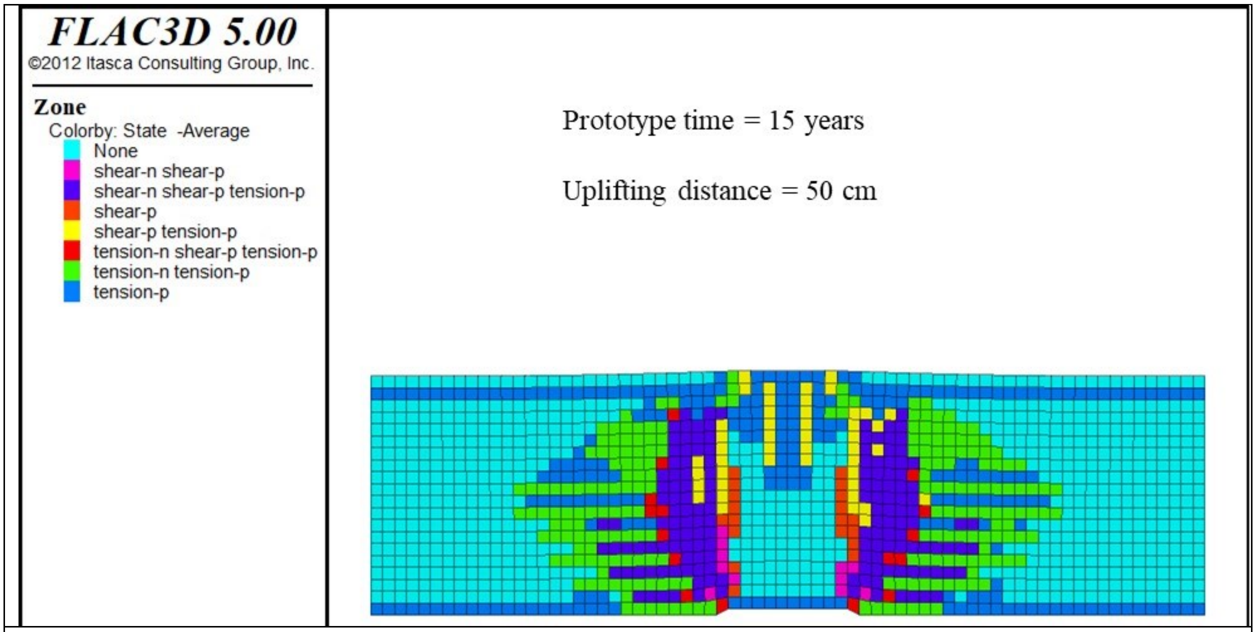

Figure E- 0-7 Zone state when the uplift displacement is 0.5 m

E.5 Summary

Although objective of this study is to identify caprock failure process through geotechnical centrifuge modelling test, numerical simulation is necessary to to provide an initial assessment of modelling applied to test results by using Mohr-Coulomb failure criteria. Moreover, as described previously, geotechnical centrifuge modelling alone cannot identify the types of forces resulting in the fractures in the model. Under this circumstances, numerical simulation is a useful tool to supplement the analysis of geotechnical centrifuge modelling results.

Results from the numerical simulation coincides well with the results of the geotechnical centrifuge modelling tests. The comparison shows that the tensile strength of the synthetic Clearwater shale for the numerical simulation test is too strong. This is mainly because the specimens for the Brazilian test are preserved in the refrigerator for over 30 days after being cured for 28 days at room temperature. Moreover, prior to the Brazilian test, the specimens are consolidated in the triaxial cell for over three weeks for the determination of permeability. Based on the experimental results of the geotechnical centrifuge modelling tests, the tensile strength for the numerical modelling tests is calibrated.

The numerical simulation test once again proves that the model can be divided into four regions based on the horizontal displacement contours, which coincides well with the experimental results of the third centrifuge modelling test.

During the centrifuge modelling test, there is a vertical fracture at the top surface of the model. The same situation exists when performing the numerical simulation test. The results show that it is the tensile stress that results in the fracture.

The uplifting table is the engine of the deformation. On any vertical plane perpendicular to the uplifting table, the vertical displacement decreases as the distance from the uplifting table increases. On the horizontal plane above the uplifting table, the vertical displacement decreases radially.

The failure plane emerges from the vertices of the uplifting table and expands to the ground surface. However, it is difficult to detect the forces that lead to the failure based on the geotechnical centrifuge modelling test. Based on the numerical simulation test, the fractures at the top of the model are induced by the tensile forces, and the inclined failure planes are the result of both the tensile force and the shear force.

Appendix F: Caprock Deformation Process − Prototype time = 15 yrs

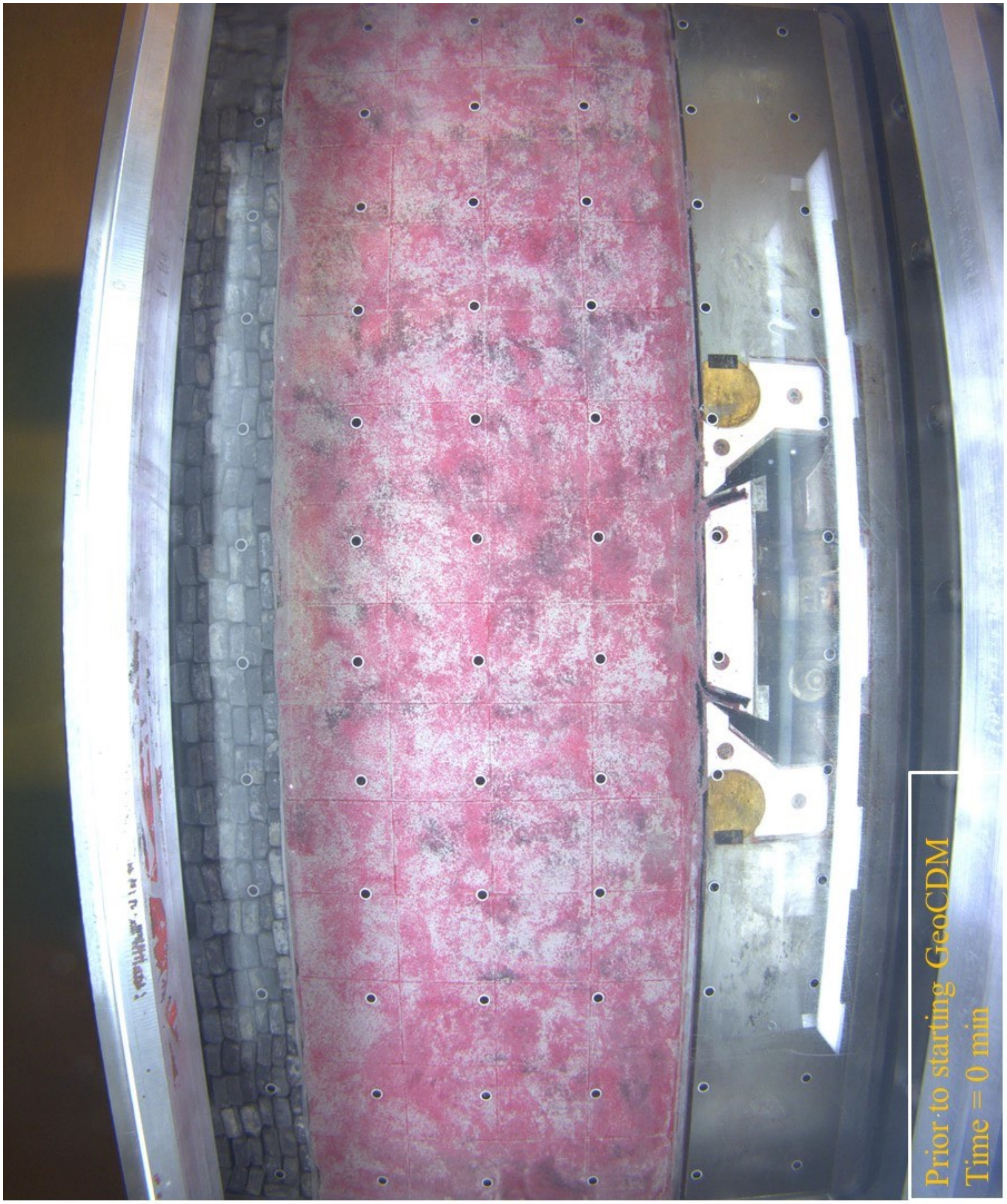

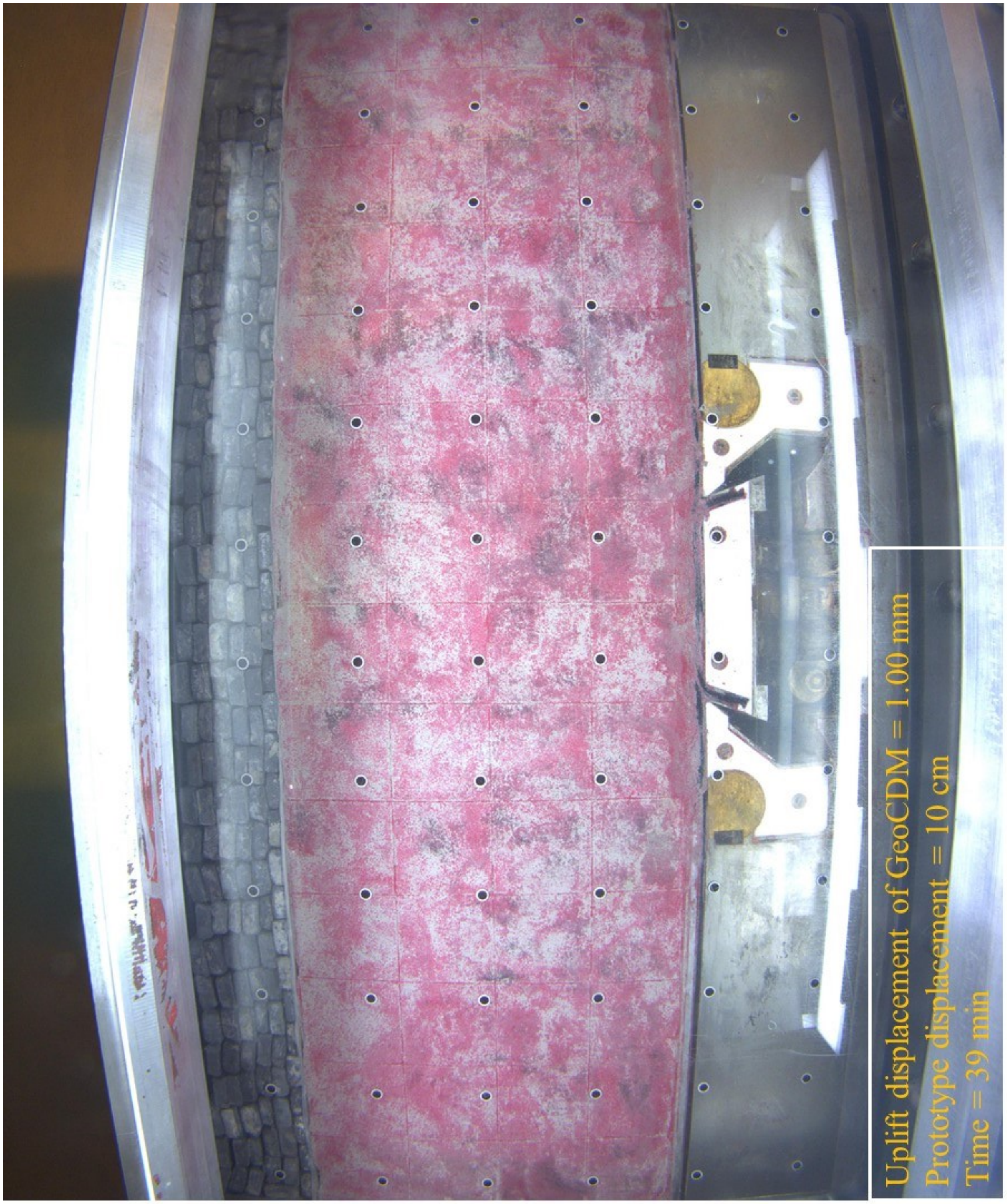
Uplift displacement of GeoCDM = 1.00 mm
Prototype displacement = 10 cm
Time = 39 min

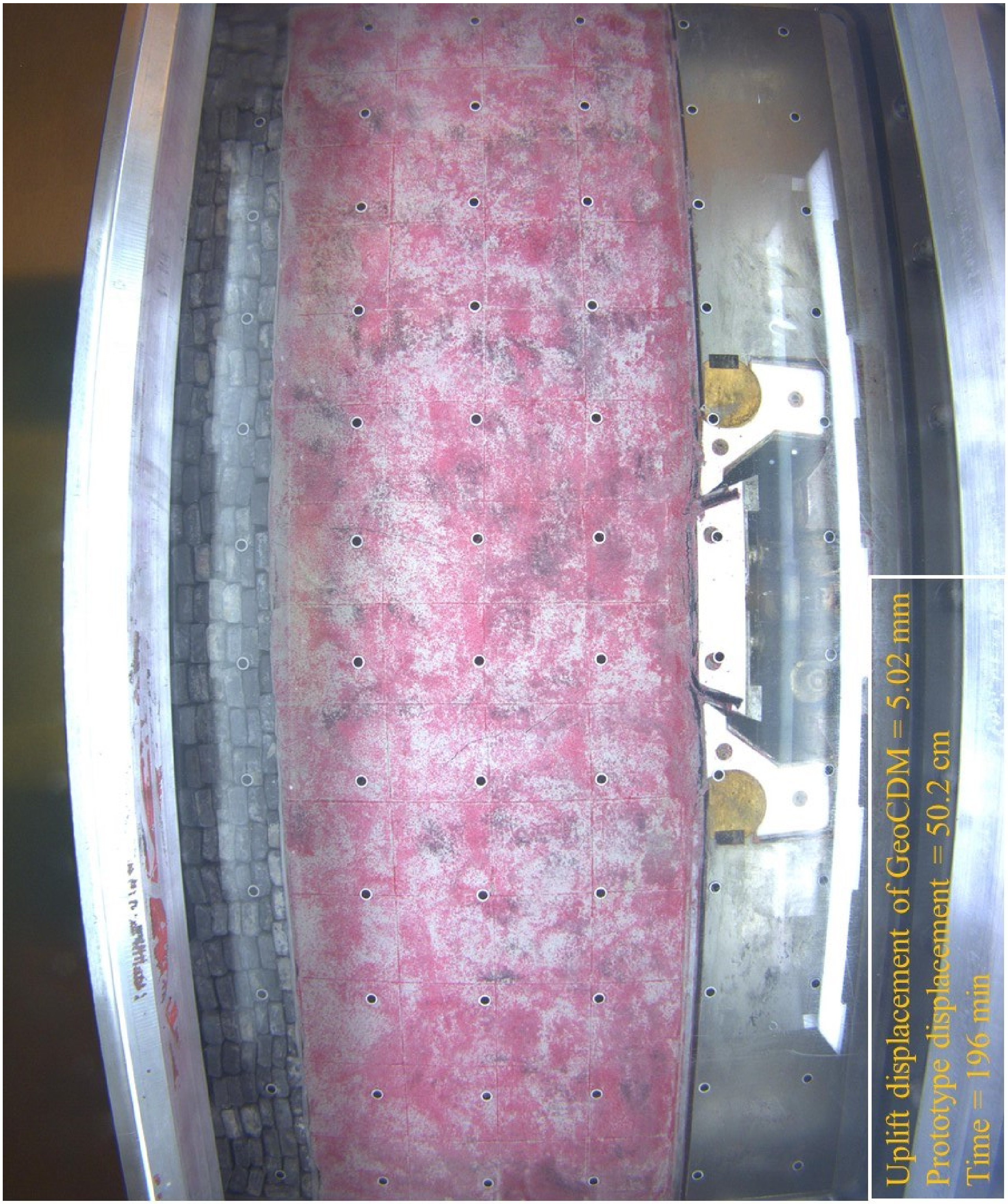
Uplift displacement of GeoCDM = 5.02 mm
Prototype displacement = 50.2 cm
Time = 196 min

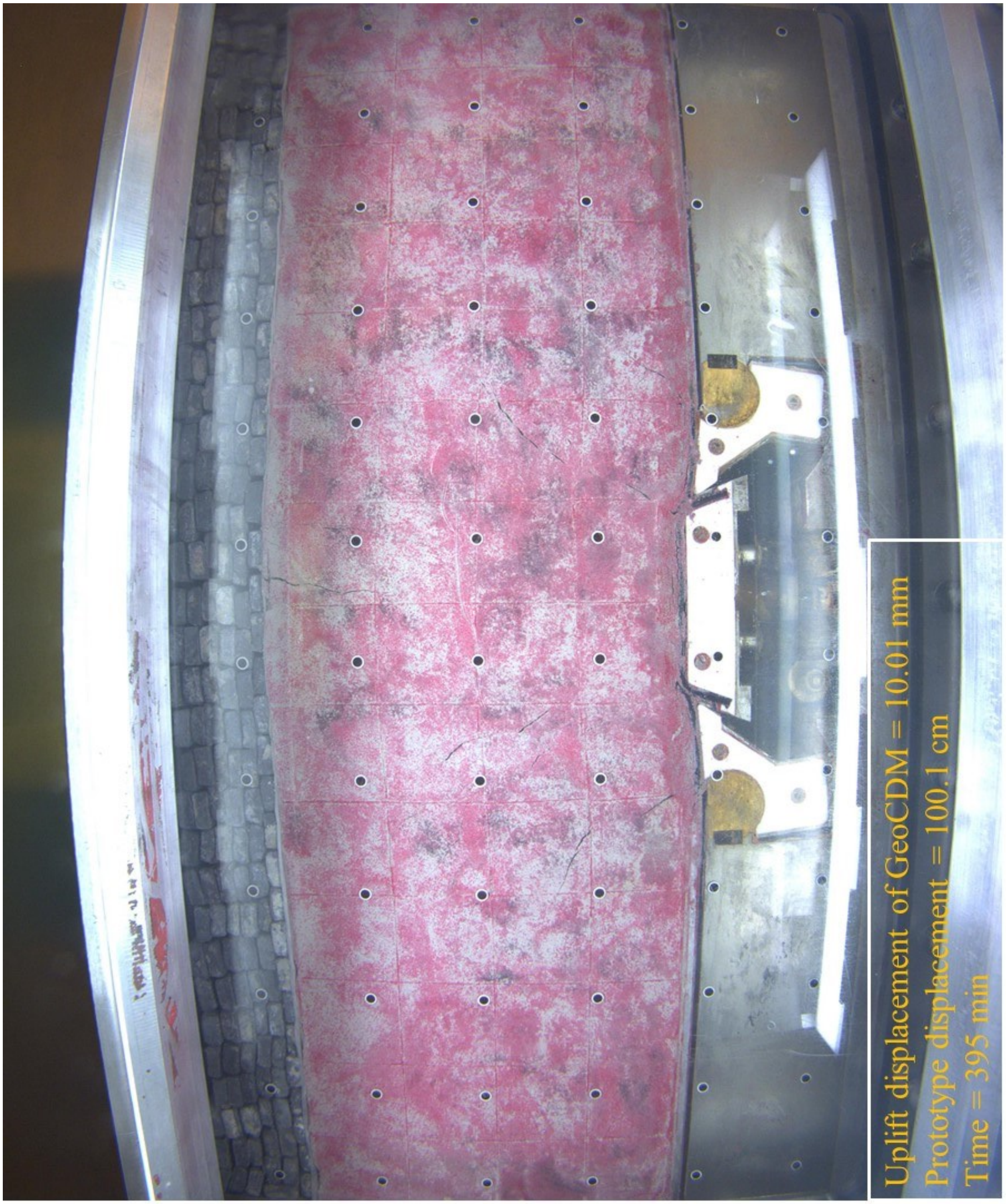
Uplift displacement of GeoCDM = 10.01 mm
Prototype displacement = 100.1 cm
Time = 395 min

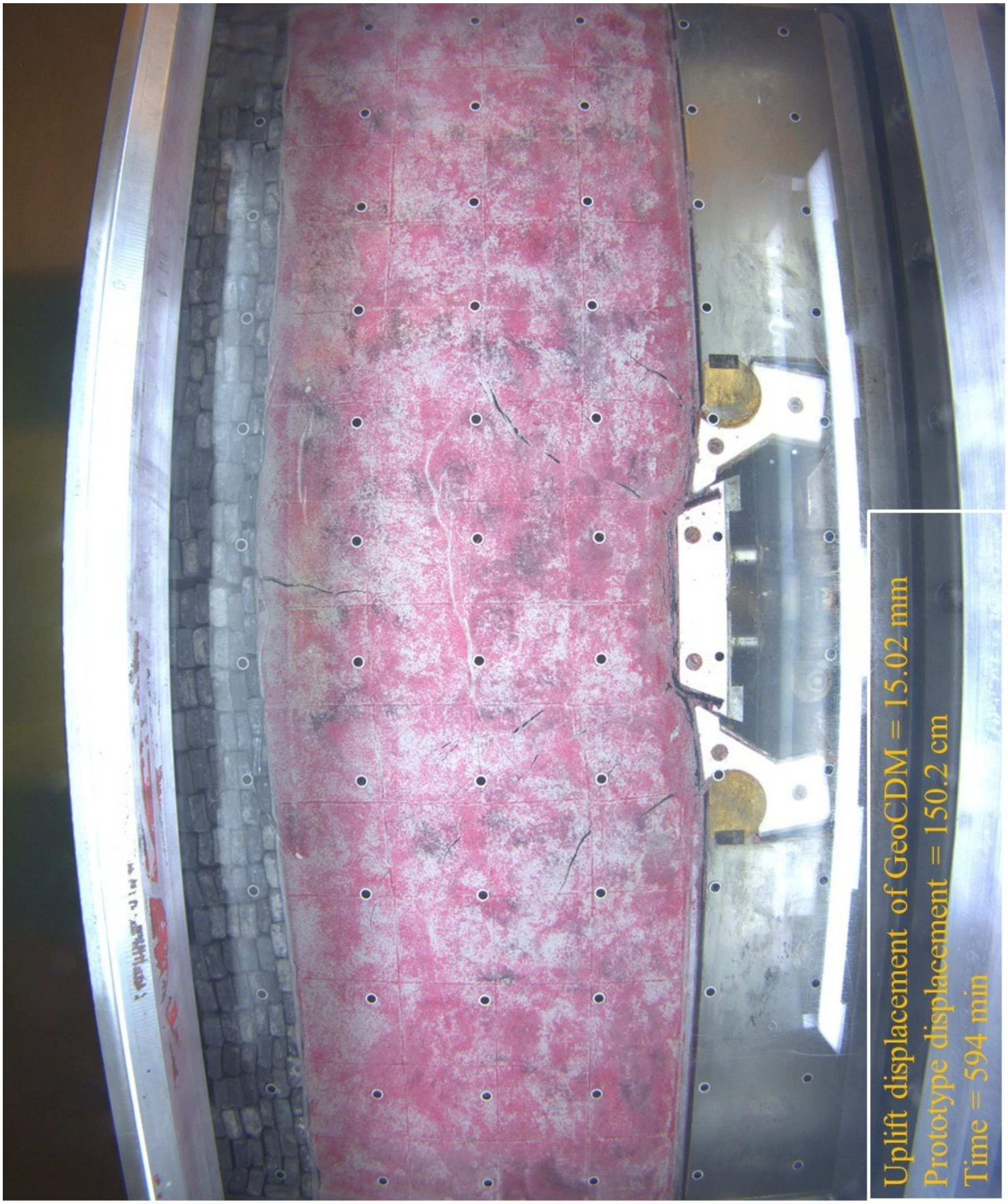
Uplift displacement of GeoCDM = 15.02 mm
Prototype displacement = 150.2 cm
Time = 594 min

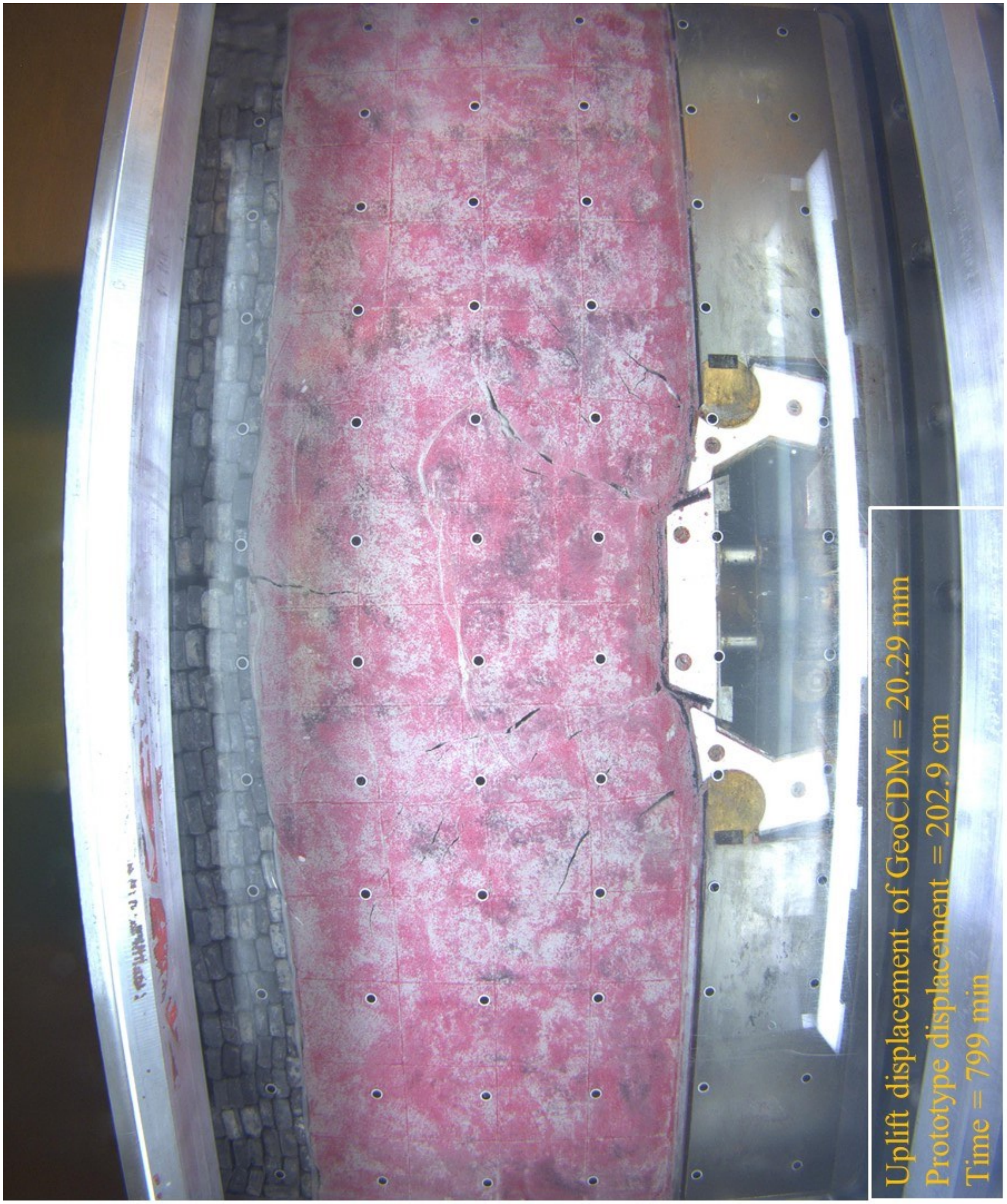
Uplift displacement of GeoCDM = 20.29 mm
Prototype displacement = 202.9 cm
Time = 799 min